Transactions of the ASME®

Transactions of the ASME, Journal of Fluids Engineering (ISSN 0098-2202) is published bimonthly (Jan., Mar., May, July, Sept., Nov.) by The American Society of Mechanical Engineers, Three Park Avenue, New York, NY 10016. Periodicals postage paid at New York, NY and additional mailing offices.
POSTMASTER: Send address changes to Transactions of the ASME, Journal of Fluids Engineering, c/o THE AMERICAN SOCIETY OF MECHANICAL ENGINEERS, 22 Law Drive, Box 2300, Fairfield, NJ 07007-2300.
CHANGES OF ADDRESS must be received at Society headquarters seven weeks before they are to be effective. Please send old label and new address.
STATEMENT from By-Laws. The Society shall not be responsible for statements or opinions advanced in papers or ... printed in its publications (B7.1, Par. 3).

INDEXED by Applied Mechanics Reviews and Engineering Information, Inc. Canadian Goods & Services Tax Registration #126148048.

Journal of Fluids Engineering

Published Bimonthly by The American Society of Mechanical Engineers

VOLUME 125 • NUMBER 1 • JANUARY 2003

(Contents continued on inside back cover)

This journal is printed on acid-free paper, which exceeds the ANSI Z39.48-1992 specification for permanence of paper and library materials. ♾™
♻ 85% recycled content, including 10% post-consumer fibers.

Journal of Fluids Engineering Volume 125, Number 1 JANUARY 2003

TECHNICAL BRIEFS

ANNOUNCEMENTS AND SPECIAL NOTICES

The ASME Journal of Fluids Engineering is abstracted and indexed in the following:

Applied Science & Technology Index, AMR Journal Article Abstracts Database, Chemical Abstracts, Chemical Engineering and Biotechnology Abstracts (Electronic equivalent of Process and Chemical Engineering), Civil Engineering Abstracts, Computer & Information Systems Abstracts, Corrosion Abstracts, Current Contents, Ei EncompassLit, Electronics & Communications Abstracts, Engineered Materials Abstracts, Engineering Index, Environmental Engineering Abstracts, Environmental Science and Pollution Management, Excerpta Medica, Fluidex, Index to Scientific Reviews, INSPEC, International Building Services Abstracts, Mechanical & Transportation Engineering Abstracts, Mechanical Engineering Abstracts, METADEX (The electronic equivalent of Metals Abstracts and Alloys Index), Petroleum Abstracts, Process and Chemical Engineering, Referativnyi Zhurnal, Science Citation Index, SciSearch (The electronic equivalent of Science Citation Index), Shock and Vibration Digest, Solid State and Superconductivity Abstracts, Theoretical Chemical Engineering

Journal of Fluids Engineering

Editorial

The end of 2002 brings about several changes to the *Journal of Fluids Engineering*. First, several Associate Editors have completed their terms and new ones have joined us. I would like to express my gratitude to the departing Associate Editors, whose valuable and thankless service is critical for the success of the Journal. Bruno Schiavello has served for two consecutive terms, and Dr. James Bridges, Prof. George Karniadakis, Prof. Yoichiro Matsumoto, and Lisa Mondy have each completed a three-year term. Prof. Yoshinobu Tsujimoto also competed a three-year term, but graciously accepted my request to stay on the Editorial board for another term. He will continue providing his unique expertise, which combines applications and theoretical modeling of complex (single phase and cavitating) turbomachinery flows.

Four new Associate Editors have joined us, and I would like to introduce and welcome them. Dr. Fernando Grinstein from the Naval Research Laboratory is an expert in computational fluid mechanics, and has done substantial research in computations of turbulent shear flows. Dr. Grinstein was also a primary driving force behind the special issue on applications of Large Eddy Simulations (LES). Prof. Sivaramakrishnan Balachandar from the University of Illinois at Urbana-Champaign is an accomplished expert in applications of Direct Numerical Simulations to modeling of heat transfer, structure and stability of wakes and boundary layers, and flows around bluff bodies. He will join the multiphase flow group and will provide essential support for the growing number of papers involving computational aspects in this area. Prof. Kyle Squires from Arizona State University has substantial experience in applications, Large Eddy Simulations, and evaluation of associated subgrid stress models. He has also been involved in the modeling of solid-particle flows, and in applications of CFD in separated flows. His wide range of experience will support both the extensive activity involving turbulence modeling and the multiphase group. We are also happy to have Prof. Dennis Siginer, the Dean of Engineering at Wichita State University, on board. He has made substantial contributions to the areas of rheology of nonlinear materials, flow and heat transfer in non-Newtonian flows and flows in porous media. I am happy that this distinguished group has agreed to join us, and am looking forward to working with them, taking advantage of their expertise and willingness to contribute.

Second, during 2002 *JFE* had parts of three issues dedicated to specific topics. Initiated and organized by Prof. Karniadakis, the March issue contained eight solicited papers dedicated to uncertainty in numerical analysis. In the June issue, we presented a series of eleven papers dealing with pump flows. These papers were selected and recommended by Dr. Adiel Guinsberg and Dr. Paul Cooper from papers presented at a symposium on pump flows that they had organized. They also assisted us in the expedited review process. The December issue contained a collection of papers on applications of Large Eddy Simulations. These papers were selected by Dr. Grinstein and Prof. Karniadakis, who also oversaw the review process. It is evident that such special issues greatly enhance the quality of the Journal, and improve the service that we provide to the community. We would like to thank our colleagues who initiated and contributed to these efforts, and hope to continue to offer these special sections on other topics.

Third, starting from January 2003, *JFE* is being transitioned from a quarterly (four issues per year) to a bimonthly, i.e., to six volumes per year. The number of pages allocated to the Journal has also been increased by about 15%, enabling us to increase the number of published papers and accommodate the increased number of submitted manuscripts.

Fourth, a primary concern is to support the authors with reliable, efficient and expedited service. In order to reduce the review time and provide closer monitoring of the review process, ASME has developed an on-line manuscript submission and review system. This new system has been in development and testing for several months, and has been made available for trial to several journals, including *JFE*. Authors are welcomed to submit papers at *http://journaltool.asme.org* effective immediately. We hope that the new journal tools will improve the service that we provide to the authors, and that adapting to it will cause few problems. For the time being, authors are also welcomed to submit their papers as before, either by e-mail or as hard copies. Once we get accustomed to this system, we believe that the review process will be significantly improved and expedited.

Last but not least, I would like to express my gratitude to Mrs. Laurel Murphy, the Editorial Assistant of *JFE*. As all of you who have communicated with our office over the past few years already know, Laurel is the primary driving force that actually makes the Journal function. In addition to managing the office, she supports several of the Associate Editors with communications/administration, helps me in finding referees for papers with uncommon topics, reviews and helps many authors to improve the style of papers, and nags me (as well as other people involved with the Journal) when certain tasks need to be performed. We are lucky to have her.

Joseph Katz
Technical Editor

Prediction of Turbulent Flow Over Rough Surfaces Using a Force Field in Large Eddy Simulation

Jie Cui

Virendra C. Patel

Ching-Long Lin

IIHR-Hydroscience and Engineering
and Department of Mechanical Engineering,
The University of Iowa,
Iowa City, IA 52242-1585

A force field model to simulate turbulent flow over a surface with arbitrary roughness is described. A given roughness is decomposed into resolved and subgrid-scale roughness, conceptually similar to the flow decomposition in large eddy simulation (LES). For a given flow and Reynolds number, a Cartesian grid is selected to satisfy LES requirements. This grid determines the geometric features of the roughness that are formally resolved. The force field used to represent this resolved roughness is determined during the LES solution process, without any empirical input. The subgrid roughness that is not resolved is modeled by a random force distribution in which a drag coefficient is specified. Use of this approach to model surface roughness is demonstrated by calculations of the flow in a duct with a wavy wall with superimposed fine-grain roughness.
[DOI: 10.1115/1.1524587]

1 Introduction

Turbulent flow over rough surfaces is hardly a new research topic. Nikuradse [1] experimented on sandgrain roughness in 1933. Subsequently, numerous experimental studies have been conducted to understand flow phenomena associated with different types of surface roughness and parameterize their effect on resistance, velocity distribution, and transport of heat and mass. Computational fluid dynamics (CFD) has not significantly advanced the understanding of this problem because it has relied mostly on concepts of equivalent sandgrain roughness and empirically determined roughness functions. In Reynolds-averaged Navier-Stokes (RANS) simulations, it is common to avoid resolution of the flow in the roughness layer and wall region adjacent to the roughness by employing the method of wall functions. An alternative, again in the framework of RANS simulations, is the so-called discrete element approach, in which roughness due to a regular array of discrete two or three-dimensional elements, such as ribs, cones, and hemispheres, is considered by adding a form drag term in the momentum equation, and under certain circumstances, accounting for the blockage effect of the roughness elements in the continuity equation, [2–7]. Patel [8] has made a review of such approaches.

Recently, roughness modeling has been extended to large-eddy simulation (LES) and direct numerical simulation (DNS). For example, Lin et al. [9] used LES to investigate surface roughness effects on flow structures in a neutrally stratified planetary boundary layer. The surface roughness treatment was similar to the wall-function approach in RANS models. Although not specifically concerned with roughness, Patton et al. [10] reported LES of turbulent flow around multiple porous windbreaks within a wheat canopy under neutral stability conditions. An empirical term representing drag of the windbreak was added to the momentum equation as in previous RANS simulations.

In the DNS of turbulent channel flow by Miyake et al. [11], a rough wall was modeled by a distribution of zero-volume ''virtual'' cones. A drag force d_i per unit length of the form

$$d_i = C_d \frac{1}{2} \rho u^2 \frac{u_i}{|u|} \frac{A}{V} \tag{1}$$

was added at the grid points inside these ''virtual'' cones, C_d being the drag coefficient, A the frontal area, and V the volume of the cone. The cone height was generated randomly with a mean value between 15 and 30 wall units, and a value of 0.5 was prescribed for C_d. The well-known effect of surface roughness in the logarithmic velocity distribution was reproduced, and the authors claimed that the effect of roughness on the eddy structure was also simulated. However, the results depend on the chosen value of C_d.

2 Present Work

The present work is inspired by some recent LES and DNS computations using ''body-force'' or ''immersed-boundary'' methods to represent very complex geometries. An example of this is the recent LES of Verzicco et al. [12] who simulated the flow in a piston-cylinder-valve assembly. The simulations were carried out in a Cartesian grid with the geometry represented by a body-force field to enforce the known (zero or prescribed) velocity within solid regions not occupied by the fluid. Although these and similar solutions were not concerned with surface roughness per se, their approaches can be extended to develop a general and powerful model of turbulent flow over rough walls. This is the purpose of the present paper.

The boundary body-force model of Verzicco et al. [12] is attractive for several reasons. First, an orthogonal Cartesian grid is used to represent complex geometry, avoiding a body-fitted (and/or deforming) grid. Second, the computation scheme remains simple and efficient, and does not introduce additional stability limits. Third, there are no parameters in the model that need to be determined beforehand by reference to experimental data because the body force magnitude is obtained internally during the numerical solution. This makes the model much more general than those involving empirical inputs. Finally, in this model, steady and moving boundaries can be treated in the same way, which is convenient for time-dependent problems.

The numerical method and decomposition of roughness into resolved and subgrid components are described in Section 3. Turbulent flow in a channel with a wavy wall is used as an example. This flow is first simulated using the traditional approach of a body-fitted grid and the results are used in Section 4 to validate the numerical method and to establish a reference to evaluate the roughness decomposition and representation by body-force distribution presented in Section 5. Section 6 describes the treatment of resolved-scale roughness, while Section 7 describes modeling of subgrid roughness. Section 8 summarizes the major results and conclusions.

Contributed by the Fluids Engineering Division for publication in the JOURNAL OF FLUIDS ENGINEERING. Manuscript received by the Fluids Engineering Division Dec. 28, 2001; revised manuscript received Aug. 6, 2002. Associate Editor: T. B. Gatski.

3 Numerical Method and Roughness Decomposition

The three-dimensional, unsteady, incompressible, filtered continuity and Navier-Stokes equations, (2) and (3), respectively, are solved with a dynamic subgrid-scale model (DSM):

$$\frac{\partial \overline{u_i}}{\partial x_i} = 0 \tag{2}$$

$$\frac{\partial \overline{u_i}}{\partial t} + \frac{\partial}{\partial x_j}(\overline{u_i u_j}) = -\frac{1}{\rho}\frac{\partial \overline{p}}{\partial x_i} + \nu\left(\frac{\partial^2 \overline{u_i}}{\partial x_j \partial x_j}\right) - \frac{\partial \tau_{ij}}{\partial x_j} + f_i . \tag{3}$$

Here $i=1$, 2, and 3, $\overline{u_i}$ are the resolved velocity components, $\overline{p}$ is pressure, ν is kinematic viscosity, f_i is the body force, and

$$\tau_{ij} = \overline{u_i u_j} - \overline{u_i}\,\overline{u_j} \tag{4}$$

is the subgrid-scale stress representing the effect of small-scale motions.

In DSM, the model coefficients are computed dynamically as the calculation progresses rather than being prescribed a priori. Two filters are introduced: the grid filter and the test filter. A test filter twice as large as the grid filter is usually chosen and is used in this paper. By applying the test filter to the equations, the subgrid-scale stresses on the test level, or subtest-scale stresses can be constructed. Then subgrid-scale stresses are parameterized by an eddy viscosity model:

$$\tau_{ij} - \frac{\delta_{ij}}{3}\tau_{kk} = -2C\overline{\Delta}^2 |\overline{S}|\overline{S}_{ij} \tag{5}$$

where

$$|\overline{S}| = (2\overline{S}_{ij}\overline{S}_{ij})^{1/2}, \quad \overline{S}_{ij} = \frac{1}{2}\left(\frac{\partial \overline{u_i}}{\partial x_j} + \frac{\partial \overline{u_j}}{\partial x_i}\right),$$

δ_{ij} is the Kronecker delta, $\overline{\Delta} = (\Delta x_1 \Delta x_2 \Delta x_3)^{1/3}$, Δx_i are the mesh distances, and C is a model constant. To obtain a single coefficient from these independent equations, C is assumed to remain unchanged between these two filters, [13–15]. Then the model constant C can be determined from

$$C = \frac{1}{2}\frac{L_{ij}M_{ij}}{M_{ij}M_{ij}} \tag{6}$$

where

$$L_{ij} = \overline{\overline{u_i u_j}} - \overline{\overline{u_i}}\,\overline{\overline{u_j}} \quad \text{and} \quad M_{ij} = \overline{\Delta}^2 |\overline{\overline{S}}|\overline{\overline{S}}_{ij} - \bar{\Delta}^2 |\bar{\overline{S}}|\bar{\overline{S}}_{ij}$$

(double overbar represents test-scale resolved quantities) can be directly computed from the resolved motion.

The finite volume LES numerical code used here was developed by Zang et al. [16]. In this method, the governing equations in general curvilinear coordinates are discretized on a nonstaggered grid. A fractional-step method is employed and the pressure Poisson equation is solved with multigrid acceleration. Time marching is semi-implicit with formal accuracy of second order in both space and time. Zang et al. [16] verified and validated the code in various flows, including decaying vortices, lid-driven flow in two-dimensional, three-dimensional and polar cavities, flow over a backward-facing step, and flow in a curved square duct.

Analogous to the basic idea of LES and the dynamic subgrid-scale model, a general approach to treat surface roughness, able to handle arbitrary roughness, is proposed. An arbitrary roughness, shown schematically in Fig. 1(a), is decomposed into two parts, a ''resolved-scale'' roughness and a ''subgrid-scale'' roughness. Since the large-scale roughness determines the most energetic flow features that vary significantly from problem to problem, it is difficult to construct a model that will work universally for all possible roughness geometry. Here we adopt the approach of Verzicco et al. [12] for the resolved-scale roughness. The length scale of the subgrid-scale roughness, as the name suggests, is much smaller than that of the resolved roughness. The subgrid-scale roughness makes a small contribution to momentum, mass and energy transport, and is expected to have common features in various problems. This portion of the roughness is modeled following the work of Miyake et al. [11].

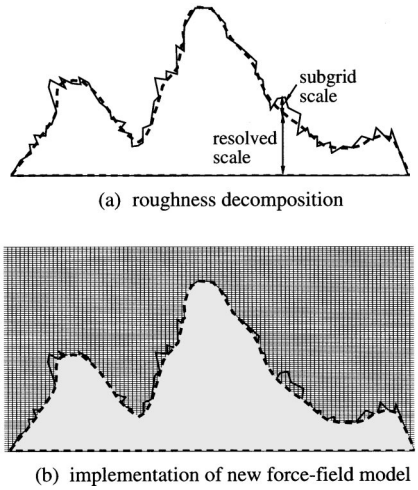

(a) roughness decomposition

(b) implementation of new force-field model

Fig. 1 Decomposition of arbitrary roughness and application of body-force model

A Cartesian grid is used for the given roughness geometry (Fig. 1(*b*)). Although the figure shows a two-dimensional geometry, the basic method is applicable to any geometry. The required grid will depend on the roughness configuration as well as the Reynolds number, as is the case in all LES applications. The grid should be fine enough to resolve the basic large-scale features of the flow as well as the roughness. The subgrid-scale roughness not resolved by the chosen LES grid is modeled as a random roughness, similar to the ''virtual'' cones in Miyake et al. [11]. The average length scale needs to be prescribed. This is a purely geometric parameter and can be obtained from the roughness geometry after the resolved-scale roughness is subtracted.

4 Flow in a Wavy-Wall Channel: Test Problem

Consider turbulent flow in a channel with plane wall on the top and a sinusoidal wavy wall on the bottom (Fig. 2). The wave profile is given by

$$h = a\sin\left(\frac{2\pi}{\lambda}x - \frac{\pi}{2}\right) \tag{7}$$

where h is the vertical height with a zero mean value, a is the wave amplitude, x is the streamwise coordinate, and λ is the wave length (Fig. 3). There is no variation in the spanwise direction,

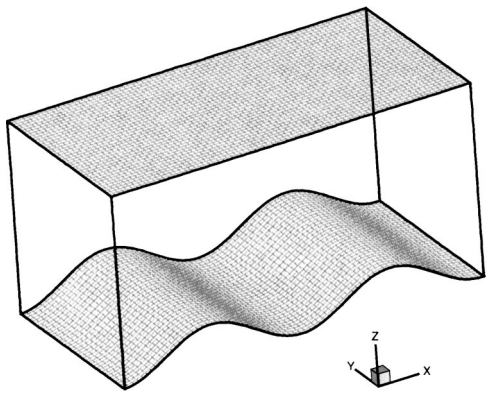

Fig. 2 Geometry of channel flow with wavy wall

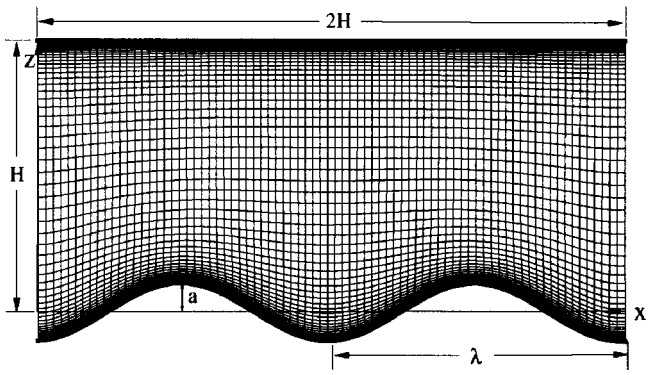

Fig. 3 Body-fitted computational grid in the wavy channel

i.e., the wavy wall is two-dimensional. In the test problem, the wavelength λ is equal to the mean channel height H, the wave steepness, $2a/\lambda$, is 0.20, and the Reynolds number (Re), based on the bulk velocity (U_b) and half-channel height ($H/2$), is 10,000.

As noted earlier, this flow problem is first solved as in conventional LES, using a body-fitted grid. The computational domain contains two waves in the streamwise direction. The spanwise and vertical dimensions are H. A grid with $82\times42\times66$ points in the streamwise (x), spanwise (y), and normal (z) directions is shown in Fig. 3. The grid points are more closely spaced near the two walls, but the grid spacing in the longitudinal and spanwise direction is uniform.

A mean streamwise pressure gradient is imposed to drive the flow, and is carefully adjusted to obtain Re=10,000. Periodic boundary conditions are imposed in the streamwise and spanwise directions, and no-slip boundary conditions are applied at the top and bottom walls. The friction Reynolds number for the upper wall Re_τ is around 570. In terms of wall units, the mesh spacing is $\Delta x^+\approx27$, $\Delta y^+\approx27$, and at least 1 for Δz^+.

As part of a validation study of the numerical method, time and spanwise-averaged mean streamwise velocity profiles at six representative locations within one wave are compared with the experimental data of Buckles et al. [17] in Fig. 4. At the wave crest, $x/\lambda=0.0$ (Fig. 4(a)), the flow is attached, and experiences strong favorable pressure gradient (acceleration) following reattachment on the previous wave. The flow accelerates rapidly in a short distance. The numerical prediction is in good agreement with the measurements except in a region close to the measured velocity maximum which occurs farther from the top wall than predicted by the LES simulation. This difference between the experiment and simulation is seen in the profiles at all streamwise locations. It may be due to the three-dimensional effects in the experiment in which the channel aspect ratio (width-to-height) was about 12:1. In the LES calculations by Henn and Sykes [18], the same trend was also observed. Henn and Sykes argued that the discrepancies could be due to the measurements, since up to 3% discrepancy in the integrated mass flux was reported from the data of Buckles et al. [17]. At $x/\lambda=0.1$, the LES profile shows a small negative velocity indicating separation, though the experiment gives only positive velocities. Thus, an earlier separation is predicted by the numerical method. Farther downstream, at $x/\lambda=0.3$, the pressure gradient is adverse and the flow separates. The reversed flow is well predicted, demonstrating success of LES in simulation of separated flow. At $x/\lambda=0.5$, the wave trough, flow is still separated. The reversed flow velocity is over estimated. Further downstream, the flow encounters a favorable pressure gradient, the near-wall flow accelerates and wall shear stress begins to increase. At $x/\lambda=0.7$, the uphill, the flow reattaches. The LES profile shows a slightly negative velocity at this location while the mea-

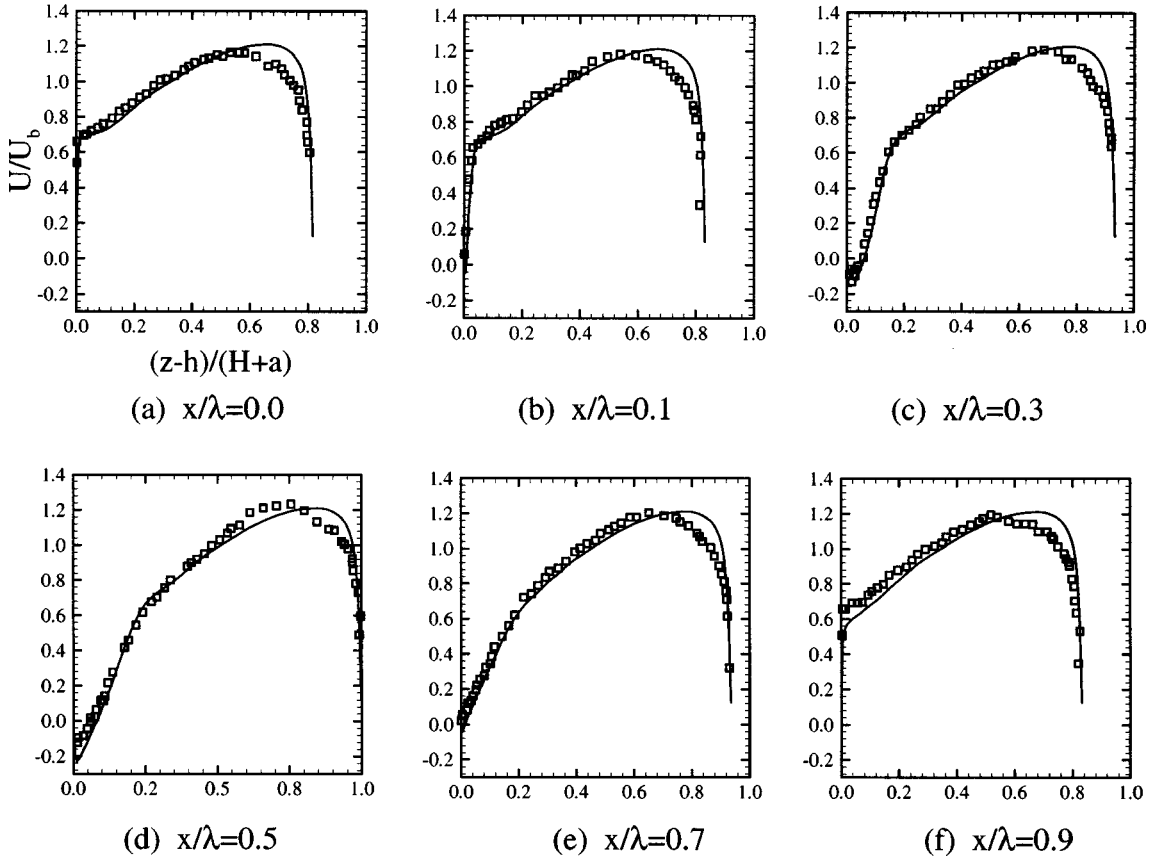

Fig. 4 Comparisons of mean streamwise velocity profiles with experimental data at selected locations

Table 1 Resistance in channel flow with wavy roughness

LES Solution	Resistance Components			Imposed Force
	Lower Boundary		Upper Boundary	
Direct solution	Pressure	Friction		
with surface-fitted grid	0.0415	0.00076	0.0067	
	Total:		0.0489	0.049
	Lower Boundary		Upper Boundary	
Resolved-scale roughness	Pressure	Friction		
and body-force	0.0416	0.00064	0.007	
	Total:		0.0492	0.049
	Lower Boundary		Upper Boundary	
Sub-grid-scale roughness and	Pressure	Friction		
random body-force model	0.0403	-0.00022	0.0071	
	Total:		0.0472	0.049

Note: Forces are per unit width of channel and are normalized by $\rho U_b^2 H$

surements do not, indicating a more downstream reattachment point. Finally, results in the last section, $x/\lambda = 0.9$, in a region of strong favorable pressure gradient, are very similar to those at the wave crest.

To check whether the size of the simulation domain and spanwise grid spacing contribute to the discrepancies with the experimental data, another run was performed on a larger domain and finer grid. The domain was extended to $3H$ in the streamwise direction and the number of spanwise grid points was doubled. The resulting domain was $3H \times H \times H$ and the grid was $122 \times 82 \times 66$. The difference between the results from the two meshes is quite small (both results show nearly identical mean velocity distribution, and that about 7% of the turbulence kinetic energy is carried by the subgrid-scale model). Therefore, it is believed that the majority of the error is due to numerical issues.

Considering the wave train as a surface roughness, albeit of regular shape, the simulation results may be used to calculate the pressure and friction components of resistance to the flow in the channel by integration along one wave. The first set of entries labeled direct solution in Table 1 summarizes the calculated resistance components. The last column in the table shows the pressure force that was imposed. It is found that the friction resistance from the lower wall is negligible due to the large separation zone in the valley behind the crest. The wavy wall generates a large pressure resistance. The contribution from the top wall only contains frictional resistance and is much smaller in comparison with the pressure resistance from the lower wall. The pressure force imposed to drive the mean flow balances the total resistance from lower and upper surfaces, further validating the numerical method and indicating sufficient sampling times to obtain the time-averaged quantities from the LES data. Detailed comparisons with experimental data with respect to other turbulent flow quantities and validation of the numerical method can be found in Cui et al. [19].

5 Modeling Resolved-Scale Roughness With Body Force

The time discretization of Eq. (3) is written as

$$\overline{u_i}^{n+1} - \overline{u_i}^{n} = \Delta t \left(- \frac{\partial \overline{u_i u_j}}{\partial x_j} - \frac{1}{\rho} \frac{\partial \overline{p}}{\partial x_i} + \nu \frac{\partial^2 \overline{u_i}}{\partial x_j \partial x_j} - \frac{\partial \tau_{ij}}{\partial x_j} + f_i \right). \tag{8}$$

To impose $\overline{u_i}^{n+1} = 0$ on points inside the roughness, the body force f_i must be

$$f_i = - \frac{\overline{u_i}^{n}}{\Delta t} + \frac{\partial \overline{u_i u_j}}{\partial x_j} + \frac{1}{\rho} \frac{\partial \overline{p}}{\partial x_i} - \nu \frac{\partial^2 \overline{u_i}}{\partial x_j \partial x_j} + \frac{\partial \tau_{ij}}{\partial x_j}. \tag{9}$$

This body force is determined internally as the solution progresses, and requires no empirical input. The body-force model may be applied to arbitrary roughness, provided a fine enough Cartesian grid resolves the roughness elements. The channel flow with wavy roughness described in the previous section is recalculated using this model, and two sets of results are compared to assess the viability of this simplified approach to modeling roughness.

Figure 5 shows the Cartesian grid for the same computational domain as before with the same number of grid points in the three directions. In the region occupied by the waves, namely, $-0.1 < z/H < 0.1$, this grid is not as fine as that used for the direct calculations of the previous section. In fact, the chosen grid defines the level of resolution of the actual surface and the scale of the subgrid roughness to be modeled.

The mean velocity vectors obtained with the new LES are shown in Fig. 6. The velocities within the waves are now blocked out by the body force. The velocity overshoot at the wave crest and the separation zone in the valley are reproduced. The flow

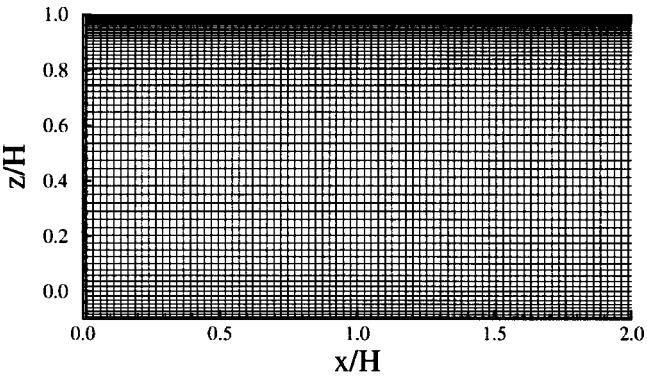

Fig. 5 Computational grid for channel flow over wavy roughness with body-force model

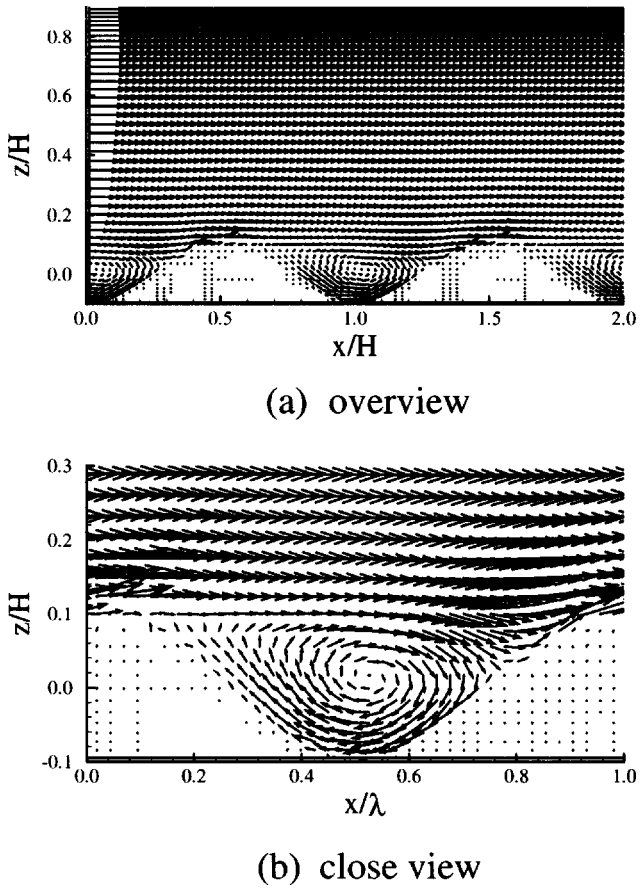

Fig. 6 Velocity vectors for channel flow over wavy roughness using body-force model

field is interpolated onto the body-fitted grid used in Section 4, so that direct comparisons between the two results can be made. In Fig. 7, similar to Fig. 4, time and spanwise-averaged mean streamwise velocity profiles using the two approaches are compared with the experimental data of Buckles et al. [17] at six representative locations. Figures 8 and 9 compare the profiles of wave-average mean velocity ($\overline{U}/U_b$) and turbulent kinetic energy ($\overline{k}/U_b^2$). Wave averaging is done by summing up the physical parameters, already time and spanwise averaged, along the streamwise grid lines, and dividing by the number of grid points on that line. It is seen that the two sets of results match well except close to the wave surface. The difference in the two simulations is due to the approximation made in the treatment of the physical shape of the boundary in the body-force model. No interpolation procedure is taken to scale the forcing at points near the curved surface and the body force is smoothed implicitly by the spatial discretization. The agreement is expected to improve with grid refinement, leaving smaller subgrid roughness effects. As noted by Fadlun et al. [20], improved results could be obtained also by using interpolation to scale the body force at points close to the curved surface.

A particularly interesting result is shown in Fig. 10 where the wave-averaged mean velocity profile is plotted in the usual semi-logarithmic coordinates. Here, $\overline{U}^+ = \overline{U}/U_\tau$ and $\overline{z}^+ = U_\tau \overline{z}/\nu$, where U_τ is the ''friction velocity'' based on the equivalent average shear stress on the wave, including the pressure and friction components, and $\overline{z}$ is distance measured from the ''virtual origin'' defined as the position where the wave-averaged velocity is zero. This plot enables the waves on the bottom wall to be viewed as roughness, and the flow features to be evaluated in the framework of surface roughness effects. It is observed that the two LES simulations, with the wavy surface resolved by a body-fitted grid and represented by a body-force field, give essentially the same result for $\overline{z}^+ > 500$. In other words, the body-force model reproduces the basic effect of roughness observed in the downward shift in the logarithmic law from the smooth-wall flow. The disagreement between the two solutions in the near-wall region, occupied by the roughness itself and the layer just beyond the roughness, is to be expected in view of the approximations made in the treatment of the roughness geometry (the chosen grid) and implementation of the body-force model.

The pressure and friction components of resistance calculated from interpolated surface pressure and shear stress are compared with those of the previous solution in Table 1. The close agreement of the forces calculated by the two methods is a measure of the success of the body-force model.

6 Modeling Subgrid-Scale Roughness by Random Force Field

As depicted in Fig. 1, use of a Cartesian grid to describe the wavy surface leaves the subgrid-scale roughness that has to be modeled. A practical example of this type of decomposition is the flow over a mountainous terrain, where the grid may be sufficiently dense to resolve the mountains and the valleys, but not the forests and buildings. This subgrid-scale roughness is most likely random and can be taken into account using the approach proposed by Miyake et al. [11]. This is demonstrated by taking the case of the wavy wall, assuming that the surface shape left unresolved by the chosen grid is random and with a mean height of 10% of the wave amplitude (i.e., $0.1a$). Following Miyake et al. [11], every grid point within the roughness element height contributes a body force, as in Eq. (1), with $C_d = 0.2$. Miyake et al. [11] used $C_d = 0.5$ for plane channel flow. In the present application, this value required very small time-steps for stability, making the computation very time-consuming. A similar problem was reported by Goldstein et al. [21] when a similar body-force model was applied to complex geometry. It should be pointed that the boundary body-force model [12] adopted for the resolved roughness in the current study does not impose additional stability requirements, while the random force model used for the subgrid-scale roughness discussed in this section does.

The effect of adding the random subgrid-scale roughness is shown in the mean velocity profile in Fig. 11. With the same imposed mean pressure gradient, addition of the ''subgrid'' roughness decreases the mean velocity. When plotted in logarithmic format, the subgrid-scale roughness increases the downward shift in the velocity profile. It is significant that much of the roughness effect is already captured by the resolved-scale LES, and the subgrid-scale roughness makes a small contribution. For many applications, therefore, it may be sufficient to obtain only a resolved-scale solution. Alternatively, a sufficiently fine grid would obviate the need to add a sub-grid component.

The resistance components with the sub-grid roughness added to the waves are summarized in Table 1. The pressure resistance decreases slightly presumably due to a smaller separation region and the friction component remains negligible. The total resistance from the bottom and top walls is less than the imposed mean pressure drop. The difference is due to the resistance added by the random subgrid roughness elements. In this case, the resistance generated by the subgrid-scale roughness is about 4% of the total resistance.

In the application of the random body-force model, the mean height of the roughness elements is the same as that obtained from the ''real'' subgrid-scale roughness. Location of the random roughness elements does not need to match that for subgrid roughness because the model attempts to simulate only the statistical effect of random roughness. Effect of individual roughness elements is insignificant as long as the generated roughness elements have the same statistical properties as the real subgrid roughness.

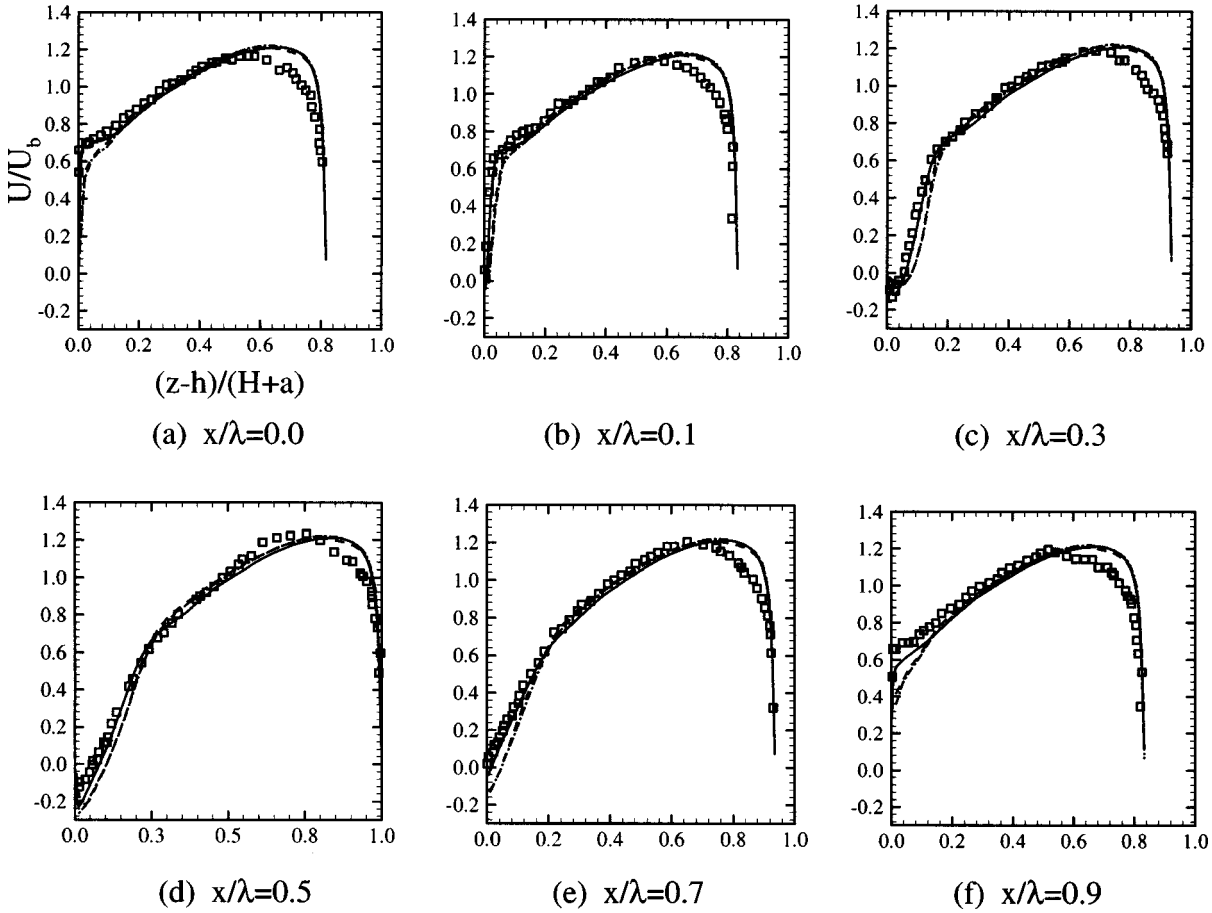

Fig. 7 Comparisons of mean streamwise velocity profiles using body-force model with experimental data at selected locations

Methods of generating random roughness elements are flexible. Height distribution of roughness elements can be simple random distribution, as in this study. Elements can be constructed on each grid point on the resolved roughness surface, or on every other grid point, or in other combinations, depending on the specific flow situation. Once random roughness elements are constructed, the body force is applied to grid points within the element.

The choice of the drag coefficient C_d needs further refinement. It is an empirical constant. Miyake et al. [11] chose 0.5 for channel flow, while Patton et al. [10] used a measured value of 0.4725 for a porous windbreak in boundary layer flow. The present example used 0.2. More numerical and laboratory experiments are needed to better correlate C_d and subgrid-scale roughness geometry. However, as subgrid roughness only accounts for the small-scale roughness, the value of C_d is unlikely to significantly affect the total flow field.

7 Summary and Conclusions

This paper has described a general method for treating the flow over a rough surface within the framework of large-eddy simulation. An arbitrary roughness is decomposed into two parts: resolved-scale and subgrid-scale roughness. The length scale of the resolved component is determined by the Cartesian grid that is chosen for a given flow situation, and is much larger than that of the subgrid roughness. For example, mountains can be treated as

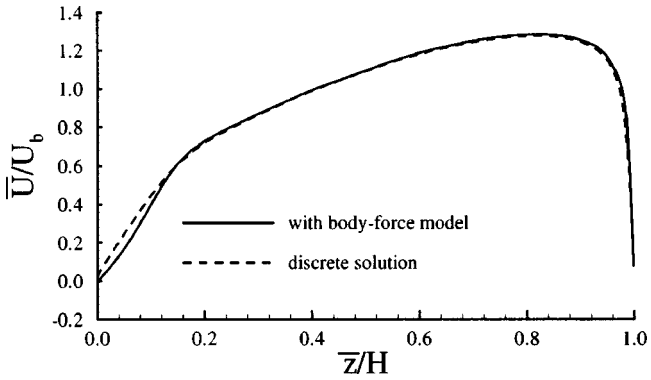

Fig. 8 Wave-averaged mean velocity profile

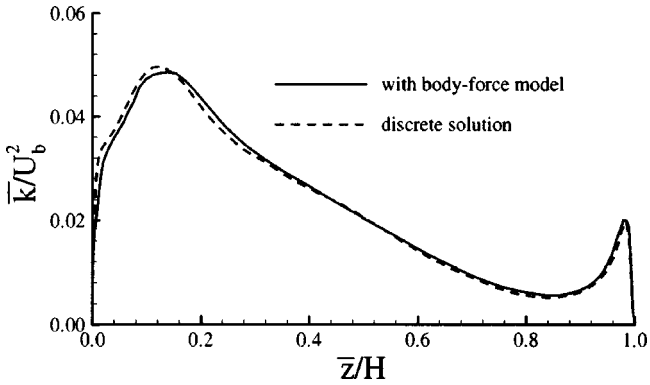

Fig. 9 Wave-averaged mean turbulence kinetic energy profile

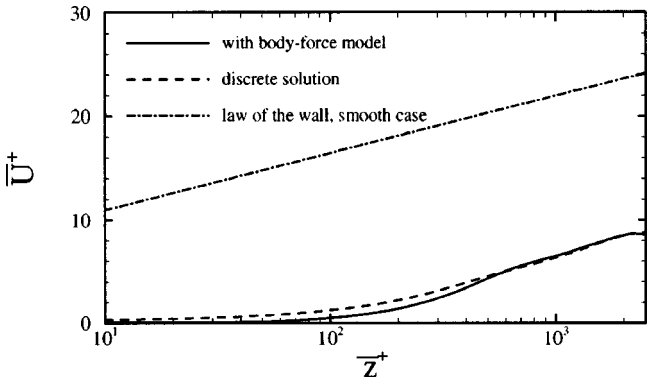

Fig. 10 Wave-averaged mean velocity profiles in wall coordinates

resolved-scale roughness, while trees and shrubs on the mountain surface are the subgrid roughness. The no-slip condition is realized by an immersed-boundary body force, which is internally determined and does not require a model. The resolved-scale roughness is accounted for directly, just as large-scale motions are solved directly in LES, and determines the major flow features. Such a simulation, by itself, may be sufficient for some applications.

For the subgrid roughness, a random body-force model is used. A drag coefficient has to be prescribed from known correlations or experiments. However, as the subgrid roughness is responsible for only a small portion of momentum, mass and energy transport, any uncertainty in this coefficient is not expected to be critical.

The new approach to modeling arbitrary roughness is demonstrated by the example of the flow over a wavy wall. Further details of turbulent flow over a wavy wall and application of the body-force model to flow over a rib roughness are given in Cui et al. [19].

Acknowledgments

The authors acknowledge the computer facilities and services provided by IIHR–Hydroscience and Engineering, National Center for Supercomputing Applications, and National Partnership for Advanced Computational Infrastructure. Prof. Robert Street and Dr. Yan Zang provided the source code developed at Stanford University.

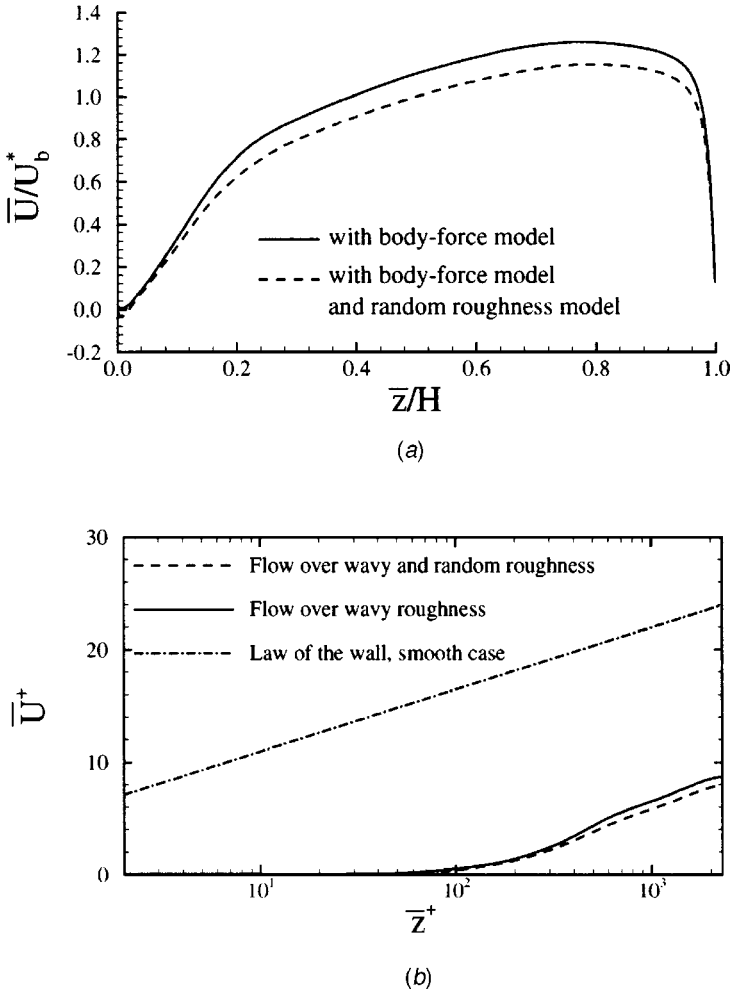

Fig. 11 Wave-averaged mean velocity profiles; effect of subgrid-scale roughness (a) In physical coordinates (U_b* is the bulk velocity in the case with body-force model only). (b) In logarithmic coordinates.

References

[1] Nikuradse, J., 1950, ''Laws of Flow in Rough Pipes,'' National Advisory Committee for Aeronautics, NACA TM 1292 (translation from VDI-Forschungsheft 361, 1933).

[2] Adams, J. C., and Hodge, B. K., 1977, ''The Calculation of Compressible, Transitional, Turbulent and Relaminarizational Boundary Layers Over Smooth and Rough Surfaces Using an Extended Mixing Length Hypothesis,'' AIAA Paper No. 77-682.

[3] Lin, T. C., and Bywater, R. J., 1980, ''The Evaluation of Selected Turbulence Models for High-Speed Rough-Wall Boundary Layer Calculations,'' AIAA Paper No. 80-0132.

[4] Finson, M. L., 1982, ''A Model for Rough Wall Turbulent Heating and Skin Friction,'' AIAA Paper No. 82-0199.

[5] Christoph, G. H., and Pletcher, R. H., 1983, ''Prediction of Rough-Wall Skin Friction and Heat Transfer,'' AIAA J., **21**, pp. 509–515.

[6] Taylor, R. P., Coleman, H. W., and Hodge, B. K., 1985, ''Prediction of Turbulent Rough-Wall Skin Friction Using a Discrete Element Approach,'' ASME J. Fluids Eng., **107**, pp. 251–257.

[7] Maruyama, T., 1993, ''Optimization of Roughness Parameters for Staggered Arrayed Cubic Blocks Using Experimental Data,'' J. Wind. Eng. Ind. Aerodyn., **46**, pp. 165–171.

[8] Patel, V. C., 1998, ''Perspective: Flow at High Reynolds Number and Over Rough Surfaces—Achilles Heel of CFD,'' ASME J. Fluids Eng., **120**, pp. 434–444.

[9] Lin, C.-L., Moeng, C.-H., Sullivan, P. P., and McWilliams, J. C., 1997, ''The Effect of Surface Roughness on Flow Structures in a Neutrally Stratified Planetary Boundary Layer Flow,'' Phys. Fluids, **9**, pp. 3235–3249.

[10] Patton, E. G., Shaw, R. H., Judd, M. J., and Raupach, M. R., 1998, ''Large-Eddy Simulation of Windbreak Flow,'' Boundary-Layer Meteorol., **87**, pp. 275–306.

[11] Miyake, Y., Tsujimoto, K., and Agata, Y., 2000, ''A DNS of a Turbulent Flow in a Rough-Wall Channel Using Roughness Elements Model,'' JSME Int. J., **43**(2), pp. 233–242.

[12] Verzicco, R., Mohd-Yusof, J., Orlandi, P., and Haworth, D., 2000, ''Large Eddy Simulation in Complex Geometric Configurations Using Boundary Body Forces,'' AIAA J., **38**, pp. 427–433.

[13] Germano, M., Piomelli, U., Moin, P., and Cabot, W. H., 1991, ''A Dynamic Subgrid-Scale Eddy Viscosity Model,'' Phys. Fluids A, **3**, pp. 1760–1765.

[14] Piomelli, U., 1993, ''High Reynolds Number Calculations Using the Dynamic Subgrid-Scale Stress Model,'' Phys. Fluids, **5**, pp. 1484–1490.

[15] Lilly, D. K., 1992, ''A Proposed Modification of the Germano Subgrid-Scale Closure Method,'' Phys. Fluids, **4**, pp. 633–635.

[16] Zang, Y., Street, R. L., and Koseff, J. R., 1994, ''A Non-staggered Grid, Fractional Step Method for Time-Dependent Incompressible Navier-Stokes Equations in Curvilinear Coordinates,'' J. Comput. Phys., **114**, pp. 18–33.

[17] Buckles, T. J., Hanratty, T. J., and Adrian, R. J., 1984, ''Turbulent Flow Over Large-Amplitude Wavy Surfaces,'' J. Fluid Mech., **140**, pp. 27–44.

[18] Henn, D. S., and Sykes, R. I., 1999, ''Large-Eddy Simulation of Flow Over Wavy Surfaces,'' J. Fluid Mech., **383**, pp. 75–112.

[19] Cui, J., Patel, V. C., and Lin, C.-L., 2000, ''Large-Eddy Simulation of Turbulent Flow Over Rough Surfaces,'' IIHR Report No. 413, IIHR—Hydroscience & Engineering (formerly Iowa Institute of Hydraulic Research), The University of Iowa, Iowa City, IA.

[20] Fadlun, E. A., Verzicco, R., Orlandi, P., and Mohd-Yusof, J., 2000, ''Combined Immersed-Boundary Finite-Difference Methods for Three-Dimensional Complex Flow Simulations,'' J. Comput. Phys., **161**, pp. 35–60.

[21] Goldstein, D., Handler, R., and Sirovich, L., 1993, ''Modeling a No-Slip Flow Boundary With an External Force Field,'' J. Comput. Phys., **105**, pp. 354–366.

Laminar, Gravitationally Driven Flow of a Thin Film on a Curved Wall

Kenneth J. Ruschak
Senior Research Associate

Steven J. Weinstein
Research Associate

Manufacturing Research and Engineering Organization,
Eastman Kodak Company,
Rochester, NY 14652-3701

Gravitationally driven flow of a thin film down an arbitrarily curved wall is analyzed for moderate Reynolds number by generalizing equations previously developed for flow on a planar wall. In the analysis, the ratio of the characteristic film thickness to the characteristic dimension of the wall is presumed small, and terms estimated to be first order in this parameter are retained. Partial differential equations are reduced to ordinary differential equations by the method of von Kármán and Pohlhausen; namely, an expression for the velocity profile is assumed, and the equation for conservation of linear momentum is averaged across the film. The assumed velocity profile changes shape in the flow direction because a self-similar profile, one of fixed shape but variable magnitude, leads to an equation that typically fails under critical conditions. The resulting equations for film thickness routinely accommodate subcritical-to-supercritical transitions and supercritical-to-subcritical transitions as classified by the underlying wave propagation. The more severe supercritical-to-subcritical transition is manifested by a standing wave where the film noticeably thickens; this standing wave is a simple analogue of a hydraulic jump. Predictions of the film-thickness profile and variations in the velocity profile compare favorably with those from the Navier-Stokes equation obtained by the finite element method. [DOI: 10.1115/1.1522412]

Introduction

The flows of thin films at moderate Reynolds number have practical applications that include liquid film coating, [1]. In coating processes, flow rates and speeds are typically high enough that inertial effects are significant, and yet flow is laminar. A consequence of the importance of inertia is that flow may undergo subcritical-to-supercritical, [2,3], or supercritical-to-subcritical, [4,5], transitions corresponding to a change in underlying wave propagation. Waves propagate upstream and downstream in subcritical flow and solely downstream in supercritical flow.

Coating flows are often designed such that film thickness changes gradually in the flow direction. When that is the case, the thin-film approximation to the Navier-Stokes equation is justified, [6]. Formally, the thin-film approximation is identical to the classical boundary layer approximation, [6,7], because of the shared underlying assumption that cross-stream derivatives of velocity greatly exceed streamwise derivatives. Consequently, approaches for solving boundary layer problems can be useful for solving thin-film problems. In particular, the boundary layer equation can often be solved approximately by averaging over a cross section of the flow and introducing an assumed velocity profile, [7]. This procedure, originated by Th. von Kármán and K. Pohlhausen, reduces the two-dimensional boundary layer equation to an ordinary differential equation for boundary layer thickness. For the flow of a thin film, the velocity profile employed in this approach is often self-similar and parabolic. One reason for this choice is that the velocity profile for purely viscous flow of a thin film in a gravitational field, [6], is parabolic. The velocity profile for fully developed film flow on an inclined, planar wall is also parabolic (Nusselt flow), and a self-similar velocity profile is useful for the approach to fully developed flow, [8], as well.

In applying the von Kármán-Pohlhausen approach to the flow of a film with inertia, any self-similar velocity profile including a parabola leads to an ordinary differential equation for film thickness that is first order in the absence of surface tension. Typically, the solution to this film equation is singular at a critical point, where the coefficient of the derivative of film thickness vanishes and the directions of wave propagation change, and no continuous solution through the critical point exists. The Navier-Stokes equation and the thin-film approximation to the Navier-Stokes equation have no such difficulty, [4,5]; consequently, the singularity is not due to a fundamental problem with the underlying assumption that the rate of change of film thickness is small, nor is it due to the neglect of surface tension. The singularity is sometimes removable for subcritical-to-supercritical flow by a particular choice of film thickness at the critical point, as for flow over a weir, [2], and for a wall moving out of a pool, [9,10]. In that case, film thickness at the critical point is chosen to remove the singularity, and the film equation is integrated from the critical point in both the upstream and downstream directions. These integrations are consistent with the propagation of the characteristics of the hyperbolic equation governing wave motion, [2,9,10]. The singularity is not removable for supercritical-to-subcritical flow, and indeed integration in the upstream direction from the critical point is impossible in that situation.

Instead of a self-similar velocity profile, Hassan [11] employed a cubic velocity profile in applying the von Kármán-Pohlhausen method to film flow under supercritical conditions. Bohr, Putkaradze, and Watanabe [12] took the same approach to a hydraulic jump on an inclined, planar wall and thereby avoided the singularity resulting from a self-similar velocity profile. Ruschak and Weinstein [4] augmented this analysis through numerical solutions of both the Navier-Stokes equation and the thin-film approximation to the Navier-Stokes equation. They found that the velocity profile varies modestly in shape as flow passes from supercritical to subcritical and that a cubic velocity profile adequately captures this variation. A velocity profile varying in shape is key to avoiding a singularity even though the variation required is modest.

The cubic velocity profile is also an effective choice for thin-film flow because it represents well, [4,12], the velocity profile for Jeffrey-Hamel flow, an exact similarity solution of the Navier-Stokes equation for radial streamlines. This flow applies to films that are driven by inertia and so thin that the effect of gravity on

Contributed by the Fluids Engineering Division for publication in the JOURNAL OF FLUIDS ENGINEERING. Manuscript received by the Fluids Engineering Division June 29, 2001; revised manuscript received June 20, 2002. Associate Editor: J. S. Marshall.

pressure is negligible. The velocity profile has an inflection point at the wall, and a parabolic profile cannot have an inflection point and therefore gives less accurate results.

The film-thickness profile for supercritical-to-subcritical flow features a standing wave where the film thickens noticeably. The underlying assumption of gradually varying film thickness remains valid in the vicinity of the standing wave, and there is no flow recirculation. The standing wave is a precursor to a hydraulic jump, a more extreme occurrence usually associated with an abrupt increase in thickness and with one or more recirculations, [13]. The focus here is the flow of thin films under critical conditions and not hydraulic jumps.

The analysis of Ruschak and Weinstein [4] for flow on an inclined plane is generalized here for flow on an arbitrarily curved wall under conditions where the Reynolds number is moderate and the ratio of the characteristic film thickness to the characteristic span of the curve, δ, is small. In simplifying the exact equations, terms estimated to be first order in δ are retained. The resulting film equation, actually a pair of coupled ordinary differential equations, is shown to handle routinely both subcritical-to-supercritical and supercritical-to-subcritical transitions. Several previous analyses of flow on curved walls have not considered moderate Reynolds numbers and critical conditions. As examples, purely viscous, time-dependent flow driven by a gradient in capillary pressure on a surface in two dimensions has been analyzed, [14], and more general and accurate equations that include the effect of gravity and a surface in three dimensions have been derived, [15]. The other extreme of nearly inviscid and irrotational flow has also been analyzed, [16].

The use of a cubic polynomial for the velocity profile necessitates an additional boundary condition that is generated by evaluating the Navier-Stokes equation at the wall, a common practice in the von Kármán-Pohlhausen approach to boundary layers, [7], and the one taken by Hassan [11] for film flow. The effectiveness of this combination for flows with critical points has only recently been recognized, [4,12]. Many previous analyses have exclusively treated film flow on a vertical wall where no critical point is encountered, [11,17], or have deliberately avoided critical conditions (see, for example, [18], p. 56). Many choices for the velocity profile have been used for boundary layer flows over submerged solid bodies, [7], but no singularity is encountered in that situation. In cases where no external pressure gradient is imposed on the boundary layer, high-order polynomials serve to improve the accuracy of the results, notably the wall shear stress (see [7], p. 206, Table 10.1). When an external pressure gradient is imposed, a polynomial velocity profile that is at least cubic is required to accommodate an inflection point and a zero slope at the wall for incipient boundary layer separation. Regardless of the assumed profile, the equation to solve for boundary layer thickness is first order. Because the pressure gradient is imposed and not calculated as part of the solution, a parabolic profile does not produce a singularity. Thus, the motivation for high-order polynomials is improved accuracy for wall shear stress and the capability to predict flow separation. In contrast, the third-order polynomial used here for film flow is essential to avoiding a singularity in the differential equation for film thickness. The singularity arises because the pressure gradient depends on the interface location and is determined as part of the solution.

The film equations resulting from a cubic velocity profile are extensive but manageable and represent an attractive option for the laminar flows of thin films.

Experimental Observation

An experiment was conducted to show a standing wave where laminar flow passes from supercritical to subcritical along a curved wall. Supercritical flow was indicated by stationary waves in the wake of a needle breaching the surface of the film. Subcritical flow was indicated by periodic flow disturbances, induced by a rotating agitator, radiating both upstream and downstream. To produce a film in supercritical flow, aqueous glycerol was pumped to a weir discharging onto a vertical wall. A smooth curve, specified by Eq. (1) below, connected the vertical wall to a plane wall inclined from horizontal by 2 deg. The wall and weir were machined from a single block of aluminum to avoid seams. Surface tension and its gradients were reduced by adding the surfactant Aerosol® OT (Cytec Industries, Inc.) at high concentration. A small amount of slurry of titanium dioxide was added to the liquid to make it white and opaque. The liquid had a viscosity of 24.7 mPa·s, a specific gravity of 1.15, and a surface tension of 30 mN/m. The flow rate was 2.6 cc/s per cm of width. Lighting by two synchronized strobe lights was adjusted to create shadows revealing the standing wave occurring where flow passes from supercritical to subcritical. Figure 1 is a photograph showing a perspective view of the standing wave.

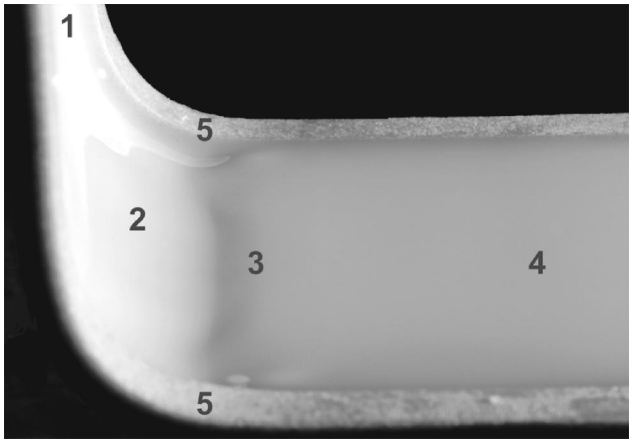

Fig. 1 Photograph of the standing wave marking the transition from supercritical to subcritical flow on a curved wall; the view is downward toward the standing wave from the side. Label 1, vertical wall; 2, curved wall; 3, standing wave with slope shadowed by the lighting; 4, wall inclined at 2 deg; 5, sidewalls. Areas beyond the sidewalls of the flow have been blackened to eliminate distractions in the surroundings. The computed film thickness profile for these conditions is plotted in Fig. 9.

Equations

A Newtonian liquid with viscosity μ, density ρ, and surface tension σ flows steadily along a curved wall at volumetric flow rate per unit width q. A Cartesian coordinate system is employed with horizontal coordinate x and unit vector $\hat{\mathbf{i}}$ and with vertical coordinate z and unit vector $\hat{\mathbf{j}}$ (Fig. 2). The outwardly directed normal to the wall, $\hat{\mathbf{n}}$, defines a local coordinate y originating at the wall. The angle of $\hat{\mathbf{n}}$ from vertical is φ with positive values indicating a downward inclination. The tangent to the wall in the flow direction is $\hat{\mathbf{t}}$, and arc length along the wall is s. With gravitational acceleration denoted g, a characteristic film thickness for gravitationally driven, viscous flow is $h_c=[\mu q/\rho g]^{1/3}$. A length scale reflecting the influence of surface tension is the capillary length, $l=\sqrt{\sigma/\rho g}$. L is a characteristic dimension of the curved wall that may be a characteristic radius of curvature. In some problems, notably a planar wall, it may be preferable or necessary to interpret L differently. For example, if $\mathrm{Re}\gg 10$ and surface tension effects are negligible, then $L=\mathrm{Re}\,h_c$ is the length scale for developing flow on a planar wall, [4].

The ambient air is assumed to exert only a uniform pressure on the liquid. There is, however, a pressure jump across the curved air interface caused by surface tension.

Dimensionless variables are employed to indicate the relative size of terms. The dimensionless coordinate along the wall is $\xi=s/L$; that normal to the wall is $\eta=y/h_c$, and the surface of the film is given by $\eta=\zeta(\xi)$. The $\hat{\mathbf{t}}$-component of velocity made di-

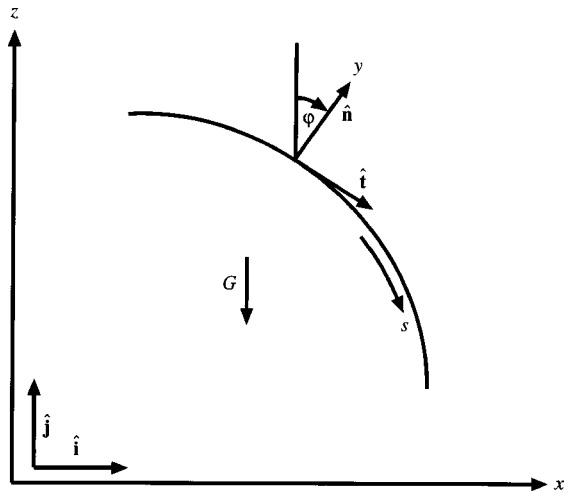

Fig. 2 Definition sketch

mensionless with q/h_c is u, and the $\hat{\mathbf{n}}$-component of velocity made dimensionless with q/L is v. Pressure, made dimensionless with ρgL, is p. Dimensionless groups that arise are the Reynolds number $\mathrm{Re}=\rho q/\mu$, the aspect ratio $\delta=h_c/L$, and the Bond number $Bo=\rho gL^2/\sigma=(L/l)^2$.

Wall shapes in the examples are determined by specifying the function $\varphi(s)$; the coordinates x and z of the wall then follow by numerical integrations of $dx/ds=\cos(\varphi)$ and $dz/ds=-\sin(\varphi)$. In one specification, the wall consists of two planar sections joined by a curved section. Upstream, the wall is planar, $\varphi=\varphi_0$, and flow is fully developed (Nusselt flow) with film thickness approaching $\zeta_0=[3/\sin(\varphi_0)]^{1/3}$. Similarly, the wall is planar downstream, $\varphi=\varphi_1$, and flow is fully developed with film thickness approaching $\zeta_1=[3/\sin(\varphi_1)]^{1/3}$. The wall is curved from $s=0$ ($\xi=0$) to $s=L$ ($\xi=1$) according to the formula

$$\varphi=\varphi_0+(\varphi_1-\varphi_0)[10\xi^3-15\xi^4+6\xi^5] \quad (0\leqslant\xi\leqslant1). \tag{1}$$

The slope and curvature of the wall are continuous, but the third derivative is discontinuous at $\xi=0$ and $\xi=1$. In a second specification of the wall, planar ends are approached asymptotically, and all derivatives are continuous.

$$\varphi=\frac{(\varphi_1+\varphi_0)}{2}+\frac{(\varphi_1-\varphi_0)}{2}\tanh(c_1\xi+c_2\xi^3) \quad (-\infty<\xi<\infty) \tag{2}$$

Here, c_1 and c_2 are adjustable constants. In light of experience, this smoother representation is preferable as more conducive to numerical solution.

In presenting the Navier-Stokes and continuity equations in wall coordinates, terms estimated to be $O(\delta)$ are retained and terms estimated to be smaller are dropped. Because moderate values of Re are contemplated, $\mathrm{Re}\,\delta$ is considered $O(1)$.

The continuity equation and the $\hat{\mathbf{n}}$-component of the Navier-Stokes equation in wall coordinates are given by

$$\frac{\partial u}{\partial\xi}+\frac{\partial}{\partial\eta}\left[\left(1+\delta\eta\frac{d\varphi}{d\xi}\right)v\right]=0 \tag{3}$$

$$\mathrm{Re}\,\delta^2u^2\frac{d\varphi}{d\xi}=\frac{\partial p}{\partial\eta}+\delta\cos(\varphi). \tag{4}$$

Because the intent is to integrate across the film, a macroscopic momentum balance is considered on a control volume extending across the film and along the wall from ξ to $\xi+\Delta\xi$. After taking the limit $\Delta\xi\to0$, the $\hat{\mathbf{t}}$-component of the balance is

$$\begin{aligned}\mathrm{Re}\,\delta\frac{d}{d\xi}\int_0^\zeta u^2d\eta+\mathrm{Re}\,\delta^2\frac{d\varphi}{d\xi}\int_0^\zeta uvd\eta&\\ =-\frac{d}{d\xi}\int_0^\zeta pd\eta-\left.\frac{\partial u}{\partial\eta}\right|_{\eta=0}+\frac{\kappa}{Bo}\frac{d\zeta}{d\xi}&\\ +\zeta\left(1+\frac{\delta\zeta}{2}\frac{d\varphi}{d\xi}\right)\sin(\varphi)+\delta\frac{d\varphi}{d\xi}\int_0^\zeta\frac{\partial u}{\partial\eta}d\eta.&\end{aligned} \tag{5}$$

Alternatively, the $\hat{\mathbf{t}}$-component of the Navier-Stokes equation can be integrated over the control volume and the divergence theorem applied. Equations (3), (4), and (5) are the primary equations for the flow of a thin film, and the required boundary conditions at the air interface and at the wall are now considered.

At the air interface, there is no shear stress

$$\frac{\partial u}{\partial\eta}-\delta\frac{d\varphi}{d\xi}u=0 \quad (\eta=\zeta). \tag{6}$$

Viscous stresses normal to the interface are negligible, but there is a pressure jump caused by surface tension.

$$p=\kappa/Bo \quad (\eta=\zeta) \tag{7}$$

Here, κ is the interfacial curvature made dimensionless with L and is given without simplification by

$$\kappa=\frac{\left[\left(1+\delta\zeta\frac{d\varphi}{d\xi}\right)^2+2\delta^2\left(\frac{d\zeta}{d\xi}\right)^2\right]\frac{d\varphi}{d\xi}-\delta\left(1+\delta\zeta\frac{d\phi}{d\xi}\right)\frac{d^2\zeta}{d\xi^2}+\delta^2\zeta\frac{d\zeta}{d\xi}\frac{d^2\varphi}{d\xi^2}}{\left[\left(1+\delta\zeta\frac{d\varphi}{d\xi}\right)^2+\delta^2\left(\frac{d\zeta}{d\xi}\right)^2\right]^{3/2}}. \tag{8}$$

This complete expression can be retained for flow entering or exiting a hydrostatic pool under conditions where surface tension is important, [19]. Then, as film thickness becomes large and the viscous and inertial terms negligible, the film equations reduce to the Young-Laplace equation of capillary hydrostatics, [20]. If surface tension effects are significant and there is no pool, then only terms $O(\delta)$ need be retained in Eq. (8) as in all other equations, i.e.,

$$\kappa\approx\frac{d\varphi}{d\xi}-\delta\zeta\left(\frac{d\varphi}{d\xi}\right)^2-\delta\frac{d^2\zeta}{d\xi^2}. \tag{9}$$

Finally, the air interface is a streamline, or equivalently, the flow rate is the same at every cross section.

$$1=\int_0^\zeta ud\eta \tag{10}$$

At the wall, velocity is zero.

$$u=v=0 \quad (\eta=0) \tag{11}$$

An additional boundary condition is required at the wall; it is generated by evaluating the $\hat{\mathbf{t}}$-component of the Navier-Stokes equation at the wall, [4,11,12].

$$0=-\frac{\partial p}{\partial \xi}+\sin(\varphi)+\frac{\partial^2 u}{\partial \eta^2}+\delta\frac{d\varphi}{d\xi}\frac{\partial u}{\partial \eta} \quad (\eta=0) \tag{12}$$

Equations (3)–(12) are solved as follows. A cubic velocity profile is selected that satisfies Eqs. (6), (10), and (11).

$$u=\frac{A}{\zeta}\left[\omega-\frac{5\omega^2}{2}+\frac{4\omega^3}{3}\right]+\frac{3}{\zeta}\left[\omega-\frac{\omega^2}{2}\right]+\frac{\delta(A-9)}{12}\frac{d\varphi}{d\xi}\left[\omega-\frac{3\omega^2}{2}\right] \tag{13}$$

Here, $\omega=\eta/\zeta$ ranges from 0 to 1, and A is a function of ξ determined as part of the solution. Previous work on a planar wall, [4], and the results that follow indicate that a cubic profile accommodates shapes determined by numerical solutions of the Navier-Stokes equation. Note that $A=0$ in Eq. (13) gives a self-similar, parabolic profile at lowest order. Similarly, $A=-3/5$ corresponds to zero curvature at the wall, and $A=-3$ corresponds to a zero velocity gradient and the onset of reverse flow at the wall. An expression for v is obtained by substituting Eq. (13) into Eq. (3), integrating with respect to η, and applying Eq. (11); only the leading term is required.

$$v=\frac{1}{\zeta}\frac{d\zeta}{d\xi}\left[A\left(\omega^2-\frac{5\omega^3}{2}+\frac{4\omega^4}{3}\right)+3\left(\omega^2-\frac{\omega^3}{2}\right)\right]-\frac{dA}{d\xi}\left[\frac{\omega^2}{2}-\frac{5\omega^3}{6}+\frac{\omega^4}{3}\right] \tag{14}$$

To determine the pressure, Eq. (4) is integrated with respect to η and Eq. (7) is applied.

$$p=\kappa/Bo+\delta\zeta\cos(\varphi)[1-\eta]-\mathrm{Re}\,\delta^2\frac{d\varphi}{d\xi}\int_{\eta}^{\zeta}u(\xi,\overline{\eta})^2 d\overline{\eta} \tag{15}$$

Equations (13), (14), and (15) are substituted into Eq. (5) and the indicated operations are performed.

$$0=D\frac{d\zeta}{d\xi}-N+\frac{\mathrm{Re}\,\delta}{\zeta^2}\frac{d\alpha}{d\xi}+\frac{\delta(A-9)}{4\zeta^2}\frac{d\varphi}{d\xi}+\frac{1}{Bo}\frac{d\kappa}{d\xi}+\frac{\mathrm{Re}\,\delta^2}{\zeta}\frac{d^2\varphi}{d\xi^2}\cdot\left(-\frac{3}{4}+\frac{23A}{420}-\frac{A^2}{315}\right)+\frac{\mathrm{Re}\,\delta^2}{\zeta}\frac{d\varphi}{d\xi}\frac{dA}{d\xi}\left(\frac{11}{420}-\frac{2A}{315}\right)+\frac{\mathrm{Re}\,\delta^2}{\zeta^2}\frac{d\varphi}{d\xi}\frac{d\zeta}{d\xi}\left(\frac{33}{40}-\frac{37A}{420}+\frac{A^2}{168}\right) \tag{16}$$

In Eq. (16),

$$D=\delta\cos(\varphi)-\mathrm{Re}\,\delta\alpha/\zeta^3 \tag{17}$$

$$N=(1+\delta\zeta d\varphi/d\xi)\sin(\varphi)-(3+A)/\zeta^3 \tag{18}$$

$$\alpha=6/5-A/15+A^2/105 \tag{19}$$

An additional equation is required because Eq. (16) has two unknowns, A and ζ, and this need is met by Eq. (12). Upon substituting Eqs. (13) and (15), Eq. (12) becomes

$$0=\delta\cos(\varphi)\frac{d\zeta}{d\xi}-\sin(\varphi)\left(1+\delta\zeta\frac{d\varphi}{d\xi}\right)+\frac{(5A+3)}{\zeta^3}-\frac{3\delta(A+7)}{4\zeta^2}\frac{d\varphi}{d\xi}+\frac{1}{Bo}\frac{d\kappa}{d\xi}+\frac{\mathrm{Re}\,\delta^2\alpha}{\zeta^2}\frac{d\varphi}{d\xi}\frac{d\zeta}{d\xi}-\frac{\mathrm{Re}\,\delta^2\alpha}{\zeta}\frac{d^2\varphi}{d\xi^2}-\frac{\mathrm{Re}\,\delta^2}{\zeta}\frac{d\varphi}{d\xi}\frac{d\alpha}{d\xi}. \tag{20}$$

As a matter of preference, Eq. (16) is replaced by the difference of Eqs. (16) and (20)

$$0=\frac{\mathrm{Re}\,\delta\alpha}{\zeta^3}\frac{d\zeta}{d\xi}-\frac{\mathrm{Re}\,\delta}{\zeta^2}\frac{d\alpha}{d\xi}+\frac{4A}{\zeta^3}-\frac{\delta(A+3)}{\zeta^2}\frac{d\varphi}{d\xi}+\frac{\mathrm{Re}\,\delta^2}{\zeta}\frac{d^2\varphi}{d\xi^2}\cdot\left(-\frac{9}{20}+\frac{A}{84}-\frac{2A^2}{315}\right)+\frac{\mathrm{Re}\,\delta^2}{\zeta}\frac{d\varphi}{d\xi}\frac{dA}{d\xi}\left(\frac{17}{420}-\frac{4A}{315}\right)+\frac{\mathrm{Re}\,\delta^2}{\zeta^2}\frac{d\varphi}{d\xi}\frac{d\zeta}{d\xi}\left(\frac{3}{8}+\frac{3A}{140}+\frac{A^2}{280}\right) \tag{21}$$

Eq. (21) has no explicit terms involving gravity or surface tension.

Equations (20) and (21) together are referred to as the film equation with varying velocity profile. The highest order derivatives are the third derivative of ζ and the first derivative of A. In the examples below, a value for ζ is specified upstream. In the cases where the film approaches fully developed flow downstream, the additional boundary conditions are $A\to 0$, $d\zeta/d\xi\to 0$, and $d^2\zeta/d\xi^2\to 0$ as $\xi\to\infty$.

In the last of the examples the wall is planar (φ is a constant) and the film flows into a pool. For that case, Eq. (8) simplifies to

$$\kappa=-\delta\frac{d^2\zeta}{d\xi^2}\Big/\left[1+\delta^2\left(\frac{d\zeta}{d\xi}\right)^2\right]^{3/2}. \tag{22}$$

To develop a downstream boundary condition, the Young-Laplace equation of capillary hydrostatics is obtained from Eq. (20) by dropping the dynamic terms

$$0=\delta\cos(\varphi)\frac{d\zeta}{d\xi}-\sin(\varphi)+\frac{1}{Bo}\frac{d\kappa}{d\xi}. \tag{23}$$

Equation (23) is integrated to get

$$0=\delta\cos(\varphi)\zeta-\sin(\varphi)(\xi-\xi_p)+\kappa/Bo \tag{24}$$

in which ξ_p is a constant of integration. The straight line giving the surface of the pool away from the wall is determined by setting $\kappa=0$ in Eq. (24),

$$\zeta\to\zeta_\infty(\xi)=\tan(\varphi)(\xi-\xi_p)/\delta. \tag{25}$$

If extended to the wall, this asymptote for the surface of the pool intersects the wall at $\xi=\xi_p$. Finally, a boundary condition that can be applied at a finite value of ξ is obtained by linearizing Eq. (24) about $\zeta=\zeta_\infty(\xi)$,

$$d^2\zeta/d\xi^2=Bo\cos(\varphi)(\zeta-\zeta_\infty)[1+\delta^2(d\zeta_\infty/d\xi)^2]^{3/2}. \tag{26}$$

Equation (26) is applied at the downstream end of the grid, which must extend beyond ξ_p.

The equations are solved by central finite differences. The grid is made sufficiently long to accommodate the asymptotic boundary conditions. Given an estimate of the film-thickness profile, an improved estimate is generated by Newton's method; that is, Eqs. (20) and (21) are linearized about estimates of ζ and A and solved to obtain improved estimates. The starting estimate is a film thickness and velocity profile corresponding to fully developed flow at the local inclination of the wall, $\zeta=[3/\sin(\varphi)]^{1/3}$ and $A=0$. Under-relaxation is usually necessary in early iterations to prevent divergence.

Additionally, selected numerical solutions of the Navier-Stokes equation were generated by the finite element method, [21]. In the formulation, velocity is piecewise linear and pressure is piecewise constant.

To obtain the equations used by Ruschak and Weinstein [4] for flow on an inclined plane, φ is made constant in Eqs. (20) and (21)

$$0=\delta\cos(\varphi)\frac{d\zeta}{d\xi}-\sin(\varphi)+\frac{(5A+3)}{\zeta^3}+\frac{1}{Bo}\frac{d\kappa}{d\xi} \tag{27}$$

$$0 = \frac{\mathrm{Re}\,\delta\alpha}{\zeta^3}\frac{d\zeta}{d\xi} - \frac{\mathrm{Re}\,\delta}{\zeta^2}\frac{d\alpha}{d\xi} + \frac{4A}{\zeta^3}. \tag{28}$$

These simplified equations can also be applied to a wall so gradually curved that it may be considered locally planar.

If the wall is slightly curved or planar and if A is a specified constant for a self-similar velocity profile, then a single equation descended from Eq. (16) is sufficient. For a parabolic velocity profile, $A=0$, and for negligible surface tension, this equation is the Nusselt film equation, [3].

$$0 = D\frac{d\zeta}{d\xi} - N \tag{29}$$

The solution to Eq. (29) is singular at a critical point, $D=0$, except in special cases where the singularity is removable by setting $N=0$ at the critical point as well, [2,3,10]. While retaining the surface tension term formally averts the singularity, standing waves of high spatial frequency appear that are not present in numerical solutions of the Navier-Stokes equation. Except by the artifact of rapidly changing curvature, surface tension cannot be important because the wall is straight or slightly curved. The cubic velocity profile, where A varies with distance along the wall, removes the singularity in Eq. (29) with or without surface tension, and formally there is no longer a critical point. However, the variation of A is significant only near $D=0$, and so wave propagation is largely unaffected elsewhere. In this light, $D=0$ can still be regarded as critical point, even though there is no critical point in a strict sense.

Results

The following examples illustrate the capabilities of the film equation with varying velocity profile. Computations of the Navier-Stokes equation support the accuracy of the approximate equation.

Consider a transition from subcritical to supercritical flow under conditions that conservatively meet the restrictions of the simplified analysis. The shape of the downwardly curving wall is given by Eq. (1) with $\varphi_0=2$ deg and $\varphi_1=90$ deg, and the flow conditions are Re=20, $\delta=0.0147$, and *Bo* effectively infinite (negligible surface tension). In this situation, flow passes from subcritical to supercritical. The Nusselt film equation, Eq. (29), the film equation with varying velocity profile, Eqs. (20) and (21), and the Navier-Stokes equation were solved. In solving the Nusselt equation, the thickness of the film at the critical point is chosen to remove the potential singularity, and the integration proceeds upstream and downstream starting at the critical point, [2]. On the other hand, the film equation with varying velocity profile requires no such special procedure. The film profiles for the film equation with varying velocity profile and the Navier-Stokes equation are shown in Fig. 3; only the critical point from the Nusselt film equation is shown because the profile is indistinguishable. A small oscillation appears at the start of the solution to the Navier-Stokes equation. This disturbance may reflect the sensitive nature of the subcritical flow and the inability of the finite elements employed (piecewise linear velocity and piecewise constant pressure) to represent perfectly the fully developed flow upstream. The plot of A in Fig. 4 shows that the velocity profile smoothly evolves. The greatest departure from a parabolic velocity profile and the most rapid rate of change of shape occur near the critical point. In Fig. 5, the range of velocity profiles is shown for the Navier-Stokes equation together with the extreme velocity profiles, $A=-0.005$ and 0.559, for the film equation with varying velocity profile. The slope of the velocity profile at the wall is greater than that for a parabolic profile. The good agreement supports the conclusion that the varying velocity profile circumvents the removable singularity in the Nusselt film equation in a manner consistent with the exact solution.

Consider next a transition from supercritical to subcritical flow, the more severe case. The shape of the upwardly curving wall is given by Eq. (1) with $\varphi_0=90$ deg and $\varphi_1=3$ deg, and the flow conditions are Re=20, $\delta=0.0093$, and *Bo* effectively infinite. Figure 6 shows film profiles for the film equation with varying velocity profile and for the Navier-Stokes equation. Figure 7 is an expanded view near the standing wave, and it is evident that the film equation with varying velocity profile over predicts the rate of thickening of the film. This bias appears to be a general result for transition from supercritical to subcritical flow. The Nusselt film equation has no continuous solution through the critical point, but it can be integrated from both upstream and downstream toward the critical point. The integration from upstream toward the critical point continues almost to the critical point before suddenly diverging, and the film profile is nearly identical to those from the Navier-Stokes equation and the film equation with varying velocity profile and so is not shown in Fig. 7. The integration from downstream toward the critical point also continues to the critical point before diverging, but near the critical point the film thickness significantly exceeds that from the Navier-Stokes equation as shown in Fig. 7. The differences among the three computations

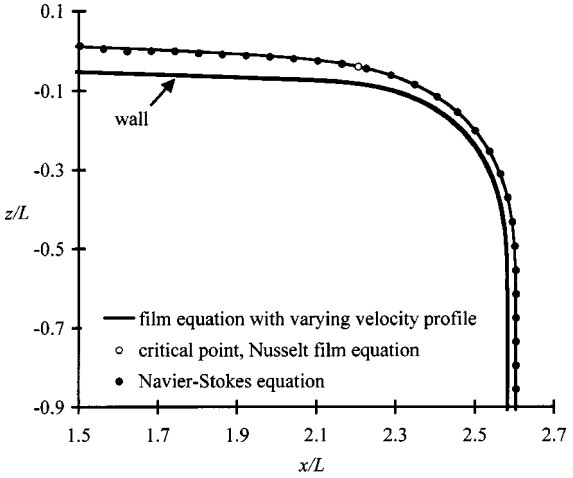

Fig. 3 Film thickness profiles for Re=20 and $\delta=0.0147$ from the film equation with varying velocity profile and the Navier-Stokes equation on a downwardly curving wall. Only the position of the critical point from the Nusselt film equation is indicated because the profile is indistinguishable. The initially subcritical flow becomes supercritical as wall inclination increases.

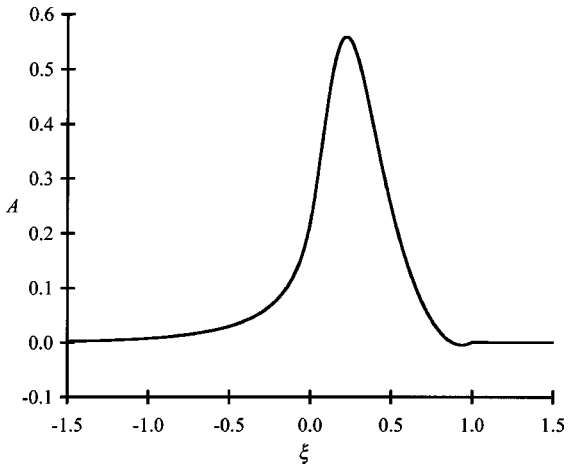

Fig. 4 Plot of the velocity profile parameter A for the conditions of Fig. 3. Upstream and downstream, $A\rightarrow 0$ as the velocity profile becomes fully developed.

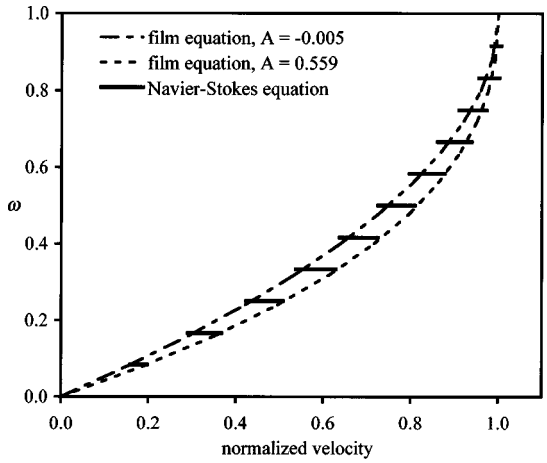

Fig. 5 The range of velocity profiles for the conditions of Fig. 3 from the film equation with varying velocity profile and from the Navier-Stokes equation. The two profiles from the film equation correspond to the extreme values of *A*. The range of velocity at each of 11 nodes is shown for the Navier-Stokes equation.

are confined to a distance downstream from the critical point of the order of magnitude of the local film thickness. Perfect agreement of the profiles for the Navier-Stokes equation and film equation with varying velocity profile is unlikely for so rapid a change in the streamwise direction. Figure 8 shows the range of velocity profiles for the Navier-Stokes equation and the extreme velocity profiles for the film equation with varying velocity profile. In contrast to the first example, the gradient of the velocity profile at the wall is less than that for a parabolic profile. The agreement is again good enough to support the contention that the incorporation of a varying velocity profile circumvents the singularity in the solution of the Nusselt film equation in a manner consistent with the exact solution.

Computations were also performed for the conditions of the experimental observation, namely $\mathrm{Re}=12$, $\delta=0.021$, and $Bo=600$. Additional calculations were performed for $\mathrm{Re}=0.1$ and $\mathrm{Re}=25$. Film profiles from the Navier-Stokes equation and from the film equation with varying velocity profile are shown in Fig. 9. The standing wave marking the transition from subcritical to supercritical flow is most apparent at a Reynolds number near that of the experiment, and the flow rate was in fact varied in the

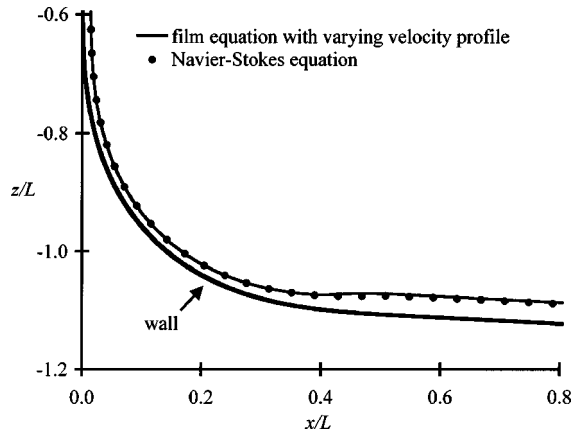

Fig. 6 Film profiles for $\mathrm{Re}=20$ and $\delta=0.0093$ from the film equation with varying velocity profile and the Navier-Stokes equation on an upwardly curving wall. The initially supercritical flow becomes subcritical as wall inclination decreases.

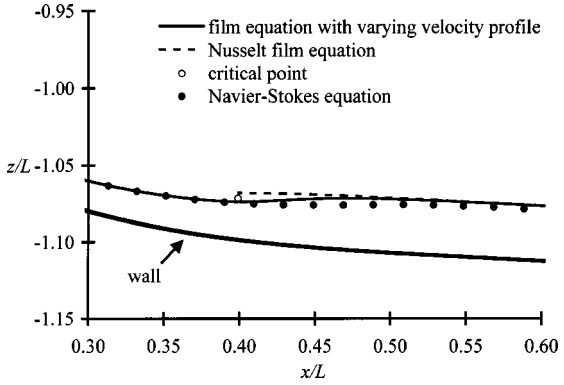

Fig. 7 An expanded view of film profiles for the conditions of Fig. 6 in the vicinity of the standing wave. The Nusselt film equation gives two sections that are discontinuous at the critical point; the section upstream of the critical point is indistinguishable and not shown

experiment until the standing wave was prominent. The tendency of the film equation with varying velocity profile to over predict the rate of film thickening at a supercritical-to-subcritical transition is again evident.

Figure 10 shows the film profile for flow on an initially horizontal wall that subsequently curves downward to vertical. The specific conditions are $\mathrm{Re}=50$, $\delta=0.05$, Bo effectively infinite, and $\varphi_0=0$ deg, $\varphi_1=90$ deg, $c_1=3$ and $c_2=0.2$ in Eq. (2). Flow passes from supercritical to subcritical on the horizontal portion of the wall and then back to supercritical on the curved portion. Near the inlet, gravitational effects are unimportant, and film thickness increases linearly with distance, [4,5,22]. This region is described by Jeffery-Hamel flow, an exact, self-similar solution of the Navier-Stokes equation, [4]. In the film equation with varying velocity profile, this limiting case corresponds to $A=-3/5$ and a velocity profile with zero curvature at the wall. Beyond the stationary wave, which occurs where the film thickens to the point that gravity becomes significant, flow is driven by a streamwise, substantially hydrostatic pressure gradient; thus, the gradually decreasing film thickness. The curved portion of the wall removes the liquid and determines the position of the standing wave. This example shows that the film equation with varying velocity profile

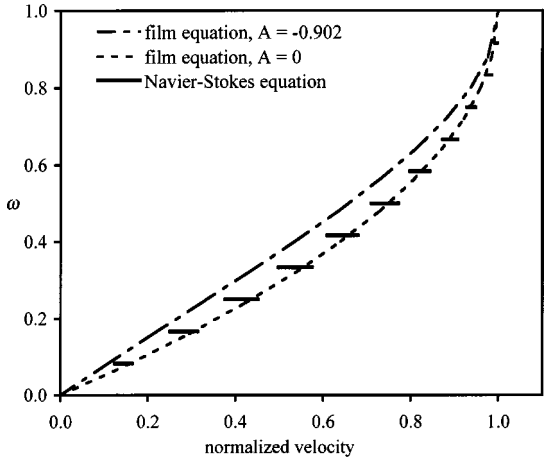

Fig. 8 The range of velocity profiles for the conditions of Fig. 6 from the film equation with varying velocity profile and from the Navier-Stokes equation. The two profiles from the film equation correspond to the extreme values of *A*. The range of velocity at each of 11 nodes is shown for the Navier-Stokes equation.

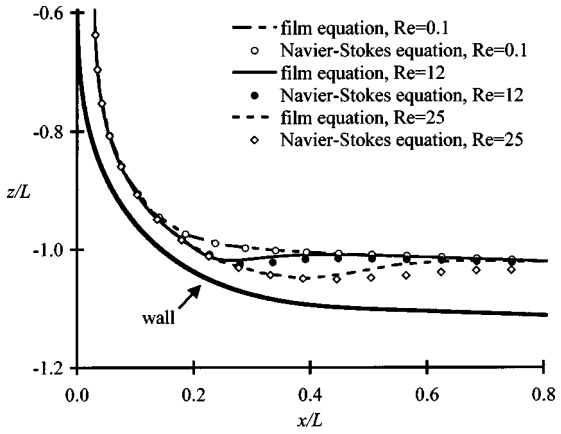

Fig. 9 Film profiles from the film equation with varying velocity profile and from the Navier-Stokes equation for flow on an upwardly curving wall. For the middle curves, Re=12, $\delta=0.021$, and $Bo=600$, the conditions of Fig. 1; for the highest curves, Re=0.1; and for the lowest curves, Re=25.

can accommodate flow driven by inertia, flow driven gravitationally by decreasing depth on a horizontal wall, and multiple transitions.

The film equation with varying velocity profile, incorporating the Young-Laplace equation of capillary hydrostatics, can also accommodate transitions to a pool. For a planar wall, the surface curvature and the boundary condition for the downstream end of the grid are given by Eqs. (22) and (26), respectively. In Fig. 11, the angle of inclination of the planar wall is 20 deg and Re=20. The figure shows the effect of surface tension with $h_c/l=0.173$. Surface tension mitigates the abruptness of the transition and creates standing waves extending upstream of the pool surface. So, high surface curvature can develop even though the geometry is planar or gently curved, and surface tension may have to be included in that case.

Concluding Remarks

The film equation with varying velocity profile appears quite versatile. The velocity gradient at the wall is free to vary, and this variation circumvents mathematical difficulties related to a self-similar velocity profile where the flow passes from supercritical to subcritical or visa versa. The cubic profile can accommodate the important special cases of a parabolic velocity profile and of Jeffrey-Hamel flow. Moreover, the Nusselt film equation, Eq. (29) with $A=0$ and $\alpha=6/5$, gives a reasonable account of inviscid flow for Re large, [3]. Of course, the film equation with varying

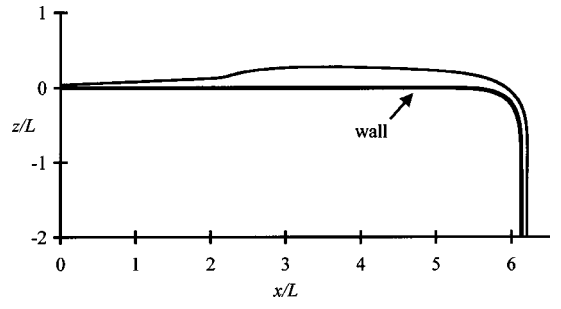

Fig. 10 Film thickness profile for Re=50 and $\delta=0.05$ from the film equation with varying velocity profile for flow on a downwardly curving wall that is horizontal upstream and vertical downstream. The initially supercritical flow becomes subcritical as film thickness increases due to drag; the flow becomes supercritical again where the wall steepens.

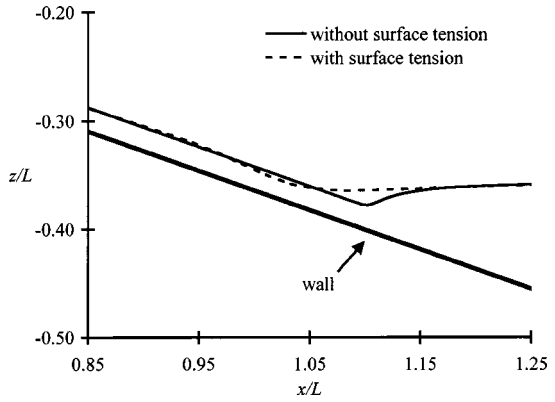

Fig. 11 Flow on a wall inclined at 20 deg from horizontal into a pool at Re=20 with and without surface tension

velocity profile is not as versatile as the thin-film approximation to the Navier-Stokes equation from which it is descended. Most obviously, there is less freedom to specify an initial velocity profile. However, the film equation captures the gradually changing flow downstream that develops as the effects of initial conditions that are possible with the Navier-Stokes equation or the thin-film approximation to the Navier-Stokes equation decay, [4]. At relatively high Reynolds numbers, a boundary layer at the wall can be combined with a plug of inviscid flow at the air interface to accommodate an initially flat velocity profile, [3].

As compared to a typical film profile equation, the proposed equations are of higher order in spatial derivatives in a consideration of wave propagation. Wave propagation is no longer hyperbolic but dispersive in nature. Nevertheless, the resulting differences are only appreciable near the critical point obtained when a self-similar parabolic profile is used. Thus, the character of the flow upstream and downstream of the critical point is essentially determined by the self-similar, parabolic form. Consequently, flow can still be characterized as subcritical or supercritical upstream and downstream of the critical point because wave motion there is essentially governed by a hyperbolic equation. The dispersive, nonhyperbolic character is manifest only near the critical point and serves to bridge the upstream and downstream hyperbolic regimes.

Acknowledgment

The photograph was taken by Paul DeVries of Eastman Kodak Company.

References

[1] Kistler, S. F., and Schweizer, P. M., eds., 1997, *Liquid Film Coating*, Chapman & Hall, New York.
[2] Ruschak, K. J., and Weinstein, S. J., 1999, "Viscous Thin-Film Flow Over a Round-Crested Weir," ASME J. Fluids Eng., **121**, pp. 673–677.
[3] Ruschak, K. J., and Weinstein, S. J., 2000, "Thin-Film Flow at Moderate Reynolds Number," ASME J. Fluids Eng., **122**, pp. 774–778.
[4] Ruschak, K. J., and Weinstein, S. J., 2001, "Developing Film Flow on an Inclined Plane With a Critical Point," ASME J. Fluids Eng., **123**, pp. 698–702.
[5] Higuera, F. J., 1994, "The Hydraulic Jump in Viscous Laminar Flow," J. Fluid Mech., **274**, pp. 69–92.
[6] Levich, V. G., 1962, *Physicochemical Hydrodynamics*, Prentice-Hall, Englewood Cliffs, NJ, Chap. 12.
[7] Schlichting, H., 1979, *Boundary-Layer Theory*, 7th Ed., McGraw-Hill, New York, pp. 157–158.
[8] Atkinson, B., and McKee, R. L., 1964, "A Numerical Investigation of Non-uniform Film Flow," Chem. Eng. Sci., **19**, pp. 457–470.
[9] Weinstein, S. J., and Ruschak, K. J., 1999, "On the Mathematical Structure of Thin Film Equations Containing a Critical Point," Chem. Eng. Sci., **54**(8), pp. 977–985.
[10] Weinstein, S. J., and Ruschak, K. J., 2001, "Dip Coating on a Planar Non-vertical Substrate in the Limit of Negligible Surface Tension," Chem. Eng. Sci., **56**, pp. 4957–4969.

[11] Hassan, N. A., 1967, ''Laminar Flow Along a Vertical Wall,'' ASME J. Appl. Mech., **34**, pp. 535–537.
[12] Bohr, T., Putkaradze, V., and Watanabe, S., 1997, ''Averaging Theory for the Structure of Hydraulic Jumps and Separation in Laminar Free-Surface Flows,'' Phys. Rev. Lett., **79**, pp. 1038–1041.
[13] Bohr, T., Ellegaard, C., Hansen, A. E., and Haaning, A., 1996, ''Hydraulic Jumps, Flow Separation and Wave Breaking: An Experimental Study,'' Physica B, **228**, pp. 1–10.
[14] Schwartz, L. W., and Weidner, D. E., 1995, ''Modeling of Coating Flows on Curved Surfaces,'' J. Eng. Math., **29**, pp. 91–103.
[15] Roy, R. V., Roberts, A. J., and Simpson, M. E., 2002, ''A Lubrication Model of Coating Flows Over a Curved Substrate in Space,'' J. Fluid Mech., **454**, pp. 235–261.
[16] Berger, R. C., and Carey, G. F., 1998, ''Free Surface Flow Over Curved Surfaces. Part I: Perturbation Analysis,'' Int. J. Numer. Methods Fluids, **28**, pp. 191–200.
[17] Roy, T. R., 1984, ''On Laminar Thin-Film Flow Along a Vertical Wall,'' ASME J. Appl. Mech., **51**, pp. 691–692.
[18] Alekseenko, S. V., Nakoryakov, V. E., and Pokusaev, B. G., 1994, *Wave Flow of Liquid Films*, Begell House, New York.
[19] Ruschak, K. J., 1978, ''Flow of a Falling Film Into a Pool,'' AIChE J., **24**, pp. 705–710.
[20] Miller, C. A., and Neogi, P., 1995, *Interfacial Phenomena: Equilibrium and Dynamic Effects*, Marcel Dekker, New York.
[21] Ruschak, K. J., 1980, ''A Method for Incorporating Free Boundaries With Surface Tension in Finite Element Fluid-Flow Simulators,'' Int. J. Numer. Methods Eng., **15**, pp. 639–648.
[22] Watson, E. J., 1964, ''The Radial Spread of a Liquid Jet Over a Horizontal Plane,'' J. Fluid Mech., **20**, pp. 481–499.

Effects of Concave Curvature on Boundary Layer Transition Under High Freestream Turbulence Conditions

Michael P. Schultz
e-mail: mschultz@usna.edu

Ralph J. Volino
e-mail: volino@usna.edu

Department of Mechanical Engineering,
United States Naval Academy,
Annapolis, MD 21402

An experimental investigation has been carried out on a transitional boundary layer subject to high (initially 9%) freestream turbulence, strong acceleration ($K=(\nu/U_w^2)\times(dU_w/dx)$ as high as 9×10^{-6}), and strong concave curvature (boundary layer thickness between 2% and 5% of the wall radius of curvature). Mean and fluctuating velocity as well as turbulent shear stress are documented and compared to results from equivalent cases on a flat wall and a wall with milder concave curvature. The data show that curvature does have a significant effect, moving the transition location upstream, increasing turbulent transport, and causing skin friction to rise by as much as 40%. Conditional sampling results are presented which show that the curvature effect is present in both the turbulent and nonturbulent zones of the transitional flow. [DOI: 10.1115/1.1522410]

Introduction

Boundary layer transition is influenced by a number of factors, including streamwise pressure gradient, freestream turbulence intensity (FSTI), surface curvature, compressibility, and surface roughness. In gas turbine environments, Mayle [1] states that a substantial fraction of the boundary layer on both sides of a gas turbine airfoil may be transitional. The extended transition zones exist due to strong favorable pressure gradients, found on both the pressure side and the leading section of the suction side, which stabilize the boundary layer and delay transition in spite of the high freestream disturbance levels in gas turbine environments. The ability to model and predict high FSTI transition is important since heat transfer rates, skin friction coefficients, and in some cases boundary layer separation depend strongly on the state of the boundary layer with respect to transition. Improved transition models and turbine designs depend, therefore, on a better understanding of high FSTI transition.

The role of surface curvature on high FSTI transition is not fully understood. Mayle [1] states that transition onset is controlled by the freestream turbulence and the periodic unsteadiness caused by wakes from upstream airfoils. He notes that the turbulent spot production rate, which determines the length of the transition region, is controlled primarily by the freestream disturbance and the streamwise pressure gradient, but that curvature may play a secondary role. The extent of this secondary role is largely unknown, as only limited data exist from convex surfaces and ''virtually no reliable data'' are available from concave surfaces for computation of spot production rates, [1]. Determining the significance of curvature is potentially important for improved turbine design. If curvature is not significant, both modeling of transitional boundary layers and future experimental studies may be simplified, as results from flat-plate studies may be directly applied to curved airfoils. If curvature is found to be significant, its effects should be incorporated into future transition models.

Reasonable arguments can be made both for and against the importance of curvature on high FSTI transition. Low FSTI results suggest that curvature is important. Görtler [2] determined theoretically that convex curvature is stabilizing and that concave curvature is destabilizing. He predicted the formation of streamwise vortices (now known as Görtler vortices) on concave surfaces. Liepmann [3] confirmed these results experimentally under low FSTI conditions. He showed that convex curvature only slightly delays transition, but that concave curvature can cause transition to occur significantly earlier. Transition occurred when the Görtler number, G, was between 6 and 9, decreasing with the FSTI. These results have been confirmed in several subsequent studies. Floryan [4] and Saric [5] provide reviews. Volino and Simon [6] provide recent documentation from a zero pressure gradient case, and Finnis and Brown [7] considered a favorable pressure gradient case. In a low FSTI, fully turbulent boundary layer, Simonich and Moffat [8] showed that concave curvature of strength comparable to gas turbine conditions resulted in about a 20% enhancement in heat transfer over flat-plate results.

While the low FSTI studies show the importance of concave curvature, the results of high FSTI investigations are less clear. Data from fully turbulent boundary layers again suggest that curvature is important. Kim et al. [9] documented cases with inlet FSTI of 8% on both flat and concave walls, and showed increased turbulent activity and an enhancement of heat transfer by about 16% on the concave wall. Kestoras and Simon [10] documented a boundary layer with 8% inlet FSTI moving from a concave wall onto a flat wall. They showed an almost immediate drop in turbulence within the boundary layer as the flow moved onto the flat wall. They postulated a synergistic effect between curvature and freestream turbulence, stating that when concave curvature and high FSTI are combined, the freestream eddies are able to penetrate closer to the wall than in a flat wall flow, resulting in significantly higher transport within the boundary layer.

Only a few studies have documented transition with high FSTI. On surfaces subject to zero streamwise pressure gradients, Blair [11], Sohn and Reshotko [12], and Kim et al. [9] all showed that at FSTI above about 3%, transition occurred rapidly near the leading edge of a test surface. Hence, little documentation of transition is provided in these cases. Kim et al. [9] included a concave curvature case, and found no evidence of Görtler vortices. They proposed that the enhanced turbulent transport caused by the high FSTI and early transition lowered the effective Görtler number and suppressed the formation of the vortices. Since Görtler vortices change the transition mechanism and promote early transition under low FSTI conditions, [6], their absence under high FSTI might suggest that curvature does not play a strong role in high

Contributed by the Fluids Engineering Division for publication in the JOURNAL OF FLUIDS ENGINEERING. Manuscript received by the Fluids Engineering Division July 12, 2001; revised manuscript received July 26, 2002. Associate Editor: K. B. M. Q. Zaman.

FSTI transition. Riley et al. [13] considered zero pressure gradient cases on concave walls with inlet FSTI as high as 7.2%. Their results indicate that with very strong curvature ($(r/\theta_s)^{0.5}<20$), transition start is delayed relative to flat wall results. They reported the presence of Görtler vortices, and attributed the delayed transition to increased near-wall velocity gradients caused by the vortices. In cases with curvature representative of gas turbine conditions ($(r/\theta_s)^{0.5}>30$), as indicated by Mayle [1]), Riley et al. [13] showed no significant difference in transition start between concave and flat wall results. They did not provide a correlation for transition end.

Extended transition regions do occur when high FSTI is combined with strong acceleration. Results are available from turbine cascade and rotating rig studies (e.g., Halstead et al. [14]), but in these cases the effects of airfoil curvature, while present, cannot be isolated. Volino and Simon [15–17] considered transition along a concave wall with inlet FSTI of 8% and acceleration with K as high as 9×10^{-6}. Acceleration rates, Reynolds numbers and FSTI were typical of the pressure side of a gas turbine airfoil. The strength of curvature, $(r/\theta_s)^{0.5}=53$, was mild relative to gas turbine conditions. An extended transition region, with intermittent turbulent and nonturbulent zones, covered most of the test surface. Although detailed documentation of the transition was provided, no comparison case from a flat wall was available, so the effect of the concave curvature could not be determined. Volino and Simon [17] stated that the curvature effect was probably small, since the strong acceleration, by suppressing the growth of the boundary layer, kept the strength of curvature low. In contrast, Volino [18] presented a model incorporating freestream turbulence and curvature effects and used it to predict that the curvature effect in the Volino and Simon [15–17] case might be substantial. As stated above, no experimental data were available to verify the prediction.

The present study addresses the significance of concave curvature directly. The case presented by Volino and Simon [15–17] has been reproduced on a flat test wall, and a concave wall with strong curvature ($(r/\theta_s)^{0.5}=27$). The flat wall results were presented in detail by Volino et al. [19]. In the present paper the concave wall results are presented and compared to the flat wall results and the weaker concave curvature case of Volino and Simon [15–17].

Experiments

Facility and Measurements. All experiments were conducted in the same low speed wind tunnel described in detail by Volino et al. [19] and shown in Fig. 1. The only change to the facility for the present study was the replacement of a flat-plate test section with a curved, converging channel. The facility is very similar to that used by Volino and Simon [17], again with the exception of the curvature of the test wall. One side of the present test section is a concave curved Plexiglas surface of 0.69 m width and 0.80 m length, which serves as the test wall. This wall has a constant radius of curvature of 25.4 cm. Pressure taps are installed along its spanwise centerline. At the leading edge of the test wall a slot is used to bleed off the boundary layer which grows in the development section between the turbulence generator and the leading edge. Opposite the test wall is a flexible convex wall that can be adjusted to set the desired pressure gradient along the test wall. For the present study the inlet velocity is set to 4.6 m/s and the velocity gradient along the wall is held constant at 13.9 s^{-1}, matching the previous flat wall, [19], and mild concave curvature, [17], cases.[1] The acceleration parameter, K, drops from a maximum of 9×10^{-6} at the inlet to the test section to 1×10^{-6} at the last measurement station. The FSTI at the inlet to the test section is 8.6%, based on all three components of the fluctuating velocity. Further details of the freestream turbulence including spectra and length scales are given in Volino et al. [19]. Within the test section, the streamwise component of the freestream turbulence, $\overline{u'_\infty}$, remains nearly constant at ~0.35 m/s, but $\overline{v'_\infty}$ increases from 0.50 m/s to 0.73 m/s. On the flat wall, $\overline{u'_\infty}$ decreased in the streamwise direction while $\overline{v'_\infty}$ remained nearly constant. It should be noted, however, that these values are based on data at the measurement point most distant from the wall ($y=30$ mm). While $\overline{u'_\infty}$ and $\overline{v'_\infty}$ on the flat wall and $\overline{u'_\infty}$ on the concave wall reach their freestream value by this location, $\overline{v'_\infty}$ is still changing with distance from the wall at several streamwise stations on the concave wall. Freestream turbulence intensity (normalized using the local freestream velocity) drops in the streamwise direction in both the concave and flat wall cases, mainly due to the increasing freestream velocity. Values of K through the test section, measurement locations, and other parameters are shown in Table 1.

Velocity profile measurements were made at nine streamwise stations along the centerline of the test wall using a single sensor, boundary layer type hot-wire probe (TSI model 1218-T1.5), a boundary layer cross-wire probe (TSI model 1243-T1.5) and a constant-temperature hot-wire anemometer (TSI model IFA-100). The probes were moved normal to the wall at each station using a manual traversing stage with a minimum increment of 10 μm. At each position in the velocity profiles, data were acquired for 26 seconds at a 20 kHz sampling rate (2^{19} data points). The hot-wire signals were low-pass filtered at 10 kHz. All raw data were stored. Sampling at 20 kHz provided essentially continuous velocity traces for subsequent processing as detailed in Volino et al. [19]. Mean and rms fluctuating velocities in the streamwise and wall-normal directions were computed from the instantaneous data. Uncertainties in these quantities are 3–5% except in the very near wall region ($y^+<5$) where near-wall corrections (Wills [22]) are applied to the mean velocity. Uncertainty in the turbulent shear stress, $-\overline{u'v'}$, is 10%. Skin friction coefficients were determined using a technique whereby τ_w was adjusted until the U^+ versus y^+ data fit profiles computed using near-wall similarity, as described by Volino and Simon [23]. This technique accounts for pressure gradient effects on the near wall profile. Uncertainty in C_f is 8%. Boundary layer thicknesses were determined from the mean velocity profiles. Uncertainties in the momentum and displacement thicknesses are 10%. These uncertainties include bias errors which tend to cancel such that the uncertainty in the shape factor, H, is 7%. The intermittency function, which indicates whether the boundary layer is instantaneously turbulent or nonturbulent, was calculated using both the instantaneous streamwise velocity, u, and the instantaneous turbulent shear stress, $-u'v'$, as described by Volino et al. [19]. The overall uncertainty in the time-averaged intermittency, γ, is 0.1. The instantaneous intermittency function was used to separate the turbulent and nonturbulent

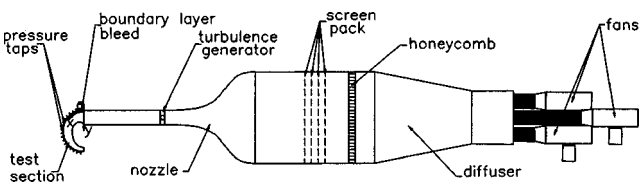

Fig. 1 Schematic of the test facility

[1]The nominal "freestream" velocity for the concave wall cases is not so clear as in the corresponding flat wall case. On a flat wall, the velocity gradient $\partial U/\partial y$ approaches zero outside the boundary layer, so the freestream velocity is independent of the distance from the wall. Curvature induces a nonzero $\partial U/\partial y$, which under low FSTI conditions approaches the potential flow solution for a curved channel. With high FSTI, however, the combination of streamwise curvature and freestream turbulence results in cross transport of momentum, as described by Eckert [20], and deviation from the potential flow solution. The gradient $\partial U/\partial y$ is approximately constant in the freestream, so following the procedure of Kestoras and Simon [21], a straight line is fit to the mean velocity data in the freestream at each station and extrapolated to the wall ($y=0$). This extrapolated velocity, designated U_w, is used as the freestream velocity for the concave wall case.

Table 1 Flow parameters at measurement stations

St	x [m]	U_w [m/s]	$\frac{\overline{u'}_\infty}{U_w}$ [%]	$\frac{\overline{v'}_\infty}{U_w}$ [%]	K $\times 10^6$	γ_{pk} [%]	$\delta_{99.5}$ [mm]	Re_x $\times 10^{-5}$
1	0.119	5.94	6.0	8.1	6.01	12.	4.89	0.39
2	0.189	7.25	4.5	7.3	4.06	11.	4.69	0.91
3	0.268	8.49	3.6	6.6	2.96	24.	5.37	1.51
4	0.345	9.53	3.2	6.0	2.35	49.	6.09	2.19
5	0.433	11.0	2.8	5.6	1.79	68.	7.00	3.14
6	0.503	12.0	2.6	5.2	1.50	81.	9.29	3.98
7	0.581	13.0	2.5	5.0	1.27	91.	10.8	5.00
8	0.659	14.0	2.4	4.9	1.10	97.	13.9	6.11
9	0.736	14.6	2.4	4.8	1.00	99.	12.6	7.13

St	Re_θ	H	G	$C_f\times 10^3$	Re_θ	H	$C_f\times 10^3$	Re_θ	H	$C_f\times 10^3$
	composite				non-turbulent			turbulent		
1	133	1.79	5.3	9.0	134	1.77	9.0	124	1.54	14.3
2	143	1.80	4.9	8.0	140	1.81	8.0	162	1.45	13.0
3	172	1.75	6.0	7.2	156	1.83	7.2	241	1.41	10.8
4	193	1.71	6.7	7.3	147	1.88	7.0	321	1.38	9.7
5	247	1.59	9.0	7.0	152	1.91	6.7	378	1.38	8.4
6	310	1.53	12.2	7.0	155	1.93	6.5	509	1.33	8.0
7	384	1.44	16.1	7.1	159	1.91	6.4	598	1.30	7.7
8	461	1.44	20.4	7.0	160	1.96	6.0	777	1.27	7.2
9	483	1.45	21.4	6.8	152	2.04	5.7	788	1.29	7.0

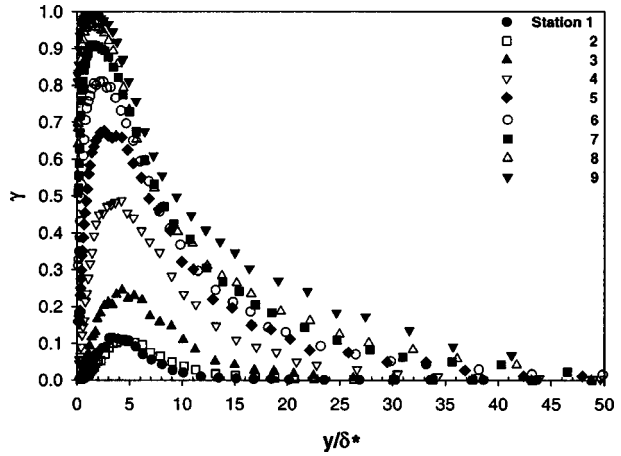

Fig. 2 Intermittency profiles based on u

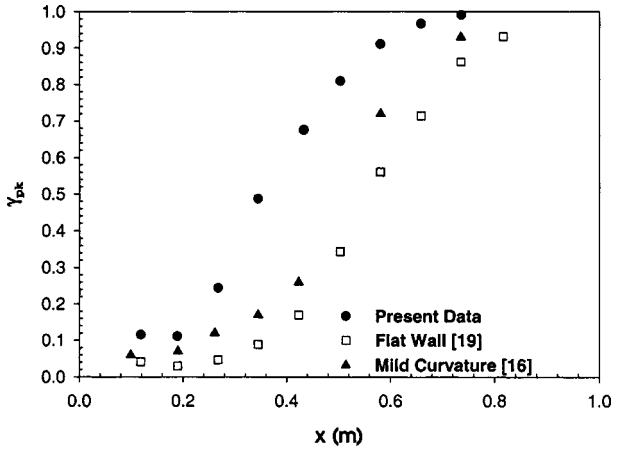

Fig. 3 Intermittency factor versus streamwise distance

zones of the boundary layer for conditional sampling. In the figures which follow, data points are shown for the nonturbulent zone only when the local $\gamma<95\%$, and for the turbulent zone only when $\gamma>5\%$. Bulk parameters such as C_f are presented when $\gamma_{pk}<95\%$ and $\gamma_{pk}>5\%$ for the nonturbulent and turbulent zones, respectively.

Results

Intermittency. Intermittency profiles for the nine measurement stations are shown in Fig. 2. These results were computed using the instantaneous streamwise velocity, u. Although not presented here, intermittency profiles based on the instantaneous tur-

Table 2 Transition start and end locations

Case	$(r/\theta_s)^{0.5}$	x_s [m]	x_e [m]	$\hat{n}\sigma\times 10^{11}$
Flat [19]	∞	0.29	0.98	4.2
Mild Curve [17]	53	0.23	0.90	5.5
Strong Curve	27	0.12	0.75	10.

bulent shear stress always agreed with those in Fig. 2 to within 0.10 and were generally within 0.05. The intermittency remains nonzero well away from the wall, to y/δ^* as high as 40. In the flat wall case, Volino et al. [19] showed γ approaching zero by $y/\delta^*=10$. Something in the concave wall case promotes turbulence well away from the wall. The peak intermittency in each profile is shown in Fig. 3 and compared to results from the flat wall and mild curvature cases. The intermittency remains fairly low ($\gamma_{pk}\sim 10\%$) for the first two stations of the strong curvature case and then starts to rise. Note that even at the first station, the intermittency is higher than that measured in the other two cases. For all these cases, the beginning of the rise in γ corresponds to K dropping below 3×10^{-6}. In low FSTI boundary layers, $K>3\times10^{-6}$ leads to relaminarization (Jones and Launder [24]). By the last station, transition is complete in the strong curvature case, whereas the flat and mildly curved wall cases are only approaching the end of transition. Following the technique of Narasimha [25], as modified by Volino and Simon [26], the function

$$f(\gamma_{pk})=(-\ln(1-\gamma_{pk}))^{1/2} \tag{1}$$

can be computed based on the peak intermittency at each station and plotted versus streamwise location. The data in these coordinates tend to lie along a straight line. The line may be extrapolated to $f(\gamma_{pk}=0)=0$ and $f(\gamma_{pk}=0.99)=2.146$, corresponding to the beginning and end of transition. Transition start and end locations for the three cases are listed in Table 2. Figure 4 shows γ_{pk} plotted versus dimensionless streamwise location within transition. Also shown is the theoretical curve

$$\gamma_{pk}=\exp\left(-4.6\left(\frac{x-x_s}{x_e-x_s}\right)^2\right) \tag{2}$$

based on the Dhawan and Narasimha [27] transition model. Agreement between the data and theory is good. Differences from Eq. (2) are seen at low γ in all the cases. This is termed ''subtransition'' [25] and is expected in favorable pressure gradient flows. The Dhawan and Narasimha [27] model assumes a concentrated breakdown or formation of turbulent spots at the transition start location. In fact, spots are formed over some finite distance in the streamwise direction in a distributed breakdown. Favorable pressure gradients stabilize the boundary layer and extend this region, resulting in the subtransition. The presence of the subtransition means that the actual start of transition does not occur at the x_s location given in Table 2. The x_s and x_e value do, however, indicate the rate at which transition proceeds. The mild curvature case completes transition slightly upstream of the flat wall case, and the strong curvature case completes transition well upstream of the other two cases. Since curvature is the only difference between the cases, it is clear that concave curvature has a significant effect on transition.

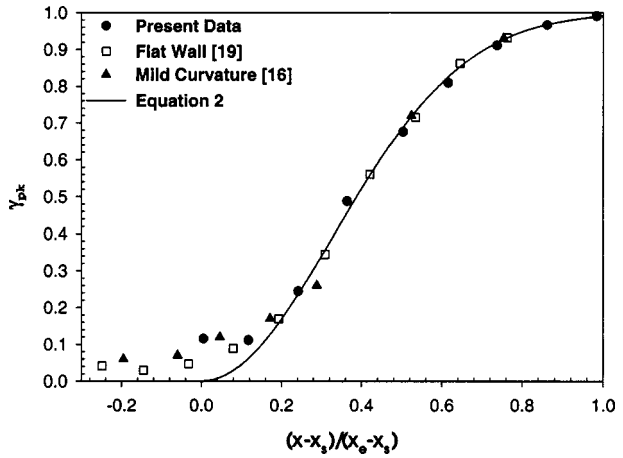

Fig. 4 Peak intermittency in profile versus dimensionless streamwise location

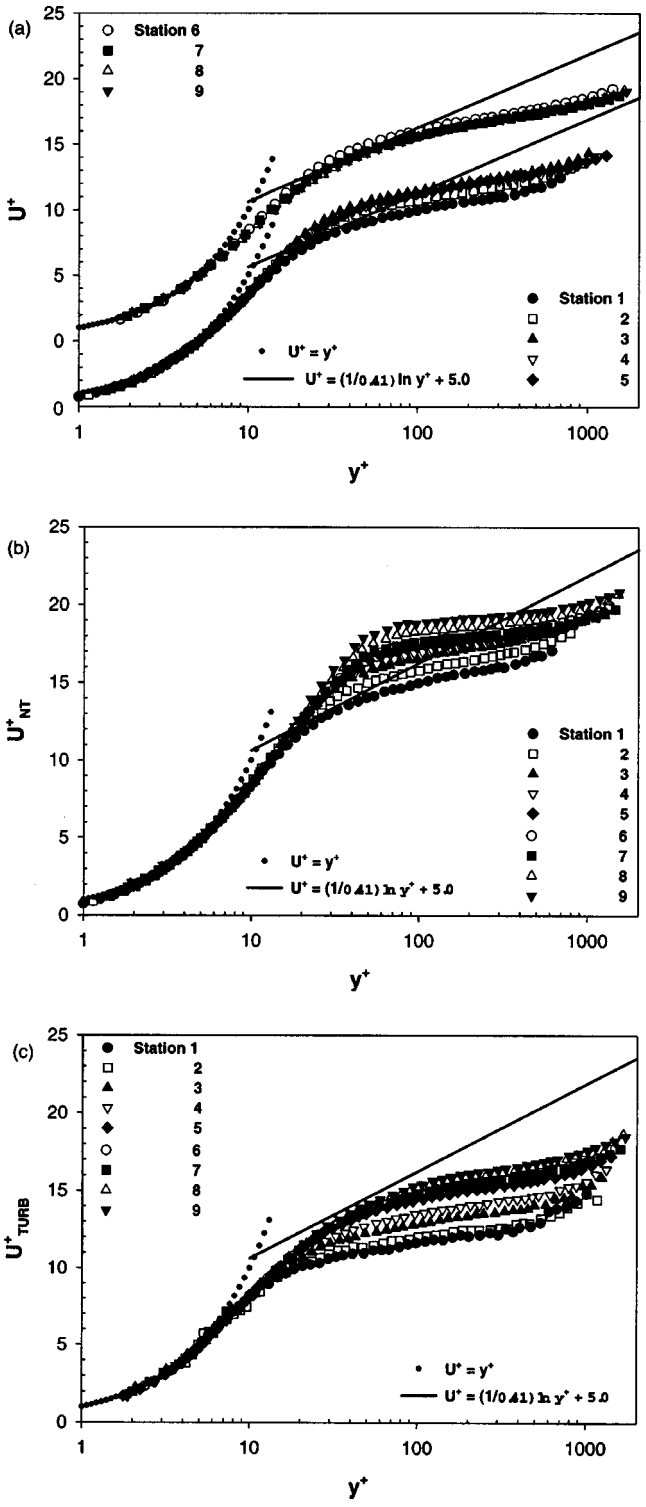

Fig. 5 Mean velocity profiles in wall coordinates: (*a*) composite; (*b*) nonturbulent; (*c*) turbulent

The dimensionless turbulent spot propagation rate (Mayle [1]) may be computed as

$$\hat{n}\sigma=\frac{4.6\nu^2\overline{U}_\infty}{(x_e-x_s)^2U_s^3} \tag{3}$$

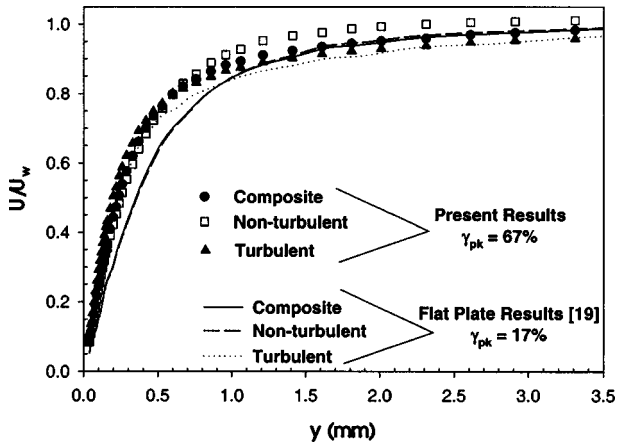

Fig. 6 Mean velocity profile for Station 5

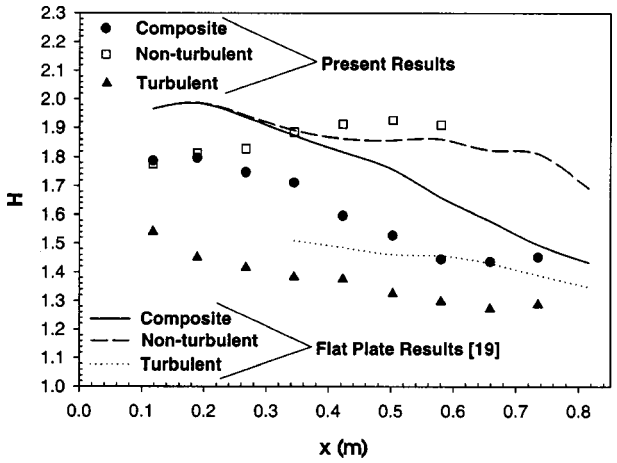

Fig. 8 Shape factor versus streamwise distance

where $\overline{U}_\infty$ is the average freestream velocity in the transition region. In the strong curvature case $\hat{n}\sigma = 1.0\times10^{-10}$. For the flat wall case and the mild curvature case, $\hat{n}\sigma$ was 4.2×10^{-11} and 5.5×10^{-11}, respectively. These values are in agreement with the trends reported by Mayle [1] for other favorable pressure gradient cases and are three to five times less than would be expected for a zero pressure gradient case with the same FSTI at the beginning of transition. It appears that wall curvature, FSTI and pressure gradient are all important parameters in determining the spot propagation rate.

Mean Velocity Profiles. Mean velocity profiles for the nine measurement stations of the strong curvature case are presented in Fig. 5 in wall coordinates. Figure 5(a) shows the composite (unconditioned) profiles. Figures 5(b) and 5(c) show turbulent and nonturbulent zone results from conditional sampling of the data. The composite profiles vary only slightly through Station 5. For the remaining downstream stations, the profiles collapse to a turbulent-like shape. Even the most upstream stations do not exhibit the laminar-like shape that was seen in the flat wall results of Volino et al. [19]. At Stations 7–9, where the acceleration rate has dropped to $K<1.5\times10^{-6}$ and transition is complete or nearly so, the profiles agree with the zero pressure gradient law of the wall, although the log-law region is quite small. The short log-law region is a consequence of the combined concave curvature and high FSTI that gives rise to significant momentum transport and result in a large, negative wake strength. The nonturbulent zone profiles (Fig. 5(b)) exhibit a laminar-like shape, even at the end of transition, as was also seen in the flat wall case. The turbulent zone profiles (Fig. 5(c)) exhibit a more turbulent-like shape, and the last five stations collapse. Note that the data at even the most downstream station falls slightly below the zero pressure gradient law of the wall, again due to the enhanced momentum transport in the outer part of the boundary layer. Examination of the results in [19] shows that this effect is not as strong on the flat wall, where there is better agreement with the zero-pressure gradient law of the wall.

Figure 6 shows the differences between the composite, nonturbulent, and turbulent profiles at Station 5, in the center of the transition zone ($\gamma_{pk}=0.67$). Also shown for comparison are the results for the flat wall at the same streamwise position, which was closer to the start of transition ($\gamma_{pk}=0.17$). On the concave wall, velocities in the near wall region are slightly higher in the turbulent zone than in the nonturbulent zone due to higher levels of turbulent mixing. Differences between the zones are not as dramatic as on the flat wall, however. While this might be attributed to the difference in the intermittency for the two cases at this streamwise position, it is also observed when comparing profiles from the two cases with the same intermittency and different streamwise locations. The enhanced mixing induced by the curvature results in higher near wall velocities, particularly in the nonturbulent zone. In the concave wall case, as in the flat wall case, the nonturbulent zone of the boundary layer never behaves as if it were laminar due to the freestream buffeting the boundary layer. This is explained further in Volino [18].

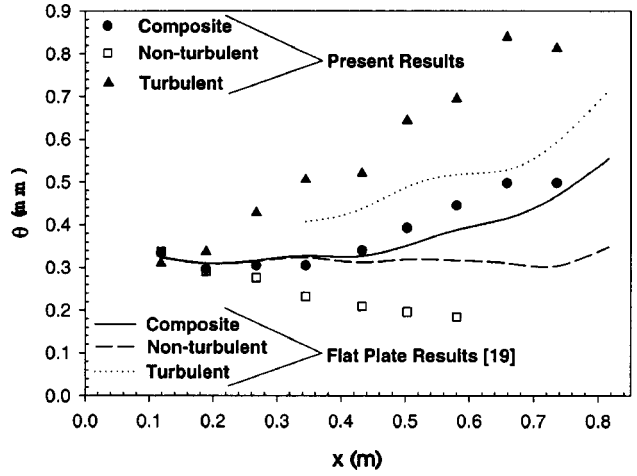

Fig. 7 Momentum thickness versus streamwise distance

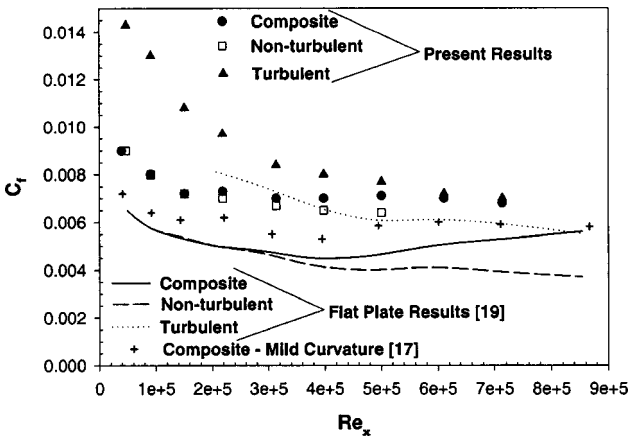

Fig. 9 Comparison of skin-friction coefficient

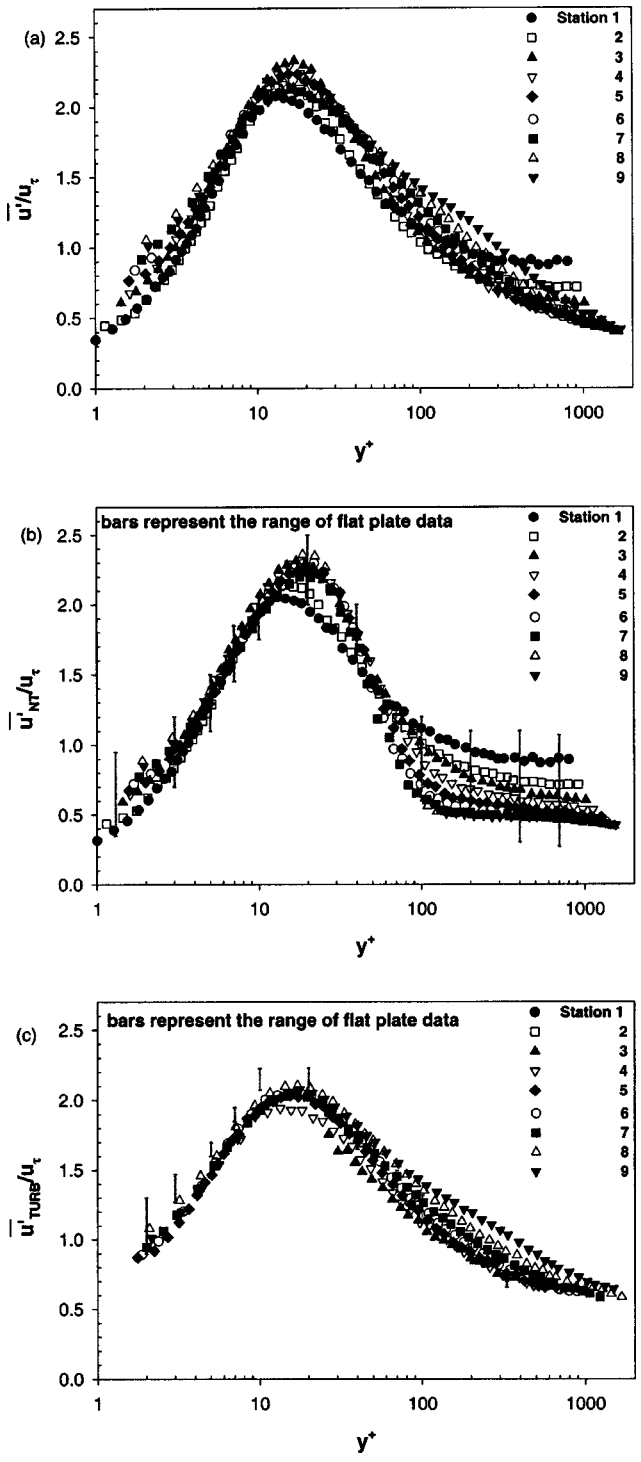

Fig. 10 Fluctuating streamwise velocity profiles in wall coordinates: (*a*) composite; (*b*) nonturbulent; (*c*) turbulent

Boundary Layer Growth. Figure 7 shows the momentum thickness plotted versus streamwise position. On the concave wall, the composite flow momentum thickness remains nearly constant through the first five stations and then increases as K drops and transition nears completion. In the nonturbulent zone, the momentum thickness drops somewhat in the streamwise direction. In contrast, the turbulent zone momentum thickness increases continuously. This is likely due to turbulent entrainment at the boundary layer edge, which appears to be more significant on the concave wall than the flat wall.

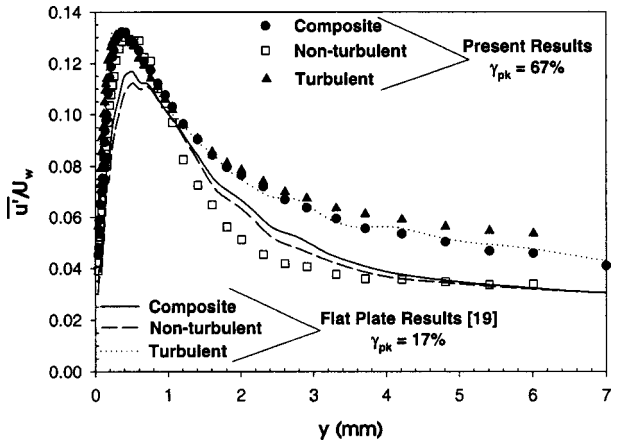

Fig. 11 Fluctuating streamwise velocity profile for Station 5

The shape factor, H, shown in Fig. 8, is an indicator of the state of the boundary layer with respect to transition. The composite flow shape factor drops from about 1.8 at Station 1 to 1.45 at Station 9. The decrease in H tracks the increase in γ_{pk} (Fig. 3). In the nonturbulent zone H increases slightly from 1.8 to about 2.0. A low FSTI laminar boundary layer on a flat wall with the same pressure gradient would have a shape factor of about 2.4. The shape factors below the laminar value agree with Fig. 6, which shows that the high FSTI makes the nonturbulent zone velocity profiles appear less laminar-like and more like those in the turbulent zone. In the turbulent zone, H drops from about 1.5 to 1.3. These values are significantly less than those for the flat wall case and suggest that the wall curvature promotes greater momentum transport in the turbulent zone even in a high FSTI, strongly accelerated boundary layer.

Skin Friction Coefficients. Skin friction coefficients, C_f, were computed from the mean velocity profiles and are plotted versus Re_x in Fig. 9. Composite flow results are presented for the flat wall, mild and strong curvature cases, and conditional sampling results are presented for the flat wall and strong curvature cases. The striking characteristic of the figure is that the nonturbulent, turbulent, and composite skin friction values in the strong curvature case are all significantly higher than in the flat wall case. The composite skin friction coefficient is as much as 56% higher and is an average of 42% higher than the flat wall case. The average increases in C_f in the nonturbulent and turbulent zone are 45% and 23%, respectively. These results indicate that wall curvature, even in the presence of strong acceleration and high FSTI, can lead to a significant increase in momentum transport in the boundary layer. The C_f values from the mild curvature case fall between the flat wall and strong curvature results as expected. The differences between the flat and curved wall cases shown in Figs. 5–9 are apparent even at the most upstream stations. This is not unreasonable since $G \approx 5$, and $(r/\theta_s)^{0.5} = 25$ by Station 1 of the strong curvature case.

Fluctuating Velocity. Figure 10 shows $\overline{u'}$ profiles in wall coordinates. The strong curvature composite flow results, shown in Fig. 10(a), are typical of transitional and turbulent boundary layers. The peak in $\overline{u'}/u_\tau$ occurs at $y^+ = 15$, and the magnitude of the peak is between 2 and 2.3. The nonturbulent and turbulent zone data are shown in Figs. 10(b) and 10(c), respectively. Included in these figures are bars showing the range of flat wall data from Volino et al. [19]. In the nonturbulent zone, the concave wall data show good agreement with the flat wall results. In the turbulent zone the data from all stations collapse, particularly near the wall, showing self-similarity throughout the transition region. In the near wall region $\overline{u'}/u_\tau$ on the concave wall is slightly but consistently reduced compared to the flat wall case. This indicates

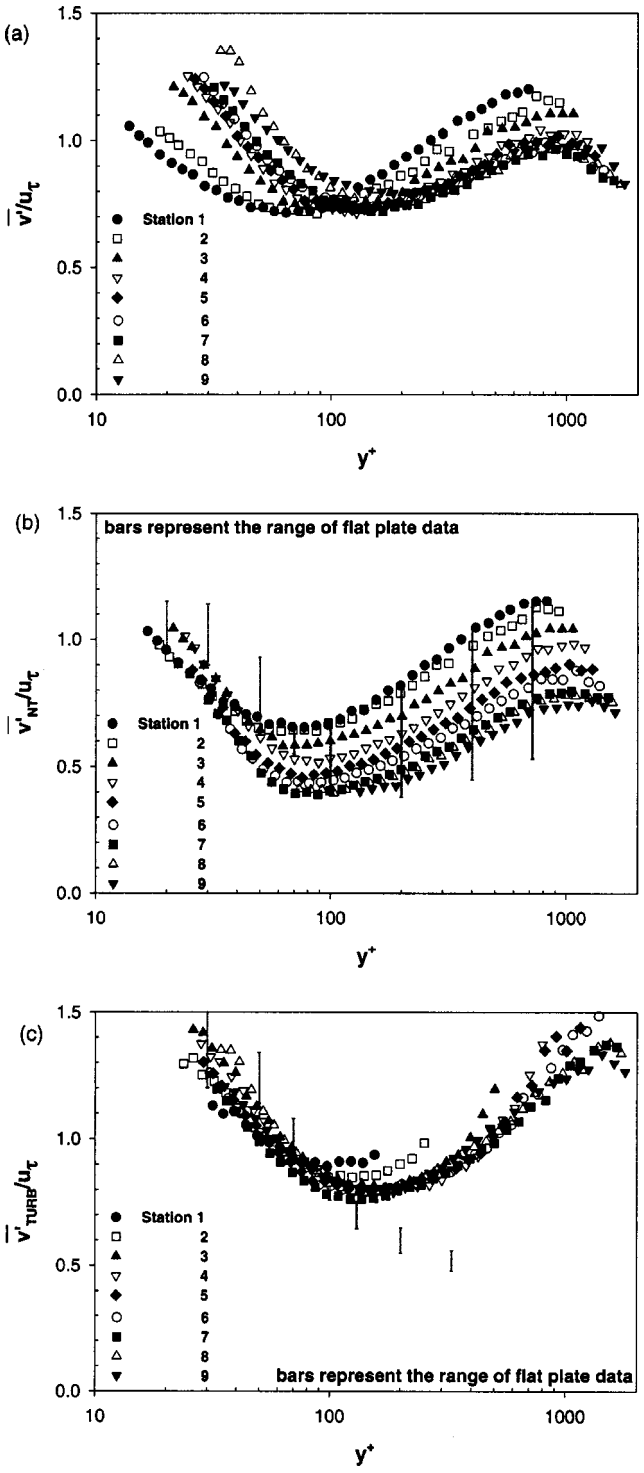

Fig. 12 Fluctuating wall-normal velocity profiles in wall coordinates: (*a*) composite; (*b*) nonturbulent; (*c*) turbulent

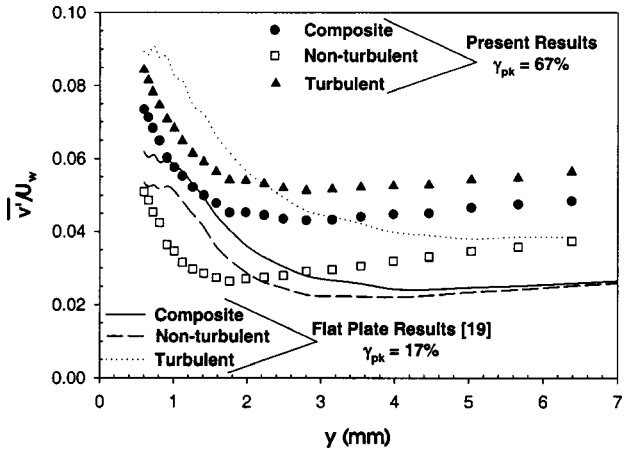

Fig. 13 Fluctuating wall-normal velocity profile for Station 5

higher skin friction relative to near wall turbulence on the concave wall, and may be due to higher mixing in the outer part of the boundary layer. In the outer region the two data sets show good agreement in wall coordinates. Figure 11 shows the $\overline{u'}$ profiles at Station 5, midway through transition on the concave wall. The peak in $\overline{u'}$ is slightly closer to the wall in the turbulent zone, but the magnitudes of the turbulent and nonturbulent peaks are very nearly equal. The difference between the turbulent and nonturbulent zones is much reduced from the flat wall case, indicating that something in the concave wall case is promoting fluctuations in the streamwise direction independent of turbulence.

Figure 12 shows the $\overline{v'}$ profiles. Figure 12(a) presents the composite flow results for the strong curvature case. The profiles are typical for a high FSTI boundary layer. They show a peak $\overline{v'}$ in the near wall region with a minimum farther from the wall followed by a rise to the freestream value. The minimum in $\overline{v'}$ results as the freestream turbulence is damped by the wall. The magnitude of $\overline{v'}/u_\tau$ rises in the near wall region as transition proceeds. As was also observed in the flat wall case of Volino et al. [19], $\overline{v'}$ is lower in magnitude and shows more change through the transition region than does $\overline{u'}$. As was the case for $\overline{u'}/u_\tau$, the turbulent zone results (Fig. 12(c)) for $\overline{v'}/u_\tau$ collapse for all of the stations. The major difference between the present results and the flat plate results is the high value of $\overline{v'}/u_\tau$ in the turbulent zone in the outer part of the boundary layer and the freestream on the concave wall. Another difference is the reduction in near wall $\overline{v'}/u_\tau$ in both zones relative to the flat wall case. As was observed for the turbulent zone $\overline{u'}/u_\tau$ profiles, higher mixing in the outer part of the concave wall boundary layer results in higher mean velocity gradients at the wall, raising the wall shear stress and u_τ. Higher u_τ reduces both $\overline{v'}/u_\tau$ and $\overline{u'}/u_\tau$ near the wall.

Figure 13 shows the $\overline{v'}$ profiles at Station 5. The magnitude of $\overline{v'}$ in the turbulent zone is almost double that in the nonturbulent zone across the entire profile. This is in contrast to the $\overline{u'}$ profiles of Fig. 11 that show the two zones to have very similar magnitudes. The same difference is also seen in the flat wall case. Volino [28] found that much of the unsteadiness in u is low-frequency unsteadiness induced by the freestream, and is a feature of both the turbulent and nonturbulent zones. The $\overline{v'}$ fluctuations, in contrast, are more closely related to near wall produced turbulence and eddy transport in the boundary layer. The differences between the turbulent and nonturbulent zones explain the rise in near wall $\overline{v'}$ in Fig. 12(a) as transition proceeds. Figure 13 also shows differences in $\overline{v'}$ between the concave and flat wall results. The concave wall $\overline{v'}$ profiles for both zones rise more rapidly near the wall, reach a minimum closer to the wall, and are higher at the edge of the boundary layer.

Turbulent Shear Stress. Turbulent shear stress profiles are shown in Fig. 14 in wall coordinates. In the composite profiles (Fig. 14(a)), the normalized turbulent shear stress increases through transition. In the nonturbulent zone the turbulent shear stress is low and comparable to the flat wall case results. In the turbulent zone (Fig. 14(c)), there is a significant increase in the normalized shear stress in the outer part of the boundary layer compared to the flat wall case. These outer region values increase

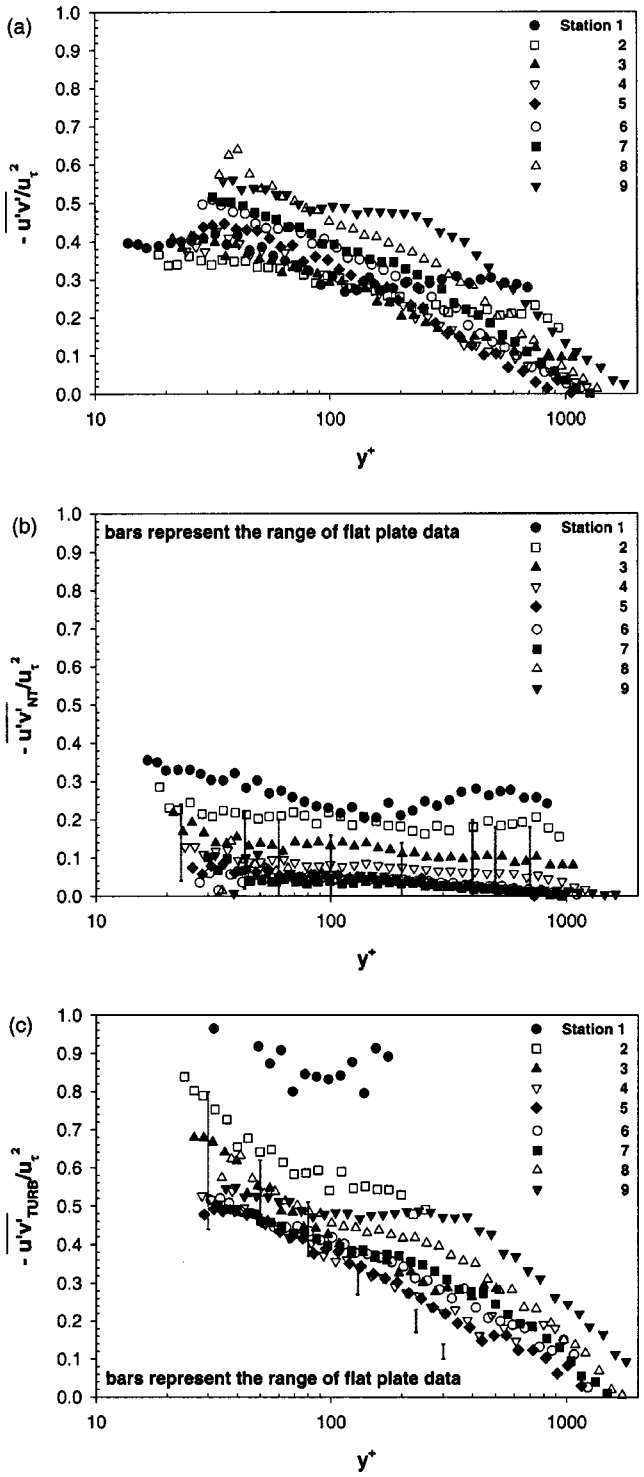

Fig. 14 Reynolds shear stress profiles in wall coordinates: (*a*) composite; (*b*) nonturbulent; (*c*) turbulent

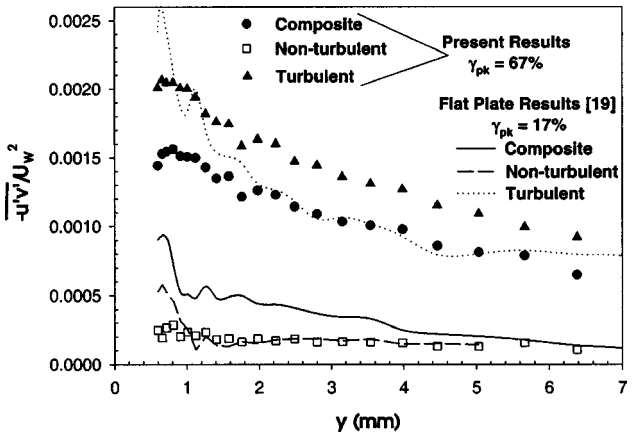

Fig. 15 Reynolds shear stress profile for Station 5

as the flow moves downstream, presumably due to the increasing strength of curvature as the boundary layer thickens. Figure 15 presents the turbulent and nonturbulent $-\overline{u'v'}$ profiles for Station 5. Similar to $\overline{v'}$ and in contrast to $\overline{u'}$, the magnitude of $-\overline{u'v'}$ is much higher in the turbulent zone than the nonturbulent. Although $-\overline{u'v'}$ is much smaller in the nonturbulent zone, it is nonzero. This indicates that some eddy transport of momentum occurs even when the boundary layer is nonturbulent. The figure also shows that turbulent zone $-\overline{u'v'}$ is about 20% higher on the concave wall than on the flat wall. The composite flow $-\overline{u'v'}$ profile is higher on the concave wall due to it being further through transition than the flat wall profile at the same streamwise location.

Profiles of the eddy viscosity are presented in Fig. 16. The composite profiles in Fig. 16(a) show that ε_M increases in the streamwise direction as the transition proceeds. Comparison of the nonturbulent and turbulent zone profiles in Figs. 16(b) and 16(c) shows that the eddy viscosity is much higher in the turbulent zone. While the difference between the two zones is clear, Fig. 16(b) shows that there is still significant eddy transport in the nonturbulent zone. It is also of note that the eddy diffusivity is significantly increased on the concave wall compared to the flat wall in both the turbulent and nonturbulent zones. As was noted for the turbulent shear stress of Fig. 14(c), the turbulent zone ε_M of Fig. 16(c) increases at the downstream stations, due to the rising strength of curvature as the boundary layer grows.

Streamwise Vortices. A possible explanation for the differences between the concave and flat wall cases might be the presence of Görtler vortices in the concave wall cases. The Görtler number at Station 3 of the strong curvature case is 6, indicating that it is possible that vortices could form. No evidence of stationary Görtler vortices was observed, however. Stationary vortices would result in spanwise variation in velocity profiles, but velocity profiles measured at different spanwise location and the same streamwise location were indistinguishable. Attempts at flow visualization using smoke did not reveal Görtler vortices, although the high FSTI tended to scatter the smoke quickly, making the flow visualization results inconclusive. If vortices were present it is unlikely that they would remain stationary. In a low FSTI case vortex location would be fixed by some small upstream disturbance such as an upstream screen in a wind tunnel. In the present case, the turbulence generating grid produces large, unsteady fluctuations which might be expected to induce nonstationary vortices. Nonstationary vortices might result in high $\overline{v'}$ away from the wall as the upwash and downwash locations of the vortices moved in the spanwise direction. Spectral analysis of $\overline{v'}$ in the present case showed a broadband peak centered at 30 Hz, which was not present in the flat wall case. This along with the high $\overline{v'}$ in the outer region (Fig. 12) suggests that nonstationary vortices may be present.

Conclusions

The effect of concave curvature on transitional boundary layers subject to high freestream turbulence and strong favorable pressure gradients has been documented. Despite the strong effects of the freestream turbulence and acceleration on transition, curvature still has a significant effect. Curvature causes higher momentum transport in the outer part of the boundary layer, resulting in a

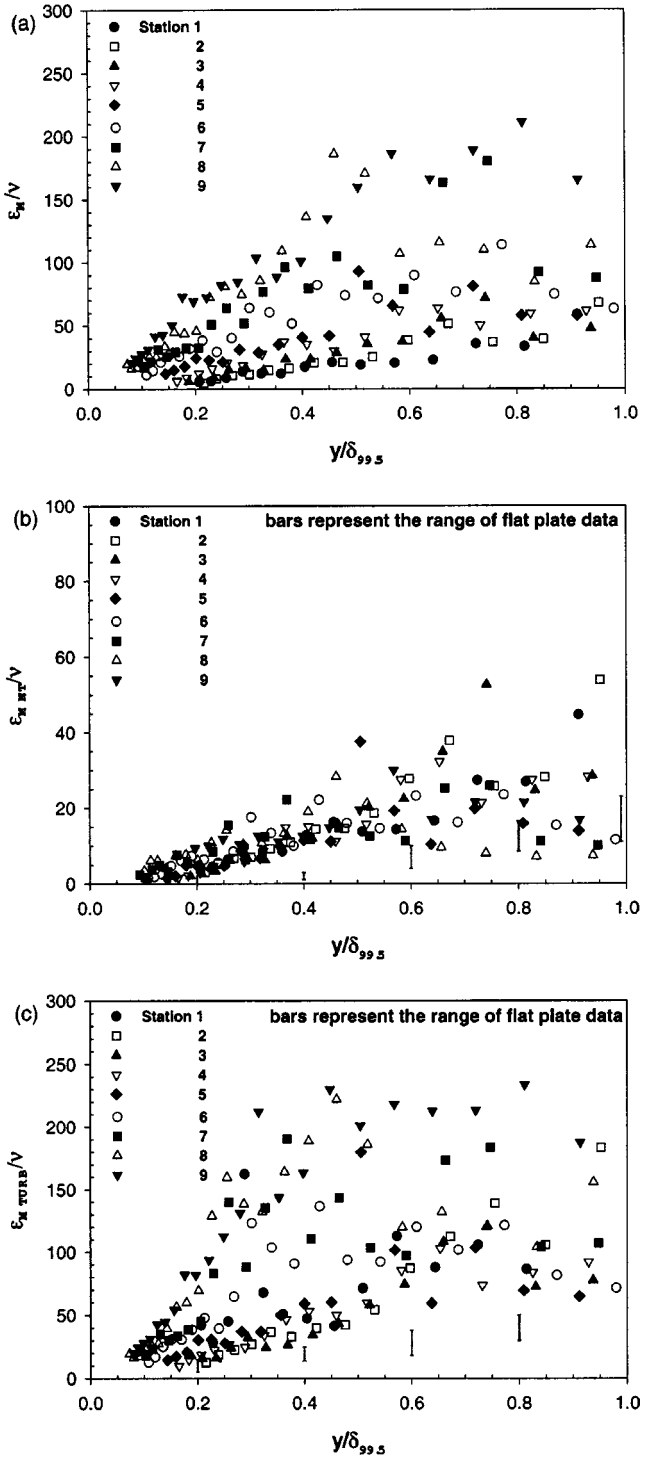

Fig. 16 Eddy viscosity profiles: (*a*) composite; (*b*) nonturbulent; (*c*) turbulent

more rapid transition to turbulence and higher skin friction. Conditional sampling shows that the curvature effect is present in both the turbulent and non-turbulent zones of the transitional flow. In the nonturbulent zone concave curvature produces mean and fluctuating velocity profiles that appear less laminar-like than in an equivalent flat wall case. In the turbulent zone curvature produces higher fluctuating velocity and turbulent shear stress in the outer part of the boundary layer. Nonstationary Görtler vortices are offered as a possible mechanism for the curvature effect on the boundary layer. Although some results which suggests the presence of vortices are presented, no direct evidence of their existence was found. Further study is needed to confirm the mechanism for the concave curvature effect.

Acknowledgments

Bill Beaver of the Technical Support Department at the U.S. Naval Academy constructed the test section. One of the authors (MPS) was supported by the Office of Naval Research as a postdoctoral fellow during the period of this work.

Nomenclature

C_f = $\tau_w/(\rho U_w^2/2)$, skin friction coefficient
FSTI = freestream turbulence intensity
$f(\gamma_{pk})$ = function of intermittency, Eq. (1)
G = $Re_\theta(\theta/r)^{0.5}$, Görtler number
H = δ^*/θ, shape factor
K = $(\nu/U_w^2)(dU_w/dx)$, acceleration parameter
$\hat{n}$ = dimensionless turbulent spot production rate
Re_x = $U_w x/\nu$, Reynolds number
Re_θ = momentum thickness Reynolds number
r = radius of curvature of test wall
U = time-averaged local streamwise velocity
U_w = local freestream velocity extrapolated to the wall
U_∞ = average freestream velocity in transition region
u = instantaneous streamwise velocity
U^+ = U/u_τ, local mean streamwise velocity in wall coordinates
$\overline{u'}$ = rms streamwise fluctuating velocity, $\sqrt{\overline{u'^2}}$
u_τ = $\sqrt{\tau_w/\rho}$, friction velocity
$-u'v'$ = instantaneous turbulent shear stress
$-\overline{u'v'}$ = time-averaged turbulent shear stress
$\overline{v'}$ = rms cross-stream fluctuating velocity, $\sqrt{\overline{v'^2}}$
x = streamwise coordinate, distance from leading edge
y = cross-stream coordinate, distance from wall
y^+ = yu_τ/ν, distance from wall-in-wall coordinates
$\delta_{99.5}$ = 99.5% boundary layer thickness
δ^* = displacement thickness
ε_M = $-\overline{u'v'}/(dU/dy)$, eddy viscosity
γ = time-averaged intermittency, fraction of time flow is turbulent
γ_{pk} = peak intermittency in profile
ν = kinematic viscosity
ρ = density
θ = momentum thickness
σ = turbulent spot propagation parameter
τ_w = wall shear stress

Subscripts

s = transition start
e = transition end
∞ = local freestream condition
w = extrapolated to the wall
NT = nonturbulent zone
TURB = turbulent zone

References

[1] Mayle, R. E., 1991, "The Role of Laminar-Turbulent Transition in Gas Turbine Engines," ASME J. Turbomach., **113**, pp. 509–537.
[2] Görtler, H., 1941, "Instabilität Laminarer Grenzchichten an Konkaven Wänder Gegenüber Gewissen Dreidimensionalen Strörungen," Z. Angew. Math. Mech., **21**, pp. 250–252 (see also NACA TM 1375, 1954).
[3] Liepmann, H. W., 1943, "Investigations on Laminar Boundary Layer Stability and Transition on Curved Boundaries," NACA Wartime Report W-87.
[4] Floryan, J. M., 1991, "On the Görtler Instability of Boundary Layers," Prog. Aerosp. Sci., **28**, pp. 235–271.
[5] Saric, W. S., 1994, "Görtler Vortices," Annu. Rev. Fluid Mech., **26**, pp. 379–409.
[6] Volino, R. J., and Simon, T. W., 1997, "Measurements in a Transitional Boundary with Görtler Vortices," ASME J. Fluids Eng., **119**, pp. 562–568.

[7] Finnis, M. V., and Brown, A., 1994, ''The Streamwise Development of Görtler Vortices in Favorable Pressure Gradient,'' ASME J. Turbomach., **118**, pp. 162–171.
[8] Simonich, J. C., and Moffat, R. J., 1982, ''Local Measurements of Turbulent Boundary Layer Heat Transfer on a Concave Surface Using Liquid Crystals,'' HMT-35, Thermosciences Division, Department of Mechanical Engineering, Stanford University.
[9] Kim, J., Simon, T. W., and Russ, S. G., 1992, ''Free-Stream Turbulence and Concave Curvature Effects on Heated, Transitional Boundary Layers,'' ASME J. Heat Transfer, **114**, pp. 338–347.
[10] Kestoras, M., and Simon, T. W., 1995, ''Effects of Free-Stream Turbulence Intensity on a Boundary Layer Recovering From Concave Curvature Effects,'' ASME J. Turbomach., **117**, pp. 240–247.
[11] Blair, M. F., 1983, ''Influence of Free-Stream Turbulence on Turbulent Boundary Layer Heat Transfer and Mean Profile Development: Part 1—Experimental Data,'' ASME J. Heat Transfer, **105**, pp. 33–40.
[12] Sohn, K. H., and Reshotko, E., 1991, ''Experimental Study of Boundary Layer Transition with Elevated Freestream Turbulence on a Heated Flat Plate,'' NASA CR 187068.
[13] Riley, S., Johnson, M. W., and Gibbings, J. C., 1989, ''Boundary Layer Transition of Strongly Concave Surfaces,'' ASME Paper No. 90-GT-321.
[14] Halstead, D. E., Wisler, D. C., Okiishi, T. H., Walker, G. J., Hodson, H. P., and Shin, H.-W., 1997, ''Boundary Layer Development in Axial Compressors and Turbines: Part 3 of 4—LP Turbines,'' ASME J. Turbomach., **119**, pp. 225–237.
[15] Volino, R. J., and Simon, T. W., 1997, ''Boundary Layer Transition Under High Free-Stream Turbulence and Strong Acceleration Conditions: Part 1—Mean Flow Results; Part 2— Turbulent Transport Results,'' ASME J. Heat Transfer, **119**, pp. 420–432.
[16] Volino, R. J., and Simon, T. W., 2000, ''Spectral Measurements in Transitional Boundary Layers on a Concave Wall Under High and Low Free-Stream Turbulence,'' ASME J. Turbomach., **122**, pp. 450–457.
[17] Volino, R. J., and Simon, T. W., 1995, ''Measurements in Transitional Boundary Layers under High Free-Stream Turbulence and Strong Acceleration Conditions,'' NASA CR 198413.
[18] Volino, R. J., 1998, ''A New Model for Free-Stream Turbulence Effects on Boundary Layers,'' ASME J. Turbomach., **120**, pp. 613–620.
[19] Volino, R. J., Schultz, M. P., and Pratt, C. M., 2003, ''Conditional Sampling in a Transitional Boundary Layer Under High Free-Stream Turbulence Conditions,'' ASME J. Fluids Eng., **125**, pp. 28–37.
[20] Eckert, E. R. G., 1987, ''Cross Transport of Energy in Fluid Streams,'' Waerme- Stoffuebertrag., **21**, pp. 73–81.
[21] Kestoras, M., and Simon, T. W., 1993, ''Combined Effects of Concave Curvature and High Free-Stream Turbulence Intensity on Boundary Layer Heat and Momentum Transport,'' ASME Paper No. 93-WA/HT-56.
[22] Wills, J. A. B., 1962, ''The Correction of Hot-Wire Readings for Proximity to a Solid Boundary,'' J. Fluid Mech., **12**, pp. 388–396.
[23] Volino, R. J., and Simon, T. W., 1997, ''Velocity and Temperature Profiles in Turbulent Boundary Layer Flows Experiencing Streamwise Pressure Gradients,'' ASME J. Heat Transfer, **119**, pp. 433–439.
[24] Jones, W. P., and Launder, B. E., 1972, ''Some Properties of Sink-Flow Turbulent Boundary Layers,'' J. Fluid Mech., **56**, pp. 337–351.
[25] Narasimha, R., 1985, ''The Laminar-Turbulent Transition Zone in the Boundary Layer,'' Prog. Aerosp. Sci., **22**, pp. 29–80.
[26] Volino, R. J., and Simon, T. W., 1995, ''Bypass Transition in Boundary Layers Including Curvature and Favorable Pressure Gradient Effects,'' ASME J. Turbomach., **117**, pp. 166–174.
[27] Dhawan, S., and Narasimha, R., 1958, ''Some Properties of Boundary Layer Flow During the Transition from Laminar to Turbulent Motion,'' J. Fluid Mech., **3**, pp. 418–436.
[28] Volino, R. J., 1998, ''Wavelet Analysis of Transitional Flow Data Under High Free-Stream Turbulence Conditions,'' ASME Paper No. 98-GT-289.

Conditional Sampling in a Transitional Boundary Layer Under High Freestream Turbulence Conditions

Ralph J. Volino
e-mail: volino@usna.edu

Michael P. Schultz

Christopher M. Pratt

Department of Mechanical Engineering,
United States Naval Academy,
Annapolis, MD 21402

Conditional sampling has been performed on data from a transitional boundary layer subject to high (initially 9%) freestream turbulence and strong ($K=(\nu/U_\infty^2)(dU_\infty/dx)$ *as high as* 9×10^{-6}) *acceleration. Methods for separating the turbulent and nonturbulent zone data based on the instantaneous streamwise velocity and the turbulent shear stress were tested and found to agree. Mean velocity profiles were clearly different in the turbulent and nonturbulent zones, and skin friction coefficients were as much as 70% higher in the turbulent zone. The streamwise fluctuating velocity, in contrast, was only about 10% higher in the turbulent zone. Turbulent shear stress differed by an order of magnitude, and eddy viscosity was three to four times higher in the turbulent zone. Eddy transport in the nonturbulent zone was still significant, however, and the nonturbulent zone did not behave like a laminar boundary layer. Within each of the two zones there was considerable self-similarity from the beginning to the end of transition. This may prove useful for future modeling efforts.* [DOI: 10.1115/1.1521957]

Introduction

Boundary layer transition is an important phenomenon experienced by the flow through gas turbine engines. Mayle [1] stated that a substantial fraction of the boundary layer on both sides of a gas turbine airfoil may be transitional. The extended transition zones exist due to strong favorable pressure gradients, found on both the pressure side and the leading section of the suction side, which stabilize the boundary layer and delay transition in spite of the high freestream turbulence intensity (FSTI) in gas turbine environments. The ability to model and predict high FSTI transition is important since heat transfer rates and skin friction coefficients may increase substantially when a boundary layer undergoes transition. Boundary layer separation, which is believed to be a significant problem on the suction side of some low-pressure turbine airfoils, also depends strongly on the state of the boundary layer with respect to transition. Improved transition models and turbine designs depend, therefore, on a better understanding of high FSTI transition.

Documentation of high FSTI transition has included work in turbine cascades and rotating rigs (e.g., Halstead et al. [2]). Several studies have considered the flow along flat and curved walls. These simpler geometries allow for more detailed in-flow measurements than are typical for cascade studies. On surfaces subject to zero streamwise pressure gradients, Blair [3], Sohn and Reshotko [4], and Kim et al. [5] all showed that at FSTI above about 3%, transition occurred rapidly near the leading edge of a test surface. Blair [6] considered cases with FSTI up to 5% and concurrent acceleration, holding the acceleration parameter, K, constant at values up to 0.75×10^{-6}. The acceleration delayed the transition, even with high FSTI. Volino and Simon [7–9] considered transition along a concave wall with inlet FSTI of 8% and acceleration with K as high as 9×10^{-6}. Acceleration rates, Reynolds numbers and FSTI were typical of the pressure side of a gas turbine airfoil. An extended transition region, with intermittent turbulent and nonturbulent zones, covered most of the test surface. The turbulent zone included a range of both large and small scale eddies, much like a fully turbulent boundary layer and the turbulent zone in a low FSTI transitional boundary layer. The nonturbulent zone and the pre-transitional boundary layer were not laminar-like as in a low FSTI flow, but instead were characterized by high-amplitude large-scale fluctuations and an absence of smaller scales. Nonturbulent zone velocity fluctuations are believed to be induced by the freestream unsteadiness through pressure fluctuations, as discussed in Volino [10]. Near-wall turbulence production is believed to be largely absent in the nonturbulent zone.

The intermittent nature of transition, both at low and high FSTI, has led to efforts to incorporate intermittency in transition models and to model the two zones of the intermittent flow separately. Among recent efforts are the work of Steelant and Dick [11], Suzen and Huang [12], and Solomon et al. [13]. Separate modeling of the nonturbulent and turbulent zones requires knowledge of the flow behavior within each zone, which can be provided through conditional sampling of experimental data. Conditional sampling results have been presented for zero streamwise pressure gradient conditions by Kim et al. [5], Sohn and Reshotko [4], and Kuan and Wang [14]. Results from favorable pressure gradient cases have been reported by Blair [6], Wang and Keller [15], and Wang and Zhou [16]. The strongest acceleration rate in these cases was $K=0.75\times10^{-6}$. This is a relatively mild acceleration for modern airfoils, and the transition zones were short in all cases with elevated FSTI.

Volino and Simon [7,9] obtained rough estimates of the time-averaged intermittency (fraction of time the flow is turbulent) in their high FSTI, strong acceleration case using an analog circuit, which determined when the flow was turbulent based on the time derivatives of hot-wire voltages. The circuit worked well in the low FSTI cases of Kim et al. [5], but in high FSTI cases differences in fluctuation level between the turbulent and nonturbulent zones are narrower, and more careful setting of thresholds and smoothing of the intermittency function are required for conditional sampling. This is difficult with an analog circuit, and is better done in post-processing after the signal has been digitized. Such post-processing requires data acquisition at a high enough sampling rate to provide an essentially continuous signal. Due to

Contributed by the Fluids Engineering Division for publication in the JOURNAL OF FLUIDS ENGINEERING. Manuscript received by the Fluids Engineering Division July 12, 2001, revised manuscript received July 26, 2002. Associate Editor: K. B. M. Q. Zaman.

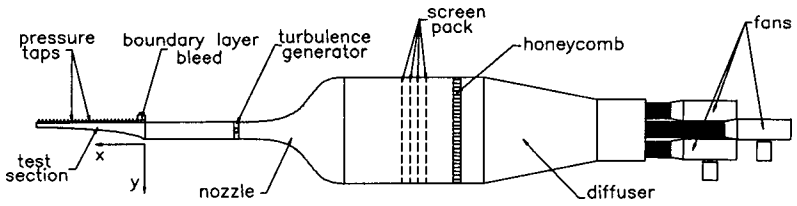

Fig. 1 Schematic of the test facility

data storage limitations at the time, Volino and Simon [7,9] only sampled at a high enough rate for such processing at a few isolated points in the boundary layer. Volino [17] examined the data from these points using wavelet analysis and presented preliminary results of conditional sampling. Uncertainties were high due to the limited amount of data. To the authors' knowledge, no other detailed conditional sampling results from boundary layers with strong acceleration, extended transition zones and FSTI greater than 5% are available in the literature.

The present paper has two objectives. The first is to provide the results of conditional sampling for a transitional boundary layer with high FSTI and strong acceleration. The case presented by Volino and Simon [7–9] has been reproduced on a flat test wall, and data have been acquired throughout the boundary layer at a sufficiently high sampling rate for conditional sampling post processing. The second objective is to provide a baseline case for a study of the significance of streamwise curvature on transitional boundary layers at elevated FSTI. A second paper (Schultz and Volino [18]) presents results from an otherwise similar case on a wall with strong concave curvature.

Experiments

Facility and Measurements. All experiments were conducted in the low speed wind tunnel shown in Fig. 1. Three fans supply air to a plenum, which is followed by a diffuser, a settling chamber containing a honeycomb, a screen pack, a second settling chamber, and a three-dimensional contraction which reduces the cross sectional area from 1.09 m×1.09 m to 0.69 m×0.18 m. A bi-planar turbulence-generating grid with 43% blockage is in the plane of the contraction exit. The grid is based on the design used by Kim et al. [5] and consists of a 3.8-cm diameter, 0.69-m long vertical pipe down the center of the contraction exit, and six 3.2-cm diameter, 0.18-m long evenly spaced horizontal pipes. Following the grid is a 1-m long rectangular development section and the test section, a converging channel. One side of this channel is a flat Plexiglas plate of 0.69 m width and 1.2 m length, which serves as the test wall. Pressure taps are installed along its spanwise centerline. At the leading edge of the test wall a slot is used to bleed off the boundary layer which grows in the development section. Opposite the test wall is a flexible wall which can be adjusted to set the desired pressure gradient along the test wall. For the present study the inlet velocity is set to 4.6 m/s and the velocity gradient along the wall is held constant at 13.9 s^{-1}. The acceleration parameter, K, drops from a maximum of 9×10^{-6} at the inlet to the test section to 1×10^{-6} at the last measurement station. Values of K through the test section, measurement locations and other parameters are given in Table 1.

At the inlet to the test section the mean flow is spatially uniform to within 3% and the turbulence is uniform to within 6%. The components of the freestream turbulence intensity are 8.8%, 8.9%, and 8.3% in the streamwise, cross-stream, and spanwise directions, respectively. The integral length scales of these components of the freestream turbulence are 3 cm, 1.6 cm, and 1.4 cm. Spectra of the freestream turbulence at the most upstream measurement station are shown in Fig. 2. In the test section, the freestream turbulence intensity (normalized using the local freestream velocity) drops to about 2% at the last measurement station. The drop is primarily due to the increasing freestream velocity. The streamwise component $\overline{u'_\infty}$ does decay somewhat due to straining of the freestream eddies in the accelerating flow, but $\overline{v'_\infty}$ remains nearly constant at all stations.

Velocity profile measurements were made at ten streamwise stations along the centerline of the test wall using a single sensor,

Table 1 Flow parameters at measurement stations

St	x [m]	U_∞ [m/s]	$\frac{\overline{u'_\infty}}{U_\infty}$ [%]	$\frac{\overline{v'_\infty}}{U_\infty}$ [%]	K $\times10^6$	γ_{pk} [%]	$\delta_{99.5}$ [mm]	Re_x $\times10^{-5}$
1	0.118	6.22	6.4	6.4	5.32	4.1	4.04	0.50
2	0.190	7.12	4.9	5.5	4.04	3.0	3.99	0.91
3	0.268	7.99	3.9	4.8	3.25	4.7	4.52	1.43
4	0.345	9.13	3.2	4.2	2.53	8.9	5.16	2.07
5	0.423	10.4	2.7	3.8	1.97	17.	4.72	2.88
6	0.503	11.4	2.4	3.4	1.63	34.	5.28	3.77
7	0.581	12.5	2.1	3.2	1.33	56.	5.67	4.84
8	0.659	13.6	1.9	2.9	1.13	71.	5.80	5.91
9	0.735	14.6	1.7	2.7	0.97	86.	6.58	7.20
10	0.817	15.9	1.5	2.5	0.83	93.	7.92	8.54

St	Re_θ	H	C_f $\times10^3$	Re_θ	H	C_f $\times10^3$	Re_θ	H	C_f $\times10^3$
	composite			non-turbulent			turbulent		
1	136	1.96	6.50	136	1.97	6.50	90	1.97	10.5
2	149	1.98	5.75	149	1.99	5.75	135	1.72	9.60
3	169	1.94	5.35	168	1.94	5.40	186	1.59	8.90
4	196	1.87	5.00	193	1.89	5.00	244	1.51	8.10
5	221	1.82	4.80	212	1.86	4.70	293	1.48	7.50
6	263	1.76	4.50	239	1.86	4.20	366	1.46	6.70
7	324	1.66	4.60	264	1.86	4.00	432	1.46	6.10
8	372	1.58	5.00	278	1.82	4.10	474	1.43	6.10
9	457	1.49	5.30	297	1.81	3.90	580	1.39	5.90
10	580	1.43	5.60	364	1.69	3.70	745	1.35	5.50

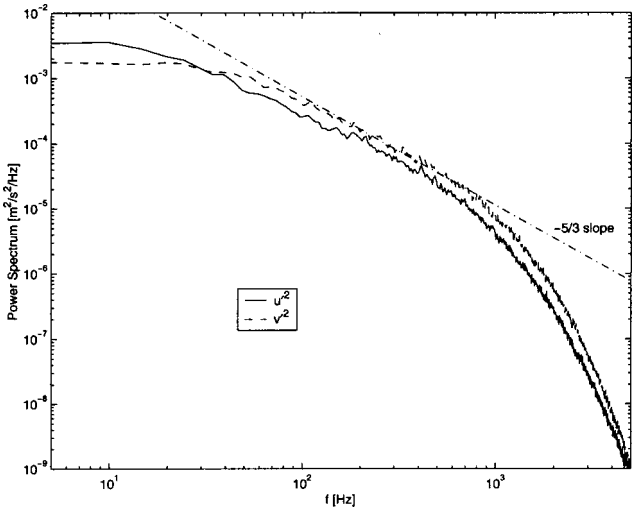

Fig. 2 Freestream spectra at Station 1

boundary layer type hot-wire probe (TSI model 1218-T1.5), a boundary layer cross-wire probe (TSI model 1243-T1.5), and a constant-temperature hot-wire anemometer (TSI model IFA-100). The probes were moved normal to the wall at each station using a motorized traverse with minimum step size of 12.5 μm. At each position in the velocity profiles, data were acquired for 26 seconds at a 20 kHz sampling rate (2^{19} data points). The hot-wire signals were low-pass filtered at 10 kHz. All raw data were stored. Sampling at 20 kHz provided essentially continuous velocity traces for subsequent processing.

Data Processing. Mean and rms fluctuating velocities in the streamwise and wall-normal directions were computed from the instantaneous data. Uncertainties in these quantities are 3–5% except in the very near wall region ($y^+<5$) where near-wall corrections (Wills [19]) are applied to the mean velocity. Uncertainty in the turbulent shear stress, $-\overline{u'v'}$, is 10%. Skin friction coefficients were determined using a technique whereby τ_w was adjusted until the U^+ versus y^+ data fit profiles computed using near-wall similarity, as described by Volino and Simon [20]. This technique accounts for pressure gradient effects on the near wall profile. Uncertainty in C_f is 8%. Boundary layer thicknesses were determined from the mean velocity profiles. Uncertainties in the momentum and displacement thicknesses are 10%. These uncertainties include bias uncertainties which tend to cancel such that the uncertainty in the shape factor, H, is 7%.

Intermittency Based on u. The intermittency function, Γ, indicates whether the boundary layer is instantaneously turbulent or nonturbulent at a measurement location. It is assigned a value of zero for nonturbulent flow and one for turbulent flow. The time average of Γ is the intermittency, γ. Keller and Wang [21] and Solomon [22] review several techniques for determining Γ. In the present study, two intermittency detection techniques were utilized and compared. The first, as used in Volino and Hultgren [23], is based on the instantaneous streamwise velocity, u. The u signal is first digitally high-pass filtered with a cutoff frequency

$$f_{HP}=200\cdot U_\infty \tag{1}$$

where f_{HP} is in Hz and U_∞ is in m/s. The filter eliminates low-frequency fluctuations, which are common to both the turbulent and nonturbulent zones. The filter was used by Volino and Hultgren [23] to remove narrow band fluctuations associated with shear layer instabilities in separated boundary layers. In the present work, this filter had little effect on the intermittency function. The filtered signal is then used to determine an intermittency function Γ_{1u}, as

$$\Gamma_{1u}(t)=\begin{matrix}1 & \text{if } |\partial u/\partial t|>8.89\cdot U_m\cdot U_\infty\\ 0 & \text{otherwise}\end{matrix} \tag{2}$$

where

$$U_m=\begin{matrix}U+2\cdot\overline{u'^3}^{1/3}-\overline{u'^2}^{1/2} & \text{if } 2\cdot\overline{u'^3}^{1/3}>\overline{u'^2}^{1/2}\\ U & \text{otherwise}\end{matrix} \tag{3}$$

The velocity U is the local mean velocity at the measurement location and U_∞ is the local freestream velocity at the measurement station. All velocities are in m/s, and the time derivative is in m/s^2. The time derivative of the velocity should scale with the magnitude of the velocity and the frequency with which eddies pass, which in turn also scales with the velocity. This explains the velocity squared term in the threshold in Eq. (2). The use of U_m instead of U_∞ allowed the threshold level to adjust in the near-wall region where the mean velocity becomes small. Very near the wall, as U approaches zero, the threshold would also approach zero and Γ_{1u} would go to 1 if U_m were set equal to U. To prevent this, U_m is adjusted using the fluctuating velocity, as shown in Eq. (3). This adjustment models the instantaneous rise in the near wall velocity which occurs during turbulent intervals when higher speed fluid sweeps toward the wall.

A second function, Γ_{2u}, is next computed based on the absolute value of the second derivative of the filtered velocity signal, $|\partial^2 u/\partial t^2|$. The threshold for Γ_{2u} is set such that the time average of Γ_{1u} and Γ_{2u} are equal. Next, a combined intermittency function, Γ_{3u} is defined as

$$\Gamma_{3u}(t)=\begin{matrix}1 & \text{if } \Gamma_1=1 \text{ or } \Gamma_2=1\\ 0 & \text{otherwise}\end{matrix} \tag{4}$$

Basing Γ_{3u} on both the first and second time derivative of the velocity helps to minimize dropouts within the turbulent zone, which occur in Γ_{1u} and Γ_{2u} when the derivatives cross zero. The final step is to smooth Γ_{3u} to minimize false turbulent points in the nonturbulent zone and false nonturbulent points in the turbulent zone. The function Γ_{3u} is low-pass filtered with cutoff frequency

$$f_{LP}=17.78\cdot U_\infty \tag{5}$$

where f_{LP} is in Hz and U_∞ is in m/s. Finally, using the filtered Γ_{3u}, the intermittency function Γ_u is set as

$$\Gamma_u(t)=\begin{matrix}1 & \text{if } \Gamma_{3u}>0.5\\ 0 & \text{otherwise}\end{matrix} \tag{6}$$

The thresholds and filter frequencies presented above were set after visual inspection of many data traces and the $\Gamma_u(t)$ resulting with several different thresholds. Visual inspection of the data is ultimately the best criteria available for determining how well an intermittency function is separating the turbulent and nonturbulent flow [17,22]. The thresholds and frequencies were useful both for the present study and the separated flow transition study of Volino and Hultgren [23]. They are not expected to be universal criteria for all flows, and other intermittency detection schemes might work as well. The thresholds might be made more general if nondimensionalized using the viscosity or a characteristic length such as the boundary layer thickness.

Intermittency Based on $u'v'$. A second intermittency function is computed based on the instantaneous turbulent shear stress. Without pre-filtering of the velocity signal, an intermittency function is computed as

$$\Gamma_{1uv}(t)=\begin{matrix}1 & \text{if } (\partial u'v'/\partial t)^2>50\cdot U_\infty^4\\ 0 & \text{otherwise}\end{matrix} \tag{7}$$

A second function Γ_{2uv} is computed based on $(\partial^2 u'v'/\partial t^2)^2$ with the threshold set such that the time averages of Γ_{1uv} and Γ_{2uv} are

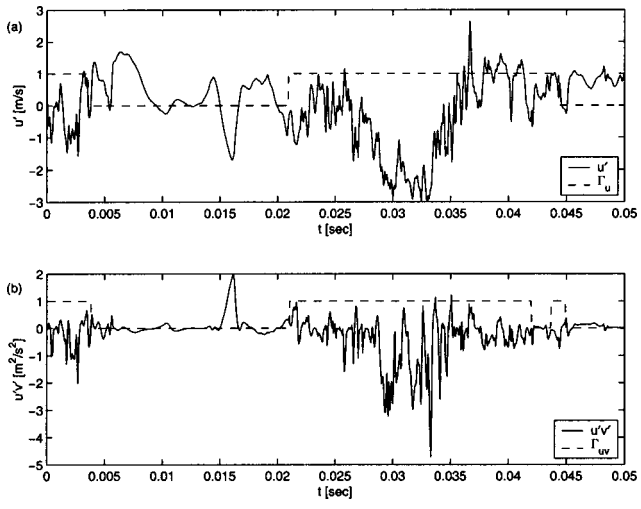

Fig. 3 Instantaneous velocity traces and intermittency function: (*a*) u and Γ_u, (*b*) $u'v'$ and Γ_{uv}

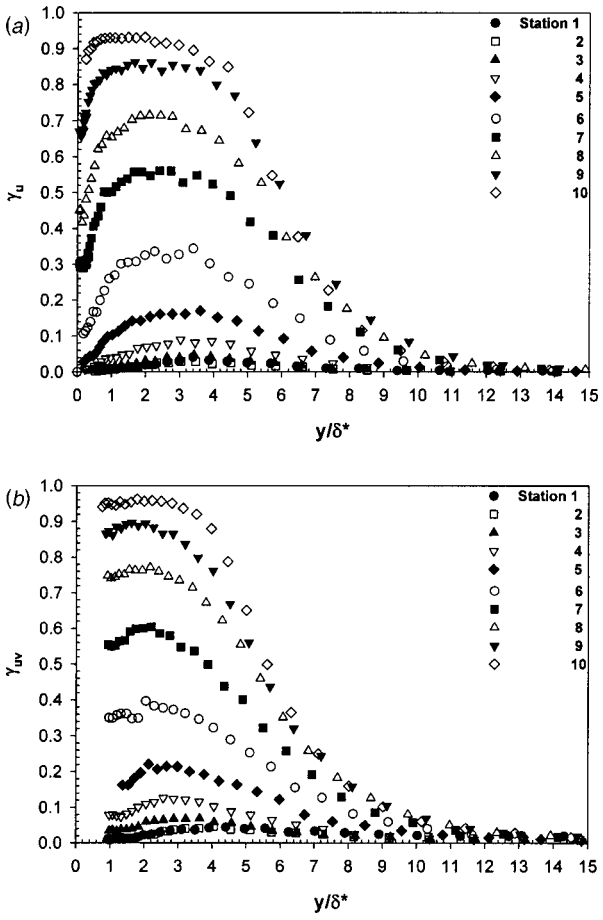

Fig. 4 Intermittency profiles based on (*a*) u and (*b*) Reynolds shear stress

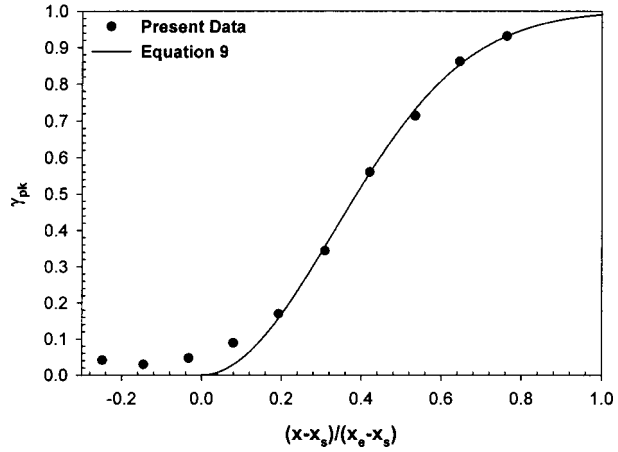

Fig. 5 Peak intermittency in profile versus dimensionless streamwise location

equal. The remaining steps in computing the intermittency function $\Gamma_{uv}(t)$ follow the steps in Eqs. (4)–(6) above.

Figure 3 presents a typical signal from the transitional boundary layer along with both intermittency functions. Some regions are clearly turbulent (e.g., 0.025 s–0.035 s) and some are clearly nonturbulent (0.01 s–0.02 s). Between zones the demarcation is not always sharp (0.04 s–0.045 s) leading to differences in $\Gamma_u(t)$ and $\Gamma_{uv}(t)$ and the possibility of some ''leakage'' of data between zones. The correlation coefficient between $\Gamma_u(t)$ and $\Gamma_{uv}(t)$ was always at least 0.8, however, and at 95% of the measurement locations it was above 0.9. Although the shear stress is often considered a better criterion function, the good agreement between $\Gamma_u(t)$ and $\Gamma_{uv}(t)$ suggest that both are acceptable. This is particularly useful very near the wall, where only u can be measured. Both functions were used in conditional sampling, providing essentially the same results. The uncertainty in the intermittency, γ, is 0.1. In the figures which follow, data points are shown for the nonturbulent zone only when the local $\gamma<95\%$, and for the tur-

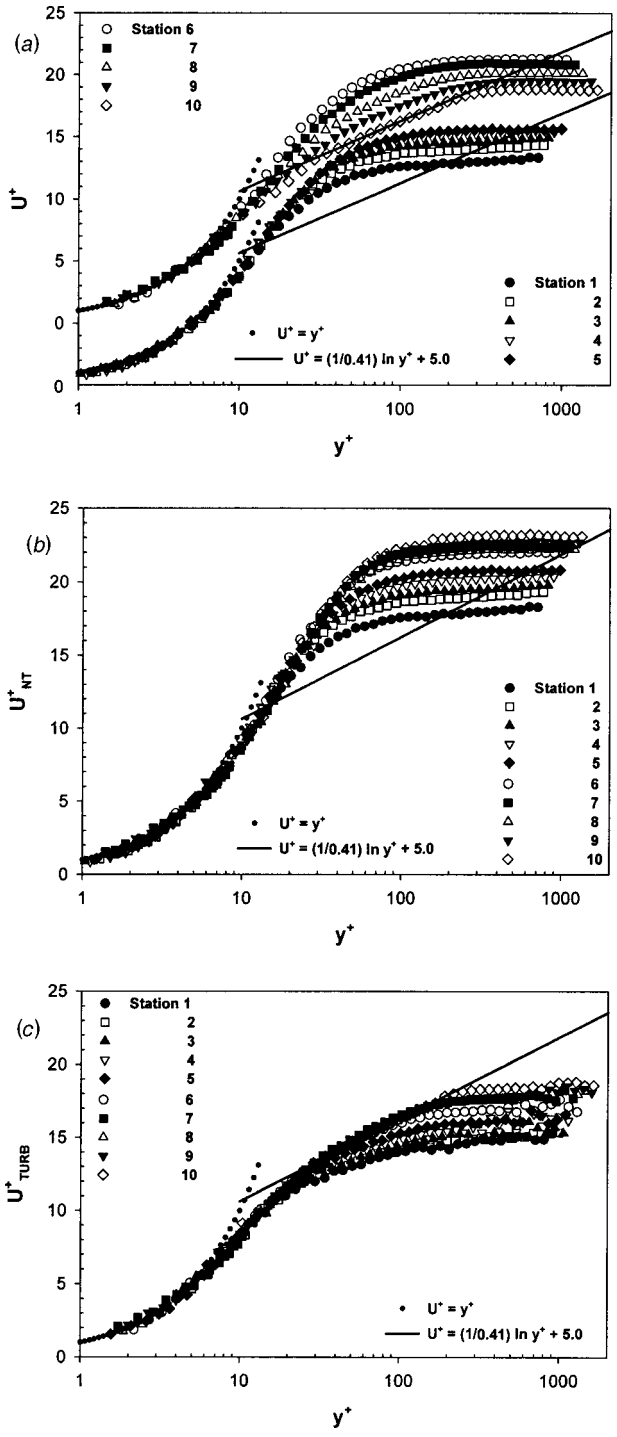

Fig. 6 Mean velocity profiles in wall coordinates: (*a*) composite; (*b*) nonturbulent; (*c*) turbulent

bulent zone only when $\gamma > 5\%$. Bulk parameters such as C_f are presented when $\gamma_{pk} < 95\%$ and $\gamma_{pk} > 5\%$ for the nonturbulent and turbulent zones, respectively.

Results

Intermittency. Intermittency profiles for the ten measurement stations are shown in Fig. 4. Agreement between the u and shear stress based γ is good. Intermittency remains low for the first three stations and then begins to rise. By the last station, transition is nearing completion. Transition criteria such as those presented by Johnson [24] and Mayle [1] indicate that the present boundary layer would be transitional by Station 1 under zero pressure gradient conditions. In fact, the intermittency is nonzero at Station 1, but the strong acceleration prevents the transition from proceeding. The beginning of the rise in γ corresponds to K dropping below 3×10^{-6}. In low FSTI boundary layers, $K>3\times10^{-6}$ leads to relaminarization (Jones and Launder [25]). Following the technique of Narasimha [26], as modified by Volino and Simon [27], the function

$$f(\gamma_{pk}) = (-\ln(1-\gamma_{pk}))^{1/2} \tag{8}$$

can be computed based on the peak intermittency at each station and plotted versus streamwise location. The data in these coordinates tend to lie along a straight line. The line may be extrapolated to $f(\gamma_{pk}=0)=0$ and $f(\gamma_{pk}=0.99)=2.146$, corresponding to the beginning and end of transition at $x_s=0.29$ m and $x_e=0.98$ m, respectively. Figure 5 shows γ_{pk} plotted versus dimensionless streamwise location within transition. Also shown is the theoretical curve

$$\gamma_{pk} = \exp\left(-4.6\left(\frac{x-x_s}{x_e-x_s}\right)^2\right) \tag{9}$$

based on the Dhawan and Narasimha [28] transition model. Agreement between the data and theory is good. In favorable pressure gradients some differences are expected and observed at low intermittency, in a region Narasimha [26] referred to as "subtransition."

The dimensionless turbulent spot propagation rate may be computed, following the development of Mayle [1], as

$$\hat{n}\sigma = \frac{4.6\nu^2\overline{U}_\infty}{(x_e-x_s)^2U_s^3} \tag{10}$$

where $\overline{U}_\infty$ is the average freestream velocity in the transition region. In the present case $\hat{n}\sigma = 4.2\times10^{-11}$. In agreement with trends reported by Mayle [1] for other favorable pressure gradient cases, this value is an order of magnitude lower than what would be expected for a zero-pressure gradient case with the same FSTI, indicating a longer transition zone with the favorable pressure gradient than with a zero-pressure gradient.

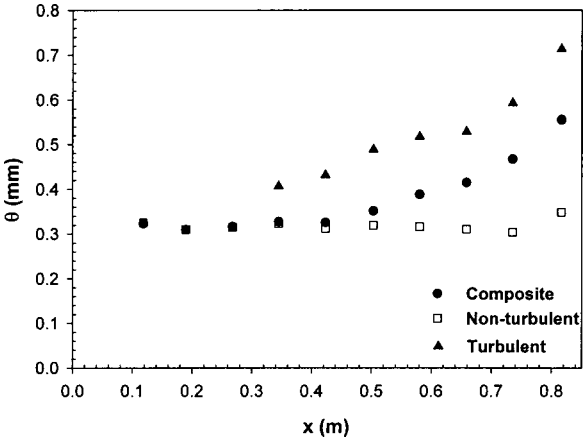

Fig. 8 Momentum thickness versus streamwise distance

Mean Velocity Profiles. Mean velocity profiles for the ten measurement stations are presented in Fig. 6 in wall coordinates. Figure 6(*a*) shows the composite (unconditioned) profiles. The profiles rise through Station 6, with a somewhat laminar-like shape. Downstream of Station 6, the profiles assume a more turbulent-like shape and by Station 10, where transition is near completion and the acceleration rate has dropped to $K=1$

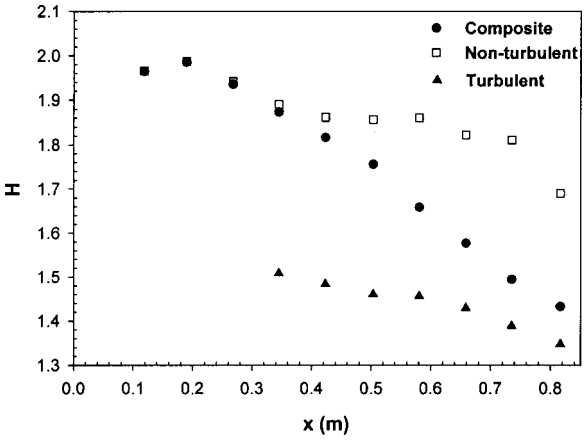

Fig. 9 Shape factor versus streamwise distance

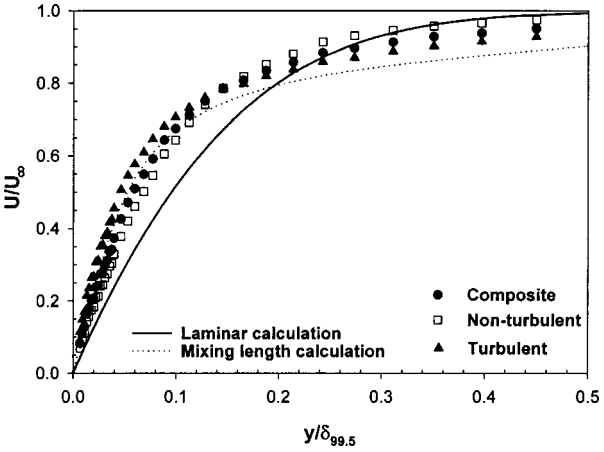

Fig. 7 Mean velocity profile for Station 7, $\gamma_{pk}=56\%$

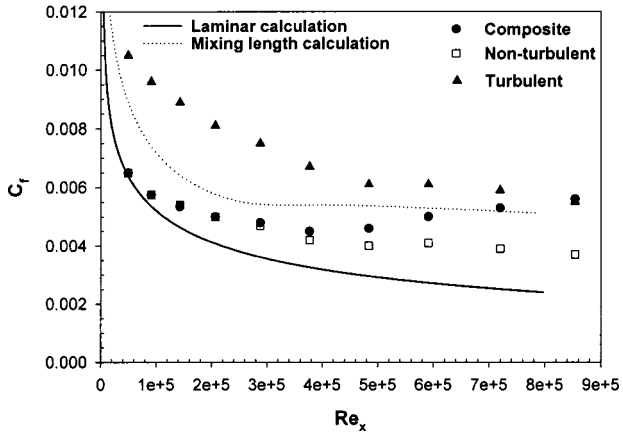

Fig. 10 Skin-friction coefficient

$\times 10^{-6}$, there is good agreement with the zero pressure gradient law of the wall. The nonturbulent zone profiles are shown in Fig. 6(*b*). All the profiles exhibit a laminar-like shape, even at the end of transition. Figure 6(*c*) shows the turbulent zone profiles. All have a turbulent-like shape, and the last five stations show good agreement with the zero-pressure gradient law of the wall. The high FSTI suppresses the wake at all stations. Figure 7 illustrates the differences between the composite, nonturbulent, and turbulent profiles at Station 7, in the center of the transition zone. Distance from the wall is normalized on the composite flow $\delta_{99.5}$. Velocities in the turbulent zone are clearly higher in the near wall region due to higher levels of turbulent mixing. Also shown in Fig. 7 are low FSTI calculations for laminar and fully turbulent

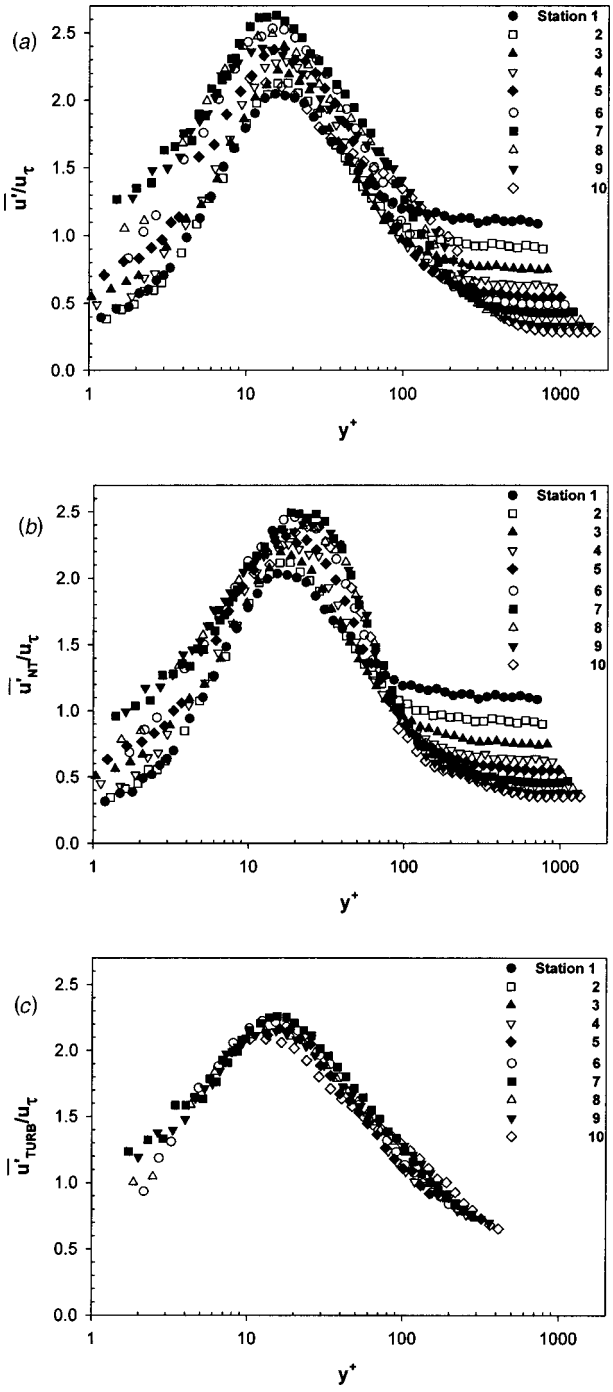

Fig. 11 Fluctuating streamwise velocity profiles in wall coordinates: (*a*) composite; (*b*) nonturbulent; (*c*) turbulent

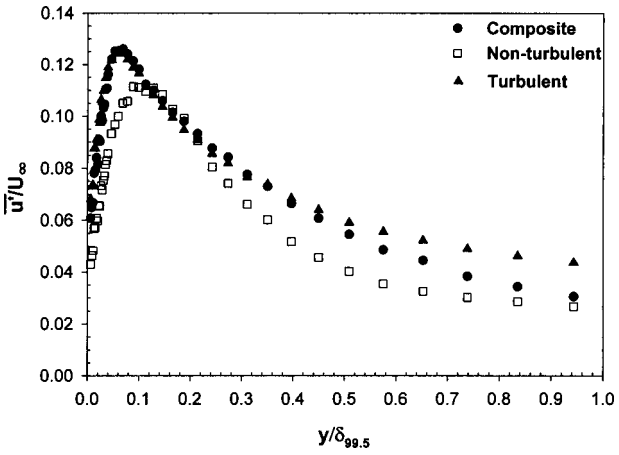

Fig. 12 Fluctuating streamwise velocity profile for Station 7, $\gamma_{pk}=56\%$

boundary layers with the same pressure gradient. The fully turbulent calculation was done with a mixing length model. The turbulent and nonturbulent zone profiles at all stations differ from the low FSTI calculations. Higher levels of transport lead to higher near wall mean velocities in the data than in the calculations. This is particularly true in the nonturbulent zone. The increased transport in the nonturbulent zone makes the differences between the turbulent and nonturbulent profiles less pronounced in the data than in the low FSTI calculations. At no point does the boundary layer behave as if it were laminar. Differences from laminar behavior have been reported in low FSTI transitional flows (e.g., [5], [15]) and attributed to the effect of the turbulent zone on the nonturbulent. In the present study, however, deviation from laminar behavior is seen even at Station 1, where the boundary layer is nearly all nonturbulent. The deviation from laminar behavior must be due to the high FSTI.

Boundary Layer Growth. Figure 8 shows the momentum thickness as a function of streamwise position. The composite boundary layer does not grow through the first five stations due to the strong acceleration. Momentum thickness increases at the downstream stations as the acceleration weakens and transition proceeds. In the nonturbulent zone, momentum thickness remains constant at all stations. The turbulent zone momentum thickness increases continuously, possibly due to turbulent entrainment at the edge of the boundary layer.

The shape factor, shown in Fig. 9, is an indicator of the state of the boundary layer with respect to transition. In the nonturbulent zone it drops only slightly from 2.0 to about 1.8. A low FSTI laminar boundary layer with the same pressure gradient would have a shape factor of 2.4. As shown in Fig. 7, the high FSTI enhances mixing and makes the nonturbulent zone appear less laminar-like. In the turbulent zone, H drops from about 1.5 to 1.35. The low FSTI fully turbulent calculation mentioned above resulted in H values about 10% higher than the experimental data. This suggests that the high FSTI promotes greater momentum transport in the turbulent zone, but the effect is not as great as in the nonturbulent zone.

Skin Friction Coefficients. Skin friction coefficients were computed from the mean velocity profiles and are shown in Fig. 10. Also shown for reference are the results from the low FSTI calculations. The skin friction coefficient is as much as 70% higher in the turbulent zone than in the nonturbulent zone. The composite C_f does not change much during transition, which if viewed alone, might suggest that there is little difference between the nonturbulent and turbulent zones. When viewed with the conditional sampling results, however, it is clear that the two zones

are quite different. In both zones the freestream turbulence results in C_f as much as 40% higher than the corresponding low FSTI calculation.

Fluctuating Velocity. Figure 11 shows $\overline{u'}$ profiles in wall coordinates. The composite flow data, shown in Fig. 11(*a*), are typical of transitional and turbulent boundary layers. The peak in $\overline{u'}/u_\tau$ occurs at $y^+ = 16$, and the magnitude of the peak is between 2 and 2.6. The peak is highest at Station 7, in the middle of transition, due in part to the unsteadiness associated with the switching between turbulent and nonturbulent states. The nonturbulent and turbulent zone data are shown in Figs. 11(*b*) and 11(*c*), respectively. In the turbulent zone the data from all stations collapse, showing self-similarity throughout the transition region. Figure 12 shows the $\overline{u'}$ profiles at Station 7, midway through transition. The peak in u' is closer to the wall in the turbulent zone, but the magnitudes of the peaks differ by only about 13% between the two zones.

Figure 13 shows $\overline{v'}$ profiles. The composite flow data are shown in Fig. 13(*a*). As expected for a high FSTI boundary layer, $\overline{v'}$ drops from a peak in the near wall region to a minimum, and then rises to the freestream value. The minimum is indicative of a damping of the freestream effect by the wall. Near the wall, there is not much change in $\overline{v'}/u_\tau$ for the first three stations. As transition begins, $\overline{v'}/u_\tau$ rises at Stations 4 and 5. Between Stations 6 and 10 there is little change. In comparison to the $\overline{u'}$ profiles of Fig. 11, $\overline{v'}$ is lower in magnitude and shows more change through the transition region. Far from the wall, normalized v' drops in the streamwise direction due to the increasing value of u_τ. The dimensional value of $\overline{v'}$ in the freestream remains essentially constant at 0.4 m/s at all stations. The nonturbulent and turbulent zone data are shown in Figs. 13(*b*) and 13(*c*). As with $\overline{u'}$, the turbulent zone profiles collapse. Figure 14 shows the $\overline{v'}$ profiles at Station 7. In contrast to the $\overline{u'}$ profiles of Fig. 12, which showed similar magnitude in the turbulent and nonturbulent zones, the $\overline{v'}$ magnitude is nearly twice as high in the turbulent zone as in the nonturbulent. Volino [17] found that much of the unsteadiness in u is low-frequency unsteadiness induced by the freestream and common to both zones. When freestream eddies buffet the boundary layer and push higher speed fluid toward the wall, the effect is an increase in u, particularly near the wall where $\partial U/\partial y$ is large. This effect is common to both the nonturbulent and turbulent zones and is not dependent on turbulence produced near the wall. It explains the similarity between the turbulent and nonturbulent $\overline{u'}$ behavior. There is no similar effect on $\overline{v'}$, so the $\overline{v'}$ fluctuations are more closely related to turbulence and eddy transport in the boundary layer, and greater differences exist between the turbulent and nonturbulent $\overline{v'}$.

Turbulent Shear Stress. Profiles of the turbulent shear stress are shown in Fig. 15 in wall coordinates. Similar to $\overline{v'}/u_\tau$ in Fig. 13(*a*), there is little change in the composite profiles in Fig. 15(*a*) for the first three stations. As transition begins, the dimensionless shear stress rises. In the nonturbulent zone (Fig. 15(*b*)) $-\overline{u'v'}$ values are low. In the turbulent zone, Fig. 15(*c*) shows that the data from beginning to end of transition all collapse onto a single line. To compare the turbulent and nonturbulent $-\overline{u'v'}$ directly, Fig. 16 shows the Station 7 profiles. In contrast to $\overline{u'}$, which had similar magnitude in the two zones, $-\overline{u'v'}$ is much higher in the

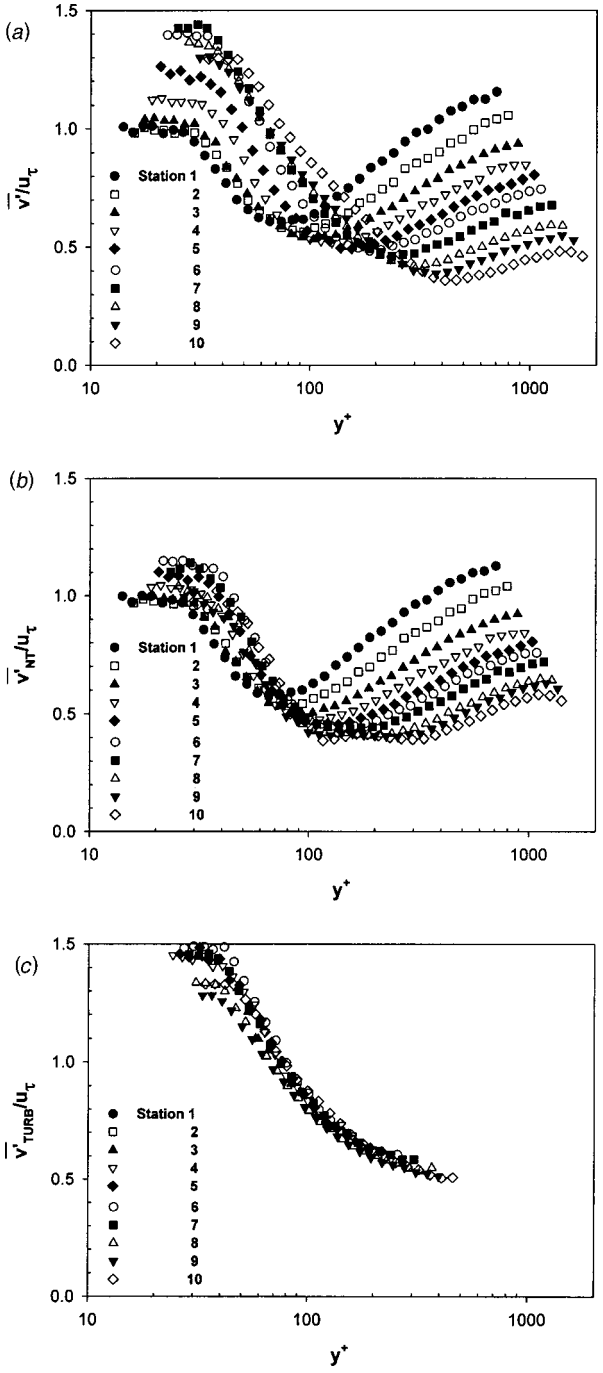

Fig. 13 Fluctuating wall-normal velocity profiles in wall coordinates: (*a*) composite; (*b*) nonturbulent; (*c*) turbulent

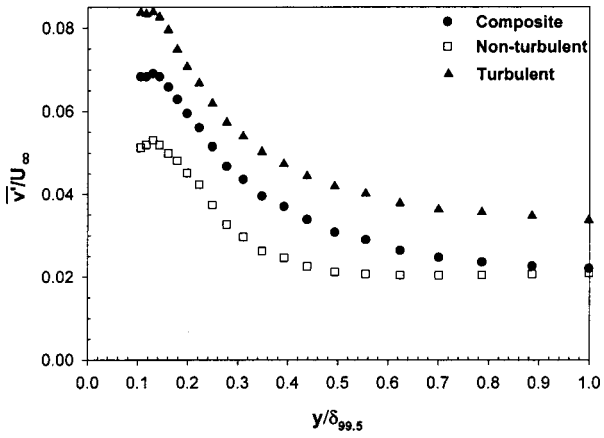

Fig. 14 Fluctuating wall-normal velocity profile for Station 7, γ_{pk}=56%

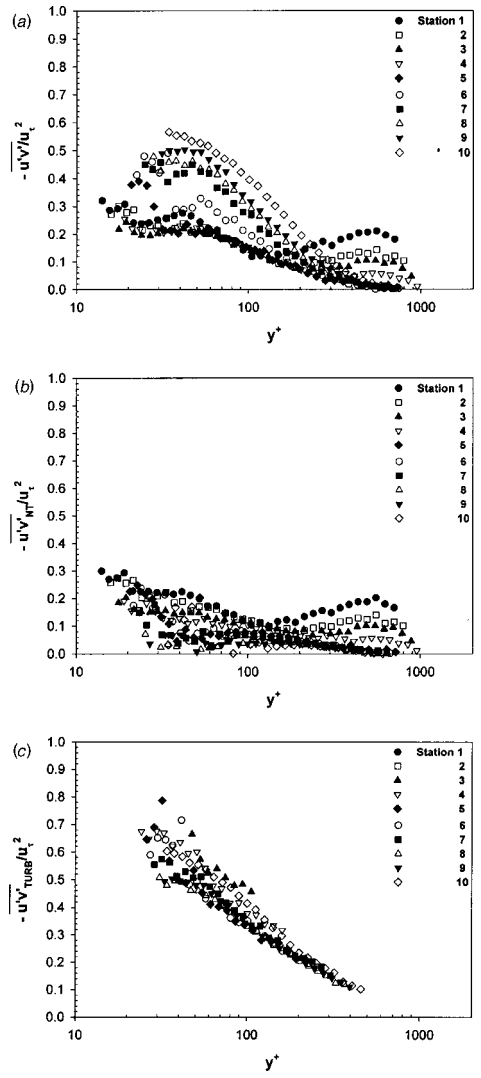

Fig. 15 Reynolds shear stress profiles in wall coordinates: (*a*) composite; (*b*) nonturbulent; (*c*) turbulent

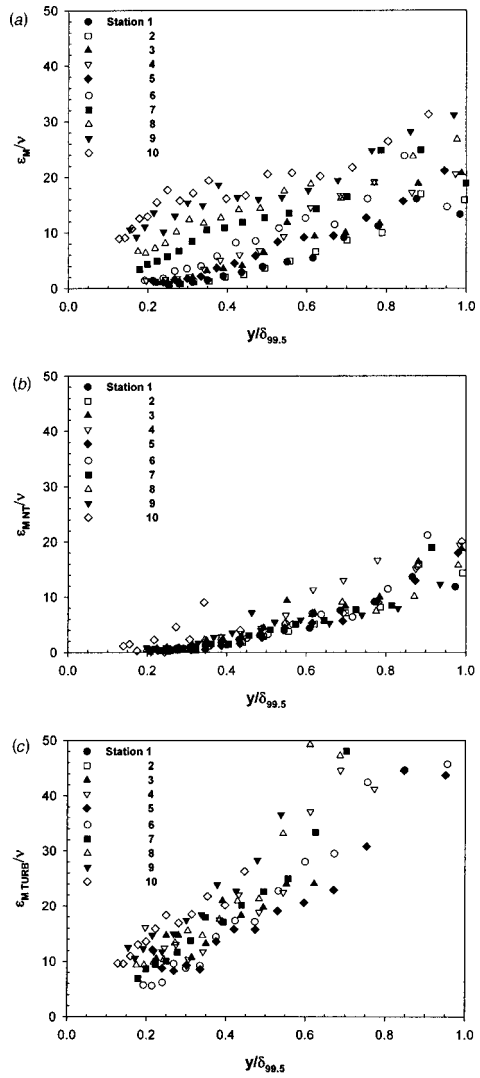

Fig. 17 Eddy viscosity profiles: (*a*) composite; (*b*) nonturbulent; (*c*) turbulent

turbulent zone. The nonturbulent $-\overline{u'v'}$ is not zero, however, indicating some eddy transport of momentum even when the boundary layer is non-turbulent. This may explain the deviation of the nonturbulent mean velocity profiles from laminar predictions and the enhancement of the skin friction above laminar values shown in Figs. 7 and 10.

The collapse of the turbulent zone data in Fig. 15(*c*), also seen in $\overline{u'}$ and $\overline{v'}$ in Figs. 11(*c*) and 13(*c*), indicates considerable similarity within the turbulent zone. The turbulence contained within the turbulent spots in the upstream part of transition (where the intermittency is low and the spots occupy only a small fraction of the total flow) appears to be very similar to the turbulence in the nearly fully turbulent region downstream. This similarity may simplify modeling of the turbulent zone. Although the collapse of the data in the coordinates of Figs. 11(*b*), 13(*b*), and 15(*b*) is not quite so good, similar arguments can be made concerning the self-similarity of the nonturbulent zone.

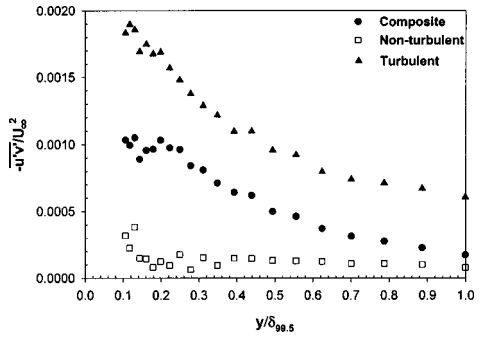

Fig. 16 Reynolds shear stress profile for Station 7, γ_{pk}=56%

Profiles of the eddy viscosity are shown in Fig. 17. The composite profiles in Fig. 17(*a*) show that ε_M increases in the streamwise direction as the transition proceeds. Comparison of the nonturbulent and turbulent zone profiles in Figs. 17(*b*) and 17(*c*) shows that the eddy viscosity is three to four times higher in the turbulent zone. While the difference between the two zones is clear, Fig. 17(*b*) again shows that there is significant eddy transport in the nonturbulent zone.

Conclusions

Conditional sampling was successfully performed on experimental data from a transitional boundary layer subject to high freestream turbulence and strong acceleration. Intermittency func-

tions based on the instantaneous streamwise velocity and the instantaneous turbulent shear stress agreed well and produced essentially equal conditional sampling results.

Mean velocity profiles differed significantly between the turbulent and nonturbulent zones, and skin friction coefficients in the turbulent zone were as much as 70% higher than in the nonturbulent zone. The $\overline{u'}$ fluctuation levels did not differ greatly between the turbulent and nonturbulent zones, but $\overline{v'}$ and the turbulent shear stress were significantly higher in the turbulent zone. Within each zone, considerable self-similarity was observed in all turbulence quantities from beginning to end of transition, particularly in the turbulent zone. The differences between the two zones and the similarity within each zone suggest the importance of properly modeling the transition process in boundary layer prediction and support arguments for the development of intermittency based models.

Although the turbulent shear stress was higher in the turbulent zone, nonturbulent zone eddy transport was still significant. In both zones there was significant deviation from low FSTI predictions.

Acknowledgments

Bill Beaver of the Technical Support Department at the U.S. Naval Academy constructed the test section. One of the authors (MPS) was supported by the Office of Naval Research as a postdoctoral fellow during the period of this work.

Nomenclature

C_f = $\tau_w/(\rho U_\infty^2/2)$, skin friction coefficient
FSTI = freestream turbulence intensity
f = frequency
$f(\gamma_{pk})$ = function of intermittency, Eq. (8)
H = δ^*/θ, shape factor
K = $(\nu/U_\infty^2)(dU_\infty/dx)$, acceleration parameter
$\hat{n}$ = dimensionless turbulent spot production rate
Re_x = $U_\infty x/\nu$, Reynolds number
Re_θ = momentum thickness Reynolds number
t = time
U = time-averaged local streamwise velocity
U_m = adjusted local velocity, Eq. (3)
U_∞ = average freestream velocity in transition region
u = instantaneous streamwise velocity
U^+ = U/u_τ, local mean streamwise velocity in wall coordinates
u' = instantaneous streamwise fluctuating velocity
$\overline{u'}$ = rms streamwise fluctuating velocity, $\sqrt{\overline{u'^2}}$
u_τ = τ_w/ρ, friction velocity

$-u'v'$ = instantaneous turbulent shear stress

$-\overline{u'v'}$ = time averaged turbulent shear stress
$\overline{v'}$ = rms cross-stream fluctuating velocity, $\sqrt{\overline{v'^2}}$
x = streamwise coordinate, distance from leading edge
y = cross-stream coordinate, distance from wall
y^+ = yu_τ/ν, distance from wall-in-wall coordinates
$\delta_{99.5}$ = 99.5% boundary layer thickness
δ^* = displacement thickness
ε_M = $-\overline{u'v'}/(dU/dy)$, eddy viscosity
Γ = intermittency function
γ = intermittency, time average of Γ (fraction flow is turbulent)
γ_{pk} = peak intermittency in profile
ν = kinematic viscosity
ρ = density
θ = momentum thickness
σ = turbulent spot propagation parameter
τ_w = wall shear stress

Subscripts

HP = high pass
LP = low pass
s = transition start
e = transition end
u = intermittency based on streamwise velocity
uv = intermittency based on turbulent shear stress
∞ = local freestream condition
1,2,3 = intermediate steps in construction of intermittency function
NT = nonturbulent zone
TURB = turbulent zone

References

[1] Mayle, R. E., 1991, "The Role of Laminar-Turbulent Transition in Gas Turbine Engines," ASME J. Turbomach., **113**, pp. 509–537.
[2] Halstead, D. E., Wisler, D. C., Okiishi, T. H., Walker, G. J., Hodson, H. P., and Shin, H.-W., 1997, "Boundary Layer Development in Axial Compressors and Turbines: Part 3 of 4—LP Turbines," ASME J. Turbomach., **119**, pp. 225–237.
[3] Blair, M. F., 1983, "Influence of Free-Stream Turbulence on Turbulent Boundary Layer Heat Transfer and Mean Profile Development: Part 1—Experimental Data," ASME J. Turbomach., **105**, pp. 33–40.
[4] Sohn, K. H., and Reshotko, E., 1991, "Experimental Study of Boundary Layer Transition with Elevated Freestream Turbulence on a Heated Flat Plate," NASA CR 187068.
[5] Kim, J., Simon, T. W., and Kestoras, M., 1994, "Fluid Mechanics and Heat Transfer Measurements in Transitional Boundary Layers Conditionally Sampled on Intermittency," ASME J. Turbomach., **116**, pp. 405–416.
[6] Blair, M. F., 1992, "Boundary Layer Transition in Accelerating Flows With Intense Freestream Turbulence: Part 1—Disturbances Upstream of Transition Onset; Part 2—The Zone of Intermittent Turbulence," ASME J. Fluids Eng., **114**, pp. 313–332.
[7] Volino, R. J., and Simon, T. W., 1997, "Boundary Layer Transition Under High Free-Stream Turbulence and Strong Acceleration Conditions: Part 1—Mean Flow Results; Part 2—Turbulent Transport Results," ASME J. Heat Transfer, **119**, pp. 420–432.
[8] Volino, R. J., and Simon, T. W., 2000, "Spectral Measurements in Transitional Boundary Layers on a Concave Wall Under High and Low Free-Stream Turbulence," ASME J. Turbomach., **122**, pp. 450–457.
[9] Volino, R. J., and Simon, T. W., 1995, "Measurements in Transitional Boundary Layers under High Free-Stream Turbulence and Strong Acceleration Conditions," NASA CR 198413.
[10] Volino, R. J., 1998, "A New Model for Free-Stream Turbulence Effects on Boundary Layers," ASME J. Turbomach., **120**, pp. 613–620.
[11] Steelant, J., and Dick, E., 1996, "Modeling of Bypass Transition with Conditioned Navier-Stokes Equations Coupled to an Intermittency Transport Equation," Int. J. Numer. Methods Fluids, **23**, pp. 193–220.
[12] Suzen, Y. B., and Huang, P. G., 2000, "Modeling of Flow Transition Using an Intermittency Transport Equation," ASME J. Fluids Eng., **122**, pp. 273–284.
[13] Solomon, W. J., Walker, G. J., and Gostelow, J. P., 1995, "Transition Length Prediction for Flows with Rapidly Changing Pressure Gradients," ASME Paper No. 95-GT-241.
[14] Kuan, C. L., and Wang, T., 1990, "Investigation of the Intermittent Behavior of a Transitional Boundary Layer Using a Conditional Averaging Technique," Exp. Therm. Fluid Sci., **3**, pp. 157–170.
[15] Wang, T., and Feller, F. J., 1999, "Intermittent Flow and Thermal Structures of Accelerating Transitional Boundary Layers, Part 1—Mean Quantities; Part 2—Fluctuation Quantities," ASME J. Turbomach., **121**, pp. 98–112.
[16] Wang, T., and Zhou, D., 1998, "Conditionally Sampled Flow and Thermal Behavior of a Transitional Boundary Layer at Elevated Free-Stream Turbulence," Int. J. Heat Fluid Flow, **19**, pp. 348–357.
[17] Volino, R. J., 1998, "Wavelet Analysis of Transitional Flow Data Under High Free-Stream Turbulence Conditions," ASME Paper No. 98-GT-289.
[18] Schultz, M. P., and Volino, R. J., 2003, "Effects of Concave Curvature on Boundary Layer Transition Under High Free-Stream Turbulence Conditions," ASME J. Fluids Eng., **125**, pp. 18–27.
[19] Wills, J. A. B., 1962, "The Correction of Hot-Wire Readings for Proximity to a Solid Boundary," J. Fluid Mech., **12**, pp. 388–396.
[20] Volino, R. J., and Simon, T. W., 1997, "Velocity and Temperature Profiles in Turbulent Boundary Layer Flows Experiencing Streamwise Pressure Gradients," ASME J. Heat Transfer, **119**, pp. 433–439.
[21] Keller, F. J., and Wang, T., 1995, "Effects of Criterion Functions on Intermittency in Heated Transitional Boundary Layers With and Without Streamwise Acceleration," ASME J. Turbomach., **117**, pp. 154–165.
[22] Solomon, W. J., 1996, "Unsteady Boundary Layer Transition on Axial Compressor Blades," Ph.D. thesis, University of Tasmania, Hobart, Tasmania, Australia.
[23] Volino, R. J., and Hultgren, L. S., 2000, "Measurements in Separated and Transitional Boundary Layers Under Low-Pressure Turbine Airfoil Conditions," ASME J. Turbomach., **123**, pp. 189–197.

[24] Johnson, M. W., 1994, ''A Bypass Transition Model for Boundary Layers,'' ASME J. Turbomach., **116**, pp. 759–764.
[25] Jones, W. P., and Launder, B. E., 1972, ''Some Properties of Sink-Flow Turbulent Boundary Layers,'' J. Fluid Mech., **56**, pp. 337–351.
[26] Narasimha, R., 1985, ''The Laminar-Turbulent Transition Zone in the Boundary Layer,'' Prog. Aerosp. Sci., **22**, pp. 29–80.
[27] Volino, R. J., and Simon, T. W., 1995, ''Bypass Transition in Boundary Layers Including Curvature and Favorable Pressure Gradient Effects,'' ASME J. Turbomach., **117**, pp. 166–174.
[28] Dhawan, S., and Narasimha, R., 1958, ''Some Properties of Boundary Layer Flow During the Transition from Laminar to Turbulent Motion,'' J. Fluid Mech., **3**, pp. 418–436.

Evaluation of the Turbulence Model Influence on the Numerical Simulations of Unsteady Cavitation

O. Coutier-Delgosha[1]
e-mail: coutier@enstay.ensta.fr

R. Fortes-Patella
e-mail: regiane.fortes@inpg.fr

LEGI-INPG, BP 53,
38041 Grenoble Cedex 9, France

J. L. Reboud
e-mail: reboud@enise.fr
ENISE-LTDS,
58, rue Jean Parot,
42023 St. Etienne, France

Unsteady cavitation in a Venturi-type section was simulated by two-dimensional computations of viscous, compressible, and turbulent cavitating flows. The numerical model used an implicit finite volume scheme (based on the SIMPLE algorithm) to solve Reynolds-averaged Navier-Stokes equations, associated with a barotropic vapor/liquid state law that strongly links the density variations to the pressure evolution. To simulate turbulence effects on cavitating flows, four different models were implemented (standard k-ε RNG; modified k-ε RNG; k-ω with and without compressibility effects), and numerical results obtained were compared to experimental ones. The standard models k-ε RNG and k-ω without compressibility effects lead to a poor description of the self-oscillation behavior of the cavitating flow. To improve numerical simulations by taking into account the influence of the compressibility of the two-phase medium on turbulence, two other models were implemented in the numerical code: a modified k-ε model and the k-ω model including compressibility effects. Results obtained concerning void ratio, velocity fields, and cavitation unsteady behavior were found in good agreement with experimental ones. The role of the compressibility effects on turbulent two-phase flow modeling was analyzed, and it seemed to be of primary importance in numerical simulations.
[DOI: 10.1115/1.1524584]

Introduction

Cavitating flows in turbomachinery lead to performance losses and modifications of the blades load. These consequences can be related to the quasi-steady cavitation effects, mainly depending on the time-averaged shapes of the vaporized structures. Moreover, turbomachinery under cavitating conditions is also submitted to transient phenomena, such as compressibility effects, flow rate fluctuations, noise, vibration, erosion, in which the unsteady behavior and the two-phase structure of the cavitating flow are influent. The study and modeling of the unsteady behavior of cavitation are thus essential to estimate the hydraulic unsteadiness in turbomachinery and the associated effects.

In this context, some numerical models taking into account the two-phase structure and the unsteady behavior of cavitation have been developed. Most of them are based on a single fluid approach: the relative motion between liquid and vapor phases is neglected and the liquid vapor mixture is treated as a homogeneous medium with variable density. The mixture density is related directly to the local void fraction and is managed either by a state law (Delannoy and Kueny [1], Song and He [2], and Merkle et al. [3]), using a supplementary equation relating the void fraction to the dynamic evolution of bubble cluster (Kubota et al. [4], and Chen and Heister [5]), or by a multiple species approach with a mass transfer law between liquid and vapor (Kunz et al. [6]). The last model can be used in a full two-fluid approach, including relative motion between the phases (Alajbegovic et al. [7]).

Main numerical difficulties are related to the strong coupling between the pressure field and the void ratio and to the coexistence of the strong compressibility of the two-phase medium with the quasi-incompressible behavior of the pure liquid flow. Moreover, the influence of the turbulence on unsteady two-phase compressible flows is not yet well known.

This paper presents unsteady cavitating flow simulations performed with a two-dimensional code. It is based on the model developed by Delannoy and Kueny [1] for inviscid fluids. Several physical modifications have been investigated by Reboud and Delannoy [8], Reboud et al. [9], and Coutier-Delgosha et al. [10] to increase the range of applications and improve the physical modeling.

In the numerical code, the two-phase aspects of cavitation are treated by introducing a barotropic law that strongly links the fluid density to the pressure variations. From the numerical point of view, this physical approach is associated with a pressure-correction scheme derived from the SIMPLE algorithm, slightly modified to take into account the cavitation process. The model has been validated on numerous cases, such as Venturi, [9,10], foils, [8,11], or blade cascades, [12,13]. The numerical results showed a good agreement with experiments. Mainly, the code leads to a reliable simulation of the cyclic self-oscillation behavior of unsteady cavitating flows.

The complex unsteady mechanism that governs this cyclic cavitation behavior is strongly affected by the applied turbulence model, [9,10]. The aim of this paper is to study the influence of different models (standard k-ε RNG; modified k-ε RNG; k-ω including or not compressibility effects) on the numerical simulation of cavitating flows. Indeed, because of the barotropic state law adopted in the model, the vaporization and condensation processes correspond mainly to highly compressible flow areas. Therefore, it is of primary importance to take into account the compressibility of the vapor/liquid mixture in the turbulence model.

The paper describes the turbulence models applied in the numerical simulations and presents comparisons between different numerical results obtained in a two-dimensional Venturi-type section, whose experimental behavior has been already studied by

[1]Currently at ENSTA UME/DFA, chemin de la Huniere, 91761 Palaiseau Cedex, France.

Contributed by the Fluids Engineering Division for publication in the JOURNAL OF FLUIDS ENGINEERING. Manuscript received by the Fluids Engineering Division August 7, 2001; revised manuscript received May 6, 2002. Associate Editor: J. Katz.

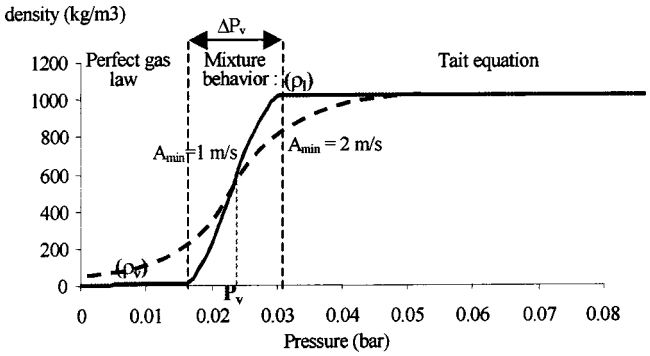

Fig. 1 Barotropic state law $\rho(P)$. Water 20°C.

Stutz and Rebouch [14,15]. In this geometry, the flow is characterized by an unstable cavitation behavior, with almost periodical vapor cloud shedding.

In addition to the standard k-ε model, three other turbulence models were applied, to investigate their influence on the two-phase turbulent flow. Mainly, the turbulence model proposed by Wilcox [16], which includes compressibility considerations, was applied, and promising results are obtained. Comparisons with experimental measurements of void ratio and velocities inside the cavity, [9], are presented.

The ability of these turbulence models to predict complex two-phase flow is discussed, and the role of the compressibility effects is studied.

Physical Model

The present work applies a single fluid model based on previous numerical and physical studies, [1,8–10]. The fluid density ρ varies in the computational domain according to a barotropic state law $\rho(P)$ that links the density to the local static pressure (Fig. 1). When the pressure in a cell is higher than the neighborhood of the vapor pressure ($P > P_v + (\Delta P_v/2)$), the fluid is supposed to be purely liquid. The entire cell is occupied by liquid, and the density ρ_l is calculated by the Tait equation, [17]. If the pressure is lower than the neighborhood of the vapor pressure ($P < P_v - (\Delta P_v/2)$), the cell is full of vapor and the density ρ_v is given by the perfect gas law (isotherm approach). Between purely vapor and purely liquid states, the cell is occupied by a liquid/vapor mixture, which is considered as one single fluid, with the variable density ρ. The density ρ is directly related to the void fraction $\alpha = (\rho - \rho_l)/(\rho_v - \rho_l)$ corresponding to the local ratio of vapor contained in this mixture.

To model the mixture state, the barotropic law presents a smooth link in the vapor pressure neighborhood, in the interval $\pm(\Delta P_v/2)$. In direct relation with the range ΔP_v, the law is characterized mainly by its maximum slope $1/A^2_{\min}$, where $A^2_{\min} = \partial P/\partial\rho$. $A_{\min}$ can thus be interpreted as the minimum speed of sound in the mixture. Its calibration was done in previous studies, [10]. The optimal value was found to be independent of the hydrodynamic conditions, and is about 2 m/s for cold water, with $P_v = 0.023$ bar, and corresponding to $\Delta P_v \approx 0.06$ bar (green chart on Fig. 1). That value is applied for the computations presented hereafter.

Mass fluxes resulting from vaporization and condensation processes are treated implicitly by the barotropic state law, and no supplementary assumptions are required. Concerning the momentum fluxes, the model assumes that locally velocities are the same for liquid and for vapor: In the mixture regions vapor structures are supposed to be perfectly carried along by the main flow. This hypothesis is often assessed to simulate sheet-cavity flows, in which the interface is considered to be in dynamic equilibrium, [3]. The momentum transfers between the phases are thus strongly linked to the mass transfers.

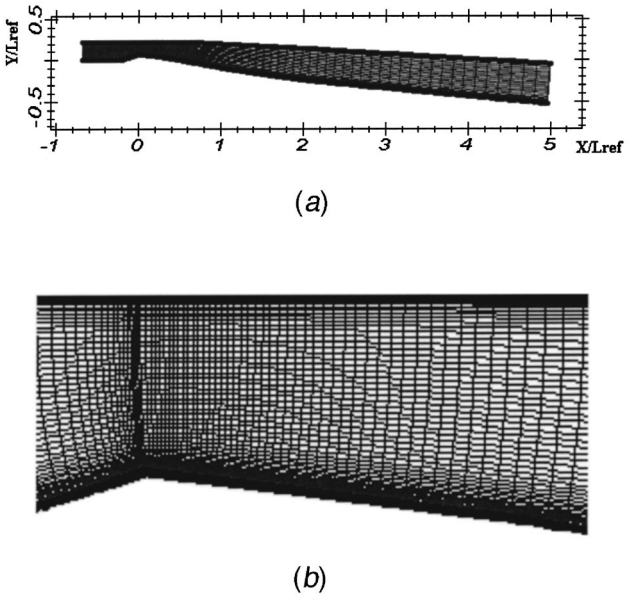

Fig. 2 (*a*) Curvilinear-orthogonal mesh of the Venturi-type section (160×50 cells). L_{ref}=224 mm. (*b*) Zoom in the throat region.

Numerical Model

To solve the time-dependent Reynolds-averaged Navier-Stokes equations associated with the barotropic state law presented here above, the numerical code applies, on two-dimensional structured curvilinear-orthogonal meshes, the SIMPLE algorithm, modified to take into account the cavitation process. It uses an implicit method for the time-discretization, and the HLPA nonoscillatory second-order convection scheme proposed by Zhu [18]. The numerical model is detailed in Coutier-Delgosha et al. [10]: A complete validation of the method was performed, and the influence of the numerical parameters was widely investigated. The present paper describes mainly the different turbulence models applied.

Boundary Conditions. In the code, the velocity field is imposed at the computational domain inlet, and the static pressure is imposed at the outlet. Along the solid boundaries, the turbulence models are associated with laws of the wall.

Initial Transients Conditions. To start unsteady calculations, the following numerical procedure is applied: First of all, a stationary step is carried out, with an outlet pressure high enough to avoid any vapor in the whole computational domain. Then, this pressure is lowered slowly at each new time-step, down to the value corresponding to the desired cavitation number σ. Vapor appears during the pressure decrease. The cavitation number is then kept constant throughout the computation.

The Geometry

Numerical simulations have been performed on a Venturi-type section whose convergent and divergent angles are, respectively, about 18 deg and 8 deg (Fig. 2(*a*)). The shape of the Venturi bottom downstream from the throat simulates an inducer blade suction side with a beveled leading edge geometry (Kueny et al. [19]) and a chord length $L_{ref} = 224$ mm.

According to experimental observations, in this geometry the flow is characterized by unsteady cavitation behavior, [14], with quasi-periodic fluctuations. Each cycle is composed of the following successive steps: The attached sheet cavity grows from the Venturi throat. A re-entrant jet is generated at the cavity closure and flows along the Venturi bottom toward the cavity upstream

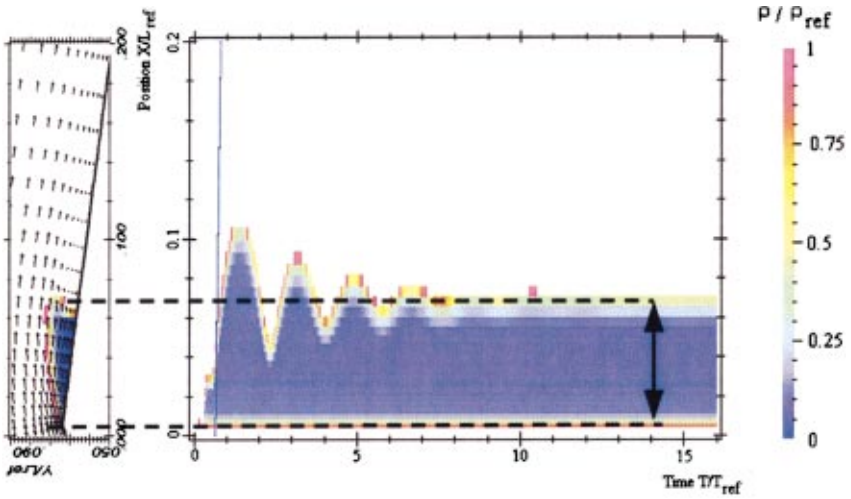

Fig. 3 Time evolution of the cavity length. The time is reported in abscissa, and the *X* position in the tunnel of cavitation is graduated in ordinate. The colors represent the density values: white for the pure liquid one and from red to dark blue for the vapor one. At a given point in time and position, the color indicates the minimum density in the corresponding cross section of the cavitation tunnel. Calculation conditions: $\sigma \approx 2.4$; $V_{ref}=7.2$ m/s; mesh=160×50-time-step $\Delta t=0.005T_{ref}$ ($T_{ref}=L_{ref}/V_{ref}$).

end. Its interaction with the cavity surface results in the cavity break off. The generated vapor cloud is then convected by the main stream, until it collapses.

For a cavitation number σ of about 2.4 (based on the time-averaged upstream pressure) and an inlet velocity $V_{ref}=7.2$ m/s, vapor shedding frequency observed experimentally is about 50 Hz for a cavity length of 45±5 mm, [14].

The standard computational grid is composed of 160×50 orthogonal cells (Fig. 2(*a*)). A special stretching of the mesh is applied in the main flow direction just after the throat, so that the two-phase flow area is efficiently simulated: about 50 grid points are used in this direction to model the 45-mm long mean cavity obtained hereafter (Fig. 2(*b*)). In the other direction, a stretching is also applied close to the walls, to obtain at the first grid point the non dimensional parameter y^+ of the boundary layer varying between 30 and 100 and to use standard laws of the walls. The grid is finer in the bottom part of the Venturi section than in its upper part, to enhance the accuracy in the cavitation domain: Cavities obtained in the following sections contain about 30 cells across their thickness.

Turbulence Models

(a) Standard k-ε RNG Model. The first model applied in the numerical code is a standard k-ε RNG model, associated with laws of the wall, [9].

In this model, the effective viscosity applied in the Reynolds equations is defined as $\mu=\mu_t+\mu_l$ where $\mu_t=\rho C_\mu k^2/\varepsilon$ is the turbulent viscosity and $C_\mu=0.085$ (Yakhot et al. [20]).

This model is originally devoted to fully incompressible fluids, and no particular correction is applied here in the case of the highly compressible two-phase mixture. Thus, the fluid compressibility is only taken into account in the turbulence equations through the mean density ρ changes.

With this model, the unstable cavitating behavior observed experimentally is not correctly simulated: After an initial transient fluctuation of the cavity length, the numerical calculation leads to a quasi-steady behavior of the cavitation sheet, which globally stabilizes (Fig. 3).

The resulting cavity length is much too small, compared with the experimental observations (in this case, the error is larger than 50 percent). Moreover, comparisons with experimental data obtained by double optical probes by Stutz and Reboud [14,15] show that the numerical mean void ratio is overestimated in the main part of the cavity. Calculations give a high time-averaged void ratio in the upstream part of the cavitation sheet (>90 percent), abruptly falling to 0 percent in the wake, while the measured void ratio never exceeds 25 percent and decreases slowly from the cavity upstream end to its wake.

This poor agreement with the real configuration seems to be related to an overprediction of the turbulent viscosity in the rear part of the cavity. The cyclic behavior of the cloud cavitation process is strongly related to the re-entrant jet development from the cavity closure, [17]. As a matter of fact, the main problem in the turbulent flow simulations consisted in the premature removal of the reverse flow along the solid wall: the re-entrant jet was stopped too early and it did not result in any cavity break off.

It is worth noting that numerical tests reported in [10] confirm that the mesh size, spatial scheme, and the time discretization applied in the model do not modify the results. Computations performed with a finer mesh (264×90) and first or second-order accurate time discretization schemes still lead to the same complete stabilization of the cavitation sheet.

(b) Modified k-ε RNG Model. To improve the turbulence modeling and to try to better simulate the re-entrant jet behavior

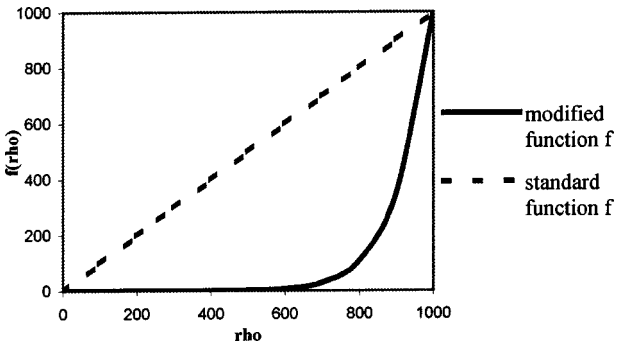

Fig. 4 Modification of the mixture viscosity ($n=10$)

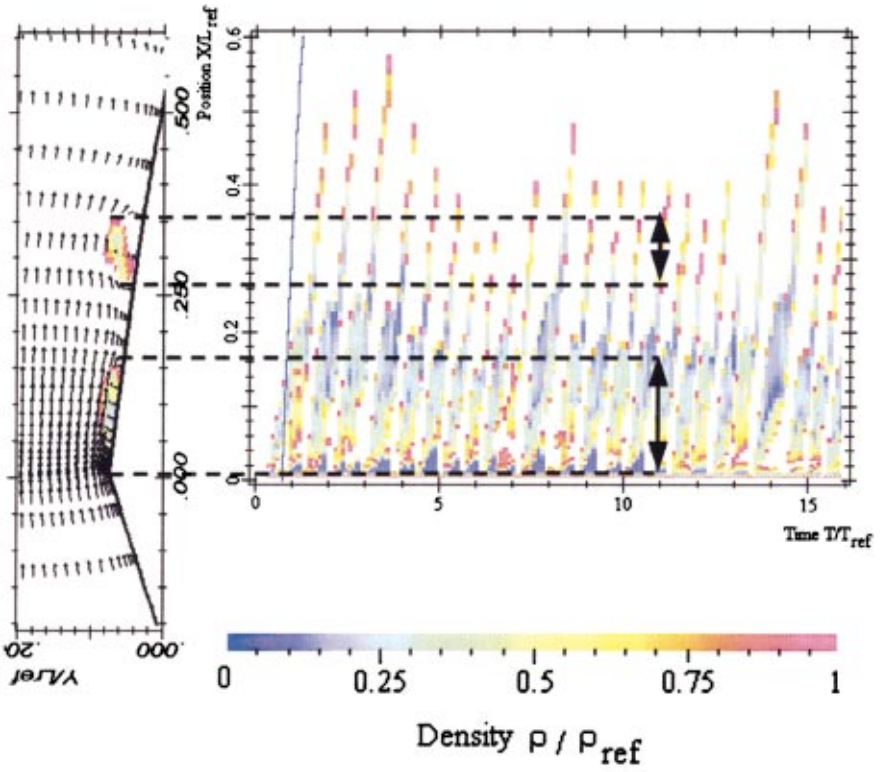

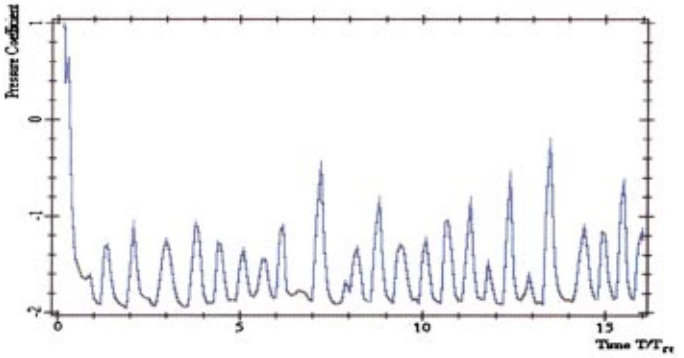

Fig. 5 Transient evolution of unsteady cavitating flow in the Venturi-type duct. (*a*) Temporal evolution (in abscissa) of the cavity length (graduated in ordinate). Instantaneous density distribution of attached and cloud cavities are drawn on the left at $T=11T_{ref}$ (velocity vectors are drawn only 1 cell over 2 in the two directions). (*b*) Time evolution of the upstream pressure.

and the vapor cloud shedding, we modified the standard k-ε RNG model simply by reducing the mixture turbulent viscosity, mainly in the low void ratio areas:

$$\mu_t = f(\rho) C_\mu k^2/\varepsilon$$

where

$$f(\rho) = \rho_v + \left(\frac{\rho_v - \rho}{\rho_v - \rho_l}\right)^n (\rho_l - \rho_v) \quad n \gg 1.$$

Indeed, according to the experimental results [15], the reentrant jet seems to be mainly composed of liquid ($\alpha \sim 0$), and thus the reduction of the mixture turbulence viscosity leads to

Table 1 Numerical tests performed on the Venturi-type section with the k-ε modified model $\sigma=2.4$, $A_{min}=2$ m/s, $\rho_v/\rho_l=0.01$

		RESULTS		
$\Delta T/T_{ref}$	Mesh	Mean Vapor Volume ($\times 10^{-4}$ m^3)	Oscillation Frequency (Hz)	Standard Deviation ($\times 10^{-4}$ m^3)
		Reference case		
0.005	160×50	11.0	55	2.4
		Influence of the time-step		
0.002	160×50	12.3	51	4.3
0.005	160×50	11.0	55	2.4
0.01	160×50	9.3	55	2.7
		Influence of the mesh		
0.002	264×90	15.6	52	2.9
0.005	264×90	14.5	54	4.3
0.005	160×50	11.0	55	2.4
0.005	110×30	6.9	64	1.9

substantial changes in the simulation. The prediction of the unsteady re-entrant jet is now obtained, and the vapor cloud shedding is well simulated (See Fig. 4.)

The transient evolution observed during this unsteady calculation is shown in Fig. 5. Fig. 5(*a*) illustrates at a given time and for each cross section of the Venturi-type duct the value of the minimal density in the section. By comparison with Fig. 3, it gives information concerning the vapor cloud shedding process: the part of the cavity that breaks off clearly appears, and the fluctuation frequency can be evaluated. Moreover, it also supplies the maximum void ratio in each section. Curve 5b presents the transient upstream pressure evolution.

The experimental self-oscillatory behavior of the cavitation sheet is correctly simulated (Fig. 5). We obtain in this case a fluctuating cavity whose mean length is about 45 mm (i.e., $L_{cav}/L_{ref}=0.2$). The mean fluctuation period is about $0.59\,T_{ref}$, and the corresponding shedding frequency equals 55 Hz. Both length and frequency are in good agreement with measurements (i.e., 45 mm and 50 Hz, respectively). The reduced frequency based on the reference velocity and the mean cavity length equals 0.33, which only slightly overestimates the classical Strouhal number St=0.3 (0.28 from the experimental measurements). The transient evolution is almost periodic, with some random disturbances affecting the oscillation regularity. This behavior is consistent with the experimental observations, which pointed out a quite regular cavitation cycle, whose frequency fluctuated around a central value, [14].

Several tests were performed to investigate the influence of the numerical parameters on the unsteady cavitating result. The whole study, including the influence of the grid size, the time-step, the order of the time discretization scheme, the ratio ρ_v/ρ_l, and the maximum slope of the barotropic law A_{min}, is detailed in [10]. Results concerning the grid resolution and the time step influence are reported in the present paper in Table 1. The effect of the mesh size appears to be small, so far it is fine enough: the cavity oscillation frequency is almost constant with the two finest grids. In contrast, the influence of the time-step cannot be completely removed: using $\Delta t=0.005\,T_{ref}$ leads to a systematic slight overestimation of the cycles frequency. Nevertheless, it must be considered that the uncertainty on experimental measurements is of the same order of magnitude.

(c) k-ω Model: Compressibility Effects. As presented before, the proposed numerical simulations take into account a single-flow physical model to describe cavitation phenomenon. According to the adopted barotropic state law, in the vapor/liquid mixture zones the sound celerity $A=\sqrt{\partial P/\partial\rho}$ is very low, the fluid is locally highly compressible. Thus the flow often reaches Mach numbers larger than 5 in the vaporization or condensation areas. As a matter of fact, Birch and Eggers [21] showed that an increase of the Mach number could modify substantially the turbulence structure in some configurations, such as mixing layers. To analyze and to evaluate the compressibility effects on the turbulence modeling of cavitating flows, we implemented in the numerical code the k-ω turbulence model proposed by Wilcox [16]. Its major advantage, compared with the previous models, consists in the corrections that are proposed by Wilcox in the turbulence equations to model the effects of density fluctuations. The main features of the models are presented hereafter. All details concerning the turbulence model can be found in [16].

Basic Model Equations. Equations are similar to the governing equations resolved in the case of the k-ε model: All the modifications result from the use of the dissipation specific rate ω instead of the turbulence dissipation ε. The turbulent viscosity expression and the k-equation are modified, and the ε equation is replaced by a ω equation:

$$\nu_t=\frac{k}{\omega}$$

$$\frac{\partial k}{\partial t}+u_j\frac{\partial k}{\partial x_j}=\tau_{ij}\frac{\partial u_i}{\partial x_j}-\beta_w^*k\omega+\frac{\partial}{\partial x_j}\left[(\nu+\sigma_w^*\nu_t)\frac{\partial k}{\partial x_j}\right]$$

$$\frac{\partial \omega}{\partial t}+u_j\frac{\partial \omega}{\partial x_j}=\alpha_w\frac{\omega}{k}\tau_{ij}\frac{\partial u_i}{\partial x_j}-\beta_w\omega^2+\frac{\partial}{\partial x_j}\left[(\nu+\sigma_w\nu_t)\frac{\partial \omega}{\partial x_j}\right]$$

where $\alpha_w=5/9$, $\beta_w=3/40$, $\beta_w^*=9/100$, $\sigma_w=0.5$, and $\sigma_w^*=0.5$ are the coefficients of the model.

$$\tau_{ij}=2\,\nu_t S_{ij}\quad\text{with}\quad S_{ij}=\frac{1}{2}(u_{i,j}+u_{j,i})$$

Compressibility Effects. By analyzing the reduction of the mixing layer growth rate as a function of the Mach number, Wilcox [16] observed that the phenomenon could not be well simulated only by taking into account the mean density evolution through the mixing length, and that an explicit supplementary correction must be applied. He concludes that the Reynolds-stress transport equation is directly concerned with the compressibility effects, and introduced the influence of the Mach number in the turbulence equations.

The modifications proposed by Wilcox are based on the previous studies of Sarkar et al. [22] and Zeman [23], who aimed to take into account the compressibility effects in a k-ε turbulence model.

He adapted this development to the k-ω model to propose the following equations giving the parameters β_w and β_w^* as functions of the turbulence Mach number defined as $M_t^2=2k/A^2$ (where A is the local sound celerity).

$\beta_w^*=\beta_{wi}^*(1+\xi^*F(M_t))$ and $\beta_w=\beta_{wi}-\beta_{wi}^*\xi^*F(M_t)$, where the index i indicates the values of the incompressible model given before

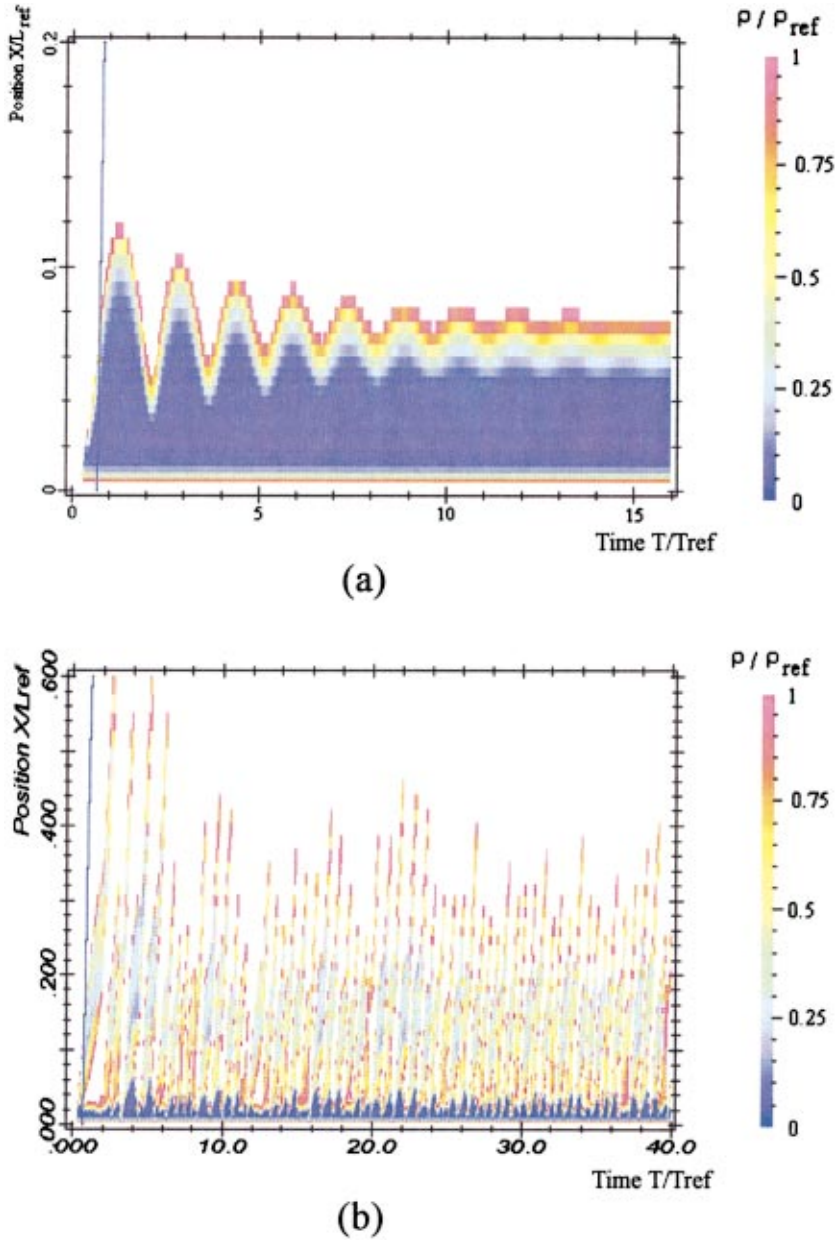

Fig. 6 Unsteady cavitation behavior calculated with the k-ω model—(*a*) without and (*b*) with compressibility effects

$$\text{with } F(M_t)=\begin{cases}(M_t^2-M_{t_0}^2) & \text{if } M_t>M_{t_0}\\ 0 & \text{if } M_t\leq M_{t_0}\end{cases}$$

$$M_{t_0}=0.25 \text{ and } \xi^*=1.5.$$

Results. Figure 6 presents calculations performed with the k-ω turbulence model.

In the first case (Fig. 6(*a*)), the influence of the compressibility is not taken into account in the model. The numerical results are not satisfactory: As in the case of standard k-ε RNG model, the unsteady cavitation behavior is not correctly simulated and the cavity length obtained by simulations is more than 50 percent smaller than the experimental one. On the other hand, numerical results obtained by taking into account the compressibility effects are in good agreement with experimental ones. They are very similar to those presented previously in the case of the modified k-ε RNG model: As can be seen in Fig. 6(*b*), the vapor cloud shedding process is correctly simulated. The mean cavity length is still correct, and the shedding frequency remains almost the same.

Comparisons are investigated with experimental data obtained by using double optical probes, [15]. This intrusive technique allows measurements of the local void ratio and the velocities of the two-phase structures inside the cavitation sheet. Their time-averaged and standard deviation values are presented for four profiles in Fig. 7.

These comparisons point out a general good agreement between experimental and numerical results. The time-averaged void ratio repartition is well predicted, and the re-entrant jet structure under the cavity appears qualitatively correct. The fluctuation levels are also in reliable close agreement with measurements. The negative velocity region at station $x=0.065$ m corresponds to the rear part of the cavity, alternatively affected by the re-entrant jet progression and by the vapor cloud shedding. Both models fail to simulate these negative velocities, because of a slight underestimation

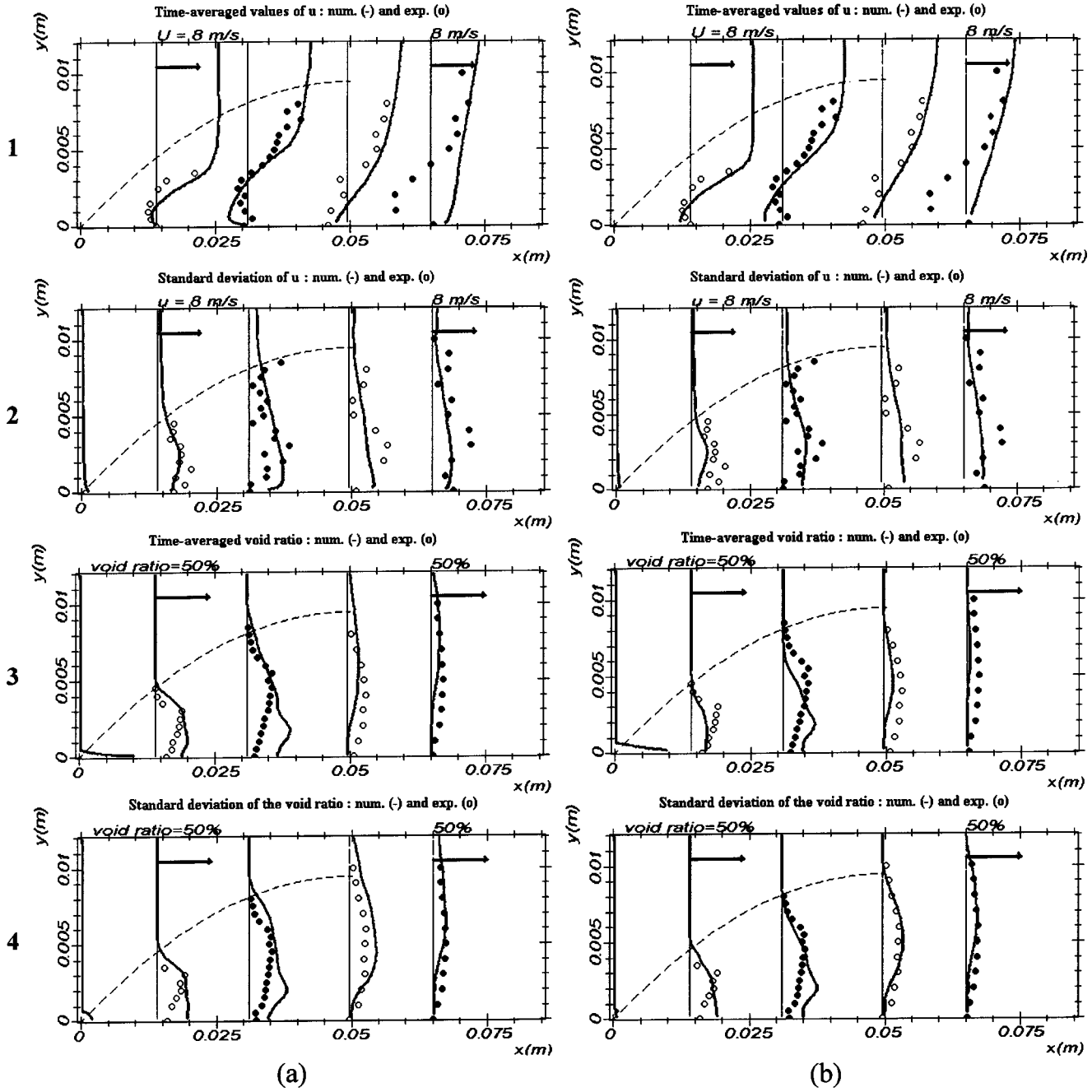

Fig. 7 Time-averaged values and standard deviation of velocity (1,2) and void ratio (3,4). Numerical results: (*a*) modified k-ε, (*b*) compressible k-ω (lines) and optical probe measurements (points)—V_{ref}=7.2 m/s. Mean cavity length 45 mm: dotted line =experimental external shape of the cavity, obtained from image processing (sigma=2.4).

of the mean cavity length in this configuration. A second discrepancy can be observed at station 0.03 m, concerning the void ratio distribution close to the wall; nevertheless, the experimental estimation of velocities and void ratio in the re-entrant jet is associated to a high uncertainty in this area, due to important fluctuations level, [14]. Thus, the comparison, along the wall, between experiments and the numerical result cannot be relevant.

Conclusion

Four turbulence models have been applied to simulate unsteady cavitating flows in a Venturi-type section.

Results obtained with the standard k-ε RNG model and with the k-ω model without taking into account compressibility effects are in poor agreement with experimental observations: the models fail to reproduce the vapor cloud shedding behavior observed experimentally. Moreover, numerical tests reported in [10] and the results presented here above indicate that the global level of dissipation induced by the numerical model seems not to be responsible for its inability to simulate the unsteady cavity behavior.

On the other hand, the modified k-ε RNG model and the k-ω model including compressibility effects lead to a very reliable simulation of the Venturi unsteady cavitation behavior. The satisfactory results obtained with the modified k-ε RNG model have been confirmed by simulations performed in other geometries,

such as a hydrofoil, [11], a foil cascade, [13], and another Venturi-type section leading to a more stable sheet of cavitation, [10]. In all cases, the general experimental behavior is correctly obtained, and oscillation frequencies are accurately predicted in unsteady configurations.

Results obtained in the present paper with k-ω models pointed out the relevant role of the compressibility effects on the turbulence model. Indeed, the corrections proposed to treat compressibility effects take into account the density fluctuations: a supplementary term appears from the averaged equations, increasing the turbulent dissipation. The final effect is a reduction of the turbulent viscosity in the compressible areas, i.e., in the vapor/liquid mixture zones.

The modifications proposed to improve the k-ε RNG model had been also based on the reduction of the turbulent viscosity in the mixture zones, which are characterized by a very low sound celerity and large Mach number. Indeed, results obtained with the modified k-ε RNG model are similar to the ones calculated by the compressible k-ω model.

According to the numerical calculations, the fluid compressibility has a strong effect on the turbulence structure, and must be taken into account to simulate unsteady cavitating flows.

Acknowledgments

The authors wish to express their gratitude to the French Space Agency: Centre National d'Etudes Spatiales (CNES) for its continuous support.

Nomenclature

$A_{\min}$ = minimum speed of sound in the medium (m/s)
Cp = $(P-P_{\text{ref}})/(\rho V_{\text{ref}}^2/2)$ pressure coefficient
k = turbulent kinetic energy per unit mass (m^2s^{-2})
L_{ref} = geometry reference length (m)
P = local static pressure (Pa)
P_{ref} = reference pressure (Pa)
P_v = vapor pressure (Pa)
V_{ref} = reference velocity ($=V_{\text{upstream}}$) (ms^{-1})
α = void ratio
ε = turbulence dissipation per unit mass (m^2s^{-3})
μ_l, μ_t = laminar and turbulent dynamic viscosity (Pa·s)
ν, ν_t = laminar and turbulent kinetic viscosity (m^2/s)
ΔP_v = range of mixture state law (Pa)
ρ = mixture density (kg/m^3)
ρ_l, ρ_v = liquid, vapor density (kg/m^3)
ρ_{ref} = reference density ($=\rho_l$) (kg/m^3)
σ = $(P_{\text{upstream}}-P_v)/(\rho V_{\text{ref}}^2/2)$ cavitation number
ω = specific dissipation rate (s^{-1})

References

[1] Delannoy, Y., and Kueny, J. L., 1990, "Two Phase Flow Approach in Unsteady Cavitation Modeling," *Cavitation and Multiphase Flow Forum*, ASME, New York, **98**, pp. 153–158.
[2] Song, C., and He, J., 1998, "Numerical Simulation of Cavitating Flows by Single-Phase Flow Approach," *3rd Int. Symp. on Cavitation*, J. M. Michel and H. Kato, eds., Grenoble, France, pp. 295–300.
[3] Merkle, C. L., Feng, J., and Buelow, P. E. O., 1998, "Computational Modeling of the Dynamics of Sheet Cavitation," *3rd Int. Symp. on Cavitation*, J. M. Michel and H. Kato, eds., Grenoble, France, pp. 307–313.
[4] Kubota, A., Kato, H., and Yamagushi, H., 1992, "A New Modeling of Cavitation Flows: A Numerical Study of Unsteady Cavitation on a Hydrofoil Section," J. Fluid Mech., **240**, pp. 59–96.
[5] Chen, Y., and Heister, S. D., 1996, "Modeling Hydrodynamic Non Equilibrium in Cavitating Flows," ASME J. Fluids Eng., **118**, pp. 172–178.
[6] Kunz, R., Boger, D., Chyczewski, T., Stinebring, D., and Gibeling, H., 1999, "Multi-phase CFD Analysis of Natural and Ventilated Cavitation About Submerged Bodies," 3rd ASME/JSME Joint Fluids Engineering Conference, San Francisco, CA.
[7] Alajbegovic, A., Grogger, H., and Philipp, H., 1999, "Calculation of Transient Cavitation in Nozzle Using the Two-Fluid Model," 12th Annual Conf. on Liquid Atomization and Spray Systems, May 16–19, Indianapolis, IN.
[8] Reboud, J. L., and Delannoy, Y., 1994, "Two-Phase Flow Modeling of Unsteady Cavitation", 2nd Int. Symp. on Cavitation, Tokyo.
[9] Reboud, J. L., Stutz, B., and Coutier, O., 1998, "Two-Phase Flow Structure of Cavitation: Experiment and Modeling of Unsteady Effects," 3rd Int. Symp. on Cavitation, Grenoble, France.
[10] Coutier-Delgosha, O., Reboud, J. L., and Delannoy, Y., "Numerical Simulations in Unsteady Cavitating Flows," submitted to the Int. J. Numer. Methods Fluids.
[11] Hofmann, M., Lohrberg, H., Ludwig, G., Stoffel, B., Reboud, J. L., and Fortes-Patella, R., 1999, "Numerical and Experimental Investigations on the Self-Oscillating Behavior of Cloud Cavitation: Part 1 Visualisation/Part 2 Dynamic Pressures," 3rd ASME/JSME Joint Fluids Engineering Conference, San Francisco, July 1999.
[12] Coutier-Delgosha, O., Reboud, J. L., and Albano, G., 2000, "Numerical Simulation of the Unsteady Cavitation Behavior of an Inducer Blade Cascade," *Proceedings of ASME FEDSM00*, ASME, New York.
[13] Lorberg, H., Stoffel, B., Fortes-Patella, R., Coutier-Delgosha, O., and Reboud, J. L., 2002, "Numerical and Experimental Investigations on the Cavitating Flow in a Cascade of Hydrofoils," Exp. Fluids, accepted for publication.
[14] Stutz, B., and Reboud, J. L., 1997, "Experiments on Unsteady Cavitation," Exp. Fluids, **22**, pp. 191–198.
[15] Stutz, B., and Reboud, J. L., 2000, "Measurements Within Unsteady Cavitation," Exp. Fluids, **29**, pp. 545–552.
[16] Wilcox, D., 1998, *Turbulence Modeling for CFD*, DCW Industries, La Canada, CA.
[17] Knapp, R. T., Daily, J. T., and Hammit, F. G., 1970, *Cavitation*, McGraw-Hill, New York.
[18] Zhu, J., 1991, "A Low Diffusive and Oscillation-Free Convection Scheme," Commun. Appl. Numer. Methods, 7.
[19] Kueny, J. L., Reboud, J. L., and Desclaux, 1991, "Analysis of Partial Cavitation: Image Processing and Numerical Prediction," *Cavitation '91*, ASME, New York. ASME-FED Vol. 116, pp. 55–60.
[20] Yakhot, V., Orszag, S. A., Thangham, S., Gatski, T. B., and Speziale, C. G., 1992, "Development of Turbulence Models for Shear Flows by a Double Expansion Technique," Phys. Fluids A, **4**, pp. 1510–1520.
[21] Birch, S. F., and Eggers, J. M., 1972, *Free Turbulent Shear Flow*, NASA SP-321, **1**, pp. 11–40.
[22] Sarkar, S., Erlebacher, G., Hussaini, M. Y., and Kreiss, H. O., 1989, "The Analysis and Modeling of Dilatational Terms in Compressible Turbulence," NASA CR-181959.
[23] Zeman, O., 1990, "Dilatational Dissipation: The Concept and Application in Modeling Compressible Mixing Layers," Phys. Fluids A, **2**(2), pp. 178–188.

Eulerian/Lagrangian Analysis for the Prediction of Cavitation Inception

Kevin J. Farrell[1]
Associate Research Engineer,
Applied Research Laboratory,
The Pennsylvania State University
P.O. Box 30,
State College, PA 16804

An Eulerian/Lagrangian computational procedure was developed for the prediction of cavitation inception by event rate. The carrier-phase flow field was computed using an Eulerian Reynolds-averaged Navier-Stokes (RANS) solver. The Lagrangian analysis was one-way coupled to the RANS solution, since at inception, the contributions of mass, momentum, and energy of the microbubbles to the carrier flow are negligible. The trajectories were computed using Newton's second law with models for various forces acting on the bubble. The growth was modeled using the Rayleigh-Plesset equation. The important effect of turbulence was included by adding a random velocity component to the mean flow velocity and by reducing the local static pressure. Simulation results for the Schiebe body indicate agreement with experimentally observed trends and a significant event rate at cavitation indices above visual inception. [DOI: 10.1115/1.1522411]

1 Introduction

The usual approach for predicting the cavitation inception pressure for a hydraulic device is to build and evaluate a small-scale model. However, a number of similarity conditions are violated for practical reasons. The methods of properly scaling the model results to full scale are unique for the type of cavitation encountered and have stimulated research for decades. For vortical flows, most methods are based on a Reynolds number scaling to an exponent, [1], and vary with the water quality. Any cavitation analysis requires an accurate determination of the fluid dynamics and knowledge of the bubble mechanics. The minimum pressure in a tip clearance vortex in a pump, for example, will depend on the tip clearance, flow coefficient, lift coefficient, and blade and end-wall boundary layers. While within certain restricted classes of turbomachines, the empirical scaling procedure may work satisfactorily (e. g., [2]), a physics-based predictive capability which integrates the known variables affecting the cavitation inception problem has not been developed.

Two-phase flow can be analyzed as two fluids in the Eulerian/Eulerian approach, or as a continuum phase and a particulate phase in the Eulerian/Lagrangian or trajectory approach. The two-fluid models can easily incorporate particle diffusion effects (if data are available) and can be extended easily to multidimensional flows. However, numerical instabilities, numerical diffusion, and large storage requirements for multiple particle sizes are inherent difficulties. The trajectory approach embodies the natural solution scheme for each phase and exhibits no numerical diffusion of the particulate phase. Also, storage requirements for poly-disperse particles are not excessive. Particle dispersion may be incorporated through an empirical diffusion velocity via Monte Carlo methods. A variety of models has been developed for the Eulerian/Lagrangian treatment of carrier-particle flows, and can be categorized based on the coupling between the phases, and the modeling approach.

Meyer, Billet, and Holl [3] correlated a numerical simulation of the cavitation on a Schiebe headform with experimental inception data. A computer code was developed to statistically model cavitation inception, consisting of a numerical solution to the Rayleigh-Plesset equation coupled to a set of trajectory equations. Using the code, trajectories and growths were computed for bubbles of varying initial sizes. An off-body distance was specified along the $C_p = 0$ isobar, and the bubble was free to follow an off-body trajectory. A Monte Carlo cavitation simulation was performed in which a variety of random processes, including stroboscopic observation, were modeled. Three different nuclei distributions were specified including one similar to that measured in the water tunnel experiment. The results compared favorably to the experiment. Cavitation inception was shown to be sensitive to nuclei distribution. The off-body effect was also found to be a significant factor in determining whether or not a bubble would cavitate. The traditional definition of a critical diameter based on the minimum pressure coefficient of the body or the measurement of liquid tension was found to be inadequate in defining cavitation inception. Results show that much larger bubbles are necessary because of the off-body pressure gradients which direct nuclei away from the region of minimum pressure.

Hsiao and Pauley [4] recently completed a Reynolds-averaged Navier-Stokes (RANS) computation of a tip vortex flow from a finite-span hydrofoil. The Rayleigh-Plesset equation for bubble growth was coupled with Johnson and Hsieh's [5] trajectory equation to track single microbubbles through the steady-state flow field and thereby infer cavitation inception. The larger bubbles controlled the cavitation index, and their likelihood of cavitation was less dependent on the release location than for the smaller bubbles. Comparative cavitation experiments were not presented. The present work builds on this type of soft coupling, yet includes a spectrum of nuclei sizes, the effect of turbulence on trajectory and pressure, and some additional forces.

Chahine [6] and colleagues have pursued a different approach to study the dynamics of traveling bubble cavitation inception using inviscid potential flow, but including modification of the flow by the nucleus, and allowing the nucleus to deform. Recently, the boundary element treatment of the bubble has been coupled with an unsteady RANS solution and Rayleigh-Plesset solution. These calculations have provided detailed information about the capture, growth, and collapse of a single bubble in a Rankine vortex. However, the large computation resources required to exercise these models are neither required for inception nor amenable to engineering design, particularly for a large sample population of nuclei.

[1]Currently with Heat Transfer Research, Inc., 150 Venture Drive, College Station, TX 77845. e-mail: kjf@htri.net.

Contributed by the Fluids Engineering Division for publication in the JOURNAL OF FLUIDS ENGINEERING. Manuscript received by the Fluids Engineering Division, Jan. 22, 2001; revised manuscript received June 28, 2002. Associate Editor: J. Katz.

2 Objective

The first application of this procedure was for an axisymmetric headform known as a ''Schiebe'' body, [7], which has been widely used for cavitation research (e. g., Gates et al. [8]; Hamilton, Thompson, and Billet [9]; Holl and Carroll [10]; Ceccio and Brennen [11]; Meyer, Billet, and Holl [3]; Kuhn de Chizzelle, Ceccio, and Brennen [12]; and Liu and Brennen [13]). The headform represents a family of half-bodies formed by the addition of a disk source and a uniform stream. The headform exhibits a relatively smooth adverse pressure gradient, and the boundary layer does not separate. Because of the large database covering a number of nuclei distributions, Reynolds numbers, and geometric scales, and the well-behaved flow field, the Schiebe body is an ideal geometry for development and demonstration of the prediction method. While the eventual goal is an inception prediction capability for the vortical flows which often control the cavitation performance of many modern pump and marine propeller designs, demonstration in axisymmetric flows is a necessary prerequisite. It is important to emphasize that the technique is to be used as an engineering design tool for hydraulic devices. The microscales of nuclei shapes and histories are not the focus. The issue is whether or not cavitation inception is imminent in the operating range of the device. As an engineering tool, one desires an efficient procedure in order to facilitate parametric studies of design concepts and attributes, in addition to the role played by the nuclei distribution.

3 Eulerian Liquid Flow Field Analysis

The main thrust of present day computational fluid mechanics efforts at ARL Penn State for turbomachinery analysis is solutions of the RANS equations. The RANS solver employed was the incompressible UNCLE (unsteady computation of field equations) code that was developed by Prof. David Whitfield and colleagues at Mississippi State University's Engineering Research Center (e.g., [14,15]). The code uses an implicit finite volume numerical approach for solving the unsteady three-dimensional incompressible Navier-Stokes equations in a general time-dependent curvilinear coordinate system. The numerical flux at cell faces is calculated using the Roe [16] approximate Riemann solver. Newton's method is the iterative process used to obtain both steady and unsteady solutions. The solution matrix operator is novel in that it is a discretized Jacobian, whose elements are obtained by using simple finite differences of the flux vectors. The discretized Jacobian is then used in a combination Newton-relaxation solution method where Newton is primary and relaxation is secondary. The Navier-Stokes equations are simulated through an explicit treatment of the diffusive fluxes. The code accommodates multiblock and dynamic grids. The UNCLE code uses artificial compressibility in order to directly couple the pressure and velocity fields and thus apply time-marching compressible flow algorithms. The code also employs the thin-layer approximation, whereby the viscous terms parallel to a vorticity generating surface are neglected as a consequence of an order-of-magnitude analysis.

The solution of the Reynolds-averaged Navier-Stokes equations requires modeling of the Reynolds stress terms. In assessing the cavitation potential of a flow-field, the turbulent fluctuations of the static pressure may be important enough to cause inception in an otherwise non-cavitating flow field. On the other hand, the stimulation of a boundary layer to the turbulent state may prevent cavitation. Aside from the effect on the local static pressure, the length and time scales of the carrier flow determine the dispersion of the nuclei. For these reasons, the modeling of the turbulence can be very important. The original turbulence model used in the code was the Baldwin-Lomax algebraic model. Other users have subsequently added the two-equation q-ω and κ-ε models (e.g., Zierke [17]). These are of particular interest here, since the turbulent kinetic energy will be used to deduce a turbulent diffusion velocity for the bubble and a turbulent pressure fluctuation which may augment bubble growth. Two-equation models are generally viewed as the minimum acceptable level of closure since the need to empirically specify either the length scale or the time scale is removed.

The specific configuration for the computational analysis is shown in Fig. 1. The stagnation point on the centerline of the body is positioned at (0, 0) in a Cartesian coordinate system. The nominal body radius normalizes the coordinate values. The domain extends ten units upstream and ten units downstream of the stagnation point. The outer boundary wall is nominally six units from the centerline, although it diverges slightly in the downstream direction. A solution was completed for a number of grids and for the Baldwin-Lomax, q-ω, and κ-ε turbulence models. Full boundary layer resolution was achieved on the surface of the body. The UNCLE code was actually run in three dimensions. Since the problem of interest was axisymmetric, a three-dimensional grid was achieved by rotating a planar grid one degree in the $+k$ and $-k$ directions. Thus there were three grid points and two cells in the k-direction. Periodic boundary conditions were applied to each k-face of the two-degree wedge.

The static pressure distribution over the Schiebe body is important for cavitation inception. Isobars near the stagnation point and along the shoulder past the minimum pressure point are shown in Fig. 2. The sharp pressure gradient along the flat face of the headform contrasts with the sharp body normal gradient near the minimum pressure point. These features have significant consequences for cavitation inception. Near the face, the pressure gradient forces nuclei away from the body—the so-called bubble screening effect, [5]. The strong gradient near the minimum pressure point indicates that the probability of a critical nucleus entering this region is small. Thus one would expect significant scale effects, i.e., $\sigma < |C_{p_{\min}}|$. Compared to the free-field theoretical minimum pressure coefficient of -0.75, the computed value for the 5.08-cm diameter body in the 30.48-cm diameter test section was -0.78. As expected, a free-field potential solution provides a fair representation of the surface pressure distribution on the Schiebe body regardless of the flow regime model. Our purpose here is to de-

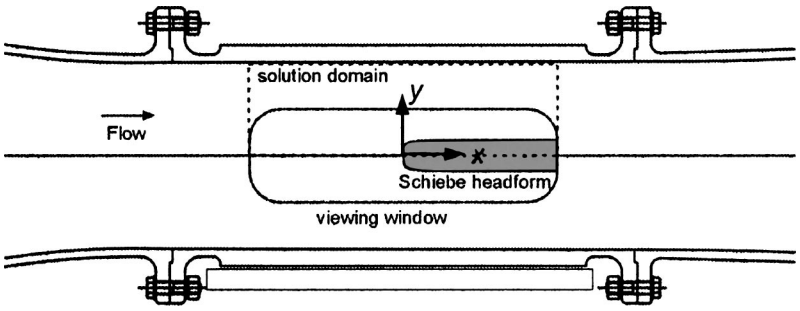

Fig. 1 Schiebe headform in the ARL Penn State 30.48-cm diameter water tunnel with solution domain

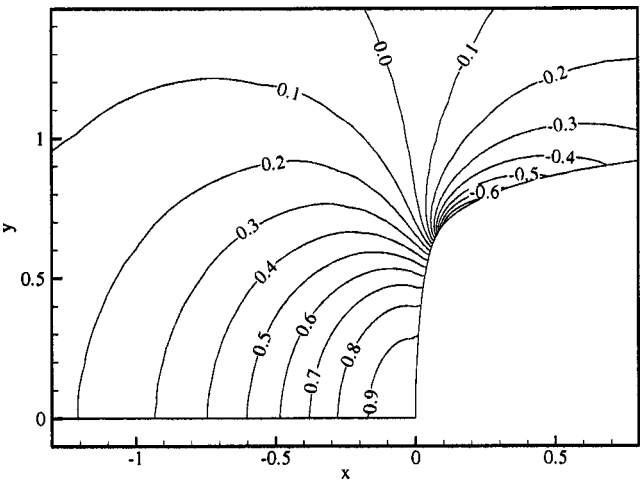

Fig. 2 Computed isobars for the Schiebe headform in the 30.48-cm diameter test section

velop a procedure which models phenomena important for predicting cavitation in the viscous flows of turbomachinery.

4 Lagrangian Analysis of Nuclei Translation and Growth

A large volume of literature describing the motion of particles, drops, and bubbles spans over 150 years. The article of Maxey and Riley [18] appears to be the definitive work on the subject based on the number of citations in the literature. A number of excellent review articles have appeared in the literature motivated by various multiphase flow interests: the dynamics and interactions of droplets, [19], the dispersion of particles in gases and the interactions of particles with turbulence, [20], the velocity fidelity of solid particles and bubbles used as flow tracers in optical techniques such as particle image velocimetry (PIV), [21], and the equation of motion and the relative importance of the various terms, [22].

Maxey and Riley [18] provided a detailed derivation of the creeping flow equation of motion, which is still considered a fairly accurate representation of the actual motion of particles. An additional consideration in the equation of motion for a bubble is its volume variation with time, [5]. Collecting terms from both of these equations yields the following trajectory equation for a bubble of changing volume:

$$\begin{aligned}\frac{1}{2}\frac{4}{3}\pi R^3\rho_L\frac{d\mathbf{V}}{dt}&=-\frac{4}{3}\pi R^3\rho_L\mathbf{g}-\frac{3}{2}\frac{4}{3}\pi R^3\rho_L\nabla p+\frac{1}{2}\rho_L(\mathbf{U}-\mathbf{V})|\mathbf{U}-\mathbf{V}|\\&\times C_D\pi R^2+6R^2\sqrt{\pi\rho_L\mu_L}\int_{t_0}^{t}\frac{\dfrac{d\mathbf{U}}{d\tau}-\dfrac{d\mathbf{V}}{d\tau}}{\sqrt{t-\tau}}d\tau\\&+2\pi\rho_L R^2(\mathbf{U}-\mathbf{V})\frac{dR}{dt}.\end{aligned}\tag{1}$$

In Eq. (1), the bubble mass and the Faxen terms are assumed negligible. The equation states that the product of the added mass and acceleration of the bubble is equal to the sum of the forces: buoyancy, pressure gradient, drag, history, and bubble volume variation, respectively, on the right-hand side of Eq. (1). Other forces such as lift and Magnus forces may also be important, particularly in the complex vortical flows of turbomachinery.

An important final consideration in the motion of particles is collision dynamics. For dilute flows of interest here, the collision of particles with solid walls can be an important consideration, particularly if the minimum pressure lies on the boundary. In contrast to the assumptions of many analytical studies of the cavitating potential flows on bodies of revolution, every nucleus in a typical streamtube, which envelops a specified range of isobars, does not pass through that minimum pressure region—in part due to collision with the headform face. Crowe et al. [23] includes an extensive discussion of particle collision models. Accurate coefficients of restitution and kinetic friction are not known, but the resulting collisional behavior is reasonable based on experimental observations of visible nuclei.

The Rayleigh-Plesset equation can be derived from the continuity and momentum equations for a spherical source, which in the absence of thermal effects and assuming polytropic behavior of the gas becomes

$$\frac{p_V-p_\infty(t)}{\rho_L}+\frac{p_{Go}}{\rho_L}\left(\frac{R_o}{R}\right)^{3\gamma}=R\ddot{R}+\frac{3}{2}(\dot{R})^2+4\frac{\mu_L}{\rho_L R}\dot{R}+2\frac{S}{\rho_L R}.\tag{2}$$

The first term of Eq. (2) is the instantaneous tension from the conditions far from the bubble. Equation (2) can be readily integrated to find $R(t)$ given the input $p_\infty(t)$, the initial conditions, and other constants. For initial conditions, it is usually appropriate to assume that the microbubble of radius R_o is in equilibrium at $t=0$ in the fluid at a pressure $p_\infty(0)$ and $dR/dt|_{t=0}=0$. Recall that the Rayleigh-Plesset equation is based on a number of assumptions: (1) that the bubble remains spherical at all times; (2) that spatially uniform conditions exist within the bubble; (3) that no body forces such as that due to gravity are present; (4) that the density of the liquid is large and its compressibility small, compared with the values of the gas; (5) that the gas content of the bubble is constant; and (6) that the vapor pressure is the equilibrium vapor pressure.

5 Effect of Turbulence on Bubble Trajectory and Growth

Depending on a number of factors: e.g., particle size/turbulent scale ratio, the relative densities of the phase, the volume fraction of the particles, and the particle Reynolds number, the presence of a dispersed phase can augment or attenuate the turbulence intensity, [24,25]. Several models have been proposed to account for the effect of turbulence on the particle trajectories, [23,26–30]). Gosman and Ioannides' [31] model allows a relative mean velocity between the eddy and the particles. A particle could pass through an eddy before the eddy decayed. The relative velocity between the particle and the eddy creates the *crossing trajectory effect*, which describes the supposed reduction in particle dispersion caused by a large relative mean velocity between the particles and local turbulent eddies. The simplicity and robustness of the Gosman and Ioannides [31] model make it the primary scheme in most commercial computational codes, [32].

In de Jong's et al. [33] analysis, turbulent diffusion is modeled by evaluating the fluid force on a particle using an instantaneous continuous phase velocity field rather than a mean velocity field. The instantaneous velocity components are obtained by adding stochastically generated turbulent velocity components to the mean velocity field for the continuous phase. The continuous phase turbulence is assumed to be isotropic, and the random turbulent velocity components are assumed to have a Gaussian probability distribution with standard deviation $\sigma_u=(2\kappa/3)^{1/2}$ where κ is the turbulent kinetic energy. The random turbulent velocity components can be obtained as $u_i=(4\kappa/3)^{1/2}\mathrm{erf}^{-1}(2x_i-1)$ where x is a uniform random deviate. This technique is less empirical than techniques traditionally used with Eulerian-Eulerian analy-

ses. Hinze [34] showed that the intensity of pressure fluctuations in a homogenous isotropic flow are given by $p' = c_1 \rho_L \kappa$ and that $c_1 = 0.47$ for large Reynolds numbers.

6 Numerical Procedure

A representative population of nuclei must be produced at the outset of the simulation. Nuclei populations have been measured in various bodies of water and in cavitation research tunnels. Usually the population is represented by a number distribution function $N(R)$ such that the concentration of nuclei between sizes R_1 and R_2 is given by $\int_{R_1}^{R_2} N(\lambda) d\lambda$. Generally $N(R)$ varies with R^{-4} or R^{-3}, [35,36]. For the purposes of simulation, a function is sought which maps a series of uniform deviates $\{x_1, x_2, \ldots, x_N\}$ to a set of nuclei sizes $\{R_1, R_2, \ldots, R_N\}$ distributed according to $N(R)$. The values are $R(x_i) = F^{-1}(x_i)$ where the cumulative normalized probability function is $F(z) = \int_0^z p(\lambda) d\lambda$, and F^{-1} is the inverse function of F, and $p(\lambda)$ is the normalized probability distribution such that $\int_0^\infty p(\lambda) d\lambda = 1$.

Newton's second law for the motion and the Rayleigh-Plesset equation are solved for each nucleus, which is introduced randomly upstream at equilibrium. A coordinate transformation is introduced to transform the equation of motion into computational coordinate space. Grid metric quantities are evaluated in the Lagrangian code in the same manner used in the Eulerian code UNCLE. Since these metric quantities are evaluated on the cell faces, repeated interpolation was required to compute metric quantities at the location of the computational bubble, which were held constant during a single time-step. Transformation between physical space and computational space is required to evaluate the bubble force terms. Once a nucleus is introduced into the flow field, various forces act upon it and determine the trajectory and hence the pressure field which will act on the nucleus. Using the local conditions along the trajectory of each nucleus, the instantaneous pressure field is computed from the mean flow and turbulence field. If the tension is greater than the critical value for the nucleus size, then the Rayleigh-Plesset equation is solved for the new radius. A cavitation event occurs if the nucleus grows to a certain size or an acoustic emission occurs. In the current study, an event occurs when the nucleus grows to a certain size, say one millimeter, which is usually visually observable, or to ten times the original size. Both criteria yielded nearly identical results. Once an event has occurred, the bubble is described as *cavitated* and is no longer tracked. The total rate of cavitation events can be computed based on the overall concentration of nuclei c, the nuclei release area A_c in the simulation, the mean velocity of transport for the nuclei V_c, and the probability of a cavitation event P_e according to $\dot{E} = cA_cV_cP_e$. The probability of a cavitation event P_e, the principal result of the simulation, is equal to the number of nuclei which cavitate over the number of nuclei in the ensemble.

7 Application

Meyer [37] conducted cavitation inception tests in the ARL 30.48-cm diameter water tunnel with a 5.08-cm diameter Schiebe headform; these data are shown in Fig. 3. Microbubbles were generated outside of the tunnel and seeded into the flow along the tunnel centerline upstream of the body. Microbubble sizes and populations were counted using in-line holography of a 7.4 cm^3 volume at each cavitation index. Cavitation bubbles were recorded on videotape. Cavitation events, denoted by growth to 1.3 mm, were counted on the videotape, and an event rate was determined. The total event rate was doubled to include the flow field shadowed by the body. Cavitation inception was observed at cavitation indices substantially lower than the negative of the computed minimum pressure coefficient, 0.78. A strong dependence on the nuclei spectrum is observed among the different seeded and unseeded cases. Additionally, one observes that the inception index generally declines slightly with increasing velocity, which is opposite of what one would expect for a particular nuclei spectrum, since the flux of nuclei increases with speed.

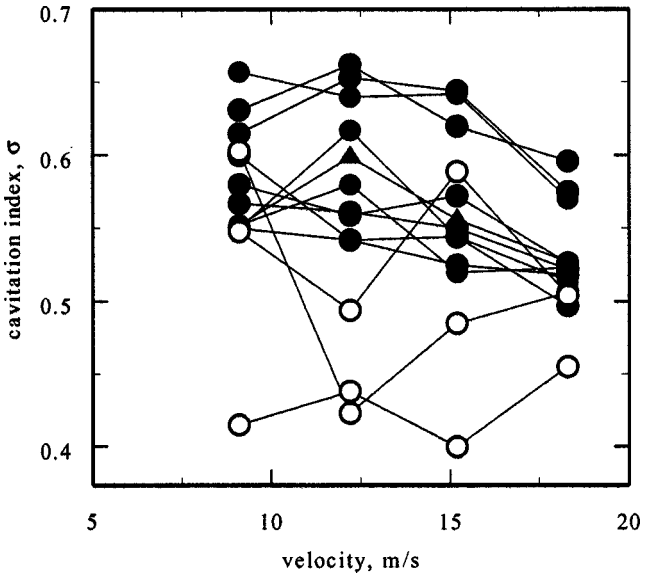

Fig. 3 Visual inception data from Meyer [37]; ○, unseeded runs; ●, ▲: seeded runs; ▲, conditions simulated in Figs. 5 and 6

Holographic images were taken during operation at the incipient cavitation index for freestream velocities of 9.1, 12.2, 15.2, and 18.3 m/s. The respective number density distributions are illustrated in Fig. 4 for the seeded case indicated by the triangles of Fig. 3. Cumulative normalized probability distributions were computed and used to generate a sample spectrum for the simulation. Figure 5 illustrates trajectories of 200 nuclei randomly placed across a portion of the inflow and shows isobars from the carrier flow. Johnson and Hsieh's [5] screening effect is obvious for several of the microbubbles which are accelerated away from the minimum pressure area by the strong pressure gradient near the stagnation point. Several of the microbubbles cross the fluid path lines and collide with the headform. These lose momentum in the collision, and some pass near the minimum pressure region which otherwise may not. Simulations were completed for $\sigma = 0.5$, 0.55, 0.6, 0.65, and 0.7 for freestream velocities of 9.1, 12.2, 15.2, and 18.3 m/s. The cavitation event rate was computed for each case, and is plotted in Fig. 6. Both the experimental data of Fig. 3 and the simulation results of Table 1 show a general trend of decreasing cavitation index with velocity, which is contrary to what one would expect given the increased flux of nuclei through the low pressure region with increasing speed. However, Fig. 4 shows that the nuclei population decreased with increasing speed. Meyer [37] reasoned that the experimental nuclei seeder worked less efficiently at higher speeds because the total pressure in the tunnel was lower at the lower tunnel velocities. At the higher velocities, the bubble generator was forced to pump against higher pressures, which resulted in lower flow rates of bubbles. A number of simulations were conducted with a nuclei population corresponding to the spectrum taken for 9.1 m/s in Fig. 5 but for velocities of 9.1, 12.2, 15.2, and 18.3 m/s. The calculated event rate does increase with velocity as expected when the nuclei population is constant for all velocities.

The data of Meyer [37] in Fig. 6 show some inconsistency relative to the event rate associated with visual inception. The inconsistency arises from the fact that the event rate was determined via interrogation of the video recording, while the visual inception index was determined in real time through visual cavitation "calling." In Table 1, interpolated values of the cavitation index are determined for the measured event rates of Meyer [37]

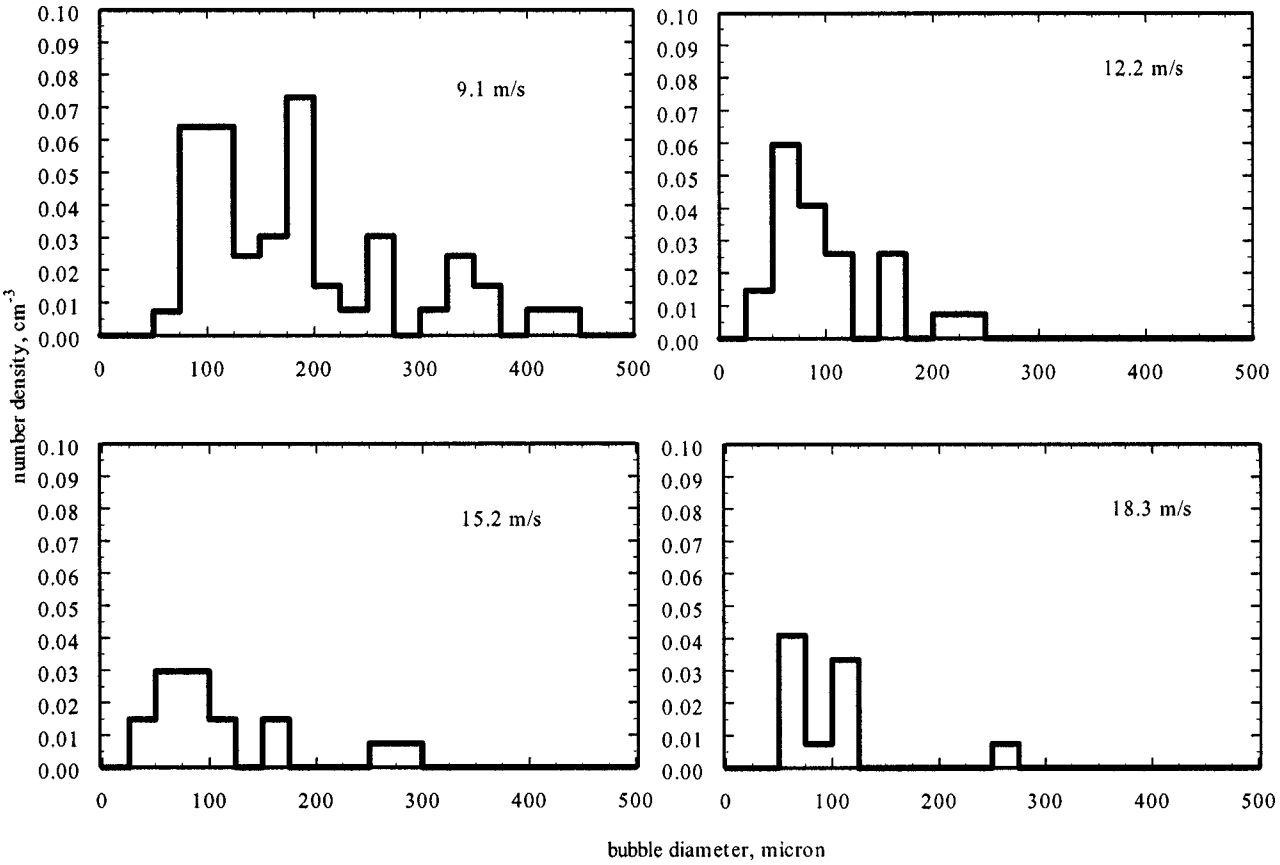

Fig. 4 Measured nuclei spectra for 9.1, 12.2, 15.2, and 18.3 m/s from Meyer [37]

and for a single representative value. The results clearly indicate the general trend of reducing cavitation index for increasing velocity.

Liu and Brennen [13] observed cavitation event rates on a Schiebe headform in two water tunnels at CalTech. The freestream nuclei number distribution was measured by a phase Doppler anemometer, which was calibrated by comparison with the holographic method. Three flush-mounted electrodes on the headform surface measured the cavitation event rate on the Schiebe headform. Liu and Brennen used an analytical approach to predict event rate which included a number of influential factors: the effect of the boundary layer, the relative motion between

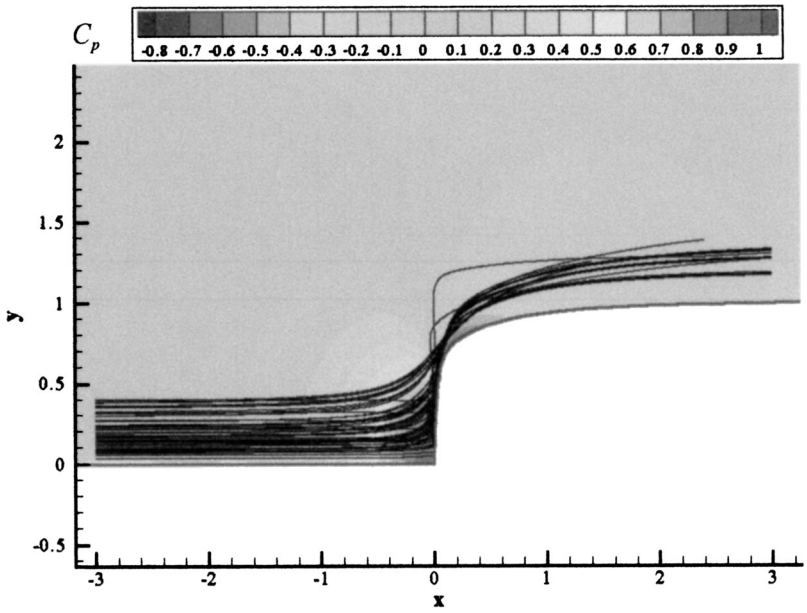

Fig. 5 Simulated nuclei trajectories over a 5.08-cm diameter Schiebe body at 9.1 m/s

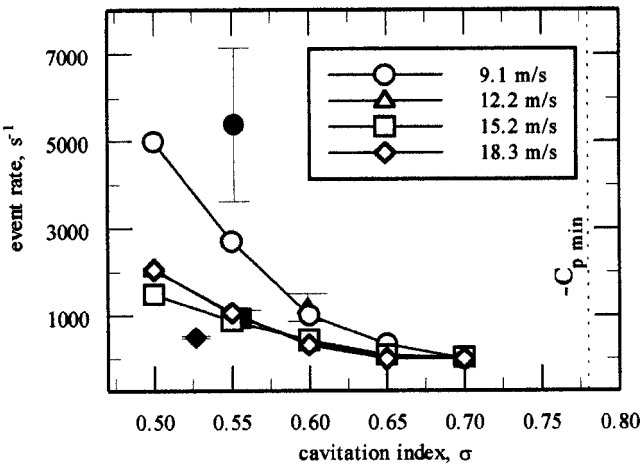

Fig. 6 Simulated cavitation event rates (nuclei spectra from Fig. 4) versus cavitation index compared to data of Meyer [37]; open symbols: simulation results; solid symbols: visual cavitation calls with event rate derived from video analysis

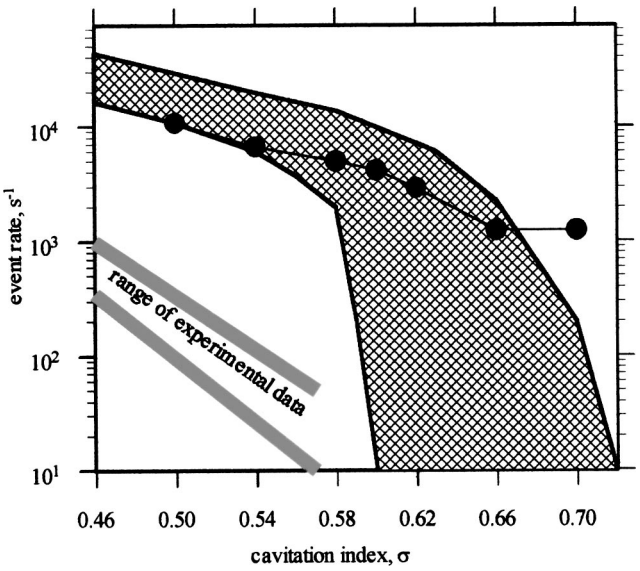

Fig. 7 Simulated cavitation event rates versus cavitation index compared to data and analysis of Liu and Brennen. Hatched area represents analytical event rate with various complications considered individually by Liu and Brennen [13].

the nucleus and the liquid, the observable bubble size effect, and the effect of bubble growth on neighboring nuclei. In the Eulerian/Lagrangian method described herein, the trajectory and growth of the nuclei are explicitly tracked through the viscous flow field, so the boundary layer and relative motion effects are inherently included. Simulations corresponding to Liu and Brennen's data are compared to their experimental measurements of event rate and their analytical predictions in Fig. 7.

The computed event rates are bracketed by the analytical results of Liu and Brennen when various complicating effects like bubble screening, boundary layer blockage, etc., are examined individually. Both the computed and analytical results are substantially higher than the measured event rates at low values of the cavitation index, which infers that smaller active microbubbles are likely over counted by the number distribution if the event rate measurements are representative. Alternatively, the events may be substantially under counted as a result of the local impedance measurement method.

8 Summary and Conclusions

An Eulerian/Lagrangian computational procedure was developed for the prediction of cavitation inception by event rate. The carrier-phase Eulerian flow field was computed using a Reynolds-averaged Navier-Stokes (RANS) solver. The Lagrangian analysis was one-way coupled to the RANS solution, since at inception, the contributions of mass, momentum, and energy of the microbubbles to the carrier flow are negligible. Probability density functions for measured nuclei populations were inverted to produce a representative population of computational bubbles, whose trajectories and growth were tracked through the flow field. The trajectories were computed using Newton's second law with models for the forces acting on the microbubbles. The growth was modeled using the Rayleigh-Plesset equation. The effect of turbulence was included by adding a random velocity component to the mean flow velocity by sampling a Gaussian probability density function with variance proportional to the turbulent kinetic energy at the location of the microbubble and by reducing the local static pressure by a value proportional to the specific turbulent kinetic energy. For the Schiebe body, turbulent pressure fluctuations are not significant contributors to the tension that causes cavitation inception. The simulation results indicate agreement with experimentally observed trends and a significant event rate at cavitation indices above visual inception.

Cavitation inception data, [12,37], show that inception indices generally decrease with increasing velocity, which is contrary to expectations based on the increased flux of nuclei to the minimum pressure region. However, nuclei populations generally are not constant for inception conditions at low and high velocities, as shown by Meyer [37]. Indeed simulations completed with Meyer's measured distributions at each velocity predict a reduction in cavitation index with increasing freestream speed. At the higher static pressures associated with the increased freestream speed, nuclei become smaller. In a more general way, this result also emphasizes the importance of an accurate microbubble number distribution; in the analyses described, all of the nuclei are assumed to be gas and not particulate.

Table 1 Comparison of experimental and simulated cavitation indices versus freestream velocity

Free-Stream Velocity (m/s)	Experimental Cavitation Index for Visual Inception	Experimental Event-Rate via Visual Interrogation (s^{-1})	Predicted Cavitation Index at Visual Event Rate	Predicted Cavitation Index at 2000 Events per Second
9.1	0.55	3638-7146	0.49–0.53	0.56
12.2	0.60	865-1507	0.53–0.55	0.52
15.2	0.56	734-1132	0.59–0.61	0.50
18.3	0.53	537-476	0.63–0.64	0.51

9 Uncertainty

Numerical uncertainties must be addressed in both the Eulerian and the Lagrangian computational analyses. For the specific case of the well-behaved nearly potential flow field of the Schiebe body, one can neglect the former relative to the latter. The numerical error associated with the cavitation event rate has two principal components. First, a resolution error occurs because every physical nucleus passing the headform minimum pressure zone is not modeled in the simulation. Instead, a smaller number of representative but computational nuclei are simulated. By releasing more computational nuclei in select areas upstream, one can limit this resolution error. For a population of 1000 computational nuclei, the resolution error is on the order of 10 events/s. Second, the value of the systematic error rests mainly on how well the mathematical model represents the motion and growth of the nuclei. The estimate of this error is 5% at a given cavitation index. Obviously, the degree to which the number and size of the computational nuclei represent the actual nuclei in the flow is an overriding concern. Given the corresponding large uncertainties for measured event rates, agreement of predicted event rates with experimental event rates within an order of magnitude is a notable achievement.

Nomenclature

A_c = nuclei release area
c = nuclei concentration
C_D = nuclei drag coefficient
C_p = pressure coefficient
$C_{p\min}$ = minimum pressure coefficient
$\dot{E}$ = cavitation event rate
$F(z)$ = cumulative nuclei size distribution function
g = acceleration of gravity
i,j,k = computational coordinate indices
$N(R)$ = nuclei number distribution function
p = static pressure
$p_\infty(t)$ = far-field pressure in Rayleigh-Plesset equation
p' = fluctuating pressure
P_e = probability of a cavitation event
$p(\lambda)$ = normalized nuclei size distribution function
p_V = vapor pressure
p_{Go} = initial noncondensible gas pressure
q = square root of the turbulent kinetic energy, $\sqrt{\kappa}$
R = nuclei radius
R_o = initial nuclei radius
S = surface tension
t = time
t_o = initial time
u = fluctuating velocity
$\mathbf{U}$ = fluid velocity at position of nucleus
$\mathbf{V}$ = nucleus velocity
V_c = mean transport velocity for nuclei in A_c
x = axial coordinate (Fig 1.); uniform random deviate
y = radial coordinate (Fig. 1)
ε = turbulent energy dissipation rate
γ = ratio of specific heats
κ = turbulent kinetic energy
μ_L = dynamic viscosity of liquid
ρ_L = density of liquid
σ = cavitation index
σ_u = standard deviation of the fluctuating velocity
ω = inverse time scale of turbulence dissipation, ε/κ

References

[1] McCormick, B. W., 1962, "On Cavitation Produced by a Vortex Trailing from a Lifting Surface," ASME J. Basic Eng., **84**, pp. 369–379.
[2] Farrell, K. J., and Billet, M. L., 1994, "A Correlation of Leakage Vortex Cavitation in Axial-Flow Pumps," ASME J. Fluids Eng., **116**, pp. 551–557.
[3] Meyer, R. S., Billet, M. L., and Holl, J. W., 1992, "Freestream Nuclei and Traveling Bubble Cavitation," ASME J. Fluids Eng., **114**, pp. 672–679.
[4] Hsiao, C.-T., and Pauley, L. L., 1999, "Study of Tip Vortex Cavitation Inception using Navier-Stokes Computation and Bubble Dynamics Model," ASME J. Fluids Eng., **121**(1), pp. 198–204.
[5] Johnson, J. E., Jr., and Hsieh, T., 1966, "The Influence of the Trajectories of the Gas Nuclei on Cavitation Inception," *Sixth Naval Hydrodynamics Symposium*, pp. 163–182.
[6] Chahine, G. L., 1995, "Bubble Interactions With Vortices," *Fluid Vortices*, S. I. Green, ed., Kluwer, Dordrecht, The Netherlands, pp. 783–828.
[7] Schiebe, F. R., 1972, "Measurement of the Cavitation Susceptibility of Water Using Standard Bodies," University of Minnesota, St. Anthony Falls Hydraulic Laboratory, Report No. 188.
[8] Gates, E. M., Billet, M. L., Katz, J., Ooi, K. K., Holl, J. W., and Acosta, A. J., 1979, "Cavitation Inception and Nuclei Distributions Joint ARL/CIT Experiments," CalTech, Division of Eng. and Applied Science, Report E244.1.
[9] Hamilton, M. F., Thompson, D. E., and Billet, M. L., 1982, "An Experimental Study of Traveling Bubble Cavitation Noise," *ASME International Symposium on Cavitation Noise*, ASME, New York, pp. 25–33.
[10] Holl, J. W., and Carroll, J. A., 1979, "Observations of the Various Types of Limited Cavitation on Axisymmetric Bodies," *Proceedings of ASME International Symposium on Cavitation Inception*, pp. 87–99.
[11] Ceccio, S. L., and Brennen, C. E., 1991, "Observations of the Dynamics and Acoustics of Traveling Bubble Cavitation," J. Fluid Mech., **233**, pp. 633–660.
[12] Kuhn de Chizelle, Y., Ceccio, S. L., and Brennen, C. E., 1995, "Observations and Scaling of Traveling Bubble Cavitation," J. Fluid Mech., **292**, pp. 99–126.
[13] Liu, Z., and Brennen, C. E., 1998, "Cavitation Nuclei Population and Event Rates," ASME J. Fluids Eng., **120**, pp. 728–737.
[14] Taylor, L. K., and Whitfield, D. L., 1991, "Unsteady Three-Dimensional Incompressible Euler and Navier-Stokes Solver for Stationary and Dynamic Grids," AIAA Paper No. 91-1650.
[15] Whitfield, D. L., 1995, "Perspective on Applied CFD," AIAA Paper No. 95-0349.
[16] Roe, P. L., 1981, "Approximate Riemann Solvers, Parameter Vectors, and Difference Schemes," J. Comput. Phys., **43**, pp. 357–372.
[17] Zierke, W. C., ed., 1997, "A Physics-Based Means of Computing the Flow around a Maneuvering Underwater Vehicle," Applied Research Laboratory Penn State, Technical Report No. TR 97-002.
[18] Maxey, M. R., and Riley, J. J., 1983, "Equation of Motion of a Small Rigid Sphere in a Non-uniform Flow," Phys. Fluids, **26**, pp. 883–889.
[19] Sirignana, W. A., 1993, "Fluid Dynamics of Sprays," ASME J. Fluids Eng., **115**, pp. 345–378.
[20] Stock, D. E., 1996, "Particle Dispersion in Flowing Gases," ASME J. Fluids Eng., **118**, pp. 4–17.
[21] Mei, R., 1996, "Velocity Fidelity of Flow Tracer Particles," Exp. Fluids, **22**, pp. 1–13.
[22] Michaelides, E. E., 1997, "Review—The Transient Equation of Motion for Particles, Bubbles, and Droplets," ASME J. Fluids Eng., **119**, pp. 233–247.
[23] Crowe, C., Sommerfeld, M., and Tsuji, Y., 1998, *Multiphase Flows with Droplets and Particles*, CRC Press, Boca Raton, FL, pp. 113–146.
[24] Gore, R. A., and Crowe, C. T., 1989, "Effect of Particle Size on Modulating Turbulence Intensity," Int. J. Multiphase Flow, **15**, pp. 279–285.
[25] Yarin, L. P., and Hetsroni, G., 1994, "Turbulent Intensity in Dilute Two-Phase Flows," Int. J. Multiphase Flow, **20**, pp. 27–44.
[26] Yuu, S., Yasukouchi, N., Hirowawa, Y., and Jotaki, T., 1878, "Particle Turbulent Diffusion in a Duct Laden Jet," AIChE J., **24**, pp. 509–519.
[27] Dukowicz, J. K., 1980, "A Particle-Fluid Model for Liquid Sprays," J. Comput. Phys., **35**, pp. 229–253.
[28] Lockwood, F. C., Salooga, A. P., and Syed, S. A., 1980, "A Prediction Method for Coal-Fired Furnaces," Combust. Flame, **38**, pp. 1–15.
[29] Jurewicz, J. T., and Stock, D. E., 1976, "Numerical Model for Turbulent Diffusion in Gas-Particle Flows," ASME Paper No. 76-WA/FE-33.
[30] Smith, P. J., Fletcher, T. J., and Smoot, L. D., 1981, "Model for Pulverized Coal Fired Reactors," *18th International Symposium on Combustion*, pp. 1285–1293.
[31] Gosman, A. D., and Ioannides, E., 1983, "Aspects of Computer Simulation of Liquid-Fueled Combustors," J. Energy, **7**, pp. 482–490.
[32] Crowe, C. T., Troutt, T. R., and Chung, J. N., 1996, "Numerical Models for Two-Phase Turbulent Flows," Annu. Rev. Fluid Mech., **28**, pp. 11–43.
[33] de Jong, F. J., Meyyappan, M., and Choi, S.-K., 1994, "An Eulerian-Lagrangian Analysis for Liquid Flows With Vapor Bubbles," Scientific Research Associates, SBI Phase II Final Report R94-9085-F, NASA Marshall Space Flight Center.
[34] Hinze, J. O., 1975, *Turbulence*, Second Ed., McGraw-Hill, New York.
[35] Billet, M. L., 1985, "Cavitation Nuclei Measurements—A Review," *ASME Cavitation and Multiphase Flow Forum—1985*, ASME, New York, FED-Vol. 23, pp. 31–38.
[36] O'Hern, T. J., Katz, J., and Acosta, A. J., "Holographic Measurements of Cavitation Nuclei in the Sea," *ASME Cavitation and Multiphase Flow Forum—1985*, ASME, New York, FED-Vol. 23, pp. 39–42.
[37] Meyer, R. S., 1989, "An Investigation of the Relation Between Free-Stream Nuclei and Traveling-Bubble Cavitation," M.S. thesis, Penn State University, State College, PA.

Scaling Effect on Prediction of Cavitation Inception in a Line Vortex Flow

Chao-Tsung Hsiao

Georges L. Chahine

Dynaflow, Inc.,
10621-J Iron Bridge Road,
Jessup, MD 20794
e-mail: info@dynaflow-inc.com

Han-Lieh Liu

U.S. Patent and Trademark Office,
Crystal Plaza 3, Room 2C02
Washington, DC 20231

The current study considers the prediction of tip vortex cavitation inception at a fundamental physics based level. Starting form the observation that cavitation inception detection is based on the "monitoring" of the interaction between bubble nuclei and the flow field, the bubble dynamics is investigated in detail. A spherical model coupled with a bubble motion equation is used to study numerically the dynamics of a nucleus in an imposed flow field. The code provides bubble size and position versus time as well as the resulting pressure at any selected monitoring position. This model is used to conduct a parametric study. Bubble size and emitted sound versus time are presented for various nuclei sizes and flow field scales in the case of an ideal Rankine vortex to which a longitudinal viscous core size diffusion model is imposed. Based on the results, one can deduce cavitation inception with the help of either an "optical inception criterion" (maximum bubble size larger than a given value) or an "acoustical inception criterion" (maximum detected noise higher than a given background value). We use here such criteria and conclude that scaling effects can be inherent to the way in which these criteria are exercised if the bubble dynamics knowledge is not taken into account.
[DOI: 10.1115/1.1521956]

1 Introduction

It is common to predict tip vortex cavitation inception in a small-scale laboratory setting. The challenge is then to find the correct scaling laws to extrapolate the results to the full scale. While the present knowledge of the scaling laws enables engineers to proceed properly in many cases, there are conditions where classical scaling as defined below needs to be reconsidered and corrected. This paper aims at contributing to the knowledge needed to describe such a more general scaling.

In practice, engineering prediction of cavitation inception is made by equating the cavitation inception number to the negative of the minimum pressure coefficient neglecting real flow effects such as nuclei presence and dynamics, and bubble/flow interactions and unsteadiness, These ignored effects sometimes lead to significant discrepancies between model and full-scale tests and to "*scale effects.*"

The nondimensional cavitation number, σ, used to characterize overall cavitation effects is defined as

$$\sigma = \frac{p_\infty - p_v}{1/2\rho V_\infty^2}, \tag{1}$$

where p_∞ and V_∞ are the characteristic pressure and velocity (usually at freestream), ρ is the liquid density, and p_v is the liquid vapor pressure. Following McCormick [1], several experimental studies have established the following scaling law to predict steady tip vortex cavitation inception:

$$\sigma_i = KC_l^2 R_e^\alpha, \quad \text{with} \quad R_e = \frac{V_\infty C_0}{\upsilon}. \tag{2}$$

K is a proportionality constant, which depends on the foil geometry and the flow incidence, C_l is the foil lift coefficient, and R_e is the flow Reynolds number based on the hydrofoil chord length, C_0. Equation (2) correlates the cavitation inception number, σ_i, to the boundary layer growth on the foil. Different values of α have been proposed in previous studies. For example, McCormick [1] found $\alpha = 0.35$ while Fruman et al. [2] and Arndt and Dugue [3] used $\alpha = 0.40$. Farrell and Billet [4] proposed a correlation model for leakage vortex cavitation inception with $\alpha = 2/7$. Arndt and Keller [5] introduced a correction term to Eq. (2) based on the "tensile strength" of the liquid to account for the presence of nuclei and the onset of cavitation in "*weak*" and "*strong*" water. However, they did not account directly for the effect of nuclei dynamics per se.

Direct experimental observation of bubble capture by the tip vortex is difficult due to the small size of the nuclei and the high local velocities. Numerical studies, therefore, have been used primarily to study these effects. The complexity of the cavitation inception process, however, has led various numerical studies to neglect one or more of the factors, and therefore to only investigate the influence of a limited set of parameters. Most models accept that tip vortex cavitation inception is due to traveling bubbles, and use a spherical bubble dynamics model coupled with a motion equation to predict cavitation inception. Latorre [6] and Ligneul and Latorre [7] applied this approach to deduce noise emission from cavitation in a Rankine line vortex. Hsiao and Pauley [8] further applied this approach to study tip vortex cavitation inception with the tip vortex flow field computed by Reynolds-averaged Navier-Stokes equations.

The current study makes a concerted effort to investigate the importance of the nuclei size on tip vortex cavitation inception. The tip vortex flow of a three-dimensional foil is idealized as a Rankine vortex. Empirical equations are used to estimate the vortex strength and core size for three different foil sizes. A modified spherical model is then implemented and used to predict inception. Both an "*acoustic*" criterion (emitted sound level higher than a threshold value) and an "*optical*" criterion (bubble size larger than a threshold value) are considered for "calling" the cavitation inception. The characteristics of the acoustic pressure signals due to the bubble dynamics are also computed and analyzed.

2 Numerical Method

2.1 Rankine Vortex Model. We consider the tip vortex generated by a finite-span hydrofoil and consider three different

Contributed by the Fluids Engineering Division for publication in the JOURNAL OF FLUIDS ENGINEERING. Manuscript received by the Fluids Engineering Division May 18, 2001; revised manuscript received July 1, 2002. Associate Editor: E. Graf.

Table 1 Conditions of the three scale tests considered

	Small Scale	Medium Scale	Large Scale
λ	1/48	1/4	1
C_0 (m)	0.0508	0.6096	2.4384
V_∞ (m/sec)	10	12.5	15
Γ (m^2/sec)	0.12767	1.91511	9.19255
R_e	5.08×10^5	7.62×10^6	3.66×10^7
a_c (m)	0.001358	0.009486	0.02770
$C_{p\ \min}$	−4.474	−13.215	−24.797

sizes of this foil, small (laboratory 1/48 scale), medium (1/4 scale), and large (full scale). These hydrofoils are geometrically similar and are operated at the same angle of attack. The tip vortex flow field is represented by a Rankine line vortex for which the rotation velocity, u_θ, and pressure, p_ω, of the vortical flow are given by

$$u_\theta(r)=\left\{\frac{\Gamma}{2\pi a_c^2}r,\quad r\leqslant a_c;\quad \frac{\Gamma}{2\pi r},\quad r>a_c\right\}, \tag{3}$$

$$p_\omega(r)=\left\{\begin{array}{cc} p_\infty-\dfrac{\rho\Gamma^2}{4\pi^2a_c^2}+\dfrac{\rho\Gamma^2r^2}{8\pi^2a_c^4}, & r\leqslant a_c \\ p_\infty-\dfrac{\rho\Gamma^2}{8\pi^2r^2}, & r>a_c \end{array}\right\}. \tag{4}$$

The circulation strength, Γ, is obtained based on the equation described in Abbott and Doenhoff [9]:

$$\Gamma=\frac{1}{2}\left(A_0+\frac{1}{2}A_1\right)2\pi C_0V_\infty, \tag{5}$$

where V_∞ is the freestream velocity. In Eq. (5) the coefficient A_0 depends only on the angle of attack and the coefficient A_1 depends only on the shape of the mean line. For the particular foils considered here, $1/2(A_0+1/2A_1)=0.04$ was empirically determined. The viscous vortex core size, a_c, is related to the turbulent boundary layer thickness on the pressure side, [1], and has the following expression:

$$a_c=\frac{0.37C_0}{R_e^{0.2}}. \tag{6}$$

The minimum pressure coefficient in the vortex center is then determined by

$$Cp_{\min}=\frac{p_\omega-p_\infty}{0.5\rho V_\infty^2}=-\frac{1}{2\pi^2V_\infty^2}\left(\frac{\Gamma}{a_c}\right)^2. \tag{7}$$

The flow conditions and parameters for the three cases considered are shown in Table 1.

2.2 Improved Spherical Bubble Dynamics Model (SAP). As in conventional spherical bubble dynamics models we assume that the bubble is too small to modify the ''basic'' flow field. It however responds dynamically to this field while remaining spherical and its dynamics can be described by the Rayleigh-Plesset equation, [10]. Conventionally, the bubble follows the flow field and sees the liquid pressure, in its absence, at the location of its center as a ''far-field'' imposed pressure. Here, we modify this equation to account for the presence of a slip velocity between the bubble and the host liquid, and to account for non-uniform pressure fields along the bubble surface. The difference between the liquid velocity $\mathbf{u}$ and the bubble translation velocity $\mathbf{u}_b$, results in an added pressure term similar to that due to a translating sphere in a liquid, and can be shown to be equal to $(\mathbf{u}-\mathbf{u}_b)^2/4$. The detailed derivation can be seen in [11]. Here we account for this term in the modified Rayleigh-Plesset equation as

$$R\ddot{R}+\frac{3}{2}\dot{R}^2=\frac{1}{\rho}\left[p_v+p_{g0}\left(\frac{R_0}{R}\right)^{3k}-P_\infty(t)-\frac{2\gamma}{R}-\frac{4\mu}{4}\dot{R}\right]+\frac{(\mathbf{u}-\mathbf{u}_b)^2}{4}, \tag{8}$$

where R is the bubble radius, R_0 *and* p_{g0} are the initial bubble radius and gas pressure, k is the polytropic gas constant, ρ, γ, and μ are the liquid density, surface tension and viscosity, and p_v is the vapor pressure. $P_\infty(t)$ in the classical spherical model is the liquid pressure at the bubble center in its absence. This obviously does not account for pressure variations around the bubble surface, and may lead here to unbounded bubble growth when the pressure in the vortex center is less than the vapor pressure. Previous studies have used this simplification to determine cavitation inception. In the current study we apply a surface averaged pressure (SAP) scheme in which $P_\infty(t)$ is taken to be the average of the outside field pressure over the bubble surface. This enables for a much more realistic description of the bubble behavior, e.g., the bubble does not continuously grow as it is captured by the line vortex. Instead, once the bubble reaches the vortex line axis, it can see an increasing pressure around it as most of its surface moves away from the axis pressure.

The bubble trajectory during capture can be predicted by the following equation of motion, [12]:

$$\frac{d\mathbf{u}_b}{dt}=\frac{3}{\rho}\nabla p+\frac{3}{4}C_D(\mathbf{u}-\mathbf{u}_b)|\mathbf{u}-\mathbf{u}_b|+\frac{3}{R}(\mathbf{u}-\mathbf{u}_b)\dot{R}, \tag{9}$$

where the drag coefficient C_D is determined using the empirical equation of Haberman and Morton [13]:

$$C_D=\frac{24}{R_{er}}(1+0.197R_{er}^{0.63}+2.6\times10^{-4}R_{er}^{1.38}), \tag{10}$$

and the relative velocity Reynolds number is defined by

$$R_{er}=\frac{2R|\mathbf{u}-\mathbf{u}_b|}{\nu}. \tag{11}$$

Equation (9) expresses the balance between drag forces, pressure gradients, and inertia forces due to bubble motion and volume variation. Detailed derivation of (9) from a complete set of motion equation for a spherical particle, [14], can be found among others in [8,15].

The liquid pressure variations at a distance l from the bubble center, resulting from the bubble dynamics is obtained using the expression

$$p=\frac{\rho}{l}[R^2\ddot{R}+2R\dot{R}^2]-\rho\left[\frac{R^4\dot{R}^2}{2l^4}\right]. \tag{12}$$

When $l\gg R$ Eq. (12) becomes the expression for the acoustic pressure p_a of Fitzpatrick and Strasberg [16] after introduction of the delayed time t' due to the finite sound speed, c:

$$p_a(t')=\frac{R\rho}{l}[R\ddot{R}(t')+2\dot{R}^2(t')],\quad t'=t-\frac{r-R}{c}. \tag{13}$$

The noise level, SPL, can then be written as:

$$\mathrm{SPL}=20\log\left(\frac{p_a}{p_{\mathrm{ref}}}\right). \tag{14}$$

We use here the conventional value $p_{\mathrm{ref}}=10^{-6}$ N/m^2.

With the prescribed pressure and velocity flow field given by Eqs. (3) and (4), a Runge-Kutta fourth-order scheme is applied to integrate Eqs. (8) and (9) through time to provide the bubble trajectory and its volume variation during bubble capture by the line vortex. Accuracy in the current numerical scheme is only determined by the time-step size which is found to depend on the initial bubble size. The time-step size should be small enough to resolve the high frequency oscillations as the bubble experiences

strong collapse. A time-step size study was conducted to determine needed time step size for each initial nuclei size to obtain less than 0.05% difference in bubble radius and 1% difference in acoustic pressure at their maximum values where the strongest collapse occurs by further reduction by half of the time-step size.

Since this paper was submitted, we have obtained extremely encouraging comparisons (especially relative to the conventional model) between the SAP Rayleigh-Plesset model and a three-dimensional model coupling three-dimensional bubble dynamics and an unsteady Reynolds-averaged Navier-Stokes code, [17].

3 Results and Discussion

3.1 Cavitation Inception Criteria. The precise notion of cavitation inception as a practically observed phenomenon is a matter of discussion. From an engineering viewpoint, cavitation inception is determined through visual or acoustical techniques. Inception is called when the measurement detects events above a predefined threshold. In the laboratory the most commonly used threshold is via visual observation when bubbles ''appear.'' This visual technique can hardly be applied to full-scale tests where an acoustic technique is preferred. In the acoustic technique, the cavitation inception event can be defined either by the sound amplitude level (absolute noise level or relative value over the background noise) and/or by the appearance of some characteristic spikes in the pressure signals. In the current study, both the acoustic and the optical criteria are investigated for determining the cavitation inception. In the following we will also show the importance for numerical simulations of the selection of the bubble dynamics model on the results.

3.2 Cavitation Inception for Line Vortex With Constant Vortex Core. To study scaling effects, the SAP modified Rayleigh-Plesset spherical model was first applied to predict for the three scales described earlier the cavitation inception number, σ_i, for a line vortex with a *nonvarying* vortex core size. Different initial nuclei sizes were also considered to study the effect of the bubble size distribution on cavitation inception. The computations were conducted by releasing the bubbles three core radii away from the vortex axis with an initial nucleus equilibrium condition.

In previous studies, [6–8], the cavitation inception number was determined as the highest cavitation number that leads to an unbounded bubble growth (see Fig. 1). Using this *conventional* model, we found that the predicted cavitation inception numbers for all cases are very close to those given by the simple criterion, $\sigma_i = -Cp_{\min}$. Scaling then follows the relationship given by (2). The results, shown in Table 2, obviously do not explain experimentally measured scaling effects. This way of determining the cavitation inception number stems directly from accepting that the bubble can grow unboundedly once it reaches the vortex center.

Table 2 Cavitation inception number using the classical spherical model approach

R_0	Small Scale	Medium Scale	Large Scale
10 μm	$\sigma_i = 4.467$	$\sigma_i = 13.212$	$\sigma_i = 24.796$
50 μm	$\sigma_i = 4.471$	$\sigma_i = 13.214$	$\sigma_i = 24.796$
100 μm	$\sigma_i = 4.473$	$\sigma_i = 13.214$	$\sigma_i = 24.796$

To account for the fact that the averaged pressure that is imposed on the bubble increases as most of the bubble surface grows away from the vortex axis, the SAP spherical model (averaging the field pressure on the bubble surface) was then applied. Figure 2 shows the bubble radius variation and the acoustic pressure for $R_0 = 50$ μm and $\sigma = 4.471$ in the small-scale case. It is seen that with the modified model both the bubble size and the acoustic pressure reach finite values instead of increasing unboundedly. Therefore, we conducted with the SAP model a series of computations to obtain bubble size and acoustic pressure for different cavitation numbers. Figure 3 shows the maximum bubble size and the maximum SPL measured at 30 cm from the vortex center versus the cavitation number for four different initial nuclei sizes ($R_0 = 10$, 25, 50, and 100 μm) for the medium scale. Similar curves for the small and the large scale can be found in [11].

Based on these curves one can determine the cavitation inception number once an optical or an acoustic threshold criterion is defined. Tables 3 and 4 show the cavitation inception number results obtained for all scales using different illustrative criteria. It is seen that different cavitation inception criteria may lead to significant differences in the resulting cavitation inception numbers. It is also found that the initial nucleus size, R_0, can significantly influence the prediction of the cavitation inception number. For *stringent* (good detection schemes) acoustic or optical criteria (e.g., $\mathrm{SPL}_{\max} > 90$ db or $R_{\max} > 100$ μm), the cavitation inception numbers are definitely not well scaled by Eq. (2) especially for the smaller nuclei. However, for *looser* (high levels needed for detection) criteria (e.g., $\mathrm{SPL}_{\max} > 130$ db or $R_{\max} > 400$ μm), the cavitation inception number is insensitive to the nuclei size and is generally well scaled by Eq. (2).

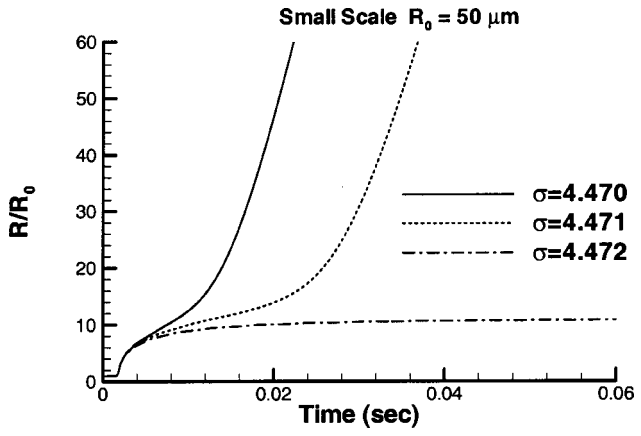

Fig. 1 Bubble radius versus time at different cavitation number obtained by the *classical* Rayleigh-Plesset equation for the small scale with $R_0 = 50$ μm

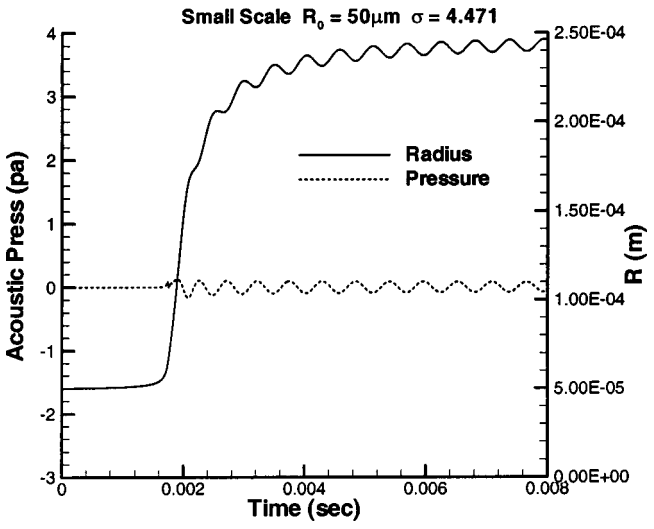

Fig. 2 Bubble radius and acoustic pressure versus time obtained by the modified SAP Rayleigh-Plesset equation for the small scale with $R_0 = 50$ μm at $\sigma = 4.471$

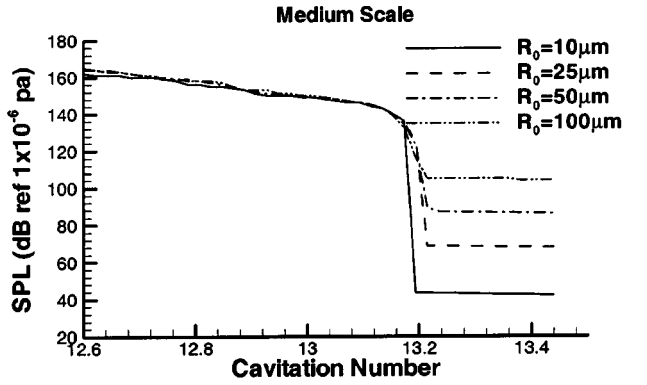

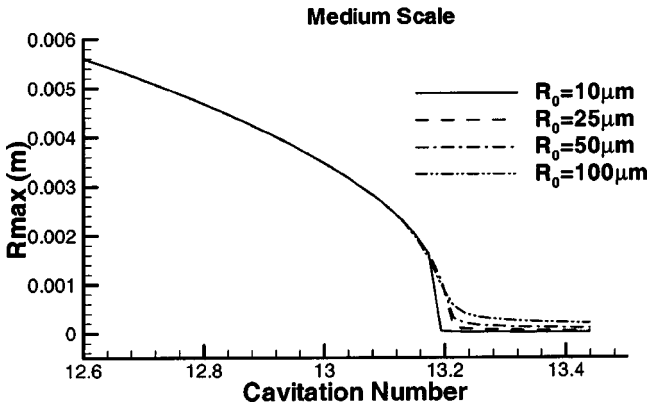

Fig. 3 Maximum SPL and bubble radius versus cavitation number for the medium scale test in the constant vortex core case

Table 3 Cavitation inception number obtained using various illustrative acoustic criteria for defining cavitation inception

Acoustic Criterion		Small Scale	Medium Scale	Large Scale
$-Cp_{min}$		4.47	13.22	24.80
SPL_{max}	$R_0=10\ \mu m$	No Inception	$\sigma_i=13.20$	$\sigma_i=24.76$
>90 db	$R_0=25\ \mu m$	$\sigma_i=4.45$	$\sigma_i=13.21$	$\sigma_i=24.77$
	$R_0=50\ \mu m$	$\sigma_i>7$	$\sigma_i=13.21$	$\sigma_i=24.78$
	$R_0=100\ \mu m$	$\sigma_i>9$	$\sigma_i>15$	$\sigma_i>26$
SPL_{max}	$R_0=10\ \mu m$	No Inception	$\sigma_i=13.17$	$\sigma_i=24.76$
>130 db	$R_0=25\ \mu m$	$\sigma_i=4.36$	$\sigma_i=13.18$	$\sigma_i=24.76$
	$R_0=50\ \mu m$	$\sigma_i=4.36$	$\sigma_i=13.18$	$\sigma_i=24.76$
	$R_0=100\ \mu m$	$\sigma_i=4.37$	$\sigma_i=13.19$	$\sigma_i=24.76$

Table 4 Cavitation inception numbers obtained using various illustrative optical criteria

Optical		Small Scale	Medium Scale	Large Scale
$-Cp_{min}$		4.47	13.22	24.80
$R_{max}>$	$R_0=10\ \mu m$	No Inception	$\sigma_i=13.20$	$\sigma_i=24.77$
100 μm	$R_0=25\ \mu m$	$\sigma_i=4.45$	$\sigma_i=13.23$	$\sigma_i=24.82$
	$R_0=50\ \mu m$	$\sigma_i=4.51$	$\sigma_i=13.42$	$\sigma_i>25$
	$R_0=100\ \mu m$	$\sigma_i>5$	$\sigma_i>14$	$\sigma_i>25.5$
$R_{max}>$	$R_0=10\ \mu m$	No Inception	$\sigma_i=13.19$	$\sigma_i=24.78$
400 μm	$R_0=25\ \mu m$	$\sigma_i=4.41$	$\sigma_i=13.21$	$\sigma_i=24.78$
	$R_0=50\ \mu m$	$\sigma_i=4.41$	$\sigma_i=13.21$	$\sigma_i=24.78$
	$R_0=100\ \mu m$	$\sigma_i=4.42$	$\sigma_i=13.23$	$\sigma_i=24.82$

3.3 Cavitation Inception for Line Vortex With Diffusive Vortex Core

3.3.1 Bubble Dynamics. In the previous section the pressure along the vortex axis was assumed to remain constant. This allowed the bubble to reach some equilibrium status after reaching the vortex axis. The acoustic emission in this case is mainly from the bubble growth and subsequent oscillations. The bubble collapse, however, is known to generate most of the cavitation noise and occurs after the grown bubble encounters an adverse pressure gradient during its motion. To investigate this effect, a diffusive line vortex was specified by taking into account a vortex core radius increase along the vortex axis as shown in Fig. 4 for the small scale. The *far-field* description of the vortex (i.e., circulation) was kept constant. This is justified by the fact that most of the bubble history occurs over a very short distance from the blade tip. The computations for the diffusive vortex core case were conducted by releasing the bubbles at one half the core radius from the vortex axis with an initial nucleus equilibrium condition. Figure 5 shows the resulting bubble radius variations and the acoustic pressure versus time during the bubble capture for $R_0=50\ \mu$m and $\sigma=4.471$ in the small-scale case.

It is seen that the bubble grows significantly then collapses when it encounters the adverse pressure gradient. Due to the presence of gas in the bubble and to the absence of acoustic energy loss it pursues many successive oscillations. This leads to high-frequency oscillations and stronger acoustic emission than generated during growth. It is interesting to isolate the importance of the slip-velocity pressure term in Eq. (8). The result for neglecting the slip-velocity term is shown in Fig. 6. One can see that much

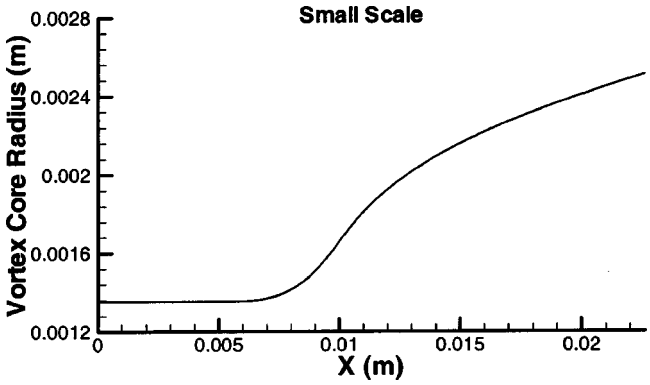

Fig. 4 Diffusion of the vortex core through increase of its radius along the longitudinal direction

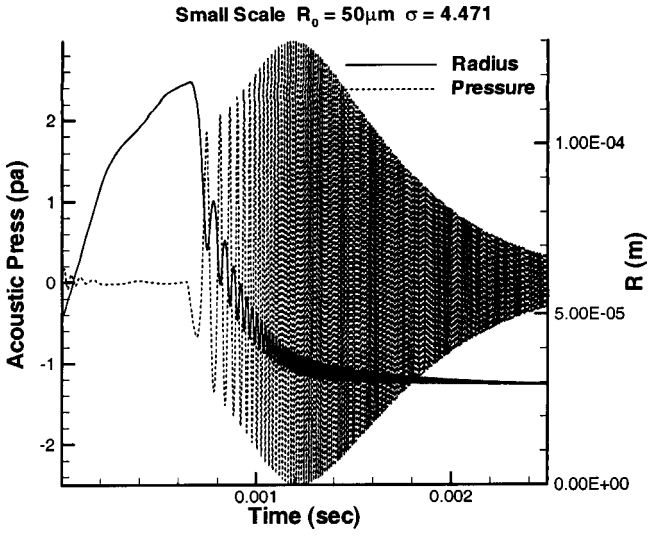

Fig. 5 Bubble radius and resulting acoustic pressure versus time for the small scale with $R_0=50\ \mu$m at $\sigma=4.471$ in a diffusive line vortex

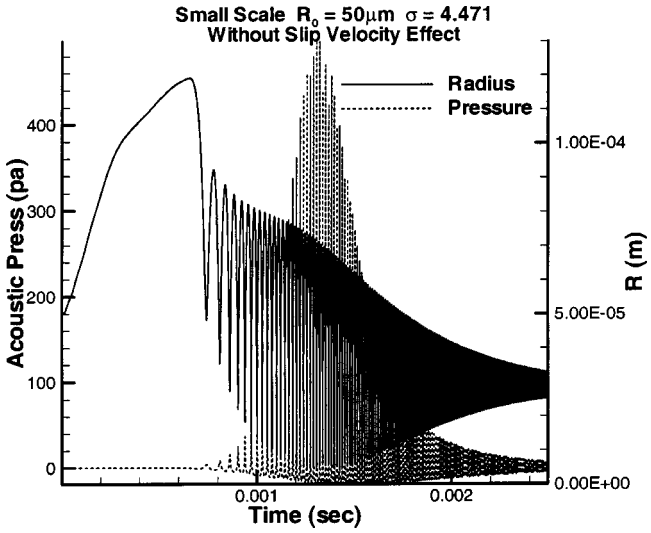

Fig. 6 Bubble radius and resulting acoustic pressure versus time for the small scale with $R_0=50$ μm at $\sigma=4.471$ in a diffusive line vortex when the slip velocity effect is neglected

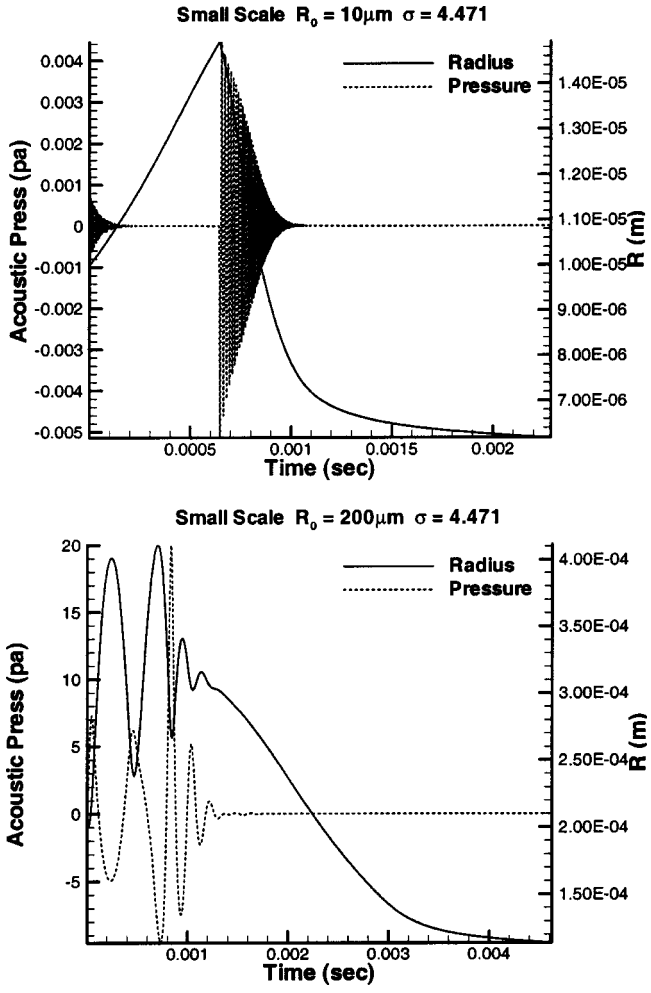

Fig. 7 Bubble radius and resulting acoustic pressure versus time for the small scale with $R_0=100$ and 200 μm at $\sigma=4.471$ in a diffusive line vortex

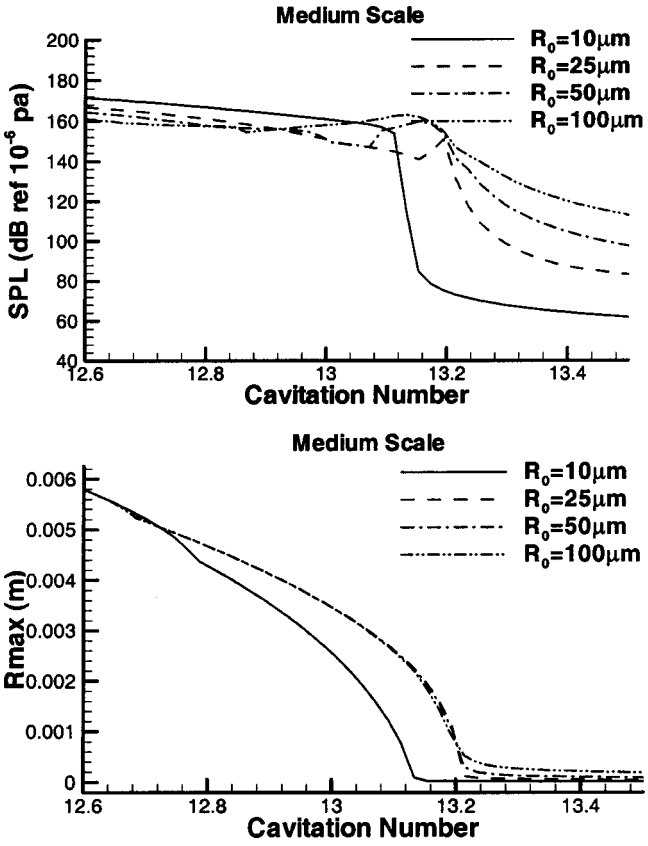

Fig. 8 Maximum SPL and bubble radius versus cavitation number for small and medium scales in the diffusive vortex core case

stronger bubble oscillations occur in this case resulting in extremely high acoustic noise during multiple collapses.

3.3.2 Influence of the Initial Bubble Radius. The influence of nuclei size is studied by releasing bubbles of different initial radii R_0 at the same cavitation number. Figure 7 shows the bubble radius and the acoustic pressure versus time during capture for two extreme sizes $R_0=10$ μm and 200 μm at $\sigma=4.471$ in the small-scale case. By including the 50 μm case of Fig. 5 one can see different bubble behaviors. The small-sized bubble collapses without strong volume rebound and generates very high frequency but very low amplitude noise, the midsized bubble collapses with strong volume rebound and generates high-frequency and high-amplitude noise. Finally, since the frequency of oscillation of the large-sized bubble is close to that of the encountered pressure field variations, large resonance pressure fluctuations occur. These three different behaviors are also found in the medium and large scales, [11].

3.3.3 Scaling. A series of computations similar to those in the previous section were conducted to obtain the maximum size of the bubble and the maximum acoustic pressure versus the cavitation number. Four initial nuclei sizes ($R_0=10$, 25, 50, and 100 μm) were used for all three scales. Figure 8 shows that the maximum bubble size and the maximum noise level SPL measured at 30 cm from the vortex center at the release location versus the cavitation number for the small scale. Similar curves for the medium and large scale can be found in [11]. By comparing Figs. 3 and 8 it is seen that the maximum radius curves are not significantly different from those obtained in the constant core case for the larger initial bubble sizes ($R_0=25$, 50, and 100 μm). For the smaller initial bubble size ($R_0=10$ μm), however, the curves are significantly different from those of constant vortex core because

Table 5 Cavitation inception number obtained using various illustrative acoustic criteria for calling inception

Acoustic Criterion		Small Scale	Medium Scale	Large Scale
$-Cp_{\min}$		4.47	13.22	24.80
SPL_{max}	$R_0=10\ \mu m$	$\sigma_i=4.37$	$\sigma_i=13.15$	$\sigma_i=24.59$
>90 db	$R_0=25\ \mu m$	$\sigma_i=4.71$	$\sigma_i=13.38$	$\sigma_i=24.88$
	$R_0=50\ \mu m$	$\sigma_i>6$	$\sigma_i>13.5$	$\sigma_i>25$
	$R_0=100\ \mu m$	$\sigma_i>7$	$\sigma_i>14$	$\sigma_i>25.5$
SPL_{max}	$R_0=10\ \mu m$	No Inception	$\sigma_i=13.13$	$\sigma_i=24.56$
>130 db	$R_0=25\ \mu m$	$\sigma_i=4.45$	$\sigma_i=13.22$	$\sigma_i=24.78$
	$R_0=50\ \mu m$	$\sigma_i=4.47$	$\sigma_i=13.25$	$\sigma_i=24.80$
	$R_0=100\ \mu m$	$\sigma_i=4.49$	$\sigma_i=13.32$	$\sigma_i=24.85$

Table 6 Cavitation inception number obtained using various illustrative optical criteria for calling inception

Optical Criterion		Small Scale	Medium Scale	Large Scale
$-Cp_{\min}$		4.47	13.22	24.80
$R_{max}>$ 100 μm	$R_0=10\ \mu m$	No Inception	$\sigma_i=13.13$	$\sigma_i=24.59$
	$R_0=25\ \mu m$	$\sigma_i=4.45$	$\sigma_i=13.23$	$\sigma_i=24.82$
	$R_0=50\ \mu m$	$\sigma_i=4.49$	$\sigma_i>13.5$	$\sigma_i>25$
	$R_0=100\ \mu m$	$\sigma_i>5.5$	$\sigma_i>14$	$\sigma_i>25.5$
$R_{max}>$ 400 μm	$R_0=10\ \mu m$	No Inception	$\sigma_i=13.12$	$\sigma_i=24.56$
	$R_0=25\ \mu m$	$\sigma_i=4.39$	$\sigma_i=13.22$	$\sigma_i=24.77$
	$R_0=50\ \mu m$	$\sigma_i=4.41$	$\sigma_i=13.22$	$\sigma_i=24.78$
	$R_0=100\ \mu m$	$\sigma_i=4.41$	$\sigma_i=13.24$	$\sigma_i=24.82$

the bubble with smaller initial size is not always able to enter the vortex center before the vortex core diffuses. To allow the smaller initial bubble size to enter the vortex center before the vortex core diffuses, further decreases of the cavitation number are required. Unlike the maximum radius curves, the maximum SPL curves of diffusive vortex core all differ significantly from those of the constant vortex core, except at high cavitation numbers where the acoustic signal created by the bubble collapse is not stronger than that of growth.

Tables 5 and 6 show the cavitation inception numbers for all the cases considered by choosing the same criteria as in Tables 2 and 3. Unlike in the constant vortex core case where one can select appropriate acoustic and optical criteria such that the cavitation inception number becomes well correlated by Eq. (2), it is very difficult to define such an acoustic or optical criterion for the diffusive vortex core case.

Another way of illustrating the scaling effect due to the nuclei size is to show the cavitation number versus the ratio of the maximum radii obtained at two different scales. This is shown in Fig. 9. To correct for viscous effects the cavitation number is normalized using $Re^{0.4}$, [18], and the maximum radius using

$$R_m \approx a_c \approx \frac{C_0}{R_e^{0.2}}. \tag{15}$$

Therefore, the ratio between scale 1 and 2 is

$$\frac{R_{m1}}{R_{m2}} = \left(\frac{C_{01}}{C_{02}}\right)\left(\frac{\mathrm{Re}_2}{\mathrm{Re}_1}\right)^{0.2}. \tag{16}$$

The ratio is shown in Fig. 9 for the three groups: middle/small, large/small, and large/middle. It is seen that for each group, the curves of different R_0 are on top of each other for high and low cavitation number but deviate *a lot* right below the cavitation inception point. The normalization factor applied in this study is also expected to merge all the curves of different groups to be equal to one at the low cavitation number. Figure 9, however, shows that the curves of middle/small and large/small approach a value less then one at the low cavitation number. This is because at the low cavitation numbers and in the small scale the bubbles

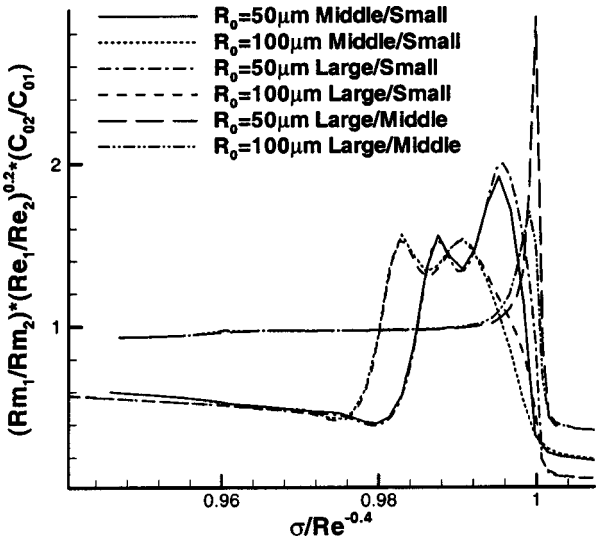

Fig. 9 The normalized curves of the ratio of maximum radius versus cavitation number for three different scale ratio and three different initial bubble size

get trapped at the streamwise location where the vortex diffusion starts to occur while the bubbles are carried downstream for the middle and large scale. An attempt for normalizing the maximum SPL curve has also been tried, but the normalized curves did not merge well due to the difficulty in finding an appropriate characteristic pressure.

3.4 Frequency Analysis. To study further the characteristics of the emitted noise during capture of a bubble in a vortex one can apply a Fourier transformation to the pressure signals. Figure 10 compares the acoustic signals of both constant and diffusive core cases in the frequency domain. Due to the stronger importance of the collapse in the case of a diffusive vortex, one can see that the higher frequencies have much higher amplitudes when compared to the constant vortex core case. The Fourier spectrum for different R_0 and in the diffusive vortex case are shown in Fig. 11 for the small scale. It is found that these curves can be categorized into three major groups according to their shapes.

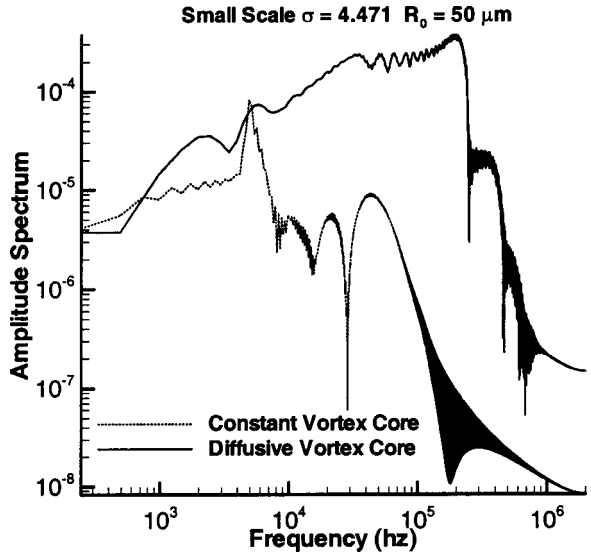

Fig. 10 Comparison of the amplitude spectra of the acoustic pressure generated in a constant and a diffusive vortex core for $R_0=50\ \mu m$ in the small scale

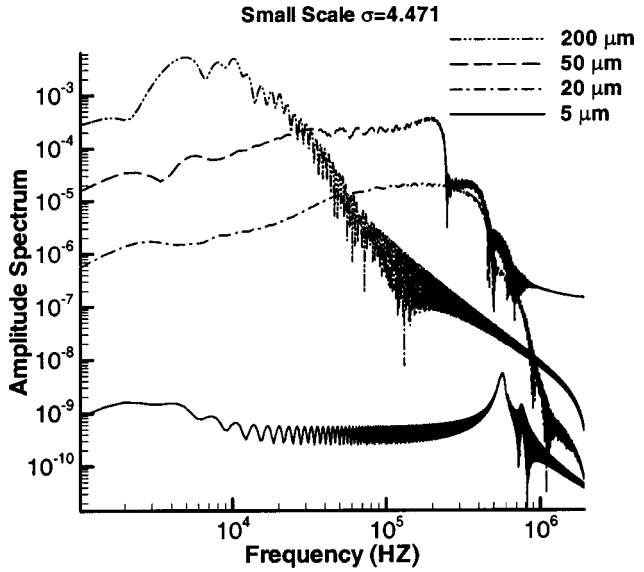

Fig. 11 Amplitude spectrum for various initial nuclei sizes in the small scale

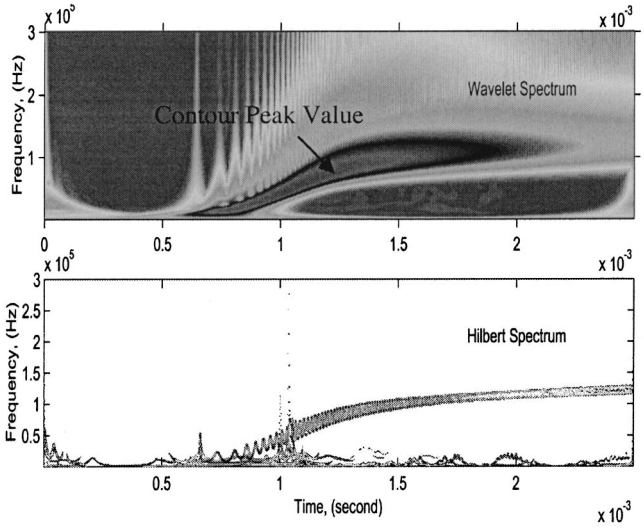

Fig. 13 Wavelet transform and Hilbert transform for R_0 = 50 μm and σ = 4.471 in the small scale

(a) In the first small bubble size group ($R_0 = 5$ μm), the curves show two major high frequency peaks, one obtained during initial bubble growth and one during bubble collapse.

(b) In the second middle bubble sizes group ($R_0 = 20$ and 50 μm), the curves show a rather flat high amplitude region, followed by a power-law decay high-frequency region mainly due to successive bubble collapses.

(c) In the third large bubble size group ($R_0 = 200$ μm), the curve shows a major amplitude peak at low frequency, which indicates the oscillation frequencies of the bubble growth and collapse, and pressure field variations are very close. This is followed by a gradual classical power-law type decay of the spectrum.

Similar curves are obtained for the other two scales, [11]. It is also found that the bubble sizes for a given group increases as the scale increases.

It is important to know what the peaks in the spectral domain correspond to. To identify these peaks we can estimate the frequency at the location of interest in the acoustic signal generated by a bubble $R_0 = 50$ μm at $\sigma = 4.471$ in the small scale as shown in Fig. 12. One disadvantage of the Fourier transformation is that it does not provide information regarding when in time the various spectral components appear. When the time localization of the spectral components is needed, either a wavelet or a Hilbert transformation, [19], can provide the time-frequency representation. Figure 13 shows the frequency versus time by applying both a wavelet and a Hilbert transformations to the same acoustic signal shown in Fig. 12. Both indicate a high amplitude at the high frequencies (~120 KHz) for a long time after the bubble first collapse. Following the first collapse the frequency of the oscillations increases with each successive collapse. In order to understand this continuous increase in the frequency, we conduct an order of magnitude analysis of the expected bubble oscillations frequency, F, based on the Rayleigh period T,

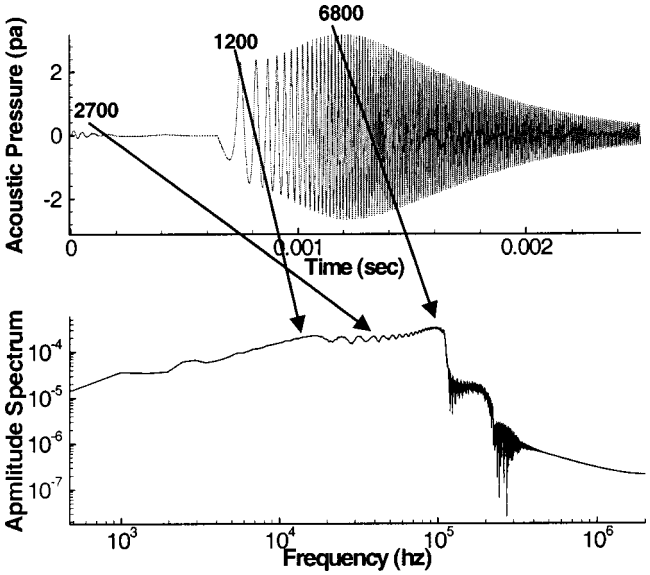

Fig. 12 Correspondence between acoustic signals and the peak frequencies in the Fourier spectrum for $R_0 = 50$ μm and $\sigma = 4.471$ in the small scale

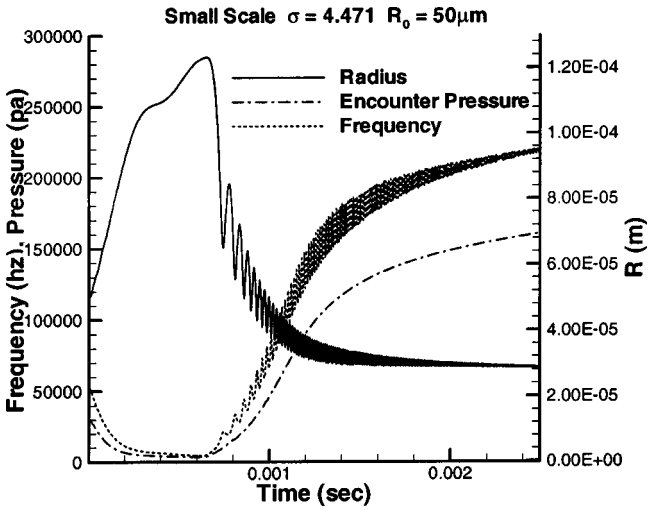

Fig. 14 Bubble radius, encounter pressure and frequency obtained using Eq. (16) versus time for $R_0 = 50$ μm and $\sigma = 4.471$ in the small scale

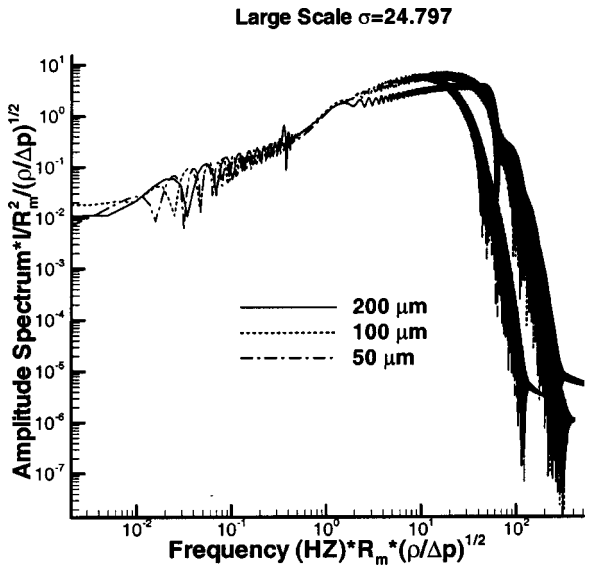

Fig. 15 Normalized amplitude spectra for various initial bubble radii in the large scale

$$F=\frac{1}{2}T^{-1}=\frac{1}{2R}\sqrt{\frac{\Delta p}{\rho}}. \tag{17}$$

Figure 14 shows F versus time computed using the pressure difference $\Delta p=P_{\infty}(t)-p_v$. This shows the same trend as the Wavelet and Hilbert spectra and appears to give a good approximation of the frequency of the acoustic signals.

From Eq. (17) it appears that the frequency of the first collapse signal is controlled by the maximum radius and pressure gradient at the location where the vortex core starts to diffuse. By appropriately choosing the normalization factor one can obtain a good normalization of the collapse frequency of the second size group discussed earlier. Figure 15 illustrates this for the large scale where more tested nuclei sizes fall in the second group in this scale. The frequencies and amplitudes are normalized by F_m and A:

$$F_m=\frac{1}{R_m}\sqrt{\frac{\Delta P}{\rho}}, \tag{18}$$

$$A=\frac{\Delta P\tau R_m}{l}=\frac{R_m^2}{l}\sqrt{\rho\Delta P}. \tag{19}$$

R_m is the maximum radius, l is the distance to the location where the acoustic signal is computed, and Δp is the difference between the encounter pressure at the first and second bubble collapse.

4 Conclusions

We have used in this study bubble dynamics to predict the cavitation inception in a line vortex flow. We have shown that using the $\sigma=-C_{p\,\min}$ conventional engineering definition of cavitation inception or the classical spherical bubble dynamics model cannot explain experimentally observed nuclei scaling effects. However, the ''improved'' SAP spherical model shows that the nuclei sizes play an important role in scaling, especially when the water contains only very small bubbles.

We have confirmed that the sources of high-frequency acoustic emission are the initial bubble growth, and more importantly, the subsequent bubble collapse when the bubble reaches the region where the vortex diffuses. The adverse pressure gradient along the vortex core was found to significantly increase both the amplitude and frequency of the acoustic emission during bubble capture by the vortex.

From frequency analysis, it was found that the amplitude spectrum of the acoustical signal can be categorized into three major groups according to their shapes. For the first group, the curves show two major peaks, one from the bubble growth signal and one from the bubble collapse signal. For the second group, the curves show a rather flat high-amplitude region, which is mainly due to successive bubble collapses. For the third group, bubble growth, collapse and pressure field have very similar frequencies and the spectra exhibit only one major peak. By appropriately choosing the normalization factor one can well normalize the first collapse signal of the second group.

Acknowledgments

This work was conducted at DYNAFLOW in execution of a Task Order under the contract N00174-96-C-0034 with the Naval Surface Warfare Center Indian Head Division, Gregory Harris monitor. Funding was provided by the Naval Surface Warfare Center Carderock Division, from the Propulsor Group, Jude Brown. We would like to thank both organizations for their support. We would also like to thank Dr. Young Shen for many useful discussions and suggestions and Dr. Ki-Han Kim for his parallel support.

References

[1] McCormick, B. W., 1962, ''On Cavitation Produced by a Vortex Trailing from a Lifting Surface,'' ASME J. Basic Eng., **84**, pp. 369–379.
[2] Fruman, D. H., Dugue, C., and Cerrutti, P., 1991, ''Tip Vortex Roll-Up and Cavitation,'' *ASME Cavitation and Multiphase Flow Forum*, FED-Vol. 109, ASME, New York, pp. 43–48.
[3] Arndt, R. E., and Dugue, C., 1992, ''Recent Advances in Tip Vortex Cavitation Research,'' *Proc. International Symposium on Propulsors Cavitation*, Hamburg, Germany, pp. 142–149.
[4] Farrell, K. J., and Billet, M. L., 1994, ''A Correlation of Leakage Vortex Cavitation in Axial-Flow Pumps,'' ASME J. Fluids Eng., **116**, pp. 551–557.
[5] Arndt, R. E., and Keller, A. P., 1992, ''Water Quality Effects on Cavitation Inception in a Trailing Vortex,'' ASME J. Fluids Eng., **114**, pp. 430–438.
[6] Latorre, R., 1982, ''TVC Noise Envelope—An Approach to Tip Vortex Cavitation Noise Scaling,'' J. Ship Res., **26**, pp. 65–75.
[7] Ligneul, P., and Latorre, R., 1989, ''Study on the Capture and Noise of Spherical Nuclei in the Presence of the Tip Vortex of Hydrofoils and Propellers,'' Acustica, **68**, pp. 1–14.
[8] Hsiao, C.-T., and Pauley, L. L., 1999, ''Study of Tip Vortex Cavitation Inception Using Navier-Stokes Computation and Bubble Dynamics Model,'' ASME J. Fluids Eng., **121**, pp. 198–204.
[9] Abbott I. H., and Doenhoff, A. E., 1959, *Theory of Wing Sections*, Dover, New York.
[10] Plesset, M. S., 1948, ''Dynamics of Cavitation Bubbles,'' ASME J. Appl. Mech., **16**, pp. 228–231.
[11] Hsiao, C.-T., Chahine, G. L., and Liu, H. L., 2000, ''Scaling Effects on Bubble Dynamics in a Tip Vortex Flow: Prediction of Cavitation Inception and Noise,'' Technical Report 98007-1NSWC, Dynaflow, Inc., Jessup, MD.
[12] Johnson, V. E., and Hsieh, T., 1966, ''The Influence of the Trajectories of Gas Nuclei on Cavitation Inception,'' *6th Symposium on Naval Hydrodynamics*, National Academy Press, Washington, DC, pp. 163–179.
[13] Haberman, W. L., and Morton, R. K., 1953, ''An Experimental Investigation of the Drag and Shape of Air Bubbles Rising in Various Liquids,'' DTMB Report 802.
[14] Maxey, M. R., and Riley, J. J., 1983, ''Equation of Motion for a Small Rigid Sphere in a Nonuniform Flow,'' Phys. Fluids, **26**, pp. 883–889.
[15] Chahine, G. L., 1979, ''Etude Locale du Phénomène de Cavitation—Analyse des Facteurs Régissant la Dynamique des Interfaces,'' doctorat d'etat essciences thesis, Université Pierre et Marie Curie, Paris, France.
[16] Fitzpatrick, N., and Strasberg, M., 1958, ''Hydrodynamic Sources of Sound,'' *2nd Symposium on Naval Hydrodynamics*, National Academy Press, Washington, DC, pp. 201–205.
[17] Hsiao, C.-T., and Chahine, G. L., 2002, ''Prediction of Vortex Cavitation Inception Using Coupled Spherical and Non-Spherical Models and UnRANS Computations'' *24th Symposium on Naval Hydrodynamics*, Fukuyoka, Japan, National Academy Press, Washington, DC.
[18] Shen, Y., Chahine, G., Hsiao, C.-T., and Jessup, S., 2001, ''Effects of Model Size and Free Stream Nuclei in Tip Vortex Cavitation Inception Scaling,'' *4th International Symposium on Cavitation*, Pasadena, CA.
[19] Huang, N. et al., 1998, ''The Empirical Mode Decomposition and the Hilbert Spectrum for Nonlinear and Non-Stationary Time Series Analysis,'' Proc. R. Soc. London, Ser. A, **454**, pp. 903–995.

Flow in a Centrifugal Pump Impeller at Design and Off-Design Conditions—Part I: Particle Image Velocimetry (PIV) and Laser Doppler Velocimetry (LDV) Measurements

Nicholas Pedersen[1]

Poul S. Larsen

Department of Mechanical Engineering,
Fluid Mechanics Section,
Technical University of Denmark,
DK-2800 Lyngby, Denmark

Christian B. Jacobsen

Fluid Dynamic Engineering,
Grundfos Management A/S,
DK-8850 Bjerringbro, Denmark

Detailed optical measurements of the flow inside the rotating passages of a six-bladed shrouded centrifugal pump impeller of industrial design have been performed using particle image velocimetry (PIV) and laser Doppler velocimetry (LDV). Results include instantaneous and ensemble averaged PIV velocity vector maps as well as bin-resolved LDV data acquired in the midplane between hub and shroud of the impeller. The flow is surveyed at both design load and at severe off-design conditions. At design load, $Q=Q_d$, the mean field of relative velocity is predominantly vane congruent, showing well-behaved flow with no separation. At quarter-load, $Q=0.25Q_d$, a previously unreported "two-channel" phenomenon consisting of alternate stalled and unstalled passages was observed, with distinct flow congruence between every second of the six passages. A large recirculation cell blocked the inlet to the stalled passage while a strong relative eddy dominated the remaining parts of the passage. The stall phenomenon was steady, nonrotating and not initiated via the interaction with stationary components. The study demonstrates that the PIV technique is efficient in providing reliable and detailed velocity data over a full impeller passage, also in the close vicinity of walls due to the use of fluorescent seeding. A quantitative comparison of blade-to-blade distributions of mean fields obtained by PIV and LDV showed a satisfactory agreement. [DOI: 10.1115/1.1524585]

1 Introduction

The internal flow that develops in a centrifugal pump impeller is exceedingly complex, involving both streamline curvature, system rotation, separation, and turbulence effects. Furthermore, the flow is often influenced by rotor-stator interaction mechanisms or other unsteady effects. In the past, a variety of measurement techniques, particularly one-point techniques such as pressure probes, hot-wire anemometry, and laser Doppler velocimetry (LDV) have been applied to turbomachines in the strive for accurate quantitative flow descriptions. These mean methods have provided much fundamental knowledge of flow phenomena occurring in centrifugal impellers. However, the quest for more flexible pumps that maintain high efficiencies at a broader range of operating conditions raises the need for a more detailed knowledge of the local and instantaneous features of the impeller flow. For this purpose, the particle image velocimetry (PIV) technique is a powerful alternative or supplement to LDV which offers both more information on the instantaneous spatial flow structures and, at the same time, considerably reduced acquisition times.

Wernet [1] provides an overview of applications of PIV to rotating machinery. Most studies have focused on the flow in the stationary components of a compressor or pump stage, with the aim of identifying the unsteady flow structures arising from rotor-stator interactions. The very first application of PIV to a turbomachine appears to be the work by Paone et al. [2] who made measurements in the blade-to-blade plane of a centrifugal compressor and described the nature of the wake from the rotating impeller blade. Akin and Rockwell [3] used PIV to study the wake from a model impeller in a simulated rotating machine and its interaction with a stationary diffuser blade. They characterized flow separation and reattachment events using instantaneous streamline patterns and vorticity contours. Eisele et al. [4] applied particle tracking velocimetry (PTV) to a vaned diffuser and found several unsteady flow features, e.g., flow separation in the diffuser channel and a recirculating backflow from the diffuser into the impeller at part-load conditions. Finally, in a recent study Sinha and Katz [5] and Sinha et al. [6] used PIV to study rotor-stator interactions between a centrifugal pump impeller and a vaned diffuser, addressing both flow structure and turbulence modeling issues.

Measurements of the instantaneous flow inside the rotating impeller passages themselves are very scarce. Oldenburg and Pap [7] performed PIV measurements in the impeller and in the volute of a purpose-made two-dimensional centrifugal pump. Planar data acquired in the mid-height plane at three different orientations of the impeller relative to the tongue showed that the flow, at part load, did not follow the vanes and thus departed from a potential-flow pattern. Hayami et al. [8] and Aramaki and Hayami [9] applied PIV in a model impeller passage with the CCD camera rotating with the impeller at a rotational speed of 30 rpm. This allowed a direct measurement of the relative velocity and a study of the spatiotemporal variation of the impeller flow.

In order to demonstrate the potential of the PIV technique as an efficient analysis tool in the design of industrial pump impellers, the objectives of the present study were, [10,11],

- to provide detailed instantaneous data of the internal flow field in the rotating passages of a centrifugal pump impeller,

[1]Presently at Fluid Dynamic Engineering, Grundfos Management A/S, DK-8850 Bjerringbro, Denmark. e-mail: nipedersen@grundfos.com.

Contributed by the Fluids Engineering Division for publication in the JOURNAL OF FLUIDS ENGINEERING. Manuscript received by the Fluids Engineering Division Sept. 20, 2001; revised manuscript received May 6, 2002. Associate Editor: Y. Tsujimoto.

• to investigate steady and unsteady flow phenomena occurring at both design and severe off-design conditions,

• to assess the accuracy of ensemble averaged PIV data by comparison with LDV data, and

• to establish a detailed database that allows the evaluation of advanced CFD techniques such as large eddy simulations.

Section 2 describes the centrifugal impeller and the test rig and Section 3 gives details on the PIV and LDV setups and techniques. Section 4 presents the experimental results, including instantaneous and ensemble-averaged PIV velocity data as well as bin-resolved LDV data, followed by conclusions in Section 5. In Part II of this paper, Byskov et al. [12], numerical results obtained using the large eddy simulation technique are presented and compared to the present database.

2 Experimental Apparatus

2.1 Centrifugal Impeller. The impeller under investigation is a shrouded low-specific speed centrifugal pump impeller that is used in multistage centrifugal pumps, see Fig. 1, [13]. Typical applications of pumps of this type are water transfer and circulation as well as pressure boosting in industrial process equipment.

Figure 2 shows the geometry of the impeller. It consists of six simple curvature backward swept blades of constant thickness and blunt leading and trailing edges. The impeller has a plane hub and a mildly curved shroud plate such that the axial height of the impeller blade is tapered nearly linearly from 13.8 mm at the inlet to 5.8 mm at the outlet. Optical access to the impeller passages was accomplished by manufacturing the entire test impeller in perspex. Table 1 summarizes the main dimensions of the test impeller.

Table 1 Impeller geometry and experimental operating conditions

Geometry				
Inlet diameter	D_1	71.0		[mm]
Outlet diameter	D_2	190.0		[mm]
Inlet height	b_1	13.8		[mm]
Outlet height	b_2	5.8		[mm]
Number of blades	Z	6		[-]
Blade thickness	t	3.0		[mm]
Inlet blade angle	β_1	19.7		[deg.]
Outlet blade angle	β_2	18.4		[deg.]
Blade curvature radius	R_b	70.0		[mm]
Specific speed	N_s	26.3		[eng.]
Flow conditions		I	II	
Q/Q_d		1.0	0.25	-
Flow rate	Q	3.06	0.76	[l/s]
Head	H	1.75	2.4	[m]
Rotational speed	n	725	725	[rpm]
Flow coefficient	Φ	0.123	0.031	[-]
Head coefficient	Ψ	0.33	0.45	[-]
Reynolds number	Re	1.4×10^6	1.4×10^6	[-]

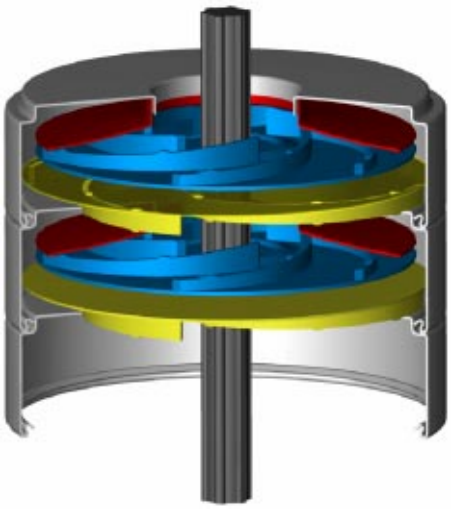

Fig. 1 Two stages of an industrial multistage pump with the shrouded centrifugal pump impeller under study, [13]

2.2 Test Rig. The measurements were performed in a compact closed-loop test rig specially designed to provide an unobstructed view of the flow within the impeller. The test rig, described in detail by Pedersen [11], consists of a 350-mm high, 400-mm diameter cylindrical tank with perspex casing. The tank holds 40 liters of demineralized water. The impeller was mounted on a 16-mm diameter shaft placed vertically in the tank. A 220-mm long, 84-mm diameter straight perspex pipe was used as inlet pipe to the impeller which discharged directly into the outer annulus of the cylindrical tank. Here the water rose and recirculated into the central inlet pipe. The impeller was driven by a 0.37 kW motor.

The flow rate through the impeller was adjusted by letting the water pass through a resistance plate, with an array of small circular holes, which was mounted at the top of the inlet pipe. By

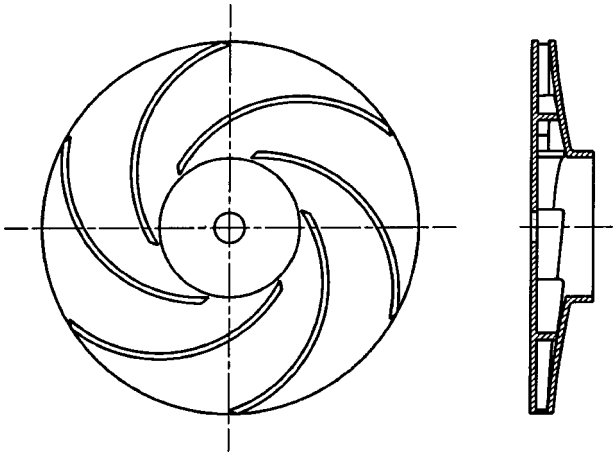

Fig. 2 Blade-to-blade (left) and meridional (right) view of the shrouded centrifugal pump impeller, [13]

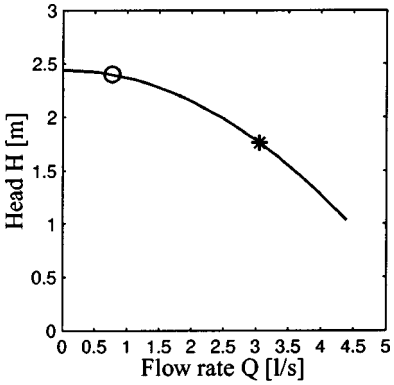

Fig. 3 Measured performance curve for a single stage of the multistage pump under investigation, [13]. The design load condition is marked by a star and the quarter-load condition by a circle.

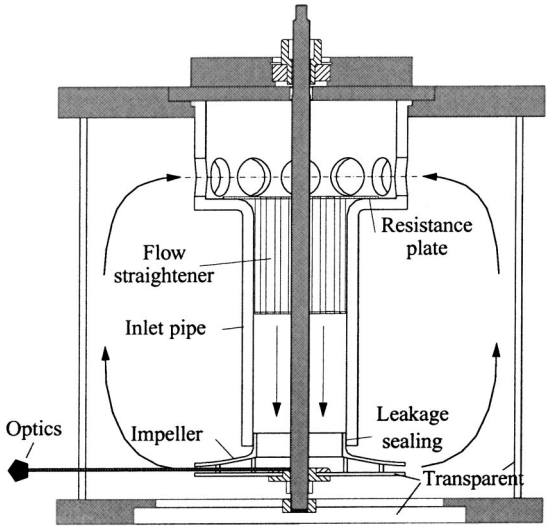

Fig. 4 Closed-loop test rig consisting of a 400-mm diameter cylindrical tank with the 190-mm diameter test impeller mounted in the vertical center plane. Optical access was provided from the sides as well as from beneath, [11].

varying the diameter of the holes the system pressure drop could be varied to achieve flow rates in the range 15–100 percent of the design flow of $Q_d = 3.06$ l/s. A flow straightener, 110-mm long and consisting of 12 7-mm diameter pipes, was mounted in the inlet pipe in order to maintain stable inlet conditions to the impeller. Furthermore, a leakage seal was installed which effectively reduced the leakage flow between inlet pipe and impeller which was measured to attain a maximum value of 10 percent of Q_d at shutoff conditions. The cylindrical tank provided optical access in all horizontal planes, as well as from beneath via a 260-mm diameter glass plate mounted in the bottom plate.

PIV and LDV data were acquired at the design load condition $Q/Q_d = 1.0$ (series I) and the quarter-load condition $Q/Q_d = 0.25$ (series II), respectively, both at a constant rotational speed of $n = 725$ rpm. Table 1 summarizes the experimental operating conditions and Fig. 3 shows the measured performance curve for the test impeller and Fig. 4 shows the test rig.

3 Experimental Technique

3.1 Particle Image Velocimetry (PIV) System. Figure 5 shows a schematic of the PIV setup, comprising a Continuum Surelite I-10 double-cavity Nd:YAG laser, a Dantec light sheet delivery system, a Kodak Megaplus ES1.0 1K×1K pixel cross-correlation CCD camera, and a Dantec Flowmap 2000 PIV processor. PIV measurements were performed inside the impeller passages in a (x,y)-plane positioned 2.9 mm above the hub, i.e., at mid passage-height, $z/b_2 = 0.5$. Figure 6 shows the positions of the two 93×94 mm^2 field-of-views which were recorded at a magnification factor of $M = 0.098$. This relatively small M was chosen in order to reveal large-scale structures in the flow. The field-of-view, denoted I, was used at design load, whereas field-of-view II was used at quarter-load where it was found advantageous to horizontally displace the camera so the image covered a full passage at the impeller outlet.

The light source, the 532 nm Nd:YAG laser, was operated at 10 Hz with a pulse duration of 4–6 ns and laser beam intensities adjusted to 30–60 mJ per pulse. An articulated light-guiding arm directed the pulsing laser beams to the test rig where cylindrical optics produced a light sheet with a thickness of approximately 1.5 mm and a divergence angle of 15 deg. The test rig was flooded with seeding particles to give a homogeneous and dense seeding distribution ensuring a minimum of 5–10 particles in each interrogation region. Fluorescent polymer particles based on melamine resin and containing Rhodamin B as fluorescent dye was used. The particles were of spherical shape and had a size range of 20–40 μm with a mean diameter of $d_p = 30$ μm. The green laser light excited the dye which subsequently emitted light in the orange spectrum centered around a wavelength of 590 nm.

Particle images were captured by the CCD camera which was aligned at right angles to the laser-sheet, see Fig. 5. The camera was equipped with a 60-mm Nikon Micro Nikkor lens and a 550-nm optical high-pass filter which only transmitted the fluorescent light and thus prevented scattered green light from reaching the CCD sensor. In order to minimize displacement estimation errors, the numerical aperture of the recording lens was chosen so

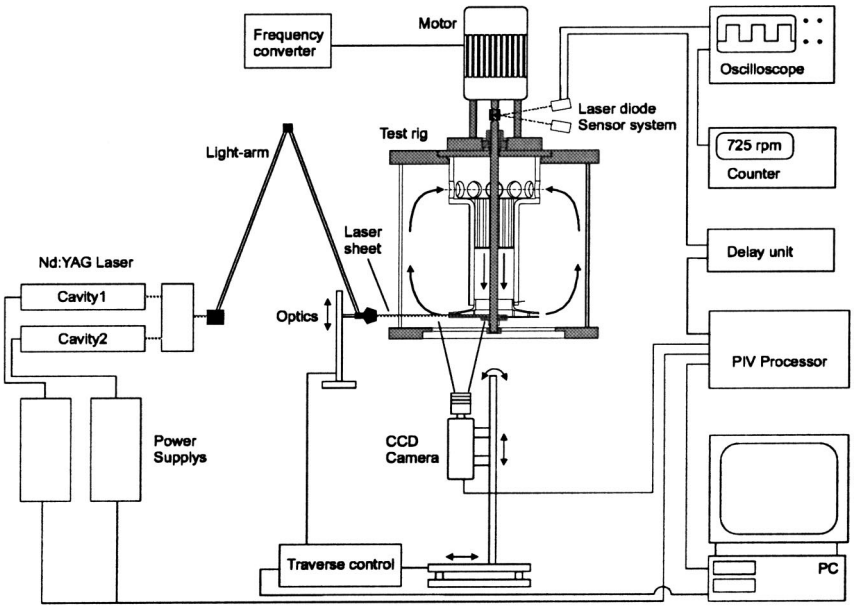

Fig. 5 Schematic of the PIV setup

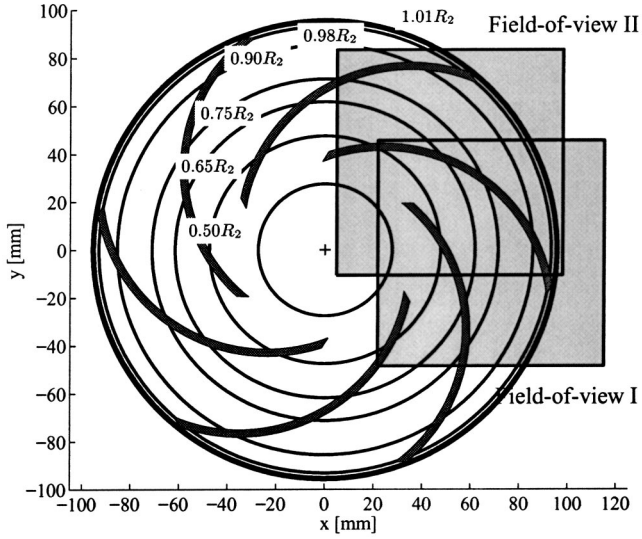

Fig. 6 Measurement positions. The squares show the locations of the two 93×94 mm² field-of-views measured with PIV, and the circles indicate the LDV measurement radii.

diffracted particle images covered at least 1–2 pixels on the CCD sensor. Based on M and the particle diameter d_p, this requirement imposed an f-number of $f^{\#}=8$, see Westerweel [14].

The image acquisition was synchronized with the rotational orientation of the impeller by means of a once-per-revolution pulse obtained from the rotor shaft, see Fig. 5. Whenever the once-per-revolution signal and the free-running 10-Hz laser pulsing coincided within a 50-μs time window, a double-frame image set was acquired. By letting the trigger signal pass an adjustable delay circuit, this procedure allowed a large number of instantaneous samples to be obtained at fixed circumferential positions of the impeller in order to calculate ensemble averages. The laser pulse separation Δt was optimized according to the 1/4 displacement rule (Keane and Adrian [15]) to 150 μs and 110 μs for series I and II, respectively. These intervals allowed the impeller to move 0.6 deg between frames, at the most, corresponding to 1 mm of its perimeter. The total recording time of a series of 1000 conditionally sampled images was of the order of 20 minutes, corresponding to a mean acquisition rate of 0.8 Hz, or one snapshot for every 15 impeller revolutions.

The PIV images were processed into vector maps using the cross-correlation method and a multiple pass interrogation algorithm, see, e.g., Scarano and Riethmuller [16] or Raffel et al. [17]. The image processing was performed off-line on a Pentium PC running an in-house FFT-based PIV processing code, [18]. A triple-pass interrogation scheme was utilized which gradually decreased the interrogation region side from 64 to 32 pixels. The Gaussian subpixel peak estimator was used as this has been shown by numerous studies, e.g., Ullum [18], to be less prone to pixel-locking effects. Remedies to avoid pixel-locking are important because the small magnification factor M in effect limits the size of the imaged particles to a diameter below 2 pixels, equivalent to a slight undersampling of the particle images. The final pass interrogation regions of 32×32 pixels were overlapped 50 percent to yield 62×62 vectors per vector map with a distance of 1.5 mm between vectors. Due to the use of fluorescent seeding, a good signal-to-noise ratio was obtained even in the close proximity of the impeller blades. Therefore, the number of spurious vectors (outliers) did not exceed 1–3 percent. Subsequently, the only validation procedure applied was a removal of the few vectors with a correlation peak signal-to-noise ratio below 1.20. These mainly corresponded to attempted velocity evaluations inside the vanes. No interpolation or data filling was applied. Table 2 summarizes essential PIV parameters.

Table 2 PIV acquisition and processing parameters

Illumination		
Light sheet source	Nd:YAG laser	
Sheet thickness	1.5	[mm]
Pulse energy	30–60	[mJ]
Pulse duration	4–6	[ns]
Pulse separation	110–150	[μs]
Seeding		
Flourescent polymer particles		
Mean diameter	30	[μm]
Density	1.5	[g/cm^3]
Recording		
Resolution	1016×1008	[px^2]
Field-of-view	93×94	[mm^2]
Lens focal length	60	[mm]
Numerical aperture	8	[-]
Image magnification	0.098	[-]
Interrogation		
Interrogation area	32×32	[px^2]
Overlap	50	[percent]
Subpixel interpolator	Gaussian	[-]
Multi-grid levels	3	[-]
Data set		
Vectors per image	62×62	[-]
Number of vector maps	1000–2000	[-]
Storage size (images)	2–4	[GB]

3.2 Laser Doppler Velocimetry (LDV) System. As a supplement to the PIV data and to allow assessment of the PIV data accuracy, a series of LDV measurements was performed in the impeller. The LDV system comprised a two-component four-beam fiber optic system with back scatter collection optics and two burst spectrum analyzers (Dantec BSA). The light source was a Coherent Innova 90 argon-ion laser operating at wavelengths of 514.5 nm (green) and 488 nm (blue). The probe consisted of an optical transducer head connected to the emitting optics and photo multipliers by means of optical fibers. The probe head was mounted on a three-axis PC-controlled traverse bench and positioned below the test rig with the optical axis oriented parallel to the impeller shaft, allowing the simultaneous measurement of the absolute radial and tangential velocity components C_r and C_t. Directional ambiguity was eliminated by means of a Bragg cell that applied a 40-MHz frequency shift to one of each pair of beams.

For the LDV measurements, the flow was seeded with neutrally buoyant polyamide seeding particles with a mean diameter of 20 μm. Velocity samples were sorted into 360 angular bins based on their arrival time relative to the once-per-revolution pulse. This ensured the proper assignment of phase angle with respect to the impeller to each velocity sample. This acquisition procedure allowed free running of the LDV system and therefore conceptually differed from the conditional sampling applied in the PIV measurements.

Figure 6 shows the LDV measurement stations. The impeller flow was surveyed at radii of $r/R_2=\{0.50,0.65,0.75,0.90,0.98,1.01\}$, respectively. At each radial station data were collected at 5–10 axial positions between hub and shroud depending on the local impeller height. At each measurement point, 200,000 samples of each velocity component were collected without coincidence filtering, yielding an average of 550 samples in each bin with an angular extent of 1 deg. However, on the grounds of flow congruence between all six impeller passages at design conditions, the statistical sample size was, in average,

Table 3 LDV parameters

Optics	Green (C_r)	Blue (C_t)	
Wavelength	514.5	488	[nm]
Beam diameter	1.35	1.35	[mm]
Beam spacing	20.3	20.3	[mm]
Lens focal length	160	160	[mm]
Seeding			
Polyamide particles			
Mean diameter	20	20	[μm]
Density	1.0	1.0	[g/cm^3]
Measurement volume			
Diameter	0.078	0.074	[mm]
Length	1.22	1.16	[mm]
Fringe spacing	3.8	4.0	[μm]
Number of fringes	19	19	[-]
Data collection			
Dead time	1–5	1–5	[ms]
Velocity samples	200.000	200.000	[per point]
Angular bins	360	360	[-]
Velocity samples	550	550	[per bin]
Statistical sample size	3333	3333	[per bin]

3333 samples per bin. As consecutive velocity realizations were placed in different phase bins, imposing a dead time of only 1–5 ms between samples ensured statistically uncorrelated samples. Effectively, though, data rates did not exceed 100 Hz due to signal loss associated with flare light. Therefore, total measurement times per series with a total of 38 measurement positions was of the order of 10 hours. Table 3 summarizes essential LDV parameters.

3.3 Measurement Errors and Uncertainty. In the PIV measurements, systematic errors include particle lag effects due to the density difference between the fluid and the fluorescent particles, the latter with a specific gravity of 1.5. According to the discussion of Agüí and Jiménez [19] this implies that a velocity slip of up to 3–4 percent between the flow and the particles may be present. However, as the focus of the present study is on the detection of large-scale structures rather than on a study of the high-frequency turbulent fluctuations in the flow, this deficiency is found not significant. Due to the presence of large velocity gradients in the flow, velocity bias effects may arise from spatial averaging over the 1.5-mm thick laser sheet.

The errors inherent in the instantaneous digital PIV velocity estimates were quantified according to Westerweel [20] to be of the order of 1 percent of full scale. Based on standard error estimates, which have been shown to apply to ensemble averaged PIV data by Ullum et al. [21], the statistical uncertainty in the mean and rms velocities based on 1000 statistically uncorrelated samples is 1.2 and 4.5 percent, respectively, stated at a confidence level of 95 percent.

In the LDV measurements, systematic errors arise from uncertainty in probe volume positioning, which was within ± 0.2 mm, and velocity bias effects due to spatial averaging over the measurement volume length of 1.2 mm. The statistical uncertainty in the LDV mean and rms velocities are estimated to 0.7 percent and 2.4 percent (c.i., 95 percent), respectively.

4 Results and Discussion

The presentation is organized as follows. First, PIV data are presented including both instantaneous samples and ensemble averages based on 1000 vector maps. Following this, blade-to-blade distributions of selected flow quantities are extracted from the PIV data and compared with mean LDV data at different radial stations. All presented data pertain to the impeller mid-height plane, $z/b_2 = 0.5$. The full data sets are included in Pedersen [11].

4.1 Design Load. Figure 7(*a*) shows a sample instantaneous PIV velocity vector map acquired at the design flow rate Q_d in field-of-view I (see Fig. 6). Since the camera frame is fixed in space, this readily obtained velocity field is the absolute velocity **C**. To allow a direct interpretation of the flow field, the relative velocity **W** as experienced by an observer rotating with the impeller was calculated by vectorial subtraction of the local circumferential impeller speed from the measured data, i.e., $\mathbf{W}=\mathbf{C}-\mathbf{U}$, inside the impeller region. Figure 7(*b*) shows the instantaneous relative velocity corresponding to the absolute vector map in Fig. 7(*a*). The impeller rotation sense is counterclockwise. Figure 7(*b*) reveals that the field of relative velocity follows the curvature of the blades in the predominant parts of the impeller passages, and that no significant separation occurs. A low-velocity zone develops on the blade pressure side, extending about two-thirds downstream the blade. This is also evident from the contour plot of the ensemble averaged relative speed $|\langle \mathbf{W} \rangle|$ shown in Fig. 8. The fact that high-momentum fluid is displaced towards the suction side in

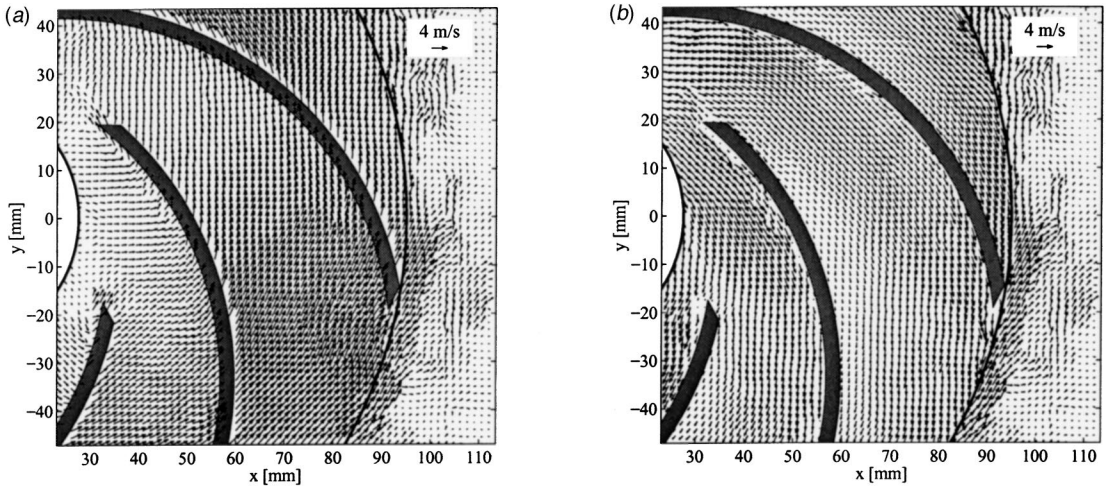

Fig. 7 Sample instantaneous velocity vector maps; (*a*) absolute velocity C, (*b*) corresponding relative velocity vector map W. ($Q/Q_d=1.0$).

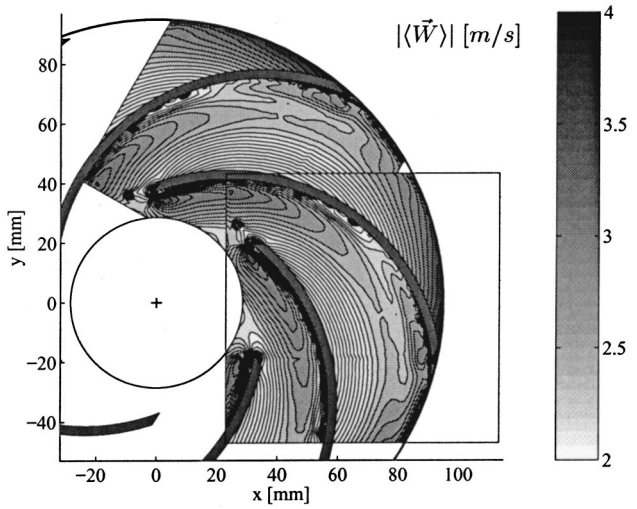

Fig. 8 Ensemble averaged relative speed $|\langle W\rangle|$. A copy of the measured data has been rotated 60 deg with respect to the rotation axis to demonstrate the flow congruence between adjacent passages. ($Q/Q_d=1.0$).

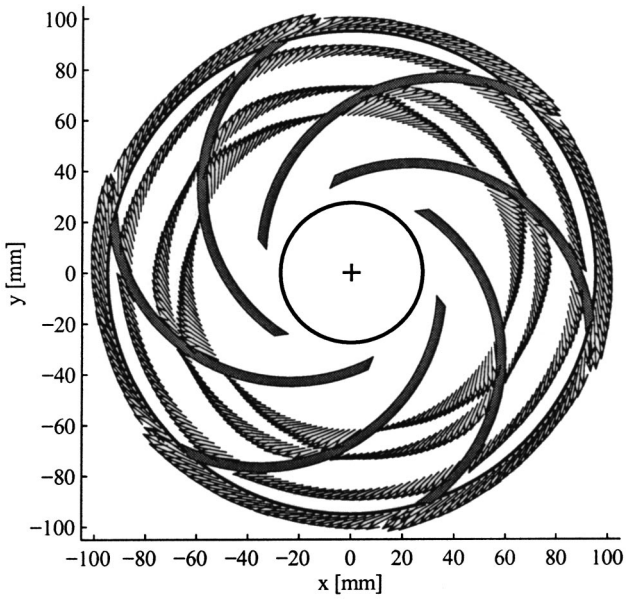

Fig. 9 Vector plot of the relative velocity $\langle W\rangle$ measured with LDV at radial stations of $r/R_2=\{0.65,0.75,0.90,1.01\}$. ($Q/Q_d=1.0$).

the inlet section is in accordance with potential theory, see, e.g., Stepanoff [22]. It also indicates that, in the inner part of the passage, the meridional curvature associated with the axial-to-radial entry bend dominates over rotational effects. However, as the fluid moves towards larger radii, the Coriolis force gains strength and pushes the fluid in the opposite direction towards the pressure side. As a result, $|\langle\mathbf{W}\rangle|$ increases on the pressure side in the outer parts of the passage, Fig. 8. The result is a fairly uniform outlet velocity distribution free from distortions or wake effects.

In the blade-to-blade plane, a measure of the relative strength between curvature and rotational effects is the Rossby number Ro given by $\mathrm{Ro}=|\langle\mathbf{W}\rangle|/\omega R_b$ where $R_b=70$ mm is the constant curvature radius of the blades. The highest Ro occurs at the inlet and attains a value of about 0.8, falling to $\mathrm{Ro}\approx 0.6$ in the central parts of the passage. This indicates that the flow in the blade-to-blade plane is mostly dominated by rotational effects, as was also the case in the impeller studied by Abramian and Howard [23].

In Fig. 8, a replicate of the measured data has been rotated 60 deg with respect to the rotation axis to illustrate the flow congruence that clearly exists between adjacent passages at design load, i.e., data acquired in one passage represent the flow in all six passages. This is clearly confirmed by the vector plot of the LDV mean relative velocity field shown in Fig. 9. The LDV velocity vectors at the inner radial station of $r/R_2=0.50$ are not shown, since excessive reflections obscured the determination of the radial velocity component C_r at this station.

A quantitative measure of the random unsteady velocity fluctuations is the measured portion k_{2D} of the turbulent kinetic energy k, defined as the mean deviation of instantaneous data from the ensemble-averaged results

$$k_{2D}=\frac{1}{2}[\langle C_x'^2\rangle+\langle C_y'^2\rangle] \tag{1}$$

where the primes denote the RMS of the velocity fluctuations, and C_x and C_y the measured planar velocity components. This quantity does not account for the spanwise velocity fluctuations, not measured. A contour plot of k_{2D} is given in Fig. 10 and demonstrates an even distribution of turbulent kinetic energy inside the passage. Disregarding image edge effects in the bottom left region and flare light effects around $(x,y)=(65,-20)$, local high levels of turbulence are confined to near-wall areas along the blade suction side, coinciding with positions of high relative velocity. Based on k_{2D}, a turbulence intensity Tu may be calculated from $Tu=\sqrt{k_{2D}}/U_2$ where U_2 is the impeller speed at the outlet. Values of Tu reach a maximum of 6 percent near the suction side, but are otherwise much lower, 2–3 percent. As noted by Ubaldi et al. [24] from similar observations in an unshrouded impeller, this low level of turbulence indicates the persistence of an inviscid potential flow core through the impeller passage at design load.

Figure 10(*b*) shows the convergence history of the first and second moments of the measured data in the three sample grid points marked in Fig. 10(*a*). The first point, P_1, is situated in the high-turbulent zone behind the leading edge on the blade suction side, the second, P_2, in the low-turbulent passage center, and the third, P_3, in the mixing-region downstream of the impeller. Figure 10(*b*) shows the effect of including more samples in the calculation of $\langle C_x\rangle$ and k_{2D}, respectively, and demonstrates that these statistics, at a sample size of $N=1000$, are well-converged even in high-turbulent regions.

In summary, the measurements at design load showed a well-behaved, predominantly vane congruent flow with no separation occurring and no significant distortions of the outlet velocity profile. A distinct flow congruence between all six passages was observed.

4.2 Quarter-Load. The main objective of the present work was to investigate the characteristics of the complex flow pattern that develops when operating the centrifugal impeller at severe off-design conditions. Figure 11(*a*) shows a snapshot of $\langle\mathbf{W}\rangle$ measured in field-of-view II at a flow rate of $0.25Q_d$, while Fig. 11(*b*) shows the corresponding ensemble average based on 1000 vector maps. Both vector maps show a clear departure from the well-behaved nonseparated flow field observed at design load and, most notable, the flow congruence between adjacent passages has been lost. In the lower passage, see Fig. 11(*b*), a large recirculation bubble has been created due to the change in incidence angle at quarter-load. This bubble covers the visible part of the suction side surface, as shown in the closeup in Fig. 12(*a*). On the contrary, the center passage shows no evidence of separated flow, but is fairly well behaved, see Fig. 11(*b*). In the upper passage, a low-velocity zone with strong instantaneous vortical structures has emerged, extending over half the passage width on almost the entire pressure side. Furthermore, at the outlet, a strong vortex

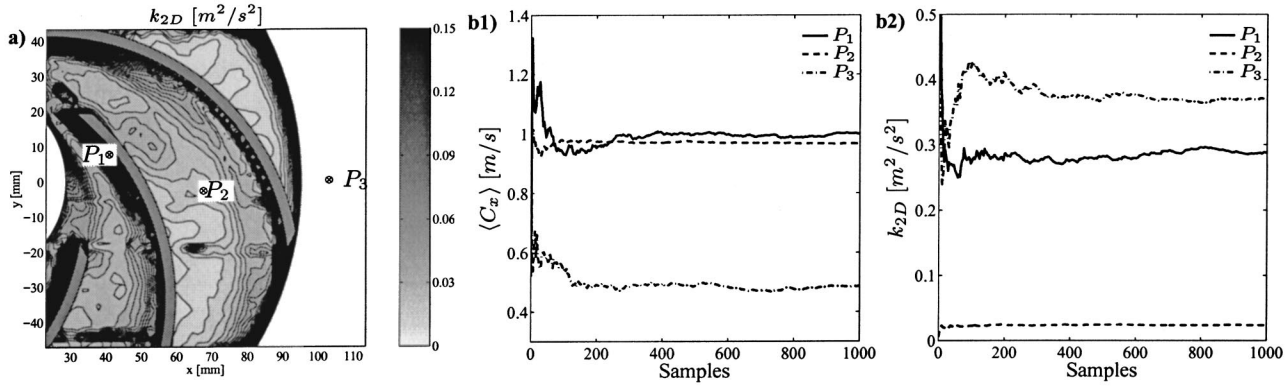

Fig. 10 (*a*) **Contour plot of the portion k_{2D} of the turbulent kinetic energy, measured by PIV.** (*b*) **Convergence history of the first and second moments in the three sample grid points P_1, P_2, and P_3.** (*b*1) **Horizontal velocity component $\langle C_x \rangle$.** (*b*2) **Turbulent kinetic energy k_{2D}.** ($Q/Q_d = 1.0$).

with a rotation sense opposite to that of the impeller reverses the flow direction and hence reduces the through-flow in this passage, see Fig. 12(*b*).

The fact that adjacent impeller passages exhibit such distinct flow characteristics at quarter-load implies the need to extend the sample area to fully grasp the flow physics. Therefore, a supplementary series of 1000 PIV velocity fields was acquired. The camera remained in the same location, but a delay of $T/6 = 13.8$ ms, corresponding to the passage time of one impeller blade, was added to the trigger signal from the rotor shaft. This procedure allowed the collection of data in a region that effectively covered two complete adjacent passages. The result is seen in Fig. 13 where the last series, although acquired at the same position in the fixed camera reference frame, has been rotated 60 deg to reflect

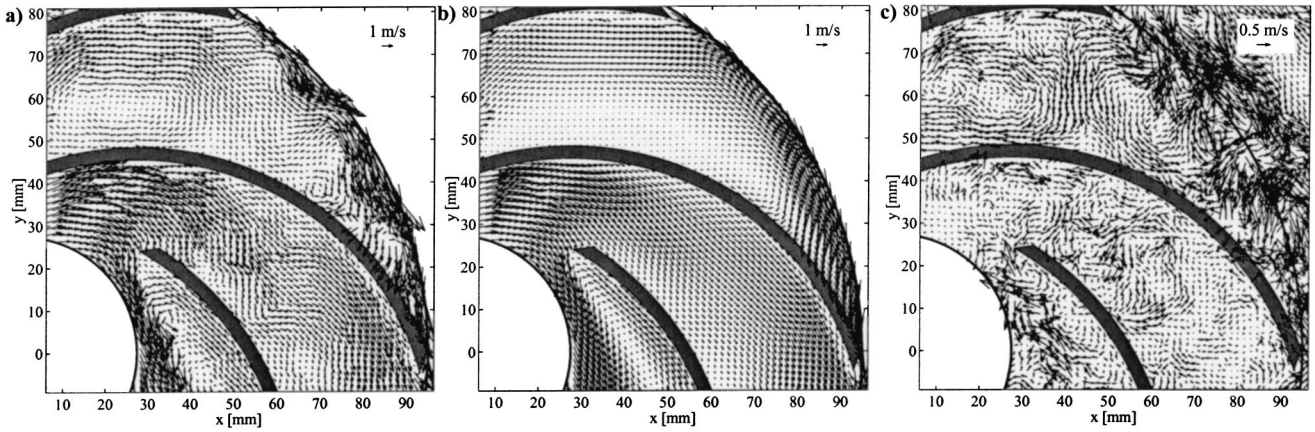

Fig. 11 PIV vector maps of the relative velocity W. (*a*) Sample instantaneous snapshot. (*b*) Ensemble average of 1000 instantaneous samples. (*c*) Sample instantaneous deviation. ($Q/Q_d = 0.25$).

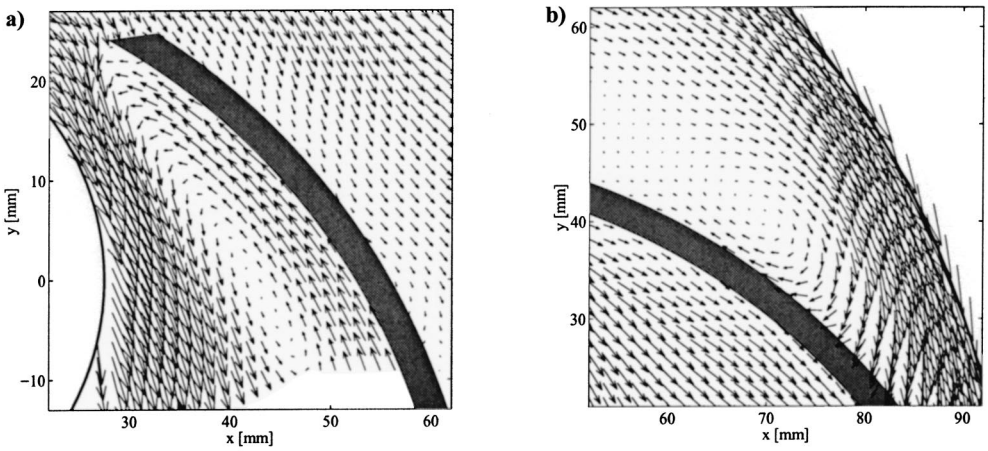

Fig. 12 Details of the ensemble averaged relative PIV velocity field $\langle W \rangle$ shown in Fig. 11(*b*). (*a*) Inlet stall cell. (*b*) Reversed flow at outlet. ($Q/Q_d = 0.25$).

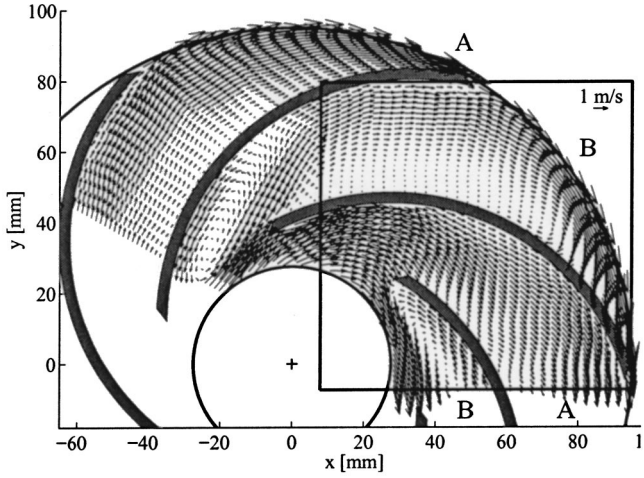

Fig. 13 Vector maps of the ensemble averaged relative velocity ⟨W⟩. The well-behaved passage is denoted *A* and the stalled passage is denoted *B*. Only every second vector is shown to avoid crowding. ($Q/Q_d=0.25$).

the effective field-of-view. A remarkable ''two-channel'' flow pattern alternately consisting of stalled and unstalled passages is revealed from Fig. 13, with an apparent flow congruence existing between every second of the six passages. The fact that the two ensemble averages fit perfectly together and therefore fully correspond with the result obtained if the two series had been acquired simultaneously with two cameras underlines the stationary nature of the detected stall phenomenon. To facilitate discussion, the impeller passage without flow separation is denoted *A* and the stalled passage *B*.

In passage *B*, see Fig. 13, the large extent of the suction side recirculation zone is notable, with flow reattaching not taking place until half way down the blade. The recirculation bubble effectively blocks three-quarters of the entrance to passage *B*. This in return unstalls passage *A* in analogy with the mechanisms leading to the propagation of a rotating stall cell. The hypothesis of every second passage being stalled is confirmed by the LDV measurements given in Fig. 14. A few outliers are visible, but in contrast to the design data in Fig. 9, the inner data at $r/R_2=0.50$ are not obscured by reflections. A detailed quantitative comparison between PIV and LDV mean data will be given later, but it is readily evident, that the LDV velocity field of Fig. 14 corresponds well to the ensemble averaged PIV flow picture in Fig. 13. Both data sets reveal the presence of a strong relative eddy that dominates the flow structure in the central and outer parts of passage *B*. It gains significant strength towards the outlet, where fluid is swept from suction to pressure side. The clockwise rotation of the eddy brings fluid backwards along the pressure surface where it is later diverted towards the suction side, with the apparent effect of suppressing separation there. A potential vortex with very similar characteristics was observed by Abramian and Howard [23] in a low-specific speed impeller operating at a flow rate of $0.50Q_d$. Visser et al. [25] also reported high passage velocities at the suction side and near-stagnation flow on the pressure side. The unusual confinement of flow separation to the blade pressure side may also be influenced by secondary flows induced due to the backward curvature of the blades, as discussed thoroughly by Farge and Johnson [26].

The deviation $\mathbf{C}$-$\langle\mathbf{C}\rangle$ of a sample instantaneous velocity from the ensemble average is shown in Fig. 11(*c*). The fluctuating velocity vectors show large spatial structures in the upper passage, passage *B*. Figure 15 reveals highly elevated levels of k_{2D} along the core of the suction side separation bubble. Significant turbulent activity is also associated with the flow reversal near the

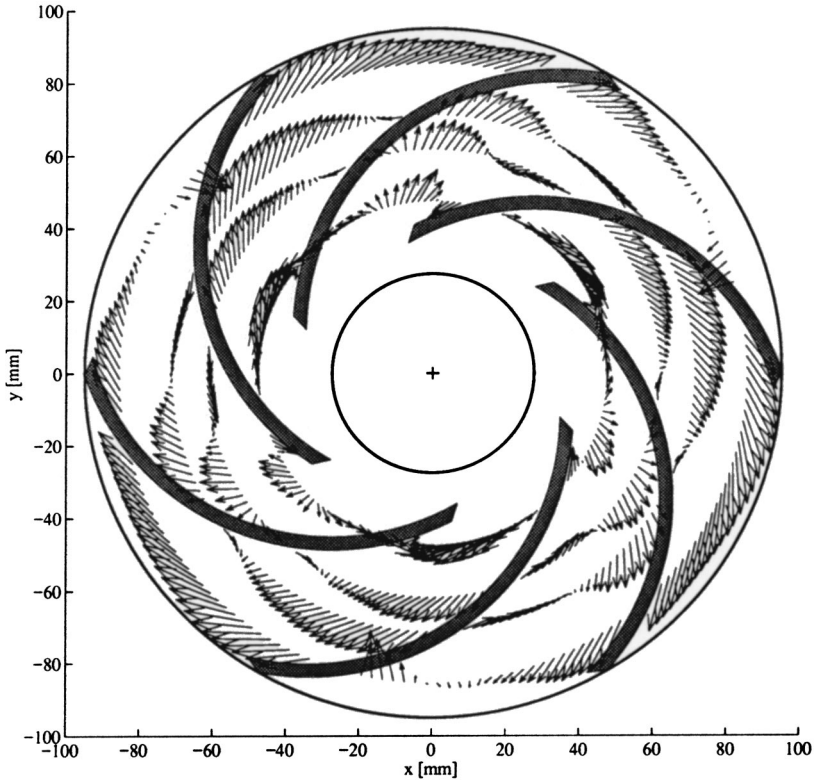

Fig. 14 Vector plot of the relative velocity ⟨W⟩ measured with LDV at radial stations of $r/R_2=\{0.50,0.65,0.75,0.90\}$. ($Q/Q_d=0.25$).

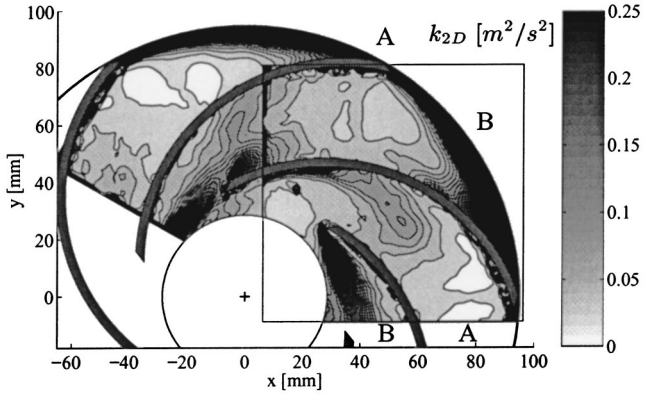

Fig. 15 Contour plot of the measured portion k_{2D} of the turbulent kinetic energy. ($Q/Q_d=0.25$).

outlet of passage *B*, although parts of this high level may be attributed to movement of the relative eddy itself, rather than to the effect of turbulence. Generally, k_{2D} attains values more than twice the level measured at design load. Expressed in terms of Tu, typical values of 8–10 percent are found in the regions described, with a peak of 15 percent just before the outlet.

Summarizing the observations done at quarter-load, a highly distorted flow with a ''two-channel'' pattern characterized by flow congruence between every second passage has emerged. The flow in the passage denoted *A* is dominated by rotational effects and resembles the well-behaved design flow, although with higher turbulent activity. In passage *B*, a stationary inlet stall cell blocks the inlet section and gives rise to a relative eddy dominating the remaining parts of the passage. Compared to observations in literature, e.g., [27,28], the detected off-design stall phenomenon is unique in the sense that it is stationary, nonrotating, and only appears in every second passage. It may be speculated that the stationary stall appearance is dictated by the even number of passages that enables a stable equilibrium mode between the forces acting on the stall cells, and subsequently locks their circumferential positions within the impeller. Any influence of geometrical asymmetries may be ruled out as consecutive runs with the impeller could cause the two-channel phenomenon to lock in different passages.

4.3 Blade-to-Blade Distributions. As demonstrated above, much knowledge of the global flow features in the centrifugal impeller may be gained from a direct study of the planar PIV velocity fields. Nevertheless, in order to substantiate the observations and to assess the accuracy of the ensemble averaged PIV data, as well as to investigate possible three-dimensional flow effects, a comparative study with LDV mean data is presented below. The six radii at which LDV data were acquired, see Fig. 6, form the basis of these comparisons between PIV and LDV.

Samples of the LDV data in the form of vector plots of **W** have already been shown in Figs. 9 and 14. Below, a closer look at the LDV data is given. Figure 16 shows the bin-resolved absolute velocity components $\langle C_r \rangle$ and $\langle C_t \rangle$ acquired at $r/R_2=0.90$ at design load, together with the RMS velocity C_r' and the number of velocity samples collected in each angular bin. The similarity between all six passages is apparent. The few local outliers result from a registration of the movement of the blade surface through the measurement volume. Figure 17 shows the LDV velocity field acquired at quarter-load, and reveals, again, flow congruence between every second of the six passages. Therefore, representative mean passage profiles were calculated from the LDV data by averaging all passages at Q_d and every second passage at $0.25Q_d$, respectively. To ensure the same statistical sample size at both flow rates, the number of velocity samples in each angular bin was

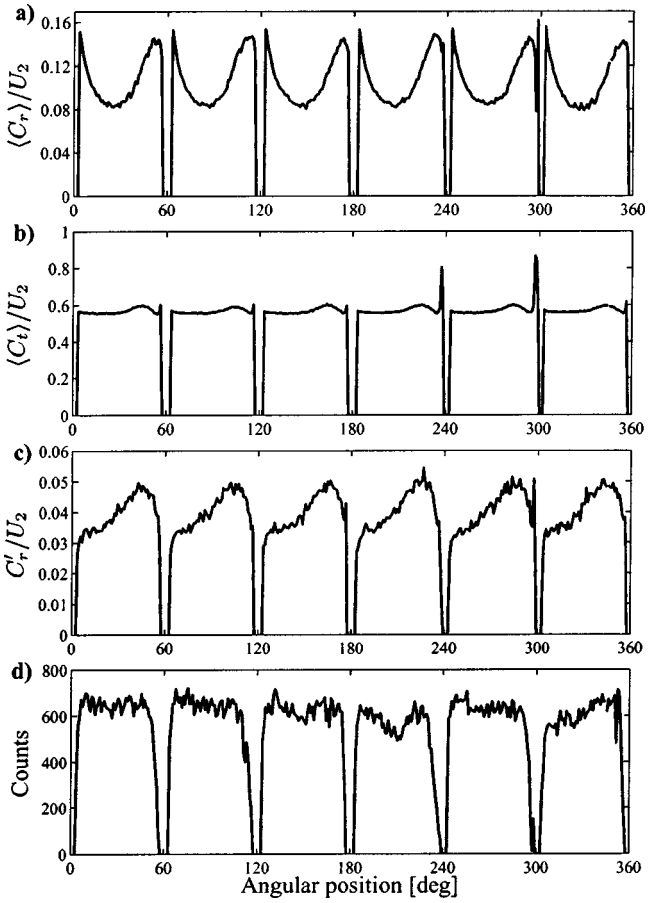

Fig. 16 Bin resolved LDV data obtained at $r/R_2=0.90$. (*a*) Radial velocity $\langle C_r \rangle$. (*b*) Tangential velocity $\langle C_t \rangle$. (*c*) RMS-velocity C_r'. (*d*) Number of radial velocity samples. ($Q/Q_d=1.0$).

doubled at $0.25Q_d$. This resulted in a uniform number of, in average, 3333 samples in each representative angular bin, comparable to the 1000 instantaneous realizations in the PIV ensemble averages. No smoothing of the LDV data was applied.

Figure 18 compares the PIV and LDV blade-to-blade distributions of the radial velocity component $\langle C_r \rangle$, assigned to representative passages as just described. The PIV profiles were obtained by bi-linear interpolation of the planar PIV data onto lines of constant radii. It should be noted that the radial components $\langle C_r \rangle$ and $\langle W_r \rangle$ are equivalent. The velocity profiles are given for radii of $r/R_2=0.50$, 0.75, and 0.98 (impeller outlet), respectively. As previously mentioned, no valid LDV data were available at the inner radial station.

In general, Fig. 18 reveals a good agreement between the two data sets. At design load, Fig. 18 (left), the flow starts off as potential flow with a radial velocity profile that is skewed markedly towards the suction side at $r/R_2=0.50$. This displacement of the flow core suggests that viscous effects have not yet developed at this radial station, leaving a flow governed by curvature and the presence of a swirl component in the inlet flow. Both effects work to raise the radial velocities near the suction side. Traveling outwards through the impeller passage, the radial velocity profile evens out under the influence of the Coriolis force. Although some discrepancy may be observed between the PIV and LDV profiles at $r/R_2=0.75$, possibly due to difference in size of seeding particles and measurement volumes, they agree well at the outlet, where large radial velocities now also exist near the pressure side due to the unloading of the blade. Overall, the design flow pattern is in accordance with classical mean line theory, [22].

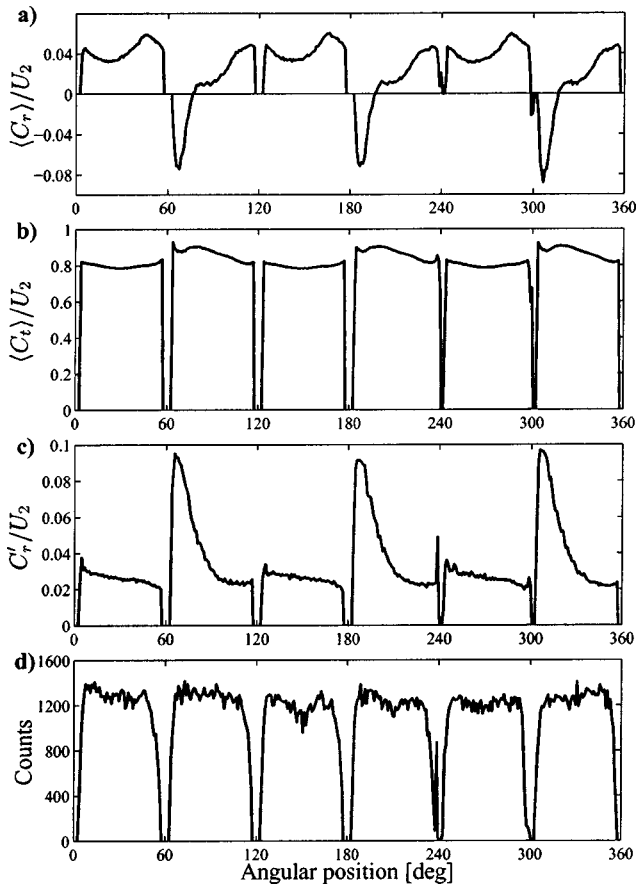

Fig. 17 Bin resolved LDV data obtained at $r/R_2=0.90$. (*a*) Radial velocity $\langle C_r \rangle$. (*b*) Tangential velocity $\langle C_t \rangle$. (*c*) RMS-velocity C_r'. (*d*) Number of radial velocity samples. ($Q/Q_d=0.25$).

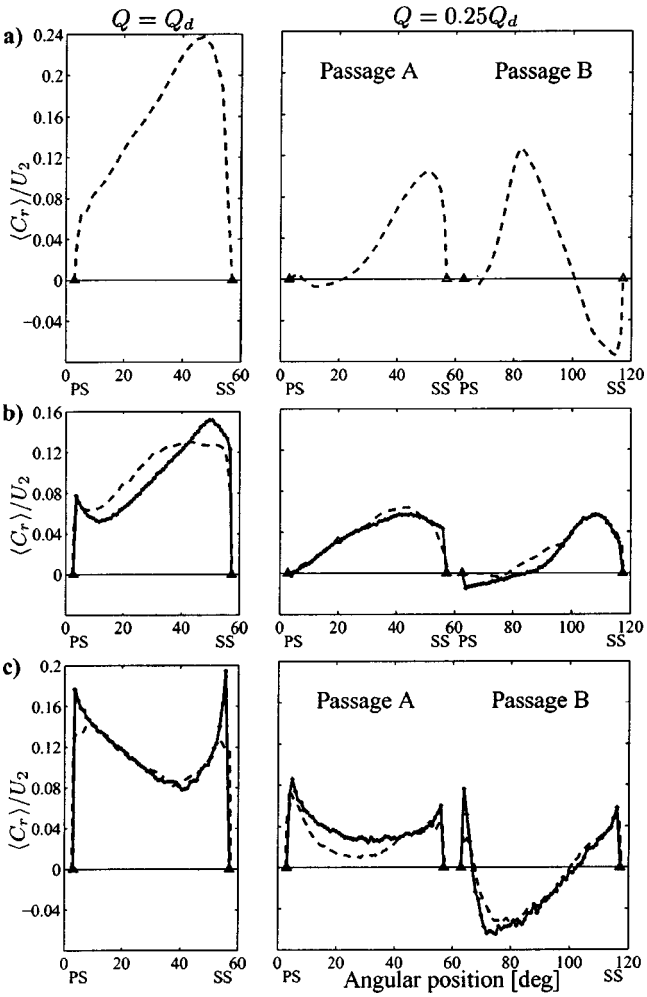

Fig. 18 Blade-to-blade distributions of the mean radial velocity $\langle C_r \rangle / U_2$ measured with PIV (— —) and LDV (——) at flow rates of Q_d (left) and $0.25Q_d$ (right). (*a*) $r/R_2=0.50$, (*b*) $r/R_2=0.75$, (*c*) $r/R_2=0.98$.

Moving on to the quarter-load data, Fig. 18 (right), passage *A* exhibits the same main characteristics as seen at design flow, with the addition of local flow features such as reversed flow near the pressure side at the inner radial station. The flow in passage *B*, however, is dictated by the suction side inlet stall cell. This is seen to cover a third of the passage at $r/R_2=0.50$ with backflow velocities reaching a magnitude of 55 percent of the maximum outward component. Large positive velocities exist in the passage center, feeding the recirculation bubble. At $r/R_2=0.75$, PIV and LDV agree on the location and height of the positive peak in passage *B* which has now moved to the suction side due to the strengthening of the relative eddy. At the outer radial station of $r/R_2=0.98$ the two profiles of passage *B* virtually collapse and uncover the significance of the flow reversal that covers two-thirds of the outlet of passage *B*. Hence, the outer radial station of passage *B* gives evidence of a stalled passage with almost no, if any, through-flow. Comparing this to the apparent net positive through-flow at $r/R_2=0.50$, suggests that some three-dimensional effects are present in the impeller. To elaborate further on this, bin-resolved LDV data obtained at a number of axial positions between hub and shroud were analyzed. Table 4 shows the integral volume flow rates Q_A and Q_B in passages *A* and *B*, respectively. The table compares passage flow rates calculated using only data at the mid-height plane, $z/b_2=0.50$, to area-averaged values based on LDV data at five different axial heights, $z/b_2=0 \ldots 1.0$, across the impeller outlet. Since the mid-height data suggest a flow rate of only $0.12Q_d$ as opposed to the actual flow rate of $0.25Q_d$ it is evident that some three-dimensional effects are in fact present at quarter-load, as is described in detail by Pedersen [11].

Figure 19 shows a comparison of the PIV and LDV blade-to-blade distributions of the tangential velocity component $\langle W_t \rangle$, and generally reveals the same levels of agreement as was seen for $\langle C_r \rangle$. The discrepancy seen at $r/R_2=0.75$ is partly due to the fact that the PIV profiles stem from bi-linear interpolation of relatively coarse planar data, and thus exhibit a stronger broadening effect than the LDV data in regions with strong gradients.

Figure 20 shows the turbulence intensities $Tu=\sqrt{k_{2D}}/U_2$ calculated from the PIV and LDV ensemble averages. The LDV data at design load show a distribution of Tu that varies almost linearly from about 3 percent in the pressure side region to 5–6 percent close to the blade suction surface. This distribution of low Tu persists throughout the impeller and is indicative of a stable flow at design load. The turbulence intensities measured by PIV at the two inner radial stations are about 40 percent smaller than the

Table 4 Integral volume flow rate distribution calculated from LDV data

Operating point	Q_A/Q_d	Q_B/Q_d	Σ
Design-load ($z/b_2=0.5$)	0.50	0.50	1.00
Design-load ($z/b_2=0 \ldots 1.0$)	0.50	0.50	1.00
Quarter-load ($z/b_2=0.5$)	0.20	-0.08	0.12
Quarter-load ($z/b_2=0 \ldots 1.0$)	0.21	0.04	0.25

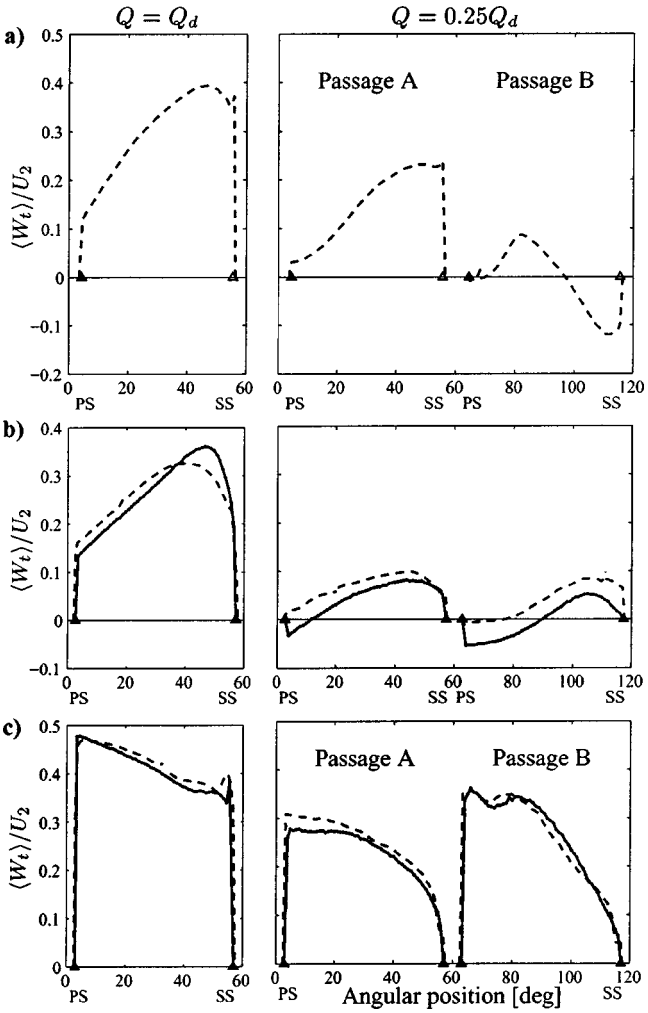

Fig. 19 Blade-to-blade distributions of the mean tangential velocity $\langle W_t \rangle / U_2$ measured with PIV (— —) and LDV (——) at flow rates of Q_d (left) and $0.25Q_d$ (right). (*a*) $r/R_2 = 0.50$, (*b*) $r/R_2 = 0.75$, (*c*) $r/R_2 = 0.98$.

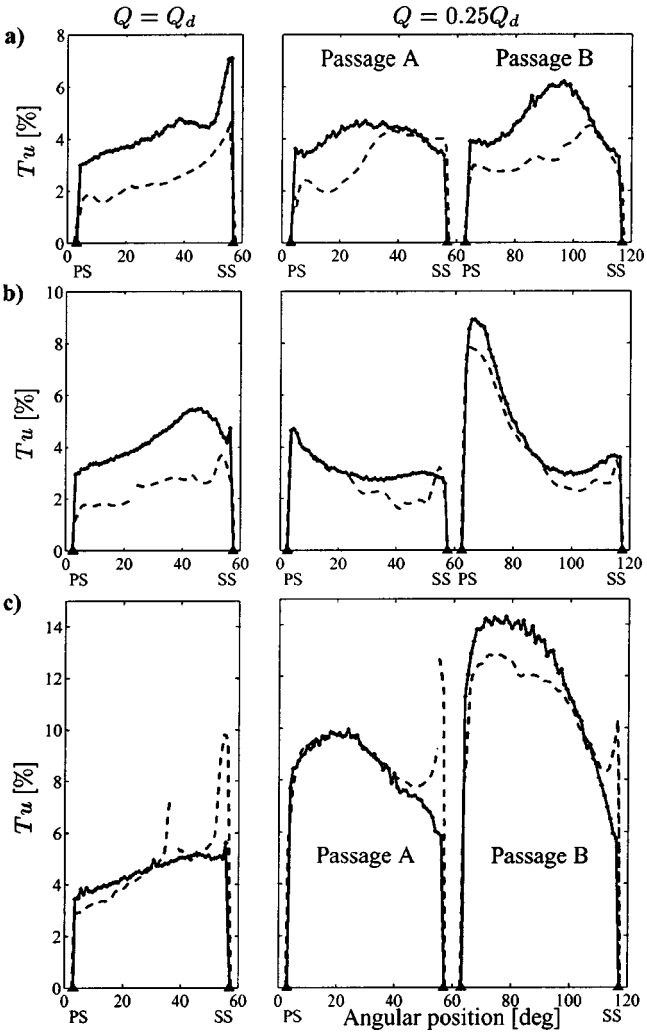

Fig. 20 Blade-to-blade distributions of the turbulence intensity $Tu = \sqrt{k_{2D}}/U_2$ measured with PIV (— —) and LDV (——) at flow rates of Q_d (left) and $0.25Q_d$ (right). (*a*) $r/R_2 = 0.65$, (*b*) $r/R_2 = 0.90$, (*c*) $r/R_2 = 0.98$.

values attained with LDV. A possible explanation for this discrepancy is the fact that Tu, apart from a turbulent contribution, may include contributions of fluctuating velocity components because of moving velocity gradients present in the flow. As noted by Hesse and Howard [29], this will result in a broadening of the probability density function of the velocity, which is falsely interpreted as turbulence. Considering that each PIV velocity realization results from a spatial averaging over a measurement volume that is in effect more than one order of magnitude larger than its LDV counterpart, the impact of this effect differs between LDV and PIV, and thus may lead to locally different levels of turbulence intensities.

Unlike the design load observations at the two inner radial stations, the agreement between the two data sets at the outlet, $r/R_2 = 0.98$, is generally good. The large peaks in the PIV profile in the passage center and at the suction side surface may be attributed to image edge effects and slight variations in the position of the blade trailing edge in consecutive PIV images, respectively. The level of agreement between the two data sets is maintained, or even improved, at the off-design condition, $0.25Q_d$. Ignoring the edge effects just mentioned, PIV predicts the same peak positions and magnitudes of turbulent intensity as LDV. In passage *B*, the values of Tu reach maxima of 9 and 14 percent at $r/R_2 = 0.90$ and $r/R_2 = 0.98$, respectively, indicating the presence of moving velocity gradients or unsteady flow effects associated with the motion of the relative eddy.

Considering the strict conditions associated with this quantitative comparison of LDV and PIV data in a rotating flow with large spatial gradients, and acquired with differently sized seeding particles and measurement volumes, a satisfactory agreement has been obtained.

5 Conclusions

Detailed measurements of the flow inside the rotating passages of a centrifugal pump impeller were obtained using particle image velocimetry (PIV) and laser Doppler velocimetry (LDV). Results included both instantaneous and ensemble averaged PIV velocity vector maps acquired in the midplane between hub and shroud of the impeller, as well as bin-resolved LDV mean fields.

At design load, $Q = Q_d$, both data sets showed a well-behaved vane congruent flow with no separation occurring, and revealed a distinct flow congruence between all six passages. Apart from local curvature effects in the inlet, the flow in the blade-to-blade plane was dominated by rotational effects. At quarter-load, $Q = 0.25Q_d$, a previously unreported ''two-channel'' phenomenon consisting of alternate stalled and unstalled passages was observed in both data sets, with distinct flow congruence between every

second of the six passages. A large recirculation cell blocked the inlet to the stalled passage while a strong relative eddy dominated the remaining parts of the same passage, causing backflow along the blade pressure side at large radii. In between the stalled passages, unstalled passages characterized by relatively well-behaved flow persisted. A quantitative study of blade-to-blade flow distributions was performed, providing additional insight into local flow features. Among other features, the strength of the inlet stall cell leading to a reduced through-flow in passage *B* was revealed.

The detected ''two-channel'' stall phenomenon was steady and nonrotating. This is possibly due to the even number of passages that enables a stable equilibrium mode between the forces acting on the stall cells, and subsequently locks their circumferential positions within the impeller. Furthermore, the stall was not initiated via the interaction with any stationary components such as a diffuser vane. In these respects, the phenomenon differs from the periodic unsteadiness of the relative flow known as rotating stall, which typically moves in the direction of rotation at a lower speed than that of the impeller.

Comparisons of PIV and LDV mean data showed a satisfactory agreement, although some discrepancies were observed, partly due to differently sized measurement volumes and seeding particles. Overall, however, the comparative study demonstrated that flow statistics calculated by ensemble averaging a large number of instantaneous PIV samples have the potential of providing accuracies comparable to LDV. A significant advantage of using the PIV technique over LDV in turbomachinery is the considerably reduced run times and the additional ability to identify instantaneous spatial flow structures. The present experimental data base may be used as a means for validating CFD simulations and turbulence models. This is demonstrated in the second part of this paper, Byskov et al. [12].

Acknowledgments

The study was partially supported by Grundfos A/S, Bjerringbro, Denmark, and partially by Technical University of Denmark.

Nomenclature

b = impeller height, m
f = impeller rotational frequency, $f=\omega/2\pi$, Hz
C = absolute speed, m/s
D = impeller diameter, m
H = head, m
n = rotational speed, rpm (revolutions per minute)
N_s = specific speed, $N_s=nQ_d^{1/2}/(H_d)^{3/4}$
Q = flow rate, m^3/s
r = radius, m
R = impeller radius, m
Re = Reynolds number, $\mathrm{Re}=U_2D_2/\nu=\pi fD_2^2/\nu$
Ro = Rossby number, $\mathrm{Ro}=|\langle\mathbf{W}\rangle|/\omega R_b$
Tu = turbulence intensity, $Tu=\sqrt{k_{2D}}/U_2$
U = circumferential velocity, m/s
W = relative speed, m/s
Φ = flow coefficient, $\Phi=Q/A_2U_2=Q/4fb_2\pi^2R_2^2$
Ψ = head coefficient, $\Psi=gH/U_2^2$

Subscripts

1 = impeller inlet
2 = impeller outlet
d = design load conditions
r = radial component
t = tangential component

Acronyms

PS = pressure side
SS = suction side

References

[1] Wernet, M. P., 2000, ''Development of Digital Particle Imaging Velocimetry for Use in Turbomachinery,'' Exp. Fluids, **28**, pp. 97–115.
[2] Paone, N., Riethmuller, M. L., and Van den Braembussche, R., 1988, ''Application of Particle Image Displacement Velocimetry to a Centrifugal Pump,'' *Proceedings of the 4th Intl. Symp. on Appl. of Laser Techniques to Fluid Mechanics*, Lisbon, Portugal, p. 6.
[3] Akin, O., and Rockwell, D., 1994, ''Flow Structure in a Radial Flow Pumping System Using High-Image-Density Particle Image Velocimetry,'' ASME J. Fluids Eng., **116**, pp. 538–544.
[4] Eisele, K., Zhang, Z., and Casey, M. V., 1997, ''Flow Analysis in a Pump Diffuser—Part 1: LDA and PTV Measurements of the Unsteady Flow,'' ASME J. Turbomach., **119**, pp. 968–977.
[5] Sinha, M., and Katz, J., 2000, ''Quantitative Visualization of the Flow in a Centrifugal Pump With Diffuser Vanes—I: On Flow Structures and Turbulence,'' ASME J. Fluids Eng., **122**, pp. 97–107.
[6] Sinha, M., Katz, J., and Meneveau, C., 2000, ''Quantitative Visualization of the Flow in a Centrifugal Pump With Diffuser Vanes—II: Addressing Passage-Averaged and Large-Eddy Simulation Modeling Issues in Turbomachinery Flows,'' ASME J. Fluids Eng., **122**, pp. 108–116.
[7] Oldenburg, M., and Pap, E., 1996, ''Velocity Measurements in the Impeller and in the Volute of a Centrifugal Pump by Particle Image Displacement Velocimetry,'' *Proceedings of the 8th International Symposium on Applications of Laser Techniques to Fluid Mechanics*, Lisbon, Portugal, pp. 8.2.1–8.2.5.
[8] Hayami, H., Aramaki, S., and Watanabe, Y., 1997, ''PC-PIV System for a Measurement of Relative Flow in a Rotating Impeller Impeller,'' *The Second International Workshop on PIV'97-Fukui*, Fukui, Japan, July, The Visualization Society of Japan, pp. 105–108.
[9] Aramaki, S., and Hayami, H., 1999, ''Unsteady Flow Measurement in a Rotating Impeller Using PIV,'' *Proceedings of the 3rd International Workshop on PIV*, Sep. 16–18, Santa Barbara, CA.
[10] Pedersen, N., and Jacobsen, C. B., 2000, ''PIV Investigation of the Internal Flow Structure in a Centrifugal Pump Impeller,'' *Proceedings of the 10th Intl. Symp. on Appl. Laser Techniques to Fluid Mechanics*, Lisbon, Portugal, July, pp. 28.3.1–28.3.10.
[11] Pedersen, N., 2000, ''Experimental Investigation of Flow Structures in a Centrifugal Pump Impeller Using Particle Image Velocimetry,'' Ph.D. thesis, Department of Mechanical Engineering, Fluid Mechanics Section, Technical University of Denmark, Copenhagen, Denmark.
[12] Byskov, R. K., Jacobsen, C. B., and Pedersen, N., 2003, ''Flow in a Centrifugal Pump Impeller at Design and Off-Design Conditions—Part II: Large Eddy Simulations,'' ASME J. Fluids Eng., **125**, pp. 73–83.
[13] Grundfos A/S, *WinCAPS Catalogue*, 1997, Ver 7.0. Product No: 41260001 CR4-20/1.
[14] Westerweel, J., 1998, ''Effect of Sensor Geometry on the Performance of PIV Interrogation,'' *Proceedings of the 9th Intl. Symp. on Appl. of Laser Techniques to Fluid Mechanics*, Lisbon, Portugal, pp. 1.2.1–1.2.8.
[15] Keane, R. D., and Adrian, R. J., 1990, ''Optimization of Particle Image Velocimeters. Part I: Double Pulsed Systems,'' Meas. Sci. Technol., **1**, pp. 1202–1215.
[16] Scarano, F., and Riethmuller, M. L., 1999, ''Iterative Multigrid Approach in PIV Image Processing With Discrete Window Offset,'' Exp. Fluids, **26**, pp. 513–523.
[17] Raffel, M., Willert, C., and Kompenhans, J., 1998, *Particle Image Velocimetry—A Practical Guide*, Springer-Verlag, New York.
[18] Ullum, U., 1999, ''Imaging Techniques for Planar Velocity and Concentration Measurements,'' Ph.D. thesis, Department of Mechanical Engineering, Fluid Mechanics Section, Technical University of Denmark, Copenhagen, Denmark.
[19] Agüí, J. C., and Jiménez, J., 1987, ''On the Performance of Particle Tracking,'' J. Fluid Mech., **185**, pp. 447–468.
[20] Westerweel, J., 1997, ''Fundamentals of Digital Particle Image Velocimetry,'' Meas. Sci. Technol., **8**, pp. 1379–1392.
[21] Ullum, U., Schmidt, J. J., Larsen, P. S., and McCluskey, D. R., 1998, ''Statistical Analysis and Accuracy of PIV Data,'' J. Visual., **1**(2), pp. 205–216.
[22] Stepanoff, A. J., 1957, *Centrifugal and Axial Flow Pumps*, 2nd Ed., John Wiley and Sons, New York.
[23] Abramian, M., and Howard, J. H. G., 1994, ''Experimental Investigation of the Steady and Unsteady Relative Flow in a Model Centrifugal Impeller Passage,'' ASME J. Turbomach., **116**, pp. 269–279.
[24] Ubaldi, M., Zunino, P., and Ghiglione, A., 1998, ''Detailed Flow Measurements Within the Impeller and the Vaneless Diffuser of a Centrifugal Turbomachine,'' Exp. Therm. Fluid Sci., **17**, pp. 147–155.
[25] Visser, F. C., Brouwers, J. J. H., and Jonker, J. B., 1999, ''Fluid Flow in a Rotating Low-Specific-Speed Centrifugal Impeller Passage,'' Fluid Dyn. Res., **24**, pp. 275–292.
[26] Farge, T. Z., and Johnson, M. W., 1992, ''Effect of Flow Rate on Loss Mechanisms in a Backswept Centrifugal Impeller,'' Int. J. Heat Fluid Flow, **13**(2), pp. 189–196.
[27] Lennemann, E., and Howard, J. H. G., 1970, ''Unsteady Flow Phenomena in Centrifugal Impeller Passages,'' J. Eng. Power, **92**(1), pp. 65–72.
[28] Yoshida, Y., Murakami, Y., Tsurusaki, T., and Tsujimoto, Y., 1991, ''Rotating Stalls in Centrifugal Impeller/Vaned Diffuser Systems,'' *Proc First ASME/JSME Joint Fluids Eng. Conf.*, ASME, New York, pp. 125–130.
[29] Hesse, N. H., and Howard, J. H. G., 1999, ''Experimental Investigation of Blade Loading Effects at Design Flow in Rotating Passages of Centrifugal Impellers,'' ASME J. Appl. Mech., **121**, pp. 813–823.

Flow in a Centrifugal Pump Impeller at Design and Off-Design Conditions—Part II: Large Eddy Simulations

Rikke K. Byskov

Christian B. Jacobsen

Fluid Dynamic Engineering,
Grundfos Management A/S,
DK-8850 Bjerringbro, Denmark

Nicholas Pedersen[1]
Department of Mechanical Engineering,
Fluid Mechanics Section,
Technical University of Denmark,
DK-2800 Lyngby, Denmark

The flow field in a shrouded six-bladed centrifugal pump impeller has been investigated using large eddy simulation (LES). The effect of the subgrid scales has been modeled through a localized dynamic Smagorinsky model implemented in the commercial CFD code FINE/Turbo. A detailed analysis of the results of LES at design load, $Q=Q_d$, and severe off-design conditions, at quarter-load $Q=0.25Q_d$, is presented. At design load LES reveals a well-behaved flow field with no significant separation. At quarter-load significant differences between adjacent impeller passages are revealed. A steady nonrotating stall phenomenon is observed in the entrance of one passage and a relative eddy develops in the remaining part of the passage. The stall unblocks the adjacent passage which exhibits a flow dominated by rotational effects. Velocities predicted by LES and steady-state Reynolds averaged Navier-Stokes (RANS) simulations based on the Baldwin-Lomax and Chien k-ε turbulence models are compared with experimental data obtained from particle image velocimetry (PIV). The complex two-channel phenomena observed by LES is with satisfactory agreement confirmed by PIV. However, it is found that the two RANS models do not reproduce the stall phenomenon observed at quarter-load and are incapable of detecting the differences between the two passages.
[DOI: 10.1115/1.1524586]

1 Introduction

The traditional approach to the hydraulic design of pumps is based on steady-state theory and depends on empirical methods, and the combination of systematic model testing and engineering experience. This approach has come a long way in producing efficient and reliable pumps. The flow field in centrifugal pumps, which is influenced by system rotation and curvature, is highly turbulent and unsteady, and due to separation and recirculation very complex. Further improvements of performance for design and off-design operating conditions will be extremely difficult with traditional steady-state methods, because it will depend more on controlling complex physical phenomena such as boundary layer separation, vortex dynamics, interactions between rotating and stationary components, vibrations and noise, etc. These unsteady phenomena are not predictable with the conventional steady simulation approach and extremely difficult to measure inside physical models. In order to improve the accuracy of the numerical simulations and to be able to analyze and understand more thoroughly the flow in centrifugal pumps, it is essential to advance from a steady state to an unsteady simulation technique. In this context a promising alternative or supplement to standard Reynolds averaged Navier-Stokes (RANS) turbulence modeling is large eddy simulation (LES).

LES has hitherto primarily been an academic research tool used for analyzing simpler flows, e.g., mixing layers, [1], flow over flat or curved plates, [2–4], and channel flows, [5–7], or to study the details of the numerical methods, e.g., development of new subgrid-scale models [8–10], discretization schemes [11], or mesh structures [12,13]. Little work has been done in the field of LES for industrial applications of practical importance and in particular on pump flows. In industrial applications the smallest resolved scales are typically orders of magnitude larger than those seen so far in classical LES. Therefore some scepticism exists on the maturity of present methods and it is necessary to investigate the limitations of the classical LES approach. It is, however, found that the present state of LES, using simple eddy-viscosity subgrid-scale models in combination with second-order numerical methods, can predict main trends for some industrial problems, and give an interesting insight into the flow dynamics in a subdomain. A few examples related to the present work can be found in literature. Eggels [14] investigated the impact of a mechanical impeller on the turbulent flow field in a baffled stirred tank reactor using the Smagorinsky model and found good agreement with experimental data. Revstedt et al. [15] performed LES on a similar test case using an implicit model also with promising results. LES of the flow through the spiral casing, impeller, and exit section of a Francis turbine system at different operating conditions have been conducted by Chen and Song [16,17] giving first an insight into the flow field present in each unit separately and later also taking into account the mutual interaction between the rotating and stationary parts. Kato et al. [18] presented the first achievements of LES of the flow in a complete stage of a mixed flow pump at 60 and 100% design flow. Again the Smagorinsky model was used. For both operating conditions the unsteady fluid forces on the impeller agreed well with measured values. Recently, Jang et al. [19] have performed LES and LDV of the vortical flow field in a propeller fan and showed that the vortex structures, the tip vorteses, the leading edge separation vortex, and the tip leakage vortex, were all simulated correctly in the LES when comparing with LDV.

The main problem in the integration of LES as an industrial analysis tool is that the methodology is not established as a standard commercial CFD tool. In order to demonstrate the potential of LES for gaining improved insight into the fluid dynamics of centrifugal pump flows, the objectives of the present work have been, [20,21],

[1]Currently at Fluid Dynamic Engineering, Grundfos Management A/S, DK-8850 Bjerringbro, Denmark. e-mail: nipedersen@grundfos.com.

Contributed by the Fluids Engineering Division for publication in the JOURNAL OF FLUIDS ENGINEERING. Manuscript received by the Fluids Engineering Division Sept. 20, 2001, revised manuscript received Aug. 23, 2002. Associate Editor: Y. Tsujimoto.

- to make LES available for numerical investigations of the flow in centrifugal pumps through the implementation of LES in a commercial CFD code tailored for turbomachinary and a subsequent validation of the implementation,
- to provide detailed flow field analysis of the flow inside a centrifugal pump impeller at design and off-design conditions, and
- to perform a comparative study of the contributions and accuracy achieved from LES and standard RANS turbulence modeling through comparison with experimental data.

Within this work LES has been implemented in the commercial CFD code FINE/Turbo and validated for plane and rotating channel flow, [21]. This paper presents the first results from simulations of the flow field in an industrial centrifugal pump impeller. A complete discussion is given in Byskov [20]. In Section 2 the numerical solution technique employed in the present work is presented. Section 3 introduces the actual impeller under investigation and describes how it has been modelled numerically. The results of the simulations are presented and discussed in Section 4, including a thorough comparison with results from standard RANS simulations based on the Baldwin-Lomax [22] and Chien k-ε [23] turbulence models as well as with experimental data obtained from particle image velocimetry (PIV). Conclusions based on the comparative study are drawn in Section 5. In Part I of this paper, Pedersen et al. [24] describes in detail the experimental apparatus and technique.

2 Numerical Solution Technique

2.1 Governing Equations. As opposed to traditional LES codes, which are often tailored for analysing simpler flows, the use of a commercial CFD code such as FINE/Turbo poses no geometrical restrictions and is thus applicable for simulating the flow in a complex geometry as a centrifugal pump impeller.

FINE/Turbo is a well-established finite volume Navier-Stokes solver based on solving the three-dimensional compressible continuity, Navier-Stokes, and energy equations, [25]. The convective fluxes are treated through a second-order central Jameson scheme, [26], with second and fourth-order scalar dissipation. In the present work the second-order term is turned off and the fourth-order dissipation is determined through the coefficient $\kappa^{(4)}=0.001$. This is two orders less than the default value of $\kappa^{(4)}=0.1$. However, the adjustment of κ needs further research. A pseudo-compressibility method and a second-order dual-time-stepping procedure implemented by Hakimi [27] allows for simulating incompressible unsteady flows.

Since the flow under investigation can be assumed to be incompressible and isothermal, the energy equation is not considered and the governing equations utilized in the present work are hence the unsteady preconditioned continuity and Navier-Stokes equations given by

$$\frac{1}{\beta^2}\frac{\partial p_g}{\partial \tau}+\frac{\partial \rho u_i}{\partial x_i}=0, \tag{1}$$

$$\frac{\partial \rho u_i}{\partial \tau}+\frac{\partial \rho u_i}{\partial t}+\frac{\partial \rho u_i u_j}{\partial x_j}+\frac{\partial p_g}{\partial x_i}=\frac{\partial}{\partial x_j}\left[\rho\nu\left(\frac{\partial u_i}{\partial x_j}+\frac{\partial u_j}{\partial x_i}\right)\right]+B_i, \tag{2}$$

where β is a preconditioning parameter, p_g the gauge pressure, and B_i the source term vector including the effects of system rotation. t is the physical time and τ the pseudo time introduced due to the dual-time-stepping. During each physical time-step an explicit fourth-order Runge-Kutta scheme is used for advancing Eqs. (1) and (2) in pseudo time.

As the flow is influenced by the rotation of the impeller Eq. (1) and (2) are formulated in a relative frame of reference. This is allowed when the two inertia forces; the Coriolis force, $\mathbf{f}_C=-2\rho(\boldsymbol{\omega}\times\mathbf{W})$, and the centrifugal force, $\mathbf{f}_c=-\rho\boldsymbol{\omega}\times(\boldsymbol{\omega}\times\mathbf{r})$, are added to the source term vector B_i as compensation. The relative velocity $\mathbf{W}$ is the velocity experienced by an observer rotating with the impeller, $\boldsymbol{\omega}$ is the angular velocity of the impeller and $\mathbf{r}$ is the position vector.

The absolute velocity $\mathbf{C}$ is computed by vectorial addition of the local circumferential impeller speed to the relative velocity, $\mathbf{C}=\mathbf{W}+\mathbf{U}$.

2.2 Large Eddy Simulation (LES). The basic philosophy in LES is, through the introduction of a filter length, to separate large eddies from small eddies. The three-dimensional time-dependent large-scale turbulent motion is resolved directly and the effect of the unresolved (or subgrid) scales is taken into account through appropriate subgrid-scale (SGS) models. The large scales in a turbulent flow are generally more energetic than the small scales and their size and strength make them the most effective transporter of conserved properties. The small scales are usually weaker, and provide little transport of these quantities. Hence the approximation of LES, which treats the large eddies more exactly than the small ones, is justified. Since only the smaller scales, which can be assumed to be isotropic, are modeled in LES, the SGS models applied can be simpler than similar models for the RANS equations.

In order to numerically define the large-scale field the idea of a traditional Reynolds decomposition is followed as shown in Eq. (3)

$$f=\overline{f}+f', \tag{3}$$

where f is any flow variable, scalar or vectorial, $\overline{f}$ is the resolved large-scale component and f' the subgrid-scale component due to spatial fluctuations of the unresolved scales. Applying the filter in Eq. (3) to the governing equations in Eqs. (1) and (2) in a manner analogous to the time averaging in the RANS approach, one achieves the filtered equations, Eqs. (4) and (5), describing the behavior of the large scales,

$$\frac{1}{\beta^2}\frac{\partial \overline{p}_g}{\partial \tau}+\frac{\partial \rho \overline{u}_i}{\partial x_i}=0, \tag{4}$$

$$\frac{\partial \rho \overline{u}_i}{\partial \tau}+\frac{\partial \rho \overline{u}_i}{\partial t}+\frac{\partial \rho \overline{u}_i \overline{u}_j}{\partial x_j}+\frac{\partial \overline{p}_g}{\partial x_i}=\frac{\partial}{\partial x_j}\left[\rho(\nu+\nu_{\mathrm{sgs}})\left(\frac{\partial \overline{u}_i}{\partial x_j}+\frac{\partial \overline{u}_j}{\partial x_i}\right)\right]+B_i, \tag{5}$$

where ν_{sgs} is the subgrid-scale viscosity introduced due to the nonlinearity of the convective term. ν_{sgs} accounts for the effect of the small unresolved scales on the large resolved scales. The overbars indicate the spatial filtering which in the present finite volume approach is implicitly represented through the numerical discretization.

2.3 Subgrid-Scale Modeling. In the few large eddy simulations of turbomachinary flows which have appeared in literature, [16–18], the Smagorinsky model has been employed. In the present work different eddy viscosity SGS models have been implemented in FINE/Turbo, [21], and plane and rotating channel flow simulations have revealed a superiority of the localized dynamic Smagorinsky model of Piomelli and Liu [9], which has therefore been employed. The SGS viscosity ν_{sgs} is given by

$$\nu_{\mathrm{sgs}}=C\Delta^2|\overline{S}_{ij}|, \tag{6}$$

where C is a model parameter, Δ a filter length related to the local cell volume $\Delta=V^{1/3}$, and $\overline{S}_{ij}$ is the strain rate tensor based on the filtered velocities. The advantage of dynamic models is the dynamic computation of the model parameter C which need therefore not be specified a priori. In the present localized dynamic Smagorinsky model, [9], the model parameter C is computed from

$$C = -\frac{(L_{ij} - 2\widehat{C^*\beta_{ij}})\alpha_{ij}}{2\alpha_{ij}\alpha_{ij}} \tag{7}$$

where $L_{ij} = \widehat{\overline{u_i}\overline{u_j}} - \hat{\bar{u}}_i\hat{\bar{u}}_j$, $\beta_{ij} = \Delta^2|\overline{S}_{ij}|\overline{S}_{ij}$ and $\alpha_{ij} = \hat{\Delta}^2|\hat{\bar{S}}_{ij}|\hat{\bar{S}}_{ij}$. C^* is a known estimate of C found from a first-order extrapolation of C from previous time-steps and I indicates spatially double filtering over a volume of the size $\hat{\Delta} = 2\Delta$. The SGS model is referred to as "localized" as it does not require averaging of the model parameter C in directions of homogeneity.

From Eq. (7) it is seen that C and consequently also ν_{sgs} can become negative. This is interpreted as an ability to predict backscatter. For reasons of stability the SGS viscosity has, however, in the present simulations been constrained to be non-negative. Further, an upper constraint limiting the model parameter to be less than 1.0 has shown necessary. With these simple constraints the model remains stable even at high Reynolds numbers.

3 Impeller Model

3.1 Pump Impeller. The impeller under investigation is a shrouded, low specific-speed pump impeller representing the rotating part of an industrial multistage pump as shown in Fig. 1, [28]. This pump type is typically applied for water distribution and pressure boosting in industry and agriculture.

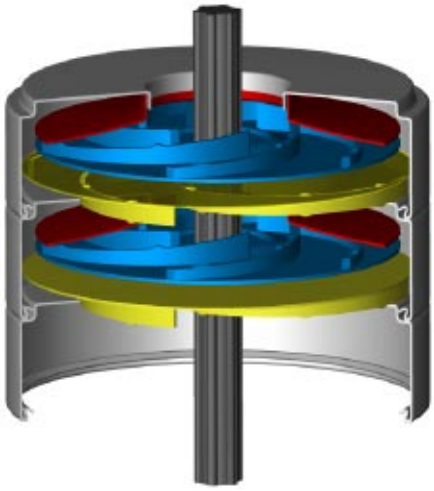

Fig. 1 Two stages of an industrial multistage pump with the shrouded centrifugal pump impeller under study, [28]

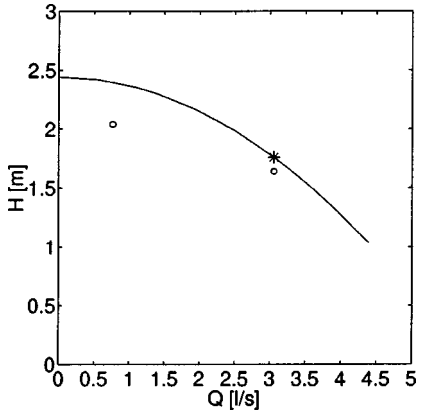

Fig. 2 Performance curve for a single stage of the multistage pump under investigation. The pump design point is marked by *, and ○ shows the static pressure rise predicted in the LES simulations.

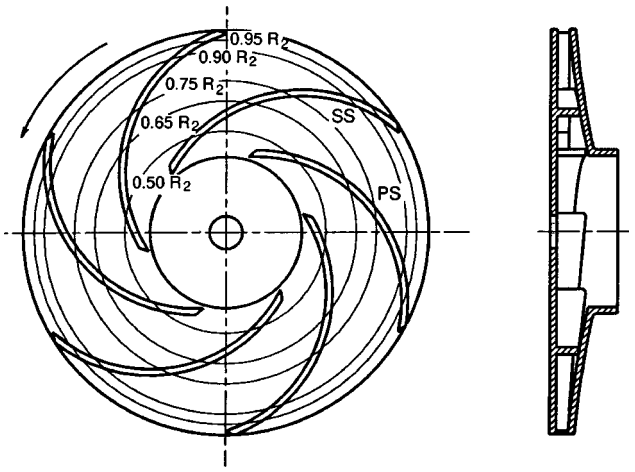

Fig. 3 Blade-to-blade (left) and meridional (right) view of the impeller under investigation, [28]. The circles indicate radii of comparison with experimental data. PS and SS refers to the blade pressure side and suction side, respectively.

The pump is designed to operate at a flow rate of $Q_d = 3.06$ l/s and provides at design load a pressure rise in a single stage equivalent to a head of $H_d = 1.75$ m. Figure 2 shows the performance curve for a single stage. Simulations at design load $Q = Q_d$ and at severe off-design load $Q = 0.25Q_d$ are performed. The predicted static pressure rise over the impeller is also shown in Fig. 2 and illustrates that 85–95% of the total pressure rise develops in the impeller and only a smaller part of the pressure rise is due to a transformation of dynamic to static pressure in the stationary parts. This corresponds to what is normally observed.

The geometry of the impeller under investigation is seen in Fig. 3. The impeller has an outer diameter of 190 mm and six simple curvature backswept blades with blunt leading and trailing edges. The Reynolds number typically used for pumps is based on the outer dimensions of the impeller, $\mathrm{Re} = U_2 D_2/\nu$, and is for the impeller under study of the order $\mathrm{Re} = 1.4 \times 10^6$ and thus very large in the context of LES. More relevant, however, when investigating the local flow behavior, is to base the Reynolds number on the local radial velocity and the blade height, $\mathrm{Re} = W_r b_1/\nu$. In this case, the Reynolds number is only $\mathrm{Re} \approx 1.5 \times 10^4$ at design load. The main geometrical data of the impeller and the operating conditions are summarized in Table 1.

3.2 Numerical Model. When modeling the impeller numerically, ideally all six impeller passages should be included in order to simulate the true flow field and detect any asymmetry of the flow. However, most numerical simulations of the flow field in turbomachines take advantage of the geometrical symmetry of the impeller and simulates one impeller passage only, e.g., [29–31]. The experimental work, described in Part I of this paper, [24], has at quarter-load revealed a pronounced correlation between every second of the six impeller passages. Modeling only one impeller passage would not allow to predict this phenomenon and consequently provide an inaccurate flow field. However, the experiments justifies modeling only two of the six passages, which still provides a significant reduction of the computation domain, which is shown in Fig. 4.

Keeping the computational effort at a realistic level compared to the available computer power, a mesh of totally 385,000 cells with roughly 150,000 cells in each impeller passage has been utilized. The grid stretching factor has been chosen to allow the first cell point to be located 1–5 μm off the surface corresponding to local y^+ values less than 5.0 in average. The main characteristics of the mesh are listed in Table 2 and a cross-sectional view is

Table 1 Impeller geometry and operating conditions

Geometry				
Inlet diameter	D_1	71.0		[mm]
Outlet diameter	D_2	190.0		[mm]
Inlet height	b_1	13.8		[mm]
Outlet height	b_2	5.8		[mm]
Number of blades	Z	6		[-]
Blade thickness	t	3.0		[mm]
Inlet angle	β_1	19.7		[deg.]
Outlet angle	β_2	18.4		[deg.]
Blade curvature radius	R_b	70.0		[mm]
Specific speed	N_s	26.3		[eng.]
Flow conditions		I	II	
Q/Q_d		1.0	0.25	
Flow rate	Q	3.06	0.76	[l/s]
Head	H	1.75	2.4	[m]
Rotational speed	n	725	725	[rpm]
Flow rate coefficient	Φ	0.123	0.031	[-]
Head coefficient	Ψ	0.33	0.45	[-]
Reynolds number	Re	1.4×10^6	1.4×10^6	[-]

Table 2 Characteristics of the mesh structure, boundary conditions, and numerical setup of the simulations

Mesh structure	
Total number of cells	385.000
Cells in inlet section	34.000
Cells in impeller	304.000
Cells in outlet section	47.000
Cell height along blades	$<1.0\mu$m
Cell height along hub & shroud	$<5.0\mu$m
Boundary Conditions	
Inflow	Turbulent velocity fields
Outflow	Uniform pressure
Wall	No-slip
Circumferential	Periodicity
Numerical Setup	
Number of pseudo time steps	100
Time step	5.0×10^{-3}s
Time steps per revolution	160
Development period	2000 time steps
Averaging period	2000 time steps
CPU time per time step	14 mins.
Total computational time	940 CPU hours

seen in Fig. 5. Kato et al. [18] utilized a total of 850,000 mesh points for a LES of an inlet section, all passages in a mixed flow impeller and a double-volute casing, and Jang et al. [19] utilized 1.3 million cells for simulating a full propeller fan which gave $y^+<2.5$ along the walls. In this context the current mesh appears to be fairly fine. However, the sensitive subject of mesh independence has not been examined.

Boundary Conditions. As opposed to RANS simulations, where the specification of a mean profile and a turbulent intensity is normally sufficient, specifying turbulent inflow conditions in the context of LES is a general matter of concern. Due to difficulties of setting up realistic turbulent inflow conditions in industrial applications, often only the mean profile is imposed, hoping that turbulence will develop due to interaction with the geometry. This approach has been utilized by both Song et al. [16] and Kato et al. [18] for large eddy simulations of the flow in a Francis turbine and a mixed flow pump, respectively.

As LES resolves the turbulent structures it is important to introduce turbulence associated with coherent structures through the inflow boundary. A straightforward approach is to superimpose random fluctuations on a mean velocity profile as done by Davidson and Nielsen [32]. While turbulence fluctuations are easily generated with a random method, the correlation between individual velocity components and the correlation in time is zero and the inflow velocity profiles are therefore not associated with organized turbulence motion, neither in space or time. In this context the development of turbulent structures requires an excessively long inlet section. Lund et al. [33] provides an overview of existing inflow generation techniques.

Balaras and Piomelli [34] concluded that the most realistic type of inflow condition available is extracting inflow velocities from an auxiliary simulation. This approach has been utilized. Simulation of a fully developed turbulent channel flow at Re=2900, [21], has allowed for the creation of a database consisting of a time series of 4000 spatially and temporally correlated velocity fields. At each time-step the velocity field in a plane is extracted from the database and applied as inflow conditions to the impeller. Due to geometrical differences the profiles have been mapped from a rectangular to a annular cross section and as the Reynolds numbers are significantly different, the velocities have been scaled according to the mass flow requirements. Naturally, these manipulations introduce some deformations of the turbulent structures, however, this approach is still believed to be far superior to the random fluctuation method.

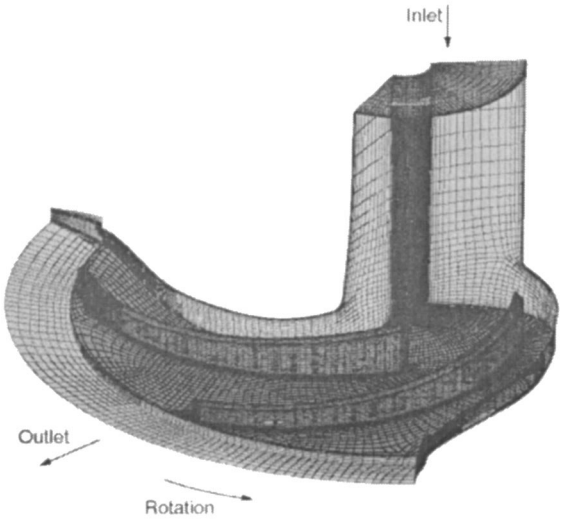

Fig. 4 Computational domain of the impeller. For reasons of visualization the shroud is not shown.

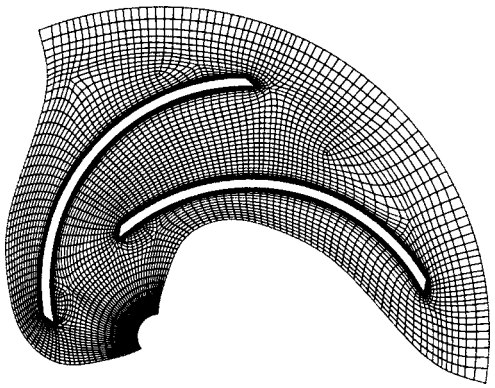

Fig. 5 Cross-sectional view of mesh structure in the impeller mid-height

The other boundary conditions are similar to what is imposed in standard RANS simulations; At the impeller outlet a uniform pressure is prescribed, thereby not imposing any restrictions on the velocities. Figure 4 illustrates how the axial height of the section after the impeller blade has been decreased in order to keep the outlet area constant. This prevents problems with flow reversal over the outlet boundary. A no-slip condition is utilized on the solid walls which are rotating with the same angular velocity as the impeller. Periodic boundaries are utilized in the circumferential direction and will be seen to ensure a smooth connection in this direction. An overview of the boundary conditions is given in Table 2.

Numerical Setup. During each physical time-step, t, the system of preconditioned equations, Eqs. (4) and (5), is solved by advancing in pseudo-time, τ. The stability of the advancement in pseudo-time is determined by a fourth-order Runge-Kutta advancement where the maximum stable CFL_τ number has shown to be 3.

The convergence rate necessary for each physical time-step to ensure a converged solution has been investigated for a turbulent channel flow, [21]. This investigation has revealed that a convergence of 0.75 orders within each physical time-step is sufficient for the continuity equation. From Fig. 6 it is seen that utilizing 100 pseudo time-steps within each physical time-step satisfies this requirement with a convergence rate from $10^{-4.2}$ to $10^{-5.0}$. This gives rise to the characteristic sawtooth pattern. Within 100 pseudo time-steps the momentum equation converges approximately one order.

In order to resolve the real temporal variations of the flow the time-step has been adjusted to $t=5.0\times10^{-3}$ s which ensures an average CFL_t number based on physical time less than 1.0. This time-step is equivalent to 160 time-steps per impeller revolution.

As initial conditions, a steady-state Baldwin-Lomax solution at 50 percent of design load has been used. With the turbulent inflow conditions described above, the flow field at both design load and quarter-load have developed for 2000 time-steps, equivalent to 12 revolutions. Time-averaged quantities have in both simulations been computed during 2000 additional time-steps. No significant differences in the mean flow profiles and the distribution of turbulent kinetic energy have been observed between averages based on 1000 and 2000 time-steps. As the flow field is statistically stable the averaging period of 2000 time-steps has therefore been found sufficient to stabilize these lower-order statistics.

The simulations have been performed on a single Alpha EV6 500 MHz processor of a COMPAQ AlphaServer DS20 situated at the Danish Computer Center, UNI-C, located at the Technical University of Denmark. The required CPU time has been about 14 minutes per physical time-step resulting in a total CPU time of about 960 hours for one operating condition. Table 2 summarizes the numerical setup.

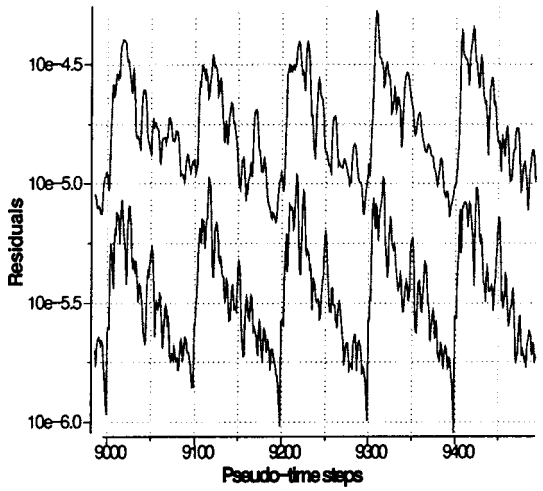

Fig. 6 Convergence history in dual-time-stepping procedure for the continuity equation (upper curve) and z-momentum equation (lower curve) at design load

4 Results and Discussion

The LES results of the flow field in the impeller are analyzed in the following. To ease the discussion it has shown advantageous to distinguish between the two impeller passages modeled, which are denoted passage *A* and *B*. For reasons of presentation the results have been replicated and rotated 120 deg and 240 deg, thereby covering the entire impeller.

4.1 Flow Field at Design Load. Figure 7 shows the time-averaged relative vector field at design load. The rotation sense is counterclockwise. It is seen that the flow follows the curvature of the impeller blades in the predominant part of the impeller passage and no significant separation occurs. In agreement with potential theory, (see, e.g., Stepanoff [35]) the flow in the inlet section is displaced towards the suction side. Along the blade suction side both passages, *A* and *B*, experience the development of a low-velocity zone at $r/R_2=0.6$. This could be interpreted as being the development phase of a jet-wake structure as reported by other investigators, [36,37]. However, at the outer radius the low-velocity zone is suppressed and a nearly uniform velocity profile across the impeller outlet has developed.

Figure 8 shows the radial velocity in hub-to-shroud sections in

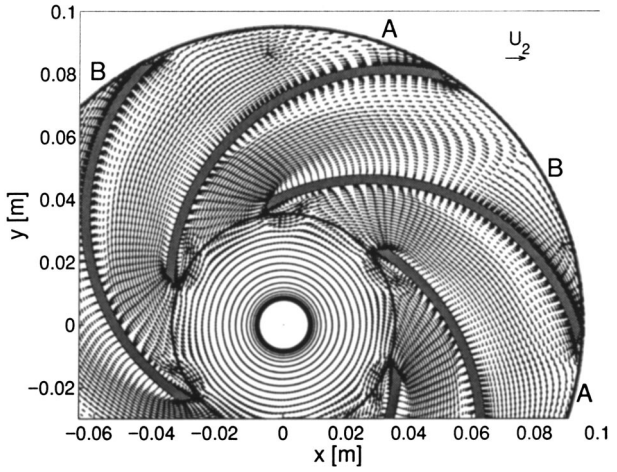

Fig. 7 Time-averaged velocity field $\langle \tilde{W} \rangle$ in the impeller mid-height, $z/b_2=0.5$. ($Q/Q_d=1.0$)

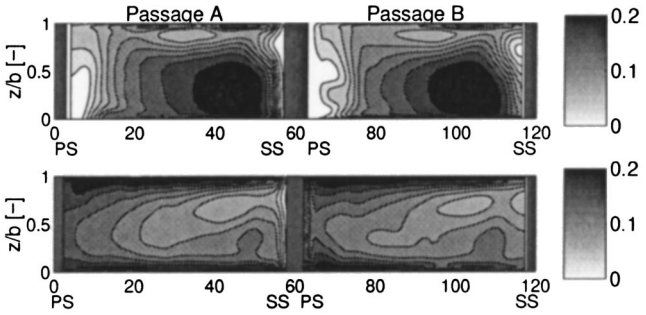

Fig. 8 Time-averaged radial velocity, $\langle W_r \rangle / U_2$ at positions of constant radius. $r/R_2=0.5$ (top) and $r/R_2=0.95$ (bottom). ($Q/Q_d=1.0$).

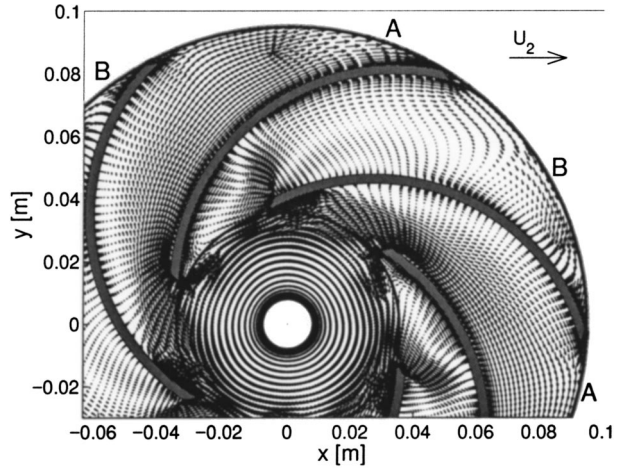

Fig. 9 Time-averaged velocity field $\langle \tilde{W} \rangle$ in the impeller mid-height, $z/b_2 = 0.5$. ($Q/Q_d = 0.25$)

the two passages. In the inlet section, $r/R_2 = 0.5$, the effect of axial-to-radial curvature is evident. High momentum fluid is concentrated in the hub-suction side corner. At $r/R_2 = 0.95$, the blade pressure surface is not covered by the suction side of the adjacent blade. As indicated in Fig. 8 and known from the literature, [38,39], this causes an increase in the velocity along the pressure side and a decrease on the suction side, resulting in an unloading of the blade.

The flow in the two adjacent passages is found to be similar, revealing no significant circumferential variations at design load conditions.

4.2 Flow Field at Quarter-Load. The time-averaged vector field at quarter-load is seen in Fig. 9 and shows a substantial departure from the well behaved nonseparated flow observed at design load.

In passage *A* the low-velocity zone along the suction side observed at design load has turned into a distinct zone of recirculation. A close analysis of the flow approaching the impeller passage reveals that the flow initially follows the curvature of the impeller blade along both suction and pressure side in passage *A*. The recirculation is thus seen as a consequence of an alteration in the Rossby number, which determines the relationship between the centrifugal force due to curvature of the blade-to-blade section and the Coriolis force, $\mathrm{Ro} = |\mathbf{W}|/\omega R_b$. $R_b = 70$ mm is the constant curvature radius of the blades. The highest Rossby number occurs at the inlet and is Ro≈0.4 but reduces rapidly to Ro≈0.2 in the dominant part of the impeller passage. At design load Ro≈0.6 in the dominant part of the passage. This indicates that the flow field

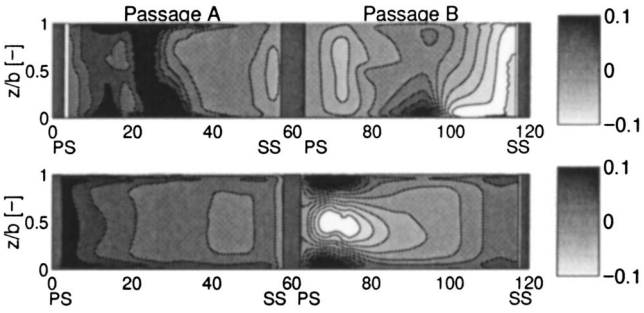

Fig. 10 Time-averaged radial velocity, $\langle W_r \rangle / U_2$ at positions of constant radius. $r/R_2 = 0.5$ (top) and $r/R_2 = 0.95$ (bottom). ($Q/Q_d = 0.25$).

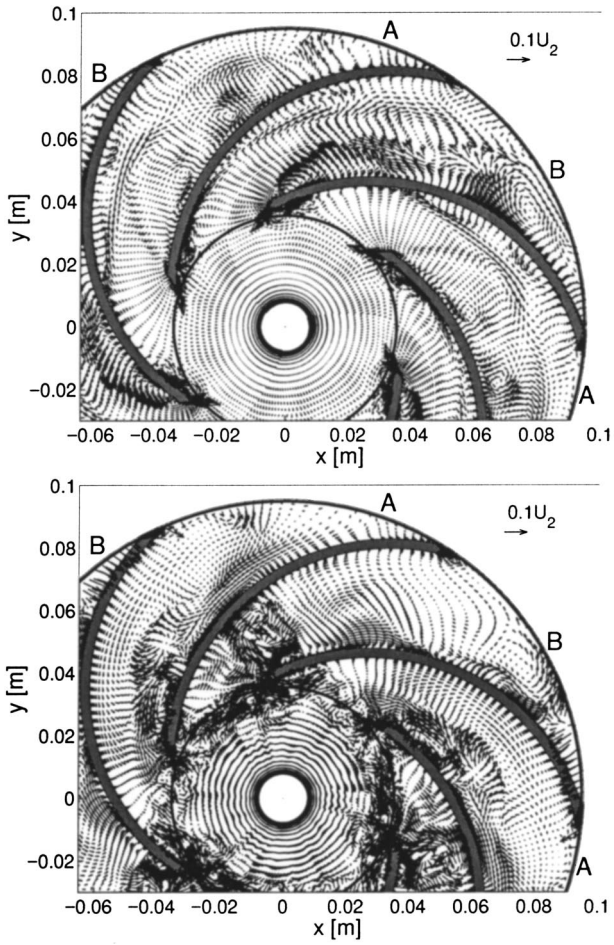

Fig. 11 Sample instantaneous velocity derivation from the time-averaged velocity, $\tilde{W} - \langle \tilde{W} \rangle$, in the impeller mid-height, $z/b_2 = 0.5$. $Q/Q_d = 1.0$ (top) and $Q/Q_d = 0.25$ (bottom).

in the blade-to-blade plane is mostly dominated by rotational effects. This was also observed in the impeller investigated by Abramian and Howard [40].

It is apparent from Fig. 9 that a significantly different flow field is present in passage *B*. This passage is largely dominated by a flow field associated with stall. A significant recirculation zone along 30 percent of the blade suction side is observed which effectively blocks the entrance to passage *B* and apparently unblocks passage *A*. In contrast to observations in literature, [41,42], the stall is stationary and nonrotating and not initiated due to interaction with stationary components. Due to the stall in passage *B* and the subsequent blocking, a minimal throughflow exists. Hence, Fig. 9 illustrates the formation of a relative eddy covering the remaining part of the passage; high positive values of the relative velocity along the blade suction side and flow reversal along the dominant part of the blade pressure side.

The distortion of the flow field becomes further evident from the velocities in the hub-to-shroud sections shown in Fig. 10.

In the entry section of the passages at $r/R_2 = 0.5$ the reversed flow along the suction side of passage *A* and both pressure and suction side in passage *B* is found to fill the entire passage height. In passage *B* flow reversal near the exit at $r/R_2 = 0.95$, due to the relative eddy, is seen to cover more than 50 percent of the passage height along the pressure side and it is apparent that the throughflow in passage *B* is minimal.

4.3 Turbulence Fluctuations. Figure 11 shows instantaneous samples of the deviation from the time-averaged velocity

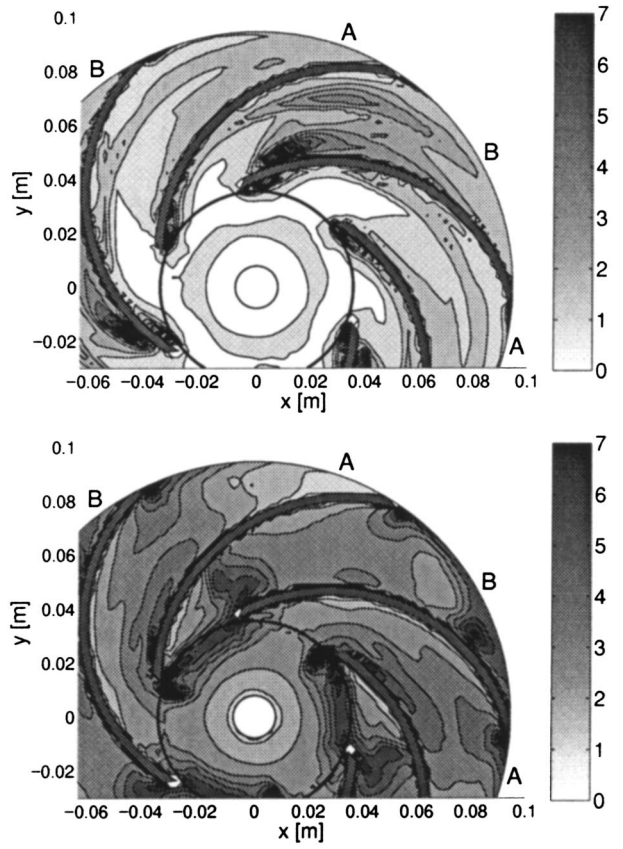

Fig. 12 Turbulence intensity Tu=100$\sqrt{k}/U_2$ in the impeller mid-height at $z/b_2=0.5$. $Q/Q_d=1.0$ (top) and $Q/Q_d=0.25$ (bottom).

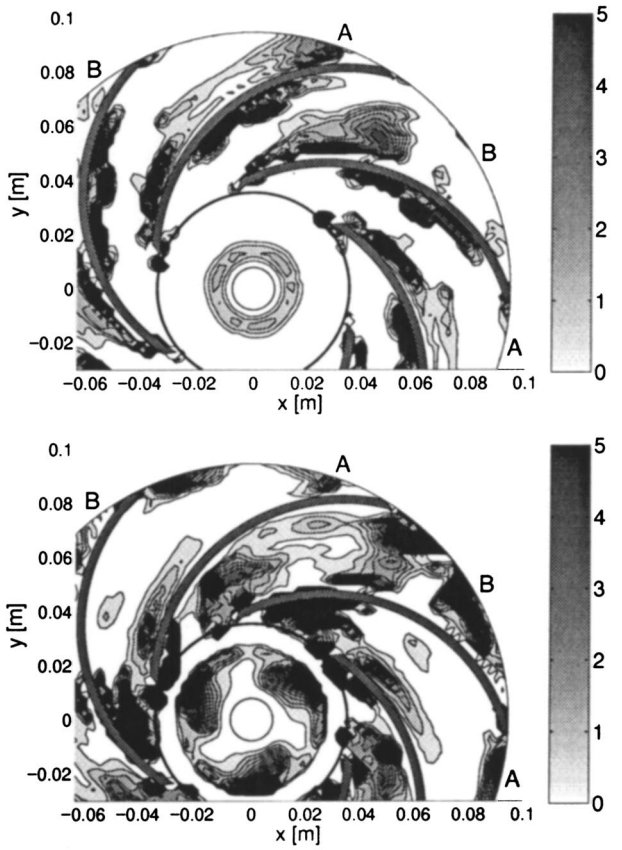

Fig. 13 Time-averaged SGS viscosity ν_{sgs}/ν in the impeller mid-height at $z/b_2=0.5$. $Q/Q_d=1.0$ (top) and $Q/Q_d=0.25$ (bottom).

profiles discussed above. The deviations give evidence of a highly fluctuating flow field superimposed with eddy structures. Due to the relatively coarse mesh only the larger eddy structures of the true turbulent flow are captured. It is seen that the level of the fluctuations increase as the flow rate decreases and the intensity associated with the stall phenomenon in passage *B* is apparent.

A qualitative measure of the velocity fluctuations is the contours of the turbulence intensity Tu=100$\sqrt{k}/U_2$ seen in Fig. 12. A significant portion of the flow at design load is characterized by turbulence levels lower than 3%, indicating a relatively stable flow. As noted by Ubaldi [39] from investigations of an unshrouded impeller, this low level indicates the presence of a potential flow core at design load. Decreasing the flow rate causes an increase in the turbulent intensity. As far as magnitude is concerned the intensity at quarter-load is almost twice the magnitude at design load with an average of around 5%. The stall phenomenon in passage *B* is observed to be associated with high turbulence activity. Also the strong reversed flow from the relative eddy in the outlet region of passage *B* gives rise to significant turbulence intensity of more than 10%.

4.4 Subgrid-Scales (SGS) Model Behavior. The time-averaged SGS viscosity is shown in Fig. 13. A qualitatively different distribution of the viscosity is revealed compared to the smooth distribution generally achieved in RANS simulations and, with an average of ν_{sgs}/ν close to 1.0 at design load and 1.2 at quarter-load, the level is significantly lower. This corresponds to that LES models only the smallest turbulent scales whereas RANS models the entire turbulent spectrum.

The main advantages of the dynamic localized Smagorinsky model [9] is an implicit and dynamic computation of the model parameter *C*, circumventing a priori specification. Figure 14

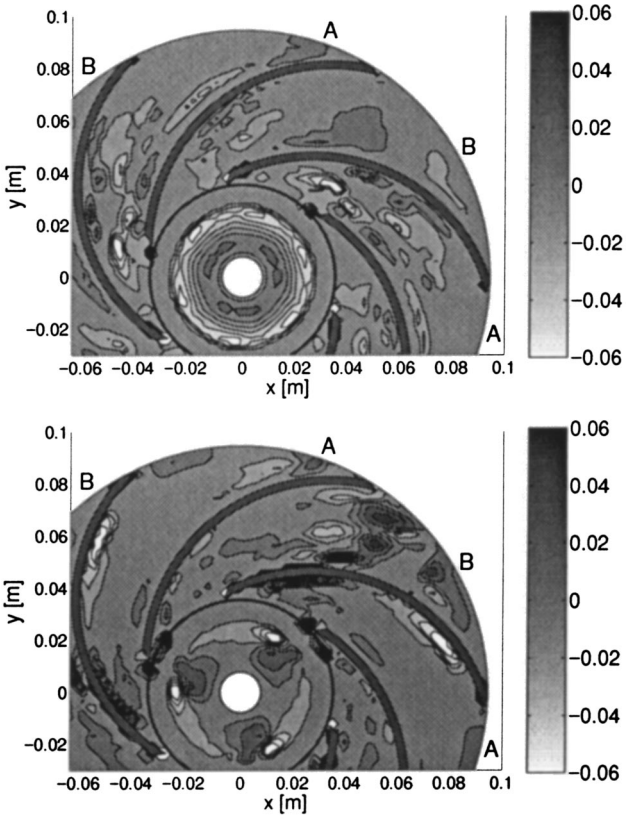

Fig. 14 Time-averaged model parameter *C* in the impeller mid-height at $z/b_2=0.5$. $Q/Q_d=1.0$ (top) and $Q/Q_d=0.25$ (bottom).

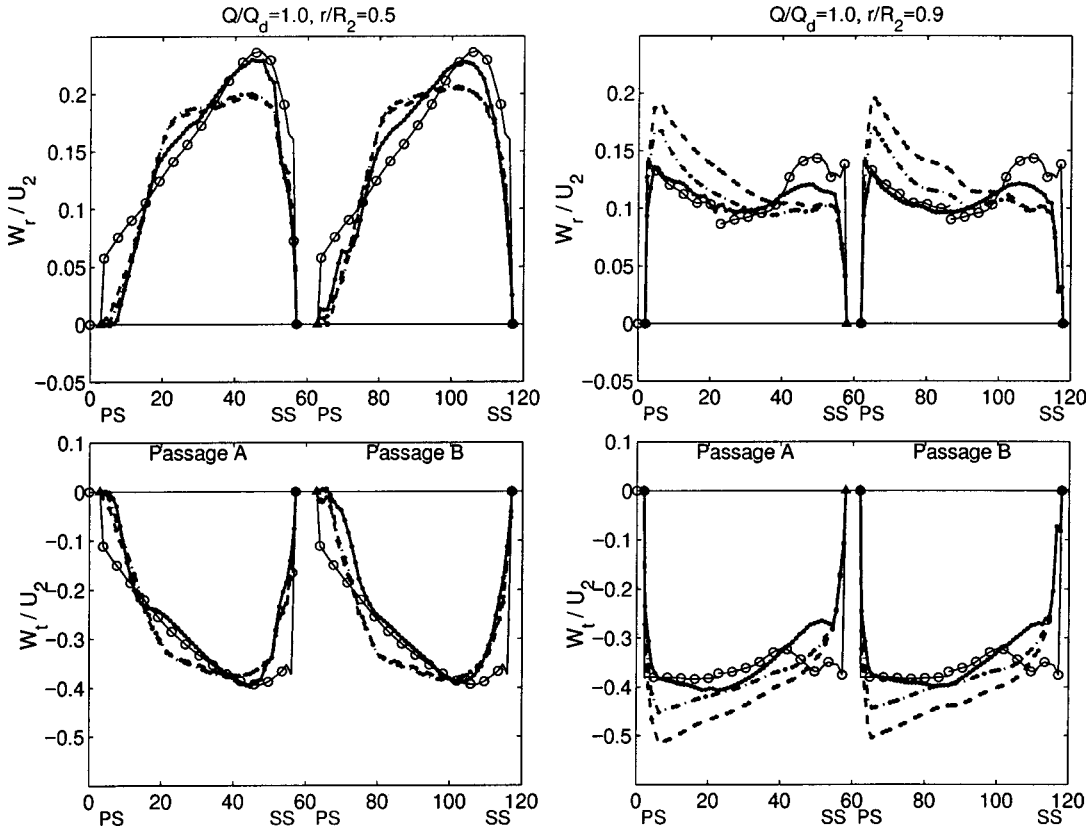

Fig. 15 Radial (top) and tangential (bottom) velocities in the impeller mid-height, $z/b_2=0.5$, at radial positions of $r/R_2=0.5$ (left) and $r/R_2=0.9$ (right). ——LES, – – – Baldwin-Lomax, —·—·—·— Chien k-ε and ○ PIV, [24]. For PIV only every third data point is shown in order to avoid crowding. ($Q/Q_d=1.0$.)

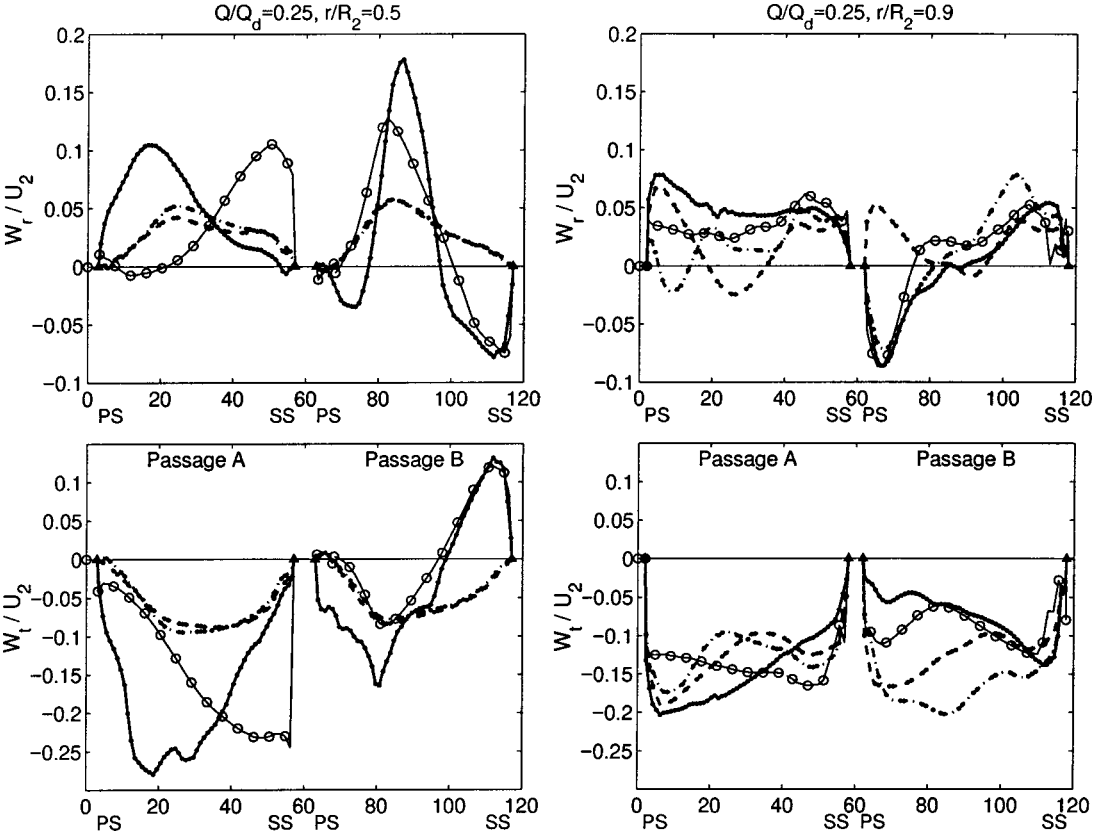

Fig. 16 Radial (top) and tangential (bottom) velocities in the impeller mid-height, $z/b_2=0.5$, at radial positions of $r/R_2=0.5$ (left) and $r/R_2=0.9$ (right). ——LES, – – – Baldwin-Lomax, —·—·—·— Chien k-ε and ○ PIV, [24]. For PIV only every third data point is shown in order to avoid crowding. ($Q/Q_d=0.25$).

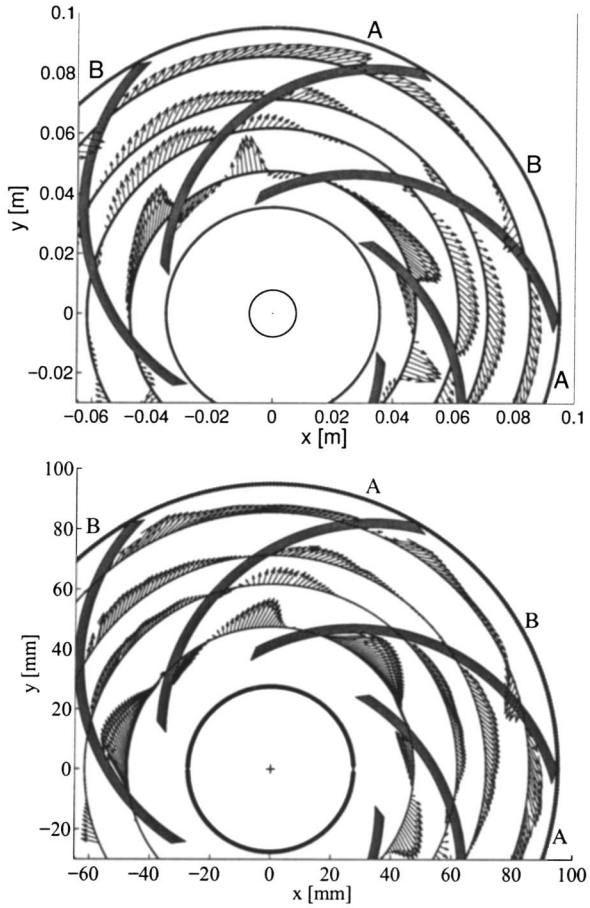

Fig. 17 Velocity field $\langle \tilde{W} \rangle$ in the impeller mid-height, $z/b_2 = 0.5$, given at radial positions of $r/R_2 = \{0.50, 0.65, 0.75, 0.90\}$. Computed using LES (top) and measured using PIV (bottom). ($Q/Q_d = 0.25$).

shows the time-averaged model parameter. An expected correlation between the model parameter C and the SGS viscosity in Fig. 13 is revealed. Significant areas of negative C are present, illustrating that the SGS model would predict backscatter had the SGS viscosity not been constrained to be non-negative. From the range of the model parameter it is evident that the constraint, specifying $|C| < 1$, is not dominating. Generally, the model parameter is seen to vary strongly in the domain with averages equivalent to Smagorinsky constants of $C_s = 0.06$ and $C_s = 0.09$ at design load and quarter-load, respectively. A difference of 33%, even on the averaged values, emphasize the difficulty of specifying the model parameter a priori. This study also reveals that the model parameter, if computed dynamically, will exhibit a very complex behavior.

4.5 Comparison with Reynolds-Averaged Navier-Stokes (RANS) and Experiments. In order to evaluate the achievements of LES relative to standard RANS turbulence modeling the LES results are compared to steady-state Chien k-ε and Baldwin-Lomax simulations, all performed on the same mesh. The basis of this comparison is ensemble averaged PIV measurements conducted by Pedersen et al. and presented in Part I of this paper, [24]. As in LES, PIV provides instantaneous whole-field information of the flow and can therefore be seen as the experimental counterpart of LES.

Flow Field at Design Load. The radial and tangential velocities at design load are compared in Fig. 15 which shows the velocities at radial positions of $r/R_2 = 0.5$ and $r/R_2 = 0.9$. The general impression is a satisfactory agreement between the numerical and experimental data for all three simulations, though a detailed analysis reveals a slightly more accurate prediction of the details of the flow behavior in the LES simulation.

Due to the dominant effect of curvature in the inlet section the velocity profiles are skewed towards the suction side at $r/R_2 = 0.5$, see Fig. 15 (left), with a peak located around 80% of the passage span for both the radial and tangential velocity. This trend is seen to be predicted very accurately in LES whereas the two RANS simulations predict flatter profiles.

Towards the outlet, $r/R_2 = 0.9$, see Fig. 15 (right), the unloading of the impeller blade is initiated. This results in increased velocities along the blade pressure side. LES predicts, in agreement with measurements, radial velocities with equal peaks at pressure and suction side and the lowest value near mid span. Experimentally, nearly uniform tangential velocities are detected at this radius. Except from some discrepencies at the suction side the LES simulation confirms this also. Both RANS simulations predict a stronger influence of the unloading and, thus, almost a linear decrease from pressure to suction side in both radial and tangential velocities.

Flow Field at Quarter-Load. At quarter-load the above discussion has revealed that LES predicts a flow field that differs substantially in the two passages. From Fig. 16 this is seen to be confirmed by the PIV measurements.

In the inlet section, $r/R_2 = 0.5$, see Fig. 16 (left), the PIV measurements reveal velocity profiles in passage *A* skewed towards the suction side. Contrary to this, LES predicts profiles displaced to the pressure side. This remarkable difference is mainly attributed to the influence of prerotation. Especially at partial load the rotation of the impeller generates upstream vorticity which, combined with the effect of leakage flow, cause a substantial swirl in the inlet velocity profile. In the experiments it has not been possible to meassure the extent of the inlet swirl. It has therefore been disregarded in the simulations, but is here seen to have a significant influence on the inflow.

In passage *B* the stall phenomenon is evident in the velocity profiles obtained by LES and PIV showing substantial variations across the passage span at $r/R_2 = 0.5$. The radial and tangential velocities illustrate reversed flow along the suction side and LES and PIV are seen to agree on the location and the size of the peak. In the mid-passage positive radial velocities feeding the recirculation are present. The peak in the radial velocity predicted by LES is slightly displaced towards the suction side giving room for a small counterrotating eddy at the pressure side. This eddy is, however, not observed experimentally. In contrast to these findings the two RANS simulations predict identical and nonseparated flows in the both passages and do not capture the complex stall phenomena.

At $r/R_2 = 0.9$, see Fig. 16 (right), both the LES and PIV radial velocity profiles are observed to become relatively flat in passage *A*. In passage *B* the LES and PIV radial velocities give evidence of the relative eddy with positive velocities along the suction side and reversed flow along the pressure side. The Chien k-ε model is observed to predict the variation in the radial velocity in passage *B*, however, flow reversal is predicted also in passage *A* instead of a uniform profile. The Baldwin-Lomax model is seen to predict substantial deviations from measurements in both passages. The variations between the three simulations and the PIV data are relatively larger when analysing the tangential velocities, though LES and PIV agree on the velocity variation in the majority of passage *B*.

The quantitative comparison given above is in Fig. 17 supplemented by a comparison of the vector field at radial positions of $r/R_2 = \{0.50, 0.65, 0.75, 0.90\}$, thereby giving an impression of the entire flow field obtained by LES and PIV. The comparison of LES and PIV illustrates that a flow field which is significantly different in the two passages is present. In passage *A* a relatively well-behaved nonseparated flow is observed in both LES and PIV. The discrepancies are due to inlet prerotation in the experiments,

as discussed previously. In passage *B* the stall in the inlet section is evident and both LES and PIV shows substantial velocity variations across the passage span at $r=0.5$. Also the relative eddy developing in the remaining part of passage *B* is clearly present in both LES and PIV.

In summary, LES is at quarter load seen to predict deviations from measurements in the inlet section of passage *A* which are attributed to differences in the inlet conditions. In passage *B*, however, LES predicts the nonrotating stall in the inlet and relative eddy in the remaining part of the passage with a satisfactory accuracy. Though the Chien k-ε model do predict flow reversal along the pressure side for larger radii it is evident that neither the Chien k-ε nor the Baldwin-Lomax models capture the stall phenomenon in passage *B*.

5 Conclusion

The flow field in a centrifugal pump impeller has been investigated at design load and quarter-load using LES.

At design load the large eddy simulation reveals a well-behaved flow dominated by curvature, causing a displacement of the flow towards the hub-to-suction side in the inlet section. The differences between the two impeller passages modelled are found to be negligible. Decreasing the flow rate to 25% of design load, significant differences are revealed between the two adjacent impeller passages. One passage is dominated by rotational effects causing high velocities along the blade pressure side. The other passage exhibits a highly separated flow field; in the entry section a significant stall is observed, blocking the entry and as the through-flow consequently is minimal, a relative eddy develops in the remaining part of the passage. Unlike stall phenomena previously reported in literature the stall is steady, nonrotating, and not initiated by interaction with stationary components.

The results from the LES simulations have been compared with steady-state RANS simulations based on the Chien k-ε and Baldwin-Lomax turbulence model and the numerical achievements have been evaluated through comparison with PIV measurements. The velocities predicted from LES compare favorably with the experimental data which confirms the presence of a nonrotating stall phenomena combined with a relative eddy. The two RANS simulations are, however, not able to predict this complex flow field.

It is thus found that using LES for analyzing the flow field in centrifugal pumps provides an improved insight into the basic fluid dynamic with a satisfactory accuracy compared to experiments. Particularly at partial load where the flow is highly separated the achievements of LES, as compared to Baldwin-Lomax and Chien k-ε models, are remarkable.

Overall the present LES approach, based on second-order accurate numerical methods combined with eddy viscosity SGS models, shows considerable promise in increasing the insight and accuracy obtained in the simulations of the flow in centrifugal pumps.

Acknowledgments

This work has been supported by the Danish Academy of Technical Sciences under the grant LESPUMP EF663.

Nomenclature

b = impeller height, m
k = turbulent kinetic energy, m^2/s^2
n = rotational speed, rpm
r = radius, m
z = height from hub, m
C = model parameter
C = absolute velocity, m/s
CFL = Courant Friedrichs Lewy number, $\mathrm{CFL}=W\Delta t/\Delta x$
D = impeller diameter, m
H = head, m
N_s = specific speed, $N_s=n\sqrt{Q}/H^{3/4}$, eng
Q = flow rate, l/s
R = radius, m
R_b = blade curvature radius, m
Re = Reynolds number, $\mathrm{Re}=U_2D_2/\nu$
Ro = Rossby number, $\mathrm{Ro}=|\mathbf{W}|\omega/R_b$
Tu = turbulent intensity, $\mathrm{Tu}=100\sqrt{k}/U_2$
U = circumferential velocity, m/s
W = relative speed, m/s
Φ = flow coefficient, $\Phi=Q/A_2U_2$
Ψ = head coefficient $\Psi=gH/U_2^2$

Subscripts

1 = inlet
2 = outlet
d = design load conditions
r = radial component
t = tangential component

Acronyms

PS = pressure side
SS = suction side

References

[1] Vreman, B., Geurts, B., and Kuerten, H., 1997, "Large-Eddy Simulation of the Turbulent Mixing Layer," J. Fluid Mech., **339**, pp. 357–390.
[2] Moser, R. D., and Moin, P., 1987, "The Effect of Curvature in Wall-Bounded Turbulent Flows," J. Fluid Mech., **175**, pp. 479–510.
[3] Wu, X., and Squires, K. D., 1998, "Numerical Investigation of the Turbulent Boundary Layer Over a Bump," J. Fluid Mech., **362**.
[4] Armenio, V., Piomelli, U., and Fiorotto, V., 1999, "Applications of a Largragian Mixed SGS Model in Generallized Coordinates," *Direct and Large-Eddy Simulation III*, Peter Voke, Neil D. Sandham, and Leonhard Kleiser, eds., Kluwer Academic Publishers, Dordrecht, The Netherlands, pp. 135–146.
[5] Moin, P., and Kim, J., 1982, "Numerical Investigation of Turbulent Channel Flow," J. Fluid Mech., **118**, pp. 341–377.
[6] Härtel, C., and Kleiser, L., 1998, "Analysis and modeling of subgrid-scale motions in near-wall turbulence," J. Fluid Mech., **356**, pp. 327–352.
[7] Lamballais, E., Metais, O., and Lesieur, M., 1998, "Spectral-Dynamic Models for Large-Eddy Simulation of Turbulent Rotating Channel Flow," Theor. Comput. Fluid Dyn., **12**, pp. 149–177.
[8] Germano, M., Piomelli, U., Moin, P., and Cabot, W. H., 1991, "A Dynamic Subgrid-Scale Eddy-Viscosity Model," Phys. Fluids A, **A3**(7), pp. 1760–1765.
[9] Piomelli, U., and Liu, J., 1995, "Large-Eddy Simulation of Rotating Channel Flow Using a Localized Dynamic Model," Phys. Fluids, **7**(4), pp. 839–848.
[10] Liu, S., Meneveau, Ch., and Katz, J., 1994, "On the Properties of Similarity Subgrid-Scale Models as Deduced From Measurements in a Turbulent Jet," J. Fluid Mech., **275**, pp. 83–119.
[11] Garnier, E., Mossi, M., Sagaut, P., Comte, P., and Deville, M., 1999, "On the Use of Shock-Capturing Schemes for Large-Eddy Simulation," J. Comput. Phys., **153**, pp. 273–311.
[12] Haworth, D. C., and Jansen, K., 1996, "LES on Unstructured Deforming Meshes: Towards Reciprocating IC Engine," *CTR, Proceedings of the Summer Program*, Center for Turbulence Reserach, Stanford University, Stanford, CA, pp. 329–346.
[13] Jansen, K. E., 1997, "Large-Eddy Simulation Using Unstructured Grids" *Advances in DNS/LES. Proceedings of the First AFOSR International Conference on DNS/LES*, C. Liu, Z. Liu, and L. Sakell, eds., Greyden Press, Columbus, OH, pp. 117–128.
[14] Eggels, J. G. M., 1996, "Direct and Large Eddy Simulation of Turbulent Fluid Flow Using the Lattice-Boltzmann Scheme," Int. J. Heat Fluid Flow, **17**, pp. 307–323.
[15] Revstedt, J., Fuch, L., and Trägård, H., 1998, "Large Eddy Simulations of the Turbulent Flow in a Stirred Reactor," Chem. Eng. Sci., **53**(24), pp. 4041–4053.
[16] Song, Ch., and Chen, X., 1996, "Simulation of Flow Through Francis Turbine by LES Method," *XVIII IAHR Symposium on Hydraulic Machinary and Cavitation*, E. Cabrera, V. Espert, and F. Martinez, eds., Kluwer, Dordrecht, The Netherlands, **1**, pp. 267–276.
[17] Chen, X., Song, Ch. C. S., Tani, K., Shinmei, K., Niikura, K., and Sato, J., 1998, "Comprehensive Modeling of Francis Turbine System by Large Eddy Simulation Approach," *Hydraulic Machinary and Cavitation*, H. Brekke, C. G. Duan, R. K. Fisher, R. Schilling, S. K. Tan, and S. H. Winnoto, eds., World Scientific, Singapore, **1**, pp. 236–244.
[18] Kato, C., Shimizu, H., and Okamura, T., 1999, "Large Eddy Simulation of Unsteady Flow in a Mixed-Flow Pump," *3rd ASME/JSME Joint Fluids Engeneering Conference*, ASME, New York, pp. 1–8.
[19] Jang, C. M., Furukawa, M., and Inoue, M., 2001, "Analysis of Vortical Flow Field in a Propeller Fan by LDV Measurements and LES—Part I: Three-

Dimensional Vortical Flow Structures,'' ASME J. Fluids Eng., **123**, pp. 748–754.
[20] Byskov, R. K., 2000, ''Large Eddy Simulation of Flow Structures in a Centrifugal Pump Impeller. Part 1: Theory and Simulation of Pump Flow,'' Ph.D. thesis, Aalborg University, Institute of Energy Technology, Aalborg, Denmark.
[21] Byskov, R. K., 2000, ''Large Eddy Simulation of Flow Structures in a Centrifugal Pump Impeller. Part 2: Code Validation,'' Ph.D. thesis, Aalborg University, Institute of Energy Technology, Aalborg, Denmark.
[22] Baldwin, B. S., and Lomax, H., 1978, ''Thin Layer Approximation and Algebraic Model of Separated Turbulent Flow,'' *AIAA Paper No. 78–257*.
[23] Chien, Y. K., 1982, ''Predictions of Channel and Boundary-Layer Flows With a Low-Reynolds Number Turbulence Model,'' AIAA J., **20**(1), pp. 33–38.
[24] Pedersen, N., Larsen, P. S., and Jacobsen, C. B., 2003, ''Flow in a Centrifugal Pump Impeller at Design and Off-Design Conditions—Part I: Particle Image Velocity (PIV) and Laser Doppler Velocimetry (LDV) Measurements,'' ASME J. Fluids Eng., **125**, pp. 61–72.
[25] Lacor, C., Alavilli, P., Hirsch, Ch., Eliasson, P., Lindblad, I., and Rizzi, A., 1992, ''Hypersonic Navier-Stokes Computations About Complex Configurations,'' *Proceedings from First European CFD Conference*, Ch. Hirsch, ed., Elsevier, Amsterdam, **2**, pp. 1089–1096.
[26] Jameson, A., Schmit, W., and Turkel, E., 1981, ''Numerical Simulation of the Euler Equations by Finite Volume Methods Using Runge-Kutta Time-Stepping Schemes,'' *AIAA Paper No. 81.1259*.
[27] Hakimi, N., 1997, ''Preconditioning Methods for Time Dependent Navier-Stokes Euations. Application to Environmental and Low Speed Flows,'' Ph.D. thesis, Department of Fluid Mechanics, Vrije Universiteit, Brussel, Belgium.
[28] Grundfos A/S. *WinCAPS Catalogue*, 1997, Ver 7.0. Product No: 41260001 CR4-20/1.
[29] Hirsch, Ch., Kang, S., and Pointel, G., 1996, ''A Numerically Supported Investigation of the 3D Flow in Centrifugal Impellers—Part I: The Validation Base,'' ASME Paper No. 96-GT-151.
[30] Chriss, R. M., Hathaway, M. D., and Wood, J. R., 1996, ''Experimental and Computational Results From the NASA Lewis Low-Speed Centrifugal Impeller at Design and Part-Flow Conditions,'' ASME J. Turbomach., **118**, pp. 55–65.
[31] Muggli, F. A., Eisele, K., Casey, M. V., Gulich, J., and Schachenmann, A., 1997, ''Flow Analysis in a Pump Diffuser—Part 2: Validation and Limitations of CFD for Diffuser Flows,'' ASME J. Fluids Eng., **119**, pp. 978–984.
[32] Davidson, L., and Nielsen, P., 1996, ''Large Eddy Simulation of the Flow in a Three-Dimensional Ventilated Room,'' *Roomvent '96, Fifth International Conference on Air Distribution in Rooms*, Yokohama, Japan, **2**, 161–168.
[33] Lund, T. S., Wu, X., and Squires, K. D., 1998, ''Generation of Turbulent Inflow Data for Spatially-Developing Boundary Layer Simulation,'' J. Comput. Phys., **140**, pp. 233–258.
[34] Baralas, N. Li. E., and Piomelli, U., 2000, ''Inflow Conditions for Large-Eddy Simulations of Mixing Layers,'' Phys. Fluids, **12**(4), pp. 935–938.
[35] Stepanoff, A. J., 1992, *Centrifugal and Axial Flow Pumps. Theory, Design and Application*, 2nd Ed., Krieger, Melbourne, FL.
[36] Hajem, EL. E., Morel, R., Champange, J. Y., and Spettel, F., 1998, ''Detailed Measurements of the Internal Flow of a Backswept Centrifugal Impeller,'' *9th International Symposium on Applications of Laser*, pp. 36.2.1–36.2.6.
[37] Liu, C. H., Vafidis, C., and Whitelaw, J. H., 1994, ''Flow Characteristics of a Centrifugal Pump,'' ASME J. Fluids Eng., **116**, pp. 303–309.
[38] Sinha, M., and Katz, J., 2000, ''Quantitative Visualization of the Flow in a Centrifugal Pump With Diffuser Vanes—Part I: On Flow Structures and Turbulence,'' ASME J. Fluids Eng., **122**, pp. 97–107.
[39] Ubaldi, M., Zunino, P., and Ghiglione, A., 1998, ''Detailed Flow Measurements Within the Impeller and Vaneless Diffuser of a Centrifugal Turbomachine,'' Exp. Therm. Fluid Sci., **17**, pp. 147–155.
[40] Abramian, M., and Howard, J. H. G., 1994, ''Experimental Investigation of the Steady and Unsteady Flow in a Model Centrifugal Impeller Passage,'' ASME J. Turbomach., **116**, pp. 269–279.
[41] Visser, F. C., and Jonker, J. B., 1995, ''Investigation of the Relative Flow in Low Specific Speed Model Centrifugal Pump Impellers Using Sweep-Beam Particle Image Velocimetry,'' *7th International Symposium on Flow Visualization*, Seattle, WA, pp. 654–659.
[42] Lenneman, E., and Howard, J. H. G., 1970, ''Unsteady Flow Phenomena in Centrifugal Impeller Passages,'' J. Eng. Power, **92**, pp. 65–72.

Effect of Pressure With Wall Heating in Annular Two-Phase Flow

Ranganathan Kumar
Lockheed Martin, Inc.,
One River Road,
Bin 109,
Schenectady, NY 12301

Thomas A. Trabold
General Motors,
Ten Carriage Street,
Honeoye Falls, NY

The local distributions of void fraction, interfacial frequency, and velocity have been measured in annular flow of R-134a through a wall-heated, high aspect ratio duct. High aspect ratio ducts provide superior optical access to tubes or irregular geometries. This work expands upon earlier experiments conducted with adiabatic flows in the same test section. Use of thin, transparent heater films on quartz windows provided sufficient electrical power capacity to produce the full range of two-phase conditions of interest. With wall vapor generation, the system pressure was varied from 0.9 to 2.4 MPa, thus allowing the investigation of flows with liquid-to-vapor density ratios covering the range of about 7 to 27, far less than studied in air-water and similar systems. There is evidence that for a given cross-sectional average void fraction, the local phase distributions can be different depending on whether the vapor phase is generated at the wall, or upstream of the test section inlet. In wall-heated flows, local void fraction profiles measured across both the wide and narrow test section dimensions illustrate the profound effect that pressure has on the local flow structure; notably, increasing pressure appears to thin the wall-bounded liquid films and redistribute liquid toward the edges of the test section. This general trend is also manifested in the distributions of mean droplet diameter and interfacial area density, which are inferred from local measurements of void fraction, droplet frequency and velocity. At high pressure, the interfacial area density is increased due to the significant enhancement in droplet concentration. [DOI: 10.1115/1.1524583]

Introduction

Annular two-phase flow is an area of active research because of its practical importance in a wide variety of applications in the chemical process and energy industries. From a scientific standpoint, annular flow is a particularly challenging phenomenon, because of the separation of the liquid phase between the wall-bounded film and dispersed droplets in the central gas core. The complication of phase separation in annular flow leads to the need for more sophisticated analyses and computations. The literature contains plenty of adiabatic tests in air-water. However, because of the attendant reliance on mathematical modeling, detailed experimental data in wall-heated high-pressure annular flow are required. The physical mechanisms and the physical models that describe the complex interactions that occur in annular flow have been discussed by Hewitt and Hall-Taylor [1] and Azzopardi [2]. Important contributions have also been made in the area of entrainment, deposition, interfacial shear, and droplet size modeling in annular flow by Hanratty and co-workers, [3–5], and by Kataoka and co-workers, [6,7]. These and numerous other papers in annular flow modeling and measurements have been referenced elsewhere, [2].

Much of the data in the literature have been obtained in circular tubes. High aspect ratio noncircular ducts have been used in many applications including compact heat exchangers. While presenting a clear optical access for fundamental experimentation, these geometries also present unique problems. Since the liquid film at the edge has been known to be much thicker than that at the flat side, the droplet breakup mechanism is nonisotropic, giving rise to three-dimensional topography in narrow ducts. Our earlier paper, [8], provided an introduction to the measurement methods and database in adiabatic annular flow, and presented void fraction and droplet velocity distributions at 2.4 MPa in a narrow duct. These data from the hot-film anemometer were further analyzed to obtain the turbulence intensity, [9], which was shown to increase with increasing droplet diameter. We also presented new measurements in adiabatic flow, [10], to illustrate the effect of pressure on flows with low surface tension and low liquid-to-vapor density ratio. The measurements from these specifically designed experiments at high pressures were used to validate the integrated effects of the annular flow models in a two-dimensional three-field formulation, [11].

In our earlier work [8–10], the adiabatic annular flow was generated upstream of the test section to produce a desired cross-sectional average void fraction. This methodology is consistent with the majority of the work reported in the literature, in which a two-phase mixture is introduced at the inlet, and the flow is considered to be fully developed after being transported over some entrance length. There is little evidence in the literature that the local structure of the phase distribution produced by this method is similar to that created by an incremental production of the vapor phase by wall heating. For the design of heated two-phase flow systems, it is important to understand if an adiabatic flow has the same basic structure as a heated flow, even if the bulk flow conditions at a given cross section are equivalent. This question is particularly relevant in connection with computational analyses in which mathematical models for heated systems are based upon data obtained in adiabatic experiments.

This paper has the primary objective of expanding upon previous experimental analysis by the current authors, [8,10], by considering the effects of wall heating in annular flow for a range of system pressures, mass flux, and void fraction in a very thin duct. These measurements have been made in a refrigerant fluid, R-134a (SUVA) at elevated temperature and pressure conditions. At 0.9 and 2.4 MPa, R-134a has a liquid-to-vapor density ratio of 27.0 and 7.3, respectively, compared to a ratio of about 850 for atmospheric pressure air-water. Similarly, the surface tension of R-134a is 0.0069 and 0.0021 N/m at 2.4 and 0.9 MPa, respectively, compared with 0.072 N/m for water at atmospheric conditions.

The specific objectives of this paper are to (a) provide detailed

Contributed by the Fluids Engineering Division for publication in the JOURNAL OF FLUIDS ENGINEERING. Manuscript received by the Fluids Engineering Division Nov. 4, 2000; revised manuscript received Aug. 9, 2002. Associate Editor: J. Katz.

local measurements of void fraction, droplet frequency, droplet velocity, and thereby infer distributions of mean droplet diameter and interfacial area concentration using hot film anemometry, (b) investigate the effect of wall heating by comparing the results with those of adiabatic flows, and (c) investigate the effect of liquid-to-vapor density ratio and surface tension on local phase distributions in both the narrow and wide directions of the cross section.

Experimental Investigation

The test section shown in Fig. 1 has been designed to be flat, thin and rectangular for easy optical access. This high aspect ratio test section and the two-phase flow facility have been described in detail in our previous papers, [8–11], and only a brief overview will be provided here. The R-134a facility consists of a chiller, pressurizer, circulating canned rotor pump, CO_2 heat exchanger, loop heaters, various throttle valves and flow meters, and a vertical test section. Loop conditions are established by programmed logic controllers. The test section has a length of 1.2 m, a cross-section aspect ratio (width/thickness) of 22.5, and a hydraulic diameter of 4.85 mm. These test section dimensions facilitate the use of thin, transparent heater films that enable visual observations and are consistent with the flow and control capabilities of the test loop. Optical access to the flow is provided by eight quartz windows, each 38.1-mm thick by 76.2-mm wide by 0.28-m long. The working fluid used in this study is refrigerant R-134a (SUVA) which is of scientific interest because of its very low liquid-to-vapor density ratio and low surface tension.

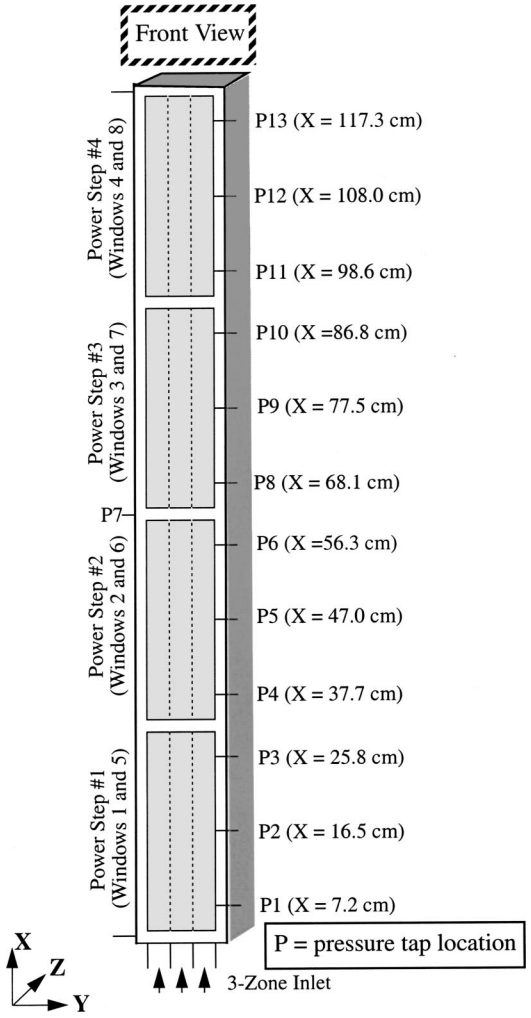

Fig. 1 Test section and measurement locations

Table 1 Flow conditions

Pressure MPa	$\frac{\rho_g}{\rho_l}$	w kg/hr	Quality, x	Void Fraction, α	V_l	V_g m/s	V_w
0.9	.037	106	.73	.94	.78	3.65	1.24
2.4	.136	106	.68	.94	1.14	1.15	1.15
0.9	.037	266	.33	.83	1.73	4.52	2.18
2.4	.136	266	.44	.83	1.76	2.08	1.84
1.4	.062	532	.46	.88	4.17	7.85	4.9
2.4	.136	532	.60	.88	3.54	5.33	4.02

A unique feature of the test section is the use of heating elements on the inside surfaces of the quartz window, which are comprised of thin transparent films that are rugged enough to provide the required heat input. The areas between the quartz windows contain the brushes to carry current to the window films. The triple-track window heater design consists of three transparent metallic oxide conductive films, vacuum deposited on the inside surface, with an antireflective coating on the outside. Three silver epoxy buses deliver the current at both ends of the window, and connect with the silver graphite brushes. The power to each of the three heater films on each window is independently controlled, so various heating profiles can be investigated.

In the present experiments, the two-phase flow field was created by a phase change in the test section due to power addition through the window heater strips. The inlet temperature was controlled by means of a heater located upstream of the test section inlet. Slightly subcooled R-134a was introduced to the test section and heat was applied uniformly to the six windows comprising the lower three power steps. For experiments conducted for comparison to earlier adiabatic annular flow tests, the window power for a given combination of pressure and mass flow rate was adjusted to produce the same cross-sectional average void fraction at $X/L = 0.86$. The total net heat addition ranged from 2.3 to 9.2 kW. The heat losses were quantified experimentally and generally accounted for less than 10 percent of the gross energy input. Majority of the losses was due to conduction at the bridge between the windows. These losses were maximum for the highest pressure of 2.4 MPa and the lowest mass flow rate of 106 kg/hr (Table 1). The heat losses were estimated to be between 5 percent and 7 percent at higher flows and about 2 percent at low pressures and all flows.

The instrumentation used in the R-134a experimental program has been extensively discussed in our previous papers [8–11]. Cross-sectional average and line-average void fraction measurements were obtained using a gamma densitometer system (GDS). This instrument features a 9-curie Cesium-137 gamma source and a NaI detector. For each experimental condition, the average void fraction was established by using a wide gamma beam that interrogated the entire duct cross section at a streamwise position of $X/L = 0.86$. The uncertainty of this measurement ($\pm 2\sigma$) has been determined empirically as ± 0.015 in void fraction.

All of the data profiles reported in this paper were measured using dual-sensor hot-film anemometer (HFA) probes (made of platinum with 25-μm diameter and 254-μm active length), which have been discussed at length in a previous publication, [8]. For each sensor pair, the upstream hot-film measurements of the local void fraction are made by quantifying the time the sensor is exposed to the vapor phase relative to the total measurement time. The local interfacial velocity is calculated by dividing the known spacing between the sensors by the mean interface transport time. The latter is obtained directly by taking the cross correlation between the output voltage signals from the upstream and downstream sensors. Two types of HFA probes were used. One was mounted in a hole in one of the quartz windows to traverse across the narrow (Z) dimension at $X/L = 0.74$. The other was mounted

in an instrument access port between windows 3 and 4 (Fig. 1), to traverse the wide (Y) dimension at $X/L=0.77$. The measurement uncertainties ($\pm 2\sigma$) associated with the HFA probes have been quantified empirically as follows: 0.027 for void fraction, 7.5 percent for near-wall velocity, and 7 percent for far-wall velocity. Limited benchmarking was done by the current authors in a previous study, [8], to confirm the results of the HFA probes. The void fraction and velocity measurements were compared by simultaneous measurements with a gamma densitometer and laser Doppler velocimeter, respectively. The effective size of the measurement volume in the narrow dimension was approximately 0.25 mm for LDV and 0.02 mm for HFA. The measurement volume can influence the measurement of mean velocity, especially in regions of large velocity gradients. Measurements made with both instruments near the middle of the test section were found to compare well with each other and were representative of the dispersed droplet velocity measurements in the vapor core. Near the wall, since LDV had a larger measurement volume, there probably was a negative bias in the mean velocity.

Measurements of local void fraction, interfacial velocity and frequency were obtained from direct analysis of the HFA output voltage signals. In the region of the two-phase flow comprised solely of dispersed liquid droplets in continuous vapor, these direct measurements were then used to compute the local mean droplet diameter:

$$d_d = 1.5 \frac{V_d \alpha_d}{f_d}. \tag{1}$$

Ishii and Mishima [12] characterized the average interfacial area concentration in annular flow by combining contributions from interfacial waves and dispersed droplets. If their expression is applied locally in the region of the flow where only the vapor core and droplets are present, the interfacial area density reduces to

$$a_i = \frac{4 f_d}{V_d}. \tag{2}$$

Galaup [13] derived the above equation from geometric considerations in bubbly flows where the characteristic size of the bubbles far exceeded the effective size of the measurement volume. In the current experiments, very small droplets (i.e., size of the same order as the 25-μm diameter HFA sensor) were measured. Therefore, it is expected that the largest error associated with the application of Eq. (2) will be for very small droplets which generally occur for cases with void fraction in excess of 90 percent. A detailed discussion of these derived parameters is given in [6,8].

Results

Detailed local measurements of void fraction, droplet frequency, diameter, velocity, and interfacial area concentration were obtained in wall heated annular refrigerant flow through a narrow duct. The three operating variables are pressure (0.9 to 2.4 MPa), mass flow rate (106 to 532 kg/hr) and cross-sectional average void fraction (0.83 to 0.94). The three system pressures investigated provide liquid-to-vapor density ratios of 7.0 to 27.0. For some of the experiments, the inlet flow was heated to produce adiabatic conditions in the test section, and to reproduce the same average void fraction obtained at the same location during similar wall-heated test runs. The HFA voltage scans were used only when the signal quality was considered adequate for accurate determination of local void fraction. For some flow conditions, in particular at high flow rates, it was difficult to define a threshold, therefore, droplet frequency and diameter measurements could not be made. However, the time-averaged interfacial velocity could be obtained using the dual-sensor HFA probe (via cross correlation) even for the highest flow rate. For all experimental runs, the cross-sectional average void fraction ($\overline{\alpha}$) was established at $X=1.03$ m using the wide beam gamma densitometer edge measurement.

The local void fraction profiles for the heated case are presented first in Figs. 2(a), 2(b), and 2(c) for each mass flow rate of 106, 266 and 532 kg/hr, and compared with the corresponding adiabatic cases. The conditions given for the mass flow rate of 106 kg/hr and 266 kg/hr for adiabatic flows are the same as those given in [8]. However, new measurements were made so that comparisons could be made at the same ambient conditions and for the same heat loss. The void profile given here in Fig. 2(a) is slightly different from that given in [8] near the wall for the lowest flow considered (where the heat loss is maximum), but still is well within the experimental uncertainty. For all flow rates, at high void fractions, the behavior of these profiles for the two types of heating is similar. There is an inversion in the void fraction profiles, as the wall-bounded film thickness decreases. The decrease in the void fraction in the center of the test section is due to the concentration of droplets emanating from the test section edge liquid film. This fact is corroborated by the interfacial area concentration profiles in Fig. 3 which show an increase in droplet concentration toward the center of the test section at high pressures. Although there is no significant difference in the overall trend displayed in the two types of heating for the same flow conditions, near-wall measurements are seen to differ. At the center, the magnitude of the dip is higher in the case of heated flow for low rates (Fig. 3(a)). Therefore, local measurements in heated flows are important for model and code validation. Having discussed the fundamental similarities and differences in adiabatic and wall-heated annular flows, further discussions will be restricted to wall-heated annular flows.

The basic structure of the phase distribution in the narrow Z-dimension is dependent on the system pressure, which is shown in Fig. 4. For $w=532$ kg/hr and $\alpha=0.71$, as the pressure is increased from 0.9 MPa to 2.4 MPa, the flow goes through several distinct transitions in the two-phase flow structure. This average void fraction was chosen so that for some conditions, a churn-turbulent flow would be produced using the window heaters. It is clear from this figure that at lower pressures of 0.9 MPa and 1.6 MPa, the void fraction profile attains the classic parabolic shape characteristic of the transition flow regime. As the pressure is increased to 2.1 MPa, the film thickness decreases on the wall, as the void profile becomes flat. At the highest pressure of 2.4 MPa (equivalent to 13.7 MPa in steam-water with the same liquid-to-vapor density ratio as the refrigerant in this study), the profile becomes inverted, with maximum void fraction near the wall and minimum void fraction at the duct centerline. This trend, also observed in earlier adiabatic experiments, may be explained as follows.

The strong inversion in the void fraction profiles in the narrow Z-dimension is caused by two mechanisms: (1) the liquid bridges in the transition regime get disintegrated into large droplets and convected into the vapor core and (2) increasing the system pressure thins the liquid film on the walls, redistributes the liquid to the edges where the disturbance waves with larger amplitudes form over a thicker base film. The disturbance waves are sheared off by the fast-moving vapor, entraining larger diameter droplets into the vapor core. The second mechanism, in conjunction with a much lower surface tension (At 2.4 MPa, R-134a has a surface tension which is significantly lower than that of water at any pressure), increases the Weber number. As the Weber number increases, the entrainment fraction increases. This phenomenon is evident from Fig. 5 which shows the void fraction distribution in both dimensions at 0.9 and 2.4 MPa for an average void fraction of 0.83 and flow rate of 266 kg/hr. As mentioned previously, the Z and Y dimension void fraction profiles were measured with HFA probes at streamwise positions of $X/L=0.74$ and 0.77, respectively. So although the X positions of the two data scans in each figure are not the same, the cross-sectional average void fraction varied little over this interval. At low pressure, the void fraction is fairly uniform across most of the duct in both the narrow and width dimensions, and quickly tapers close to the walls and the

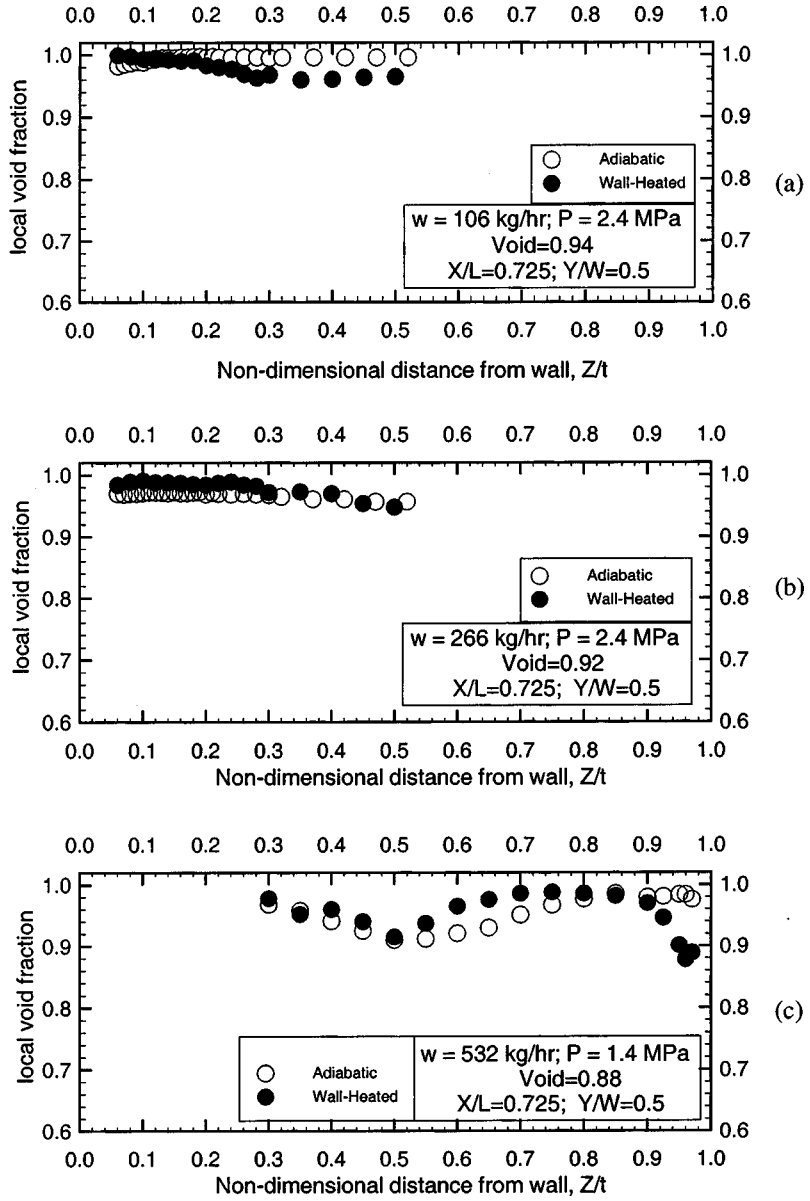

Fig. 2 Comparison of thickness dimension void fraction scans between adiabatic and wall-heated cases

edges. The near-wall gradient is especially confined within a region extending to only about 2 to 3 mm from the unheated transverse edges of the test section where the void fraction reaches a local minimum of nearly 0.4. When the pressure is increased to 2.4 MPa for the same flow rate and average void fraction, the narrow dimension profile inverts with the dip in the vapor core. The width dimension profile stays flat as it does for the lower pressure in the vapor core, however, the void fraction shows a steady decrement much farther than 2 to 3 mm from the edges. This suggests the presence of thicker liquid films at the edges and disturbance waves with large amplitudes. This phenomenon appears to be characteristic of flows in high pressure systems in high aspect ratio ducts.

Plots of void fraction, droplet frequency, droplet diameter and droplet interfacial area density are shown in Figs. 6 through 9 for different flow rates. Profiles are given for two pressures and where available, for three pressures. If reliable droplet frequency measurements could be made, interfacial area density profiles could be made available through the simple relationship, $a_i = 4f_d/V_d$, since droplet velocity measurements obtained from cross-correlation has always been reliable. However, the droplet diameter calculation requires frequency, velocity, and droplet fraction. For certain pressures in certain regions of the flow, the void fraction, α, is close to 1.0, and the diameter calculation performed using the droplet fraction, $(1\text{-}\alpha)$, would contain unacceptable uncertainty. For this reason, droplet diameter profiles are not plotted for certain flow conditions, and certain regions of the flow field.

As shown in Fig. 6, high pressure causes a void dip in the center of the test section. This dip is more profound for 266 kg/hr at a slightly lower average void fraction of 0.83. The lower the void and pressure, the more parabolic is the void profile. At the highest flow rate of 532 kg/hr, the trend continues such that the void fraction is lower near the wall for the low pressure, but a small region of void inversion exists near the center for both pressures.

The droplet frequency profiles given in Fig. 7 provide insight regarding the possible source of these droplets. For the low flow of 106 kg/hr, the frequency profile for the low pressure has a slight decreasing trend toward the vapor core since most of the entrainment occurs at the flat-side film. As the pressure is in-

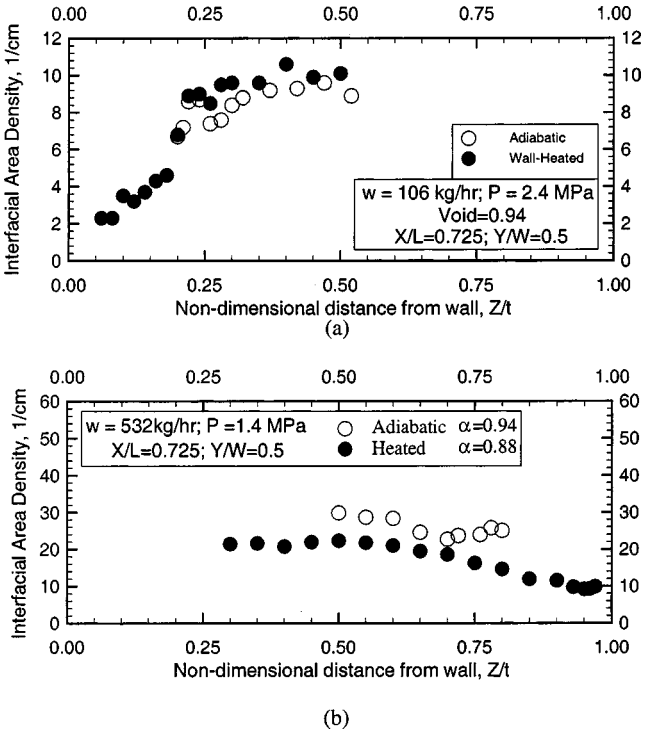

Fig. 3 Comparison of thickness dimension interfacial area density profiles between adiabatic and wall-heated cases

creased to 2.4 MPa, a complete opposite trend is seen where the frequency increases towards the core. Since the void fraction profile for this case is seen to have a slight inversion, it is reasonable to conjecture that the edge film for the higher pressure is much thicker with large amplitude waves than that at low pressure. When these waves are sheared off, some of the larger diameter droplets emanate from the edges. The other larger diameters probably arise from the liquid bridges that are disintegrated in the transition regime. This increasing trend in the frequency from the wall toward the vapor core is also seen for the highest flow of 532 kg/hr at both low and high void fractions of 0.71 and 0.88 (Figs. 7(*c*) and 7(*d*)). For this flow, the increasing trend can be noticed at both pressures. At $\alpha=0.71$, the flow has not reached a pure annular flow regime. It is probably in its late stage of transition as seen by the asymmetric distribution in droplet frequency (Fig. 7(*c*)) as well as in void fraction (Fig. 6(*c*)). At 266 kg/hr (Fig. 7(*b*)), the frequency profile is flat at the two pressures and void fractions. All the cases clearly show that the droplet concentration increases with increasing pressure.

The interfacial area density (Fig. 8) is calculated directly from droplet frequency and droplet velocity measurements. Because the velocity profiles in the droplet field are generally flat as reported previously, [6], the trend in the interfacial area closely mimics the measured frequency. To the authors' knowledge, no average or local measurements of interfacial area are available in the literature for heated flow at elevated pressures. The local interfacial area density increases with pressure for almost all flows as seen in the frequency profiles. For a constant void fraction of approximately 0.9 (Figs. 8(*a*), 8(*b*), and 8(*d*)) for $P=2.4$ MPa, the average interfacial area density increases as the flow rate increases. For the same flow rate and pressure, the interfacial area density is higher for lower void fractions due to the increased droplet frequency. These trends are expected, but the surprising result is that the magnitude of the interfacial area density is significantly higher than the values reported for the air-water flows. The largest interfacial area density reported for air-water flow was 25 cm^{-1} measured at a gas superficial velocity of 37 m/sec, [14], in circular tubes. For a measured droplet velocity field of approximately 6 m/sec, the interfacial area density reported here exceeds 25 cm^{-1} at 532 kg/hr. It may be suggested that the combination of a high Weber number due to the high pressure and a thin noncircular geometry contributed to a large frequency of droplets, thereby increasing the interfacial area compared to air-water flows at atmospheric pressure.

The droplet diameter profiles shown in Fig. 9 are another set of inferred measurements, but are significantly more difficult to obtain than interfacial area density. The uncertainty is higher at very high void fractions, since the calculation involves the volume fraction of the droplets. The droplet field features a wide range of droplets from 25 μm to 400 μm, and generally displays an in-

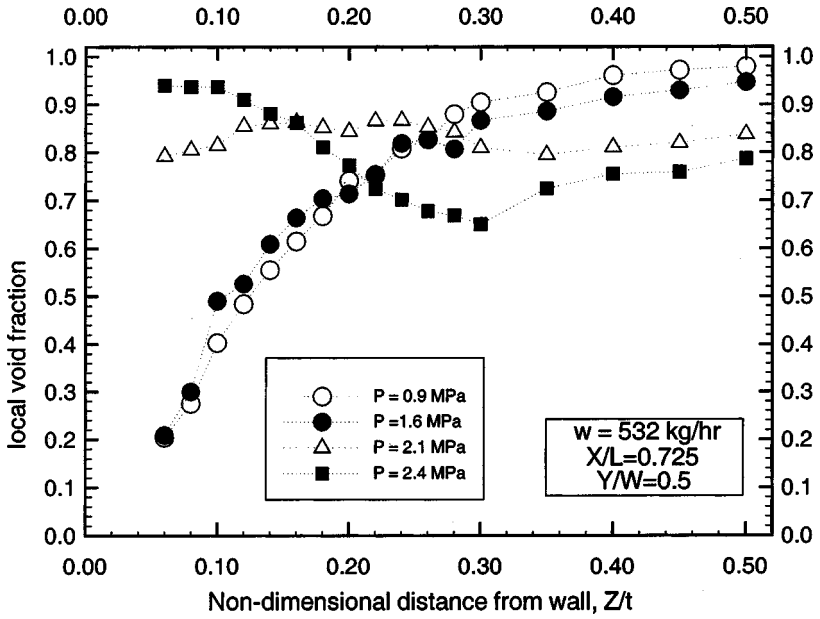

Fig. 4 Effect of pressure on void fraction scans in the thickness dimension for w=532 kg/hr and α=0.71

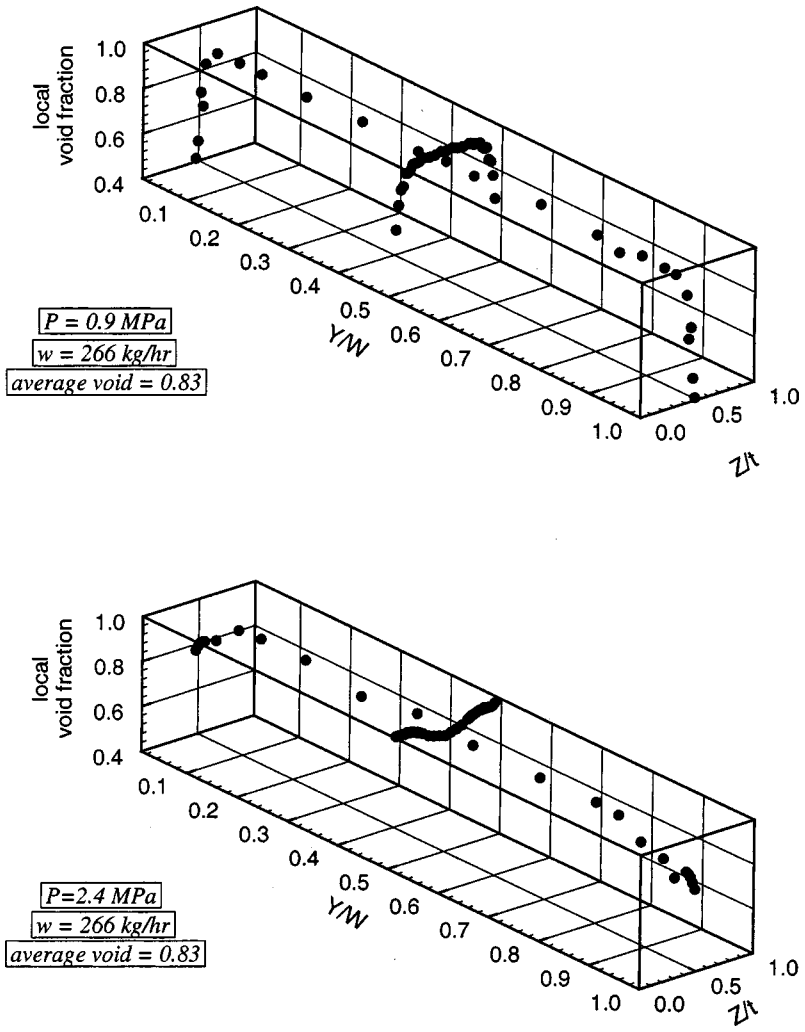

Fig. 5 Void distribution in the narrow and width dimensions at two different pressures

creasing trend in diameter from the wall to the vapor core. For high void fraction flows, the wall film is too small to contribute to large droplets. These large droplets are generated from another source, possibly the thicker edge film. The available droplet diameter profiles do not show any variation in trend as the flow rate or void fraction increases. The diameters vary only between 200 μm and 400 μm in the core of the flow ($0.2 \leq Z/t \leq 0.8$) for all the cases, whereas the droplet frequencies can vary tenfold (Fig. 7). This suggests that the increase in interfacial area density should be attributed more to the increase in droplet frequency than the droplet diameter.

Finally, the droplet velocities measured by the cross correlation of the two HFA sensors are plotted for three flow rates both in the thickness (Z) dimension (Fig. 10) and width (Y) dimension (Fig. 11). Table 1 summarizes the flow conditions and the calculated averaged liquid and vapor velocities. It also includes the wave velocity calculated for a neutrally stable film from a simple force balance at the interface between the liquid film and the vapor core yielding

$$V_w = \frac{\sqrt{\frac{\rho_g}{\rho_l}} V_g + V_l}{1 + \sqrt{\frac{\rho_g}{\rho_l}}}. \tag{3}$$

The average values of vapor velocity, V_g, and liquid velocity, V_l, can be calculated using the one-dimensional relationship in terms of the measured quality and mass flux as

$$V_g = \frac{x}{\alpha}\frac{G}{\rho_g}; \quad V_l = \frac{(1-x)}{(1-\alpha)}\frac{G}{\rho_l}. \tag{4}$$

The profiles for lower flow rates and a low pressure of 0.9 MPa in Fig. 10 offer dramatic evidence of the presence of disturbance waves on the wall. At $Z/t < 0.2$, the droplet velocity is low and follows closely the average liquid velocity (Table 1). Within this region, the velocity increases from this average liquid velocity to the wave velocity, and at $Z/t \sim 0.2$, jumps to a much higher velocity closely following vapor velocity. It is interesting that although at $Z/t < 0.2$, the droplet frequency and diameter have a higher uncertainty and are difficult to measure, the droplet velocities through the cross correlation are reliable and follow theoretical averaged velocities. It is conjectured that the measurements made close to the wall are measurements of liquid ligaments and/or large droplets and HFA is generally more biased towards bigger droplets.

The high-pressure profiles provided both in Figs. 10 and 11 are flat since the average liquid and vapor velocities for these conditions are closer to each other in magnitude. This is the uniqueness of the high pressure systems where annular flow is possible even for low vapor velocities close to 1 m/sec, whereas in air-water

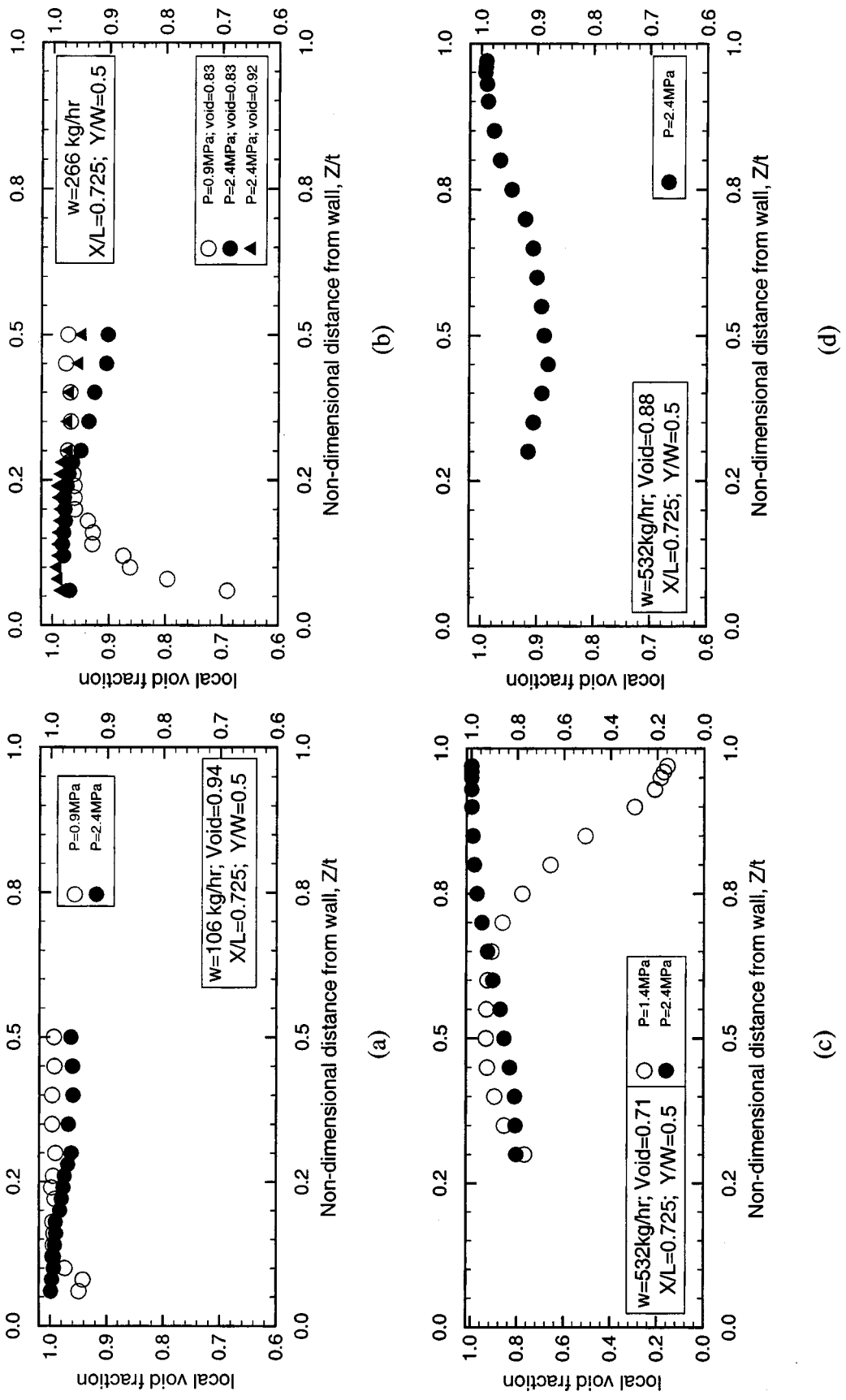

Fig. 6 Effect of pressure on thickness dimension profiles of void fraction at different flow rates

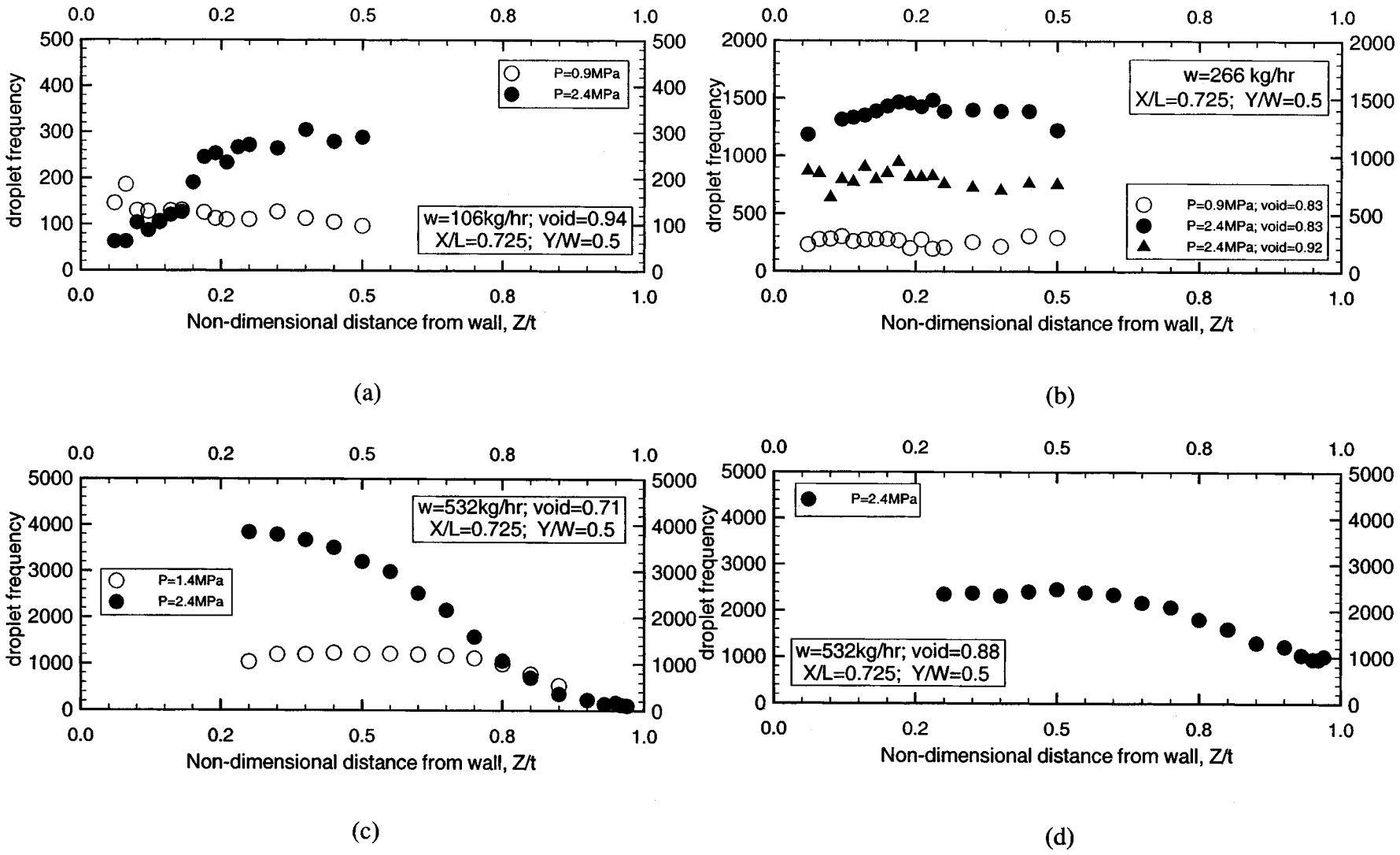

Fig. 7 Effect of pressure on thickness dimension profiles of droplet frequency

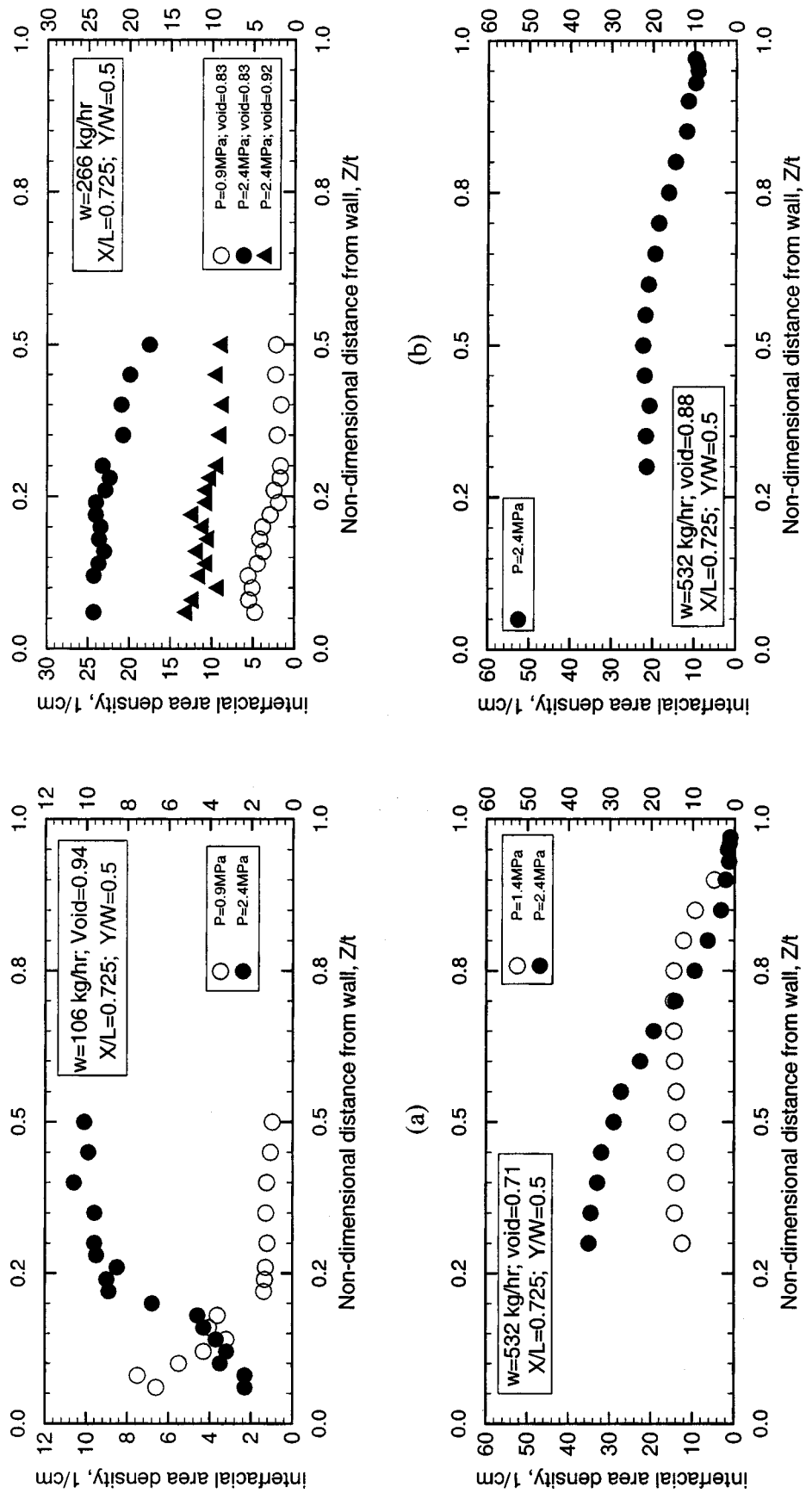

Fig. 8 Effect of pressure on thickness dimension profiles of interfacial area density at different flow rates

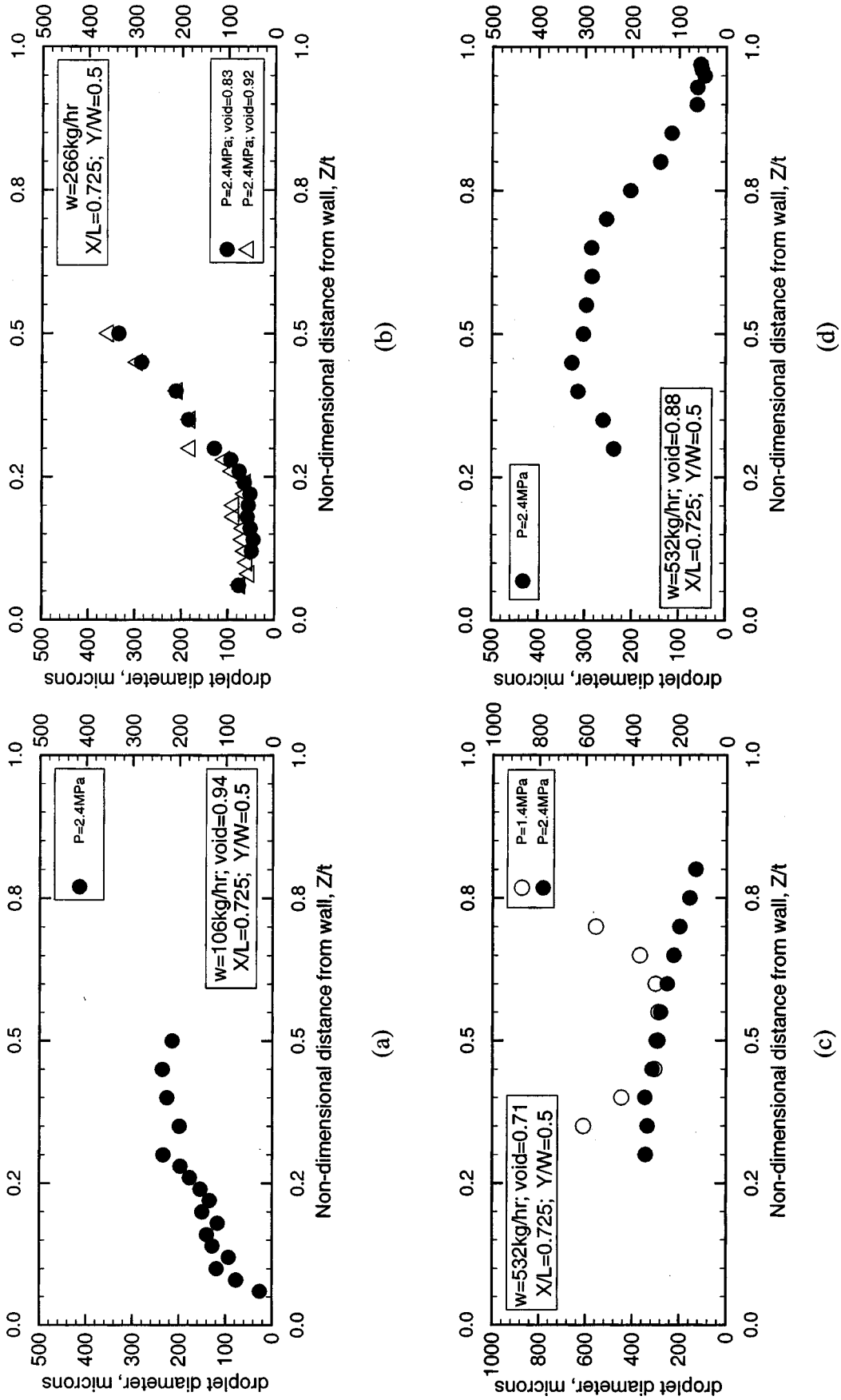

Fig. 9 Effect of pressure on thickness dimension profiles of droplet diameter

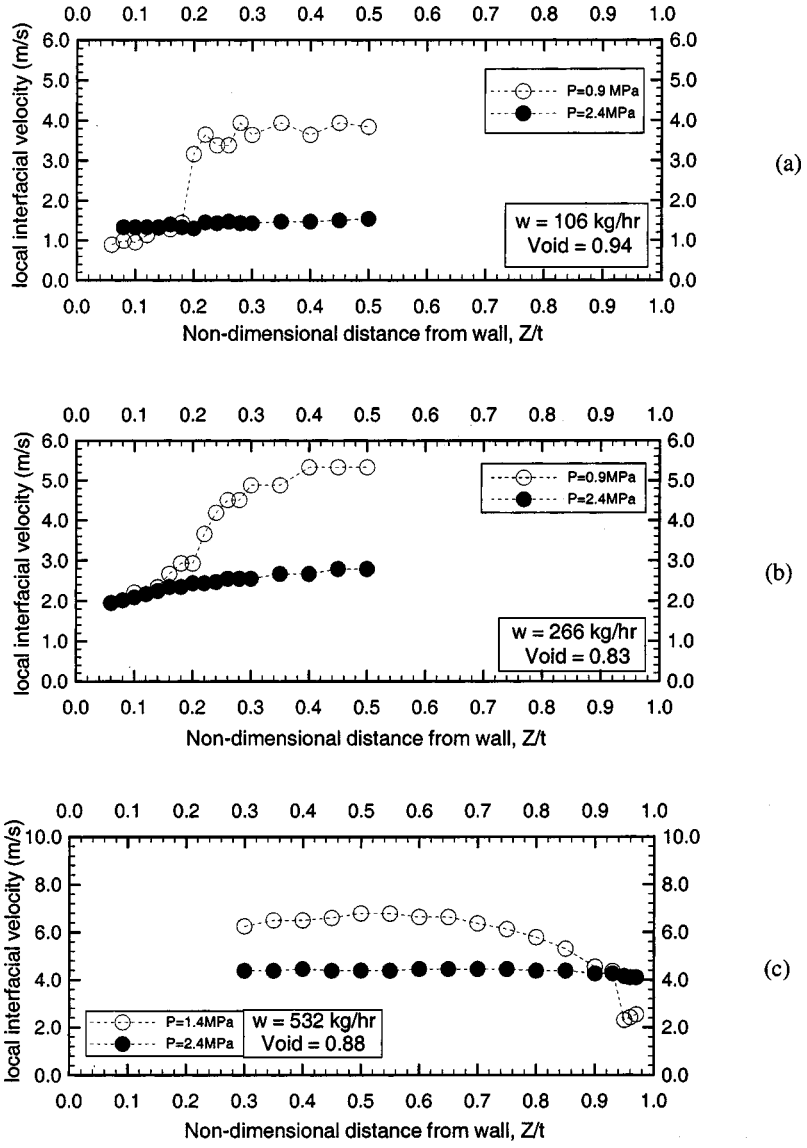

Fig. 10 Effect of pressure on thickness dimension interfacial velocity profiles

systems such low velocities are not possible in separated annular flows. The transverse profiles in Fig. 11 have a profound dip in the middle of the test section for lower pressures. Flow visualization displayed half-waves extending from one edge to the middle of the test section. These waves subsequently coalesce with half-waves from the other edge, causing a dip in the middle. In this region, the velocities are generally low because of the agglomeration of large droplets as was seen in the droplet diameter profiles at 2.4 MPa in Fig. 9.

Summary and Conclusions

An experimental study has been conducted to acquire local measurements of void fraction, interfacial velocity and droplet frequency in flows of R-134a through a vertical, high aspect ratio rectangular duct. These measurements were used to infer the local droplet size and interfacial area concentration. By considering the effect of wall heating, the results presented in this paper expand the database for annular flows in a rectangular geometry. By applying electrical power to thin, transparent metal oxide heaters on the inside surfaces of quartz windows, vapor was generated at the walls to create annular flow in the test section from a subcooled inlet. A comparison between the local phase distributions in heated flows to those obtained in earlier adiabatic experiments show generally close agreement, but there are some differences in the near-wall region, particularly for average void fractions at the lower limit of the annular flow regime.

As described in previous papers, [8–11], the unique characteristic of R-134a is that the liquid-to-vapor density ratio can be reduced by two orders of magnitude, and surface tension by an order of magnitude compared to water at atmospheric conditions. Acquisition of local two-phase flow data under these conditions has shed light on many heretofore unreported physical phenomena. Perhaps the most important of these phenomena is the manner in which the liquid phase is redistributed when the system pressure is increased, i.e., reducing the difference in density between the liquid and vapor phases and the surface tension. These property effects increase the Weber number at high pressures, thereby increasing the droplet entrainment from the edges. To fully ascertain this effect, a new hot-film anemometry device was installed to enable acquisition of local void fraction along both test section dimensions in the horizontal plane. Two-dimensional plots of local void fraction clearly demonstrate that at high pressure, the liquid is redistributed from the wide duct walls toward the edges of the test section. Incrementally increasing the pressure

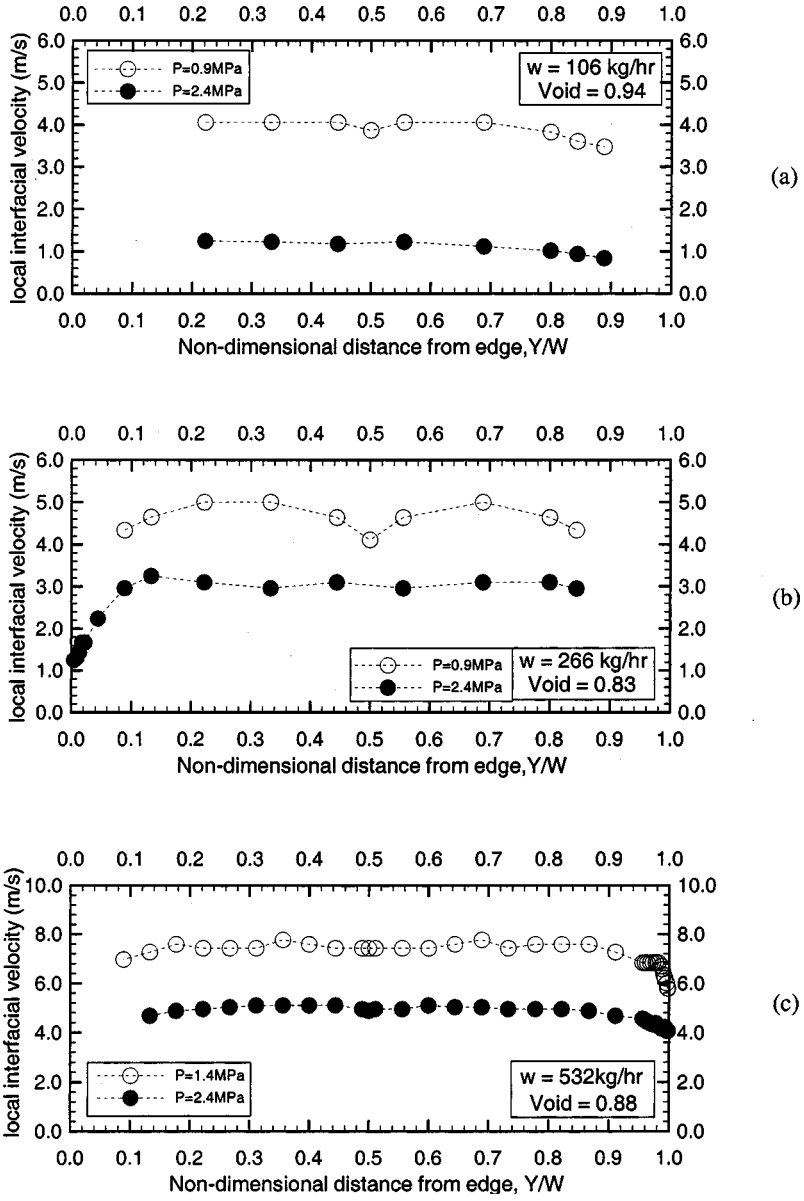

Fig. 11 Effect of pressure on width dimension interfacial velocity profiles

from 0.9 to 2.4 MPa shows a transition from a classic parabolic vapor phase distribution to one that has its maximum near the heated wall.

Pressure effects are also evident in the distributions of interfacial velocity. For data scans across the narrow (Z) dimension, the high pressure data show a small monotonic increase in velocity from the duct wall to the center of the test section, suggesting that the sensing probe is exposed only to the dispersed droplet field. At lower pressures, the velocity profile displays a clear transition from the near-wall region, where the HFA probe likely senses the interface between continuous liquid and dispersed bubbles in the wall-bounded liquid film. At the center of the test section, the local velocity is much higher, since the sensor measured predominantly the dispersed liquid droplets in the continuous vapor core. Between these two regions, the probe appears to measure the waves in the liquid film, based upon a comparison to a simple force balance derivation of a neutrally stable film.

Acknowledgments

The authors gratefully acknowledge Messrs. W. O. Morris and L. Jandzio for their efforts in the operation of the test facility. Special thanks are due to Mr. S. W. D'Amico who contributed to the development of the hot-film anemometer probe traversing and data acquisition systems.

Nomenclature

a_i = interfacial area density
d = diameter, μm
f_d = frequency of droplets, 1/sec
G = mass flux, kg/m^2/hr
L = length, mm
t = duct thickness, mm
V = average velocity, m/sec
V_d = droplet velocity, m/sec
V_w = wave velocity, m/sec
w = mass rate of flow, kg/hr
W = width, m
x = quality
X = axial dimension, m
y, Y = thickness dimension, m
z, Z = transverse dimension, m

Subscripts and Superscripts

d = droplet
g = vapor
l = liquid

Symbols

α = void fraction
ρ = density

References

[1] Hewitt, G. F., and Hall-Taylor, N. S., 1970, *Annular Two-Phase Flow*, Pergamon Press, New York.
[2] Azzopardi, B. J., 1997, ''Drops in Annular Two-Phase Flow,'' Int. J. Multiphase Flow, **23**, Suppl., pp. 1–53.
[3] Henstock, W. H., and Hanratty, T. J., 1976, ''The Interfacial Drag and Height of the Wall Layer in Annular Flow,'' AIChE J., **22**, pp. 990–1000.
[4] Tatterson, D. F., Dallman, J. C., and Hanratty, T. J., 1977, ''Drop Sizes in Annular Gas-Liquid Flows,'' AIChE J., **23**, pp. 68–76.
[5] Hanratty, T. J., and Dykhno, L. A., 1997, ''Physical Issues in Analyzing Gas-Liquid Annular Flow,'' *Exp. Heat Transfer Fluid Mech. Thermodyn.* Ed. ETS, **2**, pp. 1127–1136.
[6] Kataoka, I., and Ishii, M., 1982, ''Mechanism and Correlation of Droplet Entrainment and Deposition in Annular Two-Phase Flow,'' Argonne National Laboratory Report ANL-82-44.
[7] Kataoka, I., and Serizawa, A., 1990, ''Interfacial Area Concentration in Bubbly Flow,'' Nucl. Eng. Des., **120**, pp. 163–180.
[8] Trabold, T. A., Kumar, R., and Vassallo, P. F., 1999, ''Experimental Study of Dispersed Droplets in High-Pressure Annular Flow,'' ASME J. Heat Transfer, **121**, pp. 924–933.
[9] Trabold, T. A., and Kumar, R., 2000a, ''Vapor Core Turbulence in Annular Two-Phase Flow,'' Exp. Fluids, **28**, pp. 187–194.
[10] Trabold, T. A., and Kumar, R., 2000b, ''High Pressure Annular Two-Phase Flow in a Narrow Duct. Part I: Local Measurements in the Droplet Field,'' ASME J. Fluids Eng., **122**, pp. 364–374.
[11] Kumar, R., and Trabold, T. A., 2000, ''High Pressure Annular Two-Phase Flow in a Narrow Duct. Part II: Three-Field Modeling,'' ASME J. Fluids Eng., **122**, pp. 375–384.
[12] Ishii, M., and Mishima, K., 1981, ''Study of Two-Fluid Model and Interfacial Area,'' Argonne National Laboratory Report ANL-80-111.
[13] Galaup, J. P., 1976, ''Contribution to the Study of Methods for Measuring Two-Phase Flow,'' Center D'Etudes Nucleaires de Grenoble, Report No. 136.
[14] Wales, C. E., 1966, ''Physical and Chemical Absorption in Two-Phase Annular and Dispersed Horizontal Flow,'' AIChE J., **12**, pp. 1166–1171.

Wake Dynamics of a Yawed Cylinder

J. S. Marshall
Department of Mechanical and Industrial Engineering and IIHR–Hydroscience and Engineering,
University of Iowa,
Iowa City, IA 52242
e-mail: jeffrey-marshall@uiowa.edu

A theoretical and computational study is reported of the effect of cylinder yaw angle on the vorticity and velocity field in the cylinder wake. Previous experimental studies for yawed cylinder flows conclude that, sufficiently far away from the cylinder ends and for small and moderate values of the yaw angle, the near-wake region is dominated by vortex structures aligned parallel to the cylinder. Associated with this observation, experimentalists have proposed the so-called Independence Principle, which asserts that the forces and vortex shedding frequency of a yawed cylinder are the same as for a cylinder with no yaw using only the component of the freestream flow oriented normal to the cylinder axis. The current paper examines the structure, consequences and validity for yawed cylinder flows of a quasi-two-dimensional approximation in which the velocity and vorticity have three nonzero components, but have vanishing gradient in the direction of the cylinder axis. In this approximation, the cross-stream velocity field is independent of the axial velocity component, thus reproducing the Independence Principle. Both the axial vorticity and axial velocity components are governed by an advection-diffusion equation. The governing equations for vorticity and velocity in the quasi-two-dimensional theory can be nondimensionalized to eliminate dependence on yaw angle, such that the cross-stream Reynolds number is the only dimensionless parameter. A perturbation argument is used to justify the quasi-two-dimensional approximation and to develop approximate conditions for validity of the quasi-two-dimensional approximation for finite-length cylinder flows. Computations using the quasi-two-dimensional theory are performed to examine the evolution of the cross-stream vorticity and associated axial velocity field. The cross-stream vorticity is observed to shed from the cylinder as thin sheets and to wrap around the Kárman vortex structures, which in turn induces an axial velocity deficit within the wake vortex cores. The computational results indicate two physical mechanisms, associated with instability of the quasi-two-dimensional flow, that might explain the experimentally observed breakdown of the Independence Principle for large yaw angles.
[DOI: 10.1115/1.1523069]

1 Introduction

Cable problems typically involve flow oriented both normal and parallel to the axis of the cable. In cases such as towed cables behind ships and airplanes, the axial translation of the cable can be much larger than the cross-flow velocity. In other cases, such as cables used to tether structures or the probes used in multiwire hot-wire anemometers, the axial and cross-flow velocity components may be of a similar magnitude. Previous investigators, [1,2], using experimental flow visualization have shown that flow in the near wake of a yawed cylinder, which models a cable in the presence of combined axial and transverse flow, appears to consist of nearly two-dimensional vortex structures aligned parallel to the cylinder axis when observed sufficiently far from the cylinder ends. Experimental measurements, [1–6], also indicate that forces acting on the cylinder and the vortex shedding frequency for a yawed cylinder are approximately the same as for a cylinder with no yaw if only the normal component of the force is used. This observation is often called the Independence Principle in the literature (or the Cosine Rule in the earlier literature), since the cross-plane forces and flow field appear to be independent of the axial flow.

Several investigators, [2,7], have noted deviations from the predictions of the Independence Principle near the cylinder upstream end. Ramberg [2] demonstrated that for finite-length cylinders there exists two modes of nearly parallel vortex shedding, as illustrated in Fig. 1. Near the upstream cylinder end there is a region in which the vortices are aligned at an angle of inclination to the freestream that is greater than the cylinder yaw angle, which is followed by a region in which the shed vortices are oriented at approximately the same angle of incidence as the cylinder. These two regions of parallel vortex shedding are separated by a thin band in which the flow appears highly turbulent. Other investigators, [8–10], have demonstrated that the Independence Principle also breaks down for large yaw angles, where in the current study the yaw angle is defined such that a cylinder oriented normal to the free stream has zero yaw and a cylinder with axis parallel to the free stream has yaw angle $\phi = 90$ deg.

The current paper examines the theoretical basis of the Independence Principle. Motivated by flow visualizations of Ramberg [2], we employ a quasi-two-dimensional approximation in which the velocity and vorticity vectors have three nonzero components that are functions of time and the cross-stream coordinates x and y, but are independent of the axial coordinate z. The governing equations for the quasi-two-dimensional theory indicate that both the cross-stream velocity components and the cylinder surface pressure depend only on the axial vorticity, which evolves independently of the axial velocity and has the same form as in a purely two-dimensional flow, thus reproducing the Independence Principle. Both the axial vorticity and the axial velocity fields are governed by an advection-diffusion equation. The cross-stream vorticity field evolves both due to convection by the cross-stream flow and due to a combination of vorticity stretching and diffusion. The governing equations can be nondimensionalized such that they are independent of the yaw angle, containing only the cross-stream Reynolds number, $\mathrm{Re} = Ud/\nu$, as a dimensionless parameter. Here U is the cross-stream velocity far upstream of the cylinder, d is the cylinder diameter, and ν is the kinematic viscos-

Contributed by the Fluids Engineering Division for publication in the JOURNAL OF FLUIDS ENGINEERING. Manuscript received by the Fluids Engineering Division Jan. 29, 2002; revised manuscript received Aug. 8, 2002. Associate Editor: G. Karniadakis.

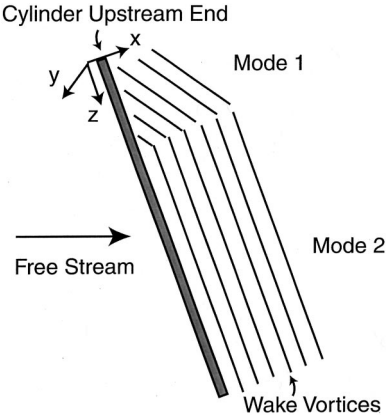

Fig. 1 Sketch showing the two modes of nearly parallel vortex shedding for flow past a yawed cylinder of finite length (based on flow visualizations of Ramberg [2])

ity. Theoretical results using quasi-two-dimensional approximation are reported by Moore [11] for flow in the boundary layer of a yawed cylinder.

The current study examines the consequences, conditions for validity, and dynamics of yawed cylinder wakes under the quasi-two-dimensional approximation. A perturbation analysis is presented in Section 2 to examine the effect of cylinder length on validity of the quasi-two-dimensional approximation. The governing equations for the quasi-two-dimensional approximation in the vorticity-velocity formulation and scaling of these equations are discussed in Section 3. An overview of the tetrahedral vorticity element (TVE) method used in the computations is given in Section 4. Computational results for evolution of the cross-stream flow are reported in Section 5, which are used to validate the computations and to assess sensitivity of the computations to change in time-step and spatial discretization. Computational results for evolution of the axial flow and the associated cross-stream vorticity field are reported in Section 6. This section also discusses two mechanisms for three-dimensional instability of the quasi-two-dimensional flow solutions, which might lead to the observed breakdown of the Independence Principle for large yaw angles. Conclusions are given in Section 7.

2 Justification of the Quasi-Two-Dimensional Approximation

We consider flow past a yawed circular cylinder of diameter d at a distance L from the cylinder upstream end. The component of the free-stream flow oriented along the cylinder normal and axial directions are given by U and W, respectively, where the cylinder yaw angle ϕ is defined by $\phi=\tan^{-1}(W/U)$. The flow is described using a Cartesian coordinate system (x,y,z), with the z-coordinate tangent to the cylinder axis and the x and y-coordinates normal to the cylinder axis. We refer to velocity and vorticity components parallel to the cylinder axis (the z-direction) as the *streamwise* components and components in the plane perpendicular to the cylinder (the x-y plane) as the *cross-stream* components. The velocity components (u,v,w), vorticity components $(\omega_x,\omega_y,\omega_z)$, pressure p, position coordinates (x,y,z), and time t are nondimensionalized as

$$\omega_x^*=\omega_x d/W,\quad \omega_y^*=\omega_y d/W,\quad \omega_z^*=\omega_z d/U,\quad x^*=x/d,$$
$$y^*=y/d,\quad z^*=z/L,\quad u^*=u/U,\quad \nu^*=\nu/U,$$
$$w^*=w/W,\quad t^*=tU/d,\quad p^*=p/\rho U^2, \tag{1}$$

where dimensionless variables are indicated by an asterisk. All variables are nondimensionalized in the remainder of the paper using (1), where for convenience the asterisks on the dimensionless variables are dropped.

The Navier-Stokes equations in the x and z-directions are given by

$$\frac{\partial u}{\partial t}+u\frac{\partial u}{\partial x}+\nu\frac{\partial u}{\partial y}+\frac{\varepsilon}{\alpha}w\frac{\partial u}{\partial z}=-\frac{\partial p}{\partial x}+\frac{1}{\mathrm{Re}}\left(\frac{\partial^2 u}{\partial x^2}+\frac{\partial^2 u}{\partial y^2}+\varepsilon^2\frac{\partial^2 u}{\partial z^2}\right) \tag{2a}$$

$$\frac{\partial w}{\partial t}+u\frac{\partial w}{\partial x}+\nu\frac{\partial w}{\partial y}+\frac{\varepsilon}{\alpha}w\frac{\partial w}{\partial z}$$
$$=-\varepsilon\alpha\frac{\partial p}{\partial z}+\frac{1}{\mathrm{Re}}\left(\frac{\partial^2 w}{\partial x^2}+\frac{\partial^2 w}{\partial y^2}+\varepsilon^2\frac{\partial^2 w}{\partial z^2}\right), \tag{2b}$$

where the y-component of the Navier-Stokes equations has a form similar to (2a). The three dimensionless parameters in (2) are the length scale ratio $\varepsilon=d/L$, the velocity ratio $\alpha=U/W$, and the cross-stream Reynolds number $\mathrm{Re}=Ud/\nu$, where ν is the kinematic viscosity.

For $\alpha\leqslant O(1)$, corresponding to moderate and large values of the yaw angle, the terms in (2) involving z-derivatives are negligible provided $\varepsilon\ll\alpha$. When this condition is satisfied, we can construct a perturbation solution of the form

$$u(x,y,z,t)=u_0(x,y,t)+\varepsilon u_1(x,y,z,t)+O(\varepsilon^2), \tag{3}$$

and similarly for the other variables, where the quasi-two-dimensional approximation appears as the leading-order term. This perturbation solution exhibits a singularity as the zero-yaw ($\alpha\to\infty$) case is approached due to blowup of the axial pressure gradient term in (2b). The case with small yaw angles can be handled using an alternative asymptotic series of the form

$$u(x,y,z,t)=u_0(x,y,t)+(1/\alpha)u_1(x,y,z,t)+O(1/\alpha)^2. \tag{4}$$

This case yields the quasi-two-dimensional approximation as a leading-order term in the perturbation solution provided $\varepsilon\ll 1$. It is of interest that with the nondimensionalization (1), the ratio W/U is eliminated from the governing equations for the quasi-two-dimensional theory, leaving the cross-stream Reynolds number Re as the only dimensionless parameter.

3 Governing Equations

In the quasi-two-dimensional idealization, the velocity and vorticity fields each have three nonzero components, but all gradients in the axial (z) direction vanish. Denoting the Cartesian velocity components by (u,v,w), the three components of vorticity are

$$\omega_x=\partial w/\partial y,\quad \omega_y=-\partial w/\partial x,\quad \omega_z=\partial v/\partial x-\partial u/\partial y. \tag{5}$$

The velocity components can be expressed in terms of the vorticity components using the Biot-Savart integral as

$$u(x,y,t)=-\frac{1}{2\pi}\int_A\frac{(y-y')\omega_z'}{(x-x')^2+(y-y')^2}da', \tag{6a}$$

$$v(x,y,t)=\frac{1}{2\pi}\int_A\frac{(x-x')\omega_z'}{(x-x')^2+(y-y')^2}da', \tag{6b}$$

$$w(x,y,t)=-\frac{1}{2\pi}\int_A\frac{(x-x')\omega_y'-(y-y')\omega_x'}{(x-x')^2+(y-y')^2}da', \tag{6c}$$

where A denotes an arbitrary cross-section of the flow in a plane $z=\text{const}$. Equations (6a) and (6b) are the standard integrals for velocity components in a two-dimensional flow, such that the cross-stream velocity components u and v depend only on the axial vorticity ω_z. The axial velocity w depends only on the cross-stream vorticity components ω_x and ω_y.

The vorticity transport equation in the quasi-two-dimensional approximation for a uniform-density incompressible fluid is

$$\frac{\partial \boldsymbol{\omega}}{\partial t} = \nabla \times (\mathbf{u} \times \boldsymbol{\omega}) + \frac{1}{\mathrm{Re}} \nabla^2 \boldsymbol{\omega}. \tag{7}$$

The vorticity stretching term vanishes for the z-component of the vorticity transport equation after using (5), giving

$$\frac{\partial \omega_z}{\partial t} = -\nabla \cdot (\omega_z \mathbf{u}) + \frac{1}{\mathrm{Re}} \nabla^2 \omega_z . \tag{8}$$

Equation (8) is an advection-diffusion equation and has the same form as the standard two-dimensional vorticity transport equation, such that the axial vorticity ω_z is independent of the axial velocity w.

4 Computational Method

The computations are performed using a quasi-two-dimensional version of the tetrahedral vorticity element (TVE) method described by Marshall et al. [12] with fixed (Eulerian) computational points. In this method, the Biot-Savart integral (6) is computed by interpolating the vorticity field using triangular elements that connect the computational points. The integration method is adjusted to yield optimal computation time while maintaining a prescribed accuracy. For a triangular element m near a point $\mathbf{x}$ where the velocity is evaluated, the contribution of the element to the Biot-Savart integral is computed using Gaussian quadratures, with either 1 or 4 quadrature points depending on the distance of the triangular element from $\mathbf{x}$. The contribution of sufficiently distant elements is computed using a $O(N \ln N)$ box-point multipole expansion acceleration method with Clarke-Tutty [13] type adaptive box structure. The acceleration method is optimized using an analytic error estimate similar to that of Salmon and Warren [14].

The vorticity transport equation is evolved in time using a second-order predictor-corrector algorithm. The spatial derivatives in the vorticity transport equation are computed using a second-order moving least-squares procedure, [15]. In this method the derivative of a function $f(\mathbf{x})$ at a point $\mathbf{x}_m$ is obtained by fitting a quadratic polynomial to the value of $f(\mathbf{x})$ at computational points near $\mathbf{x}_m$ using a least-square procedure. The first and second derivatives of $f(\mathbf{x})$ at $\mathbf{x}_m$ are obtained by differentiating the quadratic polynomial.

The vorticity field is discretized using an unstructured, fixed mesh formed of near-surface points and outer points. The near-surface points lie in a series of 25 layers of staggered points surrounding the cylinder, with 50 points in each layer and a distance of 0.0125 separating each layer. The near-surface points are embedded in a rectangular array of ''outer'' points formed of a set of 81 staggered rows consisting of 251 points each. Triangular elements are formed using a fast Delauney trangularization method similar to that described by Borouchaki and Lo [16]. Since the velocity is obtained by solution of the Biot-Savart integral, the mesh is required only to cover the region with significant vorticity. A closeup view of the mesh around the cylinder is shown in Fig. 2.

A zero-vorticity boundary condition is imposed on the upstream and two lateral sides of the mesh by setting the vorticity equal to zero at the first three points along each of these boundaries. An outflow boundary condition $\partial \boldsymbol{\omega}/\partial t = -U(\partial \boldsymbol{\omega}/\partial x)$ is prescribed at the downstream boundary. The grid is initiated just upstream of the cylinder, as shown in Fig. 2, and the outflow boundary is located at $x = 12$.

The vorticity boundary condition on the cylinder surface is set by computing at each time-step the vortex sheet strength $\boldsymbol{\gamma}_m$ at a point $\mathbf{x}_m$ due to boundary slip. The vorticity within the vortex sheet in a length l_m of the boundary surrounding $\mathbf{x}_m$ is distributed into the flow via a combination of viscous diffusion normal to the boundary and direct transport to triangular elements with nodal

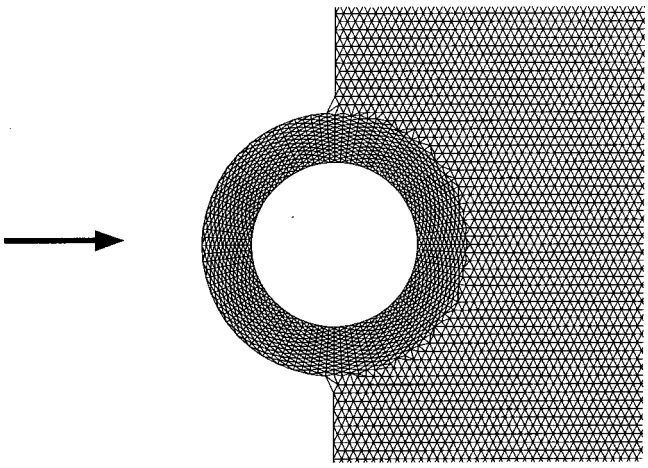

Fig. 2 Mesh used for discretization of the vorticity field near the cylinder

points on the boundary by change in the surface vorticity. If A_m is one-third of the area of all triangular elements attached to the boundary at a point m and $\mathbf{n}$ is the outward unit normal of the boundary at this point, the boundary vorticity balance can be expressed as

$$\boldsymbol{\gamma}_m l_m = A_m [\boldsymbol{\omega}(\mathbf{x}_m, t+\Delta t) - \boldsymbol{\omega}(\mathbf{x}_m, t)] - \frac{1}{\mathrm{Re}} (\mathbf{n} \cdot \nabla) \boldsymbol{\omega}(\mathbf{x}_m, t+\Delta t). \tag{10}$$

The balance equation (10) is solved iteratively, using the moving least-squares method for differentiation, and converges to a relative error of less than 10^{-4} in two to three iterations.

The computation is initiated by prescribing a Gaussian vorticity distribution with e-fold decay distance 0.1 over a layer of thickness 0.3 outside of the cylinder in both the axial and surface tangent direction. The strength of this vorticity layer was initial set using the exact potential flow solution for cylinder flow, and then refined using an iterative method such that the surface slip velocity is less than 1% of the freestream velocity.

5 Computational Results for Cross-Stream Flow

In the quasi-two-dimensional idealization, the pressure p and the cross-stream velocity components u and v vary only as functions of axial vorticity ω_z, which evolves according to the same equation as in a purely two-dimensional flow. These quantities are therefore independent of the axial flow. The computed results at $\mathrm{Re} = 300$ exhibit the usual Kárman vortex street wake in the cross-stream flow field. The slight downward drift of vortices on the right-hand side of the figure is due to the truncation of the vortex street by the presence of the outflow boundary at $x = 12$.

The drag and lift coefficients on the cylinder, defined as the force component per unit cylinder length in the x and y-directions, respectively, divided by $\rho U^2 d/2$, are plotted as functions of time in Fig. 3 for cases with $\mathrm{Re} = 100$ and 300. The initial value of the drag coefficient is dependent on the prescribed initial boundary layer thickness, and therefore has little relevance. The drag coefficient values quickly approach to close to an asymptotic value, about which they exhibit small oscillations due to the periodic vortex shedding. Reference experimental values of the time-averaged drag coefficients from Schlichting [17] are indicated by dashed lines in Fig. 3. The drag coefficient for the $\mathrm{Re} = 300$ case agrees very well with the reference data, but that for the $\mathrm{Re} = 100$ case is about 20% higher than the experimental value. Reference experimental values for lift coefficient amplitude are observed to scatter widely in the range 0.35–0.8 for Reynolds numbers from in this range, [18]. The computed lift coefficients have oscillation amplitudes in this range, with computed amplitude val-

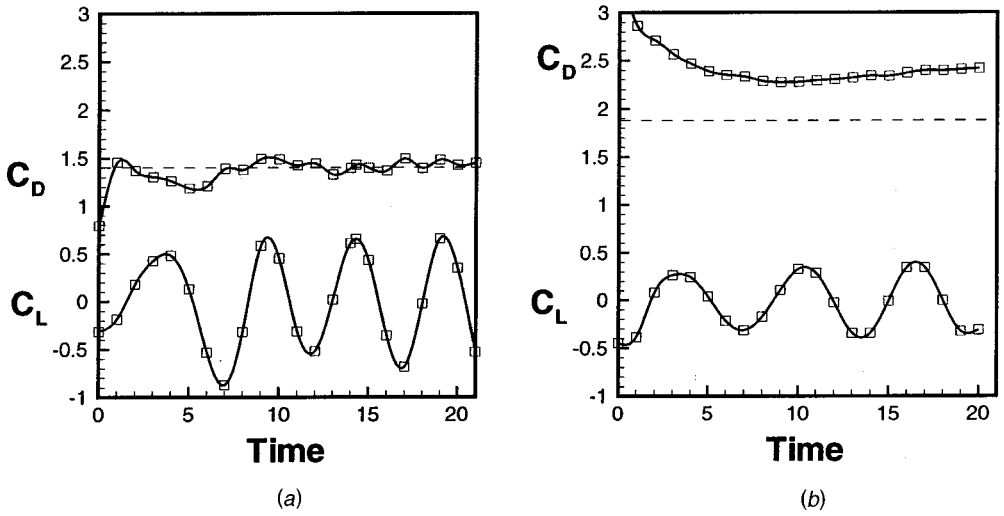

Fig. 3 Time-variation of drag and lift coefficients for (*a*) Re=300 and (*b*) Re=100. Reference drag coefficients compiled by Schlichting [17] are indicated by dashed lines.

ues 0.4 ± 0.1 and 0.7 ± 0.1 for Re=100 and 300, respectively. Experimental values of the Strouhal number for vortex shedding obtained from the data compilation of Fleischmann and Sallet [18] are 0.15 ± 0.02 for Re=100 and 0.21 ± 0.01 for Re=300. The computed Strouhal numbers are obtained by taking the reciprocal of the period for oscillation of the lift coefficient in Fig. 3, and are found to match nearly exactly to the reference data. A summary showing the comparison between the computed values of reference data for force coefficients and Strouhal number is given in Table 1.

An assessment of the sensitivity of the computations to choice of grid and time-step size was performed by performing a "coarse" computation of the Re=300 case using half as many computational points and twice the time step as used in the "high-resolution" computation reported previously. The average drag coefficient, the lift coefficient amplitude, and the Strouhal number for the coarse computation are reported in Table 1, and are found to be within the data uncertainty of those obtained for the high-resolution computation. The uncertainty in the computational data results from slight variation in force magnitudes between vortex shedding cycles. These results indicate that the computational results are not sensitive to choice of grid spacing or time-step.

6 Computational Results for Axial Flow

In the quasi-two-dimensional theory, the axial velocity is governed by an advection-diffusion equation of the same form as Eq. (8) that governs evolution of the axial vorticity. Since both production of the axial vorticity and the zero value of the axial velocity occur on the cylinder boundary and the two quantities are governed by the same equation, it is not surprising that regions of significant axial velocity deficit $W-w$ coincide with regions of significant axial vorticity magnitude. For instance, Fig. 4 shows contours of the axial vorticity, the cross-stream vorticity magnitude $\omega_C=\sqrt{\omega_x^2+\omega_y^2}$, and the axial velocity for the case Re=300 at a time near the end of the computation. The cross-stream vorticity is ejected from the cylinder boundary layer in thin sheets, which wrap around the Kárman vortices over a downstream distance of about five cylinder diameters, inducing an axial flow within the Kárman vortices that opposes the direction of the free-stream axial flow. The axial velocity deficit within the Kárman vortices varies from about 30% to 20% of the free-stream axial velocity W in the computed flow region, although the axial velocity deficit would be expected to continue to gradually diffuse and decrease in magnitude with downstream distance. Because the cross-stream flow is independent of the axial flow and the only dimensionless parameter that affects the axial flow is the cross-stream Reynolds number Re, this result holds for all values of the cylinder axial flow speed W. Computations with Re=100 exhibit similar results.

A plot of the cross-stream vorticity magnitude and the axial velocity contours within the near-wake region is given in Fig. 5 at two stages during the vortex shedding cycle. The vortex lines of the cross-stream vorticity field are plotted in Fig. 6 for the case shown in Fig. 5 for time $t=10$. The axial flow boundary layer is observed to thin on the upstream side of the cylinder and to thicken and separate on the downstream side. This effect is also evidenced in Fig. 7, in which the cross-stream vorticity magnitude on the cylinder surface is plotted as a function of azimuthal angle for both the Re=100 and 300 cases. Figure 7 exhibits high values of cross-stream vorticity in the thin boundary layer region near the front of the cylinder and low values of cross-stream vorticity near the rear of the cylinder. As shown in Figs. 5 and 6, regions of high axial velocity protrude from the cylinder shoulders due to advection by the separating cross-stream boundary flow. The associated cross-stream vorticity field exhibits a pair of thin sheets that trail from the cylinder near both the top and bottom shoulders, coin-

Table 1 Comparison of computational results with reference experimental data compiled by Fleischmann and Sallet [18].

Flow Measure	Experiment Re=100	Computation Re=100	Experiment Re=300	Computation Re=300	Coarse Computation Re=300
$\overline{C_D}$	1.9 ± 0.1	2.4 ± 0.1	1.4 ± 0.1	1.4 ± 0.1	1.4 ± 0.1
$C_{L_{\text{amp}}}$	0.6 ± 0.25	0.4 ± 0.1	0.6 ± 0.25	0.7 ± 0.1	0.6 ± 0.1
St	0.15 ± 0.02	0.15 ± 0.01	0.21 ± 0.01	0.20 ± 0.01	0.21 ± 0.01

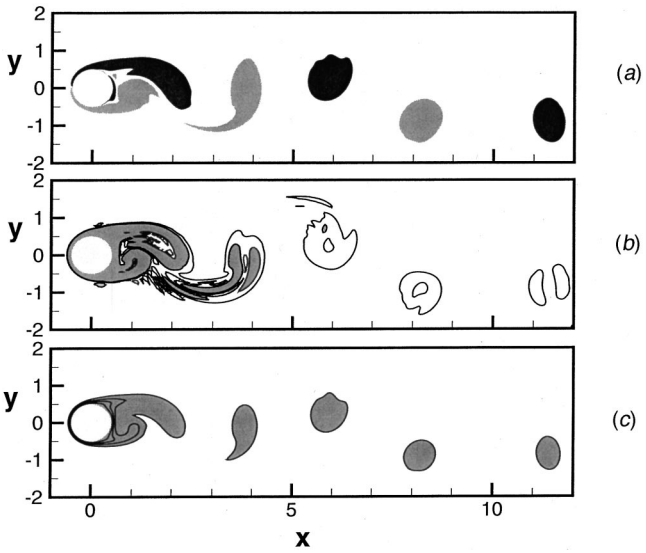

Fig. 4 Contours of (*a*) axial vorticity, (*b*) cross-stream vorticity magnitude $\omega_C=\sqrt{\omega_x^2+\omega_y^2}$, and (*c*) axial velocity in the cylinder wake for Re=300 at time $t=21$. In (*a*), regions are shaded black for $\omega_z<-1.2$ and gray for $\omega_z>1.2$. In (*b*), contours are drawn for $\omega_c=0.25$ and 0.50, and gray shading indicates $\omega_C>0.50$. In (*c*), contours are drawn for $w=0.225$, 0.45, 0.675, and 0.9, and gray shading indicates $w<0.9$.

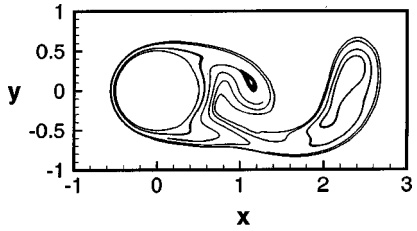

Fig. 6 Vortex lines of the cross-stream vorticity field for a case with $t=10$, corresponding to the first plot in Fig. 5(*a*)

ciding with the shear layers of the axial velocity protrusions. These sheets of cross-stream vorticity wrap around the near-wake vortices.

In the quasi-two-dimensional theory, there can be no generation of cross-stream vorticity on the cylinder surface, but rather all cross-stream vorticity present in the flow arises from advection, stretching, and diffusion of the ambient cross-stream vorticity. This assertion can be proved by writing the rate of change of vorticity in the area A occupied by the fluid, by integrating the vorticity equation over A and using the identity $\nabla^2\boldsymbol{\omega}=-\nabla\times(\nabla\times\boldsymbol{\omega})$, as

$$\rho\frac{d}{dt}\int_A \boldsymbol{\omega}da=-\int_C \mathbf{n}\times(\mathbf{u}\times\boldsymbol{\omega})dl+\frac{1}{\mathrm{Re}}\int_C \mathbf{n}\times(\nabla\times\boldsymbol{\omega})dl, \tag{11}$$

where C denotes the cylinder surface, dl is an element of length on C, and $\mathbf{n}=\mathbf{e}_r$ is a unit vector in the radial direction. Since $\mathbf{u}$ vanishes on the cylinder surface, the first term on the right-hand side of (11) also vanishes. The radial component of the last term in (11) vanishes since $\mathbf{n}$ is oriented in the radial direction. The azimuthal component of (11) is

$$\rho\frac{d}{dt}\int_A \omega_\theta da=\frac{1}{\mathrm{Re}}\int_C(\nabla\times\boldsymbol{\omega})_z dl. \tag{12}$$

The Navier-Stokes equation evaluated on the cylinder surface takes the form

$$\nabla p=-\frac{1}{\mathrm{Re}}\nabla\times\boldsymbol{\omega}. \tag{13}$$

The z-component of (13) vanishes since the pressure has zero axial gradient, so (12) indicates that the integral of ω_θ over the

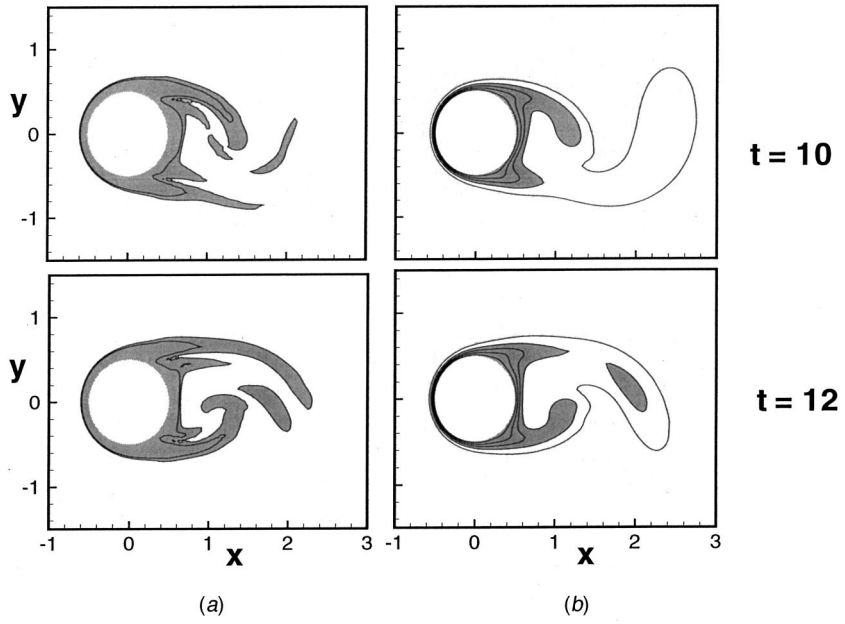

Fig. 5 Near-field of the cylinder wake showing (*a*) cross-stream vorticity magnitude and (*b*) axial velocity at two different times during the wake oscillation cycle. In (*a*), contours are shown for $\omega_C=1$ and 2, and gray shading indicates regions with $\omega_C>1$. In (*b*), contours are shown for $w=0.1$, 0.3, 0.5, 0.7, and 0.9, and gray shading indicates regions with $w<0.7$.

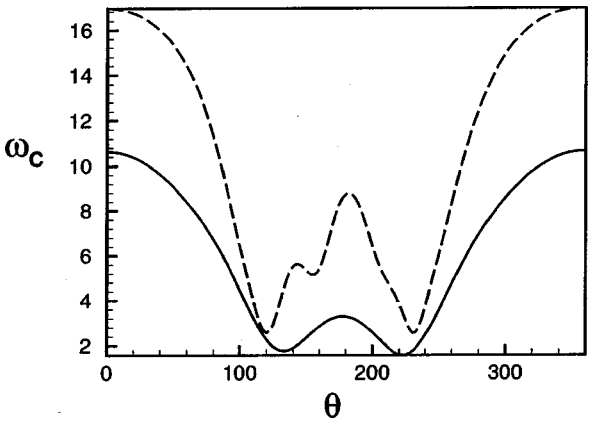

Fig. 7 Variation of axial force coefficient with time for cases with Re=100 (solid curve) and Re=300 (dashed curve)

flow is invariant. Furthermore, since the integrand of the integral on the right-hand side of (12) vanishes for any part of C, there can be no normal flux of azimuthal vorticity from any part of the cylinder surface.

The fact that there is no generation of cross-stream vorticity from the cylinder surface suggests that the thin boundary layer of axial velocity on the upstream side of the cylinder, which dominates the axial shear force on the cylinder, behaves in a manner similar to a Burger's vortex sheet, [19]. The thickness δ of the axial flow boundary layer is determined by a balance between stretching of the cross-stream vorticity along the cylinder surface by the cross-stream flow and diffusion normal to the cylinder surface, which yields $\delta \sim \mathrm{Re}^{-1/2}$. This estimate, together with the restriction $\omega_\theta \delta \sim 1$, predicts an increase of cross-stream vorticity magnitude at the cylinder leading edge by a factor of 1.7 as the Reynolds number increases from 300 to 100, whereas the computed value shown in Fig. 7 increases by a factor of 1.6.

The axial force coefficient is given by

$$C_A \equiv \frac{A}{\frac{1}{2}\rho U W(\pi d)} = -\frac{2}{\pi\,\mathrm{Re}} \int_C \omega_\theta dl, \tag{14}$$

where A is the axial force per unit cylinder length. A plot of the variation of C_A with time is given in Fig. 8. There is an initial transient that depends on the initial boundary layer thickness, after which C_A decreases slowly with time for the Re=100 case and appears to reach an asymptotic value for the Re=300 case. As

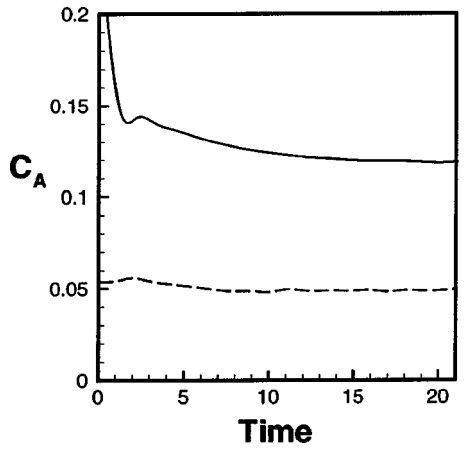

Fig. 8 Variation of cross-stream vorticity magnitude on the cylinder surface as a function of azimuthal angle for Re=100 (solid curve) and Re=300 (dashed curve)

shown in Fig. 7, the surface vorticity increases with increase in cross-stream Reynolds number. However, the division by Re on the right-hand side of (14) leads to a decrease in C_A with increase in Re.

The computations suggest two mechanisms by which the axial velocity might act to destabilize the vortex street for sufficiently large yaw angles, leading to possible breakdown of the Independence Principle. The first mechanism is Kelvin-Helmholtz-type instability of the cross-stream vorticity sheets in the cylinder near wake. This instability is partially inhibited by stretching from the cylinder wake vortices, [20], and by shear in the cross-stream plane acting orthogonally to the shear induced by the vortex sheet, [21], but for sufficiently large roll angles we anticipate formation of roller vortices in the vortex sheet that will wrap around and interact with the Kárman vortices.

The second mechanism is instability of the downstream Kárman vortices due to the presence of axial velocity deficit within the vortex cores. It is well known that axial flow in a vortex core can under certain conditions destabilize the vortex, [22]. A comprehensive mapping of the axial flow instability for both inviscid and viscous flow is given by Mayer and Powell [23]. The inviscid stability analysis indicates that a helical mode instability exists for $-1.5<q<0.074$, where $q=-\Gamma/2\pi a W_d$, with maximum instability growth rate at $q=-0.458$. Here Γ is the vortex circulation, a is the vortex core radius, and W_d is the maximum axial velocity deficit ($W_d \equiv W - w_{\mathrm{center}}$) within the vortex core. It is noted that for this value of q and $W_d>0$ only wake vortices with circulation of a positive sign will be unstable to the axial flow instability. The vortex circulation is proportional to Ud times the dimensionless time period of vortex shedding, $1/St$. By fitting a Gaussian vorticity distribution to the far wake vortices computed for the Re =300 case, we find $\Gamma/Ud \cong 0.5/St$ and $a/d \cong 0.5$. Using the computational estimate $W_d \cong 0.2W$ for the vortex axial velocity deficit gives $q \cong -4.0U/W$. This estimate indicates that vortex axial velocity deficit will lead to instability of the Kárman vortices for $W/U>2.7$ (or $\phi>70$ deg), with maximum instability occurring at $W/U=8.7$ (or $\phi \cong 83$ deg). The axial velocity deficit is about 50% greater than this far-wake estimate at the location where the vortices first form in the near wake, which yields a critical near-wake yaw angle of $\phi \cong 61$ deg and maximum instability at $\phi \cong 80$ deg.

Inclusion of viscous effects in the stability theory both inhibits the inviscid instability modes and introduces new viscous modes with longer axial wavelength than the dominant inviscid mode, [24]. These new viscous modes have growth rates of about two orders of magnitude smaller than the most unstable inviscid mode, and would hence be dominated by the inviscid instability modes in the current problem. Sufficiently high viscosity can eliminate the inviscid instability, where for helical-mode perturbations Mayer and Powell [23] report that instability is eliminated for axial-flow Reynolds numbers below the critical value 13.9. For the current study the axial-flow Reynolds number at the condition of maximum inviscid vortex instability is $W_d d/\nu \cong 0.2(W/U)\mathrm{Re} \cong 0.2 \times 8.7 \times 300 = 522$, for which case the analyses of Mayer and Powell [23] and Khorrami [24] suggest that viscosity will have a small effect on the underlying inviscid instability for the helical-mode perturbation.

The effect of combination of the axial flow vortex instability with the three-dimensional instability of a vortex street, [25], is a topic requiring further investigation. It should be kept in mind that the vortex axial velocity deficit will increase with increase in Reynolds number, causing the limiting yaw angles at instability onset and maximum instability to be somewhat smaller than the estimates given above for flows with substantially higher Reynolds numbers.

7 Conclusions

A study is reported of the wake dynamics of a yawed circular cylinder in the quasi-two-dimensional idealization. A perturbation analysis is used to motivate the restriction that, for finite-length

cylinders at moderate and large yaw angles, the quasi-two-dimensional approximation is valid at positions L along the cylinder where the ratio of cylinder diameter to L is much smaller than the ratio of normal to axial freestream velocity components. The equations of motion in the quasi-two-dimensional theory can be scaled to eliminate dependence on the yaw angle, such that the cross-stream Reynolds number is the only dimensionless parameter occurring in the governing equations. The cross-stream velocity field is determined by the axial vorticity and is the same as for a purely two-dimensional flow. Both the axial vorticity and the axial velocity fields are governed by an advection-diffusion equation. The cross-stream vorticity components are controlled by a combination of diffusion and advection and stretching by the cross-stream flow field, with no generation of cross-stream vorticity at the cylinder surface. The cross-stream vorticity is shed in thin sheets both above and below the cylinder, which wrap around the Kárman vortices in the cylinder wake. The resulting induced axial velocity deficit within the Kárman vortex cores measures between 20–30% of the free-stream axial flow speed W within the computational region, which spans about 10 cylinder diameters. Both the cross-stream vortex sheets in the cylinder near-wake region and the axial flow deficit within the downstream vortex cores may lead to instability of the vortex street and breakdown of the Independence Principle at large yaw angles for fully three-dimensional flows.

Acknowledgment

This project was supported by the Office of Naval Research under grant number N00014-01-1-0015. Dr. Thomas Swean is the program manager.

References

[1] King, R., 1977, "Vortex Excited Oscillations of Yawed Circular Cylinders," ASME J. Fluids Eng., **99**, pp. 495–502.
[2] Ramberg, S., 1983, "The Effects of Yaw and Finite Length Upon the Vortex Wakes of Stationary and Vibrating Circular Cylinders," J. Fluid Mech., **128**, pp. 81–107.
[3] Relf, E. F., and Powell, C. H., 1917, "Tests on Smooth and Stranded Wires Inclined to the Wind Direction and a Comparison of the Results on Stranded Wires in Air and Water," British A.R.C. R+M Report 307.
[4] Hanson, A. R., 1966, "Vortex Shedding From Yawed Cylinders," AIAA J., **4**(4), pp. 738–740.
[5] Van Atta, C. W., 1968, "Experiments in Vortex Shedding From Yawed Circular Cylinders," AIAA J., **6**(5), pp. 931–933.
[6] Bursnall, W. J., and Loftin, L. K., 1951, "Experimental Investigation of the Pressure Distribution About a Yawed Circular Cylinder in the Critical Reynolds Number Range," NACA TN 2463.
[7] Friehe, C., and Schwarz, W. H., 1960, "Deviations From the Cosine Law for Yawed Cylindrical Anemometer Sensors," ASME J. Appl. Mech., **35**, pp. 655–662.
[8] Thomson, K. D., and Morrison, D. F., 1971, "The Spacing, Position and Strength of Vortices in the Wake of Slender Cylindrical Bodies at Large Incidence," J. Fluid Mech., **50**, pp. 751–783.
[9] Lamont, P. J., and Hunt, B. L., 1976, "Pressure and Force Distributions on a Sharp-Nosed Circular Cylinder at Large Angles of Inclination to a Uniform Subsonic Stream," J. Fluid Mech., **76**, pp. 519–559.
[10] Snarski, S. R., and Jordan, S. A., 2001, "Fluctuating Wall Pressure on a Circular Cylinder in Cross-Flow and the Effect of Angle of Incidence," 2001 ASME Fluids Engineering Division Summer Meeting, New Orleans, LA, May 29–June 1.
[11] Moore, F. K., 1956, "Yawed Infinite Cylinders & Related Problems—Independence Principle Solutions," Adv. Appl. Mech., **4**, pp. 181–187.
[12] Marshall, J. S., Grant, J. R., Gossler, A. A., and Huyer, S. A., 2000, "Vorticity Transport on a Lagrangian Tetrahedral Mesh," J. Comput. Phys., **161**, pp. 85–113.
[13] Clarke, N. R., and Tutty, O. R., 1994, "Construction and Validation of a Discrete Vortex Method for the Two-Dimensional Incompressible Navier-Stokes Equations," Comput. Fluids, **23**(6), pp. 751–783.
[14] Salmon, J. K., and Warren, M. S., 1994, "Skeletons From the Treecode Closet," J. Comput. Phys., **111**, pp. 136–155.
[15] Marshall, J. S., and Grant, J. R., 1997, "A Lagrangian Vorticity Collocation Method for Viscous, Axisymmetic Flows With and Without Swirl," J. Comput. Phys., **138**, pp. 302–330.
[16] Borouchaki, H., and Lo, S. H., 1995, "Fast Delauney Triangularization in Three Dimensions," Comput. Methods Appl. Mech. Eng., **128**, pp. 153–167.
[17] Schlichting, H., 1979, *Boundary-Layer Theory*, McGraw-Hill, New York, p. 17.
[18] Fleischmann, S. T., and Sallet, D. W., 1981, "Vortex Shedding From Cylinders and the Resulting Unsteady Forces and Flow Phenomenon. Part I," Shock Vib. Dig., **13**(10), pp. 9–22.
[19] Burger, J. M., 1948, "A Mathematical Model Illustrating the Theory of Turbulence," Adv. Appl. Mech., **1**, pp. 171–199.
[20] Dhanak, M. R., 1981, "The Stability of an Expanding Circular Vortex Layer," Proc. R. Soc. London, Ser. A, **375**, pp. 443–451.
[21] Dritschel, D. G., 1989, "On the Stabilization of a Two-Dimensional Vortex Strip by Adverse Shear," J. Fluid Mech., **206**, pp. 193–221.
[22] Lessen, M., Singh, P. J., and Paillet, F., 1974, "The Instability of a Trailing Line Vortex. Part 1. Inviscid Theory," J. Fluid Mech., **63**, pp. 753–763.
[23] Mayer, E. W., and Powell, K. G., 1992, "Viscous and Inviscid Instabilities of a Trailing Vortex," J. Fluid Mech., **245**, pp. 91–114.
[24] Khorrami, M. R., 1991, "On the Viscous Modes of Instability of a Trailing Line Vortex," J. Fluid Mech., **225**, pp. 197–212.
[25] Robinson, A. C., and Saffman, P. G., 1982, "Three-Dimensional Stability of Vortex Arrays," J. Fluid Mech., **125**, pp. 411–427.

Mario F. Trujillo
Los Alamos National Laboratory,
Theoretical Division,
T-3 MS B285,
Los Alamos, NM 87545
e-mail: mft@lanl.gov

Chia-fon F. Lee
Department of Mechanical and Industrial Engineering,
140 Mechanical Engineering Building,
1206 W. Green Street,
Urbana, IL 61801
e-mail: cflee@uiuc.edu

Modeling Film Dynamics in Spray Impingement

A numerical and analytic study of film formation and evolution during spray impingement is presented. For the part of the film which excludes drop impact locations, the governing equations reduce to a convenient form that can be exploited using a Lagrangian particle method. At impingement points the source terms for mass and energy are calculated based on conservation principles and phenomenological results. It is shown that during the period where most of the film evolution takes place, the effect of gas shear and surface tension are negligible. Numerical testing is performed to ensure convergence. Comparisons to spray impingement experiments consisting of film extension and thickness measurements yield reasonable agreement with the exception of the shallow angle impingement case where it is suspected that the total mass deposited is overpredicted.
[DOI: 10.1115/1.1523064]

1 Introduction

Predicting the liquid film movement and the details concerning the mass distribution in the deposited film is of particular importance in spray impingement applications since it provides information such as the total surface area available for evaporation and the extent of wetting. Two methods presently exist for simulating the film dynamics. The first one is based on applying the conservation laws employing a control volume balance (Stanton et al. [1], Ahmadi-Befrui et al. [2], and Foucart et al. [3]) or integrating the conservation equations along the coordinate normal to the surface and employing a finite volume method to solve the resulting equations (Bai and Gosman [4]). The trouble arising from the numerical diffusion of the film edge is a major hurdle to this approach, but it can most likely be overcome with high-resolution methods. Alternatively, another approach used is a particle-based formulation such as the one employed by O'Rourke and Amsden [5,6] which tackles the film edge diffusion problem.

The film inertia has commonly been assumed to be negligible in some of these studies. But this assumption has been shown to be valid only under special conditions as reported by Bai and Gosman [4] in their investigation of the criteria for local equilibrium. Therefore, in general the unsteady and convective terms should be included in the film equations.

It is common to find in the literature ([1–6]) spray impingement source terms for mass, momentum, and energy directly implemented into the governing equations. But these equations are arrived at by making some crucial assumptions, e.g., neglect of surface tension, very small film surface disturbances, etc . . . , that are violated at impingement sites. Therefore in order to have a consistent formulation between the assumptions made and the governing equations employed we treat these two regions of the film separately. In the region excluding impingement sites we begin with the Navier-Stokes equations and after making certain arguments about the physical characteristic of the film we reduce these to a convenient form which is readily solved in a Lagrangian-based scheme. A nondimensional criteria for neglecting surface tension is presented, which shows that as the film velocity decays to zero it becomes increasingly hard to neglect surface tension. Estimates show that gas shear has a negligible effect excluding cases where high velocity gas flows are present. The treatment given at impingement sites is based on energy conservation of drop impact events and on experimental correlations. A number of numerical tests are performed to ensure numerical convergent results of the particle method. The model is then applied to spray impingement cases and the predictions compared to experiments.

Contributed by the Fluids Engineering Division for publication in the JOURNAL OF FLUIDS ENGINEERING. Manuscript received by the Fluids Engineering Division March 6, 2001, revised manuscript received July 26, 2002. Associate Editor: I. Celik.

2 Derivation of Film Equations

The film equations are derived in a region of the film which excludes locations where drop impact is occurring and hence is void of impingement source terms. As noted in the Introduction, some crucial assumptions do not hold in these locations. Treatment given at these impact sites is discussed in the numerical implementation section.

The velocity field $\mathbf{u}$ can be represented as $\mathbf{u}=u_1\mathbf{e_1}+u_2\mathbf{e_2}+u_3\mathbf{e_3}=u_s\mathbf{e_s}+u_3\mathbf{e_3}$, where $\mathbf{e_s}$ points in the direction of the film flow tangent to the surface and $\mathbf{e_3}$ or $\mathbf{n}$ is the outward normal to the surface. The coordinate system used is the Dupin coordinate system, [7], in which the corresponding metric coefficients are given by $(h_1,h_2,1)$ and the coordinates by $(\zeta_1,\zeta_2,\zeta_3)$. The gradient operator is split into a surface gradient and normal gradient, i.e., $\nabla=\nabla_s+\mathbf{e_3}\partial/\partial\zeta_3$ and the surface curvature J is given by

$$J=-\left(\frac{1}{h_1}\frac{\partial h_1}{\partial\zeta_3}+\frac{1}{h_2}\frac{\partial h_2}{\partial\zeta_3}\right). \tag{1}$$

For a Newtonian, incompressible fluid, continuity gives

$$\nabla\cdot\mathbf{u}=\nabla_s\cdot\mathbf{u_s}+\frac{\partial u_3}{\partial\zeta_3}-u_3J=0 \tag{2}$$

and momentum

$$\frac{\partial}{\partial t}(\mathbf{u_s}+\mathbf{u_3})+\left(\mathbf{u_s}\cdot\nabla_s+u_3\frac{\partial}{\partial\zeta_3}\right)(\mathbf{u_s}+\mathbf{u_3})$$
$$=-\frac{1}{\rho}\left(\nabla_s+\mathbf{e_3}\frac{\partial}{\partial\zeta_3}\right)p+\nu\left(\nabla_s^2+\frac{\partial^2}{\partial^2\zeta_3}-J\frac{\partial}{\partial\zeta_3}\right)(\mathbf{u_s}+\mathbf{u_3})+g\mathbf{e_g}. \tag{3}$$

To nondimensionalize these equations we introduce the film characteristic length and depth L and λ, respectively, where $L\gg\lambda$. Similarly the characteristic tangential velocity U is much greater than the corresponding value of the normal velocity w. These arguments are commonly referred to as the thin film assumptions in the literature. From these relative magnitudes, it is expected that derivatives along the normal coordinate are much greater than tangential derivatives. Consequently, the appropriate time scale should correspond to the momentum diffusion in the normal direction, i.e., λ^2/ν. The nondimensional quantities that are introduced are

$$\nabla_s = \frac{\nabla_s^*}{L}, \quad \frac{\partial}{\partial \zeta_3} = \frac{1}{\lambda}\frac{\partial}{\partial \zeta_3^*}, \quad \frac{\partial}{\partial t} = \frac{\nu}{\lambda^2}\frac{\partial}{\partial t^*},$$

$$\mathbf{u_s} = \mathbf{u_s^*} U, \quad \mathbf{u_3} = \mathbf{u_3^*} w, \quad \mathrm{Re}_\lambda = \frac{\rho U \lambda}{\mu}. \tag{4}$$

Since the pressure spike, which occurs at each drop impact event during spray impingement, is heavily localized around the impingement site, [8], and we are excluding this region in the analysis for the moment, the pressure gradient term is dropped in the momentum equation. Nondimensionalizing the governing equations gives

$$\nabla_s^* \cdot \mathbf{u_s^*} + \frac{L}{\lambda}\frac{w}{U}\frac{\partial u_3^*}{\partial \zeta_3^*} - LJ\frac{w}{U}u_3^* = 0, \tag{5}$$

for continuity and

$$\frac{\partial \mathbf{u_s^*}}{\partial t^*} + \frac{w}{U}\frac{\partial \mathbf{u_3^*}}{\partial t^*}$$

$$\mathrm{Re}_\lambda\left[\frac{\lambda}{L}(\mathbf{u_s^*}\cdot\nabla^*\mathbf{u_s^*}) + \frac{w\lambda}{UL}(\mathbf{u_s^*}\cdot\nabla^*\mathbf{u_3^*}) + \frac{w}{U}u_3^*\frac{\partial \mathbf{u_s^*}}{\partial \zeta_3^*} + \left(\frac{w}{U}\right)^2 u_3^*\frac{\partial \mathbf{u_3^*}}{\partial \zeta_3^*}\right]$$
$$= \left[\left(\frac{\lambda}{L}\right)^2\nabla_s^{*2} + \frac{\partial^2}{\partial^2\zeta_3^*} - \lambda J\frac{\partial}{\partial \zeta_3^*}\right]\left(\mathbf{u_s^*} + \frac{w}{U}\mathbf{u_3^*}\right) + \frac{\lambda^2 g}{\nu U}\mathbf{e_g} \tag{6}$$

for momentum. We will restrict our attention to surfaces that are sufficiently smooth for which LJ is at most $O(1)$. For the type of applications that we consider here, which are geared towards injection of liquid by means of pressure atomizers, the typical film velocity is of $O(10)$-$O(1)$ m/s. Velocities that are much lower than $O(1)$ m/s do not account for any substantial displacement of the film in the time frame characteristic of impingement duration. (As will be shown later, as the surface velocity decays to zero it becomes increasingly difficult to neglect surface tension effects.) The characteristic length of the film is $O(10^{-2})$ m and the film depth ranges between $O(10^{-5})$ and $O(10^{-4})$ m. The viscosity is $O(10^{-3})$ kg/m-s and the density is $O(10^3)$ kg/m^3. Overall this results in the following ranges for the nondimensional quantities: Re_λ varies between $O(10)$ and $O(10^3)$, λ/L varies between $O(10^{-3})$ and $O(10^{-2})$, and the factor $(\lambda^2 g)/\nu U$ appearing in the body force is at most $O(10^{-1})$. Therefore, if we consider only the dominant terms, continuity results in

$$\nabla_s \cdot \mathbf{u_s} + \frac{\partial u_3}{\partial \zeta_3} = 0 \tag{7}$$

and momentum

$$\frac{\partial \mathbf{u_s}}{\partial t} + \mathbf{u_s}\cdot\nabla_s\mathbf{u_s} + u_3\frac{\partial \mathbf{u_s}}{\partial \zeta_3} = \nu\frac{\partial^2 \mathbf{u_s}}{\partial^2 \zeta_3}. \tag{8}$$

Thus we see that under the aforementioned conditions, which again excludes the impaction sites, the film momentum equation to leading order is an unsteady-convective transport equation with wall-friction and negligible body forces.

We would like to express the momentum conservation, Eq. (8), in Lagrangian form in anticipation of the numerical implementation which utilizes a particle method. We have then

$$\frac{du_s}{dt} = \nu\frac{\partial^2 u_s}{\partial^2 \zeta_3}, \tag{9}$$

with the following boundary and initial conditions

$$u_s(0,t) = 0, \quad \frac{du_s(h(\mathbf{x}_p),t)}{d\zeta_3} = \gamma, \quad \text{and} \quad u_s(\zeta_3,0) = \varphi(\zeta_3). \tag{10}$$

Here $h(\mathbf{x}_p)$ is the film height at the Lagrangian particle location. The solution is

$$u_p(\zeta_3,t) = \sum_{n=0}^{\infty} C_n \exp\left(-\frac{\nu}{[h(\mathbf{x}_p)]^2}\beta_n^2 t\right)\sin\left(\frac{\beta_n\zeta_3}{h(\mathbf{x}_p)}\right) + \gamma\zeta_3, \tag{11}$$

with

$$C_n = 2\int_0^1 \varphi(zh(\mathbf{x}_p)\sin(\beta_n z)dz - 2\int_0^1 \gamma h(\mathbf{x}_p) z\sin(\beta_n z)dz, \tag{12}$$

where $z = \zeta_3/h(\mathbf{x}_p)$ and $\beta_n = \pi/2 + n\pi$.

2.1 Effect of Induced Gas Shear. The boundary condition at the top of the film, i.e., at the gas-liquid interface, is the continuity of the shear stress as one crosses the interface

$$\frac{\partial u_s^l}{\partial \zeta_3} = \frac{\mu^g}{\mu^l}\frac{\partial u_s^g}{\partial \zeta_3}, \tag{13}$$

which is valid for a constant surface tension coefficient ($\nabla_s\sigma = \mathbf{0}$). The subscripts g and l denote, respectively, the gas and liquid side. Because of the vast difference in magnitude of the gas and liquid viscosity and the very thin thickness for the film, it is expected that the gas-induced shear would be negligible. To estimate this conjecture, consider for example the shear stress as a result of gas flow moving at 10 m/sec, 1 mm away from the wall, using for instance the wall functions presented in Ref. [9]. This gives a value for $\mu^g(\partial u_s)(\partial\zeta_3)^g$ of approximately 0.6 kg/m-sec^2, which corresponds to a velocity gradient at the liquid-gas interface, $(\partial u_s)(\partial\zeta_3)^l = \gamma$ of 600 1/sec.

To investigate the effect this has on the velocity solution, consider first Eq. (12), i.e., the calculation of the Fourier coefficient, C_n. The first term accounts for the initial velocity profile and is typically of $O(10^1) - O(10^0)$ m/s. Reminding ourselves that typical film heights in spray impingement applications are $O(10^{-5})$-$O(10^{-4})$ m, the second term which accounts for the velocity gradient imposed by the gas shear has a magnitude of $O(10^{-3})$-$O(10^{-2})$ m/s. Hence we can neglected it in the calculation of C_n. If we now look at the velocity solution given by Eq. (11), we see again that the second term accounting for shear can also be neglected. Therefore, the solution for film velocity shows that the effects of gas-induced shear stress can be safely ignored which translates to $\partial u_s(\zeta_3,t)/\partial\zeta_3 = 0$, and consequently the solution for the film velocity becomes

$$u_s(\zeta_3,t) = \sum_{n=0}^{\infty} A_n \exp\left(-\frac{\nu}{[h(\mathbf{x}_p)]^2}\beta_n^2 t\right)\sin\left(\frac{\beta_n\zeta_3}{h(\mathbf{x}_p)}\right), \tag{14}$$

where

$$A_n = 2\int_0^1 \varphi(zh(\mathbf{x}_p))\sin(\beta_n z)dz. \tag{15}$$

This equation is valid for most of the evolution of the film as a result of spray impingement. Once the film has sufficiently slowed down, e.g., $\ll 0(1)$m/s, or in the presence of fast moving gas streams, the huge difference in gas to liquid viscosities is not enough to cancel the effect of gas shear.

2.2 The Effect of Surface Tension. We have shown that the momentum equation to leading order is given by Eq. (8), which can be integrated over some arbitrary volume $\mathbb{V} = \mathbb{S}\times\lambda$ of the film that extends from the bottom to the top surface yielding

$$\rho \frac{d}{dt} \int_{\mathbb{V}} \mathbf{u}_s dV + \mu \int_{\mathbb{S}} \left. \frac{\partial \mathbf{u}_s}{\partial \zeta_3} \right|_{\zeta_3=0} dS = \mathbf{0}. \tag{16}$$

This equation shows that the film exists in balance between inertia and the wall friction force. Shrinking the volume to some cylinder of small radius ϵ, we have

$$-\frac{\rho}{t_c} U \pi \epsilon^2 \lambda + \mu \frac{U}{\lambda} \pi \epsilon^2 = 0, \tag{17}$$

where the negative sign is introduced to indicate a decrease in inertia with time. Recognizing that the characteristic time t_c is λ^2/ν, we can introduce it above to show that both the inertia and wall friction are expressed by $\mu(U/\lambda)\pi\epsilon^2$. If surface tension is to be neglected in the momentum balance of an arbitrary volume its contribution must be much smaller than $\mu(U/\lambda)\pi\epsilon^2$.

The surface tension force density can be described by the following integral: $\int_{\mathbb{A}_f} \sigma \mathbf{n} J(\mathbf{x}') \delta(x-x') dS(x)$, [10], where $\mathbb{A}_f$ is the gas-liquid interface of the film, [10], and $\delta(\mathbf{x}-\mathbf{x}')$ is a three-dimensional delta function. Integrating this quantity over the same volume $\mathbb{V}$ gives $\int_{\mathbb{S}} \sigma \mathbf{n} J(\mathbf{x}') dS(\mathbf{x}')$, and allowing this volume to shrink as before we get $\sigma \mathbf{n} \cdot \mathbf{e}_s J_s \pi \epsilon^2$. Here J_f is the local curvature of gas-liquid interface. Hence for surface tension to be neglected the following condition must be satisfied:

$$\mu \frac{U}{\lambda} \pi \epsilon^2 \gg \sigma(\mathbf{n} \cdot \mathbf{e}_s) J_f \pi \epsilon^2. \tag{18}$$

Since $\mathbf{n} \cdot \mathbf{e}_s = 1$ is the upper bound of the surface tension contribution, a more limiting condition is

$$\frac{\sigma J_f \lambda}{\mu U} \ll 1. \tag{19}$$

The most apparent implication of this equation is that for a flat or nearly flat film surface, we can neglect the effect of surface tension. In spray impingement, however, this condition is for the most part not met since the impact of numerous drops inevitably leads to surface disturbances. But as long as these disturbances are not too significant and the film velocity is sufficiently large, the neglect of surface tension can be justified. As the film velocity decays, however, it becomes increasingly difficult to ignore its effects. Fortunately, at this stage the film is not evolving as fast, such that the predictions of film extension are not affected drastically.

The modeling of film dynamics from spray impingement requires modeling of the incident spray and the associated gas flow, therefore, it is prohibitively expensive to compute a full three-dimensional simulation of the film and impingement events including the necessary calculation of the interface curvature essential in incorporating the surface tension force. It is for this reason that a two-dimensional model of the film, which cannot capture accurately the surface tension, is preferred. This analysis shows that for the major part of the film spreading period this approach is justified.

3 Numerical Implementation

For the numerical simulation of the film dynamics we employ a particle method. In this approach numerical particles are used to solve the governing equations and to represent local mass and momentum. For our particular application, we deviate from the classical particle methods in two aspects. First, the solution of the equations is not fully Lagrangian; we indirectly employ one grid-based parameter, namely the film thickness. Second, the equations are not solved on a grid and then interpolated back to the particles as in the particle-in-cell (PIC) method. In our work, the equations are solved on a particle basis employing an analytical solution. This solution depends on the value of the film thickness evaluated at the particle location, $h(\mathbf{x}_p)$, which is obtained from a cell-based film thickness as follows:

$$h(\mathbf{x}_p) = \sum_{\alpha} h(\mathbf{x}_\alpha) S(\mathbf{x}_p, \mathbf{x}_\alpha), \tag{20}$$

where the quantities with subscripts α and p denote cell and particle based quantities, respectively. The function $S(\mathbf{x}_p, \mathbf{x}_\alpha)$ is an interpolation kernel having the following properties:

$$\sum_{\alpha} S(\mathbf{x}, \mathbf{x}_\alpha) = 1$$

$$\int \int_{\alpha} S(\mathbf{x}, \mathbf{x}_\alpha) d\mathbf{x} = A_\alpha. \tag{21}$$

The surface area corresponding to the wetted area in a cell indexed by $\mathbf{x}_\alpha$ is denoted by A_α. The value for $h(\mathbf{x}_\alpha)$ is calculated directly from $h(\mathbf{x}_\alpha) = \mathbb{V}(\mathbf{x}_\alpha)/A(\mathbf{x}_\alpha)$, where $\mathbb{V}(\mathbf{x}_\alpha)$ is the liquid volume of film in cell $\mathbf{x}_\alpha$. In terms of film particle volume, $\mathbb{V}_p$, this gives

$$h(\mathbf{x}_\alpha) = \frac{\Sigma_p S(\mathbf{x}_\alpha, \mathbf{x}_p) \mathbb{V}_p}{A_\alpha}. \tag{22}$$

Substituting this expression into Eq. (20) gives the film thickness evaluated at the film particle location

$$h(\mathbf{x}_p) = \frac{\Sigma_\alpha [\Sigma_j S(\mathbf{x}_\alpha, \mathbf{x}_j) V_j] S(\mathbf{x}_p, \mathbf{x}_\alpha)}{A_\alpha}, \tag{23}$$

where the sum, j, is over all particles. In the present model $S(\mathbf{x}_\alpha, \mathbf{x}_j)$ takes the nearest-grid-point form, in which $S(\mathbf{x}_\alpha, \mathbf{x}_j) = 1$ if $\mathbf{x}_j$ lies in the cell indexed by $\mathbf{x}_\alpha$ and is assigned a zero value otherwise.

If m_p is the particle mass, its conservation equation states

$$\frac{dm_p}{dt} = \dot{M}_{\text{evap}}, \tag{24}$$

i.e., film particle mass decays with evaporation (evaporation effects are incorporated from the work of O'Rourke and Amsden [5]).

As the particle position evolves through time, it does so in discrete changes of position corresponding to the discretization in time. As a consequence the film thickness field also displays this discrete nature, which can be exploited by noting that within a given time interval $(t_i, t_i + dt)$ the local film thickness is constant (the subscript i is used to denote quantities evaluated at that particular time-step). Therefore, the evolution of the velocity profile at the particle location can be performed using Eqs. (14) and (15) and the final profile corresponding to $t_i + dt$ calculated. In the next time-step the final velocity profile of the previous time-step is used as initial conditions, $\varphi(\zeta_3)$, and the velocity Eq. (14) subsequently solved.

The description of the film velocity involves three dimensions, i.e., through the particle position on the surface $\mathbf{x}_p$ and ζ_3. This three-dimensional computation is prohibitively expensive to perform and is not justified with the level of assumptions incorporated into the present model. Therefore, the particle velocity is averaged over the normal coordinate ζ_3, giving

$$\vec{u_p^i} = \sum_{n=0}^{N} \frac{A_n^i}{\beta_n} \exp\left(-\frac{\nu}{[h^i(\mathbf{x}_p)]^2} \beta_n^2 t \right). \tag{25}$$

The summation in this equation is truncated, since good accuracy is achieved with only a few Fourier modes (shown in the results). Even though we numerically solve for an averaged solution, knowledge of the profile in the normal, ζ_3, direction is still needed. The velocity profile implemented in our model has a cubic form in the region occupied by the boundary layer, whose height is given by $l(\mathbf{x}_p)$, and has an undisturbed velocity V in the region bounded by $l(\mathbf{x}_p)$ and $h(\mathbf{x}_p)$. As the profile evolves with time, the boundary layer grows to fill the entire film thickness. The cubic form is given as $u_p(\zeta_3, t)/V = a\eta + b\eta^2 + c\eta^3$, where

$\eta = \zeta_3 / l(\mathbf{x}_p)$. Immediately this profile satisfies the no-slip boundary condition. The determination of the constants comes from the following three additional conditions, [11],

$$u_p(l,t) = U_o, \quad \frac{\partial u_p(l,t)}{\partial \zeta_3} = 0, \quad \text{and} \quad \frac{\partial^2 u_p(0,t)}{\partial^2 \zeta_3} = 0, \quad (26)$$

which give $a = 3/2$, $b = 0$, and $c = -1/2$. (The last condition above is obtained directly from Eq. (9) evaluated at $\zeta_3 = 0$.) The result is a film profile described as

$$u_p^i(\zeta_3, t) = \begin{cases} V^i, & h^i(\mathbf{x}_p) \geq \zeta_3 > l^i(\mathbf{x}_p) \\ \dfrac{V^i}{2}\left[3\left(\dfrac{\zeta_3}{l^i(\mathbf{x}_p)}\right) - \left(\dfrac{\zeta_3}{l^i(\mathbf{x}_p)}\right)^3\right], & l^i(\mathbf{x}_p) \geq \zeta_3. \end{cases} \quad (27)$$

In terms of the undisturbed velocity, V^i, and a nondimensional boundary layer height defined as the ratio of boundary layer height to film thickness, namely $\delta^i \equiv l^i(\mathbf{x}_p)/h^i(\mathbf{x}_p)$, the average velocity takes the following form:

$$\bar{u}_p^i = U^i \left(1 - \frac{3}{8}\delta^i\right). \quad (28)$$

3.1 Modeling Drop/Film Interactions. In a typical spray impingement situation that consists of thousands of droplets colliding for the most part on a wetted surface from previous collisions, it is prohibitively expensive both in time and memory to compute the details concerning each individual impact. It is also not necessary or of no interest to simulate the film dynamics at that level of resolution. What is necessary is the ability to predict and understand the dynamics of the film at a more global level. For this reason the overwhelming details concerning individual drop impacts are simplified by incorporating models. For example, the treatment of drop/wall interactions in previous studies, [2–4,12], has been done by implementing source terms to represent the contribution of mass, momentum, and energy of drop impact on the film. These source terms are then introduced directly into the governing equations, which are generally integral balance statements for mass, momentum, and energy. It is important to keep in mind, however, that some major assumptions are clearly violated at the impingement site, and that modeling drop/film interactions in terms of volumetric sources is simply an option among others in treating drop/film collisions.

The drop/film impact characteristics that are of relevance to the overall film dynamics are mass deposited and the momentum exerted on the film by the collisions. The mass deposited is typically taken from experimental correlations reported in the literature and the momentum contribution is modeled. For instance, in various studies an impact pressure is assigned to the collision site. The use of the impact pressure in the literature, [1,3,6], is particularly troublesome, however, because it directly introduces a dependence on numerical parameters, not physical conditions. As the droplet collides, the impact pressure is of the order of the water hammer pressure as shown by Engel [8], not the stagnation pressure as typically cited in the literature. In addition the pressure is very localized to the immediate vicinity of the impaction site. In previous models this pressure is averaged over the entire computational cell. The implication is that with variable cell sizes, the same physical phenomenon gives different results. The droplet impact also has a very time-dependent behavior, [13]. Numerically, the interpretation of this phenomenon given in previous works, [1,3,6], inherently assigns a period of duration corresponding to the current time-step, and again the simulation of the physical phenomenon is artificially dependent on numerical parameters.

The approach taken here is fundamentally different from the one above. In our approach we inevitably make assumptions with regards to the manner in which energy and mass is distributed upon impact, but it is easier to separate the physics of impingement from numerical dependencies. The deposition of mass onto the film that occurs during an impingement event (splashing or nonsplashing) is directly accounted for by the creation of a film particle having the deposition mass. This deposition mass is calculated from the mass fraction ejection measurements of Yarin and Weiss [14], and the correlation develop in [15], namely

$$Y = 0.8 \times [1 - \exp(K_y - K_{y,\text{crit}})] \quad (29)$$

where Y is the fraction of the incident droplet's mass that is ejected upon impact, hence the fraction $1 - Y$ is deposited, and

$$K_y = \frac{1}{\Lambda^{3/8}}(\text{Oh}^{-2/5}\text{We})^{5/16}$$

$$\text{Oh} = \frac{\mu}{\sqrt{d_o \sigma \rho}}$$

$$\text{We} = \frac{\rho w_o^2 d_o}{\sigma}. \quad (30)$$

Here the incident droplet diameter is given by d_o and the normal incident velocity by w_o. The critical value for K_y is 17, $K_{y,\text{crit}} = 17$, which implies that drop impact events for which $K_y < K_{y,\text{crit}}$ result in complete deposition. The Weber and Ohnesorge numbers are, respectively, given by We and Oh.

For the momentum and energy exerted on the film, rather than simulating directly the impingement pressure and enduring its highly temporal and spatial nature, in this work we try to model the effect of the pressure, which is to spread the mass and momentum from an impinging drop to the surrounding area. In this sense the droplet impingement event can be interpreted as an analogous jet impingement case. The treatment varies depending on whether the impinging droplet completely adheres to the surface or splashes.

We consider first the splashing case and state the energy conservation applied to droplet splashing as

$$\frac{1}{2}\left(\frac{4}{3}\pi\rho r_o^3\right)U_o^2 + \sigma 4\pi r_o^2 = \text{crown surface energy} + \text{crown kinetic energy} + \text{kinetic and surface energy of secondary droplets.} \quad (31)$$

A mathematically detailed form of this equation including calculation of each of the terms as a function of We, Re, and film height is given in Ref. [16]. The terms on the LHS are the incident droplet kinetic and surface energies respectively. Out of all the different forms in which the incident energy appears after splashing, the only two that remain on the film are the crown surface energy and the crown kinetic energy. The secondary droplet contributions are clearly lost as well as the energy dissipated. The initial kinetic energy assigned to the newly created film particle from this collision corresponds to the crown kinetic energy. The crown surface energy is not necessarily neglected in this assumption, since it continues to exist as a result of the additional surface area of the disturbances created by the impact. Thus for each particle created, we have

$$\frac{1}{2}m_p(V^{i=0})^2\left(1 - \frac{3}{8}\delta^{i=0}\right)^2 = \text{crown kinetic energy} \quad (32)$$

where the term on the LHS is the kinetic energy of the wall film particle. The velocity that appears here is the normal average given in Eq. (28). We initially assigned the newly created film particle a negligible boundary layer height of $\delta^{i=0} = 0.001$ and calculate $V^{i=0}$ based on Eq. (32). With respect to the mass assigned to this particle, m_p, this value is given by $m_p = m_o(1 - Y)$.

Turning to the case where the incident droplet completely deposits on the surface, the mass balance implies $m_p = m_o$. The

energy balance during impact presented above is simpler since the secondary droplet quantities are absent, and hence all of the incident energy is diverted to the new surface energy, kinetic energy on the film, and energy dissipated. We will ignore the energy dissipated since it was observed in previous work, [16], that this term was minor. A trend, that was noted in Ref. [16], was that the crown surface and kinetic energies normalized with respect to the incident droplet kinetic energy were roughly equal throughout the ranges in We, Re, and nondimensional film height. What this implies is that relative to the incident kinetic energy the crown surface and kinetic do not change significantly for various drop impingement conditions (for practically all collisions events the Weber is such that almost all the incident energy is kinetic). We assume that this trend still holds for the deposition case and consequently the incident energy is divided equally into kinetic and surface energy, giving

$$\frac{1}{2}m_p(U^{i=0})^2\left(1-\frac{3}{8}r_s^{i=0}\right)^2=\frac{1}{2}\left(\frac{1}{2}m_oU_o^2\right) \tag{33}$$

or simply $U^{i=0}=\sqrt{U_o^2/2}$ (i.e., $r_s^{i=0}$ is negligible).

The initial trajectory, on the surface plane, for the newly created film particle is assigned stochastically from the angular distribution presented by Naber and Reitz [17]. Physically, this distribution represents the film height as a function of azimuthal angle for a liquid jet impinging obliquely on a surface, and hence bears similarities with the situation of droplet impingement.

Now that the initial condition for the particle mass and velocity characteristics have been presented what follows is a sketch of the algorithm employed in the computation of film evolution. Depending on whether the incident droplet splashes or not the appropriate calculation of $V^{i=0}$ is made based either on Eq. (32) or Eq. (33); $\delta^{i=0}$ is again set equal to a negligible small value of 0.001. This defines the initial velocity profile $\varphi^o(\zeta_3)$ from which the Fourier coefficients are calculated using Eq. (15) and the film thickness computed from Eq. (23). The film particle is displaced according to Eq. (25) and the average value, $\overline{u_p^t}(dt)$, calculated at the end of the time-step. From this average value the quantities V^{i+1} and δ^{i+1} (appearing in Eq. (28)) can be computed, that is, the boundary layer height is systematically incremented, while keeping the undisturbed velocity V^{i+1} constant. Once the boundary layer reaches the film height, then V^{i+1} is calculated from the average velocity and δ^{i+1} stays at 1. This entire process is repeated until the film particle comes to rest.

4 Results

4.1 Numerical Details. The film evolution model presented in this paper is implemented into the KIVA-3V code, [9,18], which solves the unsteady equations of a turbulent gas flow coupled to the equations governing a vaporizing spray. The gas-phase solution is based on a finite volume method called the ALE (arbitrary Lagrangian-Eulerian) method, [19]. Treatment of the turbulence is through the standard k-ϵ model. The droplets in the spray are represented by a discrete-particle technique, [20], in which each numerical particle or parcel denotes a group of physical particles having the same properties (i.e., diameter, velocity, and temperature).

4.2 Numerical Testing. The film model as described in the numerical implementation section is first isolated from the remainder of KIVA-3V and tested to determine the necessary conditions that must be met in order to ensure accurate and convergent numerical predictions. In all of the tests a prescribed quantity of fuel mass is deposited in a specified region about the center of the computational domain, such that the initial film momentum, film mass, and extent of surface wetting are the same. There are four numerical parameters that enter into our model and that we investigate they are

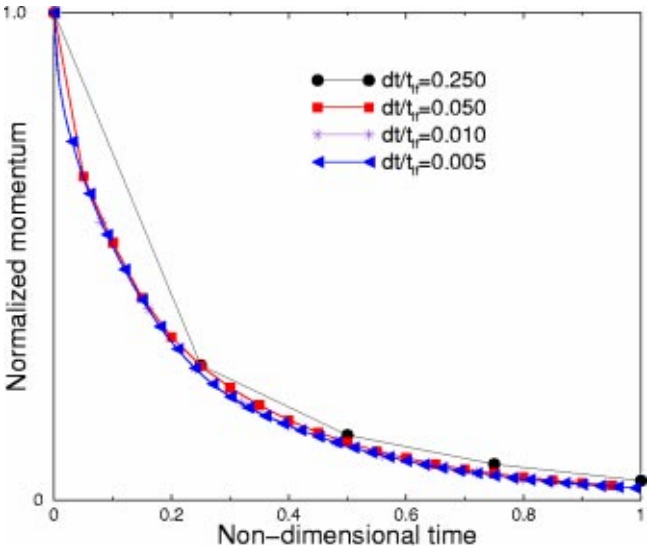

Fig. 1 Time-step size sensitivity presented in terms of dt/t_{lf}, $N_w=400$, average particle density >39, and $n_{\text{Fourier}}=6$

1. size of time-step,
2. number of Fourier modes,
3. grid size, and
4. particle number density.

The results for the tests are presented in terms of film momentum versus time. Normalization is done by respectively dividing through by the initial momentum and lifetime of film motion.

The first plot, shown in Fig. 1, presents the sensitivity to time-step size. We conclude from this plot that once the time discretization is smaller than 5% of the lifetime, the predictions have converged. In our KIVA-3V runs the ratio of time-step size to film lifetime is approximately 3.0e-3, well below this 5% mark. Also the ratio of time-step size to characteristic time, λ^2/ν, varies in the range of $O(10^{-1})-O(10^{-3})$.

In the following plot, shown in Fig. 2, the error incurred by truncating the infinite series is investigated. As a reminder the analytical solution is given in terms of a truncated infinite series

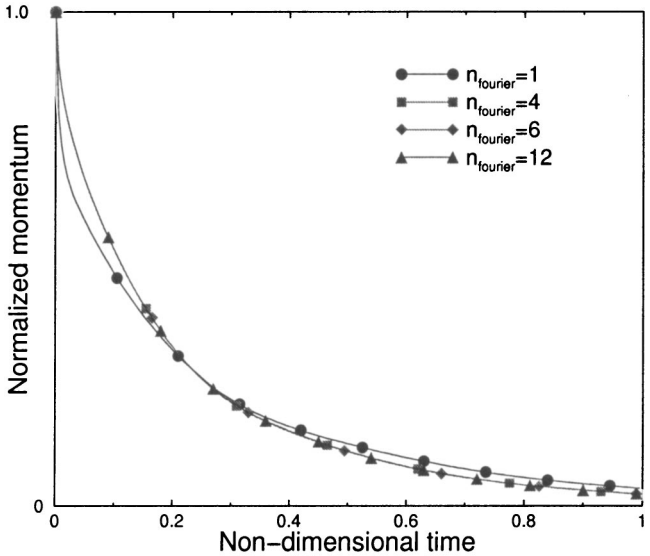

Fig. 2 The effect of truncating the number of Fourier modes in the film velocity solution, $N_w=400$, average particle density >40, and $dt/t_{lf}=0.005$

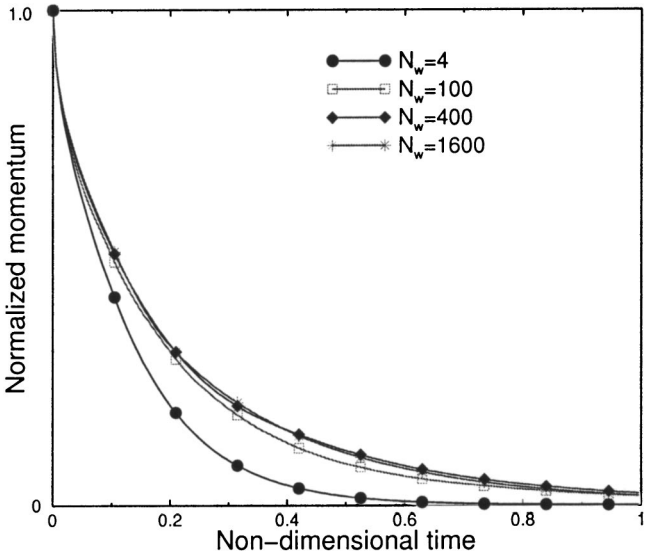

Fig. 3 Grid size sensitivity presented in terms of the number of cells occupied by the film at $t=0$, $n_{\text{Fourier}}=6$, average particle density >40, and $dt/t_{lf}=0.005$

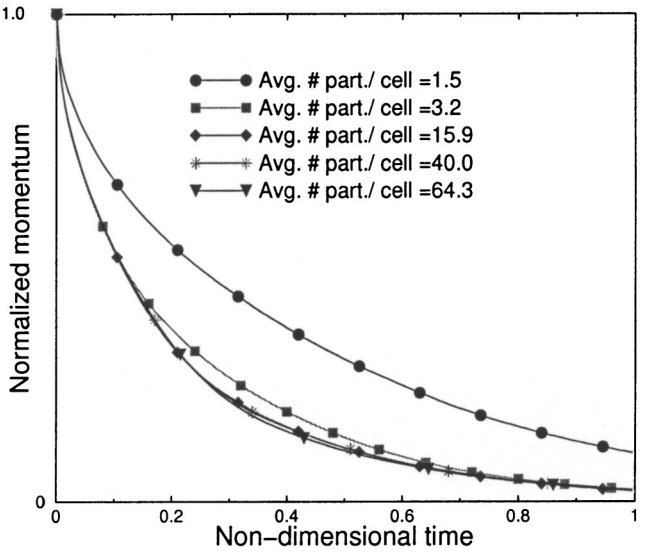

Fig. 4 Convergence with respect to the average number density, $n_{\text{Fourier}}=6$, $dt/t_{lf}=0.005$, and $N_w=400$

Eq. (25). The different curves correspond to the number of Fourier modes employed in representing the velocity profile. Once five Fourier modes are employed ($n_{\text{fourier}}=4$) the solution converges. In the KIVA-3V computations $n_{\text{fourier}}=6$ is employed.

The third plot examines the issue of grid size sensitivity. Note here that the important parameter is not the grid refinement over the entire computational domain, but the refinement in the wetted region where the film exists. Therefore, the relevant parameter is the number of cells that are occupied to some extent by the film, i.e., the number of wetted cells N_w. It should also be noted that in our Lagrangian formulation of film dynamics, differentiation along directions tangential to the surface do not exist, and hence discretization errors of this type are not introduced. However, the film height calculation depends on grid resolution, and thus it is important to shown that with increasing resolution a convergent result is obtained. This is what is shown in Fig. 3. When the film region is resolved by at least a hundred cells, our results are sufficiently close to the converged solution. In our KIVA-3V calculations the film is typically covered by over 200 cells.

The last numerical parameter that affects the solution is the average particle number density. This is simply calculated by dividing the total number of film particles by the number of cells representing the film. It is expected that with a sufficiently high density convergence is guaranteed, and since the particle density tends to decrease as the film spread, the parameter reported is the final and lowest value of particle density. We see that once the average number density exceeds ≈ 15 we have approached sufficiently the converged solution (see Fig. 4). The implications for grid refinement is that as the grid size is decrease this requires a corresponding increase in the total number of particles introduced in the computation. In our KIVA-3V computations this number density was approximately 40.

4.3 Comparison to Experiments. The computational predictions of film edge evolution and film thickness are compared to experiments performed by Mathews et al. [15,21]. The experiments consists of isooctane injection into a quiescent environment using a pintle-hole injector. The spray pulse is 8.45 ms which corresponds to 15.6 mg of fuel delivered, and the spray tip is located 10 cm from a Plexiglass surface where impingement occurs and is monitored. Three different orientation angles are chosen for the study, namely 30 deg, 45 deg, and 60 deg from normal. The typical incident drop velocities and sizes are 20 m/s and 300 μm for SMD. Additional experimental details are reported in Ref. [15].

In the experiments a number of impingement events are used to obtain film front and width time series. The film front is defined as the distance between the film edge with respect to the center of the impingement area in the forward direction, and the film width is the widest part of the film. In the experiments, however, what is measured is not the film edge but the location of maximum surface curvature, which is approximately 1 mm short of the film edge. For this reason, the computations compensate for this discrepancy with the aim of establishing more consistency in the comparisons.

The results for film front displacement are shown in Fig. 5. The time in these figures is referenced to the onset of injection. Overall reasonable agreement is observed, specially for the 30 deg and 45 deg cases. Initially, there is a discrepancy in all three curves. This discrepancy, however, is not seen in the following figure which displays film width predictions. This leads us to believe that there

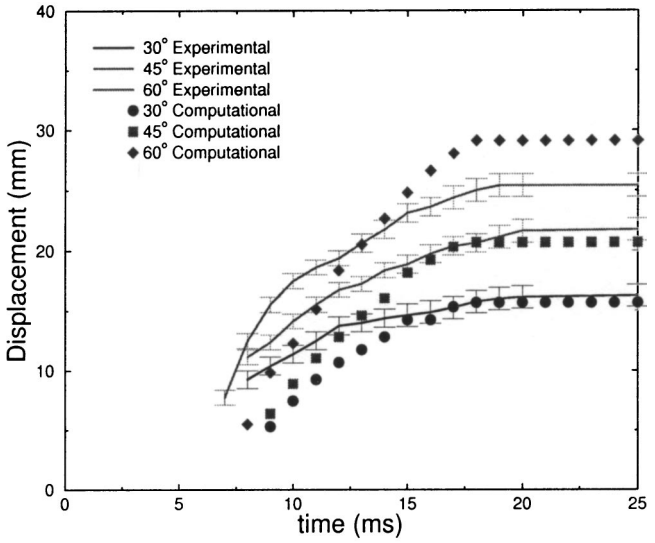

Fig. 5 Film front displacement versus time

Table 1 Mass fraction deposited as a function of incident angle

angle, degrees	30	45	60
mass fraction deposited	0.47	0.63	0.92

is good possibility that our computations are not in exact agreement with measurements of the location of the impingement center; specially, since this reference point is difficult to identify precisely in the experiments. Nevertheless, our numerical predictions overestimate somewhat the slope of film front displacement. The leveling of the curves around $t=18$ ms as well as the final film extent is, however, predicted fairly well, with the exception of the 60 deg case. We believe that the overprediction occurring for the 60 deg case is caused by an excessive amount of mass adhering to the wall in our calculations. To investigate this, Table 1 presents values for computed mass fraction deposited as a function of incident angle.

For steeper angles of impingement a greater proportion of incident droplets splash and consequently less mass is deposited. This tendency is explained by considering the behavior of the nondimensional parameter K_y (Eq. (30)). The normal velocity component varies with $\cos(\theta)$, where θ is the angle between the normal direction and incident velocity vector. Therefore, shallow impingement angles result in droplets having lower values of K_y, which means lower number of droplets overcoming the splashing threshold given by K_{crit}.

Mass fraction measurements, [22], indicate that roughly 60% of the mass adheres to the wall for all three impingement angles (The measurements are difficult to make and therefore are not very accurate.) We can argue that the 30 deg and 45 deg cases are close enough to this value, but the 60 deg case is definitely too high. The larger deposition fraction is responsible for the more accentuated discrepancy. The larger deposition mass fraction also points to another possible mechanism for removing liquid from the film during shallow angle impingement, which is at present unaccounted for with the splashing criteria of our model. We suggest that for droplets approaching the film at shallow angles, their impact with the wavy film surface could atomize some of the liquid. At present no knowledge of this mechanism of single droplet impacting on a solid dry or wetted surface has been reported in the literature, [14,23–25], because in these studies the conditions are purposefully designed to exclude any of the complications found in practical situations such as spray impingement. Future work in splashing or atomization criteria should, however, consider the possibility of this film stripping mechanism.

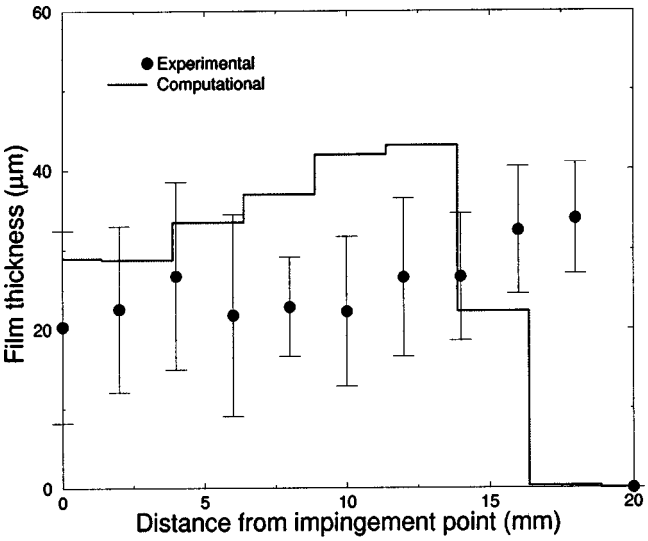

Fig. 7 Film thickness at the end of film evolution 30 deg

The comparisons of computed versus measured film width evolution are shown in Fig. 6 for the three impingement angles. Overall, good agreement is observed. The previous problem with the initial discrepancy is absent in this plot, although the computed slope is slightly larger than the measurements. The predicted film displacements come to stop at around the same times as in the measurements and the final width of the computed film is well predicted.

All the impingement angles give approximately the same film width at the end of the film evolution. This is true for both experiments and computations. There are differences, however. In the pattern observed in the experiments the final film width becomes slightly narrower with shallower impingement angles. Although this angle-to-angle variation is within the uncertainty of the measurements, it is physically reasonable to assume that for shallower impingement angles there is less of a tendency to spread the impingement mass uniformly around the site, and more of a tendency to move this mass in the forward direction. The effect would be a narrower film width and a much greater film front

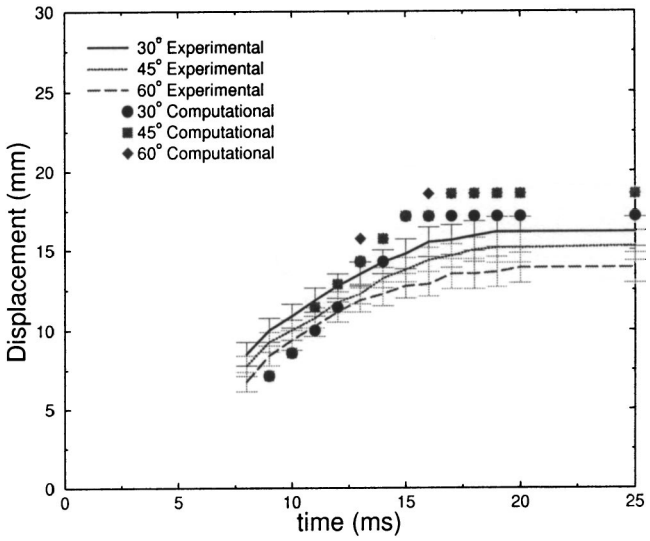

Fig. 6 Film width displacement versus time

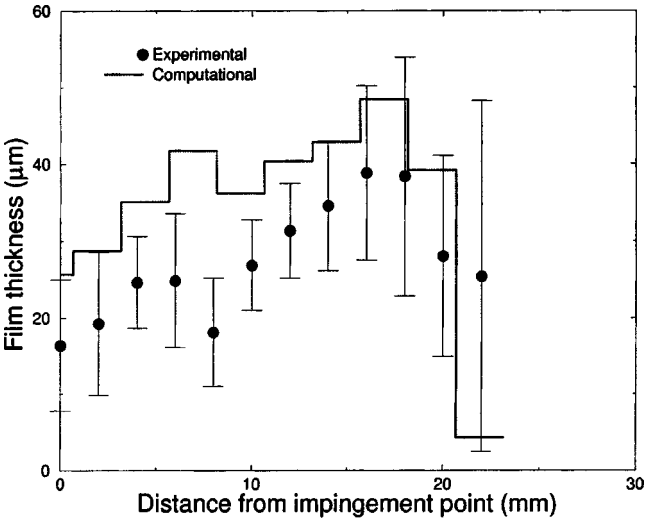

Fig. 8 Film thickness at the end of film evolution 45 deg

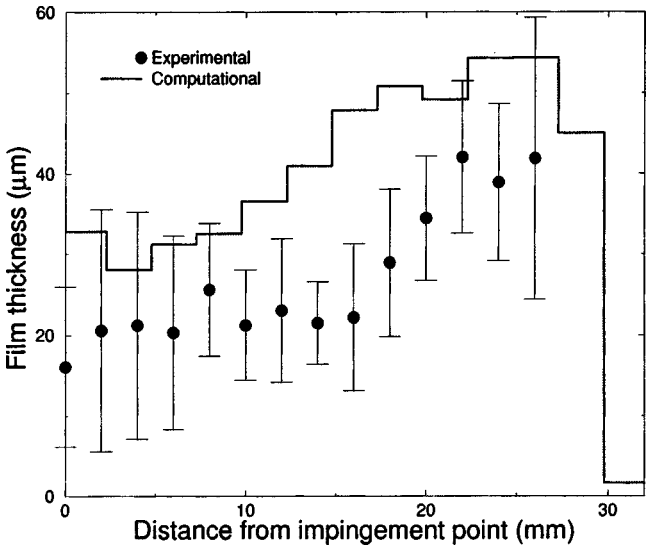

Fig. 9 Film thickness at the end of film evolution 60 deg

displacement. In the computations, due to the fact that more mass adheres with shallower impingement angle, this effect is nullified and the result is a slightly larger film width with shallower impingement angles. These angle to angle differences are relatively small, however.

To study the distribution of mass in the film, film thickness predictions at different points in the forward direction measured from the center of the impingement area are computed and compared to experiments, [21]. The results of these comparisons are shown in Figs. 7, 8, and 9 for 30 deg, 45 deg, and 60 deg respectively. The discrete nature of the computations is a result of the nearest-grid-point interpolation treatment when assigning cell quantities from particles quantities (see Eq. (23)). The average values shown in the measurements have an experimental error of approximately 8 μm. The uncertainty bar shown for each data point does not correspond directly to this error but to the standard deviation corresponding to ten measurements. It is expected that this deviation is in part due to disturbances present in the film due to spray impingement.

The numerical predictions show reasonable agreement with experiments, although the film thickness is somewhat overpredicted specially for the 60 deg impingement. We believe that the computed mass adhered is responsible for this behavior. One trend to be noted is that with shallower impingement angles, the film thickness profile becomes steeper as relatively more mass is transported from the impingement region to the edge of the film. This is due to a higher momentum component in the forward direction for incident droplets approaching the surface at shallower impingement angles. This effect, which is present in experiments, is also reproduced in the computations.

5 Conclusion

The governing equations for a liquid film formed during spray impingement have been derived with specific treatment given in the impingement sites. This is necessary since some essential assumptions that are taken to simplify the complexity of the Navier-Stokes equations do not hold at impingement regions (e.g., surface tension, surface disturbances$\leqslant$film height, etc . . .). The reduced form of the momentum equation is an unsteady-convective equation with wall friction. The assumptions of negligible gas shear and surface tension are shown to be valid for most of the film evolution period. In particular, surface tension is shown to be negligible only if $(\sigma J_s \lambda)/(\mu U) \ll 1$. However, as the film velocity decays to zero, it is very difficult to ignore these effects and prohibitively expensive to include them with the required accuracy. Fortunately, most of the film evolution, and hence the extent of surface wetting has taken place before these complications become dominant.

The governing equations casted in Lagrangian form are solved using a particle method. The solution found is semi-analytic and is based on film thickness obtained from an interpolation on particle quantities. Numerical testing demonstrates that our simulations are convergent provided some conditions are met.

The results are compared to experiments consisting of film edge displacement and film thickness measurements. Overall good agreement is obtained for the 30 deg and 45 deg impingement cases. For the 60 deg case the film front displacement is slightly larger than the experiments. It is believed that the most probable reason is an overprediction of the total amount of mass deposited on the wall. Based on this belief, it is suggested that another mechanism is responsible for the atomization of the film at shallow angle impingements.

Acknowledgments

The authors are grateful to the insights provided by Dr. P. J. O'Rourke in the early phase of this project as well as to the funding support of the Department of Energy Computational Science Graduate Fellowship and the Ford Motor Company.

Nomenclature

A_n, C_n = Fourier coefficients
d = droplet diameter
$(\mathbf{e}_1, \mathbf{e}_2, \mathbf{e}_3)$ = unit vectors
g = acceleration due to gravity
h = film thickness
(h_1, h_2, h_3) = metric coefficients
J = surface curvature
J_f = surface curvature of the gas-liquid interface
L = characteristic film spreading length
m = droplet/particle mass
$\mathbf{n}$ = unit vector in the surface normal direction
N_w = number of cells occupied by the film
p = pressure
r = droplet radius
Re_λ = Reynolds number $\rho U \lambda / \mu$
t = time
t_{fl} = duration of film motion
$\mathbf{u}$ = film velocity
U = characteristic film tangential velocity
V = undisturbed film velocity, Eq. (27)
w = normal velocity or characteristic film normal velocity
$\mathbf{x}$ = position vector
Y = mass fraction ejected during splashing
z = ζ_3 / h
β_n = $\pi/2 + n\pi$
δ = nondimensional boundary layer height (l/h)
l = boundary layer height
γ = liquid velocity gradient at the gas-liquid interface
λ = characteristic film height
μ = liquid dynamic viscosity
ν = liquid kinematic viscosity
ρ = liquid density
σ = liquid-gas surface tension
$\varphi(\zeta_3)$ = film velocity profile in the normal direction
$(\zeta_1, \zeta_2, \zeta_3)$ = film coordinates

Superscripts

i = corresponding to time interval $(t^i, t^i + dt)$
$*$ = nondimensional quantity

Subscripts

o = pertaining to the incident droplet

s = tangential
p = numerical particle quantity
α = computational cell quantity

References

[1] Stanton, D. W., and Rutland, C. J., 1996, ''Modeling Fuel Film Formation and Wall Interaction in Diesel Engines,'' SAE Paper No. 960628.
[2] Ahmadi-Befrui, B., Uchil, N., Gosman, A. D., and Issa, R. I., 1996, ''Modeling and Simulation of Thin Liquid Films Formed by Spray-Wall Interaction,'' SAE Paper No. 960627.
[3] Foucart, H., Habchi, C., Le Coz, J. F., and Baritaud, T., 1998, ''Development of a Three Dimensional Model of Wall Fuel Liquid Film for Internal Combustion Engines,'' SAE Paper No. 980133.
[4] Bai, C., and Gosman, A. D., 1996, ''Mathematical Modeling of Wall Films Formed by Impinging Sprays,'' SAE Paper No. 960626.
[5] O'Rourke, P. J., and Amsden, A. A., 1996, ''A Particle Numerical Model for Wall Film Dynamics in Port-Injected Engines,'' SAE Paper No. 961961.
[6] O'Rourke, P. J., and Amsden, A. A., 2000, ''A Spray/Wall Interaction Submodel for the Kiva-3 Wall Film Model,'' SAE 2000 Congress.
[7] Chen-To, Tai, 1992, *Generalized Vector and Dyadic Analysis*, IEEE Press, New York.
[8] Engel, O. G., 1955, ''Waterdrop Collisions With Solid Surfaces,'' J. Res. Natl. Bur. Stand., **54**(5), pp. 281–298.
[9] Amsden, A. A., O'Rourke, P. J., and Butler, T. D., 1989, ''Kiva-ii: A Computer Program for Chemically Reactive Flows With Sprays,'' Technical Report LA-11560-MS, Los Alamos National Laboratory.
[10] Pozrikidis, C., 1997, *Introduction to Theoretical and Computational Fluid Dynamics*, Oxford University Press, New York.
[11] Rao, A., and Arakeri, J. H., 1995, ''Integral Analysis Applied to Radial Film Flows,'' Int. J. Heat Mass Transf., **41**, pp. 2757–2767.
[12] Stanton, D. W., and Rutland, C. J., 1998, ''Multi-dimensional Modeling of Heat and Mass Transfer of Fuel Films Resulting From Impinging Sprays,'' SAE Paper No. 980132.
[13] Savic, P., and Boult, G. T., 1957, ''The Fluid Flow Associated With the Impact of Liquid Drops With Solid Surfaces,'' *Heat Transfer and Fluid Mechanics Institute*, California Institute of Technology, Pasadena, CA, pp. 43–84.
[14] Yarin, A. L., and Weiss, D. A., 1995, ''Impact of Drops on Solid Surfaces: Self-Similar Capillary Waves, and Splashing as a New Type of Kinematic Discontinuity,'' J. Fluid Mech., **283**, pp. 141–173.
[15] Trujillo, M. F., Mathews, W., Lee, C. F., and Peters, J. E., 2000, ''Modeling and Experiment of Impingement and Atomization of a Liquid Spray on a Wall,'' International Journal of Engine Research, **1**(1), pp. 87–105.
[16] Trujillo, M. F., 2000, ''Spray and Single Droplet Impingement on a Wall,'' Ph.D. thesis, University of Illinois.
[17] Naber, J. D., and Reitz, R. D., 1988, ''Modeling Engine Spray/Wall Impingement,'' SAE Paper No. 880107.
[18] Amsden, A. A., 1993, ''Kiva-3: A Kiva Program With Block-Structured Mesh for Complex Geometries,'' Technical Report LA-12503-MS, Los Alamos National Laboratory.
[19] Hirt, C. W., Amsden, A. A., and Cook, J. L., 1974, ''An Arbitrary Lagrangian-Eulerian Computing Method for All Flow Speeds,'' J. Comput. Phys., **14**, pp. 227–253.
[20] Dukowicz, J. K., 1980, ''A Particle-Fluid Numerical Model for Liquid Sprays,'' J. Comput. Phys., **35**, pp. 229–253.
[21] Mathews, W., Lee, C. F., and Peters, J. E., 2001, ''Experimental Measurements of the Thickness of a Deposited Film From Spray/Wall Interaction,'' 14th Annual Conference on Liquid Atomizaion and Spray Systems.
[22] Mathews, W., 2000, personal communication.
[23] Rein, M., 1993, ''Phenomena of Liquid Drop Impact on Solid and Liquid Surfaces,'' Fluid Dyn. Res., **12**, pp. 61–93.
[24] Cossali, G. E., Coghe, A., and Marengo, M., 1997, ''The Impact of a Single Drop on a Wetted Solid Surface,'' Exp. Fluids, **22**, pp. 463–472.
[25] Mundo, C., Sommerfeld, M., and Tropea, C., 1995, ''Droplet-Wall Collisions: Experimental Studies of the Deformation and Breakup Process,'' Int. J. Multiphase Flow, **21**(2), pp. 151–173.

Hui-Yuan Fan
Department of Building and Construction,
City University of Hong Kong,
Tat Chee Avenue,
Kowloon, Hong Kong, HKSAR, P. R. China
and SER Turbomachinery Research Center,
School of Energy and Power Engineering,
Xi'an Jiaotong University,
Xi'an 710049, P. R. China

Wei-zhen Lu[1]
Department of Building and Construction,
City University of Hong Kong,
Tat Chee Avenue,
Kowloon, Hong Kong, HKSAR, P. R. China
e-mail: bcwzlu@city.edu.hk

Guang Xi

Shang-jin Wang

SER Turbomachinery Research Center,
School of Energy and Power Engineering,
Xi'an Jiaotong University,
Xi'an 710049, P. R. China

An Improved Neural-Network-Based Calibration Method for Aerodynamic Pressure Probes

Calibration of multihole aerodynamic pressure probe is a compulsory and important step in applying this kind of probe. This paper presents a new neural-network-based method for the calibration of such probe. A new type of evolutionary algorithm, i.e., differential evolution (DE), which is known as one of the most promising novel evolutionary algorithms, is proposed and applied to the training of the neural networks, which is then used to calibrate a multihole probe in the study. Based on the measured probe's calibration data, a set of multilayered feed-forward neural networks is trained with those data by a modified differential evolution algorithm. The aim of the training is to establish the mapping relations between the port pressures of the probe being calibrated and the properties of the measured flow field. The proposed DE method is illustrated and tested by a real case of calibrating a five-hole probe. The results of numerical simulations show that the new method is feasible and effective. [DOI: 10.1115/1.1523063]

1 Introduction

The multihole pressure probes, such as five and seven-hole probes, have been demonstrated to be one of the easiest to use and the most cost-effective devices for three-component velocity measurement in research and industrial environment. Based on the measured five or seven pressure values at the probe's tip ports and the proper probe calibration methods, the five and seven-hole pressure probes can be used to measure the three velocity components, the total and the static pressures in a flow field at the location of its tip. The calibration of such pressure probes is an important step to establish the mapping relations between the port pressures and the properties of the flow field being measured. The conventional calibration technique usually focuses on finding some calibration curves based on the theory of potential fluid flow passing a body once the calibration data of a multihole probe obtained. Therefore, the calibrated probe has limited calibration curves, and the measured results, normally obtained through interpolating between the available curves, are, of course, only approximated.

Instead of the conventional calibration methods, Rediniotis et al. developed a novel kind of calibration method, i.e., the neural-network-based calibration method for the calibration of multihole pressure probes in recent years, [1,2]. The neural network technique is a computational strategy that simulates the biological process in the human brain. A neural network consists of a series of simple, highly interconnected processing elements called neurons. The neurons by themselves are not particularly interesting, but their interconnection creates a powerful device that can approximate arbitrary functions. Such ability of universal approximation makes neural networks very suitable to deal with highly nonlinear problems, e.g., to calibrate the multihole aerodynamic pressure probes. Previous studies show that the neural-network-based calibration methods are superior to the conventional calibration ones for multihole pressure probes, e.g., a neural-network-based calibration of a multihole probe can intrinsically eliminate the intricate tasks often encountered with a traditional calibration. These tasks include the determination of a large number of curves in the calibration phase of a probe, and/or the interpolation between the obtained curves in the use phase of the probe. Neural networks can continuously approximate the calibration relations of the probe, i.e., the relations between the five or seven port pressures and the measured flow field properties.

Neural networks must be trained with the sample solutions, i.e., training sets, to possess the ability to predict a system. The traditional training algorithm, i.e., back-propagation (BP) algorithm, is normally used to fulfill such task and was also used by Rediniotis et al. in their probe calibration studies, [1,2]. BP algorithm is a gradient-based method, and some inherent drawbacks (or difficulties) are often encountered in the use of this algorithm, e.g., the low convergence speed during the training, the unavoidable local minima situation, etc. Several techniques are required and introduced in the attempt to resolve these problems. Differential evolution (DE), developed by Storn and Price [3] in recent years, is one of the most promising novel evolutionary algorithms (EAs) to tackle the mentioned drawbacks. The method has been empirically demonstrated to be an effective and robust optimization method that outperforms some of traditional EAs (SP96). Furthermore, DE can be easily extended for handling continuous, discrete and integer variables, and for dealing with multiple nonlinear and nontrivial constraints. Besides, DE is extremely simple to implement. Although DE possesses advantages mentioned above and by Storn and Price [3], little is known about applying DE to train a neural network. In this study, DE is used to train a set of feed-forward neural networks to calibrate a five-hole aerodynamic pressure probe. The study will show the feasibility and effectiveness of DE in dealing with such problems.

2 Calibration Task and Data Acquisition

A five-hole pressure probe may have several possible geometric shapes. Among these, the most widely used types include those

[1]To whom correspondence should be addressed.

Contributed by the Fluids Engineering Division for publication in the JOURNAL OF FLUIDS ENGINEERING. Manuscript received by the Fluids Engineering Division Jan. 6, 2001; revised manuscript received July 29, 2002. Associate Editor: A. K. Prasad.

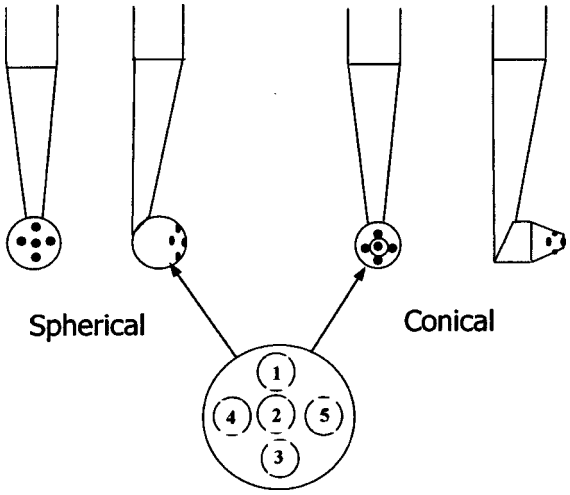

Fig. 1 Configurations of the five-hole pressure probes

with spherical and conical tips, shown in Fig. 1. Each probe tip contains five pressure ports, with one sitting at the center of the cone or the half-sphere, and the other four pressure ports being symmetrically arranged in a ring downstream, with each port connecting to a pressure measurement device.

Figure 2 presents a schematic of pressure probe calibration test. In a flow-mapping experiment, the local velocity vector can be fully characterized by four variables [1,2], i.e., the flow pitch angle α, the flow yaw angle δ, the total pressure coefficient A_t, and the static pressure coefficient A_s. The two flow angles α and δ, defined in the probe coordinate system shown in Fig. 2(b), are used to determine the direction of the flow velocity at the measured point, while the two pressure coefficients determine the magnitude of the flow velocity as well as the total and the static pressures. These four variables, also defined as output or dependent variables, are regarded as functions of the five measured pressures, i.e., the input or independent variables. These measured pressures are normally written as in Eq. (1), [1,2]. Two new parameters, i.e., the nondimensional pressure coefficients, B_α and B_δ are introduced here. B_α and B_δ can also be regarded as the input or independent variables. Therefore, calibrating a five-hole pressure probe is equivalent to determining the functional relationships between the input and output variables listed as below:

Input:

$$B_\alpha=\frac{p_4-p_5}{Q'},\quad B_\delta=\frac{p_1-p_3}{Q'} \tag{1}$$

where $$Q'=p_2-0.25\times(p_1+p_3+p_4+p_5).$$

Output:

$$\alpha,\delta,A_t=\frac{p_2-p_t}{Q'},\quad A_s=\frac{p_2-p_s}{Q'}. \tag{2}$$

The five-hole pressure probe studied here is a type of conical tip. The test rig employed in the calibration is an air jet calibration facility, including a settling chamber, a contraction section, and a jet exit nozzle, and supplied with compressed air. The probe to be calibrated is mounted such that its tip is right at the exit plane of the nozzle and centered with respect to it (see Fig. 2(a)). Two stepper motors are used to change the probe orientation corresponding to the jet axis, i.e., the motors can vary the flow angles α and δ within the range of -180, 180 deg, which covers a wide range of calibration angles. The location of probe tip is kept the same at all probe orientations. The calibration process is fully automated, except the stepper-motor assembly is manually operated to navigate the probe according to a user-defined array with desired probe orientations (α_i, δ_i, $i=1,\ldots,m$). At each orientation, the data-acquisition system is operated to collect the data, i.e., six pressure values. Five of them are probe tip pressures, i.e., p_i, $i=1,\ldots,5$. The sixth is the pressure within the settling chamber of the calibration facility. Based on the values of the sixth pressure and the atmospheric pressure, the jet velocity V at the exit can be calculated by using Bernoulli's equation. By varying the α and δ in intervals of 5 deg from -40 deg to $+40$ deg, the total 289 ($=17\times17$) data points are acquired. Such a data set can be used to establish the functions to represent the aerodynamic properties of the probe.

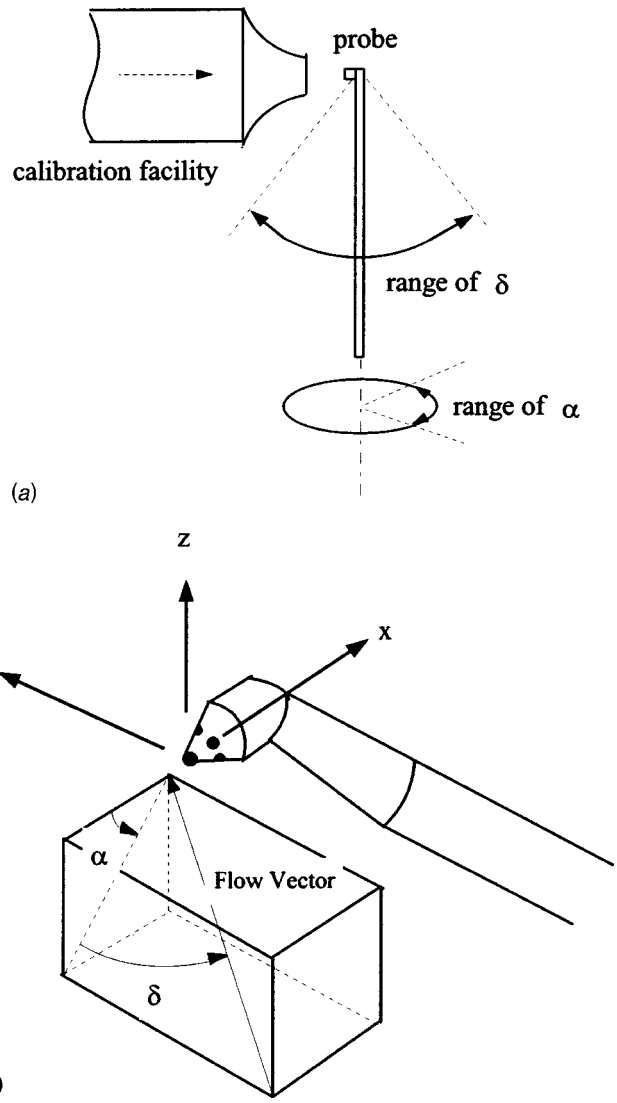

Fig. 2 (*a*) Simplified experimental scheme, (*b*) probe coordinate system

3 Neural Network Model

The artificial neural network (ANN) method is employed here to formulate the calibration method for a five-hole pressure probe in target of desired accuracy and wide range. The ANN perceptron has the ability to learn through training. The general procedure of ANN contains, [1], the following: Let X and $Y=f(X)$ represent the input and output vectors of the system to be simulated, respectively. If the function f is not explicitly known or too complicated, and the N input-output pairs $(X,Y)_i$, $i=1,\ldots,N$, are numerically known, then the idea of a neural network becomes particularly attractive. During the training, the neural network "black box" is represented with the training pairs, i.e., $(X,Y)_i$, and the

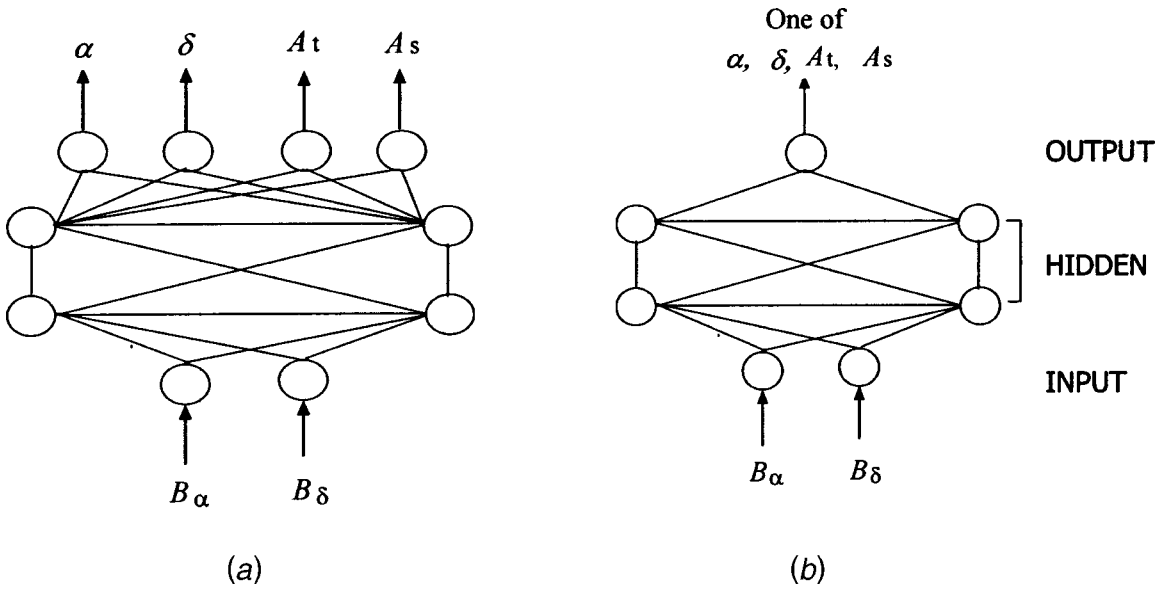

Fig. 3 Structures of neural networks: (*a*) for the semiflow forward-facing measurement case, (*b*) for the nonflow forward-facing measurement case

training algorithm will adjust its internal parameters (weights). Such procedure results in the "encoding" of the properties of function f in different parts of the neural network. If, after the training is completed, the neural network is presented with an input, X, not belonging to the N training pairs, it will be able to simulate the function f and produce an output, Y', which is an approximation of the target output, Y. The error between the actual and the predicted function values is an indication of how successful the training is. In this study, an output mean square error (MSE) of neural networks is defined as

$$\mathrm{MSE}=\frac{1}{N}\sum_{s=1}^{N}\left[\sum_{k=1}^{M}(Y_{s,k}-Y'_{s,k})^2\right] \tag{3}$$

where $k=1,\ldots,N$, and $s=1,\ldots,M$, N is the total number of training samples, and M is the dimension of the output vectors, or equivalently, the number of the output neurons.

Previous studies, [1–2,4–7], have shown the successfulness of using ANNs to model a wide diversity of systems and processes, e.g., vortex dynamics principles, [4,5], flight test data estimators, [6], control of transition from laminar to turbulence, [7], and aerodynamic multihole pressure probe calibrations, [1,2]. In this study, the "universal approximating" characteristics of ANNs is used, and mapping relations between the five port pressures and the measured flow-field properties are established within a multilayered feed-forward neural network model.

Conventionally, a five-hole pressure probe can be used in three measurement ways, i.e., "the fully flow forward-facing measurement," "the semi-flow forward-facing measurement," and "the nonflow forward-facing measurement." In a fully flow forward-facing measurement, the probe is required to be set in such a way that it is adjustable in two degrees-of-freedom at the measured point. During measurement, the probe is turned to have both flow pitch angle α and flow yaw angle δ read directly from the coordinate set. The measurement is done at the moment when the probe is facing forward the flow vector is at the measured point. A semi-flow forward-facing measurement needs the probe being adjustable only around its body axis, i.e., in one degree-of-freedom. In the measurement, the probe is turned to let the flow pitch angle being read from the coordinate set, and the flow yaw angle is calculated from the measured pressures. The probe is installed partly facing forward of the flow vector at the measured point. In a nonflow forward-facing measurement, the probe is fixed at the measured point without any degree-of-freedom. Both pitch angle and yaw angle are calculated from the measured pressures. Considering the above three different measurement methods, a five-hole pressure probe is usually calibrated with three different formulations. When the probe is used to a real work site, especially for the case of internal flow measurement, e.g., measurement inside turbomachinery, it is often impossible to implement a fully flow forward-facing measurement due to the limited space to adjust the probe in two degrees-of-freedom. In current study, the five-hole probe is only calibrated for the cases of semi-flow forward-facing measurement and nonflow forward-facing measurement.

The measured calibration data of the probe will be used as samples to train the neural network perceptrons. The trained neural network perceptrons will then be used to predict the flow properties when the probe is used to measure an unknown flow field. The neural networks selected to implement the calibrations of the five-hole probe are of the four-layer feed-forward type, as illustrated in Fig. 3. They have two input nodes representing the two nondimensional pressure coefficients, B_α and B_δ. According to the cases studied here, two types of the network outputs are chosen. The neural network used in the semi-flow forward-facing measurement case, shown in Fig. 3(a), has four outputs, i.e., the two flow angles (pitch angle α and yaw angle δ), and two pressure coefficients, A_t (the total pressure coefficient) and A_s (the static pressure coefficient). The calibration relations for the nonflow forward-facing measurement case are obviously more complicated than those for the semiflow forward-facing measurement case. To avoid an excessive large size in the neural network structure and, consequently, a time-consuming training process, we adopt four neural network perceptrons with one output node in each model, as shown in Fig. 3(b), to calibrate the above four parameters separately. In these networks, the output node in each perceptron represents the pitch angle α, the yaw angle δ, the total pressure coefficient A_t, and the static pressure coefficient A_s, respectively. Several neural network configurations are experimented by changing the node numbers in hidden layers regarding the corresponding real cases of calibration simulation. Through certain trial-and-error processes, it is found that, for the neural network with four outputs, the one with 16 nodes in the first hidden layer and 18 nodes in the second hidden layer performs satisfactorily; while for

the neural networks with one output, ten nodes in each of the two hidden layers leads to reliable and effective performance.

4 Differential Evolution (DE) Method

Based on the original DE version "DE/rand/1/bin" developed by K. Price [8], we propose a modified version of differential evolution (DE) to train the networks described in Fig. 3. Without loss of generality, let $W^{[1]}$ denote the connection weight matrix between the input layer and the first hidden layer, $W^{[2]}$ the one between the two hidden layers, and, $W^{[3]}$, the one between the second layer and the output layer, for all network structures established in the study. Further, let $W=\{W^{[1]},W^{[2]},W^{[3]}\}$. Hence, the training processes of the above neural networks with DE can be described as follows.

Similar to all EAs, DE evolves its search process in a population of N_p candidate solutions, i.e., individuals. In this study, the population to be evolved consists of individuals, $W_{i,G}=\{W_{i,G}^{[1]},W_{i,G}^{[2]},W_{i,G}^{[3]}\}$, $i=1,\ldots,N_p$, where i indexes the population and G is the generation to which the population belongs. The population is then evolved by three basic evolutionary operations, i.e., mutation, crossover, and selection. These three operations are briefly discussed below.

The essential component in the DE mutation operation is the difference vector in a population, which is the main operation different from other EAs. The mutation process at each generation begins by randomly selecting three individuals in the population. The ith perturbed individual, $V_{i,G+1}=\{V_{i,G+1}^{[1]},V_{i,G+1}^{[2]},V_{i,G+1}^{[3]}\}$, is therefore generated based on these three selected individuals as in the form

$$V_{i,G+1}^{[j]}=W_{r_3,G}^{[j]}+F\cdot(W_{r_1,G}^{[j]}-W_{r_2,G}^{[j]}) \tag{4}$$

where, $j=1,2,3$, $i=1,\ldots,N_p$, and, $r_1,r_2,r_3\in\{1,\ldots,N_p\}$ are randomly selected, except $r_1\neq r_2\neq r_3\neq i$, and a scaling factor F ($F\in[0,1+]$) is introduced by Storn and Price [9] in Eq. (4) to ensure the fastest convergence wherever possible.

In order to increase the diversity of the new individuals in the next generation, the perturbed individual, $V_{i,G+1}$, and the current individual, $W_{i,G+1}$, are selected by a given probability to perform the crossover operation to generate the population of candidate, or "trial" matrixes, $U_{i,G+1}=\{U_{i,G+1}^{[1]},U_{i,G+1}^{[2]},U_{i,G+1}^{[3]}\}$, described as follows:

$$U_{i,G+1}^{[j]}(k,m)=\begin{cases}V_{i,G+1}^{[j]}(k,m) & \text{if } r_j\leq C_r\vee(k,m)=(k^*,m^*)\\ W_{i,G+1}^{[j]}(k,m) & \text{otherwise}\end{cases} \tag{5}$$

where $i=1,\ldots,N_p$, $k=1,\ldots,K_j$, $m=1,\ldots,M_j$ are indexes of matrix's elements, K_j and M_j are row and column sizes of matrix $[\bullet]_{i,G+1}^{[j]}$, i.e., $W_{i,G+1}^{[j]}$, or $V_{i,G+1}^{[j]}$, or $U_{i,G+1}^{[j]}$; $k^*\leq K_j$ and $m^*\leq M_j$ are indexes of a matrix's element and randomly chosen once for each i, the crossover factor $C_r\in[0,1]$ is set by the user.

The selection scheme of DE also differs from other evolutionary algorithms. The population for the next generation is selected from the individuals in the current population and its corresponding trial matrix complying Eq. (6) listed as below:

$$W_{i,G+1}=\begin{cases}U_{i,G+1} & \text{if } U_{i,G+1} \text{ is better than } W_{i,G}\\ W_{i,G} & \text{otherwise}\end{cases}. \tag{6}$$

Thus, each individual of the temporary (trial) population is compared with its counterpart in the current population. The one with the lower value of objective function (OF) will survive to the population of the next generation. As a result, all the individuals of the next generation are, at least, as good as, or better than, their counterparts in the current generation. The interesting point concerning DE's selection scheme is that a trial matrix is not compared against all the individuals in the current population, but only against one individual, i.e., its counterpart in the current population.

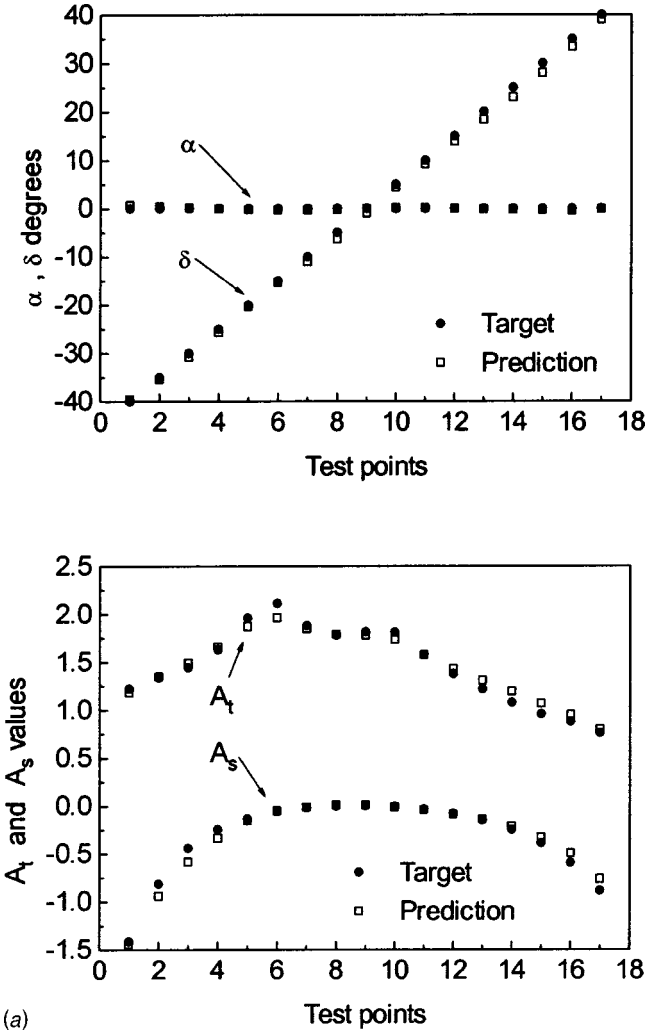

Fig. 4 Test results of neural-network-based method to calibrate five-hole probe for semiflow forward-facing measurement; (*a*) the target parameters and their predictions, (*b*) column-error plots of the testing results

In this study, a new adaptive scaling factor, F', is proposed and regarded as a proper combination of the three individuals randomly selected from the population to be used to yield the mutated current individual. The F' takes the following form:

$$F'=\left|(\mathrm{MSE}(W_{r_1,G})-\mathrm{MSE}(W_{r_2,G}))/\mathrm{MSE}(W_{r_3,G})\right|. \tag{7}$$

Hence, the new mutation operation is then expressed as

$$V_{i,G+1}^{[j]}=W_{r_3,G}^{[j]}+F'\cdot(W_{r_1,G}^{[j]}-W_{r_2,G}^{[j]}). \tag{8}$$

In Eqs. (7) and (8), the values of F' for the difference vector are determined based on the following rule: the greater the difference in objective function values between the vectors collected to comprise the vector difference, the larger the contribution of the difference vector offers to the resultant individual. Thus, the amplifications of difference vectors are scaled adaptively. Such adaptation may accelerate DE processes. Therefore, a new DE version, which is formed by embedding the adaptive mutation operation into an original version of DE, can be outlined as

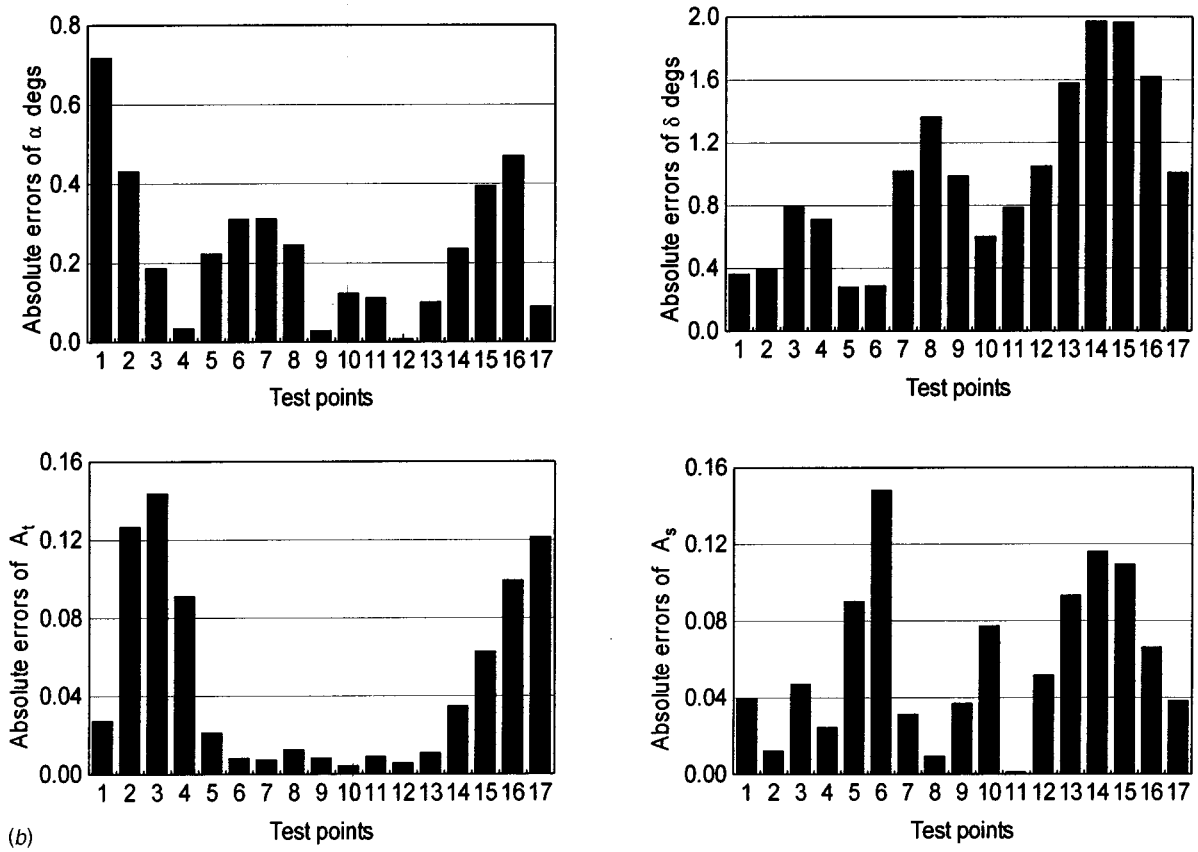

(*b*)

Fig. 4 (***continued***)

1. initialization
2. mutation operation
2.1 perform adaptive mutation with Eq. (8) with probability M_{ad}
2.2 perform original mutation with Eq. (3) with probability $(1-M_{ad})$
3. crossover operation
4. selection
5. repeat Steps 2 to 4.

In the main structural level, the improved version of DE is similar to the original one, [9], except an adaptive mutation operation step is added. This step is implemented by Eq. (8), and it occurs under a new-introduced probability, i.e., adaptive mutation factor, M_{ad}. Therefore, in the new version of DE, when an individual is mutated, it is checked with a uniformly distributed random value within range [0.0, 1.0]. If the value is smaller than M_{ad}, then a direct mutation is done for the individual; otherwise, the mutation is made by Eq. (3).

5 Simulation Results and Discussion

(i) Semiflow Forward-Facing Measurement. In this section, a neural network structure is established and used to calibrate the five-hole pressure probe for the semiflow forward-facing measurement case. The validity of the network is examined with certain measured calibration data.

The neural network with four outputs is used to analyze this case. From the available calibration data, five sets are selected to build the neural network. Each set has 17 data points, which are close to the point numbers with the pitch angle $\alpha=0$ deg and the yaw angle δ varying from -40 deg to $+40$ deg. The range of α is in the set $\{-10, -5, 0, +5, +10$ deg$\}$. Among these samples (85 samples in total), those data with pitch angle $\alpha=0$ deg are chosen as the test samples, and the rest are used as the training sets to train the neural network.

The training algorithm, i.e., DE, is performed with Matlab on a Pentium III personal computer. The evolution parameters are set by trial and error as: population size $N_p=60$, crossover factor $C_r=0.85$, scaling factor $F=0.29$, and adaptive mutation factor $M_{ad}=0.05$. The DE training process is ended at the given generation $G_{\max}=10{,}000$. The CPU time spent by the training process is about four hours.

The trained network is then used to represent the test samples to examine its prediction ability. The whole predictions are finished in a few seconds. Figure 4 shows the prediction results, in which the target data and their predictions by the established neural network are comparatively plotted (Fig. 4(*a*)), and the absolute prediction errors of neural network are also presented (Fig. 4(*b*)). It can be seen from these results that the established neural network can present the aerodynamic properties of the probe precisely. The consistencies between the target data and the predictions are quite satisfactory, i.e., the developed neural network can be used to calibrate the probe for a semiflow forward-facing measurement accurately.

By keeping the same pressures at port 4 and port 5, a conventional calibration method of five-hole probes for the semiflow forward-facing measurement can be used to determine the properties of the calibrated probe. Consequently, when it is used to measure an unknown flow field, the probe must be adjustable around its axis manually to maintain the same pressures at ports 4 and 5, and then a dividing disk on the probe coordinate carrier can indicate the flow pitch angle α accordingly. In the meantime, pressures at five ports are measured and used to calculate the yaw angle δ, the local velocity magnitudes, and the total and static pressures from a set of calibration curves. Therefore, the conven-

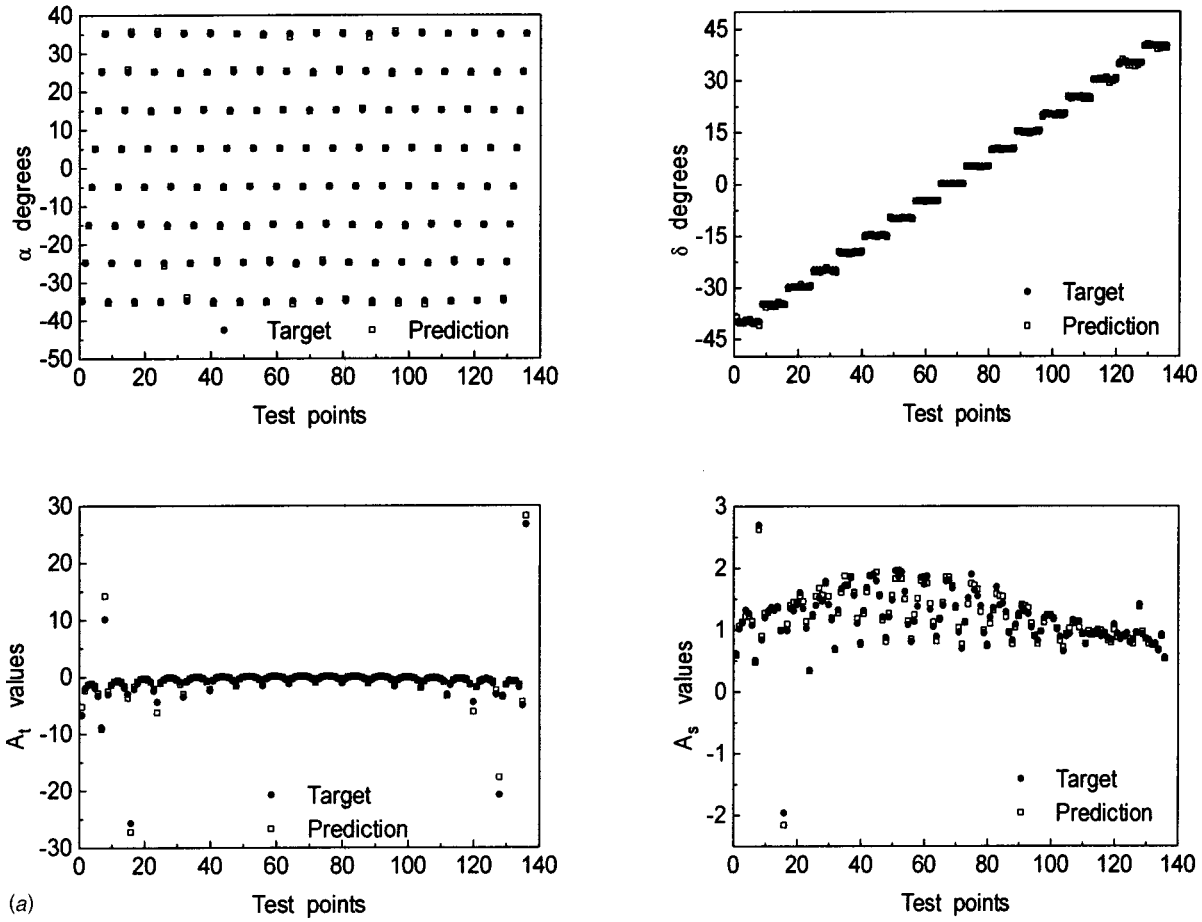

Fig. 5 Test results of neural-network-based method to calibrate five-hole probe for nonflow forward-facing case; (*a*) target parameters and their predictions, (*b*) column error plots of testing results

tional calibration of a five-hole probe for the semiflow forward-facing measurement aims to establish these calibration curves. The curves are generally plotted as some calibration coefficients, which are functions of the yaw angle δ. Such method assumes that the initial flow pitch angle $\alpha=0$ is kept the same corresponding to different yaw angles δ. But, in practice, as long as the angle δ varies, it is difficult to keep the pitch angle α as the same as the initial one if the pressures at port 4 and port 5 are in balance. This will yield errors in the measuring of the pitch angle as well as the other calibration parameters. However, if a neural network is used to prescribe the aerodynamic properties of a probe, as described above, such errors will be eliminated since a range of the pitch angle values is employed in the training samples, which cover the variation range of α corresponding to different yaw angles δ.

(ii) Nonflow Forward-Facing Measurement. The neural networks can be of more advantageous to calibrate a five-hole probe for a nonflow forward-facing measurement than the conventional method does. The conventional calibration of a five-hole probe for a nonflow forward-facing measurement is more complex than that for a semiflow forward-facing measurement, since many calibration curves need to be determined corresponding to different pitch angles α and yaw angles δ. Such a calibration task is regarded as an intricate functional approximation problem. The complexity can be greatly reduced if neural networks are used to solve such problems.

The neural network shown in Fig. 3(b) is used in this case. There are totally four neural networks, and each has one output representing α, δ, A_t, and A_s, respectively. A total of 154 calibration points are selected from the available 289 data points and used to train the neural networks. The training points are collected such that, for each group of 17 points corresponding to their pitch angles α from -40 to $+40$ deg at a given yaw angle δ, the odd points are selected as the training samples while the even ones as the testing samples.

During the DE process, the evolution parameters take the same values as in the above semiflow forward-facing measurement case. Each evolution process ends at the generation $G_{\max}=8000$. The average time period required by the training processes of the four networks is about three hours. The trained networks are then examined with the total 135 testing samples. Figure 5 presents the examination results. Again, the good predicting ability of the neural networks to the aerodynamic properties of the probe can be observed from the results. The performance and accuracy of the neural networks are quite satisfactory.

It is interesting to notice that, when the neural networks are applied to calibrate the five-hole probe for the nonflow forward-facing measurement case, its calibration for the semiflow forward-facing measurement case can be regarded as a special case of the former. In other words, a semiflow forward-facing measurement can be well facilitated if the probe is calibrated by the neural-network-based methods in the nonflow forward-facing measurement case. It means that the proposed calibration method can handle general probe calibration test and no need to distinguish the nonflow forward-facing measurement case or the semiflow forward-facing measurement case. Furthermore, even if the probe can implement a full-flow forward-facing measurement, i.e., the probe can be freely turned in its pitch (around its axis) and yaw planes, the neural-networks-based calibration for the nonflow

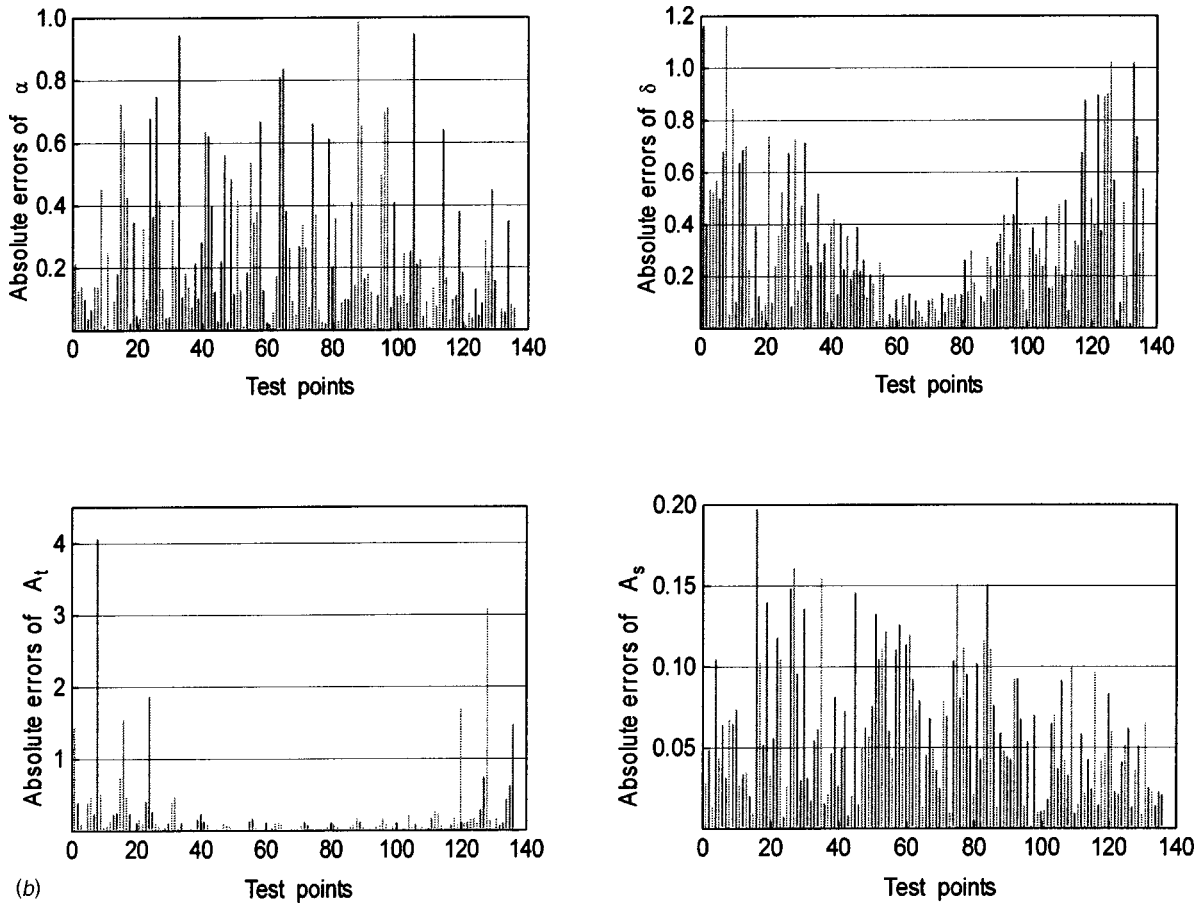

Fig. 5 (***continued***)

forward-facing measurement is still valid. From this point of view, the proposed neural-network-based methods have good reliability and generality.

(iii) Uncertainty Analysis. The following uncertainty analysis focuses on the sensitivity to random error of the proposed neural-network-based probe calibration method. The analysis is based on techniques used by Zilliac [10], Rediniotis [2], and Takahashi [11]. The nonflow forward-facing measurement case is taken for the analysis. For simplicity, only two calibration parameters, pitch angle α and yaw angle δ are considered here.

In order to implement the uncertainty analysis, a scheme is needed to perturb the data that originally used to establish the neural networks for the probe calibrations. In the current application, we follow what Rediniotis [2] and Takahashi [11] did in their studies, and specify that the pressure perturbations satisfy the Gaussian distribution with zero mean and a standard deviation of 0.25 mm H_2O. It is estimated that the worst-case error in pressure measurement is 0.5 mm H_2O and assumed that the random errors of practical pressure measurement should be beyond this error range. Similar to Rediniotis's consideration [2], the error distribution is chosen so that with, a 99.5% probability, the pressure measurement error is smaller than or equal to the worst-case error, i.e., 0.5 mm H_2O. With the perturbed pressure values, the uncertainty in the evaluation of the pressure coefficients B_α and B_δ can then be calculated using their definitions in Eq. (1) and constant-odds combination recommended by Zilliac [10] and Rediniotis [2] listed as follows:

$$\delta C_p = \sqrt{\sum_i \left(\frac{\partial C_p}{\partial p_i} \delta p_i \right)^2} \tag{9}$$

where C_p is any of the pressure coefficients B_α and B_δ, and δp_i is the uncertainty in the measurement of pressure p_i, which can be calculated by the perturbed pressure value together with its original value. For every related calibration and test data, δB_α and δB_δ are obtained and used to perturb the original values of these coefficients so as to get the perturbed neural network inputs.

The sensitivity of the established neural networks for calibrating the five-hole probe is first examined. Two calibration points, i.e., $\alpha = 0$ deg/$\delta = 0$ deg, and $\alpha = 30$ deg/$\delta = 30$ deg, are selected for this purpose. One hundred sets of perturbed neural network inputs are obtained based on the above manner. These inputs are then presented to the neural networks to predict the pitch angle and the yaw angle. The error statistics obtained from the above predictions are as follows: (a) for point of $\alpha = 0$ deg/$\delta = 0$ deg, pitch angle—average absolute error = 0.33 deg, standard deviation of error = 0.49 deg, yaw angle—average absolute error = 0.42 deg, standard deviation of error = 0.56 deg; (b) For point of $\alpha = 30$ deg/$\delta = 30$ deg, pitch angle—average absolute error = 0.51 deg, standard deviation of error = 0.77 deg, yaw angle—average absolute error = 0.71 deg, standard deviation of error = 0.92 deg. The established neural networks have quite a small uncertainty to random errors on the selected points.

To examine the sensitivity of the proposed neural-network-based calibration procedure to random error, the network structures and the training strategies are kept the same as those used in the calibration process in Section 5, the only exception is that the data used are perturbed ones produced by Eq. (9). The perturbed calibration data are first employed to train the neural networks. The trained neural networks are then used to predict the perturbed test data. The predictions obtained by this process are compared to

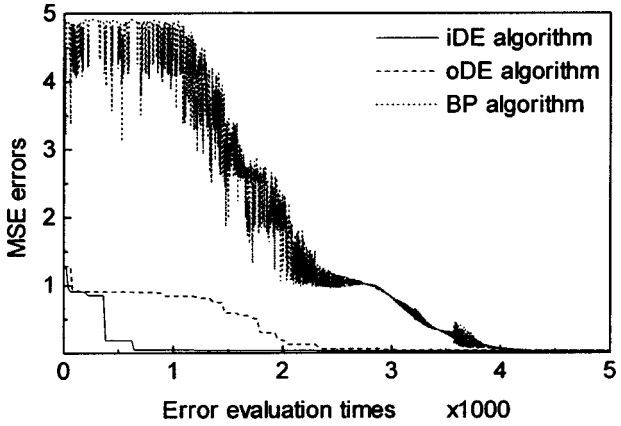

Fig. 6 Performance comparison of iDE, oDE, and BP algorithm for neural network training

those produced by the unperturbed networks. The average absolute errors and the standard deviations of the error between the comparisons can then be calculated and listed here: pitch angle—average absolute error = 0.36 deg, standard deviation of error = 0.51 deg; yaw angle—average absolute error = 0.45 deg, standard deviation of error = 0.59 deg. These results show that the proposed neural-network-based method is also less sensitive to the random error.

6 Performance Comparison

A performance comparison of the neural network training algorithms within the proposed improved version of DE (denoted as ''iDE'') described in the paper, the original version of DE (denoted as ''oDE'') and the BP algorithm is also carried out and presented here for the semiflow forward-facing measurement case. The comparisons are justified in terms of the same evaluation time verse network error. For BP algorithm, the evaluation ''time'' directly equals to the time of its updated iterations; while for DE models, it equals to a production of the population size and the evolving generations. During numerical simulations, the evolution parameters for both versions of DE algorithms are taken the same as those in previous sections. The BP algorithm is implemented with the same scheme described in Rediniotis et al. [1,2]. The convergence histories of these training processes with an average of five runs for each algorithm at different initial points are presented in Fig. 6. As expected, one can easily find that, from Fig. 6, the DE algorithms perform better than BP, and the improve DE algorithm is better than the original DE algorithm.

In addition, the time periods required by these three algorithms are also recorded for the given number of network error evaluations. The average time period for the BP algorithm with over five runs is 2.45 hours, while for iDE and oDE it is 0.99 hours and 1.01 hours, respectively. The proposed improved algorithm shows superiority to the other two algorithms in time consumed as well.

7 Conclusions

A new neural-network-based method is proposed for the calibration of a five-hole pressure probe in this paper. The method uses a novel kind of evolutionary algorithm, differential evolution, to train the connection weights of neural networks. The commonly used two cases, i.e., the semiflow forward-facing measurement case and the nonflow forward-facing measurement case, are tested for a real five-hole probe. The numerical simulations show that the new improved approach facilitates the given task of probe calibration satisfactorily. As a neural-network-based method, the proposed improved approach eliminates the intricate task, in which a larger number of calibration curves must be determined and interpolated as the conventional calibration method does. In addition, with the new approach, there is no need to distinguish an expected measurement to be a ''semiflow forward-facing measurement'' or a ''nonflow forward-facing measurement,'' thus it has good generality and reliability. Furthermore, through applying a new improved version of differential evolution to neural network training described in the study, a reliable calibration method with high accuracy and effectiveness has been obtained.

Acknowledgment

The work described in this paper was supported by a grant from the Research Grants Council of the Hong Kong Special Administrative Region, China (Project No. CityU 1013/02E), a Strategic Research Grant (Project No. 7001371(BC)), City University of Hong Kong, HKSAR, and Ph.D. Scholarship, Xi'an Jiaotong University, Xi'an, P.R. China.

References

[1] Rediniotis, O. K., and Chrysanthakopoulos, G., 1998, ''Application of Neural Networks and Fuzzy Logic to the Calibration of the Seven-Hole Probe,'' ASME J. Fluids Eng., **120**, pp. 95–101.
[2] Rediniotis, O. K., and Vijayagopal, R., 1999, ''Miniature Multihole Pressure Probes and Their Neural-Network-Based Calibration,'' AIAA J., **37**(6), pp. 666–674.
[3] Stron, R., and Price, K., 1997, ''Differential Evolution—A Simple and Efficient Heuristic for Global Optimization Over Continuous Space,'' J. Global Optim., **11**, pp. 341–359.
[4] Schreck, S. J., Faller, W. E., and Luttges, M. W., 1993, ''Neural Network Prediction of Three-Dimensional Unsteady Separated Flow Fields,'' *AIAA* Paper No. 93-3426.
[5] Schreck, S. J., and Faller, W. E., 1995, ''Encoding of Three-Dimensional Unsteady Separated Flow Field Dynamics in Neural Network Architectures,'' *AIAA* Paper No. 95-0103.
[6] McMillen, R. L., Steck, J. E., and Rokhsaz, K., 1995, ''Application of an Artificial Neural Network as a Flight Test Data Estimator,'' *AIAA* Paper No. 95-0561.
[7] Fan, X. T., Herbert, T., and Haritonidis, J. H., 1995, ''Transition Control With Neural Networks,'' *AIAA* Paper No. 95-0674.
[8] Price, K., 1999, ''An Introduction to DE,'' *New Ideas in Optimization*, D. Corne, M. Dorig, and F. Glover eds., McGraw-Hill, London, pp. 78–108.
[9] Storn, R., and Price, K., 1995, ''DE–A Simple and Efficient Adaptive Scheme for Global Optimization Over Continuous Space,'' Technical Report TR-95-012, ICSI, Mar. (via ''ftp.icsi.berkeley.edu/pub/techreports/1995/tr-95-012.ps.Z).
[10] Takahashi, T. T., 1997, ''Measurement of Air Flow Characteristics Using Seven-Hole Cone Probes,'' NASA Report No. TM-112194.
[11] Zilliac, G. G., 1993, ''Modeling, Calibration, and Error Analysis of Seven-Hole Pressure Probes,'' Exp. Fluids, **14**, pp. 104–120.

A. Arbel

A. Shklyar

Institute of Agricultural Engineering,
Agricultural Research Organization,
The Volcani Center,
P.O. Box 6,
Bet Dagan 50250, Israel

D. Hershgal

Department of Fluid Mechanics
and Heat Transfer,
Tel-Aviv University,
Ramat Aviv 69978,
Israel

M. Barak

Institute of Agricultural Engineering,
Agricultural Research Organization,
The Volcani Center,
P.O. Box 6,
Bet Dagan 50250, Israel

M. Sokolov

Department of Fluid Mechanics
and Heat Transfer,
Tel-Aviv University,
Ramat Aviv 69978,
Israel

Ejector Irreversibility Characteristics

The present study analyzes and characterizes the irreversibility of the ejector's internal processes in an effort to improve the understanding of the making of its overall performance. The analysis presented is based on entropy production methodology. Since entropy production is equivalent to performance losses, minimizing entropy production could serve as a tool for performance optimization. The three main internal processes forming sources of ejector irreversibility are mixing, kinetic energy losses, and normal shock wave. Comparison of these with those of an ideal mixing process, an ideal turbine-compressor system and stagnation conditions (of the flow after mixing) provides the benchmarks against which the actual overall performance is measured. By identifying the sources of irreversibility, the analysis provides a diagnostic tool for performance improvements. While irreversibility due to mixing can be eliminated by appropriate choice of gas and/or inlet conditions and an appropriate adjustable throat can eliminate losses associated with normal shock wave–kinetic energy losses can only be reduced but not totally eliminated. [DOI: 10.1115/1.1523067]

1 Introduction

Ejectors have a wide range of applications, [1,2], but the process is basically the same in every case: a high-pressure fluid (the primary stream) transfers part of its energy to a low-pressure fluid (the secondary stream), and the resulting mixture is discharged at a (back) pressure somewhere between the primary and the secondary pressures. Ejectors can operate with either incompressible (liquids) or compressible (gases and vapors) fluids. Most of the ejectors used by industry, [1], are of the complex compressible-flow type and are therefore the focus of the present study.

Ejector design methods are not new. Since the 1920s, many papers have been published in a continuous effort to improve the understanding of ejector processes and performance. However, knowledge of the physical mechanisms of ejector performance is still limited. The design methods can be divided into two groups, [1]: one-dimensional and two or three-dimensional. The two or three-dimensional methods are suitable for optimization of ejector dimensions. The one-dimensional analysis is often used for engineering design purposes because, despite its relative simplicity, it has been shown to yield consistent and reasonably accurate results, [1]. Pioneer research work by Keenan et al. [3] produced the first comprehensive theoretical and experimental analysis of the ejector, and is the basis of much that has taken place since. Although a number of modifications have been introduced, no attention has been given to the irreversibilities involved in the ejector processes.

The method of entropy generation minimization has emerged during the last two decades as a distinct subfield in heat transfer, [4,5]; it involves the simultaneous application of the principles of heat transfer and thermodynamics to the creation of realistic models of heat transfer processes, devices, and installations. Such ''realistic'' models account for the inherent irreversibilities of heat, mass, and fluid flow processes. Some of the most fundamental approaches deal with the optimization of power or refrigeration plants with heat transfer irreversibilities. In the case of power generation, the focus has been on the conditions for the production of maximum instantaneous power, which are equivalent to those for minimum rate of entropy generation (cf. the Gouy-Stodola theorem, [4], p. 24). In the refrigeration case, [6], as in the case of the vapor compression cycle, [7], the maximized refrigeration load corresponds to minimizing the rate of entropy generation. Recently, Bejan et al. [8] applied the entropy generation minimization technique to the optimization of a heat-driven refrigeration plant. Minimization of entropy generation is often referred to as thermodynamic optimization or thermodynamic design.

However, in all of these approaches the sources of losses of performance and their partitioning remains unknown. Identifying and quantifying such sources of performance losses is vital for pinpointing areas where design improvement may be applied effectively.

The objectives of this study were to develop the methodology and model to characterize the irreversibility sources within the ejector and to demonstrate its use in a parametric evaluation of ejector irreversibility and performance.

Contributed by the Fluids Engineering Division for publication in the JOURNAL OF FLUIDS ENGINEERING. Manuscript received by the Fluids Engineering Division September 15, 2000, revised manuscript received June 28, 2002. Associate Editor: K. M. B. Q. Zaman.

2 Method of Analysis

2.1 Methodology. In order to define sources of losses in ejector performance, an equivalent ideal processes should be theoretically defined as a processes with no entropy production. When applicable, such ''ideal'' process is equivalent to a reversible process from a thermodynamic point of view. In a mixing process, which cannot be reversible, the ''ideal process'' represents one with an upper limit of performance.

The next step is to show that the entropy production is equivalent to the losses of performance so that minimizing entropy production results in maximizing performance. In addition, benchmarking ''ideal process'' within the ejector's subprocesses indicates sources of irreversibility and can be used to evaluate performance losses.

The ejector includes three main sources of irreversibility: ''pure mixing,'' ''kinetic energy losses,'' and normal shock wave. The ''pure mixing'' and ''kinetic energy losses'' occur simultaneously (in parallel) in the mixing section followed by (in series) the normal shock wave (which is in the constant-area section).

2.2 Analysis. Unless otherwise stated, the analysis employed here is for a fixed geometry ejector of the type shown in Fig. 1. As in the case of Keenan et al. [3], the following assumptions were made: (1) flows are one-dimensional and adiabatic; (2) both streams have the same molecular weight and the same specific-heat ratio; (3) shear forces between the streams and the walls are negligible; (4) both primary and secondary flows start from stagnation conditions; (5) flows of both streams between the inlets and the cross section x are isentropic; (6) stagnation conditions prevail at the ejector exit; (7) flow is isentropic in the diffuser section; (8) a normal shock may occur in the constant-area section; (9) mixing is completed at cross section 1; and (10) mixing occurs at constant pressure. With these assumptions, and on the basis of perfect gas dynamics, Keenan et al. [3] showed that for given inlet conditions (including mass flow-rate ratio $\omega = \dot{m}_s/\dot{m}_p$), the backpressure function depends on the ''mixing pressure'' and has a maximum value. Therefore, they optimized the ejector performance for given inlet conditions by maximizing the backpressure.

This approach seems direct, but the losses of performance and their composition remain unknown. To complete the analysis, an approach based on the methodology of entropy production is used to determine and characterize the partitioning of the irreversibility sources.

Basically, an ejector can be considered as a mixer. The control volume of a general case of a mixing process is shown in Fig. 2. The energy equation for this control volume subjected to the above assumptions (1 to 4, and 6) is given by

$$h_{0_3} = h_3 = \frac{h_{0_p} + \omega h_{0_s}}{1+\omega}. \tag{1}$$

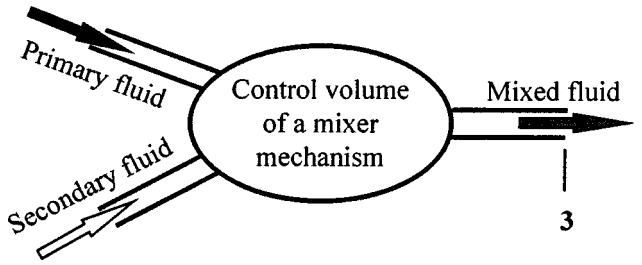

Fig. 2 Schematic diagram of a mixer mechanism control volume

Since the enthalpy of a perfect gas is a function of the temperature only, this equation can be replaced by

$$T_{0_3} = T_3 = \frac{T_{0_p} + \omega T_{0_s}}{1+\omega}. \tag{2}$$

Thus, under the above assumptions, the mixing process does not alter the stagnation temperature of the mixed stream. This means that under the same inlet conditions and with the same mass flow-rate ratio (ω), the outlet temperature of an adiabatic turbine-compressor (as shown in Fig. 3) and of a theoretical adiabatic and ideal mixing process (which is defined below) are the same as that of an adiabatic ejector. Moreover, since the mixing in the ejector is completed at cross section **1**, the stagnation temperature in this cross section is also

$$T_{0_1} = T_{3_{TC}} = T_{3_{Ip}} = T_{3_{Ej}} = T_3. \tag{3}$$

The outlet temperature ratios are given by

$$\frac{T_3}{T_{0_s}} = \frac{1+\omega\tau}{(1+\omega)\tau} \quad \text{or} \quad \frac{T_3}{T_{0_p}} = \frac{1+\omega\tau}{1+\omega} \tag{4}$$

where τ is the ratio of stagnation temperatures of the secondary stream to the primary stream ($\tau = T_{0_s}/T_{0_p}$). Thus, the outlet temperature ratios depend only on τ and ω but not on the outlet pressure (P_3). Therefore, τ and ω will be used as independent variables and the outlet pressure as a dependent variable. This means that, for given inlet conditions (τ and ω) the characteristics of the mixing process performance is signified by the outlet pressure only. In other words, while the outlet temperature is independent of the particulars of the adiabatic mixing, the outlet pressure does. Moreover, this outlet pressure indicates the mixing process performance, but not the losses of performance. Thus, attention should be focused on the irreversibility of the mixing processes. The *total* (without specifying sources or composition) entropy production of an ejector was calculated by Porter et al. [9] and Papamoschou [10]. The outlet state is defined according to these two properties (temperature and pressure), and the rate of entropy generation of the control volume (as shown in Fig. 2) is given by

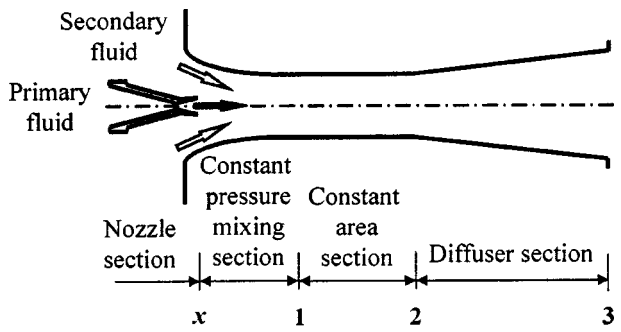

Fig. 1 Schematic view of a fixed geometry ejector

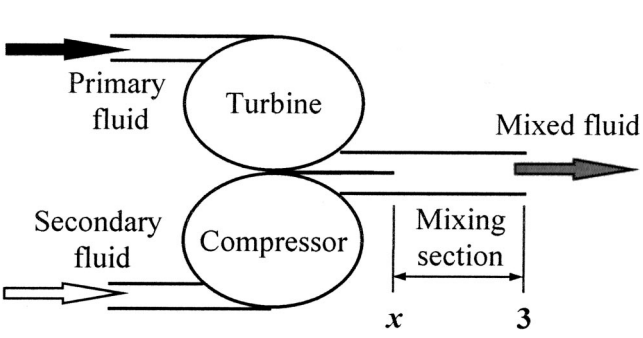

Fig. 3 Schematic view of a turbine compressor

$$\Delta \dot{S}_{\mathbf{3}} = \dot{m}_p((\mathbf{1}+\omega)s_{\mathbf{3}} - (s_{\mathbf{0}_p} + \omega s_{\mathbf{0}_s})). \tag{5}$$

For a perfect gas

$$\Delta \dot{S}_{\mathbf{3}} = R\dot{m}_p\left(\frac{k}{k-\mathbf{1}}\ln\left(\frac{T_{\mathbf{3}}^{(1+\omega)}}{T_{\mathbf{0}_p}T_{\mathbf{0}_s}{}^{\omega}}\right) - \ln\left(\frac{P_{\mathbf{3}}^{(1+\omega)}}{P_{\mathbf{0}_p}P_{\mathbf{0}_s}{}^{\omega}}\right)\right). \tag{6}$$

Since mixing is, by definition, an irreversible process let us define the criterion for an ''ideal mixing process'' as

$$\Delta \dot{S}_{\mathbf{3}_{Ip}} = 0 = R\dot{m}_p\left(\frac{k}{k-\mathbf{1}}\ln\left(\frac{T_{\mathbf{3}_{Ip}}{}^{(1+\omega)}}{T_{\mathbf{0}_p}T_{\mathbf{0}_s}{}^{\omega}}\right) - \ln\left(\frac{P_{\mathbf{3}_{Ip}}{}^{(1+\omega)}}{P_{\mathbf{0}_p}P_{\mathbf{0}_s}{}^{\omega}}\right)\right). \tag{7}$$

Thus, the ''ideal mixing process'' outlet pressure ratios are given by

$$\frac{P_{\mathbf{3}_{Ip}}}{P_{\mathbf{0}_s}} = \left(\tau^{-\omega/\mathbf{1}+\omega}\left(\frac{\mathbf{1}+\omega\tau}{\mathbf{1}+\omega}\right)\right)^{k/k-\mathbf{1}}\left(\frac{P_{\mathbf{0}_p}}{P_{\mathbf{0}_s}}\right)^{\mathbf{1}/\mathbf{1}+\omega} \quad \text{or} \quad \frac{P_{\mathbf{3}_{Ip}}}{P_{\mathbf{0}_p}} = \left(\tau^{-\omega/\mathbf{1}+\omega}\left(\frac{\mathbf{1}+\omega\tau}{\mathbf{1}+\omega}\right)\right)^{k/k-\mathbf{1}}\left(\frac{P_{\mathbf{0}_p}}{P_{\mathbf{0}_s}}\right)^{-\omega/\mathbf{1}+\omega}. \tag{8}$$

This is the highest possible theoretical outlet pressure and will therefore be used as a reference.

The rate of entropy generation of the control volume (as shown in Fig. 2) which represent an arbitrary mixing process, may be given as

$$\Delta \dot{S}_{\mathbf{3}} = \Delta \dot{S}_{\mathbf{3}} - \Delta \dot{S}_{\mathbf{3}_{Ip}} \geqslant \mathbf{0}. \tag{9}$$

Substituting Eqs. (3), (6), and (7) in Eq. (9) is used to remove the temperature term and yields

$$\Delta \dot{S}_{\mathbf{3}} = \dot{m}_p(\mathbf{1}+\omega)R\ln\left(\frac{P_{\mathbf{3}_{Ip}}}{P_{\mathbf{3}}}\right) \tag{10}$$

where $P_{\mathbf{3}}$ is the outlet pressure of a mixing process.

Three main features of this relationship should be noticed: (a) entropy production is equivalent to performance losses; (b) minimizing entropy generation is equivalent to maximizing the outlet pressure; and (c) entropy generation can be expressed as the performance ratio between the ideal and the actual mixing processes. However, this equation can be written for unit mass of the combined mixed stream

$$\Delta s_{\mathbf{3}} = R\ln\left(\frac{P_{\mathbf{3}_{Ip}}}{P_{\mathbf{3}}}\right) \tag{11}$$

or, on a mole basis,

$$\Delta \overline{s}_{\mathbf{3}} = \overline{R}\ln\left(\frac{P_{\mathbf{3}_{Ip}}}{P_{\mathbf{3}}}\right). \tag{12}$$

Note that Eqs. (11) and (12) indicate that the ratio $P_{\mathbf{3}_{Ip}}/P_{\mathbf{3}}$ does not depend on the gas constant R.

As shown in Appendix A, the lost work between the outlet states of an actual mixing process and ''ideal mixing process'' is

$$L\overline{w} = T_{\mathbf{3}}\Delta \overline{s}_{\mathbf{3}}. \tag{13}$$

Equation (13) means that the lost work is proportional to the entropy generation and, once again, that minimizing the lost work (or entropy generation) is equivalent to maximizing the outlet pressure.

According to Eq. (12), the total entropy generation in the ejector is given by

$$\Delta \overline{s}_{\mathbf{3}_{Ej}} = \overline{R}\ln\left(\frac{P_{\mathbf{3}_{Ip}}}{P_{\mathbf{3}_{Ej}}}\right) \tag{14}$$

and the entropy generation between the ejector inlets and cross section **1**, is given by

$$\Delta \overline{s}_{\mathbf{0}_1} = \overline{R}\ln\left(\frac{P_{\mathbf{3}_{Ip}}}{P_{\mathbf{0}_1}}\right). \tag{15}$$

Where the stagnation pressures ($P_{\mathbf{3}_{Ej}}$ and $P_{\mathbf{0}_1}$) are calculated following Keenan et al. [3]. While $\Delta \overline{s}_{\mathbf{3}_{Ej}}$ is the total entropy generation of the ejector, $\Delta \overline{s}_{\mathbf{0}_1}$ is the entropy generation between the ejector inlet and cross section **1**. In other words, the stagnation pressure at cross section **1** represents the mixing process in the mixing section, followed by a reversible process. Assuming that both streams flow isentropicaly between the inlets and the cross section x, $\Delta \overline{s}_{\mathbf{0}_1}$ is then due only to the mixing process (between cross sections x and **1**). Thus, the entropy generation of a normal shock (at the constant-area section) is given by

$$\Delta \overline{s}_{NS} = \Delta \overline{s}_{\mathbf{3}_{Ej}} - \Delta \overline{s}_{\mathbf{0}_1} = \overline{R}\ln\left(\frac{P_{\mathbf{0}_1}}{P_{\mathbf{3}_{Ej}}}\right). \tag{16}$$

Now, consider the case of ideal turbine-compressor as defined in Appendix B. In this case the mixing process occurs under stagnation conditions and the entropy generation is a result of ''pure mixing'' only and is given by

$$\Delta \overline{s}_{PM} = \Delta \overline{s}_{\mathbf{3}_{TC}} = \overline{R}\ln\left(\frac{P_{\mathbf{3}_{Ip}}}{P_{\mathbf{3}_{TC}}}\right) \tag{17}$$

where the outlet stagnation pressure ($P_{\mathbf{3}_{TC}}$) is calculated as shown in Appendix B. Assuming kinetic energy conservation (instead of momentum conservation) in the mixing section of the ejector, it can be shown that outlet pressure of the ideal turbine compressor is identical to the stagnation pressure at cross section **1** of the ejector. Thus, ''pure mixing'' in both ejector and turbine-compressor results in the same entropy generation.

In order to improve the performance by eliminating the entropy generation resulting from ''pure mixing,'' the entropy of both primary and secondary streams should be the same ($s_{\mathbf{0}_p} = s_{\mathbf{0}_s}$). This means that

$$\tau = \left(\frac{T_{\mathbf{0}_s}}{T_{\mathbf{0}_p}}\right) = \left(\frac{P_{\mathbf{0}_s}}{P_{\mathbf{0}_p}}\right)^{k-\mathbf{1}/k}. \tag{18}$$

Only under these (Eq. (18)) conditions the ''ideal mixing process'' and the mixing process presented by an ideal turbine compressor are reversible. Only then both streams (primary and secondary) in the mixing section of the ejector and the respective streams in the mixing section of an ideal turbine compressor are in the same thermodynamic state having identical entropy and pressure. When the two streams do not satisfy conditions set by Eq. (18), there is a difference in temperature between these two streams, which could not be adjusted to improve the performance.

The mixing process within the ejector is accompanied by velocity gradient with a consequent kinetic energy loss. The ideal gas assumption implies no change in internal energy (as shown in Appendix A) and no dissipation. Thus, the part of the entropy generation in the mixing section which is due to ''kinetic energy losses,'' is given by

$$\Delta \overline{s}_{Ke} = \Delta \overline{s}_{\mathbf{0}_1} - \Delta \overline{s}_{\mathbf{3}_{TC}} = \overline{R}\ln\left(\frac{P_{\mathbf{3}_{TC}}}{P_{\mathbf{0}_1}}\right). \tag{19}$$

Following Keenan et al. [3], the loss of kinetic energy is dissipated in a form of internal heat generation in the mixing section. However, for an ideal gas, which has no dissipation (internal friction), this conversion should be by other physical mechanisms (e.g., shock wave).

To sum up, the entropy generation in an ejector is given by

$$\Delta\bar{s}_{3_{Ej}} = \Delta\bar{s}_{PM} + \Delta\bar{s}_{Ke} + \Delta\bar{s}_{NS}$$

$$= \bar{R}\left(\ln\left(\frac{P_{3_{Ip}}}{P_{3_{TC}}}\right) + \ln\left(\frac{P_{3_{TC}}}{P_{0_1}}\right) + \ln\left(\frac{P_{0_1}}{P_{3_{Ej}}}\right)\right) \quad (20)$$

where $P_{3_{Ej}}$ and P_{0_1} are calculated following Keenan et al. [3], $P_{3_{TC}}$ from Appendix B Eq. (*B*7), and $P_{3_{IP}}$ from Eq. (8).

Since $P_{3_{Ip}}$ is the highest possible pressure at the "ideal mixing process" exit, it is convenient to define the relative performance of an arbitrary relevant mixing process as

$$Rp = \frac{P_3}{P_{3_{Ip}}} = \mathrm{Exp}\left(-\frac{\Delta\bar{s}_3}{\bar{R}}\right) \quad (21)$$

and to define the relative performance loss of the mixing process as

$$L = 1 - Rp = \frac{P_{3_{Ip}} - P_3}{P_{3_{Ip}}}. \quad (22)$$

Thus, the ejector overall relative performance losses is given by

$$L_{Ej} = L_{PM} + L_{Ke} + L_{NS} = \frac{P_{3_{Ip}} - P_{3_{TC}}}{P_{3_{Ip}}} + \frac{P_{3_{TC}} - P_{0_1}}{P_{3_{Ip}}} + \frac{P_{0_1} - P_{3_{Ej}}}{P_{3_{Ip}}} \quad (23)$$

which means that the backpressure losses is composed of "pure mixing," "kinetic energy losses," and normal shock wave losses.

Define now the efficiency of a mixing process as

$$\eta = \frac{P_3 - P_{0_s}}{P_{3_{Ip}} - P_{0_s}}. \quad (24)$$

The relative pressure lift losses can be expressed in terms of the mixing efficiency as

$$l = 1 - \eta = \frac{P_{3_{Ip}} - P_3}{P_{3_{Ip}} - P_{0_s}}. \quad (25)$$

Substituting Eq. (22) in Eq. (25) yields

$$l = L\frac{P_{3_{Ip}}}{P_{3_{Ip}} - P_{0_s}}. \quad (26)$$

Finally, the ejector relative pressure lift loss is given by

$$l_{Ej} = l_{PM} + l_{Ke} + l_{NS} = \frac{P_{3_{Ip}} - P_{3_{TC}}}{P_{3_{Ip}} - P_{0_s}} + \frac{P_{3_{TC}} - P_{0_1}}{P_{3_{Ip}} - P_{0_s}} + \frac{P_{0_1} - P_{3_{Ej}}}{P_{3_{Ip}} - P_{0_s}}. \quad (27)$$

While, according to Eqs. (8) and (*B*7), the outlet pressure of an "ideal mixing process" ($P_{3_{Ip}}$) and an ideal turbine compressor ($P_{3_{TC}}$) are functions of only four independent dimensionless parameters (τ, ω, P_{0_p}/P_{0_s} and k), following Keenan et al. [3], the exit pressure of an ejector ($P_{3_{Ej}}$) and its relevant stagnation pressure at cross section **1** (P_{0_1}) are also functions of the mixing pressure. Following Keenan et al. [3], the ejector outlet pressure function has a maximum value. This maximum defines the mixing pressure for which $P_{3_{Ej}}$ assumes it highest possible value. An ejector operating under given inlet conditions and having the maximal value of the discharge pressure, $P_{3_{Ej}}$ is referred to as an "optimal fixed ejector." Thus, for "optimal fixed ejector," all the above dimensionless dependent variables are functions of only four independent dimensionless variables (τ, ω, P_{0_p}/P_{0_s}, and k).

3 Results and Discussion

3.1 Ejector Performance Optimization. The following conditions were adopted only for demonstration purposes: $\omega = 2$, $\tau = 0.5$, $P_{0_p}/P_{0_s} = 100$, and $k = 1.4$. Figure 4(a) displays the Mach number at different cross sections as a function of the mixing pressure. As expected, reduction of the mixing pressure causes an increase of M', M'', and M_1. However, M_2 decreases when $M_1 > 1$ (supersonic) and $M_2 = M_1$ when the flow is subsonic ($M_1 \leq 1$). Each point on the curves in Fig. 4(a) represents the computed Mach number for a particular ejector comprised of a combination of primary nozzle, secondary nozzle, and a mixing tube. Such an ejector is referred to as a "fixed ejector." For example, the required secondary nozzle shape should be convergent where $M'' \leq 1$ and convergent divergent where $M'' > 1$. Figure 4(b) depicts the pressures corresponding to Mach numbers at various cross sections. Since the mixing occurs at constant pressure ($P_1 = P_x$), the mixed stream is discharged at P_2, which results from the normal shock wave. Consequently the flow reaches the stagnant backpressure ($P_{3_{Ej}}$) at the diffuser's exit. Figure 4(b) shows that for given inlet conditions, $P_{3_{Ej}}$ exhibits a maximum (point a) which determines P_x for which $P_{3_{Ej}}$ assumes its highest possible value. An ejector operating under given inlet conditions and having the maximal value of the discharge pressure, $P_{3_{Ej}}$, is referred to as an "optimal fixed ejector."

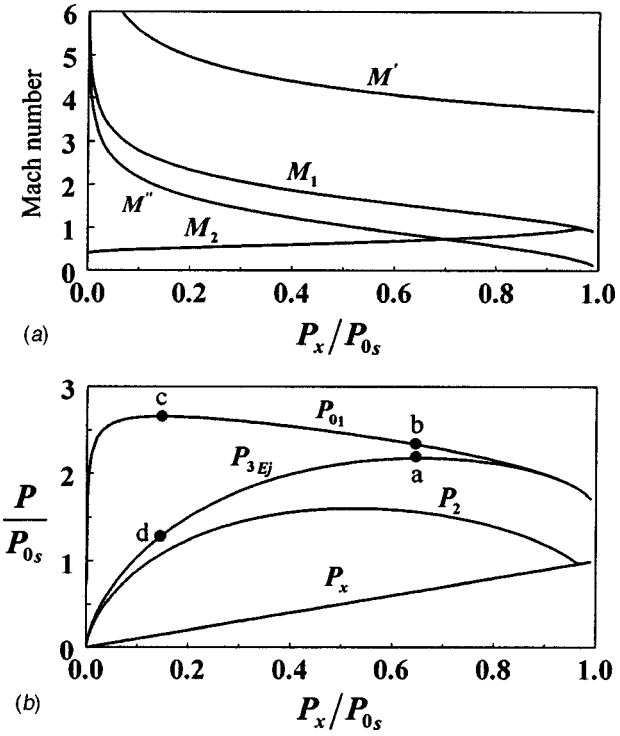

Fig. 4 Theoretical results as functions of the mixing pressure (P_x), where $\omega = 2$, $\tau = 0.5$, $P_{0_p}/P_{0_s} = 100$, and $k = 1.4$. (*a*) Mach numbers of the primary and the secondary streams at cross section *x* (M' and M'', respectively), and of the mixed stream at cross sections 1 and 2 (M_1 and M_2, respectively); (*b*) pressure at cross sections 1, 2, and 3, and the stagnation pressure at cross section 1.

Figure 4(b) also presents the stagnation pressure at cross section **1** (P_{0_1}). Thus, to retain the stagnation pressure at cross section **3** (avoid normal shock losses), the constant-area section should be replaced by adjustable throat represented by the dashed line in Fig. 5. After the flow has started (starting conditions), the adjustable throat may be varied, to provide the optimum operating area. Then, as the backpressure increases, the shock in the divergent part of the throat moves upstream toward the throat with diminishing strength. The flow is then ideal, with a maximum attainable backpressure for a given mixing pressure. This ejector

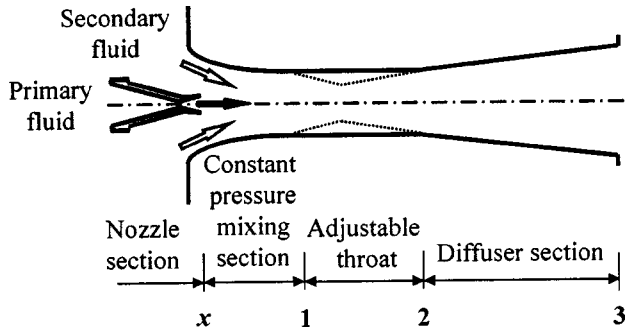

Fig. 5 Schematic view of an ejector with adjustable throat

is referred to as an ''adjustable throat ejector.'' Thus, ''adjustable throat ejector with optimal starting conditions'' is defined as an ejector with the maximum attainable backpressure (P_{0_1}-point b), which must therefore have an adjustable throat, and start with optimal starting conditions.

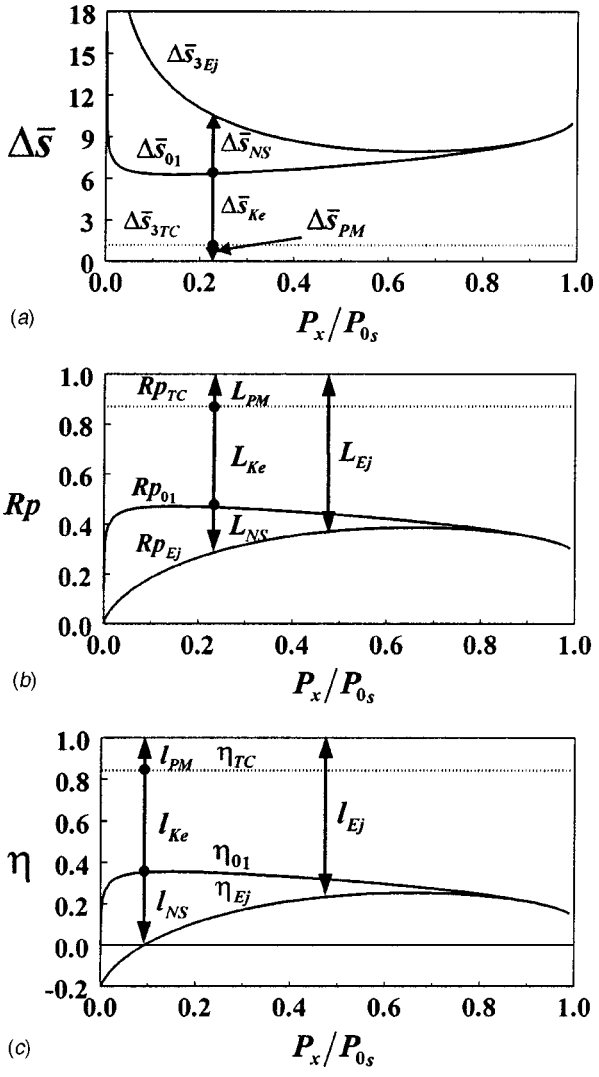

Fig. 6 Theoretical results of a ''fixed ejector,'' and an ''adjustable throat ejector,'' as functions of the mixing pressure (P_x), where $\omega=2$, $\tau=0.5$, $P_{0_p}/P_{0_s}=100$ and $k=1.4$. (*a*) Entropy generation; (*b*) relative performance; (*c*) efficiency.

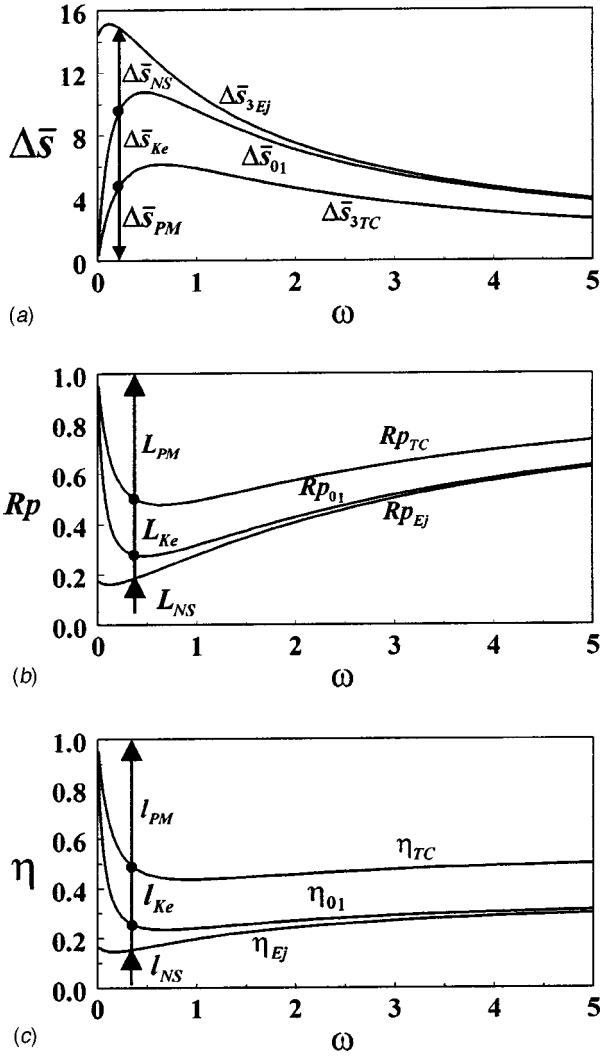

Fig. 7 Theoretical results of an ''optimal fixed ejector,'' an ideal turbine compressor, and an ''adjustable throat ejector with optimal starting conditions,'' as functions of the inlet flow rate ratio (ω), where $\tau=1$, $P_{0_p}/P_{0_s}=100$ and $k=1.4$. (*a*) Entropy generation; (*b*) relative performance; (*c*) efficiency.

As shown in Fig. 4(b), the ''adjustable throat ejector with optimal starting conditions'' does not provide the optimal operating conditions: for those conditions, the P_{0_1} function passes through a maximum (point c), which defines the P_x value for which P_{0_1} assumes its highest possible value. An adjustable throat ejector operating under given inlet conditions and having discharge pressure P_{0_1}—point c—is referred to as an ''adjustable throat ejector with optimal operating conditions.'' In order to start such an adjustable throat ejector, the required backpressure should be $P_{3_{Ej}}$—point d—(or lower), which is lower than that of the optimal fixed ejector (point a).

However, under the above conditions, the back pressures of the ideal mixing process and of the ideal turbine compressor calculated according to the Eqs. (8) and (*B*7), respectively, are $P_{3_{Ip}}/P_{0_s}=5.66$ and $P_{3_{TC}}/P_{0_s}=4.9$. The entropy generation functions for a ''fixed ejector'' ($\Delta\overline{s}_{3_{Ej}}$) and ''adjustable throat ejector'' ($\Delta\overline{s}_{0_1}$) were calculated from Eqs. (14) and (15), respectively, and are presented in Fig. 6(a). As expected, both functions pass through a minimum; this minimum defines the P_x value for which entropy generation ($\Delta\overline{s}_{3_{Ej}}$ or $\Delta\overline{s}_{0_1}$) assumes its lowest possible value. In other words, minimized entropy generation could be

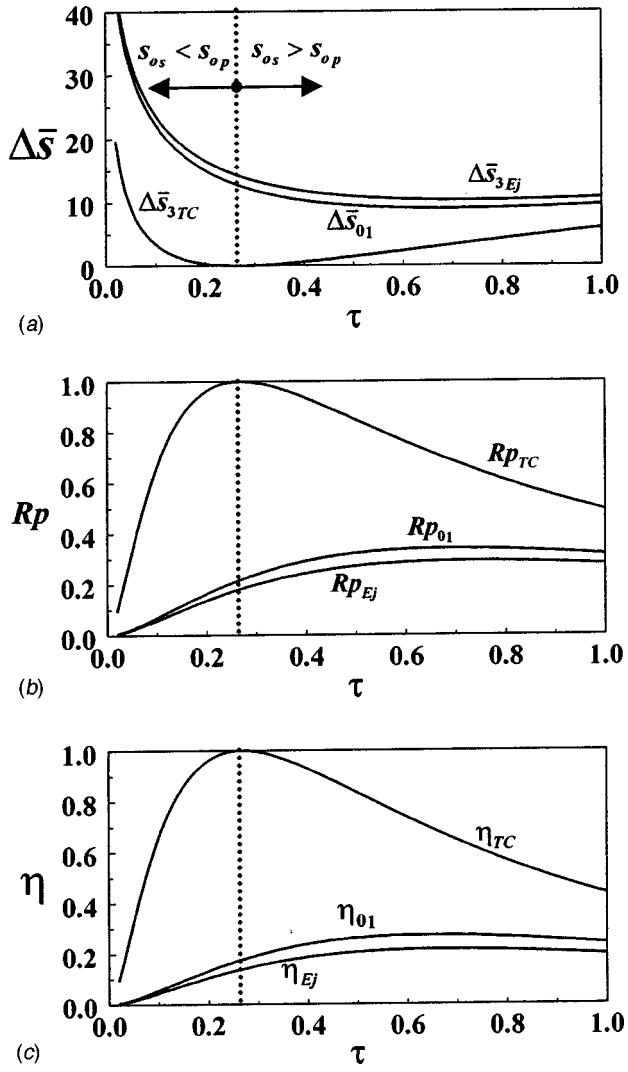

Fig. 8 Theoretical results of an "optimal fixed ejector," an ideal turbine compressor, and an "adjustable throat ejector with optimal starting conditions," as functions of the inlet temperature ratio (τ), where $\omega=1$, $P_{0_p}/P_{0_s}=100$ and $k=1.4$. (*a*) Entropy generation; (*b*) relative performance; (*c*) efficiency.

used as an equivalent criterion for performance optimization. In Fig. 6(a) the dotted line indicates the entropy generation of an ideal turbine compressor calculated according to the Eq. (17), as a reference value; this figure shows that the entropy generation is due to "pure mixing," "kinetic energy losses," and the normal shock wave. In this case, the entropy generation for all optimal ejectors (as defined above) is caused mainly by "kinetic energy losses."

It is more convenient to introduce the relative performance and relative performance losses, calculated according to Eqs. (21) and (22), respectively, as presented in Fig. 6(b). Alternatively, the efficiency and relative pressure lift losses, calculated according to the Eqs. (24) and (25), respectively, as shown in Fig. 6(c).

3.2 Sensitivity of Optimal Ejector Performance and Losses. In order to determine the sensitivity of the performance and losses of the ejector, performance analysis was conducted where three (set point) out of the four variables (τ, ω, P_{0_p}/P_{0_s}, and k) were kept constant while the fourth varied.

Only "optimal fixed ejectors" ($P_{3_{Ej}}$) and "adjustable throat ejector with optimal starting conditions" (P_{0_1}) are considered throughout this section.

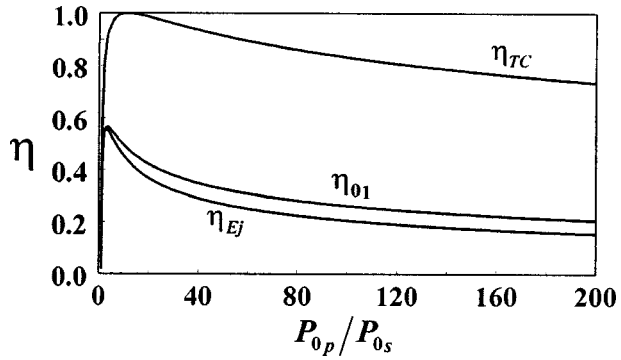

Fig. 9 Theoretical efficiency of an "optimal fixed ejector," an ideal turbine compressor, and an "adjustable throat ejector with optimal starting conditions," as functions of the inlet pressure ratio (P_{0_p}/P_{0_s}), where $\tau=0.5$, $\omega=1$ and $k=1.4$

3.2.1 Sensitivity of Results to Inlet Mass Flow-Rate Ratio (ω). For demonstration purposes a set point was chosen at $\tau=\mathbf{1}$, $P_{0_p}/P_{0_s}=\mathbf{100}$ and $k=\mathbf{1.4}$, and ω is allowed to vary in the range $\mathbf{0}>\omega\leqslant\mathbf{5}$. Figure 7(a) presents the entropy generation of an "optimal fixed ejector" ($\Delta\bar{s}_{3_{Ej}}$), of an "adjustable throat ejector with optimal starting conditions" ($\Delta\bar{s}_{0_1}$), and of an ideal turbine compressor ($\Delta\bar{s}_{3_{TC}}$). The equivalent relative performance and relative performance losses or, alternatively, the efficiency and relative pressure lift losses are shown in Figs. 7(b) and 7(c), respectively.

These figures exhibit that for small ω the performance losses caused by the normal shock wave are dominant. Thus, for small ω the effort required to construct and operate the adjustable throat may well be justified. However, for $\omega>\mathbf{0.5}$, 55% of the efficiency reduction is due to "pure mixing," 20% to "kinetic energy losses" and just a few percent to the normal shock wave. Thus for $\omega>\mathbf{0.5}$, adding an adjustable throat will have negligible effect on the overall ejector performance. This kind of information could be used to ensure effective focusing of design efforts.

3.2.2 Sensitivity of Results to Inlet Temperature Ratio (τ). Similarly to the previous section, τ is allowed to vary in the range $\mathbf{0}>\tau\leqslant\mathbf{1}$ where $\omega=\mathbf{1}$, $P_{0_p}/P_{0_s}=\mathbf{100}$ and $k=\mathbf{1.4}$. Figure 8 shows that for inlet conditions τ, P_{0_p}/P_{0_s} and k which satisfy Eq. (18), "pure mixing" losses could be eliminated for $\tau\cong\mathbf{0.27}$. Around this inlet temperature ratio, the ejector efficiency losses are mainly ($\sim$80%) due to "kinetic energy losses."

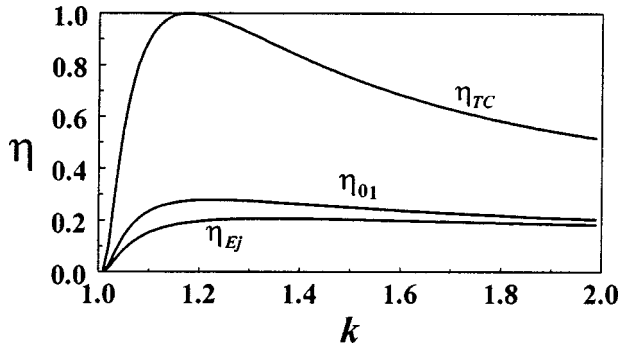

Fig. 10 Theoretical efficiency of an "optimal fixed ejector," an ideal turbine compressor, and "adjustable throat ejector with optimal starting conditions," as functions of the gas specific heat ratio (k), where $\tau=0.5$, $\omega=1$, and $P_{0_p}/P_{0_s}=100$

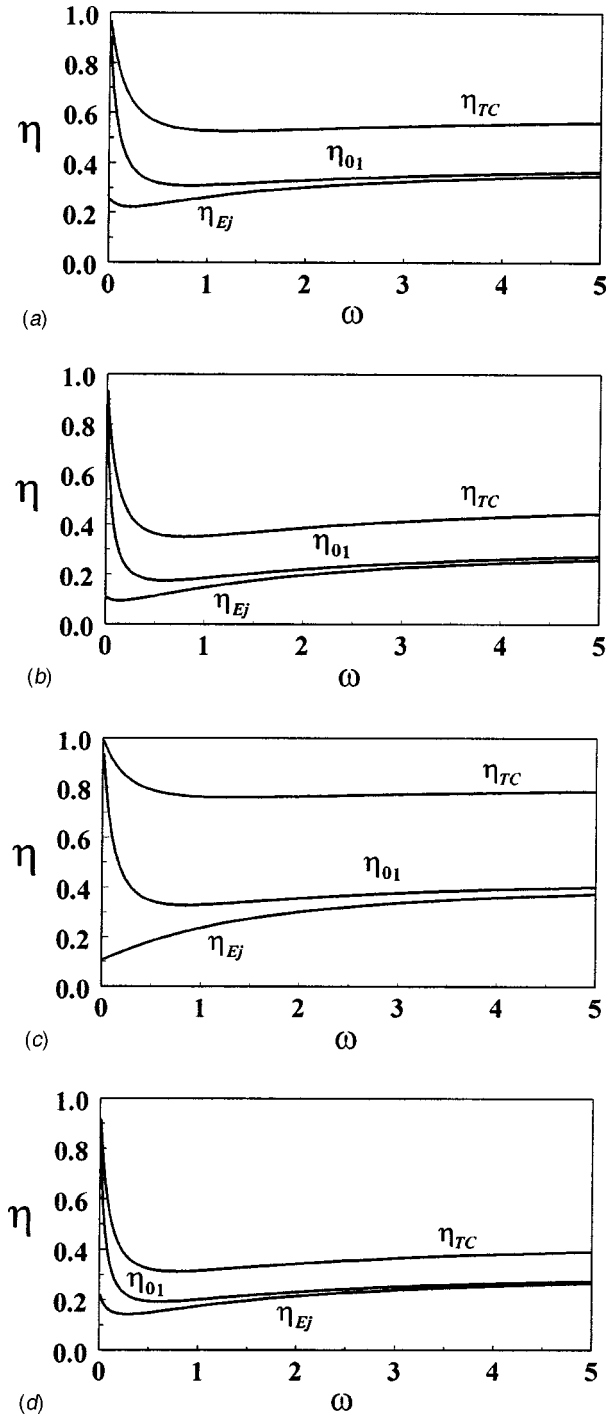

Fig. 11 Theoretical efficiency of an "optimal fixed ejector," an ideal turbine compressor, and "adjustable throat ejector with optimal starting conditions," as functions of the inlet flow rate ratio (ω), where (*a*) $\tau=1$, $P_{0_p}/P_{0_s}=50$ and $k=1.4$; (*b*) $\tau=1$, $P_{0_p}/P_{0_s}=200$ and $k=1.4$; (*c*) $\tau=1$, $P_{0_p}/P_{0_s}=100$ and $k=1.1$; and (*d*) $\tau=1$, $P_{0_p}/P_{0_s}=100$ and $k=1.7$

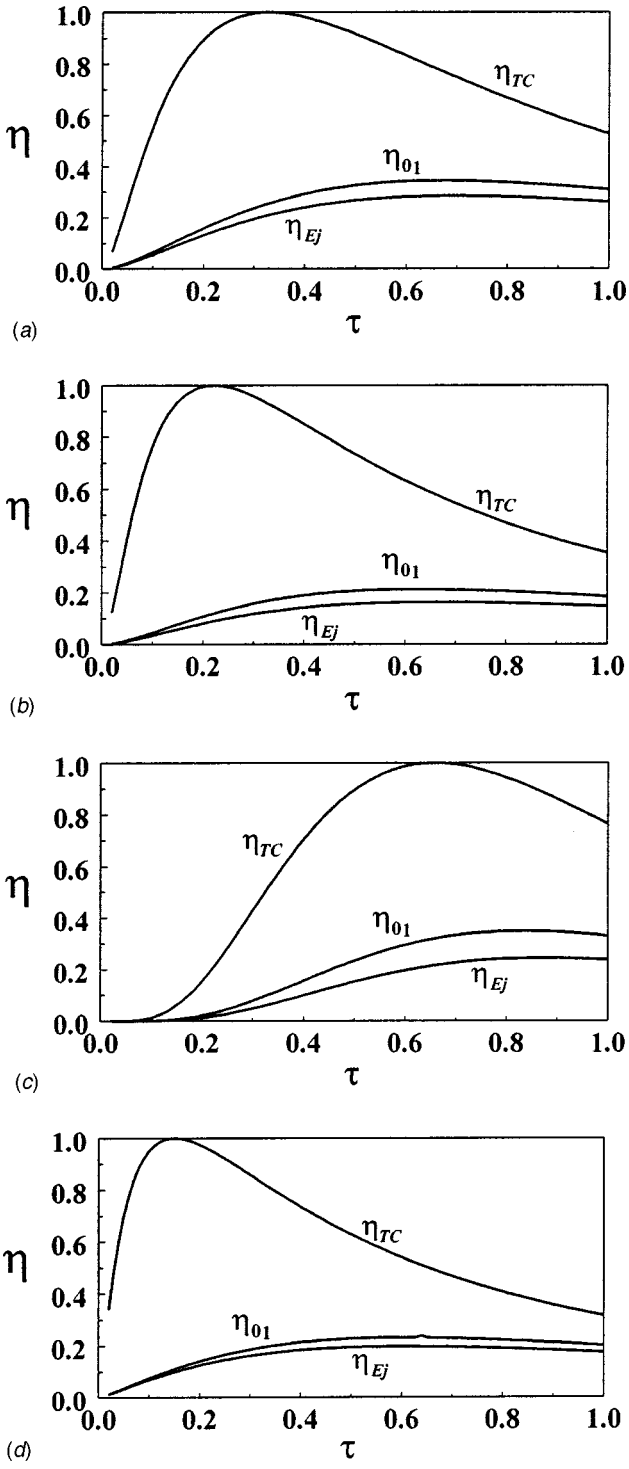

Fig. 12 Theoretical efficiency of "an optimal fixed ejector," an ideal turbine compressor, and "adjustable throat ejector with optimal starting conditions," as functions of the inlet temperature ratio (τ), where (*a*) $\omega=1$, $P_{0_p}/P_{0_s}=50$ and $k=1.4$; (*b*) $\omega=1$, $P_{0_p}/P_{0_s}=200$ and $k=1.4$; (*c*) $\omega=1$, $P_{0_p}/P_{0_s}=100$ and $k=1.1$; and (*d*) $\omega=1$, $P_{0_p}/P_{0_s}=100$ and $k=1.7$

3.2.3 Sensitivity of Results to Inlet Pressure Ratio (P_{0_p}/P_{0_s}). Here P_{0_p}/P_{0_s}, is allowed to vary in the range $\mathbf{1}>P_{0_p}/P_{0_s}\leqslant\mathbf{200}$ where the set point was $\tau=\mathbf{0.5}$, $\omega=\mathbf{1}$, and $k=\mathbf{1.4}$. As shown in Fig. 9, an inlet pressure ratio $P_{0_p}/P_{0_s}\cong\mathbf{12}$ is required to obtain the ideal mixing process in an ideal turbine compressor.

3.2.4 Sensitivity of Results to Gas Specific Heat Ratio (k). Now k is allowed to vary in the range $\mathbf{1}>k<\mathbf{2}$ around set point $\tau=\mathbf{0.5}$, $\omega=\mathbf{1}$ and $P_{0_p}/P_{0_s}=\mathbf{100}$. As shown in Fig. 10, losses due to "pure mixing," are eliminated for gas specific heat ratio, $k\cong\mathbf{1.16}$.

3.2.5 Further Sensitivity Considerations. Figure 11 shows theoretical efficiency of an ''optimal fixed ejector,'' an ideal turbine compressor, and an ''adjustable throat ejector with optimal starting conditions,'' as functions of the inlet flow rate ratio (ω) for different inlet pressure ratios (a and b) and of gas specific heat ratios (c and d). Figure 12 exhibits the same as Fig. 11 but with the inlet temperature ratio (τ) as the independent variable.

While the losses due to ''pure mixing'' and the normal shock wave could be eliminated, those due to kinetic energy losses can only be reduced. As described above, the losses due to ''pure mixing'' and the normal shock wave could be eliminated by choosing the appropriate inlet conditions or the appropriate gas, and by installing an adjustable throat, respectively. The losses arising from ''kinetic energy losses'' could be reduced, but not eliminated, by using an ''adjustable throat ejector with optimal operating conditions'' (as described in Section 3.1). From the theoretical point of view, these losses are due to the assumptions of mixing at constant pressure and with momentum conservation. Since there is no dissipation, the ''kinetic energy losses'' must be caused by shock waves. This mechanism is characterized by the formation of a series of shock cells, as presented experimentally by Desevaux et al. [11] and numerically by Choi and Soh [12].

The calculated values of pressure rise (following Keenan et al., [3]) are approximately 15% higher than the corresponding experimental values reported by Sun and Eames [1]. One may therefore conclude that this 15% of performance reduction is due to frictional effects, which were indeed neglected by Keenan et al. [3]. However, the main problem with these assumptions is the determination of the mixing-section geometry to ensure constant-pressure mixing.

The ideal turbine compressor differs from an ejector in that energy transfer is through normal forces, and that the mixing occurs under the stagnation backpressure conditions. As mentioned above, the assumption of mixing with conservation of kinetic energy (rather than momentum), results in ejector performance, which is equivalent to that of an ideal turbine compressor. This means that in order to reduce performance losses caused by the ''kinetic energy losses,'' normal forces between the primary and the secondary streams should characterize the flow. Such a flow may be obtained by, for example, swirling or interrupted primary flow. Such flows have been used in thrust augmenting ejectors, [13,14], and lead to tremendous improvement of the ejector performance.

4 Conclusions

The analysis presented, is based on the methodology of entropy production of the ejector as a whole and of each of its internal processes. It showed that entropy production is equivalent to performance losses, and that minimizing entropy production could be used as a criterion for optimization. In addition, irreversible sources were identified and their composition in the performance losses was evaluated. Such is important for the pinpointing areas where design improvement might be applied effectively.

The analysis presented indicates that the ejector irreversibility is due to three main factors: ''pure mixing,'' ''kinetic energy losses,'' and the normal shock wave. The irreversibility due to ''pure mixing'' and the normal shock wave could be eliminated by the selection of appropriate inlet conditions or gas, and by installing an adjustable throat, respectively. Further research is required which should be focused on reduction of the irreversibility attributed to ''kinetic energy losses,'' and by application of more complicated flows in the mixing section.

Nomenclature

h = enthalpy ($J\,kg^{-1}$)
$\overline{h}$ = enthalpy ($J\,mol^{-1}$)
k = specific heat ratio
L = relative performance losses, Eq. (22)
l = relative pressure lift losses, Eq. (25)
Lw = lost work ($J\,kg^{-1}$)
$L\overline{w}$ = lost work ($J\,mol^{-1}$)
M = Mach number
$\dot{m}$ = mass flux ($kg\,s^{-1}$)
P = pressure (Pa)
q = heat supply ($J\,kg^{-1}$)
$\overline{q}$ = heat supply ($J\,mol^{-1}$)
R = gas constant ($J\,kg^{-1}\,K^{-1}$)
$\overline{R}$ = universal gas constant ($J\,mol^{-1}\,K^{-1}$)
Rp = relative performance, Eq. (21)
$\Delta\dot{S}$ = entropy flux ($W\,K^{-1}$)
s = entropy ($J\,kg^{-1}\,K^{-1}$)
$\overline{s}$ = entropy ($J\,mol^{-1}\,K^{-1}$)
T = temperature (K)
u = internal energy ($J\,kg^{-1}$)
$\overline{u}$ = internal energy ($J\,mol^{-1}$)
v = specific volume ($m^3\,kg^{-1}$)
$\overline{v}$ = specific volume ($m^3\,mol^{-1}$)
$\dot{W}$ = power (W)
w = work ($J\,kg^{-1}$)
$\overline{w}$ = work ($J\,mol^{-1}$)

Greek Symbols

η = efficiency, Eq. (24)
ω = mass flow rate ratio (secondary to primary)
τ = ratio of stagnation temperatures, secondary stream to primary stream

Subscripts

Ej = ejector
Ip = ideal mixing process
Ke = kinetic energy losses
Mx = constant pressure mixing section
NS = normal shock
p = primary
PM = pure mixing
s = secondary
TC = turbine compressor
x = cross section at entrance of mixing section (i.e., Fig. 1)
0 = stagnation
1 = cross section at exit of an ejector mixing section (i.e., Fig. 1)
2 = cross section at beginning of an ejector diffuser (i.e., Fig. 1)
3 = exit (i.e., Fig. 1)

Superscripts

$'$ = primary stream at cross section x of the ejector (i.e., Fig. 1)
$''$ = secondary stream at cross section x of the ejector (i.e., Fig. 1)

Appendix A

The significance of the entropy generation for an irreversible process can be amplified by introducing the concept of lost work, $L\overline{w}$ (on a mole basis). Consider outlet stagnation conditions (**1** and **2**) of two arbitrary adiabatic mixing processes, as shown on the P-h diagram (Fig. 13). For a simple compressible substance, in the absence of motion or gravitational effects, the following two thermodynamic relations could be derived:

$$T d\overline{s} = d\overline{u} + P d\overline{v} \tag{A1}$$

$$T d\overline{s} = d\overline{h} - \overline{v}\, dP. \tag{A2}$$

These equations can be integrated for any reversible process because during such a process the state of the substance can be

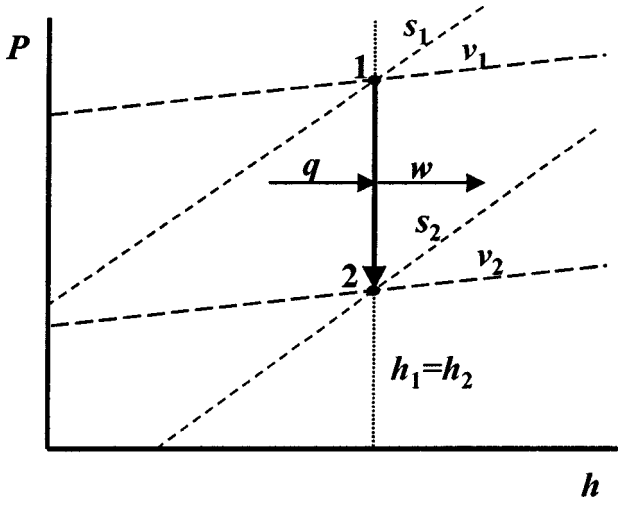

Fig. 13 Reversible process on pressure-enthalpy diagram

identified at any point. If we assume a reversible process, as shown in Fig. 13, with the path defined by $\bar{h}=$ constant, then, for an ideal gas $\bar{u}=$ constant, $T=$ constant and

$$T d\bar{s} = P d\bar{v} = -\bar{v} dP. \tag{A3}$$

Since

$$\bar{q} = T\int_1^2 d\bar{s} = T\Delta\bar{s} \quad \text{and} \quad \bar{w} = \int_1^2 P d\bar{v}, \tag{A4}$$

for this reversible process we conclude from the first law that

$$\bar{q} = \bar{w}. \tag{A5}$$

Note that Eqs. (*A*1) and (*A*2) deal only with properties. The properties of a substance depend only on its state; therefore, the changes in the properties during a given change of state are the same for an irreversible process as for a reversible one. If we assume that an irreversible process is taking place between the same two states, without actual work,

$$\bar{w} = L\bar{w}. \tag{A6}$$

Since both outlet states are due to adiabatic mixing processes with the same pair of inlets (primary and secondary) and without actual work, this lost work is the major difference between them. However, integrating the Eq. (*A*4) yields

$$L\bar{w} = T\Delta\bar{s} = \bar{R}T \ln\frac{P_1}{P_2} = \bar{R}T \ln\frac{\bar{v}_2}{\bar{v}_1} \tag{A7}$$

which is the same as Eq. (13).

Appendix B

In order to compare between an ejector and an ideal turbine compressor, the relevant assumptions should be the same (1 to 6, and 10). The power of the turbine and the compressor, respectively, are given by

$$\dot{W}_T = \dot{m}_p (h_{0_p} - h') \tag{B1}$$

$$\dot{W}_C = \dot{m}_s (h_{0_s} - h''). \tag{B2}$$

As an ideal case

$$\dot{W}_T = \dot{W}_C. \tag{B3}$$

Thus

$$T_{0_p} + \omega T_{0_s} = T' + \omega T''. \tag{B4}$$

The assumption of constant-pressure mixing yields

$$P_3 = P_x. \tag{B5}$$

Since the flows in the turbine and in the compressor are assumed to be reversible ($s_{0_p} = s'$ and $s_{0_s} = s''$, respectively), this yields

$$\frac{P_3}{P_{0_p}} = \left(\frac{T'}{T_{0_p}}\right)^{k/k-1} \quad \text{and} \quad \frac{P_3}{P_{0_s}} = \left(\frac{T''}{T_{0_s}}\right)^{k/k-1}. \tag{B6}$$

Finally, it could be shown that the outlet pressure is given by

$$\frac{P_3}{P_{0_s}} = \left(\frac{1+\omega\tau}{\omega\tau + \left(\frac{P_{0_p}}{P_{0_s}}\right)^{1-k/k}}\right)^{k/k-1}. \tag{B7}$$

References

[1] Sun, D. W., and Eames, I. W., 1995, ''Recent Developments in the Design Theories and Applications of Ejectors—A Review,'' J. Inst. Energy, **68**, pp. 65–79.
[2] Jackson, D. H., 1976, ''Steam Jet Ejectors: Their Uses and Advantages,'' Chem. Eng. Prog., **72**, pp. 77–79.
[3] Keenan, J. H., Neumann, E. P., and Lustwerk, F., 1950, ''An Investigation of Ejector Design by Analysis and Experiment,'' ASME J. Appl. Mech., **17**, pp. 299–309.
[4] Bejan, A., 1982, *Entropy Generation though Heat and Fluid Flow*, John Wiley and Sons, New York.
[5] Bejan, A., 1987, ''The Thermodynamic Design of Heat and Mass Transfer Processes and Devices,'' Int. J. Heat Fluid Flow, **8**, pp. 258–276.
[6] Bejan, A., 1989, ''Theory of Heat Transfer-Irreversible Refrigeration Plants,'' Int. J. Heat Mass Transf., **32**, pp. 1631–1639.
[7] Klein, S. A., 1992, ''Design Consideration for Refrigeration Cycles,'' Int. J. Refrig., **15**, pp. 181–185.
[8] Bejan, A., Vargas, J. V. C., and Sokolov, M., 1995, ''Optimal Allocation of Heat-Exchanger Inventory in Heat Driven Refrigerators,'' Int. J. Heat Mass Transf., **38**, pp. 2997–3004.
[9] Porter, J. L., Squyers, R. A., and Nagaraja, K. S., 1981, ''An Overview of Ejector Theory,'' AIAA Paper No. 81-1678.
[10] Papamoschou, D., 1996, ''Analysis of Partially Mixed Supersonic Ejector,'' J. Propul. Power, **12**, pp. 736–741.
[11] Desevaux, P., Prenel, J. P., and Hostache, G., 1994, ''An Optical Analysis of an Induced Flow Ejector Using Light Polarization Properties,'' Exp. Fluids, **16**, pp. 165–170.
[12] Choi, Y. H., and Soh, W. Y., 1990, ''Computational Analysis of the Flow Field of a Two-Dimensional Ejector Nozzle,'' AIAA Paper No. 90-1901.
[13] Cornelius, K. C., and Lucius, G. A., 1994, ''Multiple Hole Ejector Performance With Short Wide Angle Diffusers,'' J. Propul. Power, **10**, pp. 369–376.
[14] Quinn, W. R., 1994, ''Interrupted Jet as a Candidate for Mixing Enhancement in Aircraft Ejector,'' J. Aircr., **31**, pp. 811–817.

Shear-Driven Flow in a Toroid of Square Cross Section

J. A. C. Humphrey[1]
Department of Mechanical and Aerospace Engineering, University of Virginia, Charlottesville, VA 22904

J. Cushner
Shen Milsom & Wilke, Inc., 417 Fifth Avenue, New York, NY 10016

M. Al-Shannag

J. Herrero

F. Giralt

Department of Chemical Engineering, University of Rovira I Virgili, 43006 Tarragona, Catalunya, Spain

The two-dimensional wall-driven flow in a plane rectangular enclosure and the three-dimensional wall-driven flow in a parallelepiped of infinite length are limiting cases of the more general shear-driven flow that can be realized experimentally and modeled numerically in a toroid of rectangular cross section. Present visualization observations and numerical calculations of the shear-driven flow in a toroid of square cross section of characteristic side length D and radius of curvature R_c reveal many of the features displayed by sheared fluids in plane enclosures and in parallelepipeds of infinite as well as finite length. These include: the recirculating core flow and its associated counterrotating corner eddies; above a critical value of the Reynolds (or corresponding Goertler) number, the appearance of Goertler vortices aligned with the recirculating core flow; at higher values of the Reynolds number, flow unsteadiness, and vortex meandering as precursors to more disorganized forms of motion and eventual transition to turbulence. Present calculations also show that, for any fixed location in a toroid, the Goertler vortex passing through that location can alternate its sense of rotation periodically as a function of time, and that this alternation in sign of rotation occurs simultaneously for all the vortices in a toroid. This phenomenon has not been previously reported and, apparently, has not been observed for the wall-driven flow in a finite-length parallelepiped where the sense of rotation of the Goertler vortices is determined and stabilized by the end wall vortices. Unlike the wall-driven flow in a finite-length parallelepiped, the shear-driven flow in a toroid is devoid of contaminating end wall effects. For this reason, and because the toroid geometry allows a continuous variation of the curvature parameter, $\delta = D/R_c$, this flow configuration represents a more general paradigm for fluid mechanics research. [DOI: 10.1115/1.1523066]

Introduction

The two-dimensional wall-driven flow in a plane rectangular enclosure, also referred to as the ''lid or wall-driven cavity flow,'' has been a computational fluid dynamics paradigm of long-standing interest. Although such a flow cannot be realized experimentally, approximations have been obtained in enclosures shaped like parallelepipeds of rectangular cross section and of finite length. In the parallelepiped geometry, fluid motion is induced by the in-plane sliding of one of the four longitudinal walls of the parallelepiped, in a direction normal to the parallelepiped's longitudinal axis.

In the case of the plane square enclosure (Fig. 1(*a*)), the flow is characterized by the Reynolds number $\mathrm{Re}=DU/\nu$, where D is the enclosure cross section length, U is the sliding wall velocity, and ν is the kinematic viscosity of the fluid. In the case of a parallelepiped of square cross section (Fig. 1(*b*)) in addition to Re it is necessary to specify the longitudinal to cross section length ratio, L/D. In contrast to the two-dimensional flow in the idealized plane square enclosure, that in a finite-length parallelepiped is three-dimensional due to pressure gradient effects induced by the viscous action of the end walls. In addition, above a critical value of Re (or an equivalent Goertler number) centrifugal instabilities trigger the appearance of pairs of counterrotating vortices with axes aligned along the recirculating core flow direction. The wavelength of these vortices scales with D and in a finite-length parallelepiped their sense of rotation is permanently fixed by the end wall vortices.

We propose a new geometrical configuration for the investigation of instabilities of shear-driven flows in enclosures that is realizable experimentally and numerically without incurring the end wall bias present in the finite-length parallelepiped configuration. This consists of the shear-driven flow in a toroid of square cross section where, in the limit of low Re and large radius of curvature, R_c, fluid motion approaches that in the idealized plane square enclosure. As for the parallelepiped configuration, at a critical value of Re in a toroid centrifugal instabilities trigger the appearance of Goertler vortex pairs that, with increasing Re, become unsteady and ultimately transition to a turbulent state of motion. In addition to circumventing the end wall bias, the toroid configuration allows the investigation of the effect of the geometrical curvature parameter, $\delta = D/R_c$, on shear-driven flows. For these reasons, therefore, it represents a more general fundamental paradigm than its parallelepiped predecessors.

Earlier Work

Numerical calculations of the two-dimensional wall-driven flow in a plane rectangular enclosure have been performed by, for example, Ghia et al. [1], Iwatsu et al. [2,3], and Nishida and Satofuka [4]. Corresponding three-dimensional calculations of the parallelepiped geometry have been performed by Koseff et al. [5], Freitas et al. [6], Kim and Moin [7], Freitas and Street [8], and Iwatsu et al. [2,3]. Experimental investigations of the finite-length parallelepiped geometry include the pioneering studies performed by Koseff and Street [9–11], and later by Prasad and Koseff [12] and Aidun et al. [13]. The stability of the two-dimensional base flow to longitudinal disturbances in an infinitely long parallelepiped has been investigated numerically by Ramanan and Homsy [14], Ding and Kawahara [15,16], and Albensoeder et al. [17]. By means of linear stability analysis and experiments, Albensoeder et al. [17] demonstrate the dependence of the instabilities observed on the enclosure cross section dimensions. For parallelepipeds of cross section equal to or close to square, they conclude that the steady two-dimensional flow destabilizes to a steady three-dimensional flow of dimensionless wavenumber κ

[1]To whom correspondence should be addressed.

Contributed by the Fluids Engineering Division for publication in the JOURNAL OF FLUIDS ENGINEERING. Manuscript received by the Fluids Engineering Division August 30, 2001; revised manuscript received July 29, 2002. Associate Editor: J. S. Marshall.

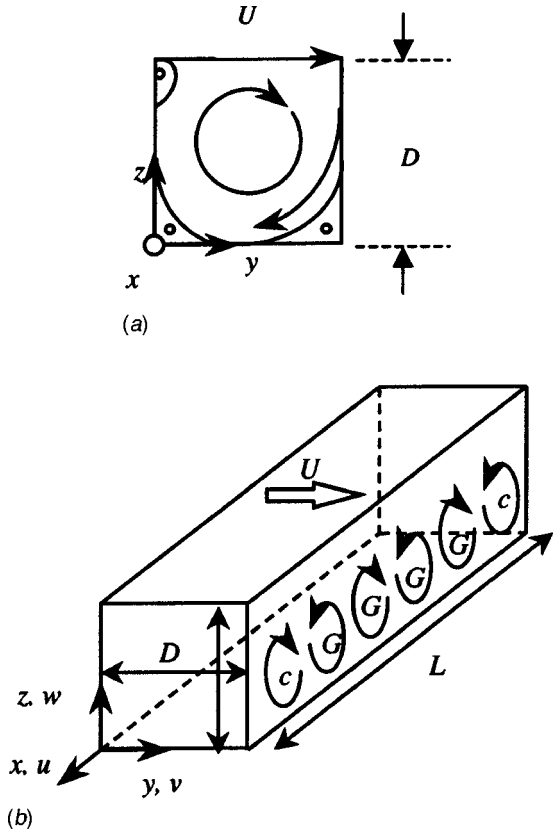

Fig. 1 Wall-driven flows in enclosures of square cross section. (*a*) Two-dimensional flow in a plane enclosure, (*b*) three-dimensional flow in a parallelepiped. At sufficiently large Re, centrifugal instabilities trigger Goertler vortices in the parallelepiped where the two end walls fix the sense of rotation of the corner (''*c*'') vortices and, as a consequence, of the remaining (''*G*'') vortices. The sense of rotation of the vortices in the bottom half of the parallelepiped is shown projected on an *x-z* plane.

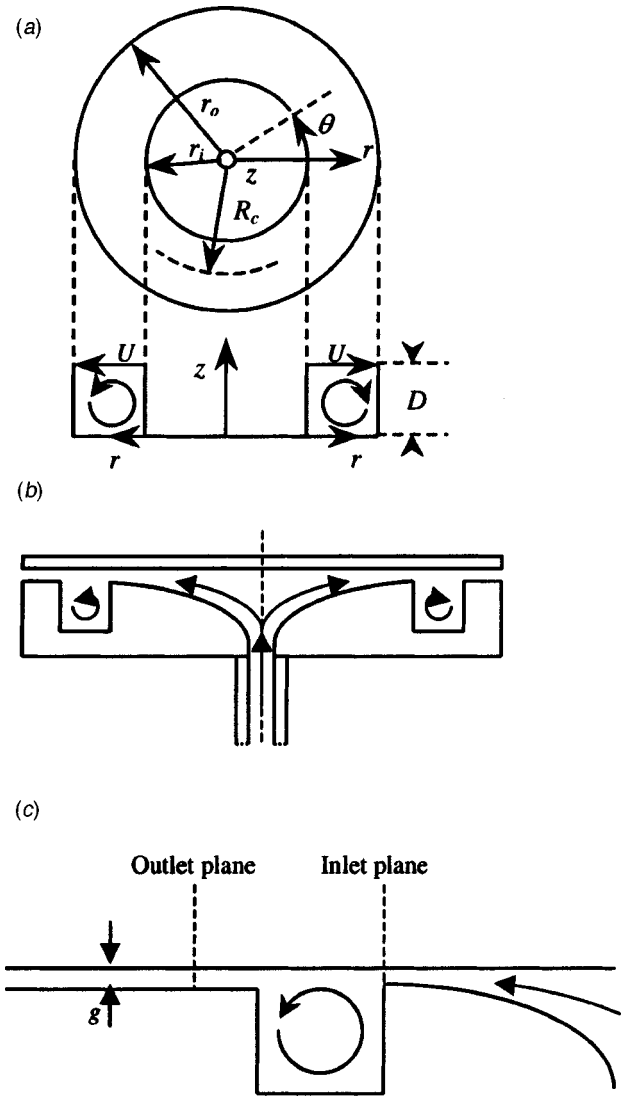

Fig. 2 (*a*) Top and side views of the idealized toroid (Configuration 1); (*b*) side view of the experimental configuration (Configuration 2); (*c*) view showing one (*r-z*) plane of the 360-deg calculation domain corresponding to Configuration 2. Note that $g/D=0$ for Configuration 1 and $g/D \ll 1$ for Configuration 2. The drawings are not to scale.

$(\equiv 2\pi/(\lambda/D))=15.43$ for a critical Re=786.3. They also find from their experiments that end wall effects can suppress instabilities in finite-length parallelepipeds.

With reference to Fig. 1, the investigations performed in infinite and finite-length parallelepipeds reveal significant (u, w) cross-stream motions in x-z planes planes perpendicular to the wall-driven recirculating core flow. These motions are induced by (a) pressure gradients arising at each of the two end walls in finite-length parallelepipeds and (b) centrifugal instabilities responsible for the Goertler vortices that arise above a critical value of the Reynolds number (or an equivalent Goertler number) in both infinite and finite-length parallelepipeds. The vortices appear as counterrotating pairs periodically distributed in the longitudinal direction (x-direction in Fig. 1(b)), and their axes are aligned with the recirculating core flow. They have been referred to as Taylor-Goertler-like vortices in the literature but, because of the manner of shearing, appear to have more in common with the centrifugal instability investigated by Goertler [18] in curved boundary layers than the centrifugal instability investigated by Taylor [19] in the space between concentric cylinders in relative rotation. In this regard, see Freitas and Street [8] for an application of the Goertler stability criterion to predict the onset of centrifugal instabilities in the wall-driven flow in a parallelepiped.

The end wall pressure gradients in finite-length parallelepipeds fix the sense of rotation of the first vortex next to each end wall. In turn, the end wall vortex fixes the sense of rotation of the Goertler vortex next to it and so on. Because the end-wall pressure-gradient forces differ in magnitude from the centrifugal forces, and because of secondary instabilities, nonlinear interactions among the vortices can induce time and space-dependent variations among them as well as in their number. Although interesting in its own right, there is an unavoidable bias in the finite-length parallelepiped configuration that unnecessarily complicates both the physical understanding and the numerical calculation of three-dimensional shear-driven enclosure flows.

A New Shear-Driven Enclosure Flow Paradigm

The end wall bias present in the finite-length parallelepiped geometry can be completely removed by converting the parallelepiped into a toroid. This is accomplished conceptually by curving the parallelepiped uniformly around a pair of parallel longitudinal walls and ''dissolving'' the end walls at the common plane where they meet to create a continuous, unobstructed toroid of square cross section (Fig. 2(a)). In this idealized configuration, one of the flat walls of the toroid (the top wall in Fig. 2(a)) is made to slide radially outwards (or inwards) with an axisymmetric velocity distribution in order to drive the flow in the toroid by viscous shear-

ing. In addition to Re, the new quantity $\delta = D/R_c$ (a geometrical curvature parameter) must be specified to characterize fluid motion. Clearly, for values of $\delta \rightarrow 0$, the effects of geometrical curvature are rendered negligible, resulting in a flow configuration which (i) at sufficiently low Re rigorously approximates the two-dimensional wall-driven flow in a plane square enclosure (ii) at sufficiently high Re will display the Goertler vortices observed in finite-length parallelepipeds, but *devoid* of end wall bias, and (iii) at even higher Re will undergo transition to turbulence. In this sense then, the shear-driven flow in a toroid represents a more general fundamental fluid mechanics paradigm than its predecessors.

Using the second order accurate (space and time) explicit CUTEFLOWS Navier-Stokes solver of Humphrey et al. [20], Phinney and Humphrey [21], and Sudarsan et al. [22] have calculated the wall-driven flow in a toroid of square cross-section corresponding to Fig. 2(*a*) to investigate the effects of varying δ and Re. The bulk of this work is for two-dimensional (axisymmetric) flow. However, time averages of three-dimensional results calculated for $\mathrm{Re}=3200$ and $\delta=0.005$ yield very good agreement with the Goertler vortices and time-averaged velocity profiles obtained by Koseff and Street [9,11] in a finite-length parallelepiped with $\mathrm{Re}=3300$; see Sudarsan et al. [22]. For $\mathrm{Re}=3200$ and $\delta=0.005$ as well as for $\mathrm{Re}=2400$ with $\delta=0.25$, the instantaneous flow is unsteady and the Goertler vortices are observed to meander chaotically. Sudarsan et al. [22] conclude that above a critical value of Re, depending on the value of δ, the flow in a toroid becomes three-dimensional due to the appearance of Goertler vortex pairs distributed periodically in the circumferential coordinate direction. They also obtain evidence to suggest that the Goertler vortices in a toroid can simultaneously alternate their sense of rotation periodically as a function of time with characteristic dimensionless frequency $\omega = 2\pi/(TU/D)$.

The present study explores more carefully the three-dimensional unsteady, shear-driven flow in a toroid of square cross section. The effort is part of an ongoing collaboration between the University of Virginia and the University of Rovira i Virgili. We are concerned with two basic flow configurations differing solely in the way fluid motion is induced. In one configuration, flow through a narrow gap, *g*, shown in Figs. 2(*b*) and (*c*), is involved. With reference to Fig. 2(*a*), Configuration 1 (the idealized case) consists of a toroid with $g/D=0$, the flow in the toroid being driven by the shearing action of the top wall sliding radially outwards with an axisymmetric, constant velocity *U*. With reference to Fig. 2(*b*), Configuration 2 (the experimental case) consists of a toroid with $0 < g/D \ll 1$, the flow in the toroid being driven by the shearing action of the wall jet that emerges from the gap, *g*, to expand radially outwards along the toroid top wall. For Configuration 2, the Reynolds number is defined as $\mathrm{Re}_g = U_g D/\nu$, where U_g is the mean velocity of the fluid in the gap at the plane where it enters the toroid.

In this communication we present results for Configuration 2. For this configuration numerical calculations are performed for $\mathrm{Re}_g=1143$ and $g/D=0.04$ in two toroids: one with $\delta=0.25$ and another with $\delta=0.51$. The main flow visualization results are obtained in a toroid with $\mathrm{Re}_g=5000$, $g/D=0.015$, and $\delta=0.25$. Following the procedure outlined by Freitas and Street [8], all three of these cases yield estimates of the Goertler number of order 10, exceeding the stability criterion for the appearance of Goertler vortices. In the calculations the upper limit on Re_g is imposed by grid refinement considerations. In the flow visualization experiments the lower limit on Re_g is imposed by the construction of the test section. Unfortunately, with the current apparatus it is not possible to obtain a large overlap in Re_g between the experiment and the calculations.

Experimental Apparatus. The experiments are performed in a flow apparatus that uses water as the working fluid. A toroid with $D=0.05$ m and $R_c=0.20$ m is accurately machined from a transparent Plexiglass block 24-in.$\times$24-in.$\times$8-in. using a CNC milling machine. With reference to Figs. 2(*b*) and 2(*c*), the inlet flow passage to the toroid is defined by a trumpet-shaped surface (machined into the same Plexiglass block) and a separate, flat, circular, Plexiglass lid of diameter 0.50 m and thickness 2.26 cm. The curvature of the trumpet-shaped surface is geometrically defined by rotating a quarter-ellipse 360 deg around the toroid axis of symmetry. The major and minor axes of this ellipse are $a=0.165$ m and $b=0.060$ m. The distance between the circular lid and the top of the toroid, defining the gap dimension *g*, is continuously adjustable between 0 and 5 mm using three UNC 10-32 fine-thread screws placed 120 deg apart. The entire Plexiglass test section rests on a laboratory table where it is leveled by means of three 6-in. long, 1/2-in. diameter, rubber-capped bolts that pass through threaded bearings 120 deg apart in the table to support the test section from below.

The test section is part of a recirculating flow system that redirects water leaving the toroid into a sump tank from where it is pumped into a constant head tank with an overflow line leading back to the sump tank. Tygon tubing is used for all flow connections and this serves to minimize the transmission of possible mechanical vibrations. A circular gutter built into the Plexiglass lid permits the continuous removal of water from the test section thus allowing unobstructed side and top views of the toroid. A globe valve controls the flow of water from the head tank into the test section, and the rate of flow is measured by means of a King flow meter (0–1.5 gpm, $\pm$0.01 gpm). After the flow meter the water passes vertically upwards through a flow conditioning section consisting of a glass tube of inner diameter 0.02 m and length 0.40 m. The inlet to this tube contains a bundle of tightly packed straws 0.20 m long located between a pair of stainless steel screens. This is followed by an unobstructed length of tube wherein the flow relaxes before passing through a third screen to finally connect with the inlet to the trumpet-shaped section, also of diameter 0.02 m. The flow in the trumpet-shaped section first decelerates slightly and then accelerates strongly as it approaches the toroid. A tendency of the flow to separate in the decelerating section is suppressed by the insertion of two relatively fine, cylindrically shaped, concentric stainless steel screens. These additional screens further reduce any residual inhomogeneities in the flow approaching the toroid.

A rheoscopic fluid manufactured by Kalliroscope Corp. (AQ-1000 Rheoscopic Concentrate, consisting of micron-sized guanine platelets in suspension) is added to the water (1% by volume) for flow visualization purposes. The flow in the toroid is illuminated using a plane of light generated by passing the beam from a 5-mW He-Ne laser through a cylindrical lens. While it is possible to obtain images of the flow in planes normal to the *r*, *z* and θ-coordinate directions, the highest quality and least optically distorted images are obtained in *r*-θ planes, normal to the *z*-coordinate direction. Photographs of the flow are taken with a Canon T90 camera using a 50 mm Canon Macrolens and Kodak Select B&W 200 ASA film.

Among the uncertainties affecting the experiment, those associated with geometrical dimensions during fabrication and assembly of the test section, water temperature variations, and mechanical vibrations are negligible, and those associated with optical distortion of images are small or correctable if necessary. Two sources of uncertainty affect the value of U_g in the Reynolds number, Re_g. One is due to the reading error ($\pm$0.01 gpm) of the flow meter scale, and the other is due to the positioning error (± 25 μm) of the circular lid which leads to an uncertainty in the gap width, *g*. The result is a final maximum percent rms uncertainty of $\pm$5% in Re_g. Of more concern is a possible misalignment of the lid leading to a nonaxisymmetric gap width, *g*. Such a misalignment will induce uneven shearing of the flow in the toroid with corresponding distortions of the flow structures in it. However, with care this effect can be minimized. For further details on the experimental apparatus, procedure and uncertainties see Cushner [23].

Numerical Calculations. A fourth-order (space and time) version of the CUTEFLOWS code referred to above is employed for the new calculations presented here, corresponding to Configuration 2. The code solves unsteady three-dimensional constant property forms of the momentum and continuity equations in Cartesian or cylindrical coordinates. The numerical procedure is based on a staggered-grid, control-volume discretization approach for deriving finite difference forms of the conservation equations in terms of the primitive variables, velocity components, and pressure. A fourth-order-accurate central differencing scheme is used to approximate the pressure and diffusion terms in the momentum equations. A quadratic upstream-weighted scheme is used for the convection terms. Continuity yields a discrete Poisson equation that is solved for pressure using the conjugate gradient method. The algorithm is explicit in time and uses a fourth-order Runge-Kutta solver. The dimensionless integration time-step is typically $t/(D/U)<0.01$ and is small enough to guarantee both stable convergence and accuracy in the course of a calculation.

The calculation domain consists of the entire toroid (full 360 deg) with the impermeable, no-slip condition imposed for velocity at all its internal surfaces. With reference to Fig. 2(*c*), the flow at the plane where it enters the toroid is taken as essentially fully developed Poiseuille flow. The flow leaving the toroid redevelops in an exit gap of the same height, g/D, as the inlet plane gap, and of length $l/D=0.55$. Calculations are started from corresponding two-dimensional (axisymmetric) solutions. Earlier linear stability analyses have shown that the two-dimensional wall-driven flow in an infinitely long parallelepiped is unstable to infinitesimal disturbances. Using the present fourth-order numerical scheme, the Goertler vortices appear spontaneously and it is unnecessary to seed disturbances. A typical run time for Configuration 2 on a dual processor Dell workstation (PWS620) is about 10 hours for 100 seconds of numerical flow development.

Substantial grid refinement tests are first performed, culminating in the choice of a grid with ($N_r=72$, $N_z=72$, $N_\theta=192$) nodes. The nodes in the *r*-*z* plane are unequally spaced while those in the θ-direction are equally spaced. Although not shown here, subsequent additional testing with this grid has yielded vortical flow structures with characteristics in excellent agreement with those obtained by Albensoeder et al. [17]. Namely, using periodic boundary conditions in the *x*-direction for the wall-driven flow in a parallelepiped of square cross-section corresponding to Fig. 1(*b*) with $g/D=0$ and $L/D=2$, we find $\kappa=15.7$ and $\omega=0$ at Re $=850$ compared to the experimental values of $\kappa=15.43$ and $\omega=0$ at Re$=786.3$.

Results and Discussion

A summary of some main findings follows below for Configuration 2.

Experimental Results. Flow visualization experiments have been performed in the range $10^3\leqslant \mathrm{Re}_g \leqslant 9\times10^3$ in a toroid with $\delta=0.25$ for gap widths corresponding to $g/D=0.015$, 0.030, 0.040, and 0.060; see Cushner [23]. Here we comment on the main observations made with a focus on the visualization results obtained for $\mathrm{Re}_g=5000$ with $g/D=0.015$.

Because of the viscous action of the circular lid on the flow, there can be a significant penetration of the radially expanding wall jet into the toroid. For each gap width, *g*, a value of Re_g exists above which this penetration is minimal and for $g/D=0.015$ this corresponds to $\mathrm{Re}_g\approx1600$. For $\mathrm{Re}_g>2000$, views of the flow in the *r*-*z* plane, made at an angle through the lid, clearly reveal the recirculating core flow and the two bottom corner eddies typical of two-dimensional wall-driven flows in plane rectangular enclosures. (Note, however, with reference to Fig. 1(*a*) that the eddy arising in the top left-hand corner of a wall-driven plane enclosure flow is not clearly visible in the experiment, and is not predicted numerically for the values of Re_g and g/D investigated.) The wall-jet penetration is discussed further below in relation to the numerical calculations performed.

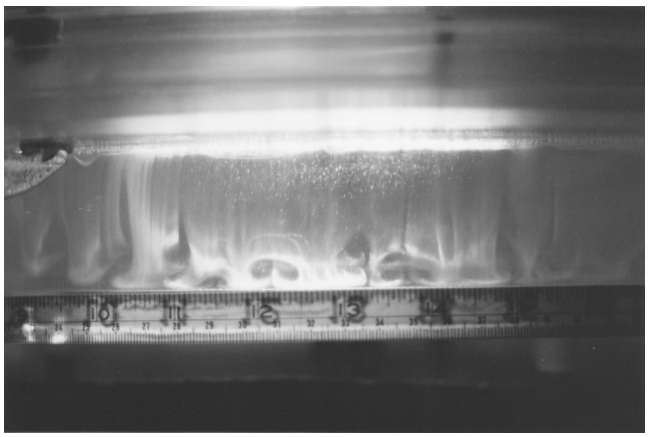

Fig. 3 Visualization of the instantaneous flow in a toroid with $\mathrm{Re}_g=5000$, $\delta=0.25$, and $g/D=0.015$. Picture shows a z^*-θ plane at $r^*=0.90$ as seen through the curved outer side wall of the toroid.

Depending on the value of g/D, between $\mathrm{Re}_g=1000$ and 2000 a first instability leads to the appearance of Goertler vortices in the flow. (The exact value of Re_g cannot be determined in the current apparatus because of the wall-jet penetration limitation.) For the flow with $g/D=0.015$ and $\mathrm{Re}_g=2000$ the dimensionless wave number of a vortex pair is $\kappa\approx6.3$, and between $\mathrm{Re}_g=3000$ and 4000, approximately, this doubles to $\kappa\approx12.6$. In the latter range of Re_g a slight meandering of the vortices (smaller in extent than half a wavelength) is observed over time periods of about 5 min. At $\mathrm{Re}_g\approx4100$ a second, marked instability, in the form of a Hopf bifurcation, is observed. This involves the continuous merging and splitting of the Goertler vortices. Beyond $\mathrm{Re}_g\approx6500$ the vortices are subjected to a strong wavy motion which, by $\mathrm{Re}_g\approx8000$, is disorganized and turbulent (although the intermittent presence of Goertler vortices is observed).

Flow visualization results corresponding to $\mathrm{Re}_g=5000$ with $g/D=0.015$ are shown in Figs. 3 and 4. (In these and subsequent figures $r^*\equiv(r-r_i)/(r_o-r_i)$ and $z^*\equiv z/D$.) The results in Fig. 3 correspond to a snapshot of the flow in the z^*-θ plane at $r^*=0.90$. Those in Fig. 4 are obtained at different times at different r^*-θ planes. Although the flow conditions correspond to an unsteady flow regime, it is not possible to extract a single characteristic frequency from the visualization observations. Notwithstanding, Goertler vortices of wave number $\kappa\approx12.5$ are clearly observed. At small values of z^* (near the toroid bottom wall), the vortices are aligned in the radial direction and fill the entire space between $r^*=0$ and 1. With increasing z^* the vortices orient themselves axially, along the z^* coordinate direction, and are especially prominent along the inner curved half of the toroid, $r^*<0.5$.

Numerical Results. Numerical calculations are performed for $\mathrm{Re}_g=1143$ and $g/D=0.04$ in two toroids: one with $\delta=0.25$ and another with $\delta=0.51$. Because the details of these two flow are very similar, and because their Goertler vortices have essentially the same wavenumber, we focus on the results obtained for $\delta=0.51$. Calculated values of the instantaneous circumferential velocity component, visualized using shades of gray ranging from white to black, are shown in Fig. 5. The results correspond to $t^*(\equiv tU_g/4D)=856$ and are in excellent qualitative agreement with the experimental observations at higher Re_g and lower δ in so far as the spatial structure, distribution, and orientation of the vortices are concerned. For the conditions calculated, the wave number of

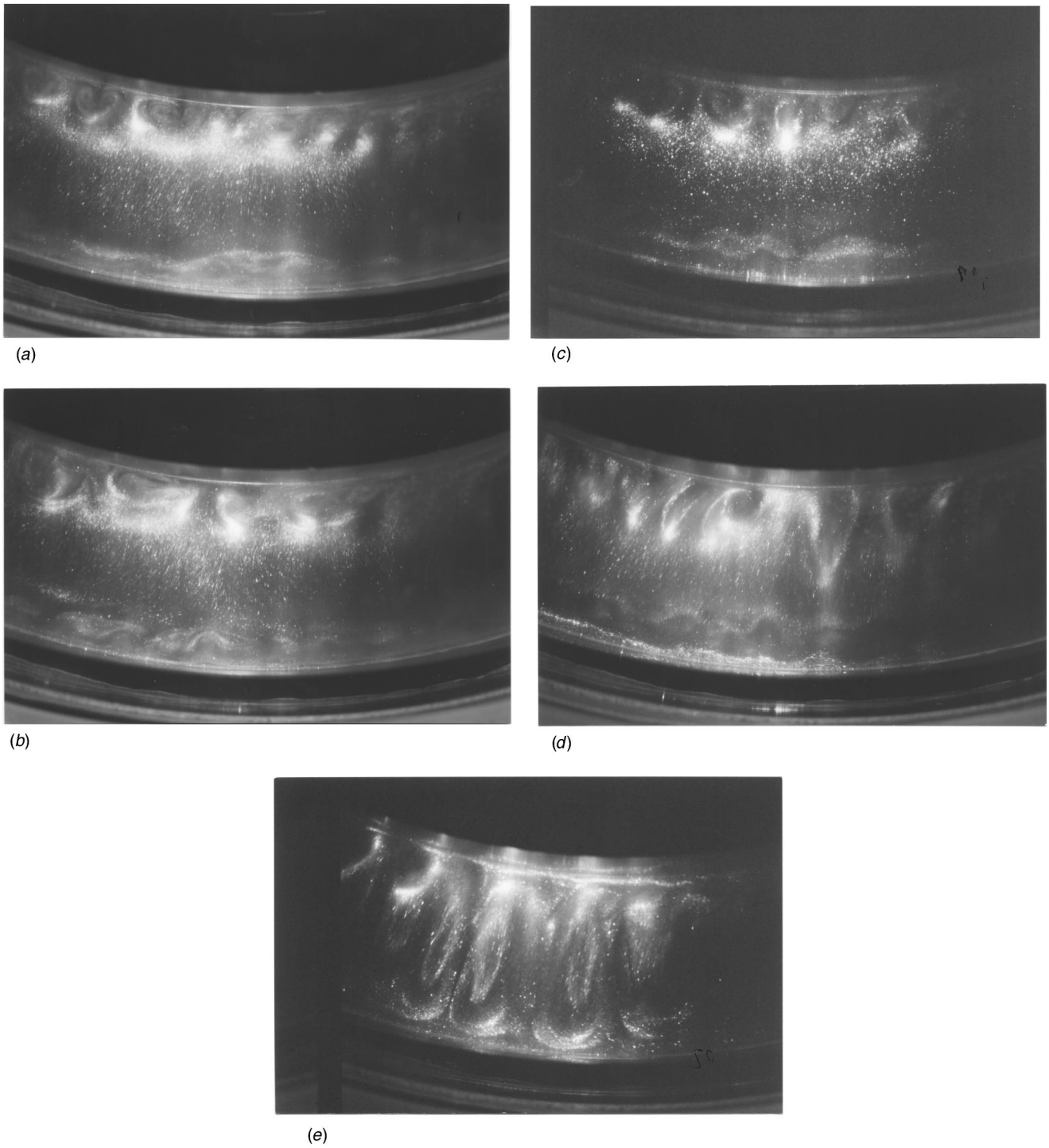

Fig. 4 Visualization of the instantaneous flow in a toroid with Re_g=5000, δ=0.25, and g/D=0.015. Pictures show views of r^*-θ planes as seen through the top wall of the toroid over a sector of 18 deg: (*a*) z^*=0.9; (*b*) 0.7; (*c*) 0.5; (*d*) 0.3; and (*e*) 0.1.

the vortices is $\kappa=8.7$ and the flow displays a time dependence of dimensionless frequency $\omega=0.154$. (Note that in the toroid the dimensionless wave number $\kappa(\equiv 2\pi/(\lambda/D))=(2\pi R_c/\lambda)(D/R_c)=N\ \delta$, where $N(=17)$ is the total number of vortex pairs in the toroid.)

Figure 6 shows calculated time records of the dimensionless circumferential velocity component ($u_\theta^*=u_\theta/U_g$) at two axial locations $z^*=0.25$ and $z^*=0.50$ with $r^*=0.5$ and $\theta=0.22\pi$. The calculations correspond to the conditions of Fig. 5. Although the magnitudes of these monitor velocity components and their changes are small, and while the recirculating flow has experienced about 22 toroid periphery ''turnovers'' in the course of its development, it appears to still be evolving. Thus, we cannot state definitively whether the flow dynamics will continue to evolve towards a final, periodic state with $\omega=0.154$, or will orbit, instead, within the basin of a strange attractor at some frequency close to $\omega=0.154$.

Nevertheless, it is especially noteworthy for the numerical conditions explored that the entire flow field in the toroid alternates between two identical but spatially displaced states of motion as a

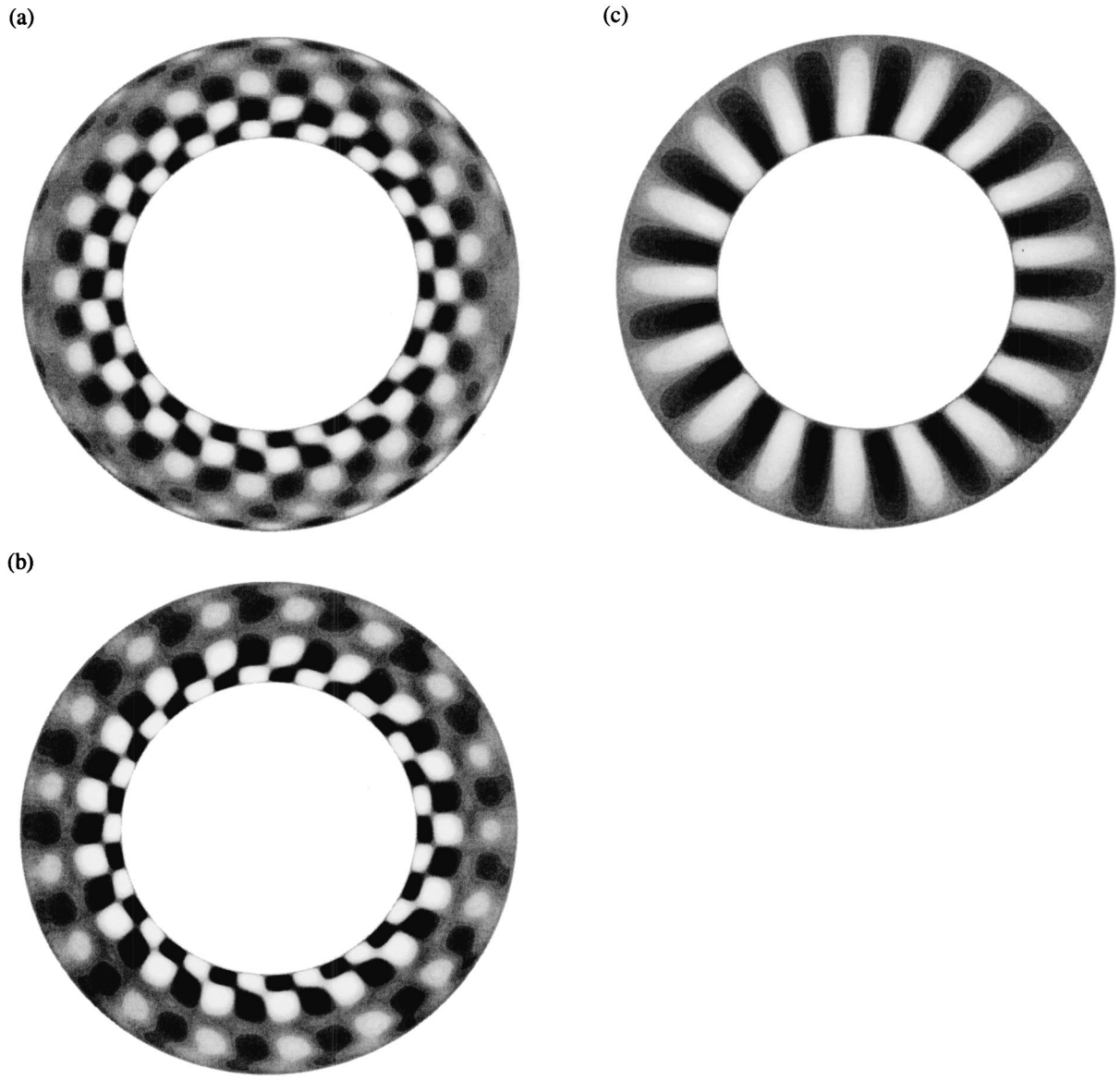

Fig. 5 Instantaneous distributions of the calculated circumferential velocity component at $t^*=856$ in r^*-θ planes of a toroid with $Re_g=1143$, $\delta=0.51$, and $g/D=0.04$: (*a*) $z^*=0.7$; (*b*) 0.5 and (*c*) 0.1. Black and white areas denote regions of opposite velocity.

function of time. This Hopf-like bifurcation is clearly illustrated by the velocity vector plots shown in Fig. 7 for two consecutive times of an oscillation cycle ($\omega=0.154$) in the z^*-θ plane located at $r^*=0.5$. While the shape, size, and number of the calculated structures are virtually the same at both times, their positions relative to a fixed reference point are displaced by half a wavelength in the θ-coordinate direction. A movie of this flow reveals a sequentially alternating pattern of Goertler vortices in the main recirculating core flow direction. At any instant in a cycle, the two vortices in any vortex pair have a particular sense of rotation, the vortices in this pair counterrotating with respect to each other. At a later time in the cycle, this vortex pair gives way to a new pair, displaced by half a wavelength in the θ-coordinate direction, in which the vortices now rotate in the opposite sense to the original pair. At all times, however, the vortices remain equally spaced in the θ-coordinate direction.

From an Eulerian viewpoint, the visual effect at a fixed location in the toroid is to observe *in situ* time-periodic alternations in sense of rotation of the vortices. This sign alternation in sense of rotation occurs simultaneously for all the vortices in a toroid, thus implying a phase shift in the recirculating core flow direction. We suggest that the periodic changes in sense of rotation of the vortices is due to a phase-shifted coupling between the tilting and stretching of circumferential, θ-component of vorticity at the convex (inner radius) wall and the tilting and stretching of the same component of vorticity at the concave (outer radius) wall.

We referred earlier to a basic difference between the toroid flows corresponding to Configuration 1 (Fig. 2(*a*)) and Configuration 2 (Fig. 2(*b*) and 2(*c*)) that has to do with the way fluid motion is induced by shearing. In Configuration 2, a wall-jet expands radially outwards along the circular lid over the toroid. The viscous action of the lid on the wall-jet results in a penetration of the flow into the toroid and the formation of a stagnation line along the outer concavely curved wall. This stagnation line falls below the exit gap by an amount p/D that depends on the values of Re_g and g/D. Figure 8 shows an instance of the calculated flow in the r^*-z^* plane corresponding to the maximum penetration depth of the wall jet when $Re_g=1143$, $g/D=0.04$ and $\delta=0.51$.

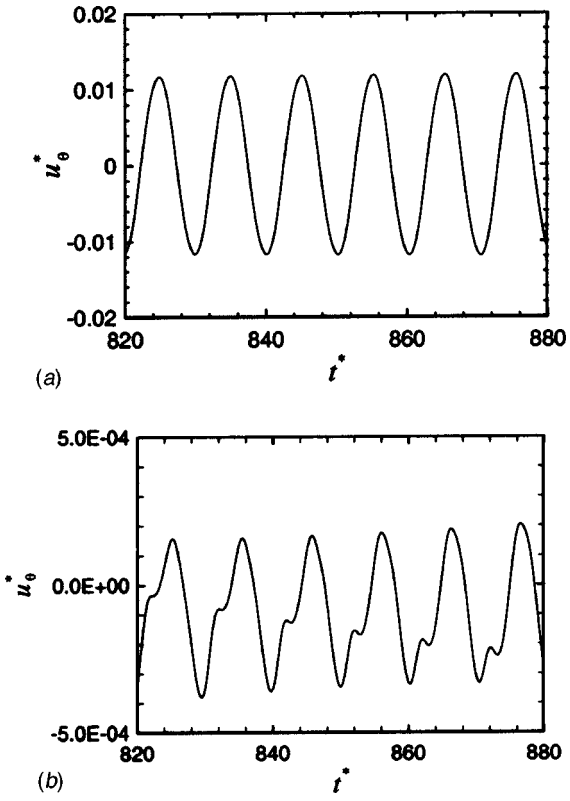

Fig. 6 Time records of the dimensionless circumferential velocity component at (*a*) $z^*=0.25$, $r^*=0.5$, and $\theta=0.22\pi$ (*b*) $z^*=0.5$, $r^*=0.5$, and $\theta=0.22\pi$ for the conditions of Fig. 5

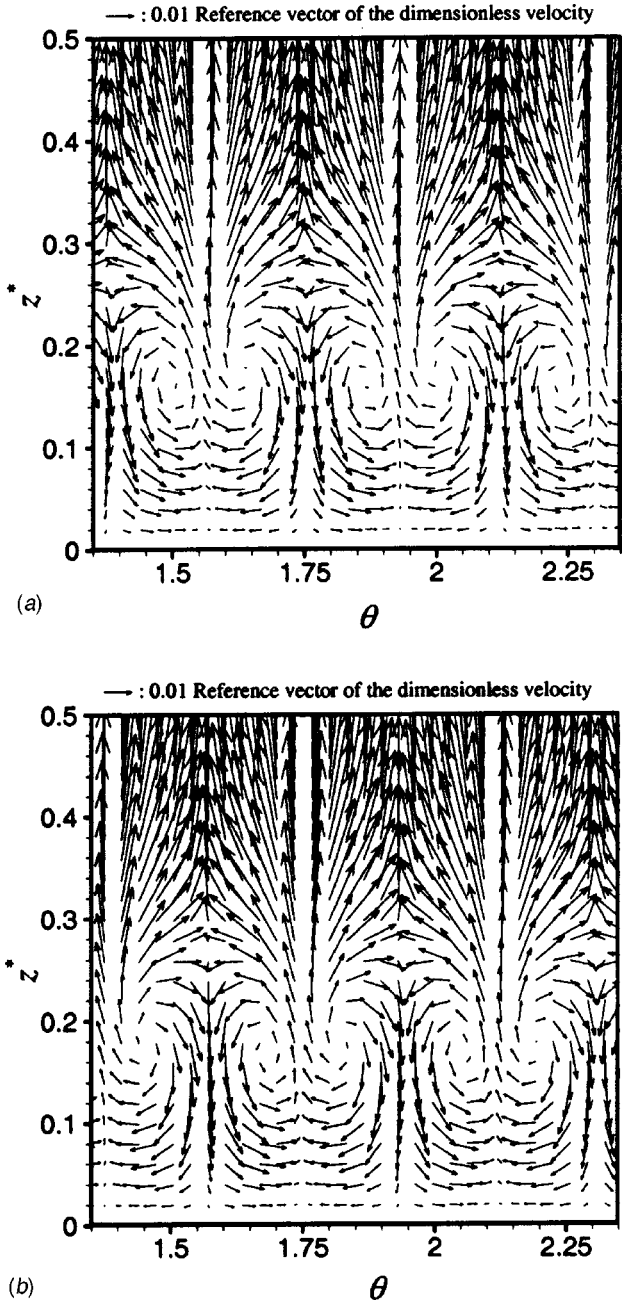

Fig. 7 Instantaneous dimensionless velocity vectors at times $t^*=860$ (*a*) and $t^*=865$ (*b*) in the lower half of the z^*-θ plane at $r^*=0.5$ for the conditions of Fig. 5

(The corresponding plot for the minimum penetration depth in an oscillation cycle is virtually the same.) While the radially decelerating expanding wall jet and the flow in the vicinity of the stagnation line represent potential sources for additional instabilities in the toroid, these are not observed in the calculations. If they exist in the experiment it is not known how much they influence the centrifugal instability leading to the formation of the Goertler vortices.

Conclusions

Because of the absence of end wall effects, the shear-driven flow in a toroid of rectangular cross section represents a more general fluid mechanics paradigm than its parallelepiped predecessors. In addition, radial accelerations and decelerations of fluid motion, induced by geometrical curvature, render this flow type especially rich in its physics.

Numerical calculations of the flow in a toroid can be performed assuming that a sliding wall shears the fluid. In contrast, an experimental realization of the flow requires the use of a wall jet to shear the fluid. We refer to the former as Configuration 1 and to the latter as Configuration 2.

In the limit $\delta\rightarrow 0$ and at sufficiently low Reynolds number, the wall-driven flow in a toroid corresponding to Configuration 1 approximates the two-dimensional flow in a plane enclosure. For $\delta=0$ and above a critical value of Re, the same configuration represents the wall-driven flow in an infinitely long parallelepiped. Our three-dimensional calculation approach yields results in excellent agreement with two-dimensional plane square enclosure flows and with the three-dimensional results of Albensoeder et al. [17] for the flow in a wall-driven parallelepiped of finite length (experiment) and infinite length (analysis). Thus, for the latter we obtain $\kappa=15.7$ and $\omega=0$ at $\mathrm{Re}=850$ compared to $\kappa=15.43$ and $\omega=0$ at $\mathrm{Re}=786.3$ for the resulting Goertler vortices. Earlier calculations in a finite-length parallelepiped for $\mathrm{Re}=3200$ and $\delta=0.005$ have yielded results in very good agreement with the Goertler vortices and time-averaged velocity profiles obtained experimentally by Koseff and Street [9,11] for $\mathrm{Re}=3300$.

Present calculations for Configuration 2 with $\delta=0.51$ (and $\delta=0.25$), $g/D=0.04$ and $\mathrm{Re}_g=1143$ reveal the same basic flow pattern as observed in Configuration 1 when the Goertler stability criterion is exceeded. This consists of a recirculating core flow and two smaller eddies at the bottom corners of the toroid, and centrifugally induced Goertler vortex pairs of wave number $\kappa=8.7$ superimposed on and aligned with the recirculating core flow. Especially noteworthy, however, is the observation that for any fixed location in the toroid, the Goertler vortex passing through that location alternates in its sense of rotation periodically as a function of time, and that this sign alternation occurs simul-

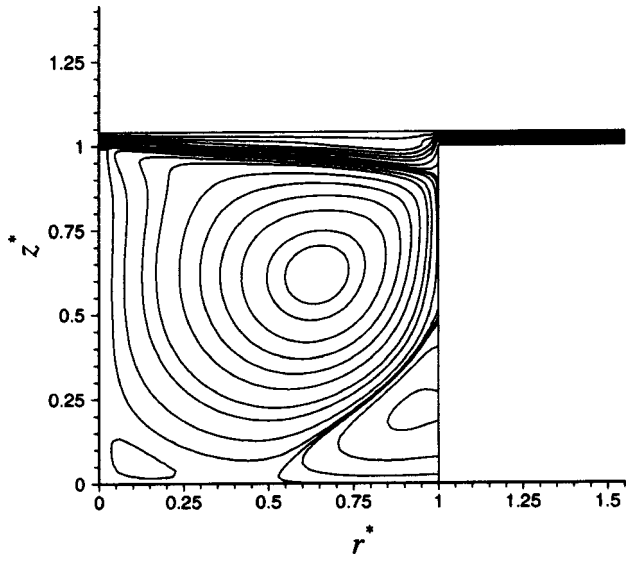

Fig. 8 Instantaneous streamlines obtained from a full domain three-dimensional flow calculation in a toroid with $Re_g=1143$, $\delta=0.51$, and $g/D=0.04$. The wall jet flows from left to right at the top of the toroid thus inducing a clockwise circulation of the core flow. Results shown correspond to the maximum penetration depth in an oscillation cycle. The maximum penetration depth is $p/D=0.079$ and the minimum is $p/D=0.076$.

taneously for all the other Goertler vortices in the toroid. From an Eulerian viewpoint, the visual effect is to observe *in situ*, simultaneous, time-periodic alternations in the sense of rotation of all the vortices in the toroid at frequency $\omega=0.154$. Such behavior is precluded for the wall-driven flows in finite-length parallelepipeds where the sense of rotation of the Goertler vortices is determined and stabilized by the sense of rotation of the end wall vortices. A comparison between the calculated results with $\delta=0.25$ and $\delta=0.51$ suggests that vortex wavenumber is independent of curvature at this value of Reynolds.

Flow visualization observations in a toroid with $\delta=0.25$, $g/D=0.015$, and $Re_g=5000$ reveal Goertler vortices of wave number $\kappa\approx12.5$ which appear to alternately merge and split around their average locations. The experimental results suggest that for a toroid with $\delta=0.25$ vortex wave number increases with increasing Reynolds number.

While these are interesting and significant findings, further work is necessary to experimentally verify the periodic alternations in sense of rotation of the Goertler vortices. (In this regard, we have made new, encouraging observations in the existing experimental apparatus but the results are not definitive.) In addition, it is important to establish (a) the dependence on Re_g, δ, and g/D for transition from two-dimensional to three-dimensional flow and the appearance of flow unsteadiness; (b) the conditions leading to, and a full understanding of, the time-dependent alternations in sense of rotation of the Goertler vortices; and (c) vortex structure breakdown and transition to turbulence as a function of the relevant geometrical and dynamical parameters.

In summary, while the physics of the shear-driven flow in a toroid has yet to be fully understood, this new configuration poses a number of significant questions related to centrifugally driven flow instabilities while serving as a well-defined and challenging test case for computational fluid dynamic procedures aimed at solving complex, three-dimensional unsteady, laminar and turbulent flows.

Acknowledgments

JACH gratefully acknowledges support received from NSF (grant CTS9504390) for this study. Thanks go to G. Waltman at Bucknell University for the construction of the toroid test section. MA, JH, and FG thank the ''Dirección General de Investigación Científica y Técnica'' (Spain), DGICYT project no. PB96-1011, and the ''Programa de Grups de Recerca Consolidats de la Generalitat de Catalunya,'' CIRIT project no. 1998SGR-00102, for their support. We are sincerely grateful to R. Eichhorn (University of Houston) and J. Heinrich (University of Arizona) for enlightening discussions.

References

[1] Ghia, U., Ghia, K. N., and Shin, C. T., 1982, ''High-Re Solutions for Incompressible Flow Using Navier-Stokes Equations and a Multigrid Method,'' J. Comput. Phys., **48**, pp. 387–411.
[2] Iwatsu, R., Hyun, J. M., and Kuwahara, K., 1990, ''Analyses of Three Dimensional Flow Calculations in a Driven Cavity,'' Fluid Dyn. Res., **6**, pp. 91–102.
[3] Iwatsu, R., Ishii, K., Kawamura, T., Kuwahara, K., and Hyun, J. M., 1989, ''Numerical Simulation of Three-Dimensional Flow Structure in a Driven Cavity,'' Fluid Dyn. Res., **5**, pp. 173–189.
[4] Nishida, H., and Satofuka, N., 1992, ''Higher Order Solutions of Square Driven Cavity Flow Using Variable-Order Multigrid Method,'' Int. J. Numer. Methods Fluids, **34**, pp. 637–653. 5.
[5] Koseff, J. R., Street, R. L., Gresho, P. M., Upson, C. D., Humphrey, J. A. C., and To, W. M., 1983, ''A Three Dimensional Lid Driven Cavity Flow: Experiment and Simulation,'' *Proceedings of the Third International Conference on Numerical Methods in Laminar and Turbulent Flow*, C. Taylor, ed., Seattle, WA, pp. 564–581.
[6] Freitas, C. J., Street, R. L., Findikakis, A. N., and Koseff, J. R., 1985, ''Numerical Simulation of Three Dimensional Flow in a Cavity,'' Int. J. Numer. Methods Fluids, **5**, pp. 561–575.
[7] Kim, J., and Moin, P., 1985, ''Application of Fractional Step Method to Incompressible Navier-Stokes Equations,'' J. Comput. Phys., **59**, pp. 308–323.
[8] Freitas, C. J., and Street, R. L., 1988, ''Nonlinear Transient Phenomena in Complex Recirculating Flow: A Numerical Investigation,'' Int. J. Numer. Methods Fluids, **8**, pp. 769–802.
[9] Koseff, J. R., and Street, R. L., 1984, ''Visualization Studies of a Shear Driven Three Dimensional Recirculating Flow,'' ASME J. Fluids Eng., **106**, pp. 21–29.
[10] Koseff, J. R., and Street, R. L., 1984, ''On End Wall Effects in Lid Driven Cavity Flow,'' ASME J. Fluids Eng., **106**, pp. 385–389.
[11] Koseff, J. R., and Street, R. L., 1984, ''The Lid Driven Cavity Flow: A Synthesis of Qualitative and Quantitative Observations,'' ASME J. Fluids Eng., **106**, pp. 390–398.
[12] Prasad, A. K., and Koseff, J. R., 1989, ''Reynolds Number and End-Wall Effects on a Lid Driven Cavity Flow,'' Phys. Fluids A, **1**, pp. 208–218.
[13] Aidun, C. K., Triantafillopoulous, N. G., and Benson, J. D., 1991, ''Global Stability of Lid Driven Cavity With Throughflow: Flow Visualization Studies,'' Phys. Fluids A, **3**, pp. 2081–2091.
[14] Ramanan, N., and Homsy, G. M., 1994, ''Linear Stability of Lid Driven Cavity Flow,'' Phys. Fluids, **6**, pp. 2960–2701.
[15] Ding, Y., and Kawahara, M., 1998, ''Linear Stability of Incompressible Fluid Flow in a Cavity Using Finite Element Method,'' Int. J. Numer. Methods Fluids, **27**, pp. 139–157.
[16] Ding, Y., and Kawahara, M., 1999, ''Three-Dimensional Linear Stability Analysis of Incompressible Viscous Flows Using the Finite Element Method,'' Int. J. Numer. Methods Fluids, **31**, pp. 451–479.
[17] Albensoeder, S., Kuhlmann, H. C., and Rath, H. J., 2001, ''Three-Dimensional Centrifugal-Flow Instabilities in the Lid-Driven-Cavity Problem,'' Phys. Fluids A, **13**, pp. 121–135.
[18] Goertler, H., 1951, ''On the Three-Dimensional Instability of Laminar Boundary Layers on Concave Walls,'' NACA Technical Memorandum No. 1375.
[19] Taylor, G. I., 1923, ''Stability of a Viscous Liquid Contained Between Two Rotating Cylinders,'' Philos. Trans. R. Soc. London, Ser. A, **45**, pp. 289–343.
[20] Humphrey, J. A. C., Schuler, C. A., and Webster, D. R., 1995, ''Unsteady Laminar Flow Between a Pair of Disks Corotating in a Fixed Cylindrical Enclosure,'' Phys. Fluids, **7**, pp. 1225–1240.
[21] Phinney, L. M., and Humphrey, J. A. C., 1996, ''Extension of the Wall Driven Enclosure Flow Problem to Toroidally Shaped Geometries of Square Cross-Section,'' ASME J. Fluids Eng., **118**, pp. 779–786.
[22] Sudarsan, R., Humphrey, J. A. C., and Heinrich, J., 1998, ''Three-Dimensional Unsteady Wall-Driven Flow in a Toroid of Square Cross-Section: A New CFD Paradigm,'' *Proceedings of the ASME FED Summer Meeting: Forum on Industrial and Environmental Applications of Fluid Mechanics*, June 21-25, Washington, DC, ASME, New York, Paper No. FEDSM98-5314.
[23] Cushner, J., 2000, ''Experimental Visualization of a Shear-Driven Toroidal LDC Flow,'' M.Sc. thesis, College of Engineering, Bucknell University, Lewisburg, PA.

Rotating Effect on Fluid Flow in Two Smooth Ducts Connected by a 180-Degree Bend

Tong-Miin Liou[1]
Professor,
College of Engineering,
Feng Chia University,
Taichung, Taiwan, ROC

Chung-Chu Chen
Microsystem Laboratory,
Industrial Technology Research Institute,
Hsin-Chu, Taiwan, ROC
e-mail: 890079@itri.org.tw

Meng-Yu Chen
Department of Power Mechanical Engineering,
National Tsing Hua University,
Hsin-Chu, Taiwan, ROC
e-mail: d853708@oz.nthu.edu.tw

Laser Doppler velocimetry (LDV) measurements are presented of turbulent flow in a two-pass square-sectioned smooth duct simulating the coolant passages employed in gas turbine blades under rotating and nonrotating conditions. For all cases studied, the Reynolds number characterized by duct hydraulic diameter and bulk mean velocity was fixed at 1×10^4. The rotation number Ro was varied from 0 to 0.2. It is found that as Ro is increased, both the skewness (SK) of streamwise mean velocity and magnitude of secondary-flow velocity increase linearly, $SK=2.3\,Ro$ and $\overline{\sqrt{U^2+V^2}}/U_h=2.3\,Ro+0.4$, and the magnitude of turbulence intensity level increases exponentially. As Ro is increased, the curvature induced symmetric Dean vortices in the turn for Ro=0 is gradually dominated by a single vortex most of which impinges directly on the outer part of leading wall. The high turbulent kinetic energy is closely related to the dominant vortex prevailing inside the 180-deg sharp turn. The size of separation bubble immediately after the turn is found to diminish to null as Ro is increased from 0 to 0.2. A simple correlation is developed between the bubble size and Ro. A critical range of Ro responsible for the switch of faster moving flow from near the outer wall to the inner wall is identified. For both rotating and nonrotating cases, the direction and strength of the secondary flow with respect to the wall are the most important fluid dynamic factors affecting local the heat transfer distributions inside a 180-deg sharp turn. The role of the turbulent kinetic energy in the overall enhancement of heat transfer is well addressed. [DOI: 10.1115/1.1522413]

Introduction

Turbulent heat transfer around a 180-deg turn is affected by flow characteristics, such as the curvature induced Dean-type vortices inside the turn, turn-induced separating bubble immediately downstream of the turn, and resulting high turbulence intensity levels, [1]. For engineering applications, such as the internal coolant path of advanced gas turbine blades, the fluid flow, and heat transfer in the coolant channel are also influenced by rotation. The effect of rotation on fluid flow in a two-pass smooth square duct with a 180-deg straight-corner turn (Fig. 1) is therefore an important issue but the experimental information regarding flow fields under rotating conditions is still lacking in the open literature.

Most previous studies of serpentine smooth passages with rotation were focused on heat transfer measurements (Wagner et al. [2,3], Han and Zhang [4], and Yang et al. [5]). Corresponding flow-field information mainly derived from numerical results. Sathyamurthy et al. [6] adopted the k-ε model with wall function treatment to calculate the rotating square coolant channel with a 180-deg bend. Stephens et al. [7] predicted the three-dimensional fluid flow in a 180-deg bend with rotation using a low Reynolds number (Re) k-ε model of turbulence. Chen et al. [8] employed a Reynolds stress model and a multiblock numerical method to calculate three-dimensional flow and heat transfer in rotating two-pass square channels. Code validation was performed for the heat transfer part. Good agreement was obtained for Nusselt number distributions. Although there is no lack of experimental heat transfer data to verify the above-mentioned numerical models, little experimental data are available for flow-field validation of rotating serpentine coolant channels. Meanwhile, for turbulent flow in a square duct with a 180-deg bend, broad agreement with measurements is achieved for local Nusselt number predictions even though significant disagreements occur between velocity field predictions in the region away from the wall and the corresponding experimental data, as pointed out by Johnson [9] in his numerical simulation of the local Nusselt number. Experimental flow-field data are therefore demanded and valued.

Some previous measurements of relevant fluid flow were performed in stationary smooth (Schabacker et al. [10]) or rotating rib-roughened (Hsieh et al. [11] and Tse and Steuber [12]) coolant passages. In the following, only the studies related to rotating smooth duct flows will be quoted. Elfer [13] investigated the rotational effect on fluid flow in a circular channel with rotation Reynolds number ($\rho\Omega D_H^2/\mu$) ranging from 0 to 3100 by using a laser two-focus method. Bons and Kerrebrock [14] used particle image velocimetry (PIV) to investigate the internal flow of a single-pass square duct with rotation number Ro up to 0.2. Their PIV results provided useful information on the Coriolis and buoyancy effects but did not provide turbulence data. In real applications the coolant duct is serpentine, fluid flow (Liou and Chen [1] and Servouze [15]) and heat transfer resulting from a 180-deg sharp turn and duct rotation is quite different from that in a rotating straight duct. Thus, Liou and Chen [1] presented a set of laser-Doppler velocimetry (LDV) data including turbulence intensity profiles for developing flows through two ducts connected by a 180-deg straight-corner turn at Ro=0.08. Servouze [15] performed three-dimensional LDV measurements in a rotating two-pass channel with a 180-deg sharp turn at Re=5000 and Ro=0.33 (600 rpm). Some results were obtained at Re=25,000 and Ro =0.033 and 0.066. He did not provide turbulence data but concluded that in the radially inward flow pass the flow is mainly affected by the bend. The studies cited above have their axis of rotation normal to the curvature axis (Y-axis in Fig. 1) of the bend, as in most turbine coolant ducts. In other applications not directly pertinent to gas turbine blade cooling, the rotational rig of Cheah et al. [16] was designed such that the axis of rotation was parallel

[1]To whom correspondence should be addressed. Current address: Department of Power Mechanical Engineering, National Tsing Hua University, Hsinchu, Taiwan 300, ROC. e-mail: tmliou@pme.nthu.edu.tw.

Contributed by the Fluids Engineering Division for publication in the JOURNAL OF FLUIDS ENGINEERING. Manuscript received by the Fluids Engineering Division Mar. 1, 2000; revised manuscript received June 17, 2002. Associate Editor: P. W. Bearman.

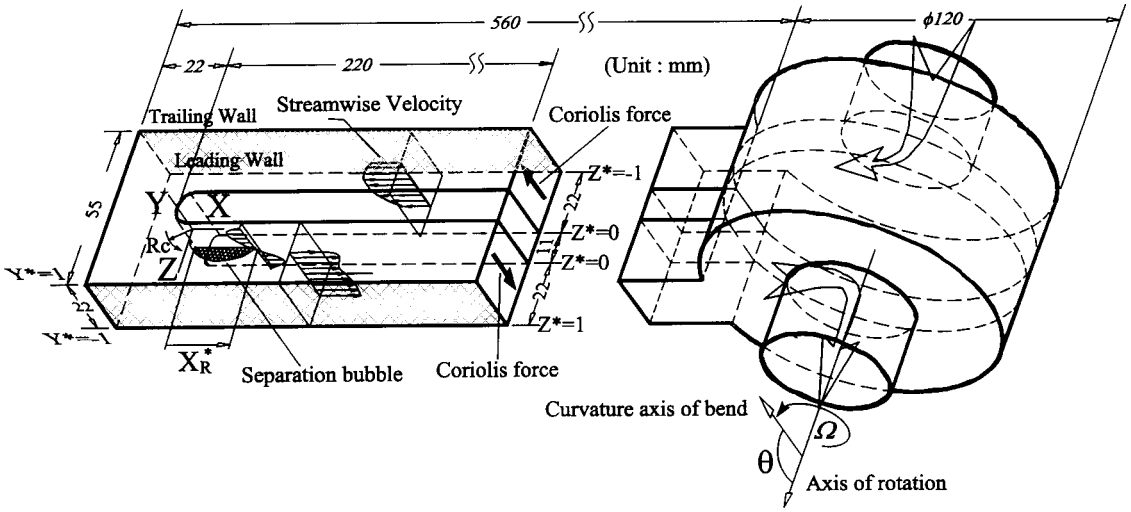

Fig. 1 Sketch of configuration, coordinate system, and dimensions of test section

to the curvature axis of the bend and located at the middle of the whole partition wall. They reported LDV measurements of a turbulent flow field in a rotating U-bend of strong curvature ($R_C/D_H=0.65$) with $Re=1\times10^5$ and Ro=0, 0.2, and −0.2.

Table 1 is a state-of-the-art list of flow-field measurements in rotating smooth ducts by various research groups. The lack of experimental measurements of turbulent velocity fields, compared to its heat transfer counterpart, in a rotating smooth duct with a 180-deg sharp turn and a bend-curvature axis normal to the rotational axis (pass number=2 and θ=90 deg) is obvious from the above survey and Table 1. In particular, the secondary flow pattern and turbulence intensity distribution inside the 180-deg sharp turn under rotating conditions are still undiscovered in the open literature and will, therefore, be investigated in the present work. Hence, the present study aims at performing measurements of the turbulent flow field in a rotating two-pass smooth duct with a straight-corner turn using nonintrusive laser-Doppler velocimetry. The reasons for adopting the straight-corner (or square-corner) turn are fourfold. First, it is used virtually in all of the previous studies (Wang and Chyu [17]). Second, it has appeared in some practical turbine blades (North [18]). Third, the square-corner turn yields the highest heat transfer enhancement among the various turning configurations examined by Wang and Chyu [17]. Fourth, the square-corner turn also makes it much easier to perform LDV measurements inside the 180-deg sharp turn. The rotation-induced spanwise variations of mean velocity profile in the internal cooling ducts were not reported previously and thus will be examined in the presented work. It is hoped that the data obtained herein lend insight to the effect of rotation on the complex flow investigation and can also be used for validation of ongoing computational predictions of internal flows in coolant ducts with and without rotation. Furthermore, heat transfer data deduced and recalculated from the previous study (Liou and Chen [19]) using transient liquid crystal thermometry in the rotating internal cooling duct is presented to provide a better understanding of the relation between the fluid flow and local heat transfer. Especially, the roles played by the turbulent kinetic energy as well as the direction and strength of the secondary flow in affecting the global heat transfer augmentation and local heat transfer distribution are documented in detail for the first time.

Experimental System and Conditions

Apparatus. The LDV experimental setup and flow system is similar to that described in Liou et al. [20], as shown schematically in Fig. 2. Based on $1/e^2$ extent of light intensity of a 4-W argon-ion laser, the forward scattering mode of the two- color four-beam two-component LDV system resulted in a probe volume of about 1.69 mm in length and 0.164 mm in diameter and the off-axis mode 0.74 mm in length and 0.164 mm in diameter inside the test section. The light scattered from salt particles with a nominal 0.8-μm diameter was collected into the photomultiplier and subsequently downmixed to the appropriate frequency shift of 0.1 to 20 MHz. Then two counter processors with 1 ns resolution were used to process the Doppler signals and feed the digital outputs into a PC-586 for storage and analysis. An optical incremental encoder (BEI H25D) attached to the rotating machinery resolver (RMR) module provided the phase angle in a given cycle.

Table 1

Lead Author	Year	Exp. Tech.	Duct Type	θ (deg)	Pass #	$Re\times10^{-4}$	Ro	Δρ/ρ	Measured	
									Quantity	Stations
Elfer	1993	L2F	○	90	1	4.5-6.0	0-0.1	0.31	U, V, u', v'	2
Cheah	1996	LDV	□	0	2	10.0	0-0.2	0	U,W,u',w',$\overline{uw}$	10
Liou	1997	LDV	□	90	2	1.4	0.082	0	U, V, u', v'	6
Servouze	1998	LDV	□	90	2	0.5-2.5	0.03-0.33	0	U, V, W	7
Bons	1998	PIV	□	90	1	0.8-1.0	0-0.3	0, 0.27	U, V	3
Present	2002	LDV	□	90	2	1.0	0-0.2	0	U, V, u', v'	20

L2F Laser-2-Focus Velocimetry
LDV Laser Doppler Velocimetry
PIV Particle Image Velocimetry
Re Reynolds number, U_bD_H/ν
Ro Rotation number, $\Omega D_H/U_b$
ρ Air density
θ Coolant passage orientation (deg)

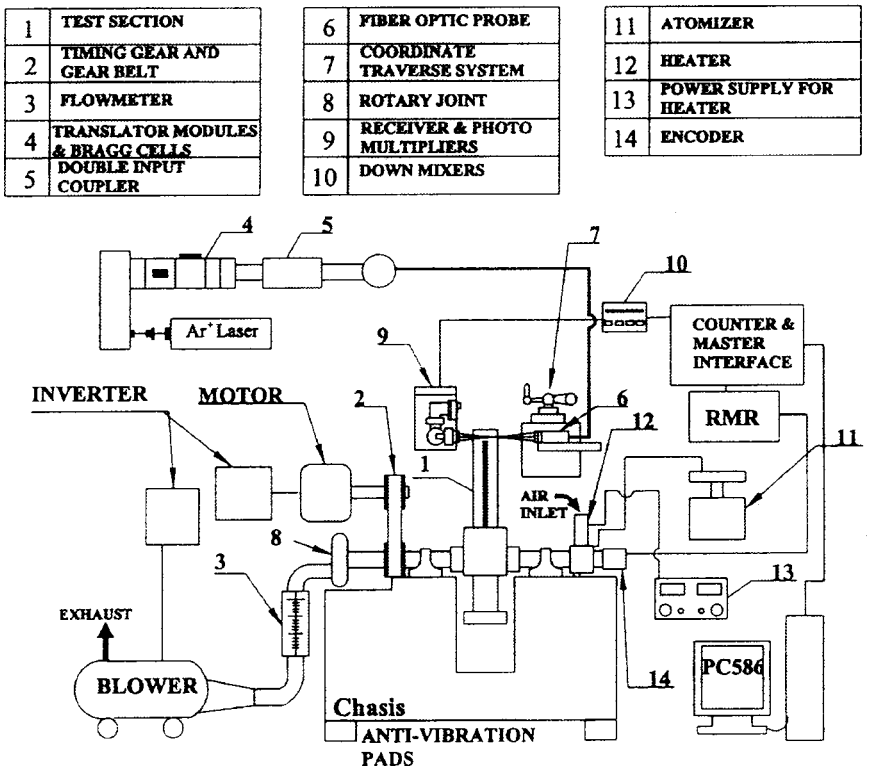

Fig. 2 Schematic drawing of overall experimental system

The minimum positioning window of each measuring location was indexed by the rotary encoder with a resolution (ER) of 0.09 deg. When a velocity measurement was validated by the counter processor, the phase angle-velocity data were concurrently transferred to the PC-586 and recorded. The circumferential length of a single data bin was from 0.51 to 0.91 mm as the measuring location varied from $X^*=10$ to $X^*=-1$. Two circumferential traverses were performed along two close radial positions to obtain profiles along straight traverse lines by data interpolation.

Air was axially drawn into one end of a hollow shaft by a 2.2 kW turbo blower, made a 90-deg turn in one side of a settling chamber, and radially flowed into the test section. The settling chamber was an enlarged part of the hollow shaft and internally partitioned into two parts by the divider of the two-pass coolant passage. As indicated in Fig. 1, the air flow in the first and second passages of the test section was radially outward and inward, respectively. Downstream of the test section, the air flow made a 90-deg turn in the other side of the settling chamber and then flowed axially through inside the hollow shaft, a rotary joint, a curved duct, a flowmeter, a bellows, and then exhausted through the exit of the blower.

Test Section and Conditions. The test section was made of 10-mm thick acrylic sheets for optical access. Figure 1 shows its configuration, coordinate system, and dimensions. The flow path has a cross section of 22 mm $\times$22 mm with a corresponding hydraulic diameter of $D_H=22$ mm. The channel height of the test section corresponds to phase angle windows of about two and four degrees at radii of 585 mm and 310 mm, respectively. The measured lengths of the first pass, sharp turn, and second pass are $10\,D_H$, $2.5\,D_H$, and $10\,D_H$, respectively. At the turn, the clearance between the tip of the divider wall and the duct outer wall is equal to $1\,D_H$ (or 22 mm) and the width of divider wall that separates the two flow passes is $0.5\,D_H$ or $W_d^*=0.25$. For the case of rotation, the mean radius-to-passage hydraulic diameter ratio is 22.7. Nevertheless, it should be noted that the coordinate origin is chosen at the tip center of the partition wall (Fig. 1) such that the X-coordinates upstream and downstream of the turn are all positive whereas in the turn negative. The streamwise mean velocity component U is taken positive along the main stream direction.

For both the stationary and rotational cases, the Reynolds number, based on the bulk mean velocity of $U_b=6.79$ m/s and hydraulic diameter, is fixed at 1.0×10^4. The choose of this value of Re is mainly limited by the LDV data rate and the practical rotation number Ro of 0.2. For the cold flow test, Ro is the major parameter documenting the effect of rotation. The rotational speeds range from 0 to 660 rpm corresponding to Ro from 0 to 0.2. The inlet reference cross section is chosen at $X^*=10$ of the first flow pass. The velocity measurements were made at 3 and 14 radial stations for the first and second flow passes, respectively. In each station the streamwise (U) and transverse (V) velocity profiles were measured along three planes ($Z^*=\pm0.23$, ±0.50, and ±0.77) for four rotation numbers (Ro=0.05, 0.10, 0.15, and 0.20). The secondary-flow velocity vector mappings were performed over three cross-sectional planes ($Z^*=-0.5$, $Z^{**}=0$, and $Z^*=0.5$) inside the turn for two rotation numbers (Ro=0.08 and 0.15). Note that the inner surface of the passage is always at $Z^*=0.0$, the outer surface is at $Z^*=\pm1.0$, and the $Y^*=0.0$ is located halfway between the leading and trailing wall.

Data Accuracy. Typically, 2000–4000 realizations were ensemble averaged at each measuring location for the stationary and rotational cases. Additional measurements of higher realizations (8000) in the high fluctuation regions were also taken to make sure the attainment of statistical convergence. For the latter case there were 40,000 to 80,000 realizations within the phase angle window over many revolutions. The presented mean velocity and turbulence intensity were calculated from the probability distribution function of the measurements. The corresponding statistical errors in the ensemble mean velocity and turbulence intensity were less than $0.018\,U_b$ and $0.031\,U_b$, respectively, for a 95% confidence level. For the rotational case, the phase angle broadening (or positioning window broadening) was estimated as 0.5 and 3.4% (relative to U_b) for mean velocity and turbulence inten-

sity profiles, respectively, for positioning window widths of 0.125 deg. An in-field balancer was used to perform the static and dynamic balance of the rotating piece. The maximum displacement of rotation-induced vibration was 28 μm for Ro=0.2. Other sources of error were documented in detail in our previous work (Liou and Chen [1]).

Results and Discussion

Flow Patterns at Inlet Reference Station. Figure 3(*a*) depicts the streamwise mean X- component velocity and turbulence intensity profiles at inlet reference station $X^*=10$ in the $Z^*=-0.5$ plane for the stationary-duct case. The profiles are only shown in the symmetrical half. It is seen that the U/U_b profile is rather uniform within 60% (with respect to $Y^*=0$) of the channel height. The corresponding boundary layer thickness, δ_{95} defined at 95% $U_{\max}$, is 3.5 mm (at $Y^*=-0.64$). The u'/U_b profile has levels of 0.09 ± 0.02, except near the wall where the levels are higher and within 0.15 ± 0.03. Because the normal vector of Z^*-planes is parallel to the axis of rotation, the Z^*-planes approximately parallel the direction of Coriolis force in the rotating duct case (Fig. 1). Therefore, the flow profiles in the Z^*-planes are expected to be influenced largely by Coriolis force. The streamwise mean velocity and turbulence intensity profiles at $X^*=10$ in the $Y^*=0$ plane for Ro=0 is depicted in Fig. 3(*b*). The data are collected in the full span and presents a slight skewness. The U/U_b profile is skewed toward the inner wall while the u'/U_b toward the outer wall. The skewness comes from the upstream 90-deg turn in the settling chamber, and has nearly diminished as a result of the flow developing length of $17.2\,D_H$.

Figure 4 shows the rotation number effect on the streamwise mean X-component velocity and turbulence intensity profiles at $X^*=10$ in the $Z^*=-0.5$ plane. It can be seen clearly that the skewness of U/U_b increases monotonically as Ro is increased from 0.05 to 0.20. The skewness indices, defined as $\int_{-1}^{1} Y^{*3}(U/U_b)dY^*/\sigma_{Y^*}^3$, [21], in the present study, are 0.12, 0.20, 0.30, and 0.48 for Ro=0.05, 0.10, 0.15, and 0.20, respectively. The maximum U/U_b accelerated by the Coriolis force occur near $Y^*=0.60$ and are $1.16\,U_b$, $1.23\,U_b$, $1.33\,U_b$, and $1.40\,U_b$ for Ro=0.05, 0.10, 0.15, and 0.20, respectively. Figure 4 also includes the mean flow results reported by Bons and Kerrebrock [14] for comparison. Their PIV-measured profile (symbol $\times$ in Fig. 4) at Ro=0.20 and Re=8100 does not skew as much as those measured in the present Ro=0.20 case. The rationale for this discrepancy can be the different flow redeveloping length in the two studies. The measuring location of Bons and Kerrebrock [14] is $7.9\,D_h$ from the tapered inlet of the test section. However, the measuring location of the inlet reference plane in the present study is about $15\,D_h$ downstream of the sudden contraction inlet after the settling chamber (Fig. 1). The velocity skewness in the $Z^*=-0.5$ plane generally increases with the development of the fluid flow in the rotating duct, as will be addressed in the following section (Flow Development in Z^* Planes). When the rotation number is increased from Ro=0.05 to Ro=0.20, the turbulence intensity in the core region, $Y^*=-0.6\sim0.6$, is augmented gradually from 0.09 ± 0.01 to 0.12 ± 0.01. The rotation-induced skewness of turbulence intensity profiles is not so obvious as that of the mean velocity profiles. Nevertheless, rotation raises turbulence intensity more notably near the trailing wall ($u'/U_b=0.20\sim0.33$ at $Y^*=0.92$) than near the leading wall ($u'/U_b=0.15\sim0.25$ at $Y^*=-0.92$) as a result of the movement of $U_{\max}/U_b$ toward the trailing wall and the increase of $U_{\max}/U_b$ with increasing Ro.

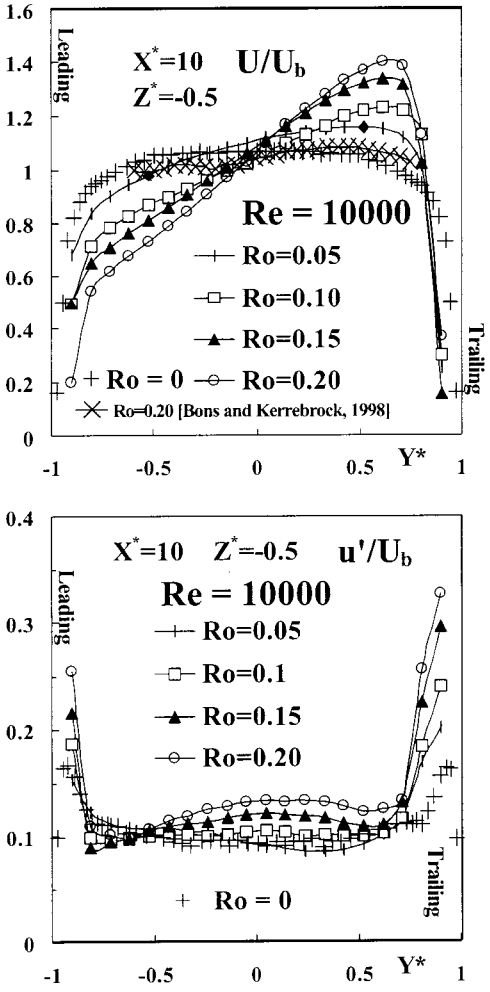

Fig. 4 Streamwise mean velocity and turbulence intensity profiles at $X^*=10$ station of the first pass in the $Z^*=-0.5$ plane for Re=10,000 with various Ro

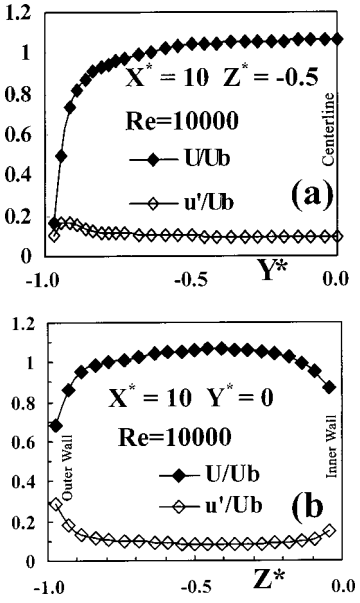

Fig. 3 Streamwise mean velocity and turbulence intensity profiles at $X^*=10$ station of the first pass in the (*a*) $Z^*=-0.5$ and (*b*) $Y^*=0$ planes for Re=10,000 and Ro=0

Flow Development in Z^* Planes. The streamwise flow developments in $Z^*=\pm0.5$ planes are depicted in Fig. 5. For Ro=0 (Liou et al. [20]), the streamwise mean velocity profiles (Ro=0,

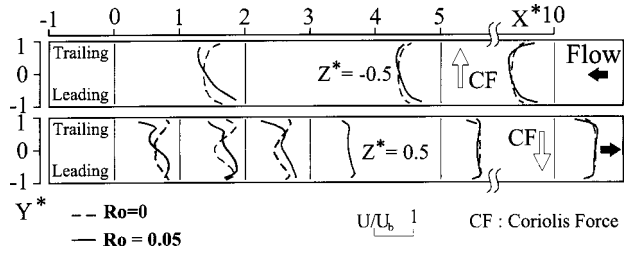

Fig. 5 Evolution of streamwise mean velocity profile in the $Z^*=\pm 0.50$ planes of the first and second passes for (*a*) Ro=0 (Liou et al., [20]) and (*b*) Ro=0.05

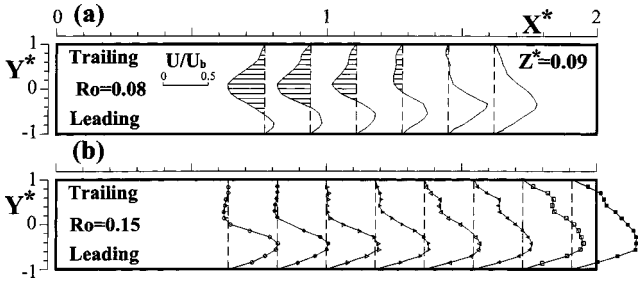

Fig. 6 Radially inward evolution of U/U_b profile within $2D_H$ immediately after the turn for (*a*) Ro=0.08 and (*b*) Ro=0.15

dashed line) in the $Z^*=-0.5$ plane of the first pass are symmetric and almost unaffected by the turning curvature. In the $Z^*=0.5$ plane within the region of about $6D_H$ after the turn, concave streamwise mean velocity profiles with lower velocity around $Y^*=0$ appear due to the combined effect of the sharp-turn-induced separation recirculation flow (will be shown shortly in this section) and the turning-curvature-induced Dean-type secondary flow. For $X^*>6$, the streamwise mean velocity profiles become a top-hat shape. Even with a small rotation number, say Ro=0.05, the symmetric velocity profiles in $Z^*=\pm 0.5$ planes are altered greatly, especially near the 180-deg sharp turn. The rotation- induced Coriolis force directs the fluid flow from the leading wall towards the trailing wall (thus increases the fluid mass there) in the outward flowing duct, whereas its direction is reversed in the inward flowing duct (Liou and Chen [1]). Solid lines in Fig. 5 show that relative to its stationary counterpart (dashed lines), the streamwise mean velocity profiles for $0\leqslant X^*\leqslant 10$ in the first pass of the rotating duct (Ro=0.05) are all skewed towards the trailing wall. The rotation-induced skewness increases gradually as the flow proceeds radially outward in the first pass since the centrifugal force increases with increasing fluid mass and distance from the rotational axis. Quantitatively, the skewness indices are 0.12, 0.26, and 0.42 for $X^*=10$, 5, and 2, respectively. At $X^*=2$, U/U_b profile has a higher peak value of $U/U_b=1.2$ occurring around $Y^*\approx 0.6$.

Conversely, the symmetric double peak U/U_b profiles in the second pass for the stationary case is skewed towards the leading wall, say at $X^*=0.1$, 1.0, 2.0, and 3.0, due to the Coriolis force as Ro is increased from 0 to 0.05. The skewness indices remain about -0.30 (negative sign represents skewing toward leading wall) from $X^*=0$ to 2.0 while the concave profiles are being leveled due to the action of the centrifugal force. As the flow proceeds radially inward to $X^*\geqslant 3.0$, the concavity of U/U_b profiles is leveled up and the skewness index drops to -0.10. The U/U_b profiles in the duct-central planes ($Z^*=0.5$) of the second pass are quite symmetric with skewness indices of -0.07 and -0.04 for $X^*=5.0$ and $X^*=10.0$, respectively. The skewness in the front portion of the second pass is the result of skewed flow profiles from first pass, the 180-deg sharp turning effect, and the ever-existing Coriolis force in the rotating duct. The resultant secondary flow directs most of flow toward leading wall before entering the second pass and shifts the recirculation separation bubble toward trailing wall in the front portion of second pass, as will be addressed in the following section (Secondary Flow Patterns in the 180-Deg Turn). This is the main reason for the skewed twin peak U/U_b profiles. Note that before entering the reference inlet plane ($X^*=10$) in the first pass, the rotation-induced Coriolis force has already affected the fluid flow for about $15D_H$, as shown in Fig. 1. This explains why one can find a well-skewed U/U_b profile at the end of first pass, say at $X^*=2.0$, but not at the exit of second pass, say at $X^*=10$, for the low rotation number case (Ro=0.05).

As mentioned previously, the twin peak U/U_b profiles result from the presence of turn-induced separation bubble. Nevertheless, no previous studies explored the variations of U/U_b distributions and dimensionless separation-bubble length (X_R^* in Fig. 1) with Ro. Such variations are plotted in Figs. 6 and 7 where the longitudinal plane $Z^*=0.09$ is 2 mm adjacent to the divider wall $Z^*=0$ (Fig. 1). As one can see from Fig. 6(*a*), there exists a separation bubble skewed slightly toward the trailing wall ($Y^*=1$). This is because the Coriolis force in the radially inward flow pass directs the fluid to flow toward the leading wall with positive U/U_b. When Ro is increased from 0.08 to 0.15, the rotation-induced Coriolis force increases accordingly. As a result, Fig. 6(*b*) shows that the region of positive U/U_b enlarges or the size of separation bubble shrinks. Figure 7 further depicts that the length of the separation bubble on the $Y^*=0$ plane and divider wall decreases with increasing Ro. This observation suggests that heat transfer uniformity immediately after the turn will be improved with increasing Ro and diminishing separation bubble. The functional relation between X_R^* and Ro can be correlated as $X_R^*=-24\,\mathrm{Ro}^2-4\,\mathrm{Ro}+1.7$ for $0\leqslant \mathrm{Ro}\leqslant 0.2$. This correlation provides a useful reference for validating the relevant CFD code.

Figure 8 depicts U/U_b and u'/U_b profiles in six Z-planes ($Z^*=\pm 0.23$, ± 0.50, and ± 0.77) for Ro=0.15. In the front part of the first pass (Fig. 8(*a*)), no apparent variations in U/U_b and u'/U_b profiles exhibit between different Z^* planes at $X^*=10.0$ and $X^*=5.0$ stations. At $X^*=2.0$, the flow has sensed the 180-deg sharp turn and, hence, displays an acceleration and deceleration in the inner plane ($Z^*=-0.23$) and outer planes ($Z^*=-0.77$), respectively, as shown in the upper left of Fig. 8(*a*). This has the same trend as the stationary case (Liou et al. [20]). However, rotating the duct with Ro=0.15 advances the outset of flow acceleration and deceleration at least $0.5D_H$ ahead of its stationary counterpart ($X^*=1.5$, Liou et al. [20]). The corresponding variations in u'/U_b profiles between $Z^*=-0.23$ and $Z^*=-0.77$ planes can be as large as 5% and 13% of U_b near the leading and trailing walls, respectively. The rotation-induced spanwise variations of

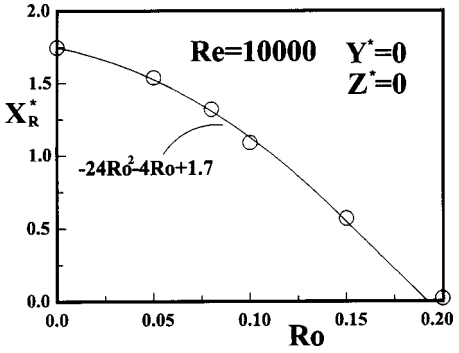

Fig. 7 Variation of separation bubble length with rotation number

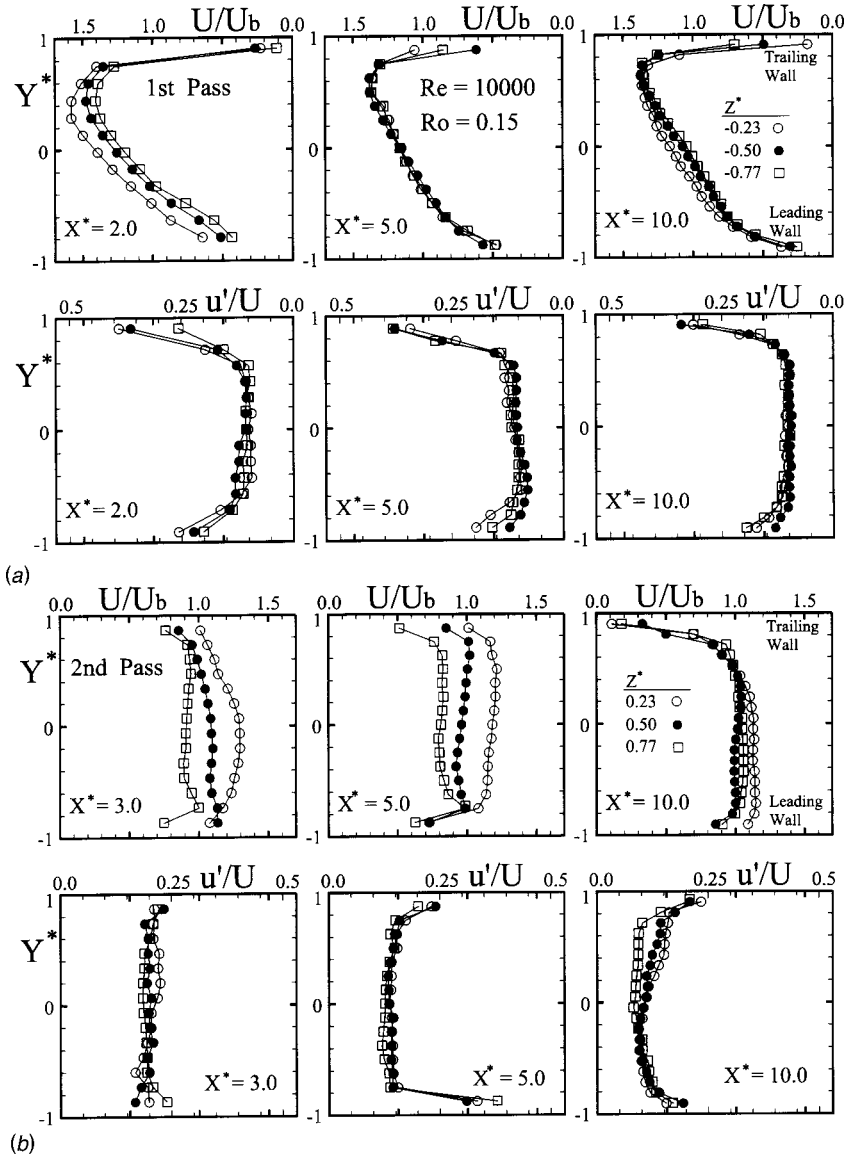

Fig. 8 (*a*) Spanwise variations of streamwise mean velocity and turbulence intensity profiles in the first pass for Ro=0.15. (*b*) Spanwise variations of streamwise mean velocity and turbulence intensity profiles in the second pass for Ro=0.15.

U/U_b mainly occur in the second pass (Fig. 8(*b*)). In the stationary case, a flow undergoes adverse (Fig. 9) and favorable pressure gradients (Liou and Liao [22]) along the inner and outer walls, respectively, in the post-turn region. The reversed trend in the streamwise mean velocity evolution results in higher and lower velocity near the outer and inner walls, respectively, throughout the second pass (Liou et al. [20]). Rotation inverses the aforementioned trend in the second pass if the value of Ro is sufficient high. As shown in Fig. 8(*b*), for Ro= 0.15 U/U_b is the highest in the $Z^*=0.23$ plane (close to inner wall) and the lowest in the $Z^*=0.77$ plane (close to outer wall) at the $X^*=3.0$ and $X^*=5.0$ stations. The physical explanation is as follows. The abovementioned reduction of the size of separation bubble with the increase of Ro lowers the turn-induced pressure loss on the inner wall side. Figure 9 is an example showing the wall static pressure drop along $Z^*=0.23$ plane near the inner wall. Please refer to Liou et al. [23] for detailed setup of pressure measurements. It is seen from Fig. 9 that as Ro is increased beyond a critical range $0.10 \leqslant Ro_c \leqslant 0.15$, the reduction in turn-induced pressure loss leads to a favorable pressure gradient from $X^*=0$ to 10 (symbol ∇ and X in Fig. 9), in contrast to an adverse pressure gradient for $Ro < Ro_c$, and in turn flow acceleration on the $Z^*=0.23$ plane shown in Fig. 8(*b*). The spanwise variation of mean velocity magnitude can be as high as 44% and 50% at $X^*=3.0$ and 5.0, re-

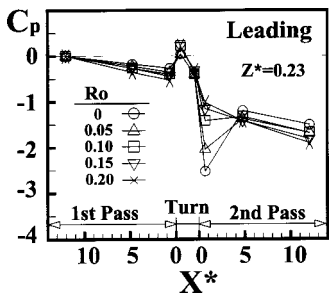

Fig. 9 Variation of dimensionless wall static pressure with *X

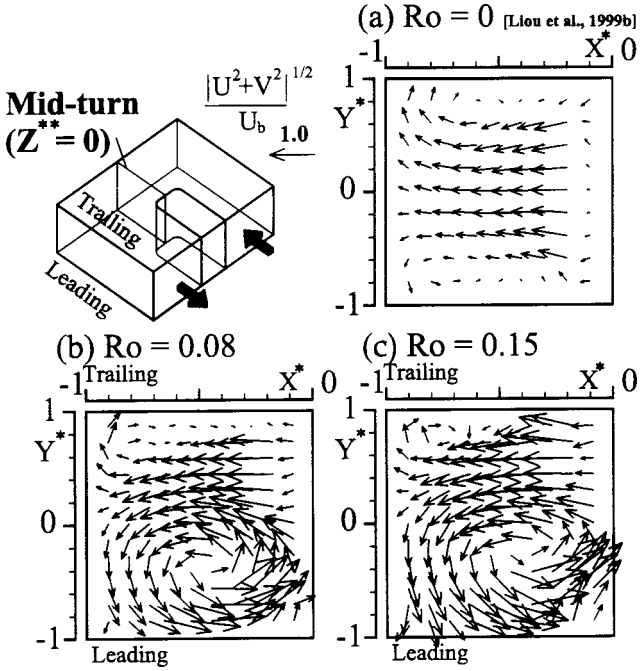

Fig. 10 Cross-stream secondary flow patterns in the midturn ($Z^{**}=0$) for (*a*) Ro=0, (*b*) Ro=0.08, and Ro=0.15 at Re=10,000 (view from downstream side)

spectively, in the second pass. In addition to the magnitude of mean velocity, the skewness of U/U_b profiles varies with different spanwise locations. The skewness indices are -0.06 ($Z^*=0.23$), -0.12 ($Z^*=0.50$), and -0.02 ($Z^*=0.77$) at $X^*=3.0$, and are 0.11 ($Z^*=0.23$), 0.05 ($Z^*=0.50$), and -0.10 ($Z^*=0.77$) at $X^*=5.0$. The spanwise variation of skewness illustrates the much more complex flow structures in the second pass than in the first pass due to the combined turning and rotating effects. Away from the turn in the second pass, the spanwise variation of U/U_b profiles is reduced, as shown by the upper right figure ($X^*=10.0$ in the second pass) in Fig. 8(*b*). In general, there are less noticeable variations, up to 7% of U_b, in u'/U_b profiles between different Z^* planes can be found from Fig. 8(*b*).

Secondary Flow Patterns in the 180-Deg Turn. Figure 10 shows the secondary-flow pattern at the midturn ($Z^{**}=0$) cross section under stationary and rotatory conditions. It is well known that a Dean-type secondary flow typically exists for a flow through a turn due to the imbalance of centrifugal force and pressure gradient, as shown by Fig. 10(*a*). Note that the secondary-flow mean-velocity vector fields are plotted in the way of the facing-upstream direction. In the stationary case, the counter rotating Dean vortex pair appears symmetrically with the vortex centers locating at $X^*=-0.60$ and $Y^*=\pm 0.80$. The maximum cross-stream mean velocity occurs at $Y^*=0$ near $X^*=-0.20$. Relatively low secondary-flow velocities appear near the divider walls ($X^*=0$). This is due to the onset of flow separation shifts from the second pass to the divider tip inside the turn for $W_d^*=0.25$ (Liou et al. [20]). Two regions with secondary flow directed toward the top and bottom walls occur around $X^*=-1$ and $Y^*=\pm 0.8\sim\pm 1$ where heat transfer is elevated. In particular, the downwash regions of the secondary flow are associated with the highest Nu/Nu_0 enhancement.

As the duct rotates, Figs. 10(*b*) and 10(*c*) clearly reveal that the difference in Ro does affect the cross-stream flow pattern inside the turn. In the first pass of the rotating duct, the streamwise mean velocity profiles are skewed towards the trailing wall (Fig. 8), as mentioned previously and further evidenced in Figs. 10(*b*) and 10(*c*) in terms of cross-stream velocity profiles. Most flow skews toward trailing wall around $X^*=0\sim-0.4$. Therefore, the symmetry of the turn-induced secondary flow is totally altered, and the lower part of the Dean vortex pair dominates the whole cross section of the midturn. The ruling vortex occupies more than a 90% area of the midturn cross section, and directs the major secondary flow to impinge and sweep the leading wall. This will cause a much greater heat transfer enhancement on the leading wall than on the trailing wall in the 180-deg sharp turn. The upper part of the distorted Dean vortex pair still exists and is confined to the upper part ($Y^*>0.85$) and upper left corner ($Y^*>0.70$ and $X^*<-0.60$) for Ro=0.08 and Ro=0.15, respectively. The upper vortex has a velocity similar to and higher than its stationary counter part for Ro=0.08 and Ro=0.15, respectively. The dominant vortex results in a strong back flow near the leading wall. One can find that the secondary flow is directed away from the leading wall near the lower right corner ($X^*=-0.25\sim 0$ and $Y^*=-1\sim-0.6$) of the midturn cross section. The upwash regions of the secondary flow are associated with the deteriorated Nu/Nu_0 enhancement (Pauley and Eaton [24] and Liou et al. [25]). Quantitatively, rotation increases the total averaged strength of secondary flow, $\overline{\sqrt{U^2+V^2}}$, from $0.39\,U_b$ (Ro=0) to $0.63\,U_b$ (Ro=0.08) and $0.73\,U_b$ (Ro=0.15) in the midturn cross section. In particular, $\sqrt{U^2+V^2}$ is remarkably increased by rotation from $0.28\,U_b$ (Ro=0) to $0.82\,U_b$ (Ro=0.08) and $0.89\,U_b$ (Ro=0.15) around the most-heat-transfer- elevated area ($Y^*<-0.8$ and $X^*<-0.4$ on the leading wall). The $(\sqrt{U^2+V^2})_{max}$ is $0.80\,U_b$, $1.20\,U_b$, and $1.45\,U_b$ for Ro=0, 0.08, and 0.15, respectively.

Velocity Vector Patterns in $Z^*=\pm 0.5(-1<X^*<0)$ Planes. Figure 11 shows flow patterns in the two selected cross sections inside the 180-deg sharp turn under rotating conditions. Note that Fig. 10 and Fig. 11 to be shown shortly are only for two- dimensional flow view due to the limitation of the LDV. The best view is in a 45-deg angle plane (Schabacker et al. [10]). At $Z^*=-0.5$, the flow patterns are quite similar to those at $Z^{**}=0$ (Fig. 10). The Dean-type vortex pair is greatly skewed by rotation-induced Coriolis force. Both the dominant vortex near the leading wall and the minor vortex confined in the upper left corner are still under developing and is smaller than those in the midturn ($Z^{**}=0$, Figs. 10(*b*) and 10(*c*)) in both size and strength. Also note that the flow vectors suggest that the presence of a vortex near the lower right corner ($X^*=0$ and $Y^*=-1$) of the $Z^*=-0.5$ cross section. This rotation-induced vortex is formed by the collision of the two opposite streams—one is the main stream from the first pass and the other is the reverse flow of the dominant vortex in the turn—near the entrance of the turn ($X^*\sim 0$). Flow patterns are much different in the $Z^*=0.5$ cross section (Fig. 11) because the flow has turned about 180 deg and is ready to enter the second pass. Note that the direction of rotation-induced Coriolis force is reversed while the turn changes outward flow (first pass) into inward flow (second pass). More fluid flow is now gathered near the leading wall for the case of $Z^*=0.5$, opposite to that for the case of $Z^*=-0.5$. This difference illustrates the skewed double-peak velocity profile shown in Fig. 5 (solid line) near the entrance of the second pass ($X^*=0$). More and more fluid flow is gathered near the leading wall while increasing Ro from 0.08 to 0.15 and, in turn, the skewness (toward the leading wall) of the concave streamwise mean velocity profiles increases with increasing Ro. The shift of the lowest velocity position in Fig. 11 from $Y^*=0.20$ (Ro=0.08) to $Y^*=0.40$ (Ro=0.15) also implies the shift of the separation recirculation zone in the second pass toward trailing wall.

Turbulent Kinetic Energy in the 180-Deg Turn. In addition to the greatly distorted secondary-flow mean velocity profiles, turbulence distributions deserve to be reported under rotating conditions since PIV measurements usually do not provide such infor-

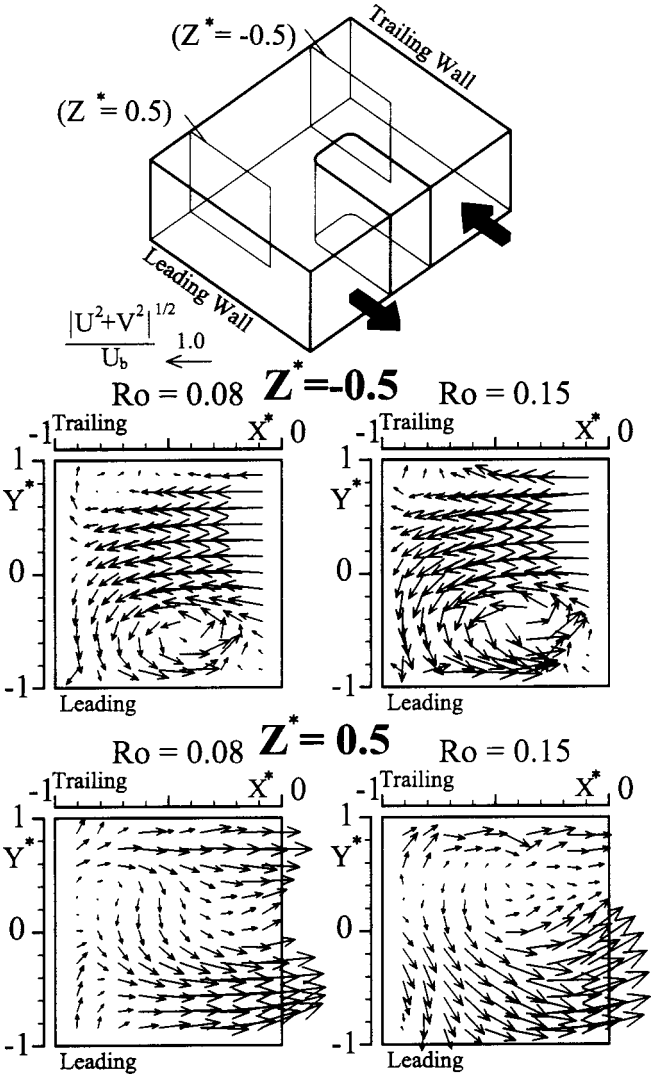

Fig. 11 Flow patterns of two cross sections ($Z^*=-0.5$ and $Z^*=0.5$) inside the turn for Ro=0.08 and Ro=0.15 at Re=10,000 (view from downstream side)

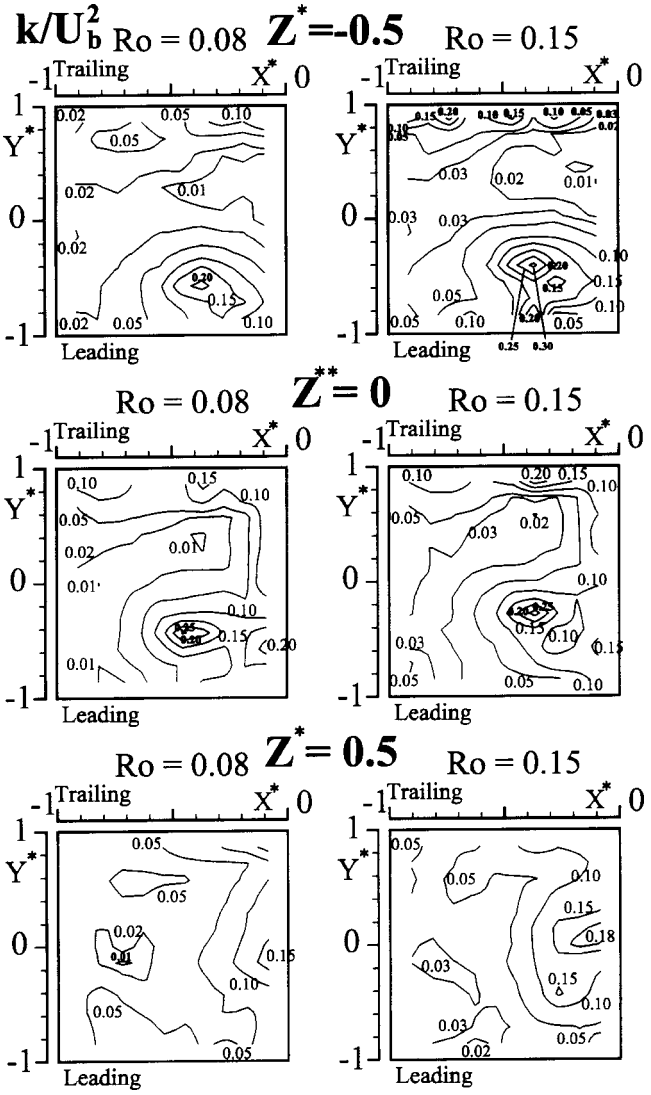

Fig. 12 Dimensionless turbulent kinetic energy contours of three cross sections ($Z^*=-0.5$, $Z^{**}=0$, and $Z^*=0.5$) inside the turn for Ro=0.08 and Ro=0.15 at Re=10,000 (view from downstream side)

mation as mentioned in Introduction. Figure 12 thus depicts the dimensionless turbulent kinetic energy (k/U_b^2) distributions in the three cross sections examined. It is seen that the distributions of k/U_b^2 for Ro$\neq$0 are quite asymmetric. For the $Z^*=-0.5$ cross section, the highest local k/U_b^2 peaks, 0.20 (Ro=0.08) and 0.30 (Ro=0.15), are associated with the dominant vortex centers (Figs. 10 and 11). The vortex structure is believed to be highly unsteady due to the combined effect of turning and rotating, and thus generates high turbulence. The shift of k/U_b^2 peak position conformably corresponds to the shift of dominant vortex center for $Z^*=-0.5$ in Fig. 11. The second high k/U_b^2 peak occurs near the trailing wall due to the collision of the main stream with the back flow of the minor vortex. The values and locations of the second high k/U_b^2 peak are (0.10, $X^*=-0.35$) and (0.20, $X^*=-0.70$) for Ro=0.08 and Ro=0.15, respectively.

In the midturn plane, the k/U_b^2 distribution is quite similar to that in the $Z^*=-0.5$ plane. For the $Z^{**}=0$ cross section, the highest local k/U_b^2 peaks located at the dominant vortex centers are 0.25 for both Ro=0.08 and Ro=0.15. The values and locations of the second high k/U_b^2 peak are (0.15, $X^*=-0.35$) and (0.20, $X^*=-0.40$) for Ro=0.08 and Ro=0.15, respectively. The relatively higher local k/U_b^2 peak near the divider wall is associated with the separation-bubble's shear layer (Liou et al. [20]) and is about 0.10 for both Ro=0.08 and Ro=0.15.

Turbulence distributions in $Z^*=0.5$ plane (Fig. 12) are quite different from those in $Z^{**}=0$ and $Z^*=-0.5$. The highest k/U_b^2 at $X^*=0$ is associated with the shear layer bounding the separating recirculation zone and the double-peak velocity profile. The values and locations of the highest k/U_b^2 peak are (0.15, $Y^*=0$) and (0.18, $Y^*=0.05$) for Ro=0.08 and Ro=0.15, respectively. Increasing Ro from 0.08 to 0.15 generally increases k/U_b^2 of the low turbulence core region from 0.01~0.02 to 0.02~0.03. The averaged values of k/U_b^2 for (Ro=0.08/Ro=0.15) are (0.044/0.062), (0.061/0.066), and (0.053/0.072) for the $Z^*=-0.5$, $Z^{**}=0$, and $Z^*=0.5$ planes, respectively. The averaged k/U_b^2 inside the turn is increased 40%, 8%, and 36% by raising rotation number from Ro=0.08 to Ro=0.15 for $Z^*=-0.5$, $Z^{**}=0$, and $Z^*=0.5$ planes, respectively.

Figure 13 summarizes the overall rotating effect on the heat transfer (Liou and Chen [19]) and fluid flow parameters in the 180-deg turning duct. The total averaged flow parameters,

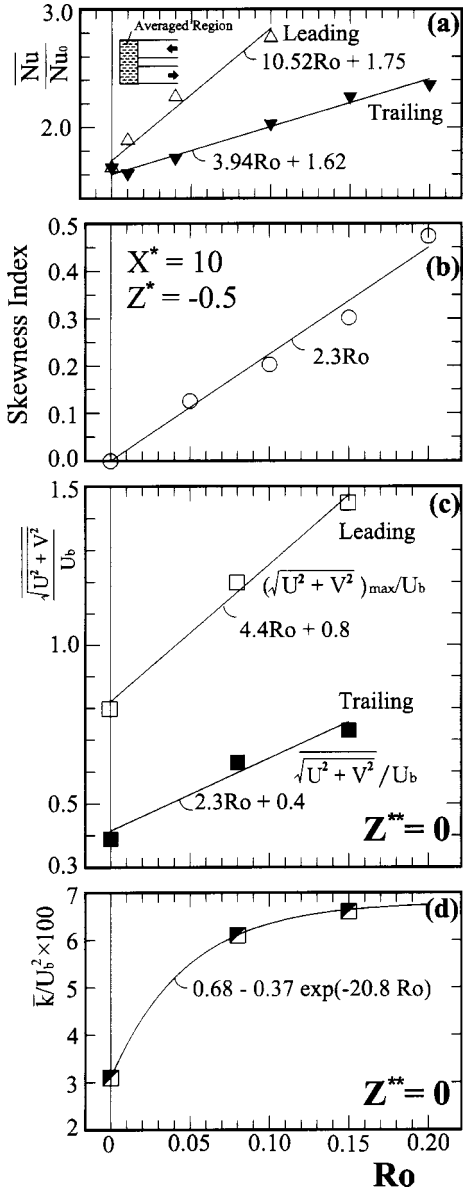

Fig. 13 Variation of Nusselt number ratio, dimensionless skewness index, magnitude of secondary-flow velocity, and turbulent kinetic energy with Ro for Re=10^4

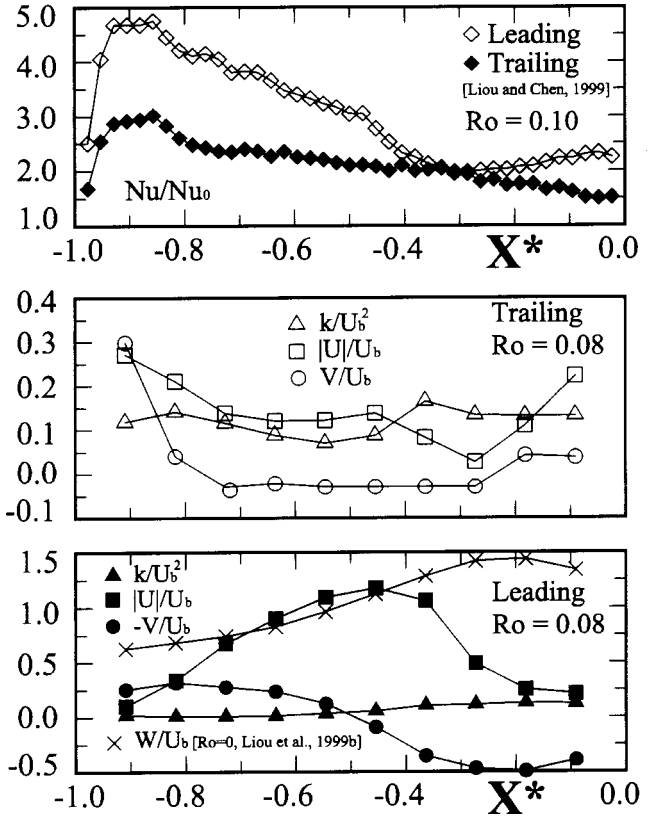

Fig. 14 Effects of rotation on radial distributions of Nu/Nu_0, k/U_b^2, $|U|/U_b$, and V/U_b at $Z^{**}=0$ for Re=10,000 (LDV measurements performed at 2-mm distance away from the leading ($Y^*=-1$) or trailing ($Y^*=1$) walls)

$\overline{\sqrt{U^2+V^2}}$ and $\overline{k}/U_b^2$, are calculated from 130 points for the rotating conditions. The measurement resolutions are 1.5 mm and 2.2 mm in transverse and spanwise directions, respectively. Rotation-induced skewness in the first pass contributes to the higher averaged Nu/Nu_0 on the leading wall than on the trailing wall inside the turn, as shown in Figs. 13(*a*) and 13(*b*). The rotation-induced increases on the magnitude of secondary-flow velocity and turbulent kinetic energy all contribute to the averaged heat transfer enhancement around the 180-deg sharp turn, as can be observed from Figs. 13(*c*) and 13(*d*), respectively. The correlation equations of these parameters are also added to Fig. 10. The RMS difference of the first-order equations are 2.8%, 2.0%, 1.9%, 0.9%, 3.8%, and 11.9% for $(Nu/Nu_0)_{Leading}$, $(Nu/Nu_0)_{Trailing}$, skewness index, $(\sqrt{U^2+V^2})_{max}$, $\overline{\sqrt{U^2+V^2}}$, and $\overline{k}/U_b^2$, respectively. All the flow parameters increase linearly with increasing Ro except turbulent kinetic energy (k/U_b) which first increases steeply and then tends to level off for Ro>0.15.

Relation Between Near-Wall Fluid Flow Parameters and Surface Heat Transfer. It is interesting to elaborate on the rotation effect on the significant role played by the secondary flow in affecting the Nusselt number augmentation in the plane $Z^{**}=0$ where convective and turbulent motions also prevail (Liou et al. [20]). Figure 14 is used to illustrate the point. The top graph of Fig. 14 presents the Nusselt number ratio curves (Liou and Chen [19]) along $Z^{**}=0$ on the leading (the hollow diamond) and trailing (the solid square) walls for Ro=0.10. The heat transfer augmentation is generally more pronounced near the outer wall ($X^*=-1$) than near the inner wall ($X^*=0$). In average, the Nu/Nu_0 is about 50% higher on the leading wall than on the trailing wall. In order to explain the effect of fluid flow on the surface heat transfer characteristics, Fig. 14 further depicts three dimensionless flow parameters, i.e., k/U_b^2 (turbulent kinetic energy), $|U|/U_b$ (velocity component parallel to the wall), and V/U_b (velocity component normal to the wall). These parameters are measured at 2-mm distance away from the leading and trailing walls ($Y^*=\pm 1$) along $Z^{**}=0$ planes. Near the trailing wall ($Y^*=1$), k/U_b^2 has about the same level (0.1~0.2) around $X^*=-0.2\sim-0.8$, where V/U_b is nearly null (Fig. 10). The U/U_b and V/U_b have the highest values near the outer wall ($X^*=-1$) where Nu/Nu_0 is also the highest. Near the leading wall, k/U_b^2 is quite low (about 0.01 for $X^*<-0.5$) relative to the mean velocity components. The $|U|/U_b$ has a bell shape with the highest value of 1.2 at $X^*=-0.45$ where the periphery of vortex strongly sweeps over and almost parallels ($-V/U_b\approx 0$) the wall surface. It is interesting that the Nusselt number ratio does not have the highest values there. On the contrary, Nu/Nu_0 is the highest at $X^*=-0.9$ where $|U|/U_b$ is the lowest. In comparison with two other flow parameters, the shapes of the $-V/U_b$ and

Nu/Nu_0 curves are most correlated. Because the current LDV experimental setup can not measure the Z-component mean velocity (W) under rotating conditions, the W/U_b profiles along $Z^{**}=0$ under stationary condition (Ro=0, Liou et al. [20]) is added to Fig. 14 for reference. Due to the acceleration and deceleration induced by the turn, W/U_b is the highest near the inner wall ($X^*=0$) and the lowest near the outer wall ($X^*=-1$), which is totally opposite to its heat transfer counterpart. In summary, one can infer the roles played by the dimensionless parameters examined in affecting Nusselt number distribution from Fig. 14. First, in the region where the mean velocity component normal to the wall prevails, say on the leading wall along $Z^{**}=0$, the Nusselt number elevation is dominated by the secondary flow impingement effect. Second, in the region where the mean velocity component normal to the wall is weak or zero, say for $X^*>-0.8$ on the trailing wall along $Z^{**}=0$, the Nusselt number augmentation is mainly affected by the mean velocity component parallel to the wall.

Conclusions

A set of comprehensive LDV measurements of turbulent fluid flows in a rotating 180-deg sharp turning smooth duct has been performed. The rotating effects on the fluid flow are documented both qualitatively and quantitatively. The following main results are drawn from the data presented:

1 In the radially outward flow pass, the skewness index (SK) of U profiles increases linearly with increasing Rotation number (Ro), SK=2.3 Ro for Ro=0 to 0.2, as a result of the rotation-induced Coriolis force and hydrodynamic centrifugal force.

2 Immediately after the turn in the radially inward flow pass, there exists a separation bubble on the inner (divider) wall side skewed slightly toward the trailing wall due to the effect of Coriolis force. Its size shrinks with increasing Ro and can be correlated as $X_R^*=-24\,\mathrm{Ro}^2-4\,\mathrm{Ro}+1.7$ along $Y^*=0$ and $Z^*=0$. The latter observation and simple correlation obtained have not been reported previously and are useful for CFD validation.

3 Rotation causes significant spanwise variations, as large as 50% of U_b, of both the magnitude and skewness of X- component mean velocity profiles near the 180-deg sharp turn and in the second pass. There exists a critical range of Ro, $0.10<\mathrm{Ro}\leqslant 0.15$, above which the turn-induced pressure loss is reduced 52~60% from its stationary counterpart. As a result, the adverse pressure gradient for $\mathrm{Ro}<\mathrm{Ro}_c$ is reversed to favorable one for $\mathrm{Ro}<\mathrm{Ro}_c$. This observation provides physical explanation to flow moving faster near the inner wall than the outer wall in the second pass from Ro=0.15.

4 As the rotation number is increased beyond 0, the curvature induced symmetric Dean-type vortices in the midturn is gradually dominated by a single vortex most of which impinges directly on the outer part of leading wall. Both the averaged and maximum magnitudes of secondary-flow velocity increase linearly with increasing rotation number, $\overline{\sqrt{U^2+V^2}}/U_b=2.3\,\mathrm{Ro}+0.4$ and $(\sqrt{U^2+V^2})_{\max}/U_b=4.4\,\mathrm{Ro}+0.8$.

5 In general, duct rotation increases the turbulent kinetic energy of the secondary flow in the 180-deg sharp turn. The averaged k/U_b^2 inside the turn is increased up to 40%, 8%, and 36% by raising rotation number from Ro=0.08 to Ro=0.15 for $Z^*=-0.5$, $Z^{**}=0$, and $Z^*=0.5$ planes, respectively. Meanwhile, the symmetrical turbulent kinetic energy contour for the stationary case is skewed and redistributed by rotation.

6 Globally, the rotation-induced increases on the secondary-flow velocity and turbulent kinetic energy all contribute to the averaged heat transfer enhancement around the 180-deg sharp turn. Locally, the direction and strength of the secondary flow with respect to the wall are the most important fluid dynamic factors affecting the local heat transfer distributions inside a rotating 180-deg sharp turn, followed by the convective mean velocity, and then the turbulent kinetic energy.

Acknowledgment

Support for this work was partially provided by the National Science Council and Taiwan Power Company of the Republic of China under contract NSC 88-TPC-E- 007-017.

Nomenclature

A = half-width of duct (m)
B = half-height of duct (m)
C_p = specific heat ($\mathrm{Jkg^{-1}K^{-1}}$)
D_H = hydraulic diameter, $4AB/(A+B)$ (m)
h = heat transfer coefficient ($\mathrm{Wm^{-2}K^{-1}}$)
k = turbulent kinetic energy $(\overline{u^2}+\overline{v^2})/2$ ($\mathrm{m^2s^{-2}}$)
k_a = thermal conductivity of air ($\mathrm{Wm^{-1}K^{-1}}$)
k_w = thermal conductivity of wall ($\mathrm{Wm^{-1}K^{-1}}$)
Nu = local Nusselt number, $h\cdot D_H/k_a$
Nu_0 = Nusselt number in fully developed tube flow $=0.023\cdot \mathrm{Re}^{0.8}\cdot \mathrm{Pr}^{0.4}$
$\overline{\mathrm{Nu}}$ = total averaged Nusselt number, $\overline{h}\cdot D_H/k_a$
Pr = Prandtl number of air, $\rho C_p\nu/k_a$
Re = Reynolds number, U_bD_H/ν
Ro = rotation number, $\Omega D_H/U_b$
T_i = initial temperature of wall (K)
T_r = bulk mean temperature of main stream (K)
T_w = wall temperature=liquid crystal green-point temperature (K)
U = streamwise mean velocity ($\mathrm{ms^{-1}}$)
U_b = duct bulk mean velocity ($\mathrm{ms^{-1}}$)
u = streamwise velocity fluctuation ($\mathrm{ms^{-1}}$)
u' = rms value of streamwise velocity fluctuation, $\sqrt{\overline{u^2}}$ ($\mathrm{ms^{-1}}$)
V = transverse mean velocity ($\mathrm{ms^{-1}}$)
v = transverse velocity fluctuation ($\mathrm{ms^{-1}}$)
v' = rms value of transverse velocity fluctuation, $\sqrt{\overline{v^2}}$ ($\mathrm{ms^{-1}}$)
W_1 = width of first-pass duct (m)
W_2 = width of second-pass duct (m)
W_d = divider thickness (m)
W_d^* = dimensionless divider thickness, $W_d/(W_1+W_2)$
X = streamwise coordinate, Fig. 1
X^* = normalized streamwise coordinate, X/D_H
X_R = separation bubble length (m)
X_R^* = dimensionless separation bubble length, X_R/D_H
Y = transverse coordinate, Fig. 1
Y^* = normalized transverse coordinate, Y/B
Z = spanwise coordinate, Fig. 1
Z^*, Z^{**} = normalized spanwise coordinate,
(i) $X<0$, $Z^{**}=Z/(2A+W_d)$ (in the turn)
(ii) $X\geqq 0$, $Z<0$, $Z^*=(Z+W_d/2)/2A$ (in the first pass)
(iii) $X\geqq 0$, $Z>0$, $Z^*=(Z-W_d/2)/2A$ (in the second pass)

Greek Symbols

α_w = thermal diffusivity of wall ($\mathrm{m^2/s}$)
δ_{99} = boundary layer thickness (m)
θ = coolant passage orientation (deg.)
ρ = air density ($\mathrm{kg/m^3}$)
σ = standard deviation
ν = kinematic viscosity ($\mathrm{m^2/s}$)
Ω = rotating speed ($\mathrm{rad\,s^{-1}}$)

Subscripts

b = bulk
rg = regional averaged

References

[1] Liou, T. M., and Chen, C. C., 1997, ''LDV Study of Developing Flows Through a Smooth Duct With 180-Deg Straight-Corner Turn,'' ASME J. Turbomach., **121**, pp. 167–174.

[2] Wagner, J. H., Johnson, B. V., and Hajek, T. J., 1991a, ''Heat Transfer in Rotating Serpentine Passages With Smooth Walls,'' ASME J. Turbomach., **113**, pp. 321–330.

[3] Wagner, J. H., Johnson, B. V., and Kopper, F. C., 1991, ''Heat Transfer in Rotating Passages With Smooth Walls and Radial Outward Flow,'' ASME J. Turbomach., **113**, pp. 42–51.

[4] Han, J. C., and Zhang, Y. M., 1992, ''Effect of Uneven Wall Temperature on Local Heat Transfer in a Rotating Square Channel With Smooth Walls and Radial Outward Flow,'' ASME J. Heat Transfer, **114**, pp. 850–858.

[5] Yang, W. J., Zhang, N., and Chiou, J., 1992, ''Local Heat Transfer in a Rotating Serpentine Flows Passage,'' ASME J. Heat Transfer, **114**, pp. 354–361.

[6] Sathyamurthy, P. S., Karki, K. C., and Patankar, S. V., 1994, ''Prediction of Turbulent Flow and Heat Transfer in a Rotating Square Duct With a 180 Deg Bend,'' ASME Paper No. 94-GT-197.

[7] Stephens, M. A., Shih, T. I-P., and Civinskas, K. C., 1996, ''Computations of Flow and Heat Transfer in a Rotating U-Shaped Square Duct With Smooth Walls,'' AIAA Paper No. 96-3161.

[8] Chen, H.-C., Jang, Y.-J., and Han, J.-C., 1999, ''Computation of Flow and Heat Transfer in Rotating Two-Pass Square Channels by a Reynolds Stress Model,'' ASME Paper No. 99-GT-174.

[9] Johnson, R. W., 1988, ''Numerical Simulation of Local Nusselt Number for Turbulent Flow in a Square Duct With a 180 Deg Bend,'' Numer. Heat Transfer, **1**, pp. 205–228.

[10] Schabacker, J., Bolcs, A., and Johnson, B. V., ''PIV Investigation of the Flow Characteristics in an Internal Coolant Passage With Two Ducts Connected by a Sharp 180 deg Bend,'' ASME Paper No. 98-GT-544.

[11] Hsieh, S., Chiang, M., and Chen P., 1997, ''Velocity Measurements and Local Heat Transfer in a Rotating Ribbed Two-Pass Square Channel with Uneven Wall Heat Flux,'' ASME Paper No. 97-GT-160.

[12] Tse, D. G. N., and Steuber, G. D., 1997, ''Flow in a Rotating Square Serpentine Coolant Passage With Skewed Trips,'' ASME Paper 97-GT-529.

[13] Elfer, M., 1993, ''The Effect of Rotation and Buoyancy on Flow Development in a Rotating Circular Coolant Channel,'' *2nd International Symposium on Engineering Turbulence Modeling and Measurements*. May 31–June 2, Florence, Italy.

[14] Bons, J. P., and Kerrebrock, J. L., 1998, ''Complementary Velocity and Heat Transfer Measurements in a Rotating Cooling Passage With Smooth Walls,'' ASME Paper No. 98-GT-464.

[15] Servouze, Y., 1998, ''3D Laser Anemometry in a Rotating Cooling Channel,'' ASME Paper No. 98-GT-123.

[16] Cheah, S. C., Iacovides, H., Jackson, D. C., Ji, H., and Launder, B. E., 1996, ''LDA Investigation of the Flow Development through Rotating U-Ducts,'' ASME J. Turbomach., **118**, pp. 590–596.

[17] Wang, T. S., and Chyu, M. K., 1994, ''Heat Convection in a 180 Deg Turning Duct With Different Turn Configurations,'' J. Thermophys. Heat Transfer, **8**(3), pp. 595–601.

[18] North, E., 1997, private communication.

[19] Liou, T. M., and Chen, C. C., 1999, ''Liquid Crystal Study on Heat Transfer in a Rotating 180-Deg Sharp Turning Square Duct,'' The 9th (Millennium) International Symposium on Flow Visualization, 22–25 Aug. 22–25, Edinburgh.

[20] Liou, T. M., Tzeng, Y. Y., and Chen, C. C., 1999, ''Fluid Flow in a 180 Deg Sharp Turning Duct With Different Divider Thickness,'' ASME J. Turbomach., **121**, pp. 569–576.

[21] Tennekes, H., and Lumley, J. L., 1972, *A First Course in Turbulence*, MIT Press, Cambridge, MA.

[22] Liou, T. M., and Liao, C. C., 1995, ''Flows in Curved Combustor Inlet With and Without a Guide Vane,'' AIAA Journal of Propulsion and Power, **11**(3), 464–472.

[23] Liou, T. M., Chen, M. Y., and Tsai, M. H., 2002, ''Fluid Flow and Heat Transfer in a Rotating Two-Pass Square Duct With In-Line 90-Deg Ribs,'' ASME J. Turbomach. **124**, pp. 260–268.

[24] Pauley, W. R., and Eaton, J. K., 1994, ''The Effect of Embedded Longitudinal Vortex Arrays on Turbulent Boundary Layer Heat Transfer,'' ASME J. Heat Transfer, **116**, pp. 871–879.

[25] Liou, T. M., Chen, C. C., and Tsai, T. W., 2000, ''Heat Transfer and Fluid Flow in a Square Duct With 12 Different Shaped Vortex Generators,'' ASME J. Heat Transf., **122**, pp. 327–335.

Comparative Evaluation of Some Existing Correlations to Predict Head Degradation of Centrifugal Slurry Pumps

Tahsin Engin[1]
Assistant Professor

Mesut Gur
Professor

Faculty of Engineering,
Department of Mechanical Engineering,
University of Sakarya,
Esentepe Campus,
54187 Sakarya, Turkey

In order to optimally design a slurry transportation system, it is necessary to know how the presence of solids will change the performance of the slurry pump to be installed. This paper makes the comparison of some existing correlations available in the literature to predict the head reduction factors of such centrifugal pumps handling slurries. For this purpose, a large number of published data for various centrifugal slurry pump tests in the literature have been used to develop a new correlation and then this correlation and all others have been tested against the data. For the proposed correlation, the mean and average deviations between the calculated and measured head reduction factor is 8.378 and 0.620%, respectively, for all data of mostly handling commercial slurries. It also produces 12.441% mean deviation in the prediction of efficiency ratio for 216 data points. Overall, the new correlation that can be applied to both metal and rubber lined pumps with impeller diameter up to 850 mm, gives remarkably closer fit to the published data of both head and efficiency ratios than all existing correlations. [DOI: 10.1115/1.1523065]

Introduction

The effect of included solids on a centrifugal pump performance is a major consideration in the pump selection and slurry system design. However, some designs of the slurry handling systems are based on the pump performance with clear water only, which may lead to an inefficient use of system and even lead to the failure of the establishment. For this reason, the accuracy of predicted head and efficiency reduction factors for a slurry pump is very important for the design and optimization of a slurry transportation system. To this end, it is necessary to know how the presence of solids will affect the pump performance. However, the amount of experimental data available in the literature is fairly limited and it is still difficult to find any reliable correlation or procedure for calculating head reduction factor over a wide range of physical properties of solids and operating conditions.

The effects of suspended solids on the performance of the centrifugal pumps have been a research interest for many years. Stepanoff [1] reviewed the past studies and proposed a useful monograph giving the relationship among the bep efficiency reduction, particle size, and concentration of solids up to 32% by volume. This monograph has been known as the first comprehensive study of solid-liquid two-phase centrifugal pump performance.

In order to predict the performance of centrifugal slurry pumps, several investigators have proposed some theoretical and empirical correlations. Fairbank [2] studied the effects of various parameters of solids (particle size, concentration, and density) on the performance characteristics of centrifugal pumps, and he developed the first theoretical model to predict these effects. Vocadlo et al. [3] presented a theoretical model showing how the individual variables contribute to the increase in relative head loss. They also concluded that the higher the concentration and larger the particle size the higher is the head reduction. According to their model, if the head output varies linearly with power consumption at the same flow rate, then the relative reduction in pump efficiency is simply a linear function of slurry specific gravity.

Most of the researchers agree that clear water head and efficiency are generally lowered by the presence of solids and they introduced empirical correlations based on their experimental data to estimate the effects of the presence of solids in the pumped liquid, [4–9]. However, these correlations are usually restricted to a few pumps and solids pumped with a carrier liquid. Therefore, none of them are wholly successful to predict performance deterioration of any centrifugal slurry pump.

Among others, Walker et al. [10] investigated the change in performance characteristics of centrifugal pumps when handling fine homogeneous type non-Newtonian slurries (coal/water and kaolin/water) using two different slurry pumps. They concluded that relative reduction in both pump head and efficiency could be correlated well with the pump Reynolds number. Mez [11] carried out experiments to investigate the effects of solid properties such as density, particle size and size distribution, and solid concentration up to 40% by weight. The maximum particle size was 125 mm. He observed that the effect of solid concentration on head reduction is linear when pumping coarse grain solids. Roco et al. [12] applied a loss analysis procedure to estimate the head-capacity characteristics of centrifugal pumps handling slurries. They divided the head losses into three major terms, namely local, secondary flow, and friction. Further, they also developed correlations to predict the various head losses for clear liquid and then incorporated the additional head losses for solid-liquid mixtures from the knowledge of the clear liquid losses and nondimensional parameters characterized by the slurry properties and the pump specific speed. They made accurate predictions for handling silica sand up to 35% concentration of solids by volume. Sneth et al. [13] carried out experiments to study the effect of various parameters on slip factor and their role on the performance characteristics of a centrifugal slurry pump. They proposed a slip factor correlation in terms of two nondimensional parameters. Sellgren and Vappling [14] conducted set of experiments using two mine tailings with concentrations up to 60% by weight and showed that the drop in head was limited to about 15% and reduction in efficiency exceeded the reduction in head for concentrations over

[1]Presently at the Department of Mechanical Engineering, ms 312, University of Nevada, Reno, NV 89557. e-mail: engint@unr.nevada.edu.

Contributed by the Fluids Engineering Division for publication in the JOURNAL OF FLUIDS ENGINEERING. Manuscript received by the Fluids Engineering Division July 16, 2001; revised manuscript received July 29, 2002. Associate Editor: B. Schiavello.

40% by weight. They also demonstrated that the effects of solids generally cannot be considered independent of the operating domain, i.e., flow rate and pump speed when pumping highly concentrated slurries. Wilson [15] presented practical methods for predicting the performance of centrifugal slurry pumps with extremely fine and coarse particles in terms of relationship between particle size, density, and concentration of solids. He concluded that when pumping slurries, the relative reductions in pump head and efficiency were independent of flow rate and pump speed. Walker et al. [16] studied the influence of pump geometry on the performance characteristics of a centrifugal pump when handling solids in suspension. The parameters examined were vane number, inlet/outlet vane angles, outlet vane width, and vane profile. They concluded that the vane shape has a vital impact on the reductions in pump head and efficiency. Sellgren and Addie [17] studied the effects of solids on large slurry pumps with impellers 0.8 and 1.2 m in diameter operating at very high slurry concentrations. They observed that the effect of solids was smaller in larger sized pumps compared to small pumps. They also concluded that the reduction in efficiency was normally less than the head reduction in large pumps and these two reductions were usually equal for smaller units. Kazim et al. [18] performed experiments to study the individual effects of particle size, particle size distribution, specific gravity, and concentration of solids on the performance characteristics of the centrifugal pumps. They found that the relative reductions in pump head and efficiency, for a constant concentration of solids, were to be fairly constant over the range of discharge investigated. They also concluded that the relative reduction in efficiency was generally lower than the relative reduction in head at any given flow rate and concentration of solids. Ni et al. [19] focused on pumping of highly concentrated slurries and concluded that the high solid concentration has a strong impact on the performance characteristics of the pump. For the medium sand slurry, they observed that there exists a critical volumetric concentration of about 35%, above which both relative reductions in pump head and efficiency dropped faster. Sellgren et al. [20] studied the effect of sand-clay slurries on the performance characteristics of centrifugal slurry pumps. They observed that the addition of clay to sand led to a reduction in pipeline friction losses, thus lowering the pumping head and power consumption. Gandhi et al. [21] developed a methodology based on a loss analysis procedure to predict the performance of centrifugal pumps handling slurries. Their methodology accounts for the constructional differences of the slurry pump when compared with the liquid pump. Although this methodology gives accurate predictions (within a $\pm 12\%$ error band) it needs accurate and detailed data of pump geometry that could not be easily obtained. In another study, Gandhi et al. [22] investigated the performance of two centrifugal slurry pumps for three different solid materials (fly ash, zinc tailing, and bed ash) with different size distribution in terms of pump performance parameters. They showed that the reduction in head was 2–10% higher than the reduction in efficiency. They also observed that, for concentrations less than 30% by weight, the increase in the input power to pump could be treated as proportional to the specific gravity of slurry. This implies that the relative reductions in pump head and efficiency can be considered to be the same for the given range of concentration of solids. Sellgren and Addie [23] investigated the effect of solids on the large centrifugal pumps head and efficiency. They used two sands and a gravel material with average particle sizes of 0.25, 1.5, and 6 mm, and showed that, for a 70% of bep flow rate, the clear water head was dropped 3.5, 7, and 10%, respectively, when pumped at a solids concentration by weight of 32% in centrifugal slurry pumps having impeller diameters of 1.1 and 1.2 m.

In the present paper, an improved correlation to predict head reduction of centrifugal slurry pumps is presented and compared to some commonly referred correlations in the literature. The new correlation takes into account the individual effects of physical properties (solid's specific gravity, particle size), concentration of solids to be transported, and impeller exit diameter of the pump. The proposed correlation shows a better consistency with the data available in the literature over a wide range of physical properties and concentration of solids and pump sizes.

The Published Data

An attempt has been made to collect data from literature taken under a broad range of operating conditions. The published data points consist of the experimentally measured values of slurry pump head and efficiency ratios as a function of solid concentration (C_w) and specific gravity (S), representative particle diameter (d_{50} or d_W), impeller exit diameter (D), and pump flow rate relative to the best efficiency point (Q/Q_{bep}). Thus, the effects of pump flow rate are included indirectly in our data analysis. However, as opposite to some exceptions, [14,19], in the majority of the studies, [1,3–6,8,9,13,15,18,23], it has been assumed or concluded that, for a given concentration of solids, the pump head reduction was independent of pump flow rate and speed.

In Table 1, a complete list of data collected from the literature is given, including the number of data points and the value of each of the parameters considered. So far as possible, all the data from a given source have been used to avoid any subjectivity in choosing just a sample. A possible disadvantage of this procedure is that the database becomes unduly weighted towards just one or two sources that happened to report a large number of readings. In the present case, there are two relatively large sources of data (Burgess and Reizes [5] and Kazim et al. [8,18]). Since these sources covered a reasonable range of the parameters, the influence of them is not excessive.

As can be seen from Table 1, the test data used in this study include a wide range of physical properties of solids, e.g., specific gravity ($1.48 \leqslant S \leqslant 6.24$), particle size ($30\ \mu\text{m} \leqslant d_w$ or $d_{50} \leqslant 26700\ \mu\text{m}$), and concentration of solids up to 65.743 by weight, pump flow rate from $Q/Q_{\text{bep}} = 0.25$ to 1.40, impeller exit diameter from 210 mm to 825 mm, and pump speed from 590 rpm to 1780 rpm. The data set covers totally 870 experimental data points (654 for head reduction, and 216 for efficiency reduction) obtained using different solid-liquid mixtures under different test conditions. The column N in Table 1 gives the number of data for head ratios. If the data of efficiency ratios are used for any source, their number is shown in the same column as a second number. The notation ''AV'' indicates the head or efficiency ratios obtained as a weighted average value over the full range of flow rate for the corresponding pump.

The weighted drag coefficient (C_D) needed for Sellgren's [6] correlation (see Table 2) was estimated using the following formula, suggested by Turton and Levenspiel [24]

$$C_D = \frac{24}{\text{Re}_p}(1 + 0.173\,\text{Re}_p^{0.657}) + \frac{0.413}{1 + 16300\,\text{Re}_p^{-1.09}} \tag{1}$$

where particle Reynolds number is defined as follows:

$$\text{Re}_p = \frac{\rho V_{ts} d_{50}}{\mu}. \tag{2}$$

The terminal settling velocity (V_{ts}) for a falling sphere in still water is given in the form

$$V_{ts} = \frac{4}{3}\frac{g d_{50}\sqrt{S-1}}{C_D}. \tag{3}$$

Equation (1) is valid for $\text{Re}_p < 3\times 10^5$, which amply covers the range encountered in most slurries, [25]. The estimated weighted drag coefficients and corresponding particle Reynolds numbers are shown in Table 1.

Construction of the Correlation

It is now well established that the performance of centrifugal pumps with slurries is different from that with clear water and

Table 1 Experimental data collected from various sources in literature

Data (ref.)	Solid	S	Particle diameter d_{50} (μm)	Particle diameter d_W (μm)	Cw (%) Min.	Cw (%) Max.	Flowrate Q/Q_{bep}	Impeller diameter D (mm)	Pump speed n (rpm)	N	C_D (Eq. 1)	Re_p (Eq. 2)
[18]	Sand-A	2.65	180	180	9.053	32.775	0.25-1.00	270 (ML)	1000	29/29	10.76	3.05
[8]	Sand-B	2.65	230	230	6.511	27.906	AV	270 (ML)	1000	4/4	6.564	5.65
[8]	Sand-C	2.65	460	460	6.714	24.720	AV	270 (ML)	1000	3/3	2.211	27.52
[18]	Sand-D	2.65	230	230	6.644	56.020	0.25-1.00	270 (ML)	1000	49/49	6.564	5.65
[18]	Sand-E	2.65	230	328	10.778	55.205	0.25-1.00	270 (ML)	1000	42/41	6.564	5.65
[8]	Sand-F	2.65	362	400	6.720	44.602	AV	270 (ML)	1000	4/4	3.063	16.322
[3]	Sand-G	2.64	105	-	12.190	53.080	1.00	280 (RL)	1780	5	38.99	0.70
[3]	Sand-H	2.64	330	-	22.680	53.080	1.00	280 (RL)	1780	4	3.558	13.14
[3]	Sand-I	2.64	570	-	22.680	53.080	1.00	280 (RL)	1780	5	1.691	43.26
[3]	Sand-J	2.64	920	-	22.680	53.080	1.00	280 (RL)	1780	5	1.036	113.36
[3]	Sand-K	2.64	1400	-	22.680	53.080	1.00	280 (RL)	1780	5	0.725	254.37
[3]	Sand-L (=G)	2.64	105	-	22.680	53.080	1.00	280 (RL)	1180	4	38.99	0.70
[3]	Sand-M (=I)	2.64	570	-	39.760	46.810	1.00	280 (RL)	1180	3	1.691	43.26
[3]	Sand-N (=J)	2.64	920	-	22.680	46.810	1.00	280 (RL)	1180	6	1.036	113.36
[3]	Sand-O (=K)	2.64	1400	-	22.680	46.810	1.00	280 (RL)	1180	5	0.725	254.37
[9]	+Sand-P	2.10	400	400	5.540	28.500	1.00	210 (ML)	1250	2	3.260	15.00
[9]	+Sand-Q	2.64	413	440	11.600	21.400	1.00	210 (ML)	1250	2	2.340	24.95
[16]	Sand-R	2.65	400	-	20.000	60.000	0.50-1.10	365 (ML)	1000	19/19	2.657	20.36
[19]	Sand-S	2.65	1840	-	15.556	65.713	0.60-1.40	400 (ML)	1200	20	0.596	423.86
[19]	Sand-T	2.65	372		14.467	65.743	0.60-1.40	400 (ML)	1200	16	2.969	17.27
[26]	Sand-U	2.64	270		22.680	39.759	0.30-0.65	810 (ML)	590	14	4.896	8.32
[26]	Sand-V	2.64	1500		22.680	53.083	0.30-1.00	810 (ML)	590	18/18	0.687	290.63
[5]	Beach sand	2.67	295	-	8.850	63.860	0.40-1.00	371 (ML)	1300	40	4.193	10.32
[5]	River sand	2.64	1290	-	13.930	56.450	0.40-1.00	371 (ML)	1300	40	0.775	217.69
[5]	Ilmenite	4.63	170	-	16.110	61.570	0.40-1.00	371 (ML)	1300	27	6.982	5.16
[5]	Heavy min.	4.35	290	-	14.770	58.160	0.40-1.00	371 (ML)	1300	39	3.007	16.83
[8]	Coal-A	1.49	185	377	9.010	57.800	AV	270 (ML)	1000	6/11	5.478	7.07
[7]	Coal-B	1.48	-	900	33.943	47.743	AV	270 (ML)	1450	6	1.596	47.81
[11]	Coal-C1	1.625	-	14900	15.840	20.670	1.00	825 (ML)	-	5	0.405	7290.35
[11]	Coal-C2	1.562	-	15500	25.310	29.250	1.00	825 (ML)	-	2	0.406	7329.29
[11]	Coal-C3	1.716	-	15300	27.230	36.150	1.00	825 (ML)	-	2	0.410	8073.48
[11]	Coal-D1	1.520	-	16700	23.580	29.660	1.00	825 (ML)	-	4	0.408	7865.40
[11]	Coal-D2	1.756	-	17600	38.460	42.680	1.00	825 (ML)	-	5	0.420	10112.14
[11]	Coal-D3	1.759	-	17300	43.170	48.670	1.00	825 (ML)	-	6	0.419	9885.71
[11]	Coal-E1	1.827	-	17300	-	18.870	1.00	825 (ML)	-	4	0.420	10302.77
[11]	Coal-E2	1.772	-	16600	30.720	33.120	1.00	825 (ML)	-	3	0.417	9396.78
[11]	Coal-E3	1.754	-	15900	42.160	45.570	1.00	825 (ML)	-	4	0.414	8737.90
[11]	Gravel	2.60	-	26700	21.440	28.590	1.00	825 (ML)	-	5	0.458	26318.57
[8]	Iron ore-A	4.35	663	663	2.511	12.558	AV	270 (ML)	1000	3	1.127	95.01
[6]	Iron ore-B	4.15	1800	-	27.930	37.270	0.50-0.80	430 (RL)	800	6	0.527	602.68
[18]	Mild Steel	6.24	230	230	5.332	23.200	AV	270 (ML)	1000	31/29	3.410	13.96
[9]	+Perlite-A	2.34	270	211	8.470	20.420	1.00	210 (ML)	1250	2	8.886	3.84
[9]	+Perlite-B	2.34	1390	1147	8.450	23.390	1.00	210 (ML)	1250	2	0.905	152.59
[6]	Perlite-C	2.34	350	-	33.060	54.930	0.50-0.80	430 (RL)	1160	11	3.580	12.94
[6]	Granite	2.67	3000	-	17.310	30.710	0.50-0.80	430 (RL)	800	6	0.452	1019.46
[7]	Zinc tailing	2.85	-	170.4	13.617	56.170	AV	270 (ML)	1450	6	11.070	2.94
[8]	Zinc	5.51	455	482	3.665	9.470	AV	270 (ML)	1000	3	1.495	54.44
[14]	Tailing	2.75	30	-	55.900	62.150	0.25-0.70	450 (RL)	800	9/9	1188,8	0.0204
[22]	Bed ash	2.44	135	209	12.100	52.100	0.30-1.00	264 (ML)	1450	17	22.630	1.277
[22]	Fly ash	2.08	42	59	13.270	60.520	0.30-1.00	264 (ML)	1450	37	716.46	0.034
[22]	Bed ash	2.44	135	209	10.070	31.800	0.25-0.70	400 (ML)	1250	27	4.012	8.51
[22]	Fly ash	2.08	42	59	14.100	48.000	0.25-0.70	400 (ML)	1250	27	269.06	0.093
[13]	Glass bead	2.42	90	-	10.000	50.000	1.00	267 (ML)	1200	5	4.106	0.64

(ML): Metal Lined, AV : averaged value over full range of flowrate

(RL): Rubber Lined, , +5% tip clearance ratio (Unshrouded impeller)

Table 2 Existing correlations in the literature

Ref.	Author(s)	K_H=
[3]	Vocadlo et al.	$\frac{C_v}{S_m}(S-1)\left[0.167+\Phi\sqrt{\frac{d_{50}(S-1)}{D}}\right]$ Φ=10 for rubber lined impeller Φ=6.02 for metal lined impeller
[4]	Cave	$0.0385(S-1)\frac{S+4}{S}C_W \ln(\frac{d_{50}}{22.7})$
[5]	Burgess and Reizes	$1-(1-C_W)^n$ *$n = S(-0.1734d_{50}^2+0.365d_{50}+0.027)$, d_{50} [mm]
[5]	Frazier	$1-\frac{1-C_V}{1+C_V(S-1)}$
[6]	Sellgren	$0.32C_W^{0.7}(S-1)^{0.7}C_D^{-0.25}$, **$C_D = f(Re_p)$ or $0.075C_1C_2$, $C_1 = f(C_w,S)$; $C_2 = f(V_{ts},d_{50})$
[7]	Gahlot et al.	$0.00056(S-1)^{0.72}\frac{S+3}{S}C_W \ln(50d_w)$
[8]	Kazim et al.	$0.13C_W\sqrt{S-1}\ln(\frac{d_w}{20})$
[9]	Engin and Gur	$0.11C_W(S-1)^{0.64}\ln(\frac{d_w}{22.7})$

* Approximated from authors' plot
** Estimated from Eq. 1.

lowered by the presence of solids in the carrier liquid. The general conclusions drawn by most previously researchers are that the head developed and efficiency of the pump decreases whereas the input power to the pump increases when any heterogeneous slurry is being pumped. In such cases, the magnitude of the reduction in the pump performance is mainly a function of weighted or volumetric concentration of solids in the mixture, physical properties of solids like their specific gravity, shape, size and size distribution of particles, and pump size. It is, however, quite difficult to consider the shape of particles, which may vary randomly. Further, pump size may reflect its effects in different ways when pumping slurries. Sellgren and Addie [17] reported that the effect of solids was smaller in larger sized slurry pumps than that in smaller units. They also reported in another study, [23], that the reduction in head decreased exponentially with D with an exponent of 0.9. In the present study, an attempt has been made to include the impeller exit diameter (D) in the developed correlation. To do this, the weighted mean particle diameter (d_w) was normalized using the impeller exit diameter (D). It was observed that the head performance of a slurry pump could be better correlated with the relative mean particle diameter (d_w/D) rather than the representative particle size (d_w or d_{50}). Therefore, when pumping slurries, the performance reduction factors of a slurry pump for a constant flow rate (e.g., bep flow rate) and rotary speed can be defined by the following expressions:

$$K_H = 1 - H_r = 1 - \frac{H_s}{H_w} = f(C_w \text{ or } C_V, S, d_w/D) \tag{4}$$

$$K_\eta = 1 - \eta_r = 1 - \frac{\eta_s}{\eta_w} = f(C_W \text{ or } C_V, S, d_w/D) \tag{5}$$

where subscripts s and w represents slurry and water, respectively. The efficiency ratio (η_r) of a slurry pump has been reported by some earlier investigators, [1,3,4,15], to be nearly equal to the corresponding head ratio (H_r), which implies that the input power to the pump, for a fixed flow rate at a given pump speed, is proportional to the slurry specific gravity ($P_s/P_w = S_s$). For this reason, the correlations given in the literature only predict H_r or K_H to obtain pump performance characteristics in slurry services.

In order to determine the functional relationship given on the right-hand side of Eq. (4), the same procedure given in our recent paper, [9], will be applied, which demonstrates that K_H can be assumed to have the following form

$$K_H = C_W(S-1)^\kappa \phi(d_w/D). \tag{6}$$

As can be seen from Table 1, the average particle size of the two materials used by Burgess and Reizes [5], namely beach sand (d_{50}=295 μm) and heavy mineral (d_{50}=290 μm) are almost the same, but they have different specific gravities. Hence, the pump head reduction factors can be compared when pumping these two materials in order to determine the effect of specific gravity on K_H. This comparison is shown in Fig. 1 for the flow rate range of Q/Q_{bep}=0.40–1.00 for each solid materials. If K^a is the head reduction factor at any given C_W (e.g., 40%), then the ratio of K^a for these two materials of different specific gravities can be written as

$$\frac{K^a_{\text{beach sand}}}{K^a_{\text{heavy min}}} = \left.\frac{0.16}{0.25}\right|_{C_W=40\%} = \frac{(2.67-1)^\kappa}{(4.35-1)^\kappa}. \tag{7}$$

Solving Eq. (7) for κ, gives a value of 0.64 which confirms that K_H varies with $(S-1)^{0.64}$ for another couple of materials reported by Engin and Gur [9].

To identify the functional relationship $\phi(d_w/D)$ in Eq. (6), which represents the effect of mean particle size, the variation of $\phi(d_w/D)$ against the relative particle diameter (d_w/D) for all

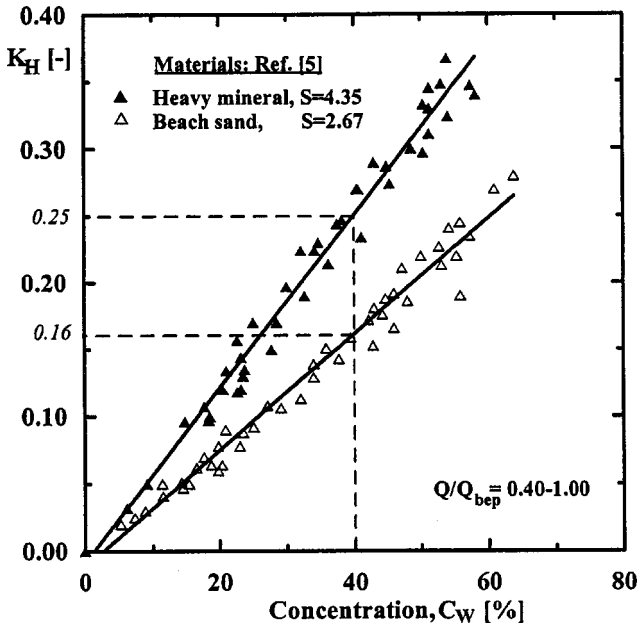

Fig. 1 Effect of particle specific gravity on head reduction factor

head ratio data is plotted. The best fit equation is in the power form with a coefficient of determination $R^2=0.90$ as follows:

$$\phi(d/D)=\frac{K_H}{C_W(S-1)^{0.64}}=2.705(d_w/D)^{0.313}. \tag{8}$$

If the weighted mean particle diameter (d_w) is not known, the mass median particle diameter (d_{50}) may be used in place of it. Consequently, the final form of the proposed correlation is given by

$$K_H=2.705C_W(S-1)^{0.64}(d_w/D)^{0.313} \tag{9}$$

Since this correlation is based on a relatively large number of data points, and involves the impeller exit diameter (D), which is an important pump parameter, one may expect it to give more accurate predictions than the previous ones.

Test of Existing Correlations Against the Experimental Data

In addition to the equation developed as part of this study [Eq. (9)], some of the correlations available in the literature were tested against the experimental data given in Table 1. These correlations, which have been widely used for prediction of head reduction of centrifugal slurry pumps, are summarized in Table 2. The correlation proposed by Frazier (from Ref. [4]) is probably the simplest equation. However, the particle diameter, which is one of the most important factors in slurry pumping performance, was not included in this equation. When this correlation was tested against the data, it was observed that it gave much higher predictions of head reductions than corresponding experimental data. Hence, this correlation is inadequate and it is not consequently included in the following comparisons.

The comparisons of the remaining seven correlations, together with the developed one (Eq. (9)), are shown in Table 3. In addition, Fig. 2 shows a comparison of the data with the equation recommended in this paper. As seen in Fig. 2, the deviation range lies within -15% to $+15\%$. However, the mean and average deviations are 8.378 and 0.620% respectively. This spread appears to be acceptable when considering the wide range of parameters and also the large number of data points. On the other hand, no other correlation has been tested against such a large number of data and they generally show a reasonable agreement with their own data.

Table 3 provides a complete comparative evaluation of the existing correlations studied in this paper. Since only the value of mass median particle diameter (d_{50}) is available for some solid materials, it has been used as the representative particle diameter in the last three equations.

It is clear from Table 3 that, the present correlation gives reasonable results for most of solid materials. The proposed correlation gives better predictions for all kinds of sand, except for beach sand slurry. Burgess's [5] correlation produces a slightly smaller deviation (7.787%) than the Eq. (9) for that solid material. However, the difference between two predictions is less than 0.14%. On the other hand, for all sands (344 data points for sand A-V, beach sand, and river sand), the proposed correlation gives about 7.4% mean deviation. Engin and Gur's [9] correlation produces 13.50% mean deviation while all other equations produce substantially larger deviations than 13.50% for the same data group.

For ilmenite, except for Vocadlo's [3] and Sellgren's [6] correlations, all other equations give reasonable predictions, while the proposed one (Eq. (9)) produces lowest deviation from the test data. As appeared in Table 3, these two correlations, [3,6], showed rather poor agreement with the data. The large deviations of the Sellgren [6] correlation could be attributed, to some extent to the assumptions in the determination of the weighted drag coefficients (C_D), which requires an iterative solution procedure. To overcome this difficulty, Wilson [15] presented a plot in log-scale to estimate C_1 and C_2 constants (see Table 2). However, it is still difficult to determine precisely the weighted drag coefficients in the Sellgren's [6] correlation and minor differences in reading can cause larger errors in the predictions.

The correlation proposed in the previous work by the present authors, [9], is marginally better (both mean and average deviation have the same value of 17.418%) than the Vocadlo's [3], Cave's [4], Burgess' [5], and Sellgren's [6] correlations. However, when the entire data are considered, it gives poorer predictions than the Kazim's [8] correlations. On the other hand, it produces almost the same deviation as the Gahlot's [7] correlation. It should be noted that the recent correlation recommended by Kazim et al. [8] provides more accurate predictions among all others, with the exception the correlation (Eq. (9)) proposed in this paper. Kazim's [8] correlation gives generally the best predictions for Coal A and B slurries as it can be seen in Table 3 showing, respectively, mean deviations 4.375%, and 4.626%. On the other hand, for another coal group (Coal C1 to E3), the proposed correlation is more accurate than all others, and causes a mean deviation of 5.332% for the 35 data points. However, it exhibits poorer predictions for Perlite C, while others show generally better agreement with the data, with the exception of Vocadlo's [3] and Gahlot's [7] correlations. The correlation proposed by Cave [4] gives the most accurate predictions (a mean deviation of 5.558%) for Bed ash slurry (Pump B) of Gandhi et al. [22], while the proposed correlation (Eq. (9)) indicates a mean deviation of 11.368% for the same slurry. However, the correlation proposed in this paper provides the closest predictions among all others and can be used over a wide range of physical properties of solids and pump sizes, depicted earlier in Table 1.

The larger deviations in the predicted values by other correlations may arise from the following reasons:

a. The correlations are generally based on a small number of test data, and the range of variables considered is relatively narrow.

b. Improper accounting for the specific gravity of solids. The exponent of "$(S-1)$" factor varies over a relatively wide range (0.5–1.0) according to various researchers.

c. The impeller exit diameter (D), which reflects the effect pump size, was generally not included in the correlations. It was

Table 3 Percentage deviations between the various correlations and experimental data

		Present (Eq. 9)		Vocadlo [3]		Cave [4]		Burgess [5]		Sellgren [6]		Gahlot [7]		Kazim [8]		Engin [9]	
Solid Material	N	Mean	Ave.	Mean	Ave.	Mean	Ave.	Mean	Ave.	Mean	Ave.	Mean	Ave.	Mean	Ave.	Mean	Ave.
Sand A to F	131	7.975	3.010	44.132	44.143	16.487	16.369	30.037	30.037	18.674	1.034	8.496	0.596	8.358	3.058	16.543	16.485
Sand G to K	24	4.876	-4.245	7.044	7.044	5.165	3.604	12.891	7.339	9.490	-0.175	8.920	-8.466	6.660	-5.708	8.401	8.401
Sand L to O	18	4.125	-3.684	4.231	4.231	4.679	2.714	13.172	5.900	9.639	-1.516	10.222	-9.299	7.985	-6.520	7.553	7.553
Sand P and Q	4	6.571	1.886	44.574	44.574	9.913	9.618	17.459	17.459	22.946	5.473	11.063	-7.552	9.463	-2.724	13.160	13.160
Sand R	19	5.837	4.246	43.332	43.332	6.771	1.591	12.365	3.004	9.627	9.627	11.143	-10.367	9.634	-7.636	7.288	6.477
Sand S and T	36	12.177	-12.177	27.922	27.922	22.356	-22.356	41.598	5.367	23.415	23.415	36.273	-36.273	32.898	-32.898	16.539	-16.288
Sand U and V	32	6.510	0.174	38.771	38.771	28.984	-28.984	9.169	-8.466	37.157	37.157	44.224	-44.224	40.557	-40.557	22.573	-22.573
Beach Sand	40	7.924	-2.087	38.133	38.133	10.337	-5.453	7.787	5.377	25.879	25.879	19.066	-18.527	16.741	-15.745	9.180	-0.300
River Sand	40	5.219	1.316	39.710	39.710	5.297	-0.172	6.566	4.827	13.786	13.786	11.319	-11.130	8.879	-8.305	6.621	4.798
Ilmenite	27	4.578	-1.471	36.773	36.773	4.692	-2.534	10.607	10.497	26.375	26.375	5.000	2.315	5.168	-3.623	4.642	1.248
Heavy Mineral	39	6.300	0.788	41.260	41.260	7.188	-1.262	9.252	7.839	25.778	25.778	7.269	2.986	7.228	-2.160	7.213	2.510
Coal A	6	14.968	14.968	65.047	65.047	44.107	44.107	39.614	39.614	32.018	32.018	13.639	13.639	4.375	-2.419	24.988	24.988
Coal B	6	15.749	15.749	61.173	61.173	26.077	26.077	13.766	-9.656	29.747	29.747	11.673	11.673	4.626	-0.650	25.731	25.731
Coal C1 to E3	35	5.322	5.307	46.007	46.007	11.272	11.272	*	*	31.923	31.923	19.939	19.939	10.135	-9.047	13.925	13.925
Gravel	5	9.826	9.826	31.653	31.653	20.108	20.108	*	*	40.134	40.134	12.011	12.011	14.480	14.480	24.088	24.088
Iron ore A	3	2.186	0.888	39.057	39.057	7.278	7.278	6.330	6.330	88.053	88.053	12.200	12.200	7.542	7.542	10.722	10.722
Iron ore B	6	2.207	-0.691	3.578	2.070	3.261	-2.165	45.427	45.427	15.349	15.349	3.993	2.714	3.137	-1.840	3.331	1.686
Mild Steel	31	13.244	-8.462	38.285	38.285	14.105	1.014	17.695	15.881	96.137	96.137	16.383	13.825	13.416	6.158	13.401	5.114
Perlite A and B	4	3.470	-2.488	30.110	30.110	4.291	1.527	18.350	18.350	42.600	42.600	8.450	-7.525	5.751	-2.560	13.477	13.477
Perlite C	11	9.578	9.578	29.178	29.178	5.036	4.900	6.692	6.692	8.578	8.578	12.311	12.311	7.160	-7.125	9.782	9.782
Granite	6	5.020	5.020	6.648	6.648	6.065	6.065	*	*	4.809	4.809	3.255	-3.220	1.683	-0.798	10.698	10.698
Zinc	3	2.735	0.829	42.553	42.553	8.854	8.854	11.732	11.732	94.819	94.819	17.405	17.405	10.872	10.872	10.620	10.620
Zinc tailing	6	4.992	-1.854	38.104	38.104	11.713	11.713	26.356	26.356	11.307	11.307	5.725	1.884	6.062	3.081	15.949	15.949
Tailing	9	15.591	15.198	28.161	28.161	81.071	81.071	38.567	38.567	61.077	61.077	70.841	70.841	71.377	71.377	82.064	82.064
Bed ash	17	18.412	12.735	53.347	53.347	37.574	37.574	52.247	52.247	26.645	26.645	18.900	8.846	19.309	12.405	26.594	26.594
Fly ash	37	11.524	5.947	41.216	41.216	65.570	65.570	48.726	48.726	58.769	58.769	28.002	28.002	32.714	32.714	49.250	49.250
Bed ash, Pump B	27	11.368	-10.294	34.334	34.334	5.558	3.148	26.576	26.576	15.142	15.142	41.422	41.422	35.901	-35.901	14.655	-14.424
Fly ash, Pump B	27	11.417	-0.725	32.614	32.614	58.003	58.003	40.809	40.809	47.525	47.525	13.945	12.179	18.259	17.927	38.096	38.096
Glass bead	5	6.393	3.240	38.744	38.744	30.198	30.198	41.902	41.902	51.465	51.465	15.157	15.157	18.589	18.589	33.797	33.797
All data	**654**	**8.378**	**0.620**	**37.258**	**37.241**	**19.210**	**10.733**	**23.629**	**19.136**	**29.443**	**25.141**	**17.494**	**-5.455**	**15.907**	**-3.160**	**17.418**	**10.642**

Mean deviation $= \frac{1}{N}\sum_{1}^{N}\left|\frac{K_{H(exp)}-K_{H(cal)}}{K_{H(exp)}}\right|$, Average deviation $= \frac{1}{N}\sum_{1}^{N}\frac{K_{H(exp)}-K_{H(cal)}}{K_{H(exp)}}$: *Not applicable

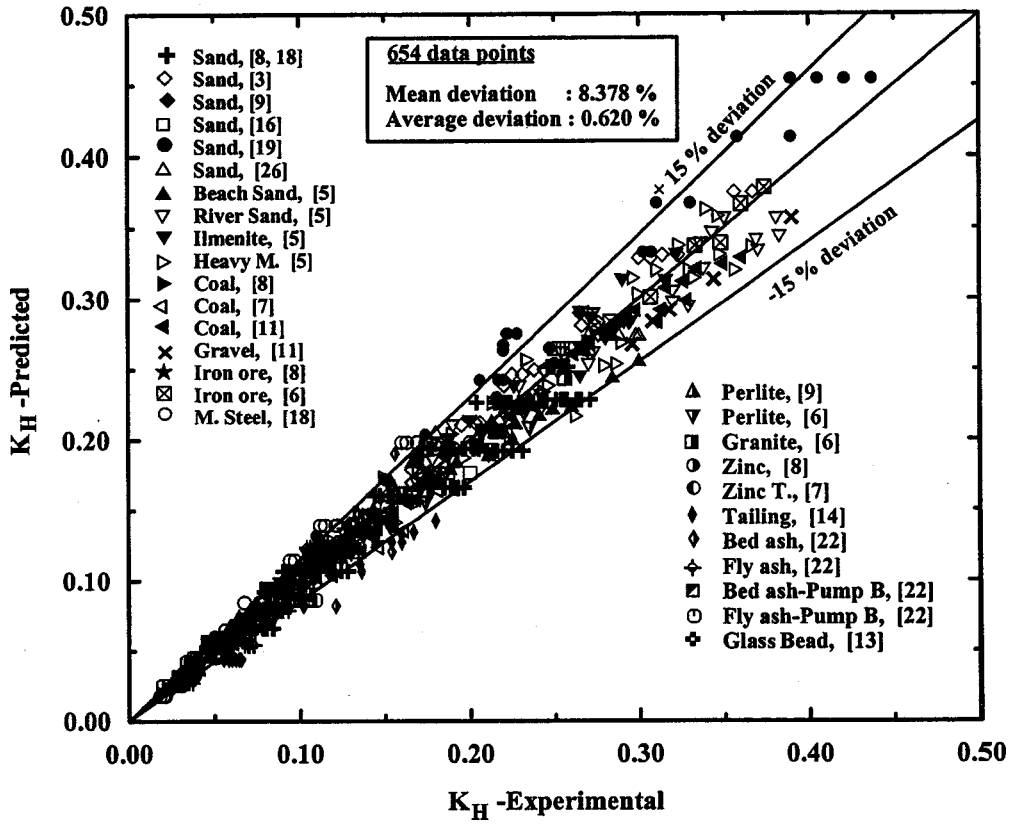

Fig. 2 Accuracy of proposed correlation for various solid materials

observed in this study that the head reduction factor could be better correlated to the (d_w/D) than the d_w alone, for the range of impeller diameters depicted in Table 1.

d. Particle size distribution is a major consideration and generally represented by either weighted mean particle diameter (d_w) or mass median particle diameter (d_{50}). The weighted mean particle diameter is defined as follows:

$$d_w = \sum_{i=1}^{n} x_i d_i \tag{10}$$

where n is the number of sieve groups in which the total sample was divided, x_i is the weight fraction of solids retained on the ith size group, and d_i is the arithmetic mean of two successive sieve openings.

The mass median diameter (d_{50}) is the sieve size through which the solid sample of 50% by weight passed. When the particle size is represented by d_{50}, as an example for a sample having a broad size distribution, particles are simply divided into two-size groups, the first group having a maximum particle size just below d_{50}, and the second group having a minimum particle size just above d_{50}. In this way, the particle size distribution in each group is not separately considered. On the other hand, when the particle size is represented by the weighted mean particle diameter (d_w), more than two particle size groups are considered and weight is given to each group. Since the individual contribution of each size group is reflected better using d_w rather than d_{50}, this method provides a more accurate determination of the representative particle size. Kazim et al. [8] showed that an identical variation of H_r (or K_H) could only be obtained if the weighted mean particle diameters of two solids are the same, regardless of equality of the d_{50} values. Sellgren and Addie [23] demonstrated that it is questionable if d_{50} is used as the representative particle size of slurries containing a considerable range of particle sizes. However, most of the correlations are based on the mass median particle diameter. This will not probably give rise to any serious errors in the predictions if the particle size distribution is narrow. Otherwise, for broad size distributions, use of d_{50} may cause larger deviations from real values. In Table 1, both d_{50} and d_w values are given for sand E, sand F, bed ash, and fly ash. When the representative particle diameter is chosen as d_w, the proposed correlation (Eq. (9)) produces mean deviations such as 4.332, 9.181, 18.412, and 11.542%, respectively, for these four solid materials. However, if the mass median diameter is used for each solid, the deviations are found to be 8.953, 15.745, 23.898, and 16.236%, respectively. It is obvious that the use of mass median diameter increased remarkably the deviations for all solids. The larger deviations in these comparisons may be attributed to some extent to the fact that we have developed the Eq. (9) based on d_w rather than d_{50}. However, it has been observed that, use of d_w in other correlations, [3–6], provide much better predictions compared to use of d_{50}.

Comparison Between Head and Efficiency Ratios

For homogeneous mixtures at a fixed flow rate (bep), Stepanoff [1] and Vocadlo et al. [3] have concluded that the power ratio $(P_r = P_s/P_w)$ is approximately equal to the specific gravity of the slurry pumped, which means that the head ratio equals to the corresponding efficiency ratio. Wilson's [15] observations supported this conclusion while he underlined that the efficiency drops at a greater rate than the head when the volumetric concentration of solids is very large. Similarly, Cave's [4] results indicated that the efficiency ratio might be slightly less than head ratio, for a particular operating condition. However, he suggested that for practical purposes efficiency ratio could be taken to be equal to the head ratio.

Sellgren [6] showed that the head and efficiency ratios could be treated equal to each other up to 20–25% concentration of solids by volume. After that, the efficiency ratio drops more sharply than the corresponding head ratio. In a later study, Sellgren and Addie

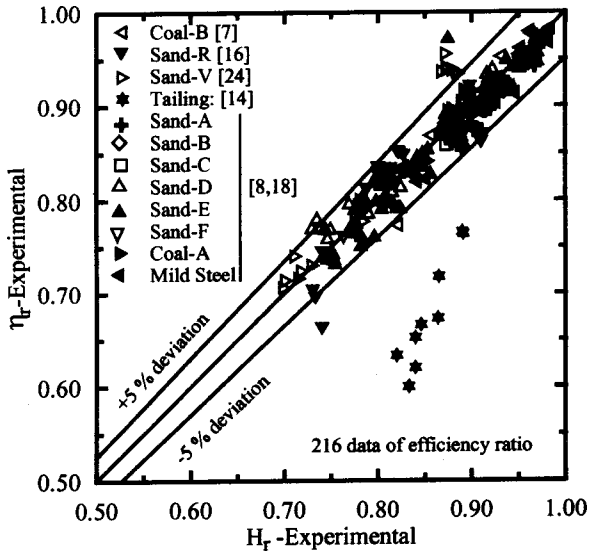

Fig. 3 Comparison between head ratio and efficiency ratio based on experimental data

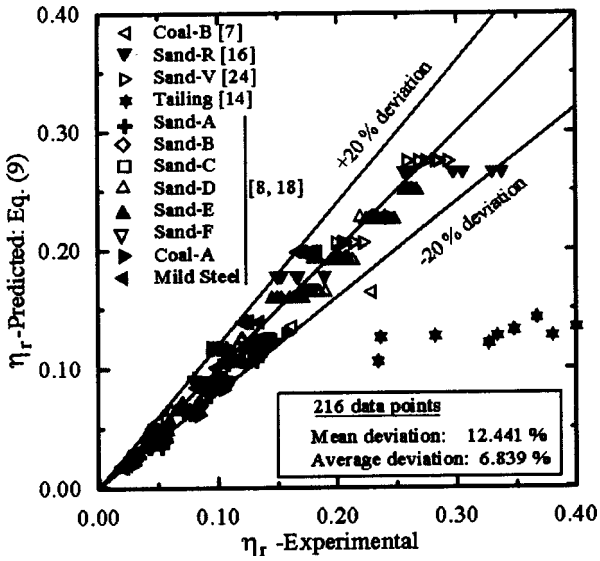

Fig. 4 Accuracy of proposed correlation for prediction of efficiency ratio

[17] noted that the reduction in efficiency was normally less than the head reduction in large pumps, while for small pumps these reductions were usually equal. However, Gahlot et al. [7] reported that efficiency ratio is higher than the corresponding head ratio in order of 2–9%, for the metal lined pump they tested. Kazim et al. [18] observed that the efficiency ratio is generally lower than the head ratio for a fixed flow rate and concentration of solids. They found the efficiency ratios to be 5% lower than the corresponding head ratios, for all materials tested. Walker et al. [16] showed that the head ratio is significantly greater than efficiency ratio for high concentrations of solids. At low concentrations, they noted that the situation is reversed with the efficiency ratio being slightly higher than head ratio. Ni et al. [19] showed that the pump efficiency for medium sand ($d_{50}=372\ \mu$m) drops faster than the head ratio when the volumetric concentration of solids exceeds 35%. In contrast to observations by Sellgren and Vappling [14], he concluded that for the fine sand ($d_{50}=123\ \mu$m) $H_r=\eta_r$ up to 35% concentration of solids by volume. On the other hand, within their experimentation limits, they found the efficiency ratio to be lower than the head ratio for coarse sand ($d_{50}=1840\ \mu$m). In a different manner, for non-Newtonian homogeneous slurries, Walker and Goulas [10] observed a dependency of both the head ratio and also the efficiency ratio with the pump Reynolds number at bep flow rate. They concluded that as the Reynolds number decreased below a critical value, both ratios dropped, the efficiency ratio being always less than the head ratio. For Reynolds numbers larger than this critical limit, they indicated that both efficiency and head ratio are independent of the pump Reynolds number. Recently, in parallel to findings by Gahlot et al. [7], Gandhi et al. [22] reported that the efficiency ratio is higher than the corresponding head ratio in order of 2–10%.

Based on the above discussion, it is clear that there is no general agreement on the relation between the efficiency ratio and head ratio for a given pump flow rate at a constant pump speed. Relatively, little experimental data for efficiency ratio is available in the literature. However, in order to reveal the relationship between these two ratios, a typical comparison could be made using data for efficiency ratios given in Table 1. This comparison is illustrated in Fig. 3. As it can be seen from this figure, the maximum deviation between the two ratios lies generally within $\pm 5\%$. The efficiency ratios for Tailing [14] appear to be considerably lower than the corresponding head ratios. This highly concentrated slurry containing average particle size 30 μm may behave in a different manner. Walker and Goulas [10] reported that if the particle sizes are smaller than 35 μm for fine sands, slit and most clay, or the solid concentration is high, the mixture was characterized as non or slow-settling. The specific gravity of the given very fine tailing is 2.75, which reasonably corresponds to non-settling slurry. The larger differences between efficiency and head ratios for that slurry may be attributed to this reason. It should be noted that this comparison is based on experimental data considered.

In practice, the correlations for prediction of the head ratio are also used for prediction of the efficiency ratios. In other words, it is usually assumed that $H_r=\eta_r$ for a constant concentration of solids at a given flow rate. It may therefore be useful to examine the correlations available for prediction of head ratios against the data of efficiency ratios given in Table 1. For this purpose, all correlations showed in Table 2 have been tested using 216 experimental data of 11 different slurries, and both mean and average deviations were calculated from the data for each correlation. The proposed correlation (Eq. (9)) gave the lowest deviations (mean deviation=12.441%, and average deviation=6.84%) among others. Kazim's [8] correlation is the second accurate correlation that gives 16.590% mean deviation for the same data group. The maximum deviation in the prediction of the efficiency ratio using the proposed correlation lies within the $\pm 20\%$ band, as illustrated in Fig. 4. A clear distinction is seen in this figure too for the tailing sand slurry. Therefore, it may be concluded that the proposed correlation can be used for prediction of the efficiency ratio of a centrifugal slurry pump handling slurries within the range of parameters considered.

Conclusions

A new correlation has been developed in order to predict head reductions of centrifugal pumps when handling slurries. The proposed correlation takes into account the individual effects of particle size, particle size distribution, specific gravity and concentration of solids, and impeller exit diameter on the pump performance. In addition to the developed correlation, eight other correlations available in the literature have been tested using a large number of data covering a wide range of specific gravity (1.48–6.24), representative particle diameter (30–26,700 μm), concentration by weight up to 65.743% and impeller exit diameter from 210 mm to 825 mm, and flow rate range relative to the bep from 0.25 to 1.40. The particle Reynolds number is also ranging

from 0.0204 to 26318.57 for the slurries included in Table 1. Furthermore, the data involves the experimental results for pumps with both metal and rubber lined impellers.

The correlation developed in this paper provides remarkably closer approximation with the experimental data compared to all others for most of experimental data used. Overall, it produces only a mean deviation of 8.378% and an average deviation of 0.620%. Furthermore, the error band in the predictions of head reduction factor, for flow rates given in Table 1 for each solid material, lies within the range of $\pm 15\%$. This spread is not surprising when considering the range of variations of parameters considered. None of other published correlations are in better agreement with all data. Thus, the present correlation is expected to predict the head reductions of centrifugal pumps, within the range of parameters considered in Table 1, with higher accuracy than all other correlations available in the literature. It can also be used for prediction of efficiency ratios within the $\pm 20\%$ error band. However, It gives generally overpredictions for both ratios for the impeller exit diameter exceeding 900 mm, which may be treated as ''large slurry pump.'' The proposed correlation is therefore recommended for the prediction of performance factors of ''small-sized'' slurry pumps having impeller diameters lower than 850 mm. It may be necessary to modify the exponent of (d_w/D) in the Eq. (9), for the large slurry pumps, which is beyond the scope of this study. It also should be noted that the proposed correlation and others are exclusively for settling slurries. They may cause extremely large errors when predicting the head ratios for slow or non-settling slurries.

Nomenclature

C_V = concentration by volume
C_W = concentration by weight
C_D = weighted drag coefficient
Re_p = particle Reynolds number $= \rho V_{ts} d/\mu$
D = impeller exit diameter
d_i = arithmetic mean of two successive sieve size
d_{50} = mass median particle diameter
d_W = weighted mean particle diameter
H_s = pump total head with slurry
H_w = pump total head with clear water
H_r = head ratio $= H_s/H_w$
K_η = efficiency reduction factor $= 1-\eta_r$
K_H = head reduction factor $= 1-H_r$
n = a constant, pump speed, number of sieve
N = number of data points
S = specific gravity of solids
S_s = specific gravity of slurry
Φ = a constant
V_{ts} = terminal settling velocity
κ = an exponent
ρ = density of water
η_s = pump overall efficiency with slurry
η_w = pump overall efficiency with clear water
η_r = efficiency ratio $= \eta_s/\eta_w$
ϕ = a functional relationship
x_i = weight fraction of solids retained on the ith size group
μ = dynamic viscosity of water

References

[1] Stepanoff, A. J., 1965, ''Pumps and Blowers, Two Phase Flow-Flow and Pumping of Solids in Suspension and Fluid Mixtures,'' John Wiley and Sons, London.
[2] Fairbank, L. C., 1942, ''Effect on the Characteristics of Centrifugal Pumps,'' Trans. Am. Soc. Civ. Eng., **107**, pp. 1564–1575.
[3] Vocadlo, J. J., Koo, J. K., and Prang, A. J., 1974, ''Performance of Centrifugal Pumps in Slurry Services,'' *Proc. Hydrotransport-3*, Paper J2, BHRA Fluid Engineering, pp. 17–32.
[4] Cave, I., 1976, ''Effects of Suspended Solids on the Performance of Centrifugal Pumps,'' *Proc. Hydrotransport-4*, Paper H3, BHRA Fluid Engineering, pp. 35–52.
[5] Burgess, K. E., and Reizes, A., 1976, ''The Effect of Sizing, Specific Gravity and Concentration on the Performance of Centrifugal Pumps,'' Proc. Inst. Mech. Eng., **190-36/76**, pp. 391–399.
[6] Sellgren, A., 1979, ''Performance of Centrifugal Pumps When Pumping Ores and Industrial Minerals,'' *Proc. Hydrotransport-6*, Paper G1, BHRA Fluid Engineering, pp. 291–304.
[7] Gahlot, V. K., Seshadri, V., and Malhotra, R. C., 1992, ''Effect of Density, Size Distribution, and Concentration of Solids on the Characteristics of Centrifugal Pumps,'' ASME J. Fluids Eng., **114**, pp. 386–389.
[8] Kazim, K. A., Maiti, B., and Chand, P., 1997, ''A Correlation to Predict the Performance Characteristics of Centrifugal Pumps Handling Slurries,'' Proc. Instn. Mech. Engrs, **21A**, pp. 147–157.
[9] Engin, T., and Gur, M., 2001, ''Performance Characteristics of a Centrifugal Pump Impeller with Running Tip Clearance Pumping Liquid-Solid Mixtures,'' ASME J. Fluids Eng., **123**, pp. 532–538.
[10] Walker, C. I., and Goulas, A., 1984, ''Performance Characteristics of Centrifugal Pumps When Handling Non-Newtonian Homogeneous Slurries,'' Proc. Instn. Mech. Engrs., **198A**(1), pp. 41–49.
[11] Mez, W., 1984, ''The Influence of Solid Concentration, Solid Density and Grain Size Distribution on the Working Behavior of Centrifugal Pumps,'' *Proc. Hydrotransport-9*, Paper H1, BHRA Fluid Engineering, pp. 345–358.
[12] Roco, M. C., Marsh, M., Addie, G. R., and Maffett, J. R., 1985, ''Dredge Pump Performance Prediction,'' *Synfuels and Coal Energy Symposium*, The 8th Annual Energy Sources Technology Conference and Exhibition, Dallas, TX, ASME, New York, pp. 31–40.
[13] Sheth, K. K., Morrison, G. L., and Peng, W. W., 1987, ''Slip Factors of Centrifugal Slurry Pumps,'' ASME J. Fluids Eng., **109**, pp. 313–318.
[14] Sellgren, A., and Vappling, L., 1989, ''Effects of Highly Concentrated Slurries on the Performance of Centrifugal Pumps,'' *ASME Fluids Engineering Div.*, FED. Vol. 38, ASME, New York, pp. 143–148.
[15] Wilson, G., 1989, ''The Effects of Slurries on Centrifugal Pump Performance,'' *Proc. of the 4th International Pump Symposium*, Houston, TX, pp. 19–25.
[16] Walker, C. I., Wells, P. J., and Pomat, C., 1992, ''The Effect of Impeller Geometry on the Performance of Centrifugal Slurry Pumps,'' *Int. Conference on Bulk Materials Handling and Transportation*, Symposium on Freight Pipelines, Wollongong, Australia, Institute of Engineers, pp. 97–101.
[17] Sellgren, A., and Addie, G. R., 1993, ''Solids Effect on the Characteristics of Centrifugal Slurry Pumps,'' *Hydrotransport-12*, 12th Int. Conf. on Slurry Handling and Pipeline Transport, Belgium, Sept. 28–30, BHRA Fluid Engineering, pp. 3–18.
[18] Kazim, K. A., Maiti, B., and Chand, P., 1997, ''Effect of Particle Size, Particle Size Distribution, Specific Gravity and Solids Concentration on Centrifugal Pump Performance,'' Powder Handl. Process, **9**(1), pp. 27–32.
[19] Ni, F., Vlasblom, W. J., and Zwartbol, A., 1999, ''Effect of High Solids Concentration on Characteristics of a Slurry Pump,'' *Hydrotransport-14*, BHRA Group, pp. 141–149.
[20] Sellgren, A., Addie, G. R., and Scott, S., 2000, ''The Effect of Sand-Clay Slurries on the Performance of Centrifugal Pumps,'' Can. J. Chem. Eng., **78**, pp. 765–769.
[21] Gandhi, B. K., Singh, S. N., and Seshadri, V., 2000, ''Improvements in the Prediction of Slurry Pumps Handling Slurries,'' Proc. Instn. Mech. Engrs., **214A**, pp. 473–486.
[22] Gandhi, B. K., Singh, S. N., and Seshadri, V., 2001, ''Performance Characteristics of Centrifugal Slurry Pumps,'' ASME J. Fluids Eng., **123**, pp. 271–280.
[23] Sellgren, A., and Addie, G., 1989, ''Effect of Solids on Large Centrifugal Pumps Head and Efficiency,'' Paper CEDA *Dredging Day*, Central Dredging Association, Amsterdam, The Netherlands.
[24] Turton, R., and Levenspiel, O., 1986, ''A Short Note on Drag Coefficient for Spheres,'' Powder Technol., **47**, p. 83.
[25] Wilson, K. C., Addie, G. R., Sellgren, A., and Clift, R., 1997, *Slurry Transport Using Centrifugal Pumps*, 2nd Ed., Blackie and Son, London.

A. Ashrafizadeh
Lecturer and Post Doctoral Fellow

G. D. Raithby
Distinguished Professor Emeritus,
Life Fellow ASME

G. D. Stubley
Professor of Mechanical Engineering

Department of Mechanical Engineering,
University of Waterloo,
Waterloo, ON N2L 3G1
Canada

Direct Design of Ducts

This paper describes a method for calculating the shape of duct that leads to a prescribed pressure distribution on the duct walls. The proposed design method is computationally inexpensive, robust, and a simple extension of existing computational fluid dynamics methods; it permits the duct shape to be directly calculated by including the coordinates that define the shape of the duct wall as dependent variables in the formulation. This "direct design method" is presented by application to two-dimensional ideal flow in ducts. The same method applies to many problems in thermofluids, including the design of boundary shapes for three-dimensional internal and external viscous flows.
[DOI: 10.1115/1.1514201]

Introduction

The present paper focuses on the flow through nozzles, diffusers, elbows, and S-bends, such as shown in Fig. 1. Elbows that also reduce the flow area are referred to as curved nozzles, and curved diffusers are elbows that increase the flow area. The following references provide excellent overviews of the large body of literature relating to the design of such components: Gibbings [1] and Johnston [2] provide reviews of the design of nozzles and diffusers respectively, Rehman and Bowyer [3] consider S-shaped diffusers used for engine intakes in the aviation industry, and curved nozzles and diffusers, frequently encountered in rotating machines, are discussed by Stanitz [4] and Parsons [5], respectively.

If a geometry is specified and the objective is to compute the flow through this geometry, the problem is referred to here as an *analysis problem*. If the objective is to compute both the flow and the surface shape that satisfies some suitable criteria (such as prescribed pressure distributions on the walls), the problem is referred to as a surface shape design (SSD) problem, or simply as a *design problem*. The focus of this paper is the solution of SSD problems involving the class of shapes shown in Fig. 1.

Several methods exist to solve SSD problems. Designers, who use analysis tools, often solve SSD problems by a cut-and-try method. This involves guessing a geometry, solving the analysis problem for the flow, correcting the geometry based on the results obtained, and repeating the process until a geometry is found that meets performance specifications. Intuition or simplified analysis (e.g., [6]) often guide the geometry update. Genetic algorithms, [7], provide a more systematic and reliable method of updating surface shape.

Optimization methods are also available to solve SSD problems. In this case, a cost functional (for example the difference between the calculated and target surface pressure) is defined and a minimum of this functional is sought subject to the constraint that the flow governing equations be satisfied. The search for the minimum can be based on sensitivities, [8], or on the solution to the adjoint equations, [9]. Optimization methods are complex to formulate, expensive to apply, and may zero in on a relative minimum in the cost functional.

The above methods usually require that many analysis problems be solved to obtain the solution of one SSD problem.

An SSD method was developed by Stanitz [4] for solving two-dimensional problems that requires about the same computational effort as the solution of one analysis problem. This was later extended to apply to three-dimensional flows, [4]. Chaviaropoulos et al. [10] provided another method for designing three-dimensional ducts. Both these methods are inherently limited to irrotational flows, and in three-dimensions they require additional constraints to ensure uniqueness of the solution.

The SSD method described in this paper is apparently new. This method provides a set of equations that, when solved, provides the fluid flow solution as well as the coordinates of nodes that define the body shape. The name *direct* design method is used because the coordinates of the body appear as dependent variables in the formulation. The method applies to one-dimensional, two-dimensional, and three-dimensional problems and is applied in physical space (most available methods work in a transformed space). It can also be used with any desired level of complexity of governing equations, from ideal to Navier-Stokes (NS), and it is a simple extension of existing CFD methods.

The present direct design method is an extension of the method used by the authors' group to compute free surface, [11], and compliant surface, [12], flows, and has been briefly described previously in the context of short duct design, [13], and heat conduction problems, [14].

The next section of the paper provides background related to design problems, and the method is then presented in the context of two-dimensional ideal (incompressible and irrotational) flow in ducts. Solutions to SSD problems, of the types shown in Fig. 1, are then presented.

Problem Overview

Consider the design of a two-dimensional curved nozzle, shown in Fig. 2, that is required to turn an incompressible flow 90 deg, and accelerate it from uniform inlet velocity V_1 to uniform outlet velocity $V_2 = 2V_1$. The locations of the inlet and outlet boundaries, Γ_1 and Γ_2, are specified, but the locations of the inside surface Γ_I and outside surface Γ_O are unknown. The "design" in Fig. 2(*a*) has simply specified smooth curves for Γ_I and Γ_O. Is this design acceptable?

A simple way to do a preliminary assessment of the design is to compute the ideal flow through the nozzle. The velocities along

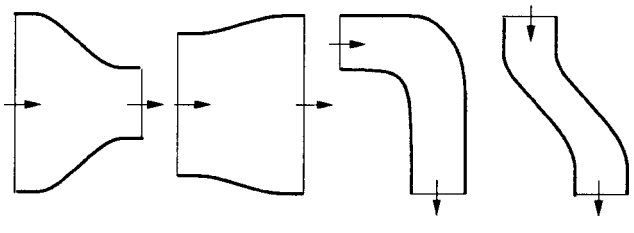

Fig. 1 Categorization of ducts

Contributed by the Fluids Engineering Division for publication in the JOURNAL OF FLUIDS ENGINEERING. Manuscript received by the Fluids Engineering Division Sept. 5, 2001; revision manuscript received June 4, 2002. Associate Editor: I. Celik.

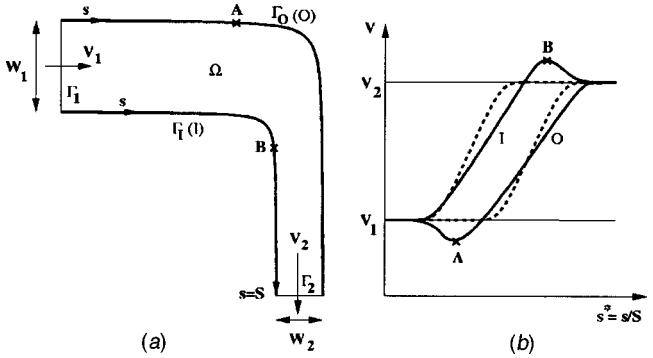

Fig. 2 A 90 deg curved nozzle. Calculated (solid curves) and target (dashed curves) wall velocities are shown in (*b*).

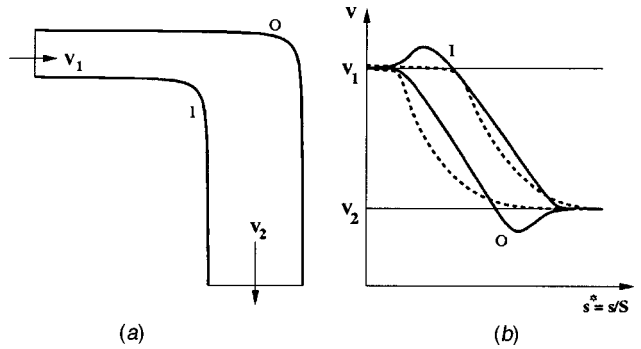

Fig. 3 A 90 deg curved diffuser. Calculated (solid curves) and target (dashed curves) wall velocities are shown in (*b*).

the inner and outer walls from an ideal flow solution are plotted as solid lines in Fig. 2(*b*) for the geometry in Fig. 2(*a*). The coordinate **s*** in this plot is the fraction of total distance along the inner and outer walls. The wall pressures are related to the wall velocities through Bernoulli's equation, so that in regions of flow deceleration the pressure gradient is adverse. The adverse pressure gradients upstream of point A on the outer wall and downstream of point B on the inner wall create conditions for possible separation in viscous flow. On seeing such predictions, a designer might wish to specify the wall velocities given by the dashed curves in Fig. 2(*b*), for which no adverse pressure gradients exist, and to calculate the duct shape that would result in these velocities. This is a surface shape design (SSD) problem.

The overall flow acceleration in the curved nozzle, just described, does allow a design to be found that avoids regions of local adverse pressure gradients. For the diverging flow in Fig. 3, there is an overall flow deceleration ($V_2 < V_1$) and hence an overall adverse pressure gradient. If one proposes the curved diffuser shape in Fig. 3(*a*), an ideal flow solution gives the wall velocities indicated by the solid curves in Fig. 3(*b*). A designer would prefer the wall velocities given by the dashed curves, which eliminate the velocity extrema and which provide the maximum flow deceleration early on when boundary layers are thinner and more able to overcome adverse pressure gradients. A SSD method would predict the duct shape that yields this wall velocity distribution.

Direct Design Method

Computational Grid. The computational grid used in this study consists of quadrilateral elements, as shown in Fig. 4. A vertex-centered finite volume method, [15,16], is used wherein a discrete volume is associated with each node. The interior volume surrounding node P in Fig. 4 is comprised of four sectors, one in each of the four elements that share node P. A typical boundary volume for node B, and a corner volume for node E, are also shown in Fig. 4.

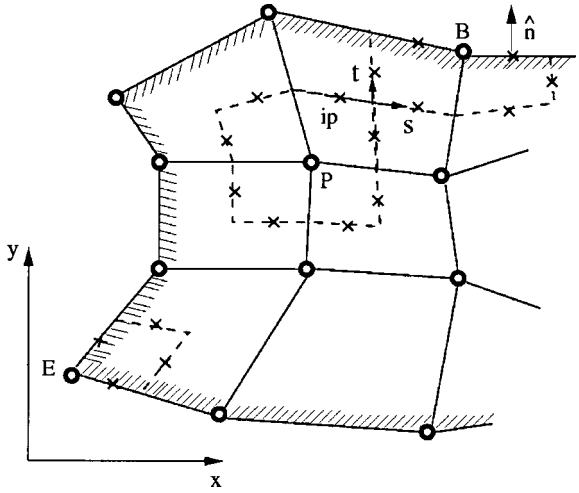

Fig. 4 The computational grid

The surface of each control volume is comprised of a number of planar panels (eight for an interior volume, six for a surface volume, and four for a corner volume). An integration point is located at the middle of each panel. These are denoted by × in Fig. 4.

Mesh Movement. Figure 5(*a*) shows a coarse grid for an initial guessed shape of curved nozzle. The solution of the ideal flow equations predicts the tangential wall velocities (e.g., the solid lines in Fig. 2(*b*)), and the objective is to adjust this geometry to give the designer-specified wall velocities (e.g., the dashed lines in Fig. 2(*b*)). This requires displacement of the boundary nodes. For example, boundary nodes C and F move from their initial locations in Fig. 5(*a*) to their final positions in Fig. 5(*b*). The interior nodes, such as D and E, must also adjust with the boundary nodes to maintain a good quality computational grid during the shape evolution.

Equations of Motion. For two-dimensional ideal flow with the stream function ψ as the dependent variable, and using the notation in Fig. 2(*a*), the governing equations are

$$\nabla^2 \psi = 0 \quad \text{in} \quad \Omega \tag{1a}$$

$$\psi = \text{specified on all boundaries} \tag{1b}$$

$$\nabla \psi \cdot \hat{n} = V_t = \text{specified tangential velocity on} \quad \Gamma_I \quad \text{and} \quad \Gamma_O \tag{1c}$$

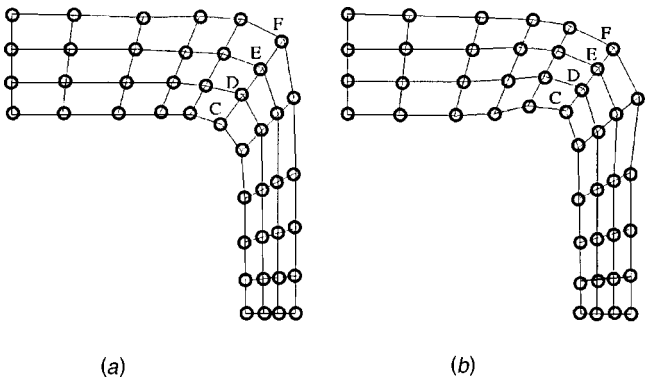

Fig. 5 Coarse mesh showing initial and final node locations

specified locations of Γ_1 and Γ_2 boundaries. (1*d*)

In analysis problems, Eqs. (1*a*) and (1*b*) plus the specified geometry would define the problem to be solved. In a surface shape design (SSD) problem, the locations of the boundaries Γ_I and Γ_O are unknown, and Eq. (1*c*) is the constraint used to compute the shapes of these boundaries. V_t in Eq. (1*c*) is referred to as the target velocity distribution, or TVD.

Finite Volume Approximation. Integrating Eq. (1*a*) over volume V with surface area A and applying the Divergence Theorem, results in:

$$\iiint_V (\nabla^2\psi)\,dV = \oint_A \nabla\psi\cdot d\mathbf{A} = 0. \tag{2}$$

The surface area A is the sum of the areas of the surface panels of the control volume associated with a node: $A=\Sigma_{ip}A_{ip}$. Equation (2) is approximated as

$$\oint_A \nabla\psi\cdot d\mathbf{A} = \sum_{ip}\int\int_{A_{ip}} \nabla\psi\cdot d\mathbf{A}$$

$$\approx \sum_{ip} [\nabla\psi]_{ip}\cdot\overline{A}_{ip} \equiv \sum_{ip} F_{ip} = 0 \tag{3}$$

where $F_{ip}\equiv[\nabla\psi]_{ip}\cdot A_{ip}$ is the "flow" of the quantity associated with ψ across the ip panel and Eq. (3) is the control volume balance equation for this quantity. Each flow term must be approximated in terms of the nodal dependent variables, which are ψ, x, and y in the present formulation. The Appendix shows that the linearized equation for F_{ip} at interior integration points has the following form:

$$F_{ip} \approx \sum_j [B1_j^{\psi}]_{ip}\psi_j + [B1_j^{x}]_{ip}x_j + [B1_j^{y}]_{ip}y_j + [C1]_{ip} \tag{4}$$

where j includes all nodes of the element which contains the integration point ip.

On the inside and outside boundaries, Γ_I and Γ_O, F_{ip} is found from

$$F_{ip} = [\nabla\psi]_{ip}\cdot\mathbf{A}_{ip} = [\nabla\psi\cdot\hat{n}]_{ip}A_{ip} = [V_t]_{ip}A_{ip} \approx [V_t^{\text{old}}]_{ip}A_{ip} \tag{5}$$

where V_t is the specified TVD on the surface. After substitution of a linearized expression for A_{ip}, and substituting the value of V_t^{old} at the integration point from the TVD, the algebraic equation can be written in the form of Eq. (4). It is necessary to evaluate V_t at the old level in Eq. (5), because V_t is specified in terms of the dimensionless coordinate $\mathbf{s}^*\equiv\mathbf{s}/\mathbf{S}$, where neither $\mathbf{s}$ at the integration points, nor the total wall length $\mathbf{S}$ are known at the new level.

Assembled Conservation Equation. Each F_{ip} in Eq. (3), whether ip lies in the interior or on the unknown boundaries, is therefore given by an equation of the form of Eq. (4). Substituting these equations into Eq. (3) for node i with neighbors j (j now includes all nodes of all elements that share node i, including i itself), the algebraic equation for the balance becomes

$$\sum_j B_j^{\psi}\psi_j + B_j^{x}x_j + B_j^{y}y_j + C_i = 0. \tag{6}$$

This is one constraint equation for the three unknowns at node i: ψ_i, x_i, and y_i.

Closure Relations. Because there are three unknowns per node, two additional relations are required for each node to close the system of equations. At interior nodes both these relations come from the strategy used to locate each node relative to its neighbors (i.e., the grid generation scheme). Many alternatives exist for generating the grid. In the present paper the grid was algebraically generated. The method starts by defining a reference line. For the geometry shown in Fig. 6, AB is the reference line from which spines are erected that cross both boundaries of the duct. For example, spine k in Fig. 6 has origin (x_*^k, y_*^k) on this line, and lies at specified angle θ^k to the x-axis. This spine intersects the duct inner and outer boundaries at R_I^k and R_O^k. Node i on this spine is defined to lie at a constant fraction r_i^k, of the distance between R_I^k and R_O^k. The distance from the origin of the spine k to node i (R_i^k) is

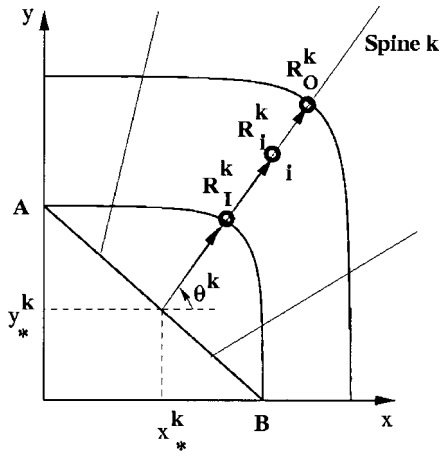

Fig. 6 Definition sketch showing spines used for grid generation

$$R_i^k = (1-r_i^k)R_I^k + r_i^k R_O^k, \tag{7}$$

so the equations for the Cartesian coordinates of node i on spine k (x_i and y_i) are

$$x_i = x_*^k + R_i^k\cos\theta^k \quad \text{and} \quad y_i = y_*^k + R_i^k\sin\theta^k. \tag{8}$$

Specification of r_i^k and θ^k in Eqs. (7) and (8) provide the two additional constraints required to close the system of equations for interior node i on spine k. Substituting these equations into Eq. (6) to eliminate x_i and y_i results in

$$\sum_j B_j^{\psi}\psi_j + \sum_m B_m^{R_I}R_I^m + B_m^{R_O}R_O^m + \hat{C}_i = 0. \tag{9}$$

For interior node i, this algebraic equation involves nine values ψ_j and the values of R_I^m and R_O^m for the three spines containing these nine nodes. Equation (9) still contains the unknowns R_I^m and R_O^m, to be determined from the control volume equations for the boundary nodes.

For node i on spine k on the inner boundary, the control volume equation has the form of Eq. (9) but the number of nodes is reduced to six. But by Eq. (1*b*), all nodal values of ψ on this boundary are known. Specifying the value of ψ_i permits this equation to become the constraint equation for R_I^k. Similarly Eq. (9) becomes the equation for R_O^k when applied at the node on the outer boundary. This is the key to the present method.

On the inlet and outlet boundaries, the nodal locations are given by Eqs. (7) and (8), but the locations of the inlet and outlet planes are user-specified, so the values of R_I^k and R_O^k are known. The values of ψ are also specified at the nodes on these boundaries.

The system of equations is now closed, and the linear set can be solved.

The formation of the equations for direct design of a duct has just been described. The formation of the analysis equations, Eqs. (1*a*) and (1*b*) with specified boundary location, is very similar. In fact, the same computer code is used to form and solve both sets

of equations. It is used in *analysis mode* to solve analysis problems, or in *design mode* to solve design problems.

Solution Algorithm. In the finite volume equations, Eq. (9) at each node, coefficients depend on the dependent variables. Solution is achieved by computing the coefficients based on the best available dependent variables, solving the linear set by application of a direct solver, and repeating the process until convergence is achieved.

The convergence is measured by the normalized residual, RES_i^*, defined as the residual of Eq. (9) at node i normalized by the product of the diagonal coefficient and the range of ψ in the problem. The error due to lagging the specified TVD at boundary node i is

$$E_i = |(V_t)_i - (V_t^{\mathrm{old}})_i| / (V_t^{\mathrm{old}})_i . \tag{10}$$

To start the solution, a shape is guessed, and the ideal flow for this shape is calculated to obtain the initial boundary velocity distribution V_t^0. Let the designer specified TVD be V_t^N. If the initial shape is far from the shape that corresponds to V_t^N, then underrelaxation may be desirable. This is achieved by using *intermediate* TVDs defined by

$$V_t^n = V_t^0 + \frac{n}{N}[V_t^N - V_t^0] \tag{11}$$

where $n = 1,2,\ldots,N-1$. The iteration algorithm is the following:

1 Guess an initial shape and solve the analysis problem for V_t^0. Initialize $n=0$.

2 Increment $n(n \leftarrow n+1)$. Specify V_t^n using Eq. (11).

3 Set $V_t^{\mathrm{old}} = V_t^n$.

4 Update the coefficients of the linear equations.

5 Calculate residuals RES_i^* for every node i.

6 Check the maximum value of RES_i^*. For $n<N$ the convergence criterion is usually 10^{-3} while for $n=N$ a criterion of about 10^{-5} is used. Also check the maximum value of E_i: The convergence criterion used for both intermediate and final TVDs is 10^{-4}. If both convergence criteria are satisfied, go to Step 11; else continue.

7 Solve the linear equations for ψ_i, R_I^k and R_O^k.

8 Update the nodal point locations (x_i, y_i), and update the $\mathbf{s}^*$ locations of nodes on the boundaries.

9 Find V_t^n at the new positions of boundary nodal points and calculate E_i.

10 Go to Step 3.

11 If $n<N$ go to Step 2; else stop.

The intermediate convergence criteria used in this study have been selected for illustrative purposes only and have not been optimized for best convergence.

Solved Problems

Validation, Accuracy, and Order of the Method. Stanitz [4] specified TVDs for a contracting 90-deg elbow with an area ratio of $W_1/W_2 = 2$. These target velocities are plotted in Fig. 7(*d*) as a function of the dimensionless wall coordinate $\mathbf{s}^*$. The dashed lines in Fig. 7(*c*) show the corresponding elbow profile reported by Stanitz for a 65×15 grid, with 15 nodes across the duct.

The initial guessed shape for the present method is shown in Fig. 7(*a*). For this geometry the code, run in analysis mode, yields the wall velocities in Fig. 7(*b*). These provide the V_t^0 wall velocities in Eq. (11). Stanitz' specified TVDs (Fig. 7(*d*)) provide the target velocity V_t^N. Using a 65×15 grid, the present method predicts the duct profile shown with solid lines in Fig. 7(*c*). These are in good agreement with Stanitz' predictions. To obtain this solution, no intermediate TVD was used ($N=1$ in Eq. (11)), and a total of 15 iterations were required to meet the convergence criteria.

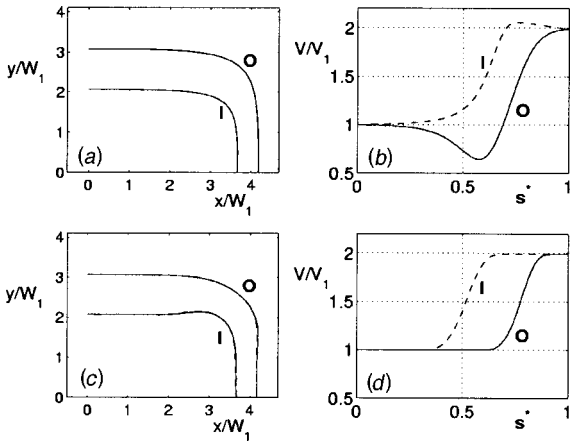

Fig. 7 Validation using the Stanitz' elbow problem. Initial guessed shape (*a*), initial wall velocity (*b*), and designed shape (*c*) for TVD in (*d*). Dashed line in (*c*) is Stanitz' solution, [4].

Accurate profile predictions were obtained using the present method with much coarser grids. Results for a 10×6 mesh were not much different, and even a 10×3 mesh gave quite good agreement with Stanitz' 90-deg elbow.

The discretization errors for the method, as implemented, should reduce at second order. Note that there are no first-order derivatives in the governing equations so that false diffusion is not an issue. To verify second order accuracy, this problem was run using $M\times M$ meshes with $M=19$, 37, and 73, and values of R_I and R_O were examined for the spines that were common to all three grids. These values were fit with an equation of the form $R = a + b(1/M)^c$. The values of c in this fit were found to be very close to 2, verifying second-order reduction of the discretization error with mesh refinement.

Straight Nozzles. The present method is now applied to design a nozzle with area ratio $W_1/W_2 = 10$. The initial guessed shape is shown in Fig. 8(*a*). Application of the code in analysis mode predicts the wall velocities in Fig. 8(*b*), which have velocity extrema at A and B. The corresponding locations on the nozzle are marked in Fig. 8(*a*). Despite the smooth contraction of the flow, it

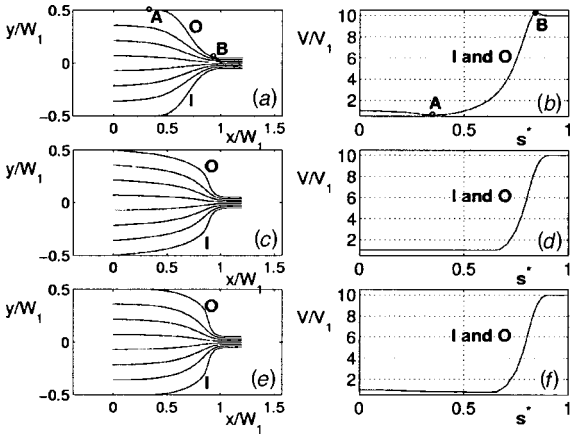

Fig. 8 Design of a straight nozzle. Initial guessed shape (*a*) and initial wall velocity (*b*). (*c*) and (*e*) are designed shapes for the TVDs in (*d*) and (*f*), respectively.

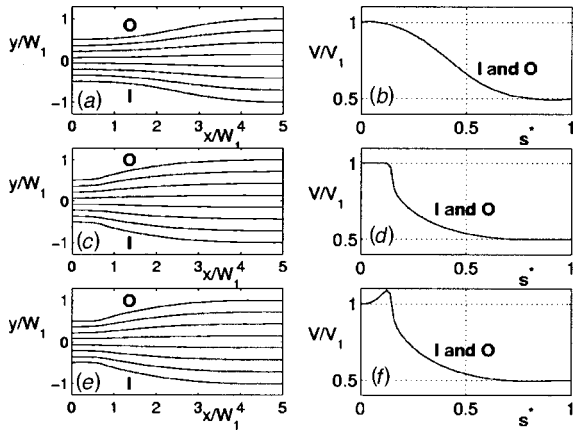

Fig. 9 Design of a straight diffuser. Initial guessed shape (*a*) and initial wall velocity (*b*). (*c*) and (*e*) are designed shapes for the TVDs in (*d*) and (*f*), respectively.

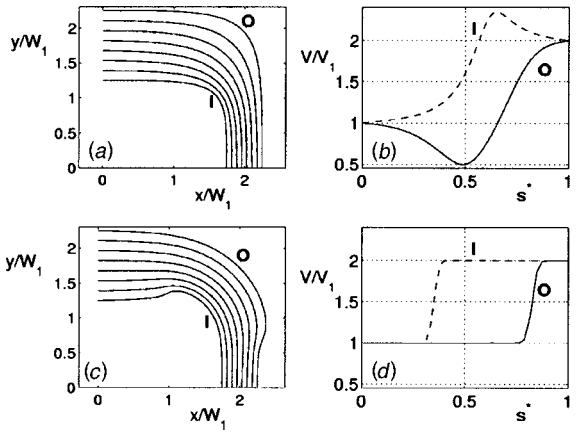

Fig. 10 Design of a 90 deg curved nozzle. Initial guessed shape (*a*), initial wall velocity (*b*), and designed shape (*c*) for TVD in (*d*).

is quite likely that the adverse pressure gradients would, in a viscous flow, cause flow separation upstream of A and downstream of B.

It is much more desirable to have a TVD that increases monotonically, as shown in Fig. 8(*d*). The steeper the TVD profile, the shorter will be the nozzle. For the TVD in Fig. 8(*d*), the predicted nozzle shape is shown in Fig. 8(*c*). This problem was solved on a 65×15 grid, no intermediate TVD was used, and convergence was obtained in 40 iterations. Nearly half of the iterations were required to satisfy the convergence criterion on E_i in Eq. (10).

The wall of the designed nozzle in Fig. 8(*c*) has nonzero slope at the inlet. Making the nozzle longer reduces this slope, but it only asymptotically approaches zero. The slope can also be reduced or eliminated by specifying an undershoot in the TVD (that should be small enough to avoid separation). For the TVDs shown in Fig. 8(*f*), the designed duct shape in Fig. 8(*e*) has a uniform inlet area. The resulting shape is remarkably similar to the optimized shape of a wind tunnel contraction with the same area ratio obtained experimentally by Bradshaw [17].

Straight Diffusers. A guessed shape for a straight diffuser with area ratio $W_2/W_1=2$ is shown in Fig. 9(*a*); the analysis of ideal flow in this shape leads to the wall velocities in Fig. 9(*b*). To decelerate the flow more quickly near the inlet, where the boundary layers would be better able to overcome the adverse pressure gradient, the TVD in Fig. 9(*d*) is specified. This results in the diffuser shape shown in Fig. 9(*c*). To achieve a uniform parallel flow at the inlet, Fig. 9(*e*), a small overshoot in the target velocity is needed, as shown in Fig. 9(*f*). This solution was achieved with a 65×15 grid, and required only five iterations without using any intermediate TVD. Boundary layer calculations were performed for the diffusers in Figs. 9(*a*) and 9(*e*). These showed that, with the same inlet conditions, the initial shape (Fig. 9(*a*)) resulted in separation while the final design (Fig. 9(*e*)) did not, [6,20]. Experimental studies on the effect of wall profiles on the boundary layer flow in straight diffusers also support this design philosophy, [18].

Curved Nozzles. The Stanitz elbow problem in Fig. 7 is an example of this class of geometry. Stanitz never explained the motivation behind his choice of wall velocity profiles in Fig. 7(*d*), and one may ask how the elbow profile changes with the shape of these TVDs.

The TVDs specified in Fig. 10(*d*) have much sharper changes than the Stanitz' TVDs in Fig. 7(*d*). The guessed shape is shown in Fig. 10(*a*), the V_t^0 profiles obtained by analysis of the flow in this shape are plotted in Fig. 10(*b*), and the designed shape is shown in Fig. 10(*c*). The result of the more rapid flow acceleration is to separate the flow acceleration zone from the zone where the flow is turned. From Fig. 10(*c*), the flow is first accelerated by the inner wall, then turned at nearly constant area, and then finally accelerated by the outer wall.

This zone separation could have been anticipated by the much larger distance between the I and O TVD profiles in Fig. 10(*d*), compared to those in Fig. 7(*d*). This raises the question of how these profiles are specified in order to achieve the required turning. The designer might look at the V_t^0 profiles to get an initial estimate of the positions of I and O TVD profiles. Then by running the code in the design mode for a few different TVDs, TVDs can be quickly found that result in the specified turning angle. It is not necessary to obtain the converged solution for each one of the trial TVDs and obviously the experience of the designer is an important factor to find appropriate TVDs.

The problem shown in Fig. 10 was solved on a 65×15 grid, to a maximum residual of 10^{-5} and a maximum TVD error of 10^{-4}. This required a total of 23 iterations using 1 intermediate TVD (i.e., $N=2$).

Uniform Elbow. Flow in an elbow with area ratio $W_2/W_1=1$ is now considered. The guessed shape is plotted in Fig. 11(*a*), and analysis of the ideal flow in this shape leads to the wall velocities in Fig. 11(*b*). The objective is to reduce the velocity overshoots and, where flow deceleration is required, to cause the

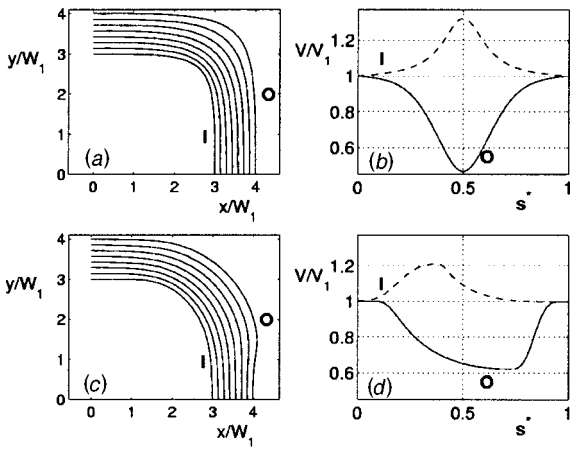

Fig. 11 Design of a 90 deg uniform elbow. Initial guessed shape (*a*), initial wall velocity (*b*) and designed shape (*c*) for TVD in (*d*).

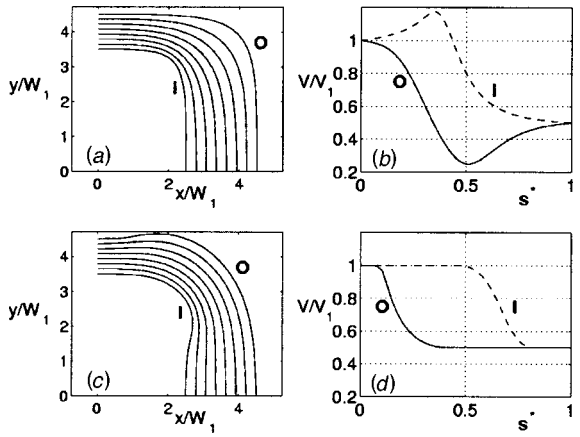

Fig. 12 Design of a 90 deg curved diffuser. Initial guessed shape (*a*), initial wall velocity (*b*), and designed shape (*c*) for TVD in (*d*).

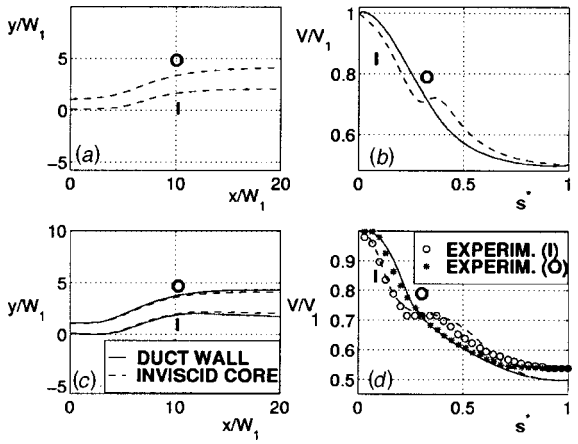

Fig. 14 Design of an expanding S-bend. Initial guessed shape (*a*), initial wall velocity (*b*), and designed shape (*c*) for TVD in (*d*). Data in (*d*) are from [3].

highest deceleration early. The profiles specified in Fig. 11(*d*) have these properties with much more gradual decelerations compared to the V_t^0 profiles. The resulting designed shape is plotted in Fig. 11(*c*). A 65×15 grid was used and the solution was obtained after ten iterations with $N=1$.

Curved Diffusers. The problem of flow in an expanding elbow was already discussed in relation to Fig. 3. For $W_2/W_1=2$ and the guessed shape in Fig. 12(*a*), the wall velocities from the analysis are plotted in Fig. 12(*b*). The specified wall velocities in Fig. 12(*d*) eliminate the velocity overshoots and would load the boundary layer more heavily at the beginning of the deceleration. The designed shape for these specified TVDs is plotted in Fig. 12(*c*). This solution was obtained with a 65×15 grid, and required a total of nine iterations with $N=1$.

S-Bends. A typical design of a contracting S-bend with $W_1/W_2=2$ is shown in Fig. 13. For the initial guess, shown in Fig. 13(*a*), the calculated V_t^0 are shown in Fig. 13(*b*). The designer specifies the TVDs shown in Fig. 13(*d*) to eliminate the extrema in the V_t^0 profiles. Note that the specified TVDs resemble the TVDs of two curved nozzles separated by a constant area duct. There are degrees of freedom for the designer to decide about the position of the crossover point in the TVDs. The designed duct, shown in Fig. 13(*c*), was obtained with a 65×15 grid after 15 iterations with $N=1$.

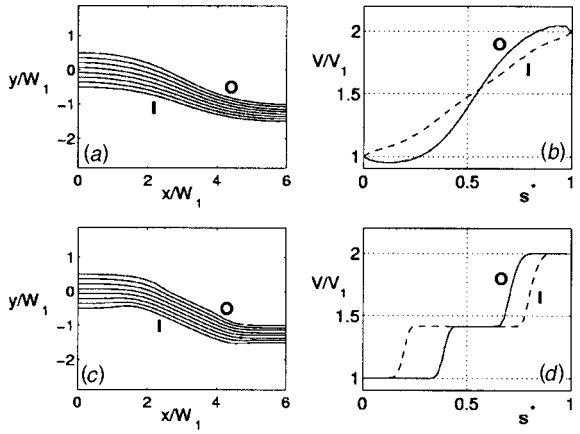

Fig. 13 Design of a contracting S-bend. Initial guessed shape (*a*), initial wall velocity (*b*), and designed shape (*c*) for TVD in (*d*).

The design of an S-bend diffuser was reported by Rehman and Bowyer [3]. The TVDs shown by the solid and dashed curves in Fig. 14(*d*) were specified to design an ideal flow duct with an area ratio of $W_2/W_1=2$. They used Stanitz' method to compute the ''inviscid core'' shape shown with the dashed lines in Fig. 14(*c*). The inviscid core was then corrected for the viscous effects with an integral boundary layer analysis method to obtain the duct walls (solid curves in Fig. 14(*c*)). This diffuser was built and the near wall velocities were deduced from wall pressure measurements. These near wall velocities are plotted in Fig. 14(*d*), and are seen to be in reasonable agreement with the specified TVDs.

The present method started with the guessed shape of inviscid core shown in Fig. 14(*a*). Analysis of the flow in the initial shape provided the V_t^0 profiles shown in Fig. 14(*b*). When TVDs shown with the solid and dashed curves in Fig. 14(*d*) were used, the present method predicted a flow core that was very close to that shown by the dashed lines in Fig. 14(*c*). An integral boundary layer analysis method based on the inner variable theory of Das [19] was developed and applied to this problem using the boundary layer information given in [3]. Adding our calculated displacement thickness to the inviscid core resulted in duct wall profiles indistinguishable from those of Rehman and Bowyer. Further details may be found in [3,20].

Discussion

The biggest questions about all SSD methods are

1. how does one prescribe a TVD?
2. what happens if the TVD is not realizable?
3. if a solution is found for a TVD, is that solution unique?

The Problem Overview section of this paper provides some guidelines for choosing a TVD. For a new problem, and if an ideal flow solver is used to solve the SSD problem, many designs can be quickly generated for a wide range of TVDs and a few of the shapes that look particularly attractive can be subjected either to CFD analysis using the full NS equations, or to experiment. This should quickly lead to a satisfactory design, and a good designer will rapidly learn the desirable properties of the TVD for future applications. It is more natural for a designer to improve a design by trying new TVDs, which are more directly related to performance criteria, than by directly guessing shape improvements.

Particularly for new problems, some of the TVDs chosen will be unrealizable (i.e., no corresponding duct shape exists). With application of the present SSD method with no (or very few) intermediate TVDs, a nonrealizable TVD will lead to rapid divergence of the iteration loop. If rapid divergence is encountered, a

large value of N is specified (e.g., $N=10$) and shapes can be found for several values of $0<n/N<1$. This allows one to usually get a solution for an intermediate TVD that is close to the specified TVD. Also, by plotting the evolution of the shape with increasing values of n/N (or animating the shape evolution), it usually becomes clear why a solution for the TVD is not achievable. This allows one to specify a more reasonable TVD.

For the problems considered in this paper, the shape of a boundary was designed by specifying an extra boundary condition on that boundary. For such problems, only one solution was ever found for a wide range of initial guesses and iteration parameters. It may sometimes be desirable to apply an extra boundary condition on one boundary to constrain the shape of the other boundary; this may lead to nonuniqueness, as discussed in [14].

Concluding Remarks

A direct surface shape design method was proposed in this paper. The method is based on a simple extension of a standard CFD method used to solve analysis problems. The only additional complexity of the method, compared to existing CFD methods, arises from the non-linearities due to the grid motion.

The method is computationally efficient and converges very quickly for the examples discussed in this paper. While the ideal flow equations were used for the present calculations, the method could be applied to the Euler equations or the Navier-Stokes equations. In these applications various control volume balance equations, with different flow terms, are used. For example F_{ip} can be the flow of momentum by advection and diffusion across the panel containing integration point ip in the momentum balance equations.

At the present time there are design problems which can be solved by optimization methods that may be intractable with the proposed direct design method. We believe, however, that where the direct design method applies, a designer may obtain greater physical insight than with mathematically more intensive, and computationally more expensive, optimization methods.

Acknowledgment

The first author was supported in his Ph.D. studies by the Ministry of Higher Education of Iran. Supplementary support of this research was provided through a research grant from the National Sciences and Engineering Research Council of Canada to the second author.

Nomenclature

A = Surface area
E_i = TVD error at node i; Eq. (10)
F_{ip} = flow associated with ψ across area A_{ip}
N = number of TVDs
$\hat{n}$ = normal outward unit vector
R = spine coordinate
RES_i^* = normalized residual at node i
$\mathbf{S}$ = length of the duct wall
SSD = surface shape design
$\mathbf{s}$ = body fitted coordinate
TVD = target velocity distribution
V = fluid velocity
V_t = tangential velocity at the duct wall, Eq. (5)
W = width of duct
x, y = Cartesian coordinates
Γ = boundary of the domain
θ = spine angle
ψ = stream function
Ω = solution domain

Subscripts

I = inside wall
ip = integration point
O = outside wall
1,2 = inlet and outlet
$*$ = reference coordinate

Superscripts

k, m = spine identifier
N = number of TVDs
old = old value
0 = initial guessed wall velocity distribution
$*$ = nondimensional

Appendix

Linearized Equation for F_{ip}. The bilinear distribution of ϕ within an element is given by

$$\phi(s,t)=\sum_j N_j(s,t)\phi_j \equiv N_j(s,t)\phi_j, \tag{12}$$

where ϕ may be ψ, x, or y and (s,t) are the nondimensional element parametric coordinates. Subscript j denotes a nodal value and the summation is over all nodes of the element. $N_j(s,t)$ is the bilinear shape function associated with node j and evaluated at (s,t). Repeated indices in this Appendix imply summation over the nodes of the element, as indicated by the second equality in Eq. (12).

Equation (12) allows the normal outward area vector at the integration point ip to be calculated as

$$\mathbf{A}_{ip}=([A_x]_{ip},[A_y]_{ip})=([\alpha_j]_{ip}y_j,-[\alpha_j]_{ip}x_j). \tag{13}$$

For example, for the area of the panel containing integration point ip in Fig. 4, which lies between $(s,t)=(-1,0)$ and (0,0), $[\alpha_j]_{ip}=-(N_j(0,0)-N_j(-1,0))$. Note that $[\alpha_j]_{ip}$ does not change with the evolution of the grid.

Also from Eq. (12), the derivative of ϕ at an integration point is

$$\left[\frac{\partial\phi}{\partial s}\right]_{ip}=\left[\frac{\partial N_j}{\partial s}\right]_{ip}\phi_j. \tag{14}$$

The vector $\nabla\psi$ at the integration point ip within the element is found by implicit differentiation to be

$$[\nabla\psi]_{ip}=\left(\left[\frac{\partial\psi}{\partial x}\right]_{ip},\left[\frac{\partial\psi}{\partial y}\right]_{ip}\right)$$
$$=\frac{1}{J_{ip}}\left(\left[\frac{\partial\psi}{\partial s}\frac{\partial y}{\partial t}-\frac{\partial\psi}{\partial t}\frac{\partial y}{\partial s}\right]_{ip},-\left[\frac{\partial\psi}{\partial s}\frac{\partial x}{\partial t}-\frac{\partial\psi}{\partial t}\frac{\partial x}{\partial s}\right]_{ip}\right) \tag{15}$$

where

$$J_{ip}\equiv\left[\frac{\partial x}{\partial s}\frac{\partial y}{\partial t}-\frac{\partial y}{\partial s}\frac{\partial x}{\partial t}\right]_{ip}. \tag{16}$$

For convenience in writing the equations, the array of constants $[\gamma_{mn}]_{ip}$, which does not change with the evolution of the grid, is defined as

$$[\gamma_{mn}]_{ip}\equiv\left[\frac{\partial N_m}{\partial s}\frac{\partial N_n}{\partial t}-\frac{\partial N_m}{\partial t}\frac{\partial N_n}{\partial s}\right]_{ip}. \tag{17}$$

Now the equations for J_{ip} and F_{ip} can be written in the following compact forms:

$$J_{ip}=[\gamma_{pq}]_{ip}x_p y_q, \tag{18a}$$

$$F_{ip}=[\nabla\psi]_{ip}\cdot\mathbf{A}_{ip}=\left(\frac{[\gamma_{mn}\alpha_i]_{ip}(y_n y_i+x_n x_i)}{[\gamma_{pq}]_{ip}x_p y_q}\right)\psi_m\equiv[G_m]_{ip}\psi_m, \tag{18b}$$

where i, m, n, p, and q all refer to values at the nodes of the element containing the integration point ip. In Eq. (18b), $[G_m]_{ip}$,

which represents the effect of the geometry of the element on the flow term (F_{ip}) at integration point ip, is a highly nonlinear function of the element nodal coordinates. When the grid evolves from a known (old) grid to a new one, all quantities are subject to change. Linearizing about the values denoted by superscript$^{\text{old}}$ (old values), and defining the differential for an arbitrary quantity ϕ as $\delta\phi=\phi-\phi^{\text{old}}$, the new value of F_{ip} can be approximately calculated as

$$F_{ip}\approx F_{ip}^{\text{old}}+[G_m]_{ip}^{\text{old}}\delta\psi_m+\psi_m^{\text{old}}\delta[G_m]_{ip}. \tag{19}$$

To obtain a linear expression for the flow term in terms of the unknown nodal values, $\delta[G_m]_{ip}$ in Eq. (19) is linearized as follows:

$$\delta[G_m]_{ip}\approx\left(\frac{\partial[G_m]_{ip}}{\partial y_n}\right)^{\text{old}}\delta y_n+\left(\frac{\partial[G_m]_{ip}}{\partial x_i}\right)^{\text{old}}\delta x_i+\cdots+\left(\frac{\partial[G_m]_{ip}}{\partial y_q}\right)^{\text{old}}\delta y_q. \tag{20a}$$

Each of the coefficients is easily computed. For example,

$$\left(\frac{\partial[G_m]_{ip}}{\partial y_n}\right)^{\text{old}}=\frac{[\gamma_{mn}\alpha_i]_{ip}y_i^{\text{old}}}{J_{ip}^{\text{old}}}\equiv[\beta 1_{mn}^{y}]_{ip}. \tag{20b}$$

Other terms in Eq. (20*a*) can be calculated similarly. Defining $[\beta 1_n^y]_{ip}\equiv[\beta 1_{mn}^y]_{ip}\psi_m^{\text{old}}$, $[\beta 2_i^y]_{ip}\equiv[\beta 2_{mi}^y]_{ip}\psi_m^{old}$ etc., Eq. (19) can now be written as

$$F_{ip}\approx F_{ip}^{\text{old}}+[\beta_m^{\psi}]_{ip}\delta\psi_m+([\beta 1_n^y]_{ip}\delta y_n+[\beta 2_i^y]_{ip}\delta y_i+[\beta 3_q^y]_{ip}\delta y_q)+([\beta 1_n^x]_{ip}\delta x_n+[\beta 2_i^x]_{ip}\delta x_i+[\beta 3_p^x]_{ip}\delta x_p). \tag{21}$$

Collecting terms and inserting the equation for each differential results in:

$$F_{ip}\approx[\beta_j^{\psi}]_{ip}\psi_j+[\beta_j^y]_{ip}y_j+[\beta_j^x]_{ip}x_j+(F_{ip}^{\text{old}}-[\beta_j^{\psi}]_{ip}\psi_j^{\text{old}}-[\beta_j^y]_{ip}y_j^{\text{old}}-[\beta_j^x]_{ip}x_j^{\text{old}}). \tag{22}$$

It can be shown that the last term in Eq. (22) is identically zero. Equation (22) is Eq. (4) in the body of the paper, in which $[C1]_{ip}=0$.

References

[1] Gibbings, J. C., 1993, "Incompressible Flow in Contracting Ducts," Aeronaut. J., **97**, pp. 230–246.

[2] Johnston, J. P., 1998, "Review: Diffuser Design and Performance Analysis by a Unified Integral Method," ASME J. Fluids Eng., **120**, pp. 6–18.

[3] Rehman, F., and Bowyer, Jr., J. M., 1989, "Turbulent Incompressible Air Flow Through S-Shaped Ducts With Cross-Sectional Area Change," *Forum on Turbulent Flows*, ASME, The Fluids Engineering Division (FED) Vol. 76, ASME, New York, **76**, pp. 49–57.

[4] Stanitz, J. D., 1988, "A Review of Certain Inverse Methods for the Design of Ducts With 2 or 3-Dimensional Potential Flow," Appl. Mech. Rev., **41**(6), pp. 217–238.

[5] Parsons, D. J., and Hill, P. G., 1973, "Effects of Curvature on Two-Dimensional Diffuser Flow," ASME J. Fluids Eng., **95**(3), pp. 349–360.

[6] Ashrafizadeh, A., and Raithby, G. D., 1999, "Prediction of Efficient Shapes for Nozzles and Diffusers," *Proceedings of 46th Annual CASI Conference*, Canadian Aerospace and Space Institute, pp. 169–178.

[7] Fabbri, G., 1997, "A Genetic Algorithm for Fin Profile Optimization," Int. J. Heat Mass Transf., **40**(9), pp. 2165–2172.

[8] Cheng, Chin-Hsiang, and Wu, Chun-Yin, 2000, "An Approach Combining Body Fitted Grid Generation and Conjugate Gradient Methods for Shape Design in Heat Conduction Problems," Numer. Heat Transfer, Part B, **37**, pp. 69–83.

[9] Jameson, A., 1994, "Optimum Aerodynamic Design Via Boundary Control," Optimum Design Methods for Aerodynamics, AGARD Report No. R-803, pp. 3.1–3.33.

[10] Chaviaropoulos, P., DeDoussis, V., and Papailiou, K. D., 1995, "On the 3-D Inverse Potential Target Pressure Problem. Part 1. Theoretical Aspects and Method Formulation," J. Fluid Mech., **282**, pp. 131–146.

[11] Raithby, G. D., Xu, W.-X., and Stubley, G. D., 1995, "Prediction of Incompressible Free Surface Flows With an Element-Based Finite Volume Method," Computational Fluid Dynamics J., **4**(3), pp. 353–371.

[12] Xu, W.-X., Raithby, G. D., and Stubley, G. D., 1996, "Prediction of Compliant-Surface Flows," *Proceedings of 4th Conference of CFD Society of Canada*, pp. 293–300.

[13] Ashrafizadeh, A., and Raithby, G. D., 2000, "A New Direct Solution Technique for Internal Flow Design Problems," *Proceedings of 8th Annual Conference of CFD Society of Canada*, pp. 715–720.

[14] Ashrafizadeh, A., Raithby, G. D., and Stubley, G. D., 2002, "Direct Design of Shape," Numer. Heat Transf.—Part B, **41**, pp. 501–510.

[15] Ronel, J. K., and Baliga, B. R., 1979, "A Finite Element Method for Unsteady Heat Conduction in Materials With and Without Phase Change," ASME Paper No. 79-WA/HT-4.

[16] Schneider, G. E., and Raw, M. J., 1987, "Control-Volume Finite Element Method for Heat Transfer and Fluid Flow Using Co-Located Variables-1. Computational Procedure," Numer. Heat Transfer, **11**, pp. 363–390.

[17] Bradshaw, P., 1970, *Experimental Fluid Mechanics*, Oxford University New York; Pergamon Press, 2nd Ed.

[18] Carlson, J. J., Johnston, J. P., and Sagi, C. J., 1967, "Effects of Wall Shape on Flow Regimes and Performance in Straight, Two-Dimensional Diffusers," J. Basic Eng., **89**(1), pp. 151–160.

[19] Das, D. K., 1992, "An Inverse Inner-Variable Theory for Separated Turbulent Boundary Layers," ASME J. Fluids Eng., **114**, pp. 543–553.

[20] Ashrafizadeh, A., 2000, "A Direct Shape Design Method For Thermo-Fluid Engineering Problems," Ph.D. thesis, University of Waterloo, Waterloo, Ontario, Canada.

Performance Analysis of a Two-Stage Electrohydraulic Servovalve in Centrifugal Force Field

Y. B. He
e-mail: mybhe@ntu.edu.sg

P. S. K. Chua

G. H. Lim

School of Mechanical Production Engineering,
Nanyang Technological University,
50 Nanyang Avenue,
Singapore 639798, Singapore

Electrohydraulic servosystems are commonly used in various engineering applications due to their high power-to-weight ratio, good performance, and ease of control. Electrohydraulic servovalves are affected by centrifugal forces when they are used in the fields of spaceflight, earthquake simulation, and geotechnique. Based on theories of fluid dynamics and performance of an electrohydraulic servovalve, the fluid flow and structure of a two-stage electrohydraulic servovalve are analyzed when the valve is affected by centrifugal forces in operation. From calculation and experimental data it is found that centrifugal acceleration is directly proportional to null shift and the scale factor is formulated. Relevant methods to reduce the influence of the centrifugal force are provided.
[DOI: 10.1115/1.1516573]

Introduction

Centrifugal test as part of environment testing is becoming more and more widely used to some products in the fields of spaceflight, earthquake simulation, and geotechnique. Centrifugal environment test is normally needed for high-precision electrohydraulic servovalves.

In certain environments, electrohydraulic servovalves, as well as hydraulic actuators, are installed on the centrifuge arm to provide vibration power when vibration testing is needed for some special parts of spaceflight, geotechnique, and earthquake simulation. In the 1980s, research institutes and universities in America and Japan had successfully applied hydraulic actuators on the centrifuge arms. These included the California Institute of Technology (Caltech), University of California at Davis (UC Davis), the Rensselaer Polytechnic Institute (RPI), Colorado University in Boulder, the Port and Harbour Research Institute of Japan, the Tokyo Institute of Technology, and the Disaster Prevention Research Institute of Kyoto University. In UC Davis, a hydraulic actuator controlled by an electrohydraulic servovalve is used to simulate an earthquake on a centrifuge called Schaevitz. RPI designed an electrohydraulic shaking table to simulate an earthquake also. The table was installed on the RPI centrifuge to test the liquefaction of soil in an earthquake. At Colorado University, an electrohydraulic servovibrator was installed on a geotechnique centrifuge for use in earthquake simulation and geotechnique tests. The vibrator is widely used in experiments for material testing, structure load, and base vibration stimulation. The Delft centrifuge (at Delft Geotechnics, Netherlands), one of the biggest centrifuges in the world, can offer centrifugal force up to 6500 kN for the study of soil mechanics, foundation engineering, and civil engineering. Delft Geotechnics has abundant experience in using hydraulic actuators on the centrifuge. Two standard D760 MOOG electrohydraulic servovalves and two hydraulic cylinders were used to test piling in clay and dynamic unbalance of the equipment, [1–9].

Nowadays, electrohydraulic servovalves are frequently used in a centrifugal force field but no research paper has been published to show the influence of centrifugal force to electrohydraulic servovalves. In this paper a creative study on the influence of centrifugal force to the fluid and electrohydraulic servovalve is carried out to overcome the shortfall of research in this field.

Contributed by the Fluids Engineering Division for publication in the JOURNAL OF FLUIDS ENGINEERING. Manuscript received by the Fluids Engineering Division Jan. 23, 2001; revised manuscript received May 29, 2002. Associate Editor: A. K. Prasad.

Theoretical Analysis of a Centrifugal Force Field

A typical two-stage servovalve is shown as Fig. 1. The first stage is a double nozzle-flapper valve. The flapper is positioned by a torque motor which includes the polepiece, armature, and magnet. Displacement of the flapper results in a pressure difference between two sides of the spool, the second stage of the valve. The spool displacement results in loading fluid flow. In the paper it is assumed that the oil is incompressible and acceleration of earth gravity on the fluid in the servovalve can be neglected when compared with the centrifugal acceleration.

Figure 2 shows a sketch of the double nozzle-flapper valve. At first we discuss forces acting on the flapper when the direction of flapper's deflection is opposite to that caused by the acceleration. Figure 2 shows surface "1," surface "*N*," and the direction of acceleration. Using Bernoulli equation, we get

$$\frac{P_N}{\rho}-ax_N+\frac{\alpha_N V_N^2}{2}=\frac{P_1}{\rho}-ax_1+\frac{\alpha_1 V_1^2}{2} \tag{1}$$

where, $x_1-x_N=L$. Here we suppose velocity of flow distributes evenly at any cross section of the pipeline. Then $\alpha_1=\alpha_N=1$. Obviously V_1 is much less than V_N. We consider $V_1=0$. From Eq. (1), we get

$$P_N=P_1-\rho aL-\frac{\rho V_N^2}{2}. \tag{2}$$

Using the momentum principle of flow fluid, we have

$$F_1=P_N A_N+\rho Q_N V_N-\rho a A_N(x_{f0}-x_f) \tag{3}$$

$Q_N=V_N A_N$. From Eqs. (2) and (3) we get

$$F_1=\left(P_1-\rho aL-\frac{\rho V_N^2}{2}\right)A_N+\rho A_N V_N^2-\rho a A_N(x_{f0}-x_f) \tag{4}$$

where V_N can be expressed as

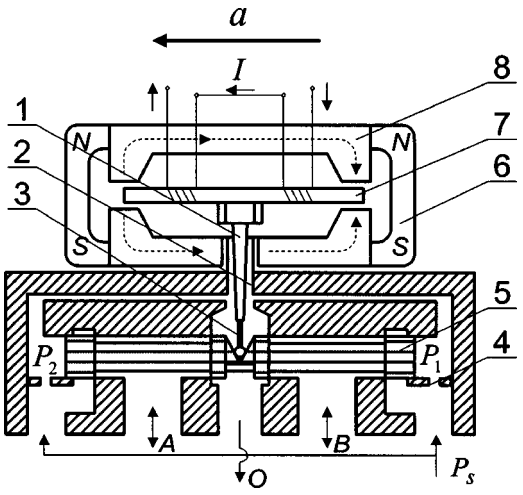

Fig. 1 Configuration principium drawing of a two-stage electrohydraulic servovalve. 1: flexure tube, 2: nozzle, 3: feedback spring, 4: inlet orifice, 5: spool, 6: magnet, 7: armature, 8: polepiece.

$$V_N=\frac{Q_N}{A_N}=\frac{C_{df}\pi D_N(x_{f0}-x_f)\sqrt{\frac{2}{\rho}P_1}}{\pi D_N^2/4}=\frac{4C_{df}(x_{f0}-x_f)\sqrt{\frac{2}{\rho}P_1}}{D_N}. \tag{5}$$

From Eqs. (4) and (5) we get

$$F_1=P_1A_N\left[1+\frac{16C_{df}^2(x_{f0}-x_f)^2}{D_N^2}\right]-\rho aA_N(L+x_{f0}-x_f). \tag{6}$$

Equation (6) expresses the fluid forces acting on a single nozzle-flapper valve in the centrifugal force field. Here we call the derivative of flow force F_1 to flapper's offset x_f "stiffness" of fluid forces acting on a single flapper-nozzle valve. The stiffness is

$$\left.\frac{dF_1}{dx_f}\right|_0=-4\pi C_{df}^2P_sx_{f0}+\rho aA_N. \tag{7}$$

Assuming equal hydraulic impedances at the inlet orifices and the nozzle/flapper orifices, we have $P_s=2P_1|_0$. From Eq. (7) we know that the stiffness (the derivative of flow force F_1 to flapper's offset x_f) of the single nozzle-flapper valve is negative. The negative stiffness causes instability. It needs to be counteracted by positive stiffness of the driving torque. In the centrifugal force field, the stiffness is increased by "ρaA_N."

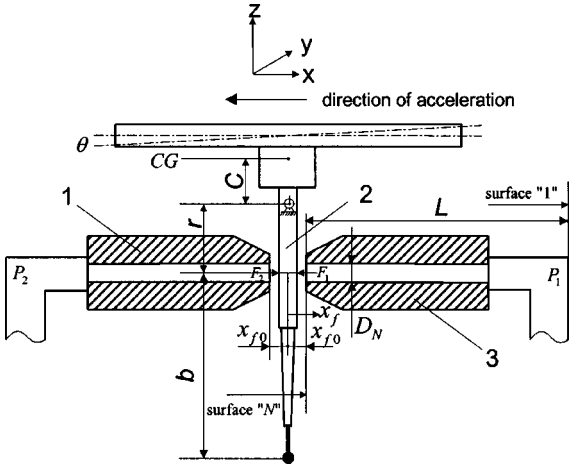

Fig. 2 Sketch of the double nozzle flapper valve. 1: nozzle, 2: flapper, 3: nozzle.

Fluid forces acting on the flapper from the other side can be formulated as

$$F_2=P_2A_N\left[1+\frac{16C_{df}^2(x_{f0}+x_f)^2}{D_N^2}\right]+\rho aA_N(L+x_{f0}+x_f). \tag{8}$$

Then

$$F_1-F_2=P_LA_N+4\pi C_{df}^2x_{f0}^2P_L+4\pi C_{df}^2x_f^2P_L-8\pi C_{df}^2x_{f0}P_sx_f-2\rho aA_N(L+x_{f0}). \tag{9}$$

For nozzle-flapper valves, as a general rule, $x_{f0}/D_N=1/8\sim1/16$, [10,11], and $P_L\approx0$, $x_f\approx0$ around the flapper's middle position. Then two items in Eq. (9), $4\pi C_{df}^2x_{f0}^2P_L$ and $4\pi C_{df}^2x_f^2P_L$, can be neglected because they are much less than the item, $8\pi C_{df}^2x_{f0}P_sx_f$. The stiffness (derivative of fluid forces F_1-F_2 to flapper's offset x_f) can be expressed as

$$\left.\frac{d(F_1-F_2)}{dx_f}\right|_0=-8\pi C_{df}^2P_sx_{f0}. \tag{10}$$

From Eqs. (9) and (10), we know that differential force acting on the flapper is increased, but the centrifugal force does not affect the stiffness of the double nozzle-flapper valve.

Equation of motion of the flapper can be expressed as

$$T_d=J_a\frac{d^2\theta}{dt^2}+B_a\frac{d\theta}{dt}+K_a\theta+(F_1-F_2)r+maC+T_2. \tag{11}$$

It is apparent that $\tan\theta=x_f/r\approx\theta$. Then

$$T_d=\frac{J_a}{r}\frac{d^2x_f}{dt^2}+\frac{B_a}{r}\frac{dx_f}{dt}+rP_LA_N+\left[\frac{K_a}{r^2}-8\pi C_{df}^2P_sx_{f0}\right]rx_f+maC-2\rho aA_N(L+x_{f0})r+T_2. \tag{12}$$

From Eq. (12), it can be deduced that the torque is increased by the component $maC+2\rho aA_N(L+x_{f0})r$ according to the acceleration. It must be recognized that $K_a/r^2>8\pi C_{df}^2P_sx_{f0}$ so as to prevent valves from being unstable. That is to say, spring stiffness should be larger than the stiffness of fluid forces. Centrifugal force increases the torque, but does not affect the stiffness of the torque acting on the flapper.

When the direction of the centrifugal acceleration is reversed, P_N', F_1', F_2', and T_d' are corresponding to P_N, F_1, F_2, and T_d. It can be deduced that

$$P_N'=P_1+\rho aL-\frac{\rho V_N^2}{2} \tag{13}$$

$$F_1'=P_1A_N\left[1+\frac{16C_{df}^2(x_{f0}-x_f)^2}{D_N^2}\right]+\rho aA_N(L+x_{f0}-x_f) \tag{14}$$

$$\left.\frac{dF_1'}{dx_f}\right|_0=-4\pi C_{df}^2P_sx_{f0}-\rho aA_N \tag{15}$$

$$F_2'=P_2A_N\left[1+\frac{16C_{df}^2(x_{f0}+x_f)^2}{D_N^2}\right]-\rho aA_N(L+x_{f0}+x_f) \tag{16}$$

$$F_1'-F_2'=P_LA_N+4\pi C_{df}^2x_{f0}^2P_L+4\pi C_{df}^2x_f^2P_L-8\pi C_{df}^2x_{f0}P_sx_f+2\pi aA_N(L+x_{f0}) \tag{17}$$

$$\left.\frac{d(F_1'-F_2')}{dx_f}\right|_0=-8\pi C_{df}^2P_sx_{f0} \tag{18}$$

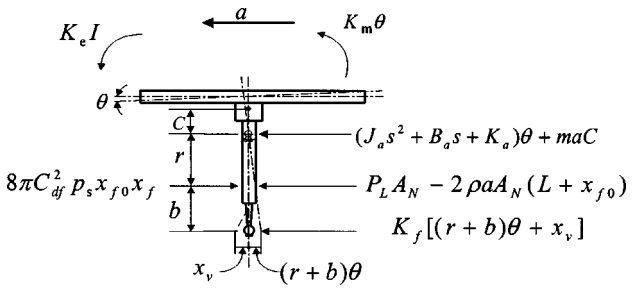

Fig. 3 Torque and forces on the armature/flapper assembly

$$T_d' = \frac{J_a}{r}\frac{d^2x_f}{dt^2} + \frac{B_a}{r}\frac{dx_f}{dt} + rP_L A_N + \left[\frac{K_a}{r^2} - 8\pi C_{df}^2 P_s x_{f0}\right] r x_f - maC + 2\rho a A_N (L + x_{f0}) r + T_2 . \quad (19)$$

From the analysis of force and torque acting on the flapper, conclusions are summarized as follows: First, centrifugal force affects not only magnitude but also stiffness (derivative of fluid forces to flapper's offset x_f) of fluid forces acting on single nozzle-flapper valves. When direction of acceleration is the same as the direction of flapper's deflection, stiffness of fluid forces is reduced. Secondly, centrifugal force only affects magnitude of fluid forces and torque acting on double nozzle-flapper valves, but does not affect the stiffness of the fluid forces.

Torque Equation Determination

T_d can be expressed as

$$T_d = K_e I + K_m \theta. \quad (20)$$

T_2 can be expressed as

$$T_2 = (r+b) K_f [(r+b)\theta + x_v]. \quad (21)$$

The torque acting on the flapper can be expressed as

$$K_e I + K_m \theta = \frac{J_a}{r}\frac{d^2x_f}{dt^2} + \frac{B_a}{r}\frac{dx_f}{dt} + rP_L A_N + \left[\frac{K_a}{r^2} - 8\pi C_{df}^2 P_s x_{f0}\right] \times r x_f + maC - 2\rho a A_N (L + x_{f0}) r + (r+b) K_f [(r+b)\theta + x_v]. \quad (22)$$

The torque acting on the flapper is shown in Fig. 3. The compressibility and leakage of oil inside the spool valve can be ignored. We get

$$q_n = A_v \frac{dx_v}{dt} = K_{qn} x_f - K_{ln} P_L . \quad (23)$$

From Eq. (23), we get

$$x_f = \frac{A_v}{K_{qn}}\frac{dx_v}{dt} + \frac{1}{K_{pn}} P_L . \quad (24)$$

The pressure gain of nozzle orifice near the middle position of the flapper can be expressed as

$$K_{pn} = \frac{K_{qn}}{K_{ln}} = \frac{P_s}{x_{f0}}. \quad (25)$$

The offset can be expressed as

$$x_f = r\theta. \quad (26)$$

From synthesizing Eqs. (22), (24), (25), and (26), we get

$$K_e I = \frac{J_a A_v}{r K_{qn}}\frac{d^3x_v}{dt^3} + \frac{B_a A_v}{r K_{qn}}\frac{d^2x_v}{dt^2} + \frac{K_{mf} A_v}{r K_{qn}}\frac{dx_v}{dt} + (r+b) K_f x_v + \frac{J_a}{r K_{pn}}\frac{d^2P_L}{dt^2} + \frac{B_a}{r K_{pn}}\frac{dP_L}{dt} + \frac{K_{mf} + r^2 A_N K_{pn}}{r K_{pn}} P_L + maC - 2\rho a A_N (L + x_{f0}) r \quad (27)$$

where the integrated stiffness of the torque motor is

$$K_{mf} = K_{an} + (r+b)^2 K_f \quad (28)$$

and where the net stiffness of the torque motor is

$$K_{an} = K_a - K_m - r^2 (8\pi C_{df}^2 P_s x_{f0}). \quad (29)$$

Forces Acting on the Spool (the Second Stage) in Centrifugal Force Field. Forces acting on the spool include the pressure difference between two ends of the spool, friction, flow force, inertia force, damp, elasticity produced by the feedback rod, and the centrifugal force. These forces are formulated as

$$A_v P_L = m_v \frac{d^2x_v}{dt^2} + B_v \frac{dx_v}{dt} + K_f [(r+b)\theta + x_v] + F_{f1} + m_v a + F_{fv} . \quad (30)$$

We ignore oil leakage in the spool valve and consider that the axial flow force varies linearly. The axial flow force can be expressed as $F_{f1} = K_v x_v$. From amalgamating and coordinating Eqs. (24) and (30), we get

$$\frac{A_v r K_{pn} - K_f (r+b)}{r K_{pn}} P_L = m_v \frac{d^2x_v}{dt^2} + \left(B_v + \frac{K_f (r+b) A_v}{r K_{qn}}\right)\frac{dx_v}{dt} + (K_f + K_v) x_v + m_v a + F_{fv} . \quad (31)$$

Experimental Results

Figure 4 shows the principium sketch of an electrohydraulic test stand on a centrifuge. The centrifuge provides centrifugal force. The centrifuge's drive spindle rotates with a constant angular velocity ω in the plane fixed by axes x and y. An electrohydraulic servovalve and a hydraulic actuator are mounted on the centrifuge arm. Both the servovalve and the actuator are affected by the centrifugal force. The pump, which supplies fluid power, is built on the ground with an oil tank. Rotary joints connect pipelines on the centrifuge arm with those on the ground. This allows pressurized oil to be conveyed into and out of the hydraulic actuator. Counterweight counterpoises the centrifuge arm.

During the experiments, the servovalve's orifices A and B (See Fig. 1) were plugged up when the spool was in its middle position and $x_v = \dot{x}_v = \ddot{x}_v = 0$. Friction F_{fv} is very small and can be ignored. When the centrifugal acceleration varies smoothly, from Eqs. (27), (28), and (31), the relationship between null shift due to the centrifugal force field, ΔI, and the centrifugal acceleration, a, can be formulated as

$$\Delta I = Ka \quad (32)$$

where the scale factor

$$K = \frac{mC}{K_e} + \frac{m_v [K_{an} + (r+b)^2 K_f + r^2 K_{pn} A_N]}{K_e r K_{pn} A_v - K_e K_f (r+b)} - \frac{2\rho A_N (L + x_{f0}) r}{K_e}. \quad (33)$$

Equation (12) can also be expressed as

$$I = Ka + I_0 . \quad (34)$$

Table 1 shows some parameters and their values of a nozzle-flapper valve. (Rated current, I_n, is 10 mA and rated flow, Q_n, is 1 L/min). From calculation, the scale factor K is 2.28×10^{-6} As^2/m, or $0.228\% I_n/g$, where g is the acceleration due to gravity and its value is 10 m/s^2. Experimental data from acceleration test is shown in Table 2. Results from calculation and experiments are shown in Fig. 5. The negative current shown in Fig. 5

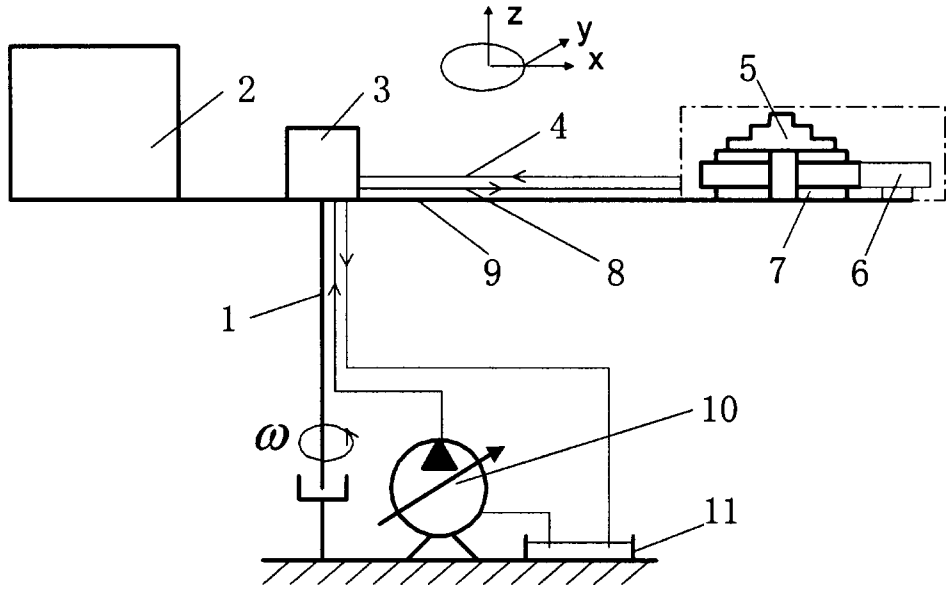

Fig. 4 Sketch of an electrohydraulic test stand on a centrifuge. 1: centrifuge spindle, 2: counterweight, 3: rotary joints, 4: return line, 5: electrohydraulic servovalve, 6: test stand, 7: hydraulic actuator, 8: in line, 9: centrifuge arm, 10: hydraulic pump, 11: oil tank

shows the opposite direction of the current compared to the positive current. Comparing the theoretically deduced K with the linearized experimental scale factor K', 2.31×10^{-6} As^2/m ($0.231\% I_n/g$), the error is very small, just 0.05×10^{-6} As^2/m (relative error of 2.17%).

From computation, the influence of mass of the armature/flapper assembly, mass of the spool, and flow effects in Eq. (33) are 2.201×10^{-6} As^2/m, 0.069×10^{-6} As^2/m and 0.011×10^{-6} As^2/m, respectively. The influence of mass of the armature/flapper assembly is much bigger here. But the distance between CG (the Center of Gravity) and the center of rotation of the armature/flapper assembly, C, is (or could be) much smaller (even approaching zero) for other servovalves when the influence of the acceleration is considered. Thus the influence of the spool and that of flows are the main roles. Acceleration effects on flows are small. But the effects can't be ignored because the value is of the same order of magnitude as that of the influence of the spool mass.

Discussion

The final calculation results are based on the static condition of the system. The movement of the spool and the centrifugal acceleration are assumed to be static. In order to keep the integrality of hydraulic and force equations, some dynamic items are included in some of the above equations before the movement of the spool is supposed to be static. In fact, the analysis of the dynamic situation is very complex and the dynamic items are not just those mentioned in some of the above equations. Many dynamic factors, such as the dynamics of the armature/flapper assembly, shock and vibration, and the dynamic acceleration environment, as well as the servovalve frequency response characteristic, should be considered if dynamic analysis is needed.

Table 1 Parameters of the double nozzle-flapper valve

m	3.45×10^{-3} kg	A_N	4.9×10^{-8} m^2
C	1.627×10^{-3} m	$L+x_{f0}$	2.5×10^{-2} m
ρ	900 kg/m^3	r	12.4×10^{-3} m
m_v	2.84×10^{-3} kg	K_{an}	2.45 Nm/rad
K_{pn}	7.74×10^{11} N/m^3	K_f	3.626×10^3 N/m
A_v	1.59×10^{-5} m^2	b	5.2×10^{-3} m
K_e	2.55 Nm/A	I_n	10 mA

Conclusions

Centrifugal forces affect the efficient application of electrohydraulic servovalves in certain centrifugal force fields. Centrifugal forces acting on double nozzle-flapper valves affect the magnitude of fluid forces and torque. This leads to the change of null shift of the electrohydraulic servovalves. From the analysis it can be concluded that null shift is linear to the centrifugal acceleration and the linear scale factor is deduced. The influence must be considered and should be minimized or eliminated when the centrifugal acceleration is great (i.e., $a \geqslant 100\,g$). It is suggested that to minimize the influence of acceleration:

1. the influence of centrifugal force to null shift can be balanced out by adding proportional reverse voltage or current to the servovalve,
2. when servovalves are designed to apply in centrifugal force fields, the distance between the center of gravity and the center of rotation of the armature/flapper assembly, C, should be very small. The influence of the mass of armature/flapper assembly can be effectively reduced by diminishing the distance C. The best situation is where C is zero. Then the influence of the mass of armature/flapper assembly, which has been the greatest influence as studied in this paper, is zero and can be ignored.
3. when mass of the armature/flapper assembly, mass of the spool, and net stiffness of the torque motor are becomingly decreased, correspondingly the moment constant of the

Table 2 Experimental data of the double nozzle-flapper valve in acceleration tests

$a\cdot g^{-1}$	0	2	4	6	8	10	12	14	16	18	20
$I\cdot I_n^{-1}(\%)$	−0.4	−0.3	0.1	0.6	1.2	1.8	2.2	2.8	3.0	3.4	4.0

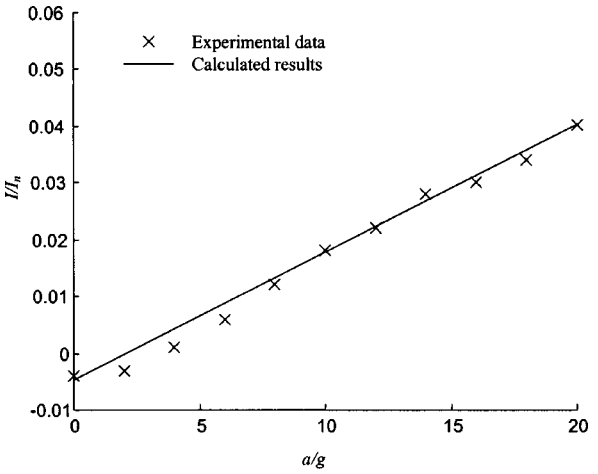

Fig. 5 Experimental data and calculated results of double nozzle-flapper valves

torque motor and pressure gain of the nozzle orifice are increased, the influence of centrifugal force can also be reduced.

Nomenclature

A_N = cross-section area of the nozzle orifice, m^2
A_v = spool end area, m^2
a = centrifugal acceleration, m/s^2
B_a = damping coefficient of the armature/flapper assembly, Nms/rad
B_v = damping coefficient of the spool, Nms/rad
b = distance from the end of the feedback rod to the axis of each nozzle, m
C = distance between the center of gravity and the center of rotation of the armature/flapper assembly, m
C_{df} = orifice discharge coefficient
F_1, F_2 = fluid forces acting on the flapper, N
F_{f1} = the axial flow force acting on the spool, N
F_{fv} = friction acting on the spool, N
g = acceleration of gravity, m/s^2
I = input current, A
I_0 = null shift, A
I_n = rated current, mA
J_a = inertia coefficient of the flapper, kgm^2/rad
K = scale factor, As^2/m
K_a = stiffness of the supporting spring, Nm/rad
K_{an} = net stiffness of the armature/flapper assembly, Nm/rad
K_f = stiffness of the feedback rod, N/m
K_e = torque constant of the electromagnetic torque motor, Nm/A
K_{ln} = flow-pressure coefficient, m^5/Ns
K_m = magnetism-elasticity torque coefficient of the electromagnetic torque motor, Nm/rad
K_{mf} = integrated stiffness of the torque motor, Nm/rad
K_{pn} = blocked load differential pressure gain of the double nozzle/flapper orifices, N/m^3
K_{qn} = flow gain of nozzle orifice, m^2/s
K_v = stiffness of the steady-state axial flow force acting on the spool, N/m
L = distance along axis x between surface "1" and surface "N," m
m = mass of the armature/flapper assembly, kg
m_v = mass of the spool, kg
P_1, P_2 = pressure at the spool ends, N/m^2
P_L = differential pressure on spool ends, N/m^2
P_N = pressure at surface "N," N/m^2
P_s = oil supply pressure, N/m^2
Q_N = flow rate through the nozzle orifice, m^3/s
Q_n = rated flow, L/min
q_n = flow output, m^3/s
r = distance between the rotation axis of the flapper and the axis of each nozzle, m
T_2 = torque provided by the second stage, Nm
T_d = driving torque of the electromagnetic motor acting on flapper, Nm
V_1, V_N = velocity of flowing fluids at surface "1" and surface "N," m/s
x_1, x_N = distance between surface "1" and "N" along axis x, m
x_f = flapper's offset along with the axis of the nozzle orifice, m
x_{f0} = distance between nozzle and flapper when the flapper is in middle position, m
x_v = displacement of the spool, m
ρ = density of oil, kg/m^3
θ = angle of rotation of the flapper, rad
α_1, α_N = kinetic energy correct modulus of fluids at surface "1" and surface "N"

References

[1] Ortiz, L. A., Scott, R. F., and Lee, J., 1983, "Dynamic Centrifuge Testing of a Cantilever Retaining Wall," Earthquake Eng. Struct. Dyn., **11**, pp. 251–268.
[2] Hushmand, B., Scott, R. F., and Crouse, C. B., 1988, "Centrifuge Liquefaction Tests in a Laminar Box," Geotechnique, **38**(2), pp. 253–262.
[3] ANS&A Report 26-02-R-004, 1992, "Earthquake Centrifuge Modeling-A General Review of Equipment Development," AD-A257 721, **12**, pp. 1–33.
[4] Campbell, D. J., Cheney, J. A., and Kutter, B. L., 1991, "Boundary Effects in Dynamic Centrifuge Model Tests," *Centrifuge 91*, Balkema, Rotterdam, pp. 441–448.
[5] Elgamal, A. W., Dobry, R., Laak, P. V., and Nicolas J. F., 1991, "Design, Construction and Operation of 100 g-ton Centrifuge at RPI," *Centrifuge 91*, Balkema, Rotterdam, pp. 27–34.
[6] Ketcham, S. A., Ko, H. Y., and Sture, S., 1991, "Performance of an Earthquake Motion Simulator for a Small Geotechnical Centrifuge," *Centrifuge 91*, Balkema, Rotterdam, pp. 361–368.
[7] Hjortnaes-Pedersen, A. G. I., and Nelissen, H. A. M., 1991, "Application of Hydraulic Actuators in the Delft Geotechnics Centrifuge," *Centrifuge 91*, Balkema, Rotterdam, p. 385.
[8] Nelissen, H. A. M., 1991, "The Delft Geotechnical Centrifuge," *Centrifuge 91*, Balkema, Rotterdam, pp. 35–36.
[9] Allard, M. A., and Schenkeveld, F. M., 1994, "The Delft Geotechnics Model Pore Fluid for Centrifuge Tests," *Centrifuge 94*, Balkema, Rotterdam, pp. 133–138.
[10] Wang, C. X., 1981, *Hydraulic Control Sevosystems*, Mechanical Industry, Beijing.
[11] Li, H. R., 1981, *Hydraulic Control Systems*, National Defense Industry, Beijing.

Experimental Characterization of Compact Heat Exchangers With Short Flow Lengths at Simulated Elevated Altitudes

J. A. Mathias[1]
e-mail: mathias.32@osu.edu

J. Cao

M. E. Ewing

R. N. Christensen

Department of Mechanical Engineering,
The Ohio State University,
206 W. 28th Avenue
Columbus, OH 43210

This paper presents experimental pressure drop and heat transfer results of compact heat exchangers made with plain rectangular fins of short flowlengths tested with air at very low Reynolds numbers. Experiments were performed at sea level and at simulated elevated altitudes up to 25,298 m (83,000 ft). From the experimental results, the additional pressure drop of the air caused by the developing boundary layers and the hydrodynamic entrance length were determined. An equation was produced that predicted the average Nusselt number of the air, which significantly decreased with nondimensional length. The experimental results varied with respect to the aspect ratio of the rectangular duct and nondimensional length, which is inversely related to the Reynolds number.
[DOI: 10.1115/1.1516574]

Introduction

There is a need to design heat exchangers that operate in a subsonic high-altitude aircraft at altitudes up to 25,298 m (83,000 ft). These heat exchangers should impose a low pressure drop on the ambient air, while still transferring the required amount of heat. Compact heat exchangers made with plain rectangular fins of short lengths were examined to determine if they meet this need. Some of the most noted experimental and numerical research performed with compact heat exchangers and surfaces used in compact heat exchangers are discussed in the following paragraph.

Kays and London [1] measured heat transfer and pressure drop characteristics of fluids traveling along many surfaces used in heat exchangers, including an approximately 0.229 m (9 in.) square surface consisting of plain rectangular fins. Clark and Kays [2] determined the heat transfer of fluids in entire heat exchangers that were approximately 0.305 m (12 in.) long also consisting of plain rectangular fins. Montgomery and Wibulswas [3] numerically determined the average Nusselt number of a fluid traveling through rectangular ducts of different aspect ratios. Shah and London [4] extensively reviewed experimental and numerical literature about the heat transfer and pressure drop characteristics of fluids with developing or fully developed boundary layers traveling through rectangular ducts or other geometries.

Sparrow et al. [5] and Lundgreen et al. [6] both determined the additional pressure drop that results from the development of the boundary layers in the entrance region of rectangular ducts. Sparrow et al. accomplished this experimentally with two long rectangular ducts of different aspect ratios. Lundgreen et al. completed this numerically for many individual ducts of different aspect ratios. Fleming and Sparrow [7] and Han [8] both determined the length of the hydrodynamic entrance region in a rectangular duct. Fleming and Sparrow completed this experimentally with two ducts of different aspect ratios, whereas Han accomplished this numerically for ducts of many different aspect ratios.

The previous experimental research tested exchangers with long lengths and with fluids at atmospheric pressure. The research previously performed using numerical methods examined a single rectangular duct or other geometric shape and not an entire heat exchanger. None of the previous research that was found experimentally tested heat exchangers with plain fins of short lengths with fluids at pressures other than atmospheric. However, the design need requires heat exchangers with short lengths that perform adequately using air at subatmospheric pressure.

This paper presents and compares experimental pressure drop and heat transfer results collected at atmospheric and simulated elevated altitudes up to 25,298 m (83,000 ft) performed with compact heat exchangers made with plain rectangular fins of short lengths of 2.79 cm (1.100 in.) In all the experiments, the air traveling through the rectangular ducts was laminar with Reynolds numbers between 100 and 1000, and the boundary layers of the air are developing for the entire or large portion of the length of the duct. The additional pressure drop and heat transfer of the developing boundary layers are quantified in this paper.

Analysis

Compact Heat Exchangers. Compact heat exchangers are made in a plate-fin arrangement with plates separating the two different fluids. Fins are generally placed in the path of the fluids that are gases. These fins have parameters associated with them that help define the heat exchanger. These parameters are the distance between the fins called fin spacing (s), height of the fins (h_f), thickness of the fins (t), the length of the duct formed by the fins (L), and the total height in the nonflow direction (H). These parameters are shown in Fig. 1.

Once the parameters of the fins and plates are known, other relevant parameters are calculated. These are the hydraulic diameter of an individual rectangular duct formed by the rectangular fins, D_h, the aspect ratio, α, the free flow area, A_{ff}, and the porosity, σ; these parameters are defined in the Nomenclature Section. The aspect ratio was varied in the heat exchangers used in the experiments and is equal to the fin spacing divided by the fin height; because the fin height was always greater than the spacing, the aspect ratio varied between one and zero, corresponding to square ducts and parallel plates, respectively.

Pressure Drop Analysis of Compact Heat Exchangers. The pressure losses of the air traveling through a compact heat exchanger are mainly due to skin friction and to expansion and contraction in area. The heat exchangers tested in these experiments have relatively high porosities, greater than 70%; therefore,

[1]Corresponding author. Research Scientist, 506 Mahoning Court, Columbus, OH 43210.

Contributed by the Fluids Engineering Division for publication in the JOURNAL OF FLUIDS ENGINEERING. Manuscript received by the Fluids Engineering Division Mar. 27, 2001; revised manuscript received May 29, 2002. Associate Editor: A. K. Prasad.

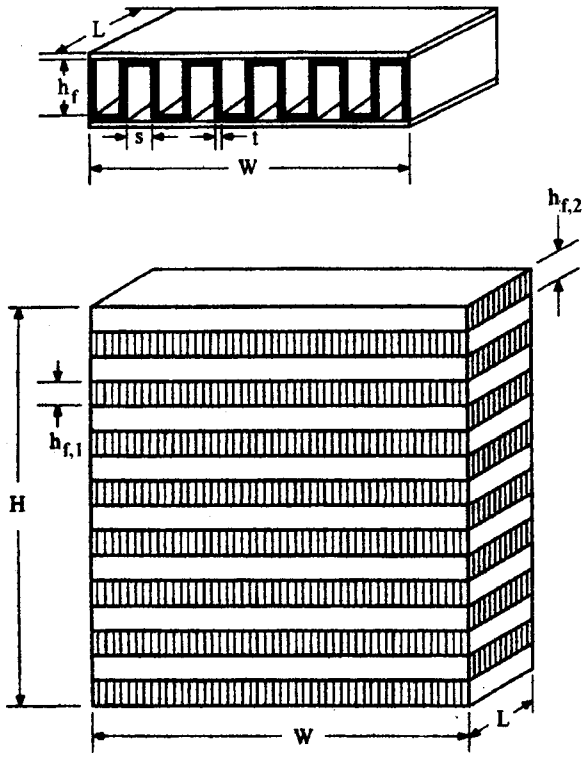

Fig. 1 Parameters of fins and overall design of a compact heat exchanger

the pressure drop is largely due to skin friction losses. Form losses were assumed to be negligible for flow around the thin fins and tubes; this assumption is more valid for flow around the fins than the tubes.

The pressure losses due to contraction and expansion occurred when the air entered and excited the heat exchanger. These losses always accounted for less than 10% of the total pressure drop; in a specific example of the heat exchanger with rectangular ducts of aspect ratio 1/6 being tested at a Reynolds number of 650, the pressure losses due to contraction and expansion of area was 4.6% of the total pressure drop measured. The pressure drop of air from these losses is calculated in Eq. (1) by using K_c and K_e for the loss coefficient for contraction or expansion, respectively. The contraction and expansion loss coefficients, K_c and K_e, are given in graphical form in Fox and McDonald [9]. These graphs were generated from the data of Streeter [10].

$$\Delta P = K_{c,e}\rho V^2/2 \tag{1}$$

The pressure loss of the air due to skin friction is a result of the shear force between the air and the duct wall, which is greater where the boundary layers of the air are developing and is constant in the laminar flow regime after the boundary layers are fully developed. Equation (2) calculates the pressure loss due to skin friction in both regions of the rectangular duct where the boundary layers are developing and fully developed, [11]. The first term on the R.H.S. of Eq. (2) accounts for the pressure drop in the fully developed region and f_{fd} for laminar flow is equal to a constant divided by Reynolds number. The term in Eq. (2) that includes K, accounts for the additional pressure drop in the region of a rectangular duct where the boundary layers of the air are developing. If the boundary layers of the air become fully developed in a duct, then K approaches a constant value of $K(\infty)$.

$$\Delta P = \left(\frac{4f_{fd}L}{D_h} + K\right)\frac{\rho V^2}{2}. \tag{2}$$

In the Results section, the results of the pressure drop experiments are shown with nondimensional parameters. Equation (3) defines a nondimensional pressure drop, referred to as loss coefficient, and Eq. (4) defines a nondimensional length. In Eq. (4), x represents a length over which the experimental measurements were made. Because the difference in pressure was measured before the inlet and after the exit of the heat exchanger, x corresponded to the length, L, of the rectangular duct.

$$\text{Loss coefficient} = \Delta P/(\rho V^2/2) \tag{3}$$

$$x^+ = \text{nondimensional length} = x/(D_h\,\text{Re}) \tag{4}$$

A relationship between nondimensional length and loss coefficient is shown in Eq. (5), which compares data from experimental flows to the theoretical pressure drop of flows with fully developed boundary layers from the entrance of the duct. This relationship, used by other researchers (e.g., [4]), is obtained from the pressure drop and the first term on the R.H.S. of Eq. (2). In the Results section this relationship is shown in a graph of the data of loss coefficient versus nondimensional length. These graphs show that the data have a greater loss coefficient at the same nondimensional length than theoretical flow because the boundary layers of the air are developing at the entrance of a rectangular duct; K represents the difference between these loss coefficients. The difference of the loss coefficients increases until the boundary layers of the flow become fully developed; after this occurs, the difference of the loss coefficients remain constant, represented by $K(\infty)$, so that a linear fit of the data and the line representing flow with fully developed boundary layers are parallel.

$$\frac{4f_{fd}x}{D_h} = \frac{4Cx}{D_h\,\text{Re}} = \frac{\Delta P}{\frac{1}{2}\rho V^2} = 4Cx^+ \tag{5}$$

Heat Transfer Analysis of Compact Heat Exchangers. The objective of the heat transfer experiments was to determine the average heat transfer coefficient and average Nusselt number of the air in the compact heat exchanger. Heat was transferred to the air by flowing heated water through the inside of the tubes of the heat exchanger. The heat transfer coefficient of the air was calculated by first calculating the overall heat transfer coefficient times area, UA, shown in Eq. (6).

$$\dot{Q} = UA\ \ F\Delta T_{\text{lm}} \tag{6}$$

The total rate of heat transferred, $\dot{Q}$, was calculated from an average of the heat lost by the water and the heat gained by the air, which amounts always agreed within 3% of each other. The log-mean temperature difference, ΔT_{lm}, was calculated for countercurrent flow and a correction factor, F, was used to account for cross flow versus countercurrent flow and was always within 2% of unity. After UA was calculated, the average heat transfer coefficient of the air was calculated from the following equation.

$$1/UA = 1/(\eta_{o,\text{air}}h_{\text{air}}A_s) + t_p/(k_pA_p) + 1(\eta_{o,\text{water}}h_{\text{water}}A_s) \tag{7}$$

The heat transfer coefficient of the water, h_{water}, was calculated from a correlation by Gnielski [12] and the accuracy of this correlation was stated to be equal to or better than 10% of the calculated value. The heat transfer coefficient of the water was very large; the thermal resistance of the water and metal wall always represented less than 5% of the total thermal resistance of the system, which allowed for good accuracy when calculating the thermal resistance of the air. The overall surface efficiencies of the air and water side, $\eta_{o,\text{air}}$ and $\eta_{o,\text{water}}$, were calculated by knowing the efficiency of the fins on the air and water sides from Eq. (8); there were fins in the water side due to the internal ribs of the tubes. Equation (9) calculated the efficiency of a fin that has no heat transfer at the tip. Because of symmetry in a compact heat exchanger, in Eq. (9) l is equal to one half of the height of the fin and the parameter "m" is defined in Eq. (10).

Table 1 Parameter of the fins used in compact heat exchangers

Aspect Ratio	Fin Pitch Fins/cm (Fins/in.)	Fin Height cm (in.)	Fin Length cm (in.)	Fin Thickness Cm (in.)	Hydraulic Diameter, D_h cm (in.)
1/3	3.9 (10.0)	0.737 (0.290)	2.794 (1.1)	0.0127 (0.005)	0.363 (0.143)
1/6	3.9 (10.0)	1.468 (0.578)	2.794 (1.1)	0.0127 (0.005)	0.414 (0.163)
1/9	3.9 (10.0)	2.184 (0.860)	2.794 (1.1)	0.0127 (0.005)	0.434 (0.171)
1/15	5.9 (15.0)	2.362 (0.930)	2.794 (1.1)	0.0127 (0.005)	0.295 (0.116)

$$\eta_o = 1 - (1 - \eta_f) A_f / A_s \tag{8}$$

$$\eta_f = \tanh(ml)/(ml) \tag{9}$$

$$m = [(h_{\text{avg}} p_f)/(k_f A_{cf})]^{1/2} \tag{10}$$

The average heat transfer coefficient of the air is implicit in these equations because it appears in the parameter "m" and in the equation of overall heat transfer coefficient times area, hence the equations must be solved iteratively. Lastly, after the average heat transfer coefficient of the air was calculated, the average Nusselt number of the air was calculated by Eq. (11).

$$\text{Nu} = h_{\text{air}} D_h / k_{\text{air}} \tag{11}$$

Experimental Setup

Four heat exchangers were made with rectangular fins that formed rectangular ducts of aspect ratios of 1/3, 1/6, 1/9, and 1/15. Table 1 shows the important parameters of the rectangular fins. The length of each aluminum tube and the rectangular ducts that the air traveled through was 2.79 cm (1.100 in.). The total width (W) of each heat exchanger and each section of fins was 0.305 m (1.00 ft.). The height of each aluminum tube was 0.241 cm (0.095 in.). The total height (H) of the heat exchanger was required to be less than 0.305 m (1.00 ft.) to fit into the experimental apparatus that was built to test the heat exchangers; therefore, the total height of each heat exchanger was determined by the number of fin and tube sections that could be brazed together and still have the height be less than 0.305 m (1.00 ft.).

Ewing [13] constructed the experimental apparatus, a diagram of which is shown in Fig. 2, that allowed pressure drop and heat transfer measurements to be taken of the air traveling through the ducts of the compact heat exchangers. In the following paragraphs, the path of the air is described as it traveled through the experimental apparatus and the rectangular ducts of the heat exchanger.

Air was drawn through a bell-mouth opening and then traveled through a screen with square holes of length 1.1 mm (0.045 in.). The air then traveled through a honeycomb section that acted as a flow straightener that had round holes with a diameter of 0.63 cm (0.25 in.) and a length of 20.3 cm (8.0 in.). After the flow straightener, the air traveled through another screen similar to the first one and then entered and exited the ducts of the compact heat exchanger. Then the air entered into another 0.3048 m (1.00 ft.) square box that is 19.1 cm (7.5 in.) long and proceeded 0.914 m (3.00 ft.) through a 10.16 cm (4.00 in.) diameter PVC pipe to a vortex shedding flowmeter, which measured the volumetric flow rate of air. The density and mass flow rate of the air were calculated by measuring the temperature and pressure of the air at the flow meter. Following this, the air proceeded down the PVC pipe to the fan and then outside.

A manometer that was connected to pressure taps that were before and after the heat exchanger measured the difference in static pressure of the air before and after the rectangular ducts of the heat exchanger. From the pressure drop measurements, the loss coefficient was calculated by subtracting the pressure drop due to the contraction and expansion of the air from the measured pressure drop and then dividing this term by $\rho V^2/2$.

Heat transfer experiments were performed by passing air through the experiment as just described and by flowing water through the inside of the tubes of the heat exchanger. After the water exited the tubes it was pumped past electrical immersion heaters, which transferred heat back to the water, then the water flowed into a reservoir and to the inlet of the pump. Temperatures of air and water were approximately steady after 30 minutes of operation and were recorded when all temperatures varied less than 0.6°C (1°F) over a ten minute period.

Results and Discussion

Pressure Drop Experiments at Isothermal Conditions. Many experiments were performed from which data of K and x^+ were calculated; the values of K increased at small values of x^+ and were approximately constant at larger values of x^+. Values of $K(\infty)$ for ducts of aspect ratios of 1/3, 1/6, 1/9, and 1/15 were determined by averaging the approximately constant values of K at larger values of x^+. An equation of the form of Eq. (12) was used to predict K at any x^+. C_1 is a constant determined from the curve fit of the data and depends on the aspect ratio of the rectangular duct. C_1 was positive for each heat exchanger made with rectangular ducts of a different aspect ratio; therefore, K approached $K(\infty)$ as the nondimensional length approached infinity and was zero when x^+ was zero. The nondimensional hydrodynamic entrance length, L_{hy}^+, needed for the boundary layers of the

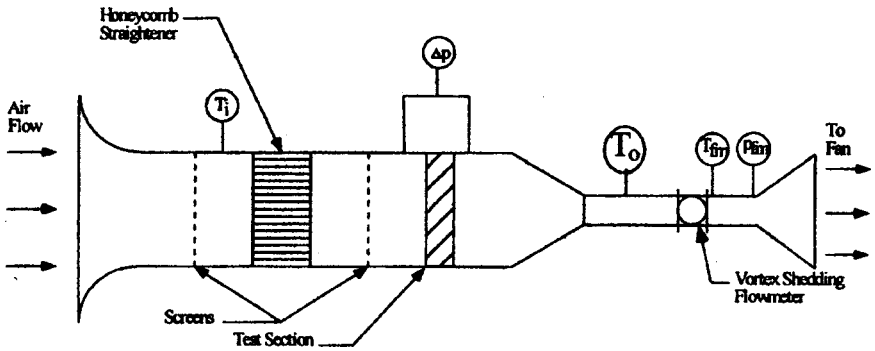

Fig. 2 Diagram of the experimental apparatus

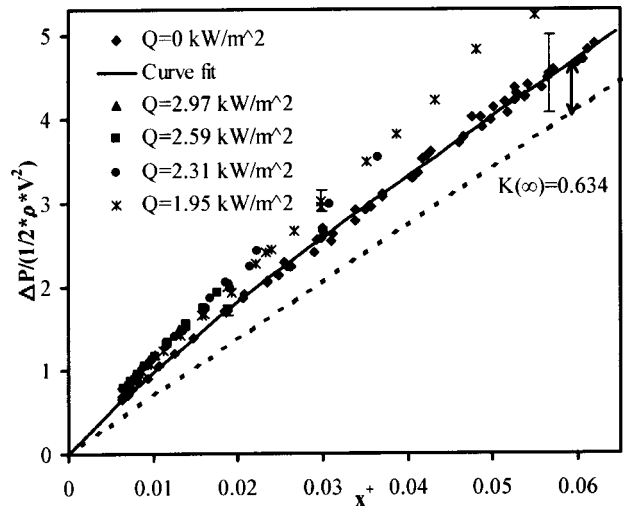

Fig. 3 Loss coefficient versus x^+ for rectangular ducts with an aspect ratio of 1/3

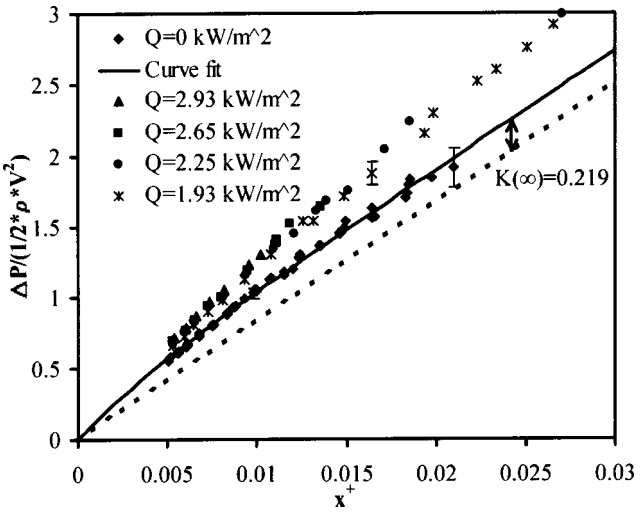

Fig. 5 Loss coefficient versus x^+ for rectangular ducts with an aspect ratio of 1/9

air to become fully developed was calculated by assuming that the boundary layers were fully developed when $K/K(\infty)$ of the curve fit was equal to 0.98.

$$\frac{K}{K(\infty)} = 1 - e^{-C_1 x^+} \tag{12}$$

The results of the experiments are shown in a graph of $\Delta P/(0.5\rho V^2)$ versus x^+ in Figs. 3–6 for heat exchangers made with rectangular ducts of aspect ratios of 1/3, 1/6, 1/9, and 1/15, respectively. Each graph shows $K(\infty)$ and the curve fit from Eq. 12 and Table 2 shows all the important results from the data points collected at isothermal conditions, such as $K(\infty)$, L_{hy}^+, and constant C_1 of Eq. (12).

Many trends were seen from the results of the pressure drop experiments performed at isothermal conditions. The pressure drop data at large nondimensional lengths for each aspect ratio were parallel to the line representing flow with fully developed boundary layers. This supports the published friction factor values of the aspect ratios tested. The additional pressure drop due to the developing boundary layers significantly increased as the aspect ratio increased from 1/6 to 1/3, as shown in Figs. 4 and 3, respectively. The additional pressure drop due to the developing boundary layers did not increase significantly for the heat exchangers made with ducts with aspect ratios of 1/6, 1/9, and 1/15, as shown in Fig. 4–6, respectively. The nondimensional hydrodynamic entrance length, L_{hy}^+, decreased by approximately one half between the ducts of aspect ratios of 1/3 and 1/6, and 1/6 and 1/9. The boundary layers developed in such a short distance for the ducts of an aspect ratio of 1/15 that it was not possible to detect an entrance length from the experimental data, as shown in Fig. 6.

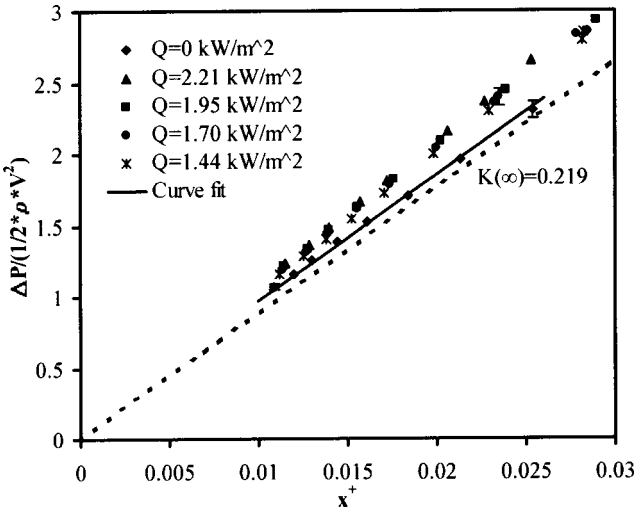

Fig. 6 Loss coefficient versus x^+ for rectangular ducts with an aspect ratio of 1/15

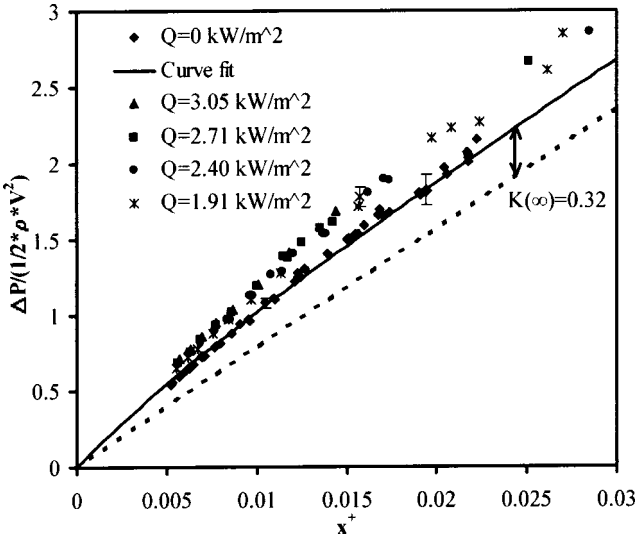

Fig. 4 Loss coefficient versus x^+ for rectangular ducts with an aspect ratio of 1/6

Table 2 Major results from the experiments performed at isothermal conditions

Aspect Ratio	$K(\infty)$	Entrance Length, L_{hy}^+	C_1 of Eq. (12)	Fully Developed Friction Factor, $f=4C/\mathrm{Re}$
1/3	0.634	0.0641	61.16	68.47/Re
1/6	0.320	0.0315	125.54	79.06/Re
1/9	0.219	0.0166	237.02	83.85/Re
1/15	0.0905			88.31/Re

Pressure Drop Experiments With Heat Transfer Simultaneously Occurring. Figures 3–6 show the data points collected from the pressure drop experiments performed with heat transfer simultaneously occurring with heat exchangers made with ducts of aspect ratios of 1/3, 1/6, 1/9, and 1/15, respectively. This data at nonisothermal conditions had greater loss coefficients at the same nondimensional length than the pressure drop experiments at isothermal conditions.

Two factors were identified that contributed to the larger loss coefficients for the pressure drop experiments with heat transfer simultaneously occurring. The first factor is the velocity of the air at the exit of the heat exchanger was greater than the velocity of the air at the inlet of the heat exchanger due to the decrease in density of the higher temperature air for the experiments performed with heat transfer occurring. The static pressure drop was greater for the experiments with heat transfer occurring due to the difference in the velocity and momentum at the inlet and exit of the heat exchanger.

A greater pressure drop also resulted from the greater viscosity of the air in the pressure drop experiments that were performed with heat transfer occurring. The results were calculated assuming an air viscosity at the average bulk temperature of the air at the inlet and exit of the heat exchanger; however, a more accurate calculation of air viscosity would be to calculate it at the temperature of the wall, which for these experiments was very close to the temperature of the water.

The values of K were recalculated accounting for the change in density and calculating the viscosity of the air at the temperature of the water; the recalculated values compared very closely to the values of K that were obtained at isothermal conditions. Therefore the differences in the values of K were accounted for by variations in density and viscosity of the air.

Pressure Drop Experiments at Simulated Elevated Altitudes. Pressure drop and heat transfer measurements were obtained at simulated elevated altitudes by placing the apparatus in a chamber that remained partially evacuated as the specified flow rate of air passed through the experimental apparatus. The experiments at simulated elevated altitudes were performed in the following way. First, the chamber was partially evacuated to simulate an altitude of 4572 m (15,000 ft.) and the flow rate of air through the experiment was adjusted to correspond to a Reynolds number of approximately 250. When the conditions were steady, the pressure drop across the heat exchanger and the temperatures of the air and water were recorded. After this, the chamber was further evacuated to simulate an altitude of 9144 m (30,000 ft) and the procedure was repeated at this altitude and at altitudes of 15,240 m (50,000 ft), 19,202 m (63,000 ft), 24,384 m (80,000 ft), and 25,298 m (83,000 ft).

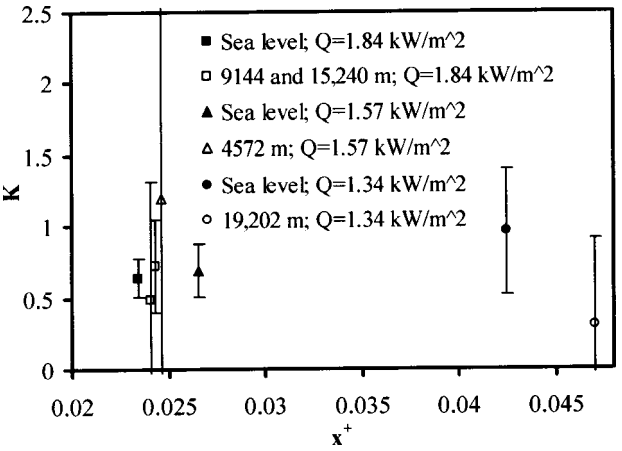

Fig. 8 Comparison between sea level and elevated altitude for aspect ratio 1/9

The pressure drop data collected from the experiments performed at sea level and at simulated high altitude conditions are compared in graphs of K versus x^+ in Fig. 7–9, corresponding to ducts of aspect ratios of 1/3, 1/9, and 1/15, respectively. In Fig. 7, the values of K compare very well for the experiments performed at simulated altitudes of 4572 and 9144 m to the experiments performed at sea level at the same x^+ value and with the same amount of heat transfer occurring. The values of K compare reasonably well for the experiment performed at a simulated altitude of 19,202 m to the corresponding experiment performed at sea level. In Fig. 8 the values of K compare very well for the experiments performed at simulated altitudes of 9144 and 15,240 m to the experiments performed at sea level. In Fig. 9, three of the four values of K of the experiments performed at simulated altitudes of 4572 and 9144 m and at sea level compare very well. The values of K somewhat differ between the experiments performed at a simulated altitude of 19,202 m and sea level.

Generally, these experiments indicate a good correlation between pressure drop experiments performed at sea level and at simulated elevated altitude at the same x^+ value, which corresponds to the same Reynolds number because x and D_h remained constant. Therefore, from the good correlation of results between the pressure drop experiments performed at sea level and simu-

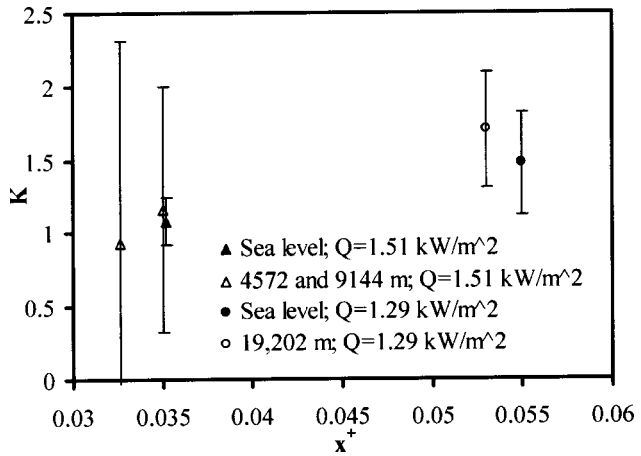

Fig. 7 Comparison between sea level and elevated altitude for aspect ratio 1/3

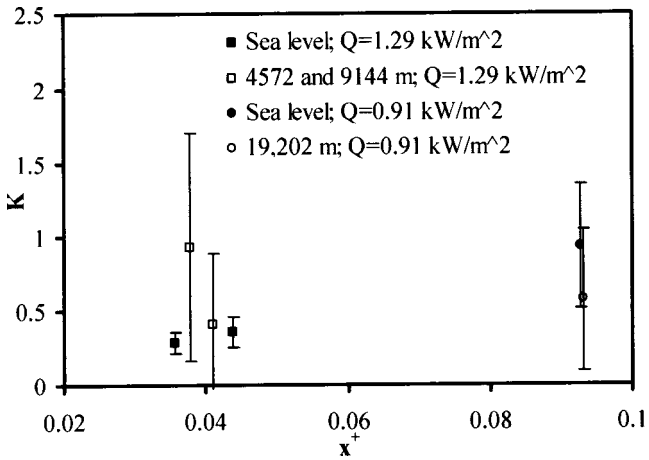

Fig. 9 Comparison between sea level and elevated altitude for aspect ratio 1/15

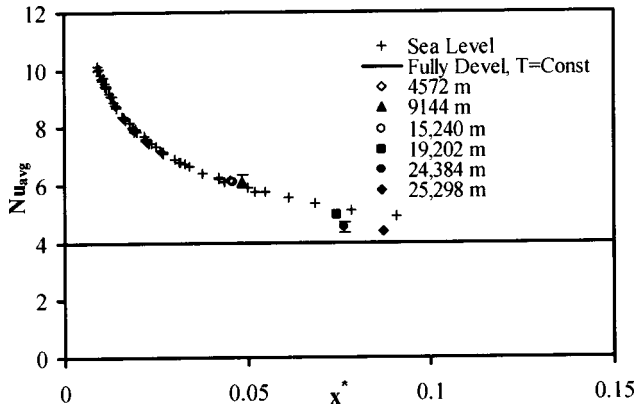

Fig. 10 Heat transfer experiments for aspect ratio 1/3

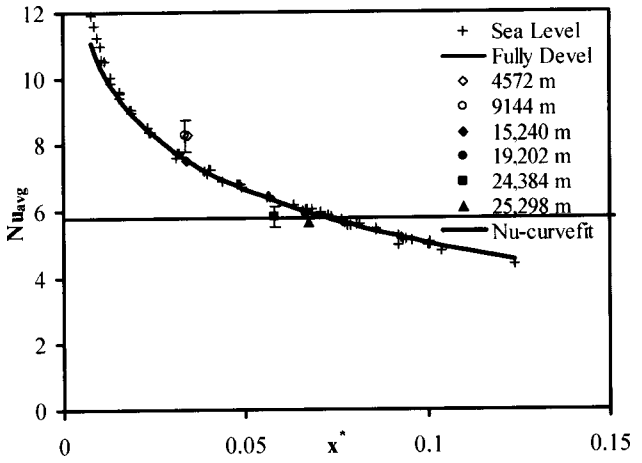

Fig. 12 Heat transfer experiments and graph of Eq. (13) for aspect ratio 1/9

lated elevated altitudes, heat exchangers tested at sea level conditions will perform comparably at elevated altitudes.

The confidence intervals of the data from the pressure drop experiments performed at simulated elevated altitudes are relatively large due to the manometer used during the experiments. Confidence that the results from the pressure drop experiments performed at sea level and simulated elevated altitudes are nearly equivalent is gained from the pressure drop data with smaller confidence intervals and correct trends are seen when examining all the data together. The experimental results with relatively large confidence intervals are presented to show the complete set of experimental data and no conclusions were made from this portion of data.

Heat Transfer Experiments. The results of the heat transfer experiments are shown in graphs of Nu_{avg} versus nondimensional thermal length, x^* in Figs. 10–13 for heat exchangers with rectangular ducts of aspect ratios of 1/3, 1/6, 1/9, and 1/15, respectively. The trends of these experimental data show that the Nusselt number for laminar flow through short rectangular ducts, less than 2.8 cm (1.1 in.), depends on the aspect ratio and x^*, which is inversely proportional to Reynolds number. Also, illustrated in these graphs is the increase in the average Nusselt number of the air due to the developing boundary layers of the air. In Figs. 10–12, the average Nusselt number decreased significantly as x^* values increased to 0.025. The Nusselt number continued to decrease at a lower rate as the x^* value increased to values greater than 0.025. The Nusselt numbers appear to be decreasing at the largest x^* values for the experiments performed with aspect ratios of 1/6, 1/9, and 1/15.

The Nusselt numbers calculated from the experiments with ducts of aspect ratios of 1/3, and 1/6 at larger x^* values very closely approach the theoretical Nusselt number for flow with fully developed boundary layers at a constant wall temperature. Comparing the data to Nusselt numbers corresponding to constant wall temperature condition is more appropriate due to the high flow rate of water inside the tubes, which resulted in essentially a constant wall temperature. The Nusselt numbers calculated from the experiments with rectangular ducts of aspect ratios of 1/9 and 1/15, fall below the theoretical Nusselt numbers. There is a trend noticed that as the aspect ratio decreases the average Nusselt number further decreases below the fully developed value. Also, the experimental Nusselt numbers appear to be approximately equal at x^* values of 0.1 for all the heat exchangers tested; however, the theoretical Nusselt number for fully developed boundary layers increases as the aspect ratio decreases. The following paragraphs give possible explanations for the experimental Nusselt numbers decreasing below the theoretical value.

The theoretical Nusselt numbers for flow with fully developed boundary layers at a constant wall temperature were determined by numerical methods for a single rectangular duct and by assuming that heat conduction in the axial direction of the fluid is negligible, [3]. Singh [14] determined that in circular tubes, heat conduction in the axial direction is negligible for fluids with Peclet numbers (Pe) greater than 100. Many experiments were performed with air at low Reynolds numbers, which resulted in Peclet numbers of approximately 70, therefore axial conduction may have been significant in these experiments. Axial conduction

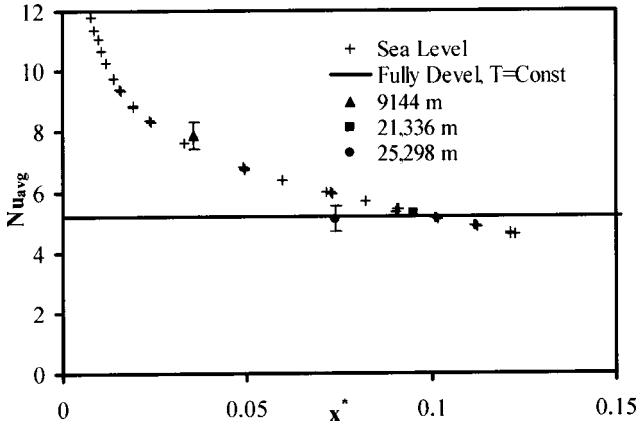

Fig. 11 Heat transfer experiments for aspect ratio 1/6

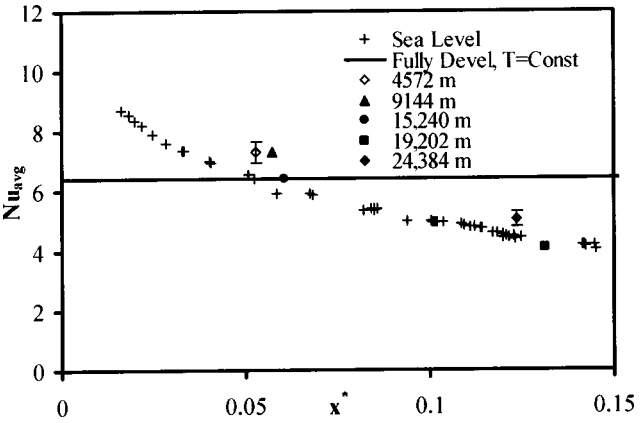

Fig. 13 Heat transfer experiments for aspect ratio 1/15

would decrease the temperature difference between the air and the wall and decrease the heat transfer to the air and the Nusselt numbers calculated from the experiments because the Nusselt numbers were calculated from the amount of energy gained by the air. Taitel and Tamir [15] determined that the Nusselt number for fully developed flow in round tubes decreased 5% below the fully developed value at a Peclet number of 50. In addition axial conduction in the fluid may be more significant in the region where the boundary layers are developing or in certain aspect ratios of rectangular ducts.

The geometry of a compact heat exchanger with many rectangular ducts is significantly different than a single rectangular duct; this difference in geometry may partially account for the experimental Nusselt numbers falling below the theoretical Nusselt number. In addition, the air could have experienced some nonideal flow such as separation from the fin or tube as it entered or exited the rectangular duct and this would impact the heat transfer ability and Nusselt number of the air.

The graph of Nusselt number versus nondimensional thermal length of each aspect ratio is represented well by a logarithmic curve. Equation (13) was obtained for the Nusselt number, which is valid for aspect ratios between 1/15 and 1/3, for nondimensional thermal lengths between 0.01 and 0.12, and for Reynolds numbers between 100 and 1000. The raw correlation coefficient (R^2) factor for this equation compared to all the experimental data is equal to 0.9986 and the average percent error between the equation and the experimental measurements is 3.1%. The greatest percent error occurred at the smallest and largest nondimensional thermal lengths. The graph of the experimental data collected from the heat exchanger made with rectangular ducts with an aspect ratio of 1/9 is shown along with the graph of Eq. (13) in Fig. 12.

$$\mathrm{Nu} = -2.3393^* \ln(x^*) - 3.2870^*(\alpha)$$

$$0.01 < x^* < 0.12, \quad 1/15 < \alpha < 1/3, \quad \text{and} \quad 100 < \mathrm{Re} < 1000 \quad (13)$$

Comparisons to Other Studies. The experimental results were compared to experimental or numerical results of other studies. The values of $K(\infty)$ were compared to $K(\infty)$ values obtained by numerical methods by Lundgren et al. [6] and the experimental values obtained by Sparrow et al. [5]. When calculating $K(\infty)$, Lundgren et al. [6] assumed the air had a uniform velocity profile at the entrance of the duct and a fully developed velocity profile at a downstream distance greater than the entrance length. The momentum of the air with a fully developed profile is greater than the momentum of the air at the entrance of the duct with a uniform velocity profile. This necessary increase in momentum comes at the expense of a greater pressure drop and hence a substantially greater $K(\infty)$. Sparrow et al. [5] measured the pressure of the air before it entered a single rectangular duct and in the duct where the boundary layers are fully developed; hence, the air also experienced an increase in momentum in the rectangular duct.

The present experiments measured the pressure drop before the air entered the duct and after the air exited the duct, both locations having an approximately uniform velocity profile of the air; therefore, the momentum of the air was equal where the pressure drop measurements were made, from which $K(\infty)$ was calculated. The momentum difference reported by Lundgren et al. [6] was added onto the $K(\infty)$ of the present data and the favorable comparisons between the three different studies are shown in Fig. 14.

The hydrodynamic entrance lengths calculated from the curve fit of the pressure drop data were compared to the numerical studies of Fleming and Sparrow [7] and Han [8]. This study determined the hydrodynamic entrance length to be the length where $K/K(\infty) = 0.98$; whereas Fleming and Sparrow [7] determined the entrance length to be where $K/K(\infty) = 0.95$. Han [8] determined the entrance length as the distance where the centerline velocity is 99% of the fully developed centerline velocity, i.e., u_o/u_∞

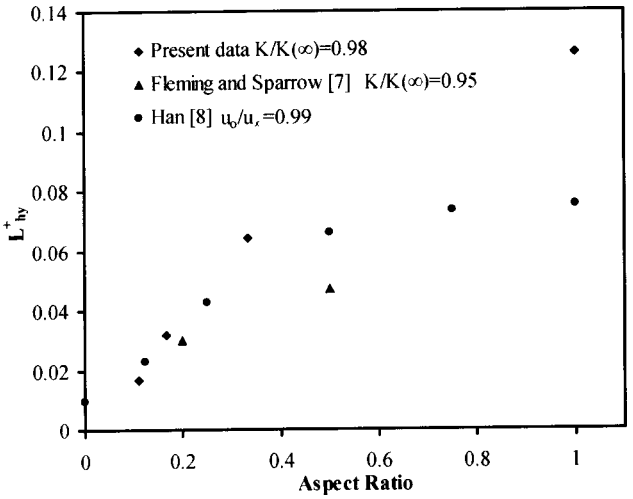

Fig. 15 Comparison of entrance lengths of the present data to previous studies

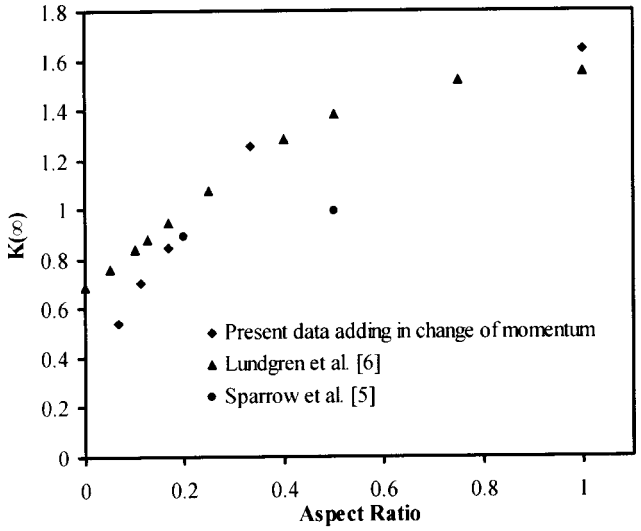

Fig. 14 Comparison of $K(\infty)$ of the present data to previous studies

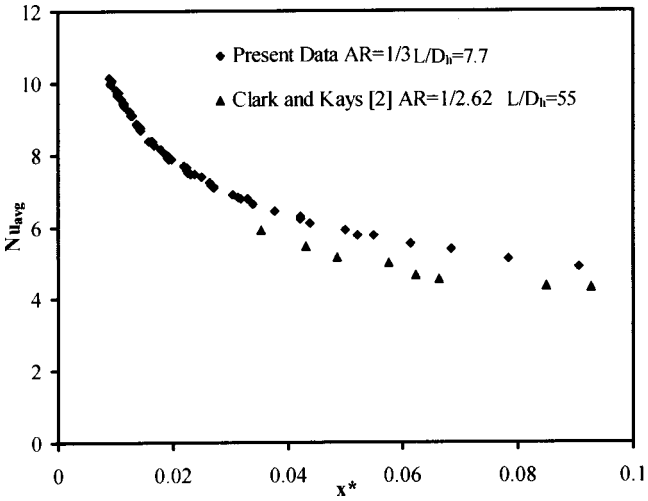

Fig. 16 Comparison of Nusselt numbers of the present data to a previous study

$=0.99$. The entrance lengths calculated from the present experiments and the two previous studies are shown in Fig. 15 and compare well at aspect ratios less than 0.4; there are noticeable discrepancies at larger aspect ratios.

The Nusselt numbers calculated from the heat transfer experiments were compared to the experimental Nusselt numbers calculated by Clark and Kays [2]. Clark and Kays [2] tested a compact heat exchanger made with rectangular ducts with an aspect ratio of 1/2.62 and a length of 12 in. The rectangular ducts of the heat exchanger tested by Clark and Kays [2] had a ratio of length-to-hydraulic-diameter of 55; whereas, the rectangular ducts tested in this study had an aspect ratio of 1/3, a length of 1.1 in., and a length to hydraulic diameter ratio of 7.7. Clark and Kays [2] performed the heat transfer experiments with air at Reynolds numbers between 840 and 2200; whereas, the experiments of this study were performed with air at Reynolds numbers between 120 and 1150.

The Nusselt numbers calculated from the experiments by Clark and Kays [2] are shown in Fig. 16 and illustrate that there is not a large increase in the Nusselt number calculated from the experiments due to the fact that the rectangular ducts were relatively long compared to the length of the developing boundary layers. The Nusselt numbers of this study are slightly greater than those obtained by Clark and Kays [2] because of the slightly different aspect ratios of the heat exchangers tested. There is no literature available where the developing boundary layers represent a large portion of the relatively short rectangular duct, therefore, there is no comparison to the Nusselt numbers of the present experiments performed at nondimensional thermal lengths less than 0.035.

Uncertainty Analysis

An uncertainty analysis was performed to determine the accuracy of $\Delta P/(0.5\rho V^2)$, K, and Nusselt number, and to determine how sensitive these values are to measurements taken during the experiment. The measurements that affect the calculation of $\Delta P/(0.5\rho V^2)$ and K are the pressure drop across the heat exchanger measured by a manometer, the flow rate of air measured by a vortex shedding air flowmeter, the pressure reading at the flowmeter measured by a U-tubed manometer, the atmospheric pressure measured by a barometer, and the inlet and exit temperature of the air measured by thermocouples. The pressure drop measurement directly affects $\Delta P/(0.5\rho V^2)$, which is also used to calculate K. The accuracies of the other measurements affect the calculation of the mass flow rate and density of air that are used to calculate the average velocity, the calculation of $\Delta P/(0.5\rho V^2)$, and the pressure drop of theoretical flow with fully developed boundary layers.

The effect that the accuracy of these measurements have on $\Delta P/(0.5\rho V^2)$ and K is determined by computing the partial derivative of $\Delta P/(0.5\rho V^2)$ or K with respect to a measurement and then multiplying this by the accuracy of the instrument. The partial derivatives were calculated numerically and the accuracy of each measurement device was determined by the accuracy reported by the manufacturer or by general observations. This procedure is repeated for each measurement that affects the value of $\Delta P/(0.5\rho V^2)$ or K. After each of these products of the partial derivative with respect to the measurement multiplied by the accuracy of the measurement are obtained, they are each squared, summed together and then the square root is taken of this sum, as described by Moffat [16]. This method to calculate the accuracy of K in this experiment is shown in Eq. (14). The accuracy of $\Delta P/(0.5\rho V^2)$ was calculated by replacing K with $\Delta P/(0.5\rho V^2)$ in Eq. (14).

$$K=\left[\begin{array}{l}\left(\dfrac{\partial K}{\partial \text{Press Drop}}\right)^2(\Delta \text{ Manometer})^2+\left(\dfrac{\partial K}{\partial \text{Exit Temp}}\right)^2(\Delta \text{ Thermocouple})^2+\\ \left(\dfrac{\partial K}{\partial \text{Flowmtr Press}}\right)^2(\Delta \text{ Flowmtr Press})^2+\left(\dfrac{\partial K}{\partial \text{Flowmeter}}\right)^2(\Delta \text{ Flowmeter})^2+\\ \left(\dfrac{\partial K}{\partial \text{Atm Pressure}}\right)^2(\Delta \text{ Barometer})^2+\left(\dfrac{\partial K}{\partial \text{Inlet Temp}}\right)^2(\Delta \text{ Thermocouple})^2\end{array}\right]^{1/2} \tag{14}$$

The accuracy reported by the manufacturer for the manometer used in the experiments performed at sea level conditions is ± 0.062 Pa (± 0.00025 inches of water). After experimentally determining the repeatability of the manometer and accounting for possible vibrations, it was decided to use an accuracy of the manometer of ± 0.093 Pa (± 0.000375 inches of water). For the experiments performed at simulated elevated altitude conditions the accuracy of the monometer was ± 1.24 Pa (± 0.005 inches of water).

The accuracy of the air flowmeter was reported by the manufacturer as $\pm 1\%$ of the measurement. The value of $\Delta P/(0.5\rho V^2)$ or K is affected very little by the accuracy of the thermocouples, the barometric pressure, and the pressure measured at the flowmeter. The accuracy of these devices is more than adequate for the experiments performed.

The value $\Delta P/(0.5\rho V^2)$ or K is very sensitive to the accuracy of the pressure drop measurement. Pressure drop is very low through relatively short rectangular ducts. The uncertainty of the manometer can be as large as 10% of the total pressure drop measurement. To decrease the significance of one pressure drop measurement, for each experimental data point at sea level conditions, the pressure drop was measured five times and the average pressure drop was used. There were many data points collected for each heat exchanger at isothermal conditions to assure that the measurements were repeatable.

$\Delta P/(0.5\rho V^2)$ or K is somewhat sensitive to the measurement of the volumetric flow rate of air, used to calculate an average velocity through each rectangular duct. When pressure drop measurements were being made, the volumetric flow rate was recorded every four seconds for approximately a two-minute interval. The average volumetric flow rate from the two-minute interval was used to calculate the average velocity through each rectangular duct of the heat exchanger that was being tested.

The accuracy of $\Delta P/(0.5\rho V^2)$ or K was determined for each experimental data point by using Eq. (14). The confidence intervals are shown in Figs. 3–6 for $\Delta P/(0.5\rho V^2)$ and Figs. 7–9 for K. The confidence intervals of $\Delta P/(0.5\rho V^2)$ become significantly larger at larger values of x^+ due to the smaller pressure drop measured from the experiment. The confidence intervals become

large for the values of K for the experiments at simulated elevated altitudes but there is good correlation between much of the data and correct trends in the data can be seen.

A typical example given of the accuracy of the pressure drop experiment performed at sea level with the heat exchanger made with rectangular ducts with an aspect ratio of 1/9. The flow rate of this particular experiment resulted in a Reynolds number of 348. For this experiment the nominal value of K was 0.244 and the accuracy calculated was ± 0.139. The accuracy of the manometer measuring the pressure drop accounted for 78% of the total accuracy of K.

The confidence intervals shown for the Nusselt numbers in Figs. 10–13 were calculated using an equation in the same form as Eq. (14); the equation used the accuracy of the thermocouples measuring the inlet and exit temperatures of the air and the water, and the flowmeters measuring the air and water flow rates.

Conclusions

The additional pressure drop due to the developing boundary layers was calculated for ducts of different aspect ratios. Also, the length of the region where the boundary layers are developing was determined for ducts of specific aspect ratios and a curve fit was obtained that calculated K at any location in the developing region of a rectangular duct. Values of K were comparable at the same nondimensional length for the experiments performed at simulated elevated altitudes and sea level; therefore, heat exchangers can be tested at sea level conditions to determine the pressure drop at elevated altitudes.

The average Nusselt number was predicted by the aspect ratio of the duct and the nondimensional thermal length; the increase in the average Nusselt number was noticeable at small nondimensional thermal lengths, which is attributed to the boundary layers developing in a significant portion of the rectangular duct. The average Nusselt number of the air decreased below the theoretical fully developed values at experiments performed at larger nondimensional lengths for aspect ratios of 1/9, and 1/15. This decrease may be partially attributed to axial conduction occurring and the difference in geometry between many ducts of a heat exchanger and a single rectangular duct.

Acknowledgments

The experimental testing of compact heat exchangers reported in this paper was funded by a grant from the NASA-Glenn Research Center. In addition, appreciation is expressed to David Bents at the NASA-Glenn Research Center for technical contributions.

Nomenclature

A_{cd} = cross-sectional area of a duct
A_{cf} = cross-sectional area of a fin
A_f = surface area of fins
A_{ff} = free flow area $= Wh_f s/(t+s)[H/(h_{f,1}+h_{f,2})]$
A_s = total surface area
c_p = specific heat
C = constant of friction factor for fully developed laminar flow
C_1 = constant of the curve fit of Eq. (12)
D_h = hydraulic diameter $= 4A_{cd}/p_w = 4h_f s/(2(h_f+s))$
F = factor to account for cross flow
f_{fd} = fanning friction factor in the fully developed region
h_{avg} = heat transfer coefficient
h_f = height of rectangular fins
H = total height of heat exchanger
k = conductivity
K_c = contraction loss coefficient
K_e = expansion loss coefficient
K = coefficient for calculating additional pressure drop due to the developing boundary layers
$K(\infty)$ = constant value of K, $x^+ \geqslant L_{hy}^+$
l = one-half the height of a fin
L = flow length of rectangular duct
L_{hy}^+ = nondimensional entrance length
m = parameter to calculate fin efficiency
Nu_{avg} = Nusselt number $= h_{\text{avg}} D_h/k$
p_f = perimeter of fin
p_w = wetted perimeter of duct
ΔP = static pressure drop
P = static pressure of air
Pe = Peclet number = Re*Pr
Pr = Prandtl number $= c_p \mu/k$
$\dot{Q}$ = total rate of heat transferred
R = correlation coefficient
Re = Reynolds number $= \rho V D_h/\mu$
s = spacing of rectangular fins
T = temperature
t = thickness of rectangular fins
UA = overall heat transfer coefficient times area
u_o = centerline velocity
u_∞ = fully developed centerline velocity
V = average air velocity through a rectangular duct
W = width of rectangular fin section
x = length along a rectangular duct
x^+ = nondimensional length $= x/(D_h \text{ Re})$
x^* = nondimensional thermal length $= x/(D_h \text{ Re Pr})$

Greek Letters

α = aspect ratio $= s/h_f$, $0 \leqslant \alpha \leqslant 1$
η_f = fin efficiency
η_o = overall surface efficiency
μ = viscosity
ρ = density
σ = porosity $= A_{ff}/(W^*H)$

Subscripts

a = air
avg = average
f = fin
fm = flowmeter
i = inlet
lm = log-mean average
o = outlet
p = plate

References

[1] Kays, W. M., and London, A. L., 1984, *Compact Heat Exchangers*, 3rd Ed., McGraw-Hill, New York.
[2] Clark, S. H., and Kays, W. M., 1953, "Laminar-Flow Forced Convection in Rectangular Tubes," Trans. ASME, **75**, pp. 859–866.
[3] Shah, R. K., and London, A. L., 1978, *Laminar Flow Forced Convection in Ducts*, Academic Press, San Diego, CA.
[4] Sparrow, E. M., Hixon, C. W., and Shavit, G., 1967, "Experiments on Laminar Flow Development in Rectangular Ducts," Transaction of the ASME. J. Basic Eng., **89**, pp. 116–124.
[5] Lundgren, T. S., Sparrow, E. M., and Starr, J. B., 1964, "Pressure Drop due to the Entrance Region in Ducts of Arbitrary Cross Section," Transaction of the ASME. J. Basic Eng., **86**, pp. 620–626.
[6] Fleming, D. P., and Sparrow, E. M., 1969, "Flow in the Hydrodynamic Entrance Region of Ducts of Arbitrary Cross Section," ASME J. Heat Transfer, **91**, pp. 345–354.
[7] Han, L. S., 1960, "Hydrodynamic Entrance Lengths for Incompressible Laminar Flow in Rectangular Ducts," ASME J. Appl. Mech., **28**, pp. 403–409.
[8] Montgomery, S. R., and Wibulswas, P., 1967, "Laminar Flow Heat Transfer for Simultaneously Developing Velocity and Temperature Profiles in Ducts of Rectangular Cross Section," Appl. Sci. Res., **18**, pp. 247–259.
[9] Fox, R. W., and McDonald, A. T., 1992, *Introduction to Fluid Mechanics*, 4th Ed., John Wiley and Sons, New York, p. 355.
[10] Streeter, V. L., ed., 1961, *Handbook of Fluid Dynamics*, McGraw-Hill, New York.

[11] Hewitt, G. F., 1992, *Handbook of Heat Exchanger Design*, Begell House, New York.
[12] Gnielinski, V., 1976, ''New Equations for Heat and Mass Transfer in Turbulent Pipe and Channel Flow,'' Int. Chem. Eng., **16**, p. 359.
[13] Ewing, M. E., 1998, ''Fundamental Studies of Enhanced Heat Exchanger Surfaces at Low Reynolds Numbers,'' Ph.D. dissertation, The Ohio State University, Columbus, OH.
[14] Singh, S. N., 1958, ''Heat Transfer by Laminar Flow in a Cylindrical Tube,'' Appl. Sci. Res., **7**, pp. 325–340.
[15] Taitel, Y., and Tamir, A., 1972, ''Application of the Integral Method to Flows With Axial Diffusion,'' Int. J. Heat Mass Transf., **15**, pp. 733–740.
[16] Moffat, R. J., 1988, ''Describing the Uncertainties in Experimental Results,'' Exp. Fluid Therm Sci., **1**, pp. 3–17.

Parallel Particle Simulation of the Near-Continuum Hypersonic Flows Over Compression Ramps

J.-S. Wu[1]
Assistant Professor,
e-mail: chongsin@cc.nctu.edu.tw

K.-C. Tseng
Graduate Student

Department of Mechanical Engineering,
National Chiao-Tung University,
1001 Ta-Hsueh Road,
Hsinchu 30050, Taiwan

This paper describes the analysis of the near-continuum hypersonic flow over a compression ramp using the two-dimensional parallel direct simulation Monte Carlo (DSMC) method. Unstructured and triangular solution-based adaptive mesh depending on the local mean free path is used to improve the resolution of solution for the flow field with highly varying properties. In addition, a freestream parameter is defined to help reduced the cell numbers in the freestream area, resulting in appreciable decrease of the computational time (20–30%) without sacrificing the accuracy of the solution. The two-step multilevel graph partition technique is used for physical domain decomposition, employing estimated particle number distribution in each cell as the graph vertex weight. 32 IBM-SP2 processors are used throughout the study unless otherwise specified. The Effect of the outflow vacuum boundary condition, compression ramp angle, freestream condition, and length of the ramp to the flow field are investigated. Computational results are compared with previous numerical results whenever available.
[DOI: 10.1115/1.1523068]

Introduction

Due to the complicated physical features possessed by hypersonic compression ramp flow and its importance to the design of hypersonic vehicles, it has been studied extensively in the past, [1–6]. Details of the general physics can be found in Refs. [1–6] and references cited therein. Several points, however, are worthy of mentioning here. First, the tip flows are in strong nonequilibrium and hence continuum assumption breaks down in this regime, where the Navier-Stokes equation fails to approximate the flow features. Second, most flows relevant to hypersonic vehicles are in the range of transition to near-continuum, thus the direct simulation Monte Carlo method (DSMC), [7], is well-suited to study this complicated flow field, although the computational cost is extremely high in the near-continuum regime. Third, the flow possesses very complicated physical features involving highly varying flow properties, which are very difficult to resolve using nonadaptive mesh.

In order to well resolve the complicated flow features of a compression ramp using the DSMC method, two issues are required to handle it properly. First, the distribution of computational cells should be adapted to the variation of the flow properties. Hence, solution-based adaptive mesh is generally required. In traditional computational fluid dynamics (CFD), unstructured mesh rather than structured mesh is more flexible for the purpose of mesh adaptation. The same applies to the DSMC method. There were, however, relatively few studies developed along this line, [8,9], in the DSMC community. Robinson [8] first applied the re-meshing technique to adapt the unstructured mesh, then Wu et al. [9] applied the mesh-embedding scheme instead to adapt the unstructured mesh. Second, due to the high computational cost of the DSMC simulation, especially in the near-continuum regime, parallel processing is highly expected. Fortunately, DSMC is readily paralleled using domain decomposition due to its particle nature and high locality due to assumed binary collisions. Detailed reviews of parallel processing of DSMC can be found in Refs. [8,10], which will not be repeated here for brevity.

As mentioned earlier, the hypersonic flow over a compression ramp involves rather complicated flow phenomena with highly varying flow properties. Hence, integration of parallel processing and unstructured adaptive mesh is highly expected to accelerate the computational speed to an acceptable level as well as to improve the resolution.

Therefore, the specific objectives of the current study are

1. to integrate the previously developed DSMC method using unstructured adaptive mesh, [9], and the parallel DSMC method, [10], using unstructured mesh;
2. to apply this method to compute a hypersonic compression ramp flow and compare the results with those of Moss et al. [6]; and
3. to study the effects of ramp angles, free-stream conditions, outflow vacuum boundary conditions, and ramp length on the flow properties, including pressure, shear stress, and heat transfer coefficients.

The paper begins with descriptions of numerical methods. Results of short compression are compared to those of Moss et al. [6] and different effects on surface properties are discussed in turn.

Numerical Method and Procedures

Parallel Direct Simulation Monte Carlo (DSMC) Method. The DSMC algorithm is readily parallelized through the physical domain decomposition as mentioned previously. The cells of the computational grid are distributed among the processors. Each processor executes the DSMC algorithm in serial for all particles and cells in its own domain. Parallel communication occurs when particles cross the domain (processor) boundaries and then particle data are transferred between processors. Figure 1 shows a simplified flow chart of the parallel DSMC method proposed in the current study. Note that CPUs are numbered from 0 to np-1 in the figure.

In this method, an approach of handling the cell related data is proposed. An unstructured triangular mesh is first constructed using the advancing front method by a commercial code, HyperMesh™, [11]. Then, a preprocessor (or ''converter'') is designed to convert the unstructured mesh data into the *globally sequential but locally unstructured* mesh data for each processor in confor-

[1]To whom correspondence should be addressed.

Contributed by the Fluids Engineering Division for publication in the JOURNAL OF FLUIDS ENGINEERING. Manuscript received by the Fluids Engineering Division Jan. 2, 2002; revised manuscript received Aug. 20, 2002. Associate Editor: Y. Matsumoto.

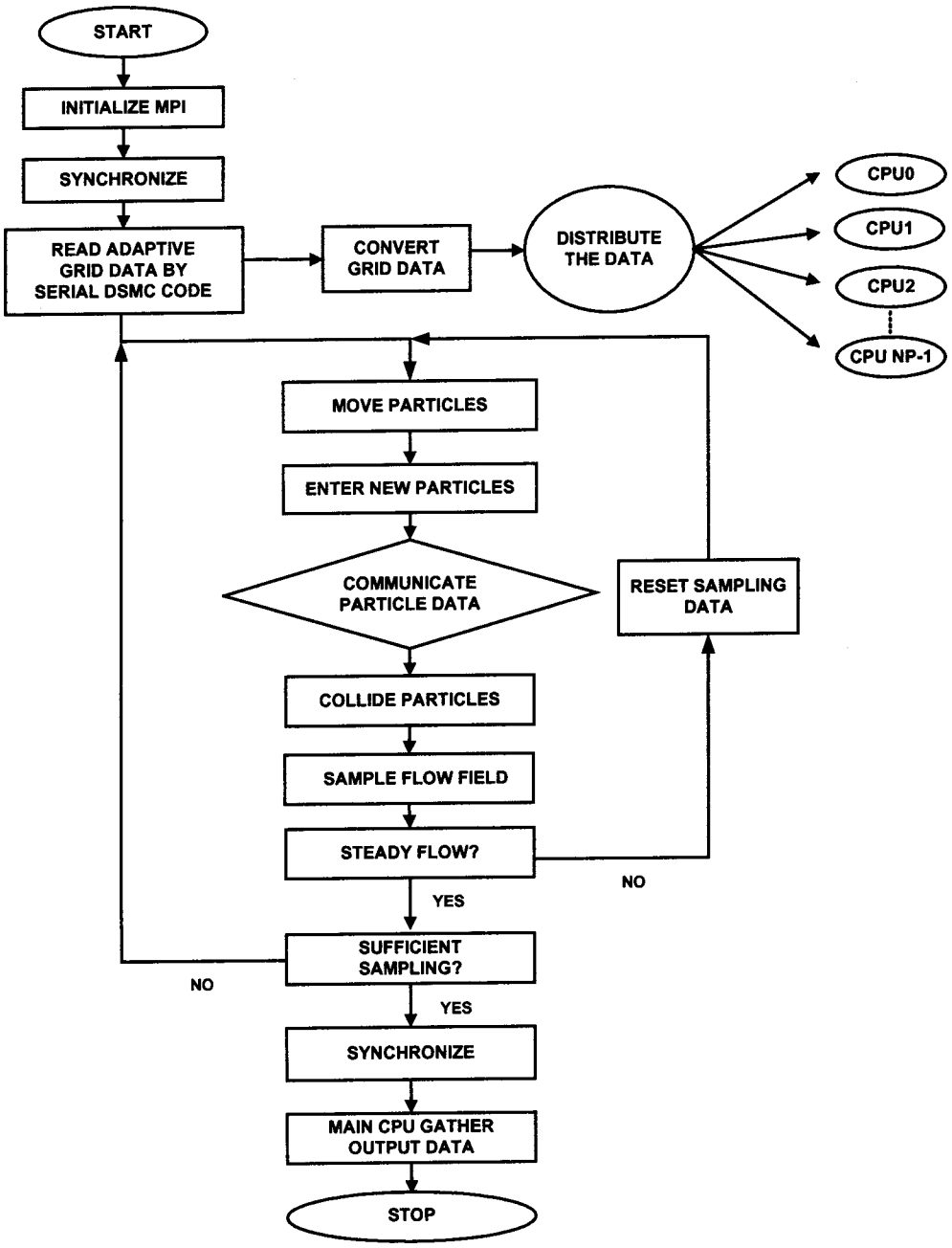

Fig. 1 Flow chart of the parallel DSMC method

mation with the partitioning information from graph partitioner (e.g., JOSTLE [12]), as schematically presented in Fig. 2. In each processor, the cell numbering is unordered (unstructured), but the starting (and ending) cell number increases sequentially with the processor number. We term this as ''globally sequential but locally unstructured.'' Thus, in each processor the memory is only needed to record the starting and ending cell numbers. This simple conversion dramatically reduces the memory cost otherwise required for storing the mapping between the local cell number in each processor and the global cell number in the computational domain if unstructured cells are used, [10]. The resulting mesh data is then imported into the parallel DSMC code.

After reading the mesh data on a master processor (cpu 0), the mesh data are then distributed to all other processors according to the designated domain decomposition. All the particles in each processor then start to move as in sequential DSMC algorithm. The particle related data are sent to a buffer and are numbered sequentially when hitting the inter-processor boundary (IPB) during its journey within a simulation time-step. After all the particles in a processor are moved, the destination processor for each particle in the buffer is identified via a simple arithmetic computation, owing to the previously mentioned approach for cell numbering, and the transferred data are then packed into arrays. Considering communication efficiency, the packed arrays are sent as a whole to its surrounding processors, in turn based on the tagged numbers recorded earlier. Once a processor sends out all the packed arrays, it waits to receive the packed arrays from its surrounding processors in turn. This ''send'' and ''receive'' operation serves practically as a synchronization step during each simulation time-step. Received particle data are then unpacked and each particle continues to finish its journey for the remaining

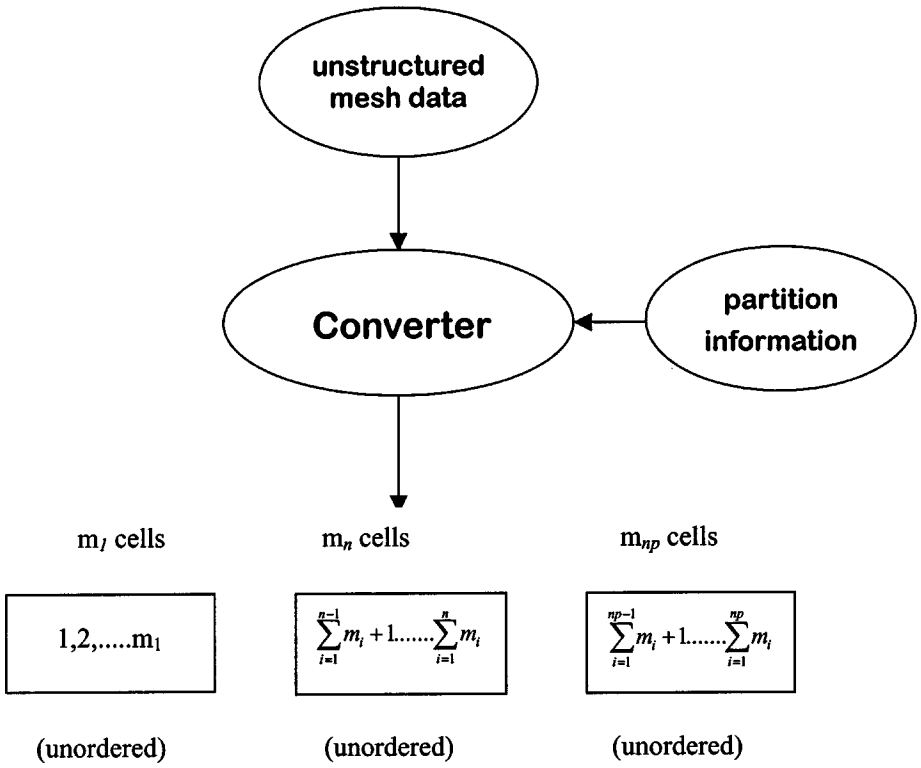

Fig. 2 Cell renumbering scheme in the parallel DSMC method

time-step. The above procedures are repeated twice since there might be some particles crossing the IPB twice during a simulation time-step.

After all particles on each processors have come to their final destinations at the end of a time-step, the program then carries out the indexing of all particles and the collisions of particles in each computational cell in each processor as usual in a sequential DSMC code. The particles in each cell are then sampled at the appropriate time as specified.

The current parallel code, in SPMD (single program multiple data) paradigm, is implemented on the IBM-SP2 machines (distributed memory system) using the message passing interface (MPI) to exchange information between processors. It is thus essentially no code modification required to adapt to other parallel machines (e.g., IBM-SMP, PC-clusters) with a similar distributed memory system once they use the same MPI libraries for data communication.

The DSMC Method With Mesh Adaptation. All mesh adaptation methods need some means to detect the requirement of local mesh refinement to better resolve the features in the flow fields and hence to achieve more accurate numerical solutions. This also applies to DSMC. It is important for the adaptation parameters to detect a variety of flow features but does not cost too much computationally. Often the gradient of the properties, such as pressure, density, or velocity, is used as the adaptation parameter to detect rapid changes of the flow-field solution in traditional CFD. However, by considering the statistical nature of

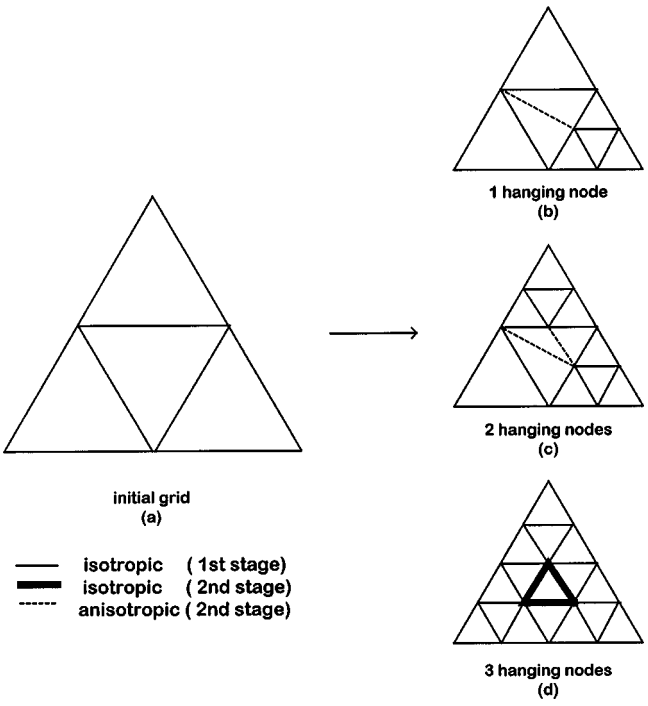

Fig. 3 Mesh refinement scheme for unstructured triangular mesh

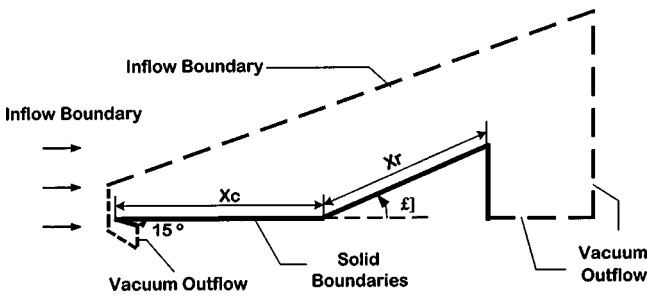

Fig. 4 Sketch of the two-dimensional hypersonic compression corner flow

Table 1 Flow conditions of simulation

							$x_c = 71.4$ mm		
Case	x_r (mm)	$\rho_\infty x10^{-5}$ (Kg/m^3)	V_∞ (m/s)	T_∞ (K)	T_w (K)	M_∞ (–)	λ_∞ (mm)	Kn_∞ (–)	Re_∞ (–)
1	31.55	5.14	1340	8.3	383	22.8	0.475	0.0066	3938.66
2	31.55	10.72	1452	8.6	394	24.3	0.230	0.0032	8670.23
3	31.55	18.09	1448	14.1	340	18.9	0.154	0.0022	10120.06
4	31.55	39.12	1740	15.6	341	21.6	0.073	0.0010	24402.49
5	71.4	39.12	1740	15.6	341	21.6	0.073	0.0010	24402.49

the DSMC method, density is adopted instead as the adaptation parameter in the current study. Using density as the adaptation parameter in DSMC is justified since it is generally required that the cell size be much smaller than the local mean free path to better resolve the flow features as advocated by Bird [7]. To use the density as an adaptation parameter, a local cell Knudsen number is defined as

$$\mathrm{Kn}_c = \frac{\lambda_c}{\sqrt{A_c}}, \tag{1}$$

where λ_c is the local cell mean free path based on VHS model and A_c is the magnitude of the local cell area. When the mesh adaptation module is initiated, the local Knudsen number at each cell is computed and compared with a preset value, Kn_{cc}. If this value is less than the preset value, then mesh refinement is required. If not, check the next cell until all cells are checked. This adaptation parameter is expected to be most stringent on mesh refinement (more cells are added); hence, the impact to the DSMC computational cost might be high, but it is required to obtain an accurate solution.

Considering the practical applications of mesh adaptation in external flows, we have added another constraint, $\phi \geqslant \phi_0$, in addition to the constraint of the local cell Knudsen number. Note that the freestream parameter, ϕ, is defined as

$$\phi = \frac{\rho}{\rho_\infty}, \tag{2}$$

where ϕ_0 is a preset value. Not only does the above constraint helps to reduce the total refined cell numbers to an acceptable level by reducing the cell numbers in the freestream region a great deal, but it also reduces the total computational time up to 30%.

Two general rules of mesh adaptation are described as follows:

(1) *Isotropic mesh refinement is employed for those cells which flag for mesh refinement*. A new node is added on each edge (face) of a *parent cell* and connecting them to form four *child cells*. In general, this will create one to three hanging nodes in the nonrefined interfacial cell, which is next to the isotropically refined cell. Existence of hanging node(s) not only complicates the particle movement, but also increases the cost of the cell-by-cell particle tracing due to the increase of face numbers. Hence, a remedy is proposed as follows in item (2).

(2) *Anisotropic mesh refinement is utilized in the (interfacial) cells next to those cells have just been isotropically refined*. Triangular child cells are formed no matter how many hanging nodes exist. Typical methods of interfacial mesh refinement in the triangular cells are schematically shown in Fig. 3.

The mesh adaptation procedures are performed using a serial DSMC code using very few particles (<1%). As a rule of thumb, about 10,000 particles sampled in a cell are considered enough for the mesh adaptation purpose. The mesh adaptation module is initiated and checks through all the cells to determine if mesh enrichment is required based on the specific adaptation parameter, which was explained previously. If mesh enrichment is conducted, associated neighbor identifying arrays are updated or created, coordinates and number of faces for new cells are recorded, and sampled data on the coarse *parent cell* are redistributed (based on the magnitude of cell area) to the finer *child cells* accordingly. The above procedures are repeated until the prescribed maximum number of adaptation levels has been reached or no mesh enrichment is required for all the cells in the computational domain. Finally the adaptive mesh due to the above procedures is outputted as the computational cells for further parallel DSMC processing. In summary, output adaptive mesh and density distribution is then used as the information for domain decomposition using the graph partitioner, JOSTLE, [12]. Finally, the previously developed parallel DSMC code, [10], is then utilized for computation.

Results and Discussion

Figure 4 illustrates the sketch of a hypersonic flow over a compression ramp as previously simulated by Moss et al. [6]. Current flow conditions are summarized in Table 1, where cases 1–4 ($x_c = 71.4$ mm, $x_r = 31.55$ mm) corresponds to those simulated in Moss et al. [6] except for case 5 ($x_c = 71.4$ mm, $x_r = 71.4$ mm) with a longer ramp. For completeness, they are briefly described here as follows: VHS nitrogen gas, freestream Mach number $M_\infty = 18.9 \sim 24.3$, freestream density $\rho_\infty = 5.14\text{E-}5 \sim 39.12\text{E-}5$ Kg/m^3, freestream temperature $T_\infty = 8.3 \sim 15.6$ K, and a fully thermally accommodated and diffusive flat and ramp wall

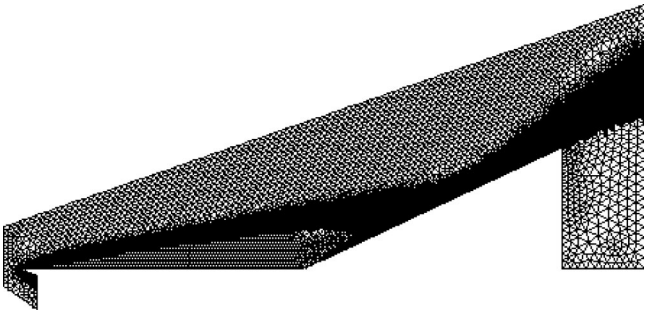

Fig. 5 Unstructured adaptive mesh for case 5 ($x_r = 71.4$ mm, $\beta = 25$ deg) (163,658 cells, 3 levels of mesh adaptation)

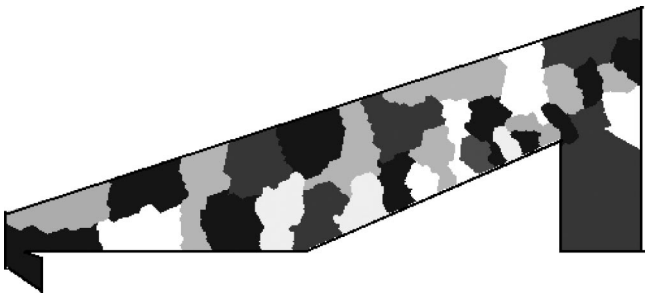

Fig. 6 Multilevel graph partition for case 5 ($x_r = 71.4$ mm, $\beta = 25$ deg) (32 CPUs)

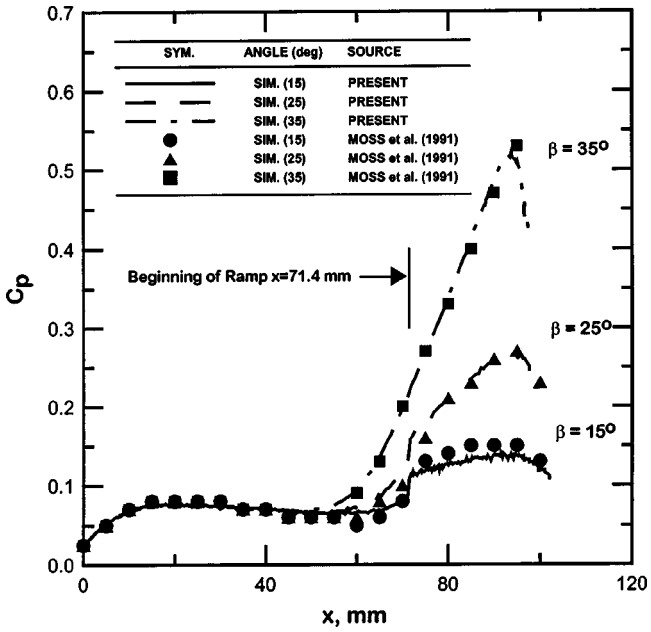

Fig. 7 Pressure coefficient distribution along the solid wall for β=15 deg, 25 deg, and 35 deg (case 1, Kn_∞=0.0066)

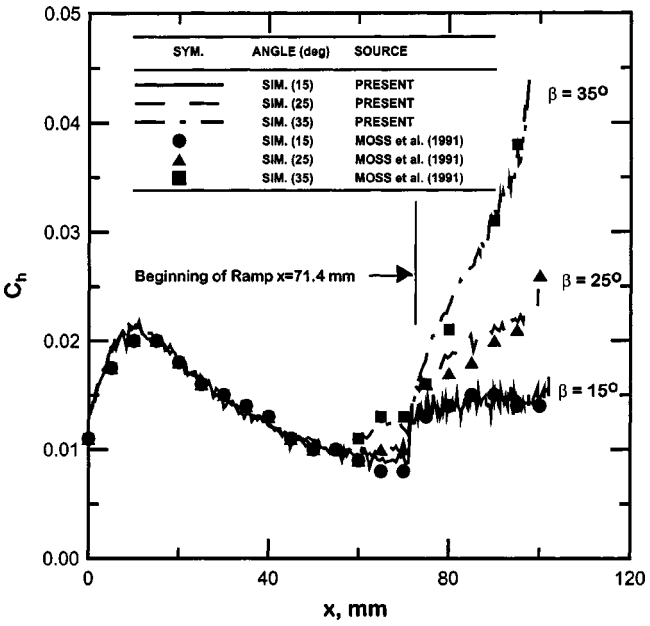

Fig. 9 Heat transfer coefficient distribution along the solid wall for β=15 deg, 25 deg, and 35 deg (case 1, Kn_∞=0.0066)

with $T_w = 340 \sim 394$ K. The resulting Knudsen numbers and Reynolds numbers based on x_c are in the range of 0.0010–0.0066 and 3938.66–24402.49, respectively. Temperature-dependent rotational energy exchange model of Parker [7] is used to model the diatomic nitrogen gas. Vibration energy transfer is neglected due to the low temperature involved. Typical particle numbers and cell numbers are in the range of 0.8–8 million and 19,000–250,000, respectively, depending upon the rarefaction of the problem. Additionally, ϕ_0 is normally set to 1.03 unless otherwise specified. Typical adaptive mesh distribution is shown in Fig. 5 for the case 5 at ramp angle of 25 deg (163,658 cells). Corresponding distribution for domain decomposition using the graph-partitioning technique is illustrated in Fig. 6. Note that the size of each subdomain is obviously different due to the variations of estimated

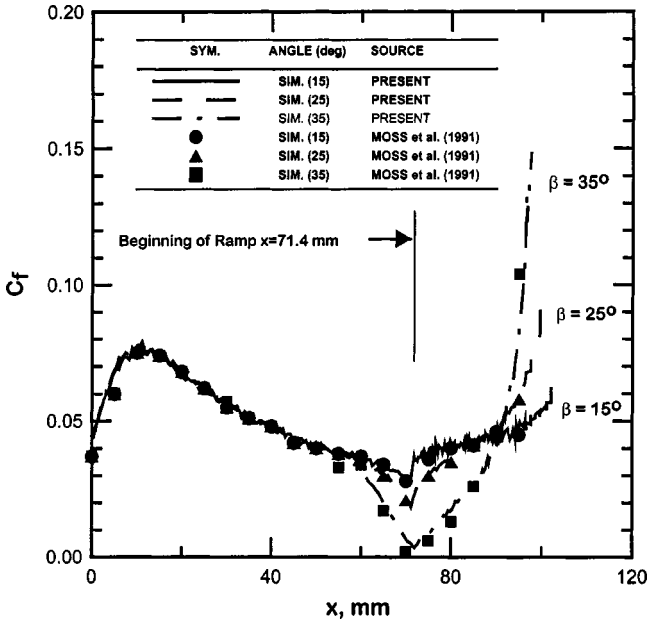

Fig. 8 Shear stress coefficient distribution along the solid wall for β=15 deg, 25 deg, and 35 deg (case 1, Kn_∞=0.0066)

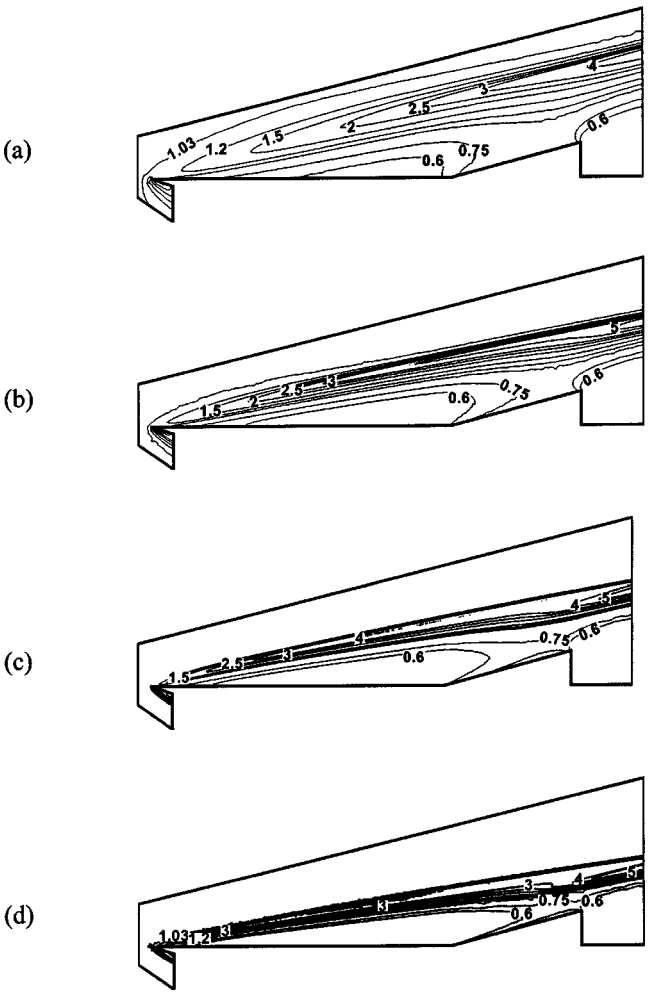

Fig. 10 Density contours at different freestream Knudsen number for β=15 deg (*a*) Kn_∞=0.0066; (*b*) Kn_∞=0.0032; (*c*) Kn_∞=0.0022; (*d*) Kn_∞=0.0010

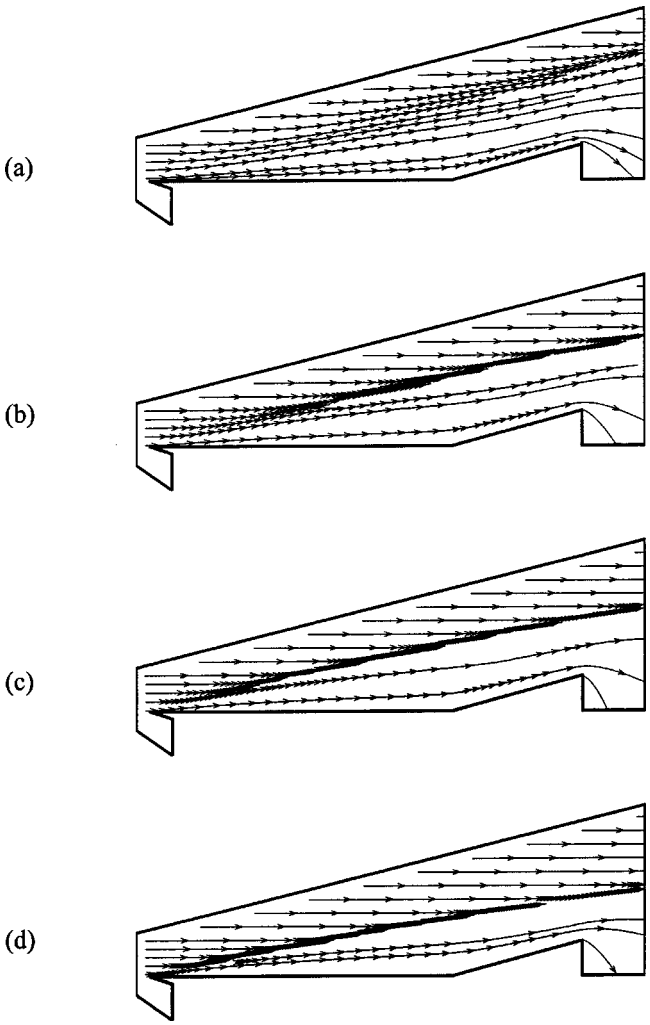

Fig. 11 Streamline contours at different freestream Knudsen number for β=15 deg (*a*) Kn_∞=0.0066; (*b*) Kn_∞=0.0032; (*c*) Kn_∞=0.0022; (*d*) Kn_∞=0.0010

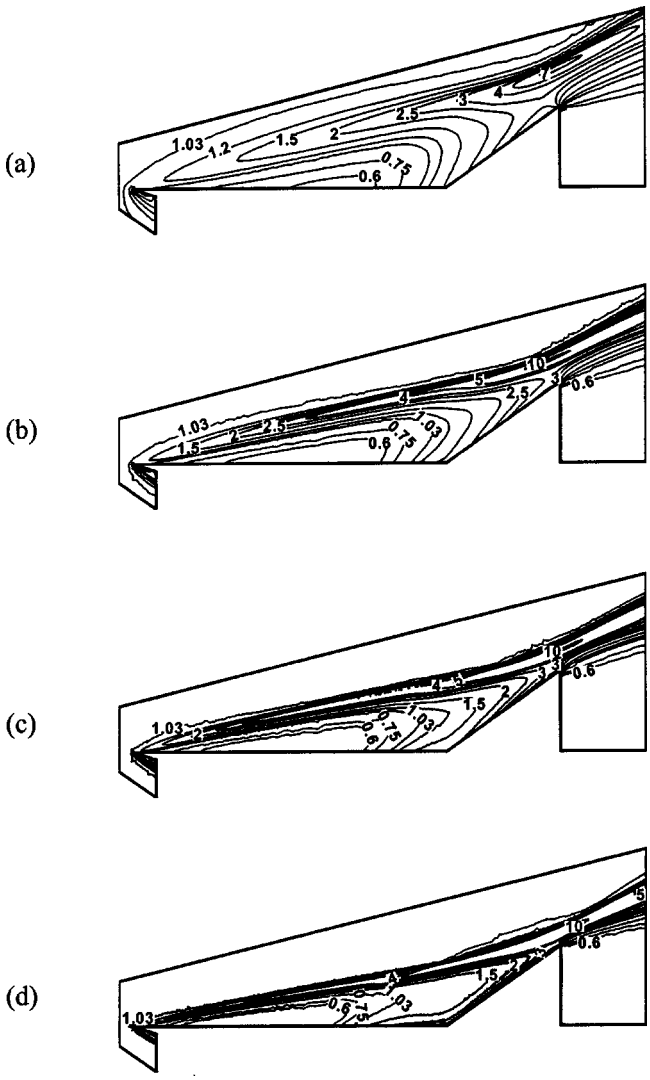

Fig. 12 Density contours at different freestream Knudsen number for β=35 deg (*a*) Kn_∞=0.0066; (*b*) Kn_∞=0.0032; (*c*) Kn_∞=0.0022; (*d*) Kn_∞=0.0010

density distribution (or equivalently computational load) in the computational domain. Note that 32 IBM-SP2 processors are used throughout the current study unless otherwise specified.

Verification of the Present Implementation. In Moss et al. [6], the outflow vacuum condition was placed right at the end of the ramp instead of the current position as shown in Fig. 4. It was, however, problematic since previous results showed a large circulation bubble formed at the compression corner for a large ramp angle with the flow reattached near the end of the ramp. This might cause subsonic outflow (or even reversed flow) near the end of the ramp wall, which renders the vacuum outflow conditions unphysical. In the current study, we have moved the outflow vacuum boundary condition further downstream to the wake region as shown in Fig. 4, which coincides more with the experimental conditions, [6].

Figures 7, 8, and 9 illustrate the pressure, shear stress, and heat transfer coefficient distribution, respectively, along the solid wall for case 1 (the most rarefied case in Table I with a short ramp) at three different ramp angles (15 deg, 25 deg, and 35 deg). Detailed discussion on the physics of the flow field is relatively brief since it can be found in Moss et al. [6]. As shown in Fig. 7, the pressure distribution generally increases with the distance from the leading edge, reaches a maximum value 0.077 at approximately the position of $x=20$ mm, and then decreases to some value before the ramp corner, depending upon the ramp angle. Pressure increases appreciably starting from the corner region due to the existence of ramp, especially for the 35 deg case. For the cases considered, the data generally coincide very well with those of Moss et al. [6] except at the end of the ramp for the 35 deg case, due to the position of outflow vacuum condition. Current prediction shows that strong expansion occurs in this regime for the 35 deg case, which will be shown later. This is reasonable since the flow close to the end of the ramp wall is slowed down most due to the large angle of the ramp corner although no reverse flows occur. The placement of the outflow vacuum boundary condition in Ref. [6] will prevent the flow from expanding at this regime. In addition, shear stress and heat transfer coefficient distributions for all three ramp angles (Fig. 8) along the solid wall agree reasonably well with those of Moss et al. [6]. The current cell numbers for this case is on the order of 20,000, which is larger than that used by Moss et al. [6] ($\approx$7,000). But the distribution of cells is definitely better due to the solution-based adaptive mesh. Also the particle numbers is about 0.8–2 million that is much larger than that ($\approx$0.1–0.2 million) used in Ref. [6]. This represents that the current parallel DSMC simulation using unstructured adaptive mesh is at least as accurate as (or may be more accurate than) previous simulation study for the most rarefied case.

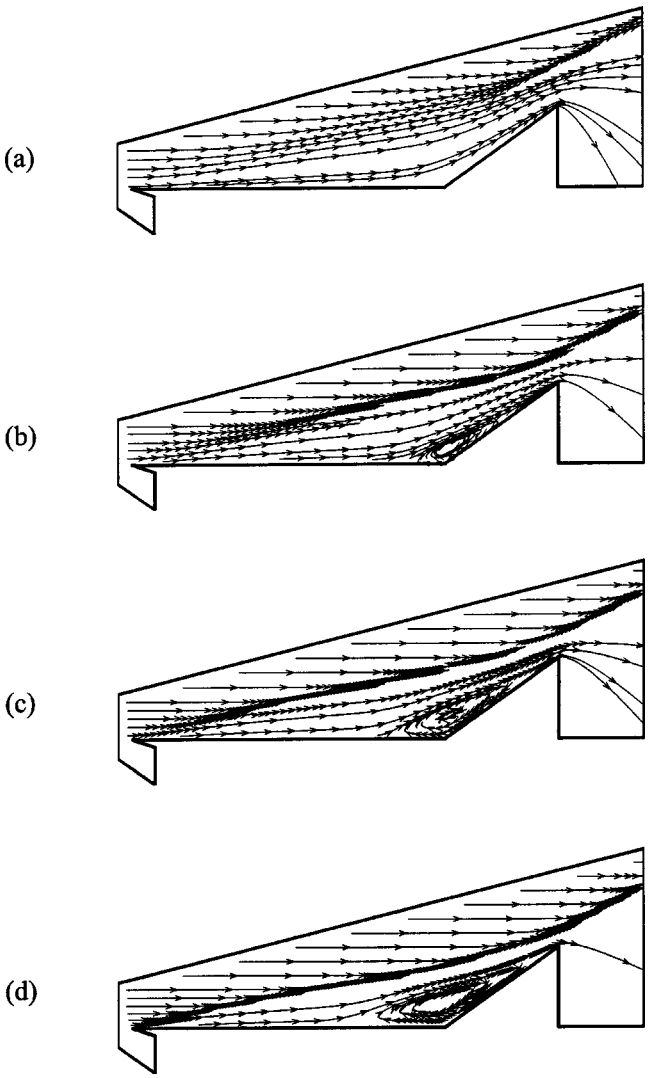

Fig. 13 Streamline contours at different freestream Knudsen number for $\beta=35$ deg (*a*) $Kn_\infty=0.0066$; (*b*) $Kn_\infty=0.0032$; (*c*) $Kn_\infty=0.0022$; (*d*) $Kn_\infty=0.0010$

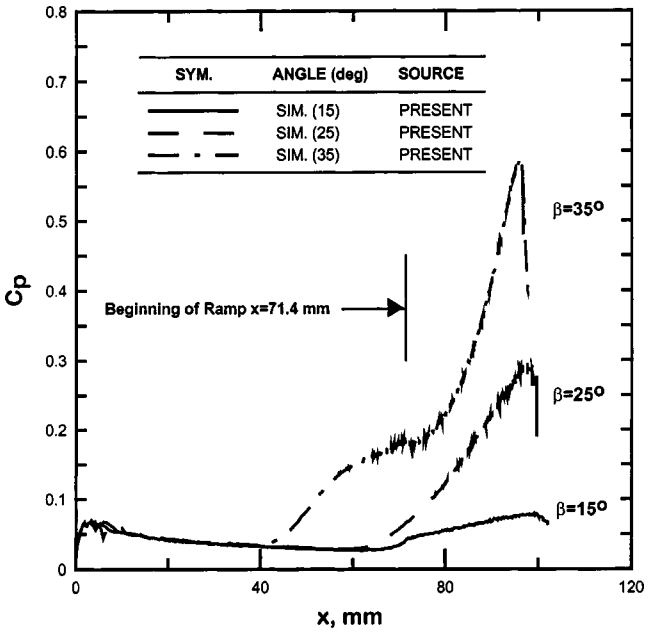

Fig. 14 Pressure coefficient distribution along the solid wall for $\beta=15$ deg, 25 deg, and 35 deg (case 4, $Kn_\infty=0.0010$)

Effects of Freestream Rarefaction and Ramp Angle. Effects of rarefaction for the short ramp can be clearly demonstrated in Figs. 10, 11 (15 deg) and Figs. 12, 13 (35 deg). In Figs. 11(*a*)–11(*d*) ($\beta=15$ deg, density distribution), the density gradient across the leading-edge shock increases with decreasing freestream rarefaction. In addition, rarefied region above the flat-plate increases with decreasing freestream rarefaction as well. In addition, strong gas expansion occurs at the end of the ramp wall, which causes the pressure to decrease as shown earlier in Fig. 7. Because of the short ramp length considered, the oblique shock due to compression corner is not very clearly formed even in the case of the densest flow (Fig. 11(*d*)). No separation bubble can be identified for all the cases considered with ramp angle of 15 deg (Figs. 11(*a*)–11(*d*), streamline contour). From Figs. 11(*b*)–11(*d*), the leading-edge shock extends over the ramp due to the very blur (weak) oblique shock. Additionally, the strength of the leading-edge shock increases with decreasing rarefaction as expected.

In Figs. 12(*a*)–12(*d*) ($\beta=35$ deg, density distribution), physical trend for density distribution is similar to those of 15 deg as shown in Fig. 10. There is, however, one distinct feature caused by the large ramp angle. Density in the corner region is more uniform than that of 15 deg case as compared with Figs. 10(*a*)–10(*d*). This is caused by the circulation bubble formed in the compression corner as shown in Figs. 13(*a*)–13(*d*) for lower freestream rarefaction cases. In addition, the gas expansion at the end of the ramp wall is more obvious as compared with that of the 15 deg case, which is expected due to the adverse pressure gradient along the ramp caused by the large ramp angle. From both Figs. 12 and 13, the leading-edge shock is deflected upwards and mingled with oblique shock (due to the corner) at the end of the ramp due to the large ramp angle. Note that the oblique shock due to the ramp corner is not very clear because of the short ramp. In addition, the size of the separation bubble increases with decreasing rarefaction. The separation bubble even extends over 1/3 upstream of the flat-plate length and almost covers the entire ramp

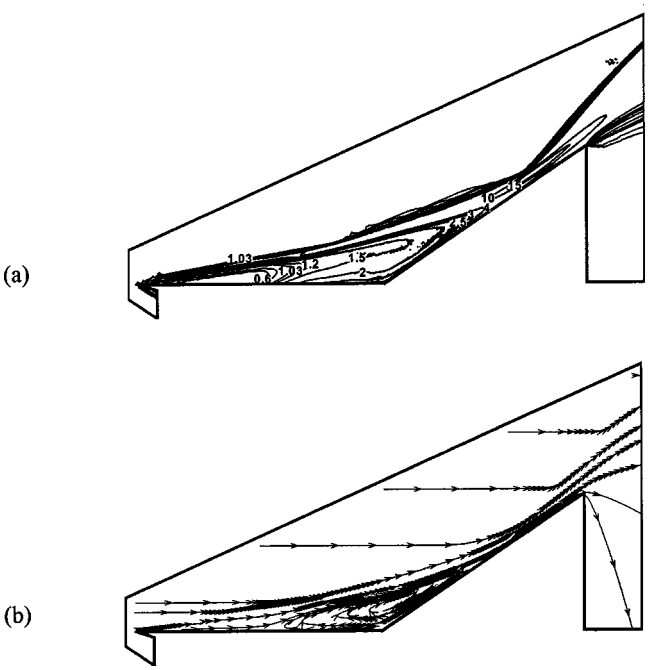

Fig. 15 Density and streamline contours at $\beta=35$ deg (long ramp, case 5, $Kn_\infty=0.0010$)

wall. This definitely will dramatically change the surface properties as can be seen, for example, in Fig. 14, where the pressure coefficient is much higher in the corner region for the $\beta=35$ deg case as compared with the other two cases ($\beta=15$ deg and 25 deg).

Generally speaking, the strength of leading-edge shock, gas expansion at the end of the ramp, as well as the separation bubbles size in the corner increases with decreasing rarefaction.

Effects of Length of the Ramp. Effects of the ramp length on the flow structure can be illustrated in Fig. 15, where $\mathrm{Kn}_\infty = 0.001$ (case 5, $x_r = 71.4$ mm, $\beta=35$ deg) which is in the near-continuum regime. The formation of the strong oblique shock is very clear at the later portion of the ramp due to the longer ramp considered. For the short ramp case at the same angle (Fig. 12(*d*)), the oblique shock is comparably blurred due to the short ramp. In addition, the gas expansion fan the corner of the ramp (to the wake region) is clearly seen because of the formation of the strong oblique shock. A well-known neck region is clearly formed along the ramp wall. Comparing Fig. 15(*b*) and Fig. 13(*d*), we can see that the circulation bubble is larger because of the long ramp. Hence, the rarefied region above the flat-plate (as compared with the freestream value) becomes smaller due to the large circulation bubble. The nature of the interaction among the leading-edge shock, the viscous boundary layer along the solid wall and the oblique shock is rather complicated. The related discussion can be found in Robinson [8] and are skipped here.

Conclusions

A two-dimensional parallel DSMC method using unstructured solution-based adaptive mesh has been developed. Simulated data of a hypersonic flow over a compression ramp at a most rarefied condition are used to compare with previous reported results. It is then applied to simulate similar flow to study the effects of the freestream rarefaction, ramp angle, and the effects of the ramp length. This study shows that simulation of near-continuum flow using the DSMC method is possible using parallel processing. Future work considering dynamic load balancing during simulation for parallel DSMC is in progress and will be reported elsewhere.

Acknowledgment

This investigation was supported by the National Science Council of Taiwan, Grant No. NSC 90-2212-E-009-046. The authors also would like to express their sincere thanks to the computing resources provided by the National Center for High-Speed Computing of National Science Council of Taiwan.

Nomenclature

a_∞ = freestream sound speed
C_w = shear stress coefficient, $2\tau_w/\rho_\infty V_\infty^2$
C_p = pressure coefficient, $2p_w/\rho_\infty V_\infty^2$
C_h = heat transfer coefficient, $2q_w/\rho_\infty V_\infty^3$
Kn_∞ = freestream Knudsen number, λ_∞/x_c
M_∞ = freestream Mach number, U_∞/a_∞
p = pressure
q = heat transfer rate
$\mathrm{Re}_{\infty,x}$ = local Reynolds number, $\rho_\infty V_\infty x/\mu_\infty$
T = temperature
T_{tr} = translational temperature
U_∞ = freestream velocity
x_c = distance from leading edge to the ramp corner
x_r = ramp length
β = ramp angle
λ_∞ = mean-free path in freestream
μ = viscosity
ρ = density
τ = shear stress

Subscripts

c = corner
ref = reference condition
w = wall
∞ = free-stream condition

References

[1] Anderson, J. D., Jr., 1989, *Hypersonic and High Temperature Gas Dynamics*, McGraw-Hill, New York.
[2] Pullin, D. I., and Harvey, J. H., 1976, "A Numerical Simulation of the Rarefied Hypersonic Flat Plate Problem," J. Fluid Mech., **78**, pp. 689–707.
[3] Vogenitz, F. W., Broadwell, J. E., and Bird, G. A., 1969, "Leading Edge Flow by the Monte Carlo Direct Simulation Technique," 7th Aerospace Science Meeting, AIAA Paper No. 69–141.
[4] Chun, C.-H., 1991, "Experiments on Separation at a Compression Corner in Rarefied Hypersonic Flow," *Rarefied Gas Dynamics*, A. Beylich, ed., VCH Publishers, New York, pp. 562–569.
[5] Moss, J., Rault, N., and Price, J. M., 1994, "Direct Monte Carlo Simulations of Hypersonic Viscous Interactions Including Separation," *Rarefied Gas Dynamics: Space Science and Engineering*, B. D. Shzgal and D. P. Weave, eds., Washington, DC.
[6] Moss, J. N., Price, J. M., and Chun, C. H., 1991, "Hypersonic Rarefied Flow About a Compression Corner—DSMC Simulation and Experiment," 26th Thermophysics Conference, AIAA Paper No. 91-1313.
[7] Bird, G. A., 1994, *Molecular Gas Dynamics and the Direct Simulation of Gas Flows*, Oxford University Press, New York.
[8] Robinson, C. D., 1998, "Particle Simulation on Parallel Computers With Dynamic Load Balancing," Ph.D. thesis, Imperial College of Science, Technology and Medicine, U.K.
[9] Wu, J.-S., Tseng, K.-C., and Kuo, C.-H., 2001, "The Direct Simulation Monte Carlo Method Using Unstructured Adaptive Mesh and Its Application," Int. J. Numer. Methods Fluids, accepted for publication.
[10] Wu, J.-S., Tseng, K.-C., and Yang, T.-J., 2001, "Parallel Implementation of the Direct Simulation Monte Carlo Method Using Unstructured Mesh and Its Application," Int. J. Numer. Methods Heat Fluid Flow, submitted for publication.
[11] Hypermesh, Version 2.0, Altair Computing, Altair Engineering, Inc., Maplelawn, MI.
[12] Walshaw, C., Cross, M., Everett, M. G., Johnson, S., and McManus, K., 1995, "Partitioning and Mapping of Unstructured Meshes to Parallel Machine Topologies," *Proc. Irregular Parallel Algorithms for Irregularly Structured Problems*, A. Ferreia and J. Rolim, eds., **980**, LNCS, Springer, Berlin, pp. 121–126.

Journal of Fluids Engineering

Technical Briefs

Euler Number Based Orifice Discharge Coefficient Relationship

Gerald L. Morrison
Nelson-Jakson Professor of Mechanical Engineering,
Texas A&M University, College Station, TX 77843-3123
e-mail: gmorrison@mengr.tamu.edu

A new relationship for orifice flow meter discharge coefficients has been developed which replaces the Reynolds number dependence with the Euler number. Both relationships have the same accuracy for the calculation of the discharge coefficient but the new relationship eliminates the need to know fluid viscosity.
[DOI: 10.1115/1.1521955]

Introduction

The equations used to calculate the discharge coefficient for an orifice flow meter are complex and dependent upon the Reynolds number, pipe diameter, and orifice diameter. The general equation for the mass flow rate calculation given the discharge coefficient for an orifice flow meter is presented as follows:

$$\dot{m} = \frac{C_d}{\sqrt{1-\beta^4}} Y \frac{\pi}{4} \beta^2 D^2 \sqrt{2\rho \Delta P} \tag{1}$$

where $\dot{m}$ is the mass flow rate, C_d is the discharge coefficient, β is the ratio of the orifice diameter to pipe diameter, Y is the expansion factor, D is the pipe diameter, ρ is the fluid density, and ΔP is the pressure drop across the orifice plate. The discharge coefficient, C_d, as a function of the Reynolds number and β ratio for flange pressure taps, is shown in Fig. 1. These data represent the well-conditioned flow data set contained in *GRI/NIST Orifice Meter Discharge Coefficient Database, Version 1.0* by Scott, Brennan, and Blakeslee [1] which represent the majority of the data used in the establishment of the ANSI/API 2530, [2], orifice standard. The criteria for well-conditioned flow used are piping configurations, as described in the database, that will produce well conditioned flow according to ANSI/API 2530, [2]. Secondly, the discharge coefficient calculated according to ANSI/API 2530, [2] (contained in the GRI/NIST database) differ from the measured discharge coefficient by less than 0.5% was considered well conditioned flow. Any data which were over 0.5% different from the ANSI/API 2530 calculated value were discarded. These data were obtained for flows using nitrogen, air, water, gas-oil, and natural gas for β ratios from 0.10 to 0.75 for flange tap orifice flow meters. The discharge coefficient was calculated directly from data recorded in the following laboratories: British Gas, CEESI, Delft Hydraulics Lab, Gasunie, NEL, NIST-Boulder, NIST-Gaithersburg, and Southwest Research Institute. As the figure illustrates, the discharge coefficient varies significantly with β ratio and Reynolds number. Some of the data spread within a given β ratio is due to pipe diameter effects.

New Analysis

During the analysis of two-phase flow, there arose a need to re-examine the basic assumption of representing the discharge coefficient as a function of pipe diameter, β ratio, and Reynolds number. Following the technique of nondimensionalizing the equation governing the specific flow condition under study, the orifice flow equation, Eq. (1), was examined. The generalized mass flow rate equation can be rearranged using the definition of the Euler number which results in the following equation:

$$C_d Y \sqrt{Eu} \frac{\beta^2}{\sqrt{1-\beta^4}} = 1 \quad \text{where} \quad Eu = \frac{\Delta P}{1/2\ \rho U^2}. \tag{2}$$

Sometimes the Euler number does not include the half-term. This analysis states that the important nondimensional parameter is the Euler number, not the Reynolds number. If true, the viscosity of the fluid will no longer enter into the calculation of the flow rate. This will increase the accuracy of the flow rate calculation by deleting the uncertainty in the viscosity term. The calculation of C_d will also be simplified since one of the fluid properties is no longer needed.

Analyzing Eq. (2) with emphasis on how the equation can be used to interpret measurements from obstruction flow meters to yield mass flow rate the following observations are made. The

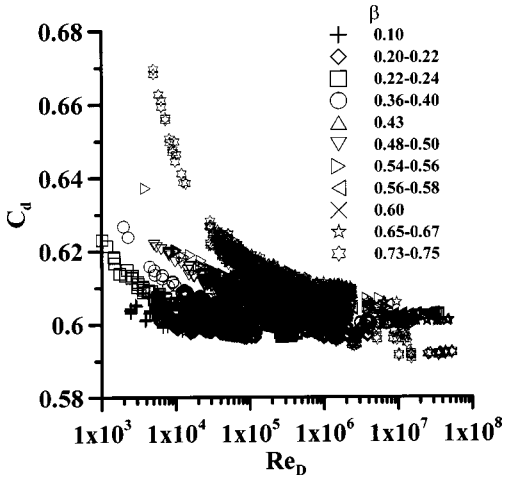

Fig. 1 Discharge coefficient from GRI/NIST database, [1], as a function of β ratio and Reynolds number

Contributed by the Fluids Engineering Division for publication in the JOURNAL OF FLUIDS ENGINEERING. Manuscript received by the Fluids Engineering Division January 29, 2002; revised manuscript received June 17, 2002. Associate Editor: S. L. Ceccio.

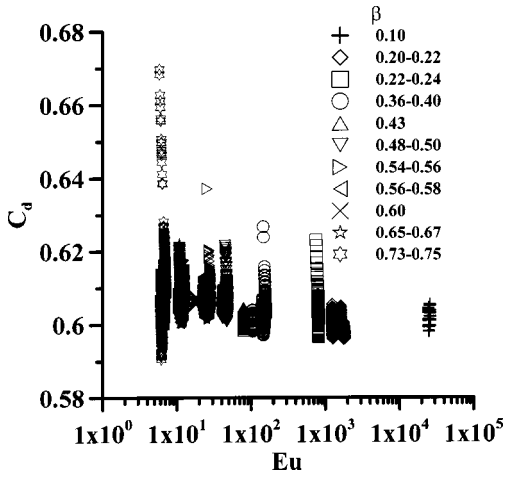

Fig. 2 Discharge coefficient as a function of β ratio and Euler number. Data from GRI/NIST database, [1].

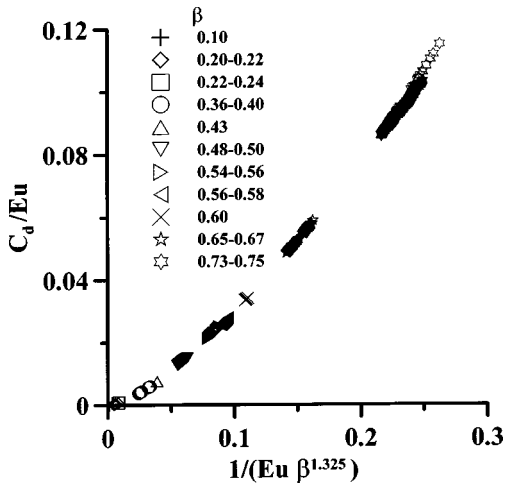

Fig. 3 Ratio of discharge coefficient to Euler number as a function of Euler number and β ratio. Data from GRI/NIST database, [1].

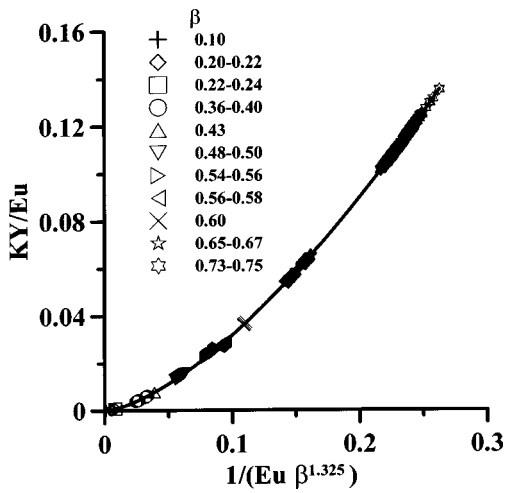

Fig. 4 Ratio of the product of flow coefficient and expansion factor to Euler number as a function of Euoer number and β ratio. Data from GRI/NIST database, [1].

current standard expresses the expansion factor (Y) as a function of the absolute static pressure in the pipe, the pressure drop across the orifice plate, ΔP, the β ratio, and the ratio of specific heats. Thus, the expansion factor is calculated from the known geometry of the orifice run and properties measured in the orifice run and will be considered a known quantity. Assuming the density of the fluid is known, as is currently done for orifice flow meters, the Euler number has only one unknown in it, the velocity of the fluid, U, since ΔP is measured. This leaves as the only unknowns in Eq. (2) the bulk averaged velocity, U, and the discharge coefficient, C_d. If the discharge coefficient can be expressed in terms of the Euler number, there will be one equation with one unknown, U.

Pursuing the goal of representing C_d as a function of Euler number, the GRI/NIST database was used to evaluate various schemes. The Euler number was calculated by using the standard mass flow Eq. (1) along with the other data listed in the database to calculate the mass flow rate. From this, the bulk averaged velocity in the pipe, U, was calculated. This value of U, along with the tabulated values of ΔP and density, were used to calculate the Euler number. Figure 2 illustrates the results of this endeavor where the discharge coefficient is plotted as a function of the Euler number for various ranges of β ratio. These data show that there is a relationship between β ratio and Euler number which is expected since smaller β ratios produce larger values of ΔP for a fixed value of mass flow rate and density. However, within a given β ratio, there is a large variation in discharge coefficient at a given Euler number.

Continued analysis of the data determined that if the ratio of the discharge coefficient to Euler number is plotted as a function of $1/(\mathrm{Eu}\,\beta^{1.325})$, a reasonable collapse of the data is obtained as shown in Fig. 3. There is some spread in the data for the higher β ratio data. Substituting the flow coefficient, $K = C_d/\sqrt{1-\beta^4}$, for the discharge coefficient, and including the expansion factor, Y, Fig. 4 is obtained. This shows a very good collapse of the data onto a single common curve. This graph includes 9645 data points recorded at eight different installations, for five fluids, in pipes from 50 mm (2 in.) to 600 mm (24 in.) diameter and β ratios from 0.10 to 0.75. These data follow a single curve very closely and exhibit a smooth trend with KY/Eu increasing monotonically with $1/(\mathrm{Eu}\beta^{1.325})$. Comparing Figs. 1 and 4 it is easy to see that a simple curve fit is possible for the data in Fig. 4 while the spread in data in Fig. 1 eliminates the possibility of a simple curve fit in terms of Reynolds number.

Figure 4 shows that this new discharge coefficient dependency representation does not depend upon pipe diameter or fluid vis-

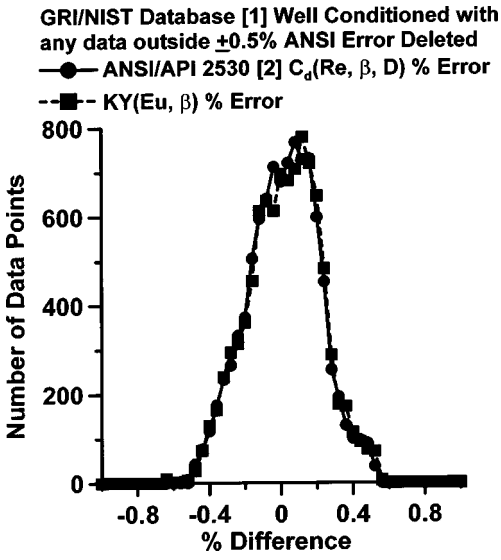

Fig. 5 Accuracy of ANSI/API 2530, [2], and Euler number method

cosity (the Reynolds number has been eliminated). The simple functional representation of this relationship will reduce the overall uncertainty of the measured mass flow rate. Additional increases in flow rate calculation accuracy are possible since the uncertainty of viscosity has been eliminated from the calculations. One other advantage of the new relationship is the reduction of the computational capability of flow computers required to calculate mass flow rates.

Results—Application of New Analysis

Figure 5 shows the error distribution for the ANSI/API 2530 calculated discharge coefficient. The percent difference between the ANSI/API 2530 calculated value and the measured discharge coefficient has a mean value of -0.0045% with a standard deviation of 0.1970% for the 9645 data points considered. Utilizing Fig. 4, the discharge coefficient was calculated from the flow coefficient as a function of β ratio and Euler number. The percent error histogram for these data are also shown in Fig. 5. The mean is 0.0014% with a standard deviation of 0.2077%. In essence, both the ANSI/API 2530 and the Euler number technique produce the same result.

Conclusions

The accuracy of the ANSI/API 2530 discharge coefficient equation and the Euler-based discharge coefficient equation are essentially the same. However, there are some advantages of the Euler-based equation including the possibility of more accurate discharge coefficients when used in the field. The increased accuracy comes about by the elimination of fluid viscosity as an input parameter. This will reduce the uncertainty of the calculated discharge coefficient since there is some uncertainty in the viscosity value which propagates into an increase in the discharge coefficient calculation. Another advantage is the simplicity of the relationship between discharge coefficient, β ratio, and Euler number. For a given geometry of the obstruction flow meter (i.e., pipe diameter and β ratio being known), Eq. (2) states that the only unknowns are the discharge coefficient, expansion factor, and Euler number. Figure 4 effectively states that the product of the flow coefficient and expansion factor are known as a function of Euler number and β ratio, hence, the discharge coefficient is known. The only unknown in Eq. (2) is the Euler number, $\mathrm{Eu} = 2\Delta P/\rho U^2$. The pressure differential, ΔP, is directly measured. This leaves two unknown parameters, the fluid velocity and density. If the meter is treated as an ordinary obstruction flow meter, then the density is specified based upon pressure and temperature measurements of the fluid. The fluid velocity is then calculated. An interesting second possibility is the combination of an obstruction flow meter with a volumetric flow meter such as a turbine meter, vortex shedding meter, or ultrasonic flow meter. The volumetric flow meter will provide the fluid velocity and then the obstruction flow meter can be used as a densitometer to determine the density of the fluid.

Acknowledgments

The opportunity to develop this work has been provided by Dr. Ken Hall at Texas A&M University, the Gas Research Institute, Southwest Research Institute, and the Advanced Technology Program of the State of Texas.

References

[1] Scott, J. L., Brennan, J. A., and Blakeslee, D. M., 1994, "GRI/NIST Orifice Meter Discharge Coefficient Database, Volume 1," NIST Standard Reference Database 45, U.S. Department of Commerce, National Institute of Standards and Technology, Gaithersburg, MD.

[2] AGA, ANSI, API, and GPA, 1992, "Orifice Metering of Natural Gas and Other Related Hydrocarbon Fluids," ANSI/API 2530, Third Ed., American Gas Association, Arlington, VA.

A Nonlinear k-ε-k_p Two-Phase Turbulence Model

L. X. Zhou
e-mail: zhoulx@mail.tsinghua.edu.cn

H. X. Gu

Department of Engineering Mechanics, Tsinghua University, Beijing 100084, China

Nonlinear relationships of two-phase Reynolds stresses with the strain rates together with the transport equations of gas and particle turbulent kinetic energy and the two-phase correlation turbulent kinetic energy are proposed as the nonlinear k-ε-k_p turbulence model. The proposed model is applied to simulate swirling gas-particle flows. The predicted two-phase time-averaged velocities and Reynolds stresses are compared with the PDPA measurements and those predicted using the second-order moment model. The results indicate that the nonlinear k-ε-k_p model has the modeling capability near to that of the second-order moment model, but the former can save much computation time than the latter.

[DOI: 10.1115/1.1522414]

1 Introduction

The two-phase turbulence model is the key problem for developing two-fluid models of turbulent gas-particle flows. Several years ago, we proposed the two-phase Reynolds stress or unified second-order moment (USM) and k-ε-k_p models, [1], based on Reynolds time averaging. The particle Reynolds (kinetic) stress models have also been developed by Simonin [2] and Zaichik [3] based on PDF approaches. It has been found that the conventional or linear k-ε-k_p model is rather simple and can well simulate nonswirling and weakly swirling gas-particle flows. However, for strongly swirling flows the USM model is better, [4], but the USM model is rather complex and is not convenient for engineering application. A best compromise between the reasonability and simplicity is either an implicit algebraic two-phase Reynolds stress model, or a nonlinear k-ε-k_p two-phase turbulence model. Since the implicit algebraic Reynolds stress models frequently cause some divergence problem due to lack of diffusion terms in the momentum equation, particularly in three-dimensional flows, a nonlinear k-ε-k_p two-phase turbulence model, i.e. an explicit algebraic stress model, is preferred. This is because the momentum equations and k, ε, k_p equations have the same form for both linear and nonlinear k-ε-k_p models, so it is easier to get the convergent results.

Recently, remarkable strides have been made in developing the nonlinear stress-strain k-ε models for single-phase flows, [5]. In the nonlinear stress-strain model, the equivalent eddy viscosity is anisotropic. The nonlinear k-ε model has been validated in simple flows and applied to simulate complex flows. The comparison with experiments shows that this model does make significant improvement over the standard isotropic k-ε model and this model is almost as economical as the linear k-ε model is. For turbulent gas-particle flows, a nonlinear k-ε-k_p two-phase turbulence model is proposed in this paper. Nonlinear relationships of

Contributed by the Fluids Engineering Division for publication in the JOURNAL OF FLUIDS ENGINEERING. Manuscript received by the Fluids Engineering Division January 19, 2000, revised manuscript received June 20, 2002. Associate Editor: Y. Matsumoto.

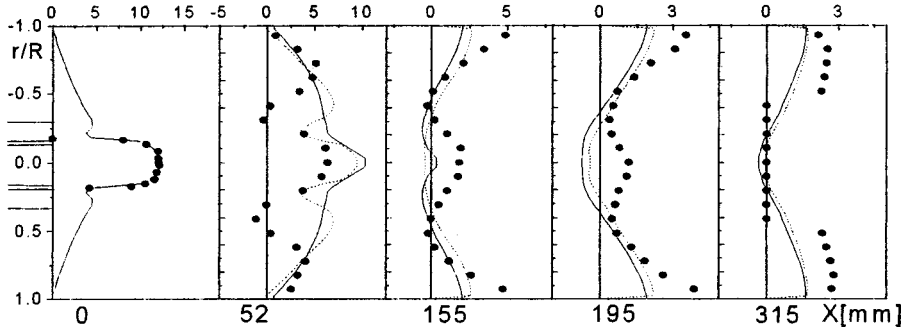

Fig. 1 Axial velocity of 45 μm particles (m/s, $s=0.47$) (● Exp, —NKP, ···USM)

two-phase Reynolds stresses and two-phase fluctuation velocity correlations with the strain rates are derived from the algebraic two-phase Reynolds stress expressions. The nonlinear k-ε-k_p model is applied to simulate swirling gas-particle flows. The comparison is made between the predictions using the nonlinear k-ε-k_p, USM models and the PDPA measurement data to access the proposed model.

2 A Nonlinear k-ε-k_p Model

Consider the algebraic expressions of two-phase Reynolds stresses and two-phase fluctuation velocity correlations [6],

$$\overline{v_i v_j} = (1-\lambda)\frac{2}{3}k\delta_{ij} + \lambda\frac{k}{\varepsilon}\left(\overline{v_i v_k}\frac{\partial V_j}{\partial x_k} + \overline{v_j v_k}\frac{\partial V_i}{\partial x_k}\right) + \frac{k}{c_1\rho\varepsilon}(\overline{v_{pi}v_j} + \overline{v_i v_{pj}} - 2\overline{v_i v_j})$$

$$\overline{v_{pi}v_{pj}} = -\frac{\tau_{rp}}{2}\left(\overline{v_{pi}v_{pk}}\frac{\partial V_{pj}}{\partial x_k} + \overline{v_{pj}v_{pk}}\frac{\partial V_{pi}}{\partial x_k}\right) + \frac{1}{2}(\overline{v_i v_{pj}} + \overline{v_{pi}v_j})$$

$$\overline{v_{pi}v_j} = -\frac{\rho\tau_{rp}}{\rho+\rho_p}\left(\overline{v_{pi}v_k}\frac{\partial V_j}{\partial x_k} + \overline{v_j v_{pk}}\frac{\partial V_{pi}}{\partial x_k}\right) + \frac{\rho}{\rho+\rho_p}\overline{v_i v_j} + \frac{\rho_p}{\rho+\rho_p}\overline{v_{pi}v_{pj}} - \frac{\rho\tau_{rp}}{\rho+\rho_p}\frac{1}{\tau_e}\overline{v_{pi}v_i}\delta_{ij}$$

where $\overline{v_i v_j}$ and $\overline{v_{pi}v_{pj}}$ are gas-phase and particle-phase Reynolds stresses, respectively. $\overline{v_{pi}v_j}$ is the two-phase fluctuation velocity correlation. We can transform the above-listed expressions into their explicit form, on the right-hand side of which there are no terms containing $\overline{v_{pi}v_j}$, $\overline{v_{pi}v_{pj}}$, $\overline{v_i v_j}$. The obtained nonlinear stress-strain relationship written to quadratic-power terms of the strain rates, for example, for $\overline{v_{pi}v_{pj}}$ is

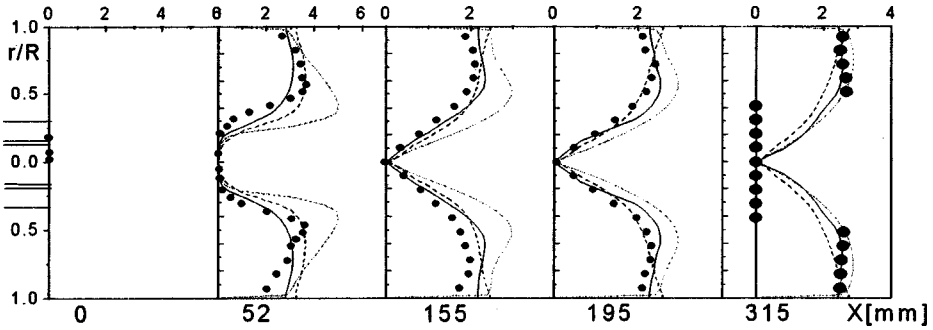

Fig. 2 Tangential velocity of 45 μm particles (m/s, $s=0.47$) (● Exp, —NKP, ···USM)

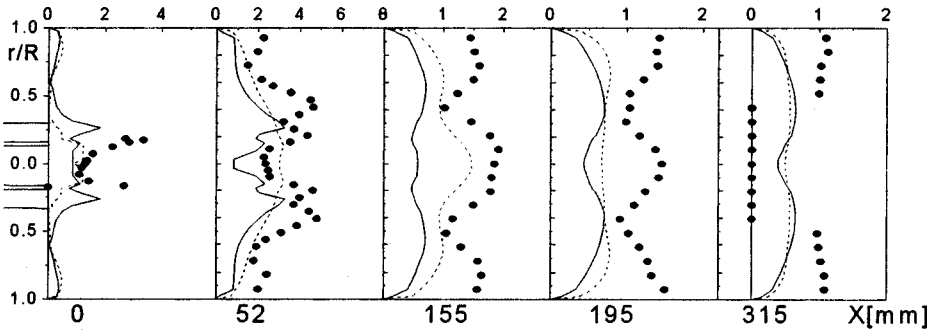

Fig. 3 Axial fluctuation velocity of 45 μm particles (m/s, $s=0.47$) (● Exp, —NKP, ···USM)

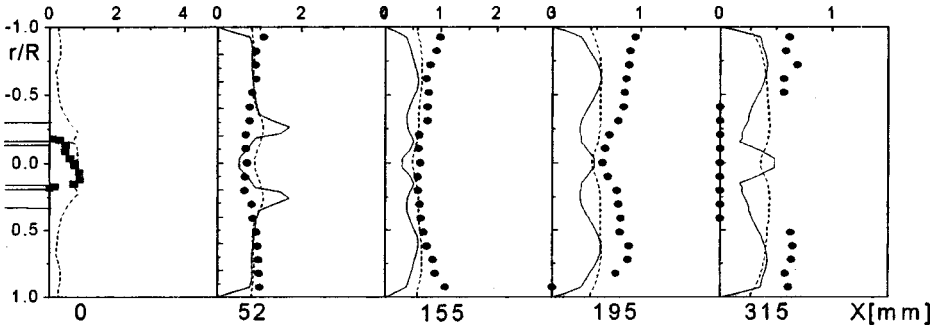

Fig. 4 Tangential fluctuation velocity of 45 μm particles (m/s, $s=0.47$) (● Exp, —NKP, ···USM)

$$\overline{v_{pi}v_{pj}} = P_1\delta_{ij} + P_2\left(\frac{\partial V_i}{\partial x_j} + \frac{\partial V_j}{\partial x_i}\right) + P_3\left(\frac{\partial V_{pi}}{\partial x_j} + \frac{\partial V_{pj}}{\partial x_i}\right) + P_4\left(\frac{\partial V_i}{\partial x_k}\left(\frac{\partial V_j}{\partial x_k} + \frac{\partial V_k}{\partial x_j}\right) + \frac{\partial V_j}{\partial x_k}\left(\frac{\partial V_i}{\partial x_k} + \frac{\partial V_k}{\partial x_i}\right)\right) + P_5\left(\frac{\partial V_{pi}}{\partial x_k}\left(\frac{\partial V_{pj}}{\partial x_k} + \frac{\partial V_{pk}}{\partial x_j}\right) + \frac{\partial V_{pj}}{\partial x_k}\left(\frac{\partial V_{pi}}{\partial x_k} + \frac{\partial V_{pk}}{\partial x_i}\right)\right) + P_6\left(\frac{\partial V_i}{\partial x_k}\left(\frac{\partial V_{pj}}{\partial x_k} + \frac{\partial V_{pk}}{\partial x_j}\right) + \frac{\partial V_j}{\partial x_k}\left(\frac{\partial V_{pi}}{\partial x_k} + \frac{\partial V_{pk}}{\partial x_i}\right)\right) + P_7\left(\frac{\partial V_{pi}}{\partial x_k}\left(\frac{\partial V_j}{\partial x_k} + \frac{\partial V_k}{\partial x_j}\right) + \frac{\partial V_{pj}}{\partial x_k}\left(\frac{\partial V_i}{\partial x_k} + \frac{\partial V_k}{\partial x_i}\right)\right) + P_8\left(\left(\frac{\partial V_i}{\partial x_k} - \frac{\partial V_{pi}}{\partial x_k}\right)\left(\frac{\partial V_j}{\partial x_k} - \frac{\partial V_{pj}}{\partial x_k}\right)\right) \quad (1)$$

where the coefficients P1∼P8 are functions of k, ε, k_p, k_{pg}, ρ_p, ρ, and τ_{rp}; k is the gas turbulent kinetic energy, ε is its dissipation rate, k_p is the particle turbulent kinetic energy, and k_{pg} is defined by $k_{pg}=\overline{v_i v_{pi}}$. We can obtain the similar expressions for $\overline{v_i v_j}$ and $\overline{v_{pi}v_j}$. The variables k, ε, k_p, and k_{pg} will be determined by their transport equations

$$\frac{\partial}{\partial t}(\rho k) + \frac{\partial}{\partial x_k}(\rho V_k k) = \frac{\partial}{\partial x_k}\left(\rho c_s \frac{k}{\varepsilon}\overline{v_k v_l}\frac{\partial k}{\partial x_l}\right) - \rho\overline{v_i v_k}\frac{\partial v_i}{\partial x_k} - \rho\varepsilon + \frac{\rho_p}{\tau_{rp}}(2k_{pg} - 2k) \quad (2)$$

$$\frac{\partial}{\partial t}(\rho\varepsilon) + \frac{\partial}{\partial x_k}(\rho V_k \varepsilon) = \frac{\partial}{\partial x_k}\left(\rho c_\varepsilon \frac{k}{\varepsilon}\overline{v_k v_l}\frac{\partial \varepsilon}{\partial x_l}\right) + \frac{\varepsilon}{k}\left(c_{\varepsilon 1}\left(-\rho\overline{v_i v_k}\frac{\partial v_i}{\partial x_k} + \frac{\rho_p}{\tau_{rp}}(2k_{pg} - 2k)\right) - c_{\varepsilon 2}\rho\varepsilon\right) \quad (3)$$

$$\frac{\partial}{\partial t}(\rho_p k_p) + \frac{\partial}{\partial x_k}(\rho_p V_{pk} k_p) = \frac{\partial}{\partial x_k}\left(\rho_p c_{kp}\frac{k_p}{\varepsilon_p}\overline{v_{pk}v_{pl}}\frac{\partial k_p}{\partial x_l}\right) - \rho_p\overline{v_{pi}v_{pk}}\frac{\partial v_{pi}}{\partial x_k} + \frac{\rho_p}{\tau_{rp}}(2k_{pg} - 2k_p) \quad (4)$$

$$\frac{\partial}{\partial t}(k_{pg}) + (V_k + V_{pk})\frac{\partial}{\partial x_k}(k_{pg}) = \frac{\partial}{\partial x_k}\left(\left(c_s\frac{k}{\varepsilon}\overline{v_k v_l} + c_{kp}\frac{k_p}{\varepsilon_p}\overline{v_{pk}v_{pl}}\right)\frac{\partial k_{pg}}{\partial x_l}\right) - \frac{1}{2}\left(\overline{v_i v_{pk}}\frac{\partial v_{pi}}{\partial x_k} + \overline{v_{pi}v_k}\frac{\partial v_i}{\partial x_k}\right) - \frac{1}{\tau_e}k_{pg} + \frac{1}{\rho\tau_{rp}}(\rho_p k_p + \rho k - (\rho + \rho_p)k_{pg}). \quad (5)$$

3 Simulation Results and Discussion

The nonlinear k-ε-k_p (NKP) model was used to simulate swirling gas-particle flows measured by Sommerfeld and Qiu [7] using PDPA. The adopted grid nodes are 20×43, but a fine grid system of 40×86 was also used, and it gives the same results. For the axial and tangential velocities of 45 μm particles (Figs. 1 and 2), except for individual cross sections, in most regions of the flow field, the difference between two model predictions is small and both of them are in good agreement with experiments. Figures 3 and 4 give the predicted axial and tangential fluctuation velocities of 45 μm particles. In most regions the difference between two model predictions is not obvious and is small than that for the gas phase. The particle fluctuation velocities are underpredicted using either of these two models. The discrepancy between predictions and experiments may be caused by PDPA measurements including the effect of particle size and the effect of particle-wall collision not taken into account in both two models.

4 Conclusions

1. The NKP model has the modeling capability nearly to that of the USM model in simulating the swirling gas-particle flows.
2. Both of NKP and USM models can give the predicted two-phase averaged velocities in good agreement with those measured.

3. Both of these two models can simulate the anisotropic two-phase turbulence, but underpredict the two-phase fluctuation velocities, and the difference between the two model predictions is not obvious.
4. The nonlinear k-ε-k_p model has no problem of convergence encountered in the implicit algebraic stress model.
5. In two-dimensional flows with small geometrical sizes the NKP model can save about 50% computation time than the USM model. However, in three-dimensional flows with large geometrical sizes the NKP model can save much more computation time.

Acknowledgment

This study was supported by the Special Funds for Major State Basic Research, under the Project G1999-0222-08, PRC.

References

[1] Zhou, L. X., 1993, *Theory and Numerical Modeling of Turbulent Gas-Particle Flows and Combustion*, Science Press, Beijing and CRC Press, Boca Raton, FL, pp. 156–161.
[2] Simonin, O., 1996, "Continuum Modeling of Dispersed Turbulent Two-Phase Flows" (Lecture Series 1996-02 at the von Karman Institute for Fluid Dynamics: Combustion and Turbulence in Two-phase Flows), Von Karman Institute for Fluid Dynamics, Rhode-St. Ganèse, Belgium, pp. 1–47.
[3] Zaichik, L. I., 1996, "An Equation for the Particle Velocity Probability Density Function in Inhomogeneous Turbulent Flow," Fluid Dyn., **31**(2).
[4] Zhou, L. X., and Chen, T., 2001, "Simulation of Strongly Swirling Gas-Particle Flows Using USM and k-ε-k_p Two-Phase Turbulence Models," Powder Technol., **114**, pp. 1–11.
[5] Shih, T.-H., and Lumley, J. L., 1993, "Remarks on Turbulent Constitutive Relations," Math. Comput. Modell., **18**, pp. 1377–1387.
[6] Zhou, L. X., Liao, C. M., and Chen, T., 1994, "A Unified Second-Order Moment Two-Phase Turbulence Model for Simulating Gas-Particle Flows," *Numerical Methods in Multiphase Flows*, ASME-FED-185, ASME, New York, pp. 307–313.
[7] Sommerfeld, M., and Qiu, H. H., 1991, "Detailed Measurement of a Swirling Particulate Two-Phase Flow by a Phase Doppler Anemometer," Int. J. Heat Fluid Flow, **12**, pp. 20–28.

A Finite Element Model and Electronic Analogue of Pipeline Pressure Transients With Frequency-Dependent Friction

Jian-Jun Shu
Associate Professor, School of Mechanical and Production Engineering, Nanyang Technological University, 50 Nanyang Avenue, Singapore 639798
e-mail: mjjshu@ntu.edu.sg

A finite element model and its equivalent electronic analogue circuit has been developed for fluid transients in hydraulic transmission lines with laminar frequency-dependent friction. Basic equations are approximated to be a set of ordinary differential equations that can be represented in state-space form. The accuracy of the model is demonstrated by comparison with the method of characteristics. [DOI: 10.1115/1.1522415]

1 Introduction

If external perturbations are superimposed onto a steady system, the equilibrium no longer exists. These perturbations will propagate in the form of waves. Some waves chase each other to form weakly discontinuous rarefaction waves and strongly discontinuous shock waves. In hydraulic systems, transient flow usually occurs when there is either a retardation of the flow due to closure of a pump valve or an acceleration due to the opening of the valve. This may cause damage to hydraulic components, reduce volumetric efficiency, and hence disturb normal operations by forming the rarefaction wave, commonly known as waterhammer, and the shock wave generated by cavitation.

Dynamic analysis in a time domain is one of the most important parts of computer simulation of hydraulic systems. Most transient distributed models can be described by hyperbolic partial differential equations. The method of characteristics, [1–4], has been widely and successfully used in tackling the problems of fluid transients such as waterhammer, [5,6], and cavitation, [7,8]. In the calculation procedures of the method of characteristics, due to the determination between time-step and space-step, there is some difficulty in determining the compatible time-step and boundary conditions to connect with other hydraulic lumped or distributed models, especially in the design of expert systems, large-scale power system packages and parallel processing. For example, at least 2000 computing elements are needed for a time-step with 10^{-2} millisecond along a tube 20 m in length. When variable time-steps are required, the calculation for intermediate interpolations becomes very expensive. Another disadvantage of using the method of characteristics is that some mathematical transformations are required before a numerical scheme is implemented.

In an attempt to overcome these limitations, finite element formulations were devised by Rachford and Ramsey [9], Watt et al. [10], Paygude et al. [11], and others listed in [12] without considering frequency-dependent friction. These formulations produce many numerical oscillations due to using a conventional uniformly spaced grid system with two degrees-of-freedom, pressure and flow rate. In the work that follows, the Galerkin finite element method, [13], is re-examined by including frequency-dependent friction and using one degree-of-freedom, pressure, or flow rate. The objective of this paper is to illustrate a simple and well-defined problem as an example to demonstrate how the Galerkin finite element method is applied in the space variables only, and gives rise to an initial value problem for a system of ordinary differential equations in order to decouple time-step from space-step. In addition, an equivalent electronic analogue circuit is established. There is no difficulty in applying the presented procedures to solve other waterhammer problems and even cavitation problems.

2 Basic Governing Equations

Before introducing the procedure itself, the physical problem to which it will be applied is described. Because of sudden valve closure at the start of a fluid transmission line, the flow within the transmission line is to be calculated under the assumptions of one-dimensional, unsteady and compressible flow. The independent variables of space and time are denoted x and t. The dependent variables are P, the pressure and Q, the flow rate. In the analysis of fluid transients, two basic principles of mechanics namely (a) the conservation of mass law and (b) Newton's momentum law give rise to two partial differential equations.
(a) Continuity Equation

$$\frac{1}{c_0^2}\frac{\partial P}{\partial t}+\frac{\rho}{\pi r_0^2}\frac{\partial Q}{\partial x}=0. \tag{1}$$

(b) Momentum Equation

$$\frac{\rho}{\pi r_0^2}\frac{\partial Q}{\partial t}+\frac{\partial P}{\partial x}+F(Q)+\rho g\sin\theta_0=0, \tag{2}$$

Contributed by the Fluids Engineering Division for publication in the JOURNAL OF FLUIDS ENGINEERING. Manuscript received by the Fluids Engineering Division June 25, 2001; revised manuscript received July 29, 2002. Associate Editor: J. S. Marshall.

Table 1 n_i and m_i

i	1	2	3	4	5	6	7	8	9	10
n_i	2.63744 $\times 10^1$	7.28033 $\times 10^1$	1.87424 $\times 10^2$	5.36626 $\times 10^2$	1.57060 $\times 10^3$	4.61813 $\times 10^3$	1.36011 $\times 10^4$	4.00825 $\times 10^4$	1.18153 $\times 10^5$	3.48316 $\times 10^5$
m_i	1.0	1.16725	2.20064	3.92861	6.78788	1.16761 $\times 10^1$	2.00612 $\times 10^1$	3.44541 $\times 10^1$	5.91642 $\times 10^1$	1.01590 $\times 10^2$

where c_0 is the acoustic velocity, ρ is the density, g is the acceleration due to gravity, r_0 is the internal radius of the transmission line tube, and θ_0 is the angle of the transmission line tube inclined with the horizontal. The friction term $F(Q)$ can be expressed as a steady friction term F_0 plus a frequency-dependent friction term, for which a model applicable to laminar flow has been developed by Zielke [14] and Kagawa et al. [15].

$$F = F_0 + \frac{1}{2}\sum_{i=1}^{k} Y_i \tag{3}$$

$$\begin{cases} \dfrac{\partial Y_i}{\partial t} = -\dfrac{n_i \mu}{\rho r_0^2} Y_i + m_i \dfrac{\partial F_0}{\partial t} \\ Y_i(0) = 0 \end{cases} \tag{4}$$

μ is the viscosity. The constants n_i and m_i are tabulated in Table 1 and the number of terms k to be selected should be determined according to the relationship between the break frequency of the approximated weighting function and the frequency range of the system, [15], which is assumed in steady state when time $t=0$.

3 Galerkin Finite Element Method

Finite element formulations using the Galerkin method in time domain analysis have been presented by Rachford and Ramsey [9], Watt et al. [10], and Paygude et al. [11] without considering frequency-dependent friction by using a conventional uniformly spaced grid system with two degrees-of-freedom, pressure, and flow rate. These formulations produce many numerical oscillations. In the work that follows, the Galerkin finite element method is re-examined by including frequency-dependent friction and using one degree-of-freedom, pressure, or flow rate.

Let $U=\rho/\pi r_0^2 Q$, $F_0(Q)=8\mu/\pi r_0^4 Q$, $R=8\mu/\rho r_0^2$ and $H_0=\rho g \sin\theta_0$ for the case of linear steady friction, the Eq. (1), (2), and (4) can be rearranged in terms of the operator equations

$$L_1(U,P,Y_i) \equiv \frac{1}{c_0^2}\frac{\partial P}{\partial t} + \frac{\partial U}{\partial x} = 0 \tag{5}$$

$$L_2(U,P,Y_i) \equiv \frac{\partial U}{\partial t} + \frac{\partial P}{\partial x} + RU + \frac{1}{2}\sum_{i=1}^{k} Y_i + H_0 = 0 \tag{6}$$

$$L_3(U,P,Y_i) \equiv \frac{\partial Y_i}{\partial t} + \frac{n_i R}{8} Y_i - m_i R \frac{\partial U}{\partial t} = 0. \tag{7}$$

When the transmission line is divided into $2N+1$ equal elements, each Δx in length, as shown in Fig. 1 and a suitable finite dimensional space is spanned by shape functions, [13],

$$w_j^+(x) = \frac{x_{j+2}-x}{x_{j+2}-x_j} \quad w_j^-(x) = \frac{x-x_j}{x_{j-2}-x_j}. \tag{8}$$

The Galerkin method consists in finding approximations to U, P, and Y_i of the form

$$U(x,t) = u_{2j}(t) w_{2j}^+(x) + u_{2j+2}(t) w_{2j+2}^-(x) \tag{9}$$

$$P(x,t) = p_{2j+1}(t) w_{2j+1}^+(x) + p_{2j+3}(t) w_{2j+3}^-(x) \tag{10}$$

$$Y_i(x,t) = y_{i,2j}(t) w_{2j}^+(x) + y_{i,2j+2}(t) w_{2j+2}^-(x) \tag{11}$$

for $j=0,1,\ldots,N-1$, where the unknown coefficients u, p, and y_i, which are nodal values of U, P, and Y_i, respectively, are determined by an inner product $(\bullet,\bullet)$ so that

$$(L_i, w_j^+) \equiv \int_{x_j}^{x_{j+2}} w_j^+ L_i dx = 0 \quad \text{and} \quad (L_i, w_j^-) \equiv \int_{x_j}^{x_{j-2}} w_j^- L_i dx = 0 \tag{12}$$

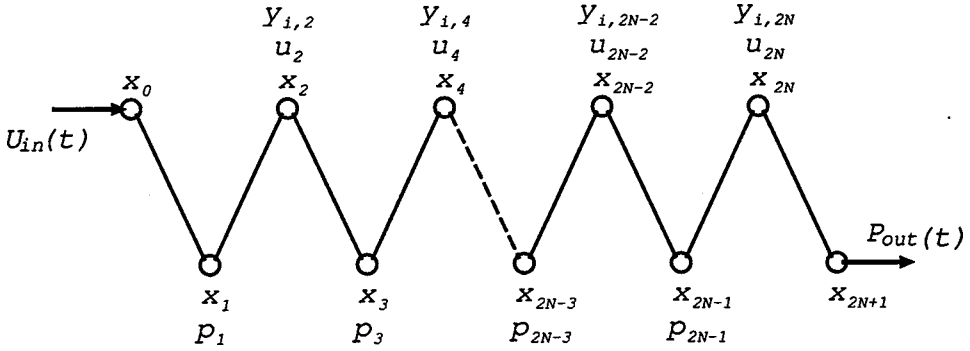

Fig. 1 Interlacing grid system

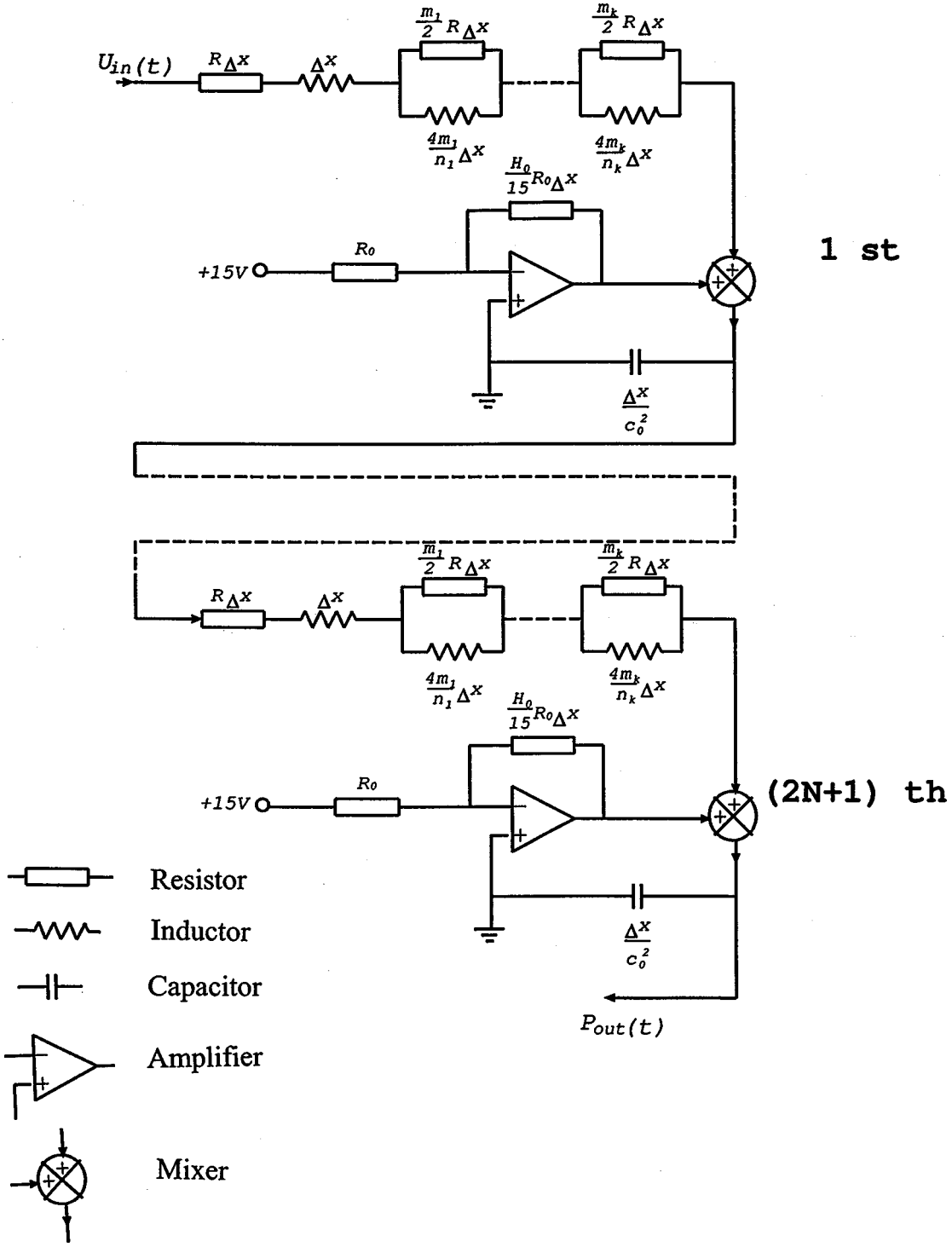

Fig. 2 Equivalent electronic analogue circuit

Table 2 Parameter list

Upstream Pressure (MPa)	Downstream Pressure (MPa)	Radius r_0 (mm)	Length L (km)	Density ρ (kg/m^2)	Acoustic Velocity c_0 (m/s)	Viscosity μ (cP)
3	2	4	0.02	871	1392	50.518

when $i=1$, j is chosen as an odd number and when $i=2$ or 3, j is chosen as an even number.

Taking account of the boundary conditions that flow rate $u_0 = U_{\text{in}}(t)$ is known at this end and pressure $p_{N+1} = P_{\text{out}}(t)$ is known at another end, the resultant ordinary differential equation is of the following form:

$$\frac{d}{dt}\begin{pmatrix}\mathbf{u}\\ \mathbf{p}\\ \mathbf{y}\end{pmatrix} = \begin{pmatrix} -R\mathbf{I} & \frac{1}{16\Delta x}\mathbf{A} & -\frac{1}{2}(\Xi\otimes\mathbf{I})^T \\ \frac{c_0^2}{16\Delta x}\mathbf{B} & \mathbf{O} & \mathbf{O} \\ -R^2\mathbf{M}\otimes\mathbf{I} & \frac{R}{16\Delta x}\mathbf{M}\otimes\mathbf{A} & -\frac{R}{8}[\mathbf{F}+4\mathbf{M}\otimes(\Xi\otimes\mathbf{I})^T] \end{pmatrix} \times \begin{pmatrix}\mathbf{u}\\ \mathbf{p}\\ \mathbf{y}\end{pmatrix} + \frac{c_0^2}{16\Delta x}U_{\text{in}}\begin{pmatrix}\mathbf{O}\\ \mathbf{C}\\ \mathbf{O}\end{pmatrix} + \frac{1}{16\Delta x}P_{\text{out}}\begin{pmatrix}\mathbf{D}\\ \mathbf{O}\\ R\mathbf{M}\otimes\mathbf{D}\end{pmatrix} - H_0\begin{pmatrix}\mathbf{E}\\ \mathbf{O}\\ R\mathbf{M}\otimes\mathbf{E}\end{pmatrix} \tag{13}$$

Here the abbreviations for matrix and vector elements appear in expanded form in the Appendix for clarity.

4 Electronic Analogue

The new ordinary differential equation allows us to simulate the fluid transients by constructing an equivalent electronic analogue circuit as shown in Fig. 2. The value and type for each electronic component are indicated.

For a section of transmission line of length Δx, this can be considered to offer a resistor due to the steady fluid friction, an inductor due to the fluid inertia and a capacitor due to the fluid compressibility. The frequency-dependent friction can simply be formed by a set of subcircuits, each of which is made of a resistor and a inductor hooked in parallel. The inverting operational amplifier indicates a constant pressure drop due to gravity for an inclined tube. On reading the analogue circuit, we may get the impression that, without the frequency-dependent friction, the circuit is almost identical to a π-type LC butterworth passive low-pass filter, [16,17]. With time, the wave generated by changes of boundary conditions becomes smoother and smoother due to the rejection of the high frequencies superimposed upon the wave. The parallel RL subcircuit, which is representative of frequency-dependent friction, enhances the function of the low-pass filter by means of raising passing impedance to high-frequency signals.

The great advantage in using the analogue circuit to analyses the fluid transients has been found in the following three major points:

a. A quantitative analysis for the analogue circuit is able to help us fully to understand the fluid transients by means of existing well-established electronic theory.
b. An equivalent electronic analogue circuit is able to provide a monitoring base, such as differentiating cavitation noise from system noise.
c. The low-pass filter design theory is able to modify the circuit to get more precise mathematical models, such as the frequency-dependent friction model.

5 Numerical Results

Transient responses of the finite element formulation have been compared with those of the method of characteristics to demonstrate the accuracy of the Galerkin method. Comparison with previously published data, [18], listed in Table 2, for studying pressure changes at the vicinity of an upstream valve after the sudden closure of the valve in a flowing liquid line, show good agreement between experimental results and numerical computation by means of the method of characteristics for transient flow under negative pressure, in which liquids can withstand tensile strength against vaporization.

It is to be noted at this stage that ordinary differential equations, [13], are based on the Galerkin finite element method in the space

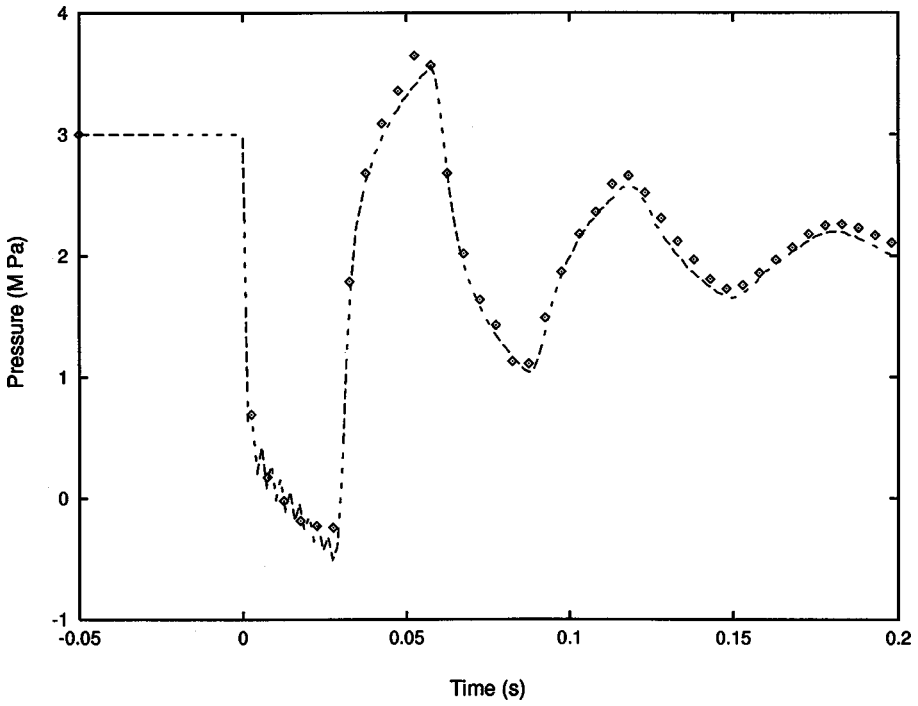

Fig. 3 Finite element method (point) versus method of characteristics (line)

domain only. If the finite element is to be adopted for the time domain also, the problem becomes unmanageable even on large computers. A compromise is to have another numerical scheme in the time domain. Although many different methods are available for solving the ordinary differential equations, [19], the Dormand and Prince fifth-order Runge-Kutta method, [20], has been adopted here.

The comparison for p_0 is usually meaningful, but p_0 is not explicitly computed for the arrangement shown in Fig. 1. The interpolation using the Galerkin method

$$\int_{x_0}^{x_1} w_0^+ L_1(U,P,Y_i)dx = 0$$

$$\text{gives} \quad \frac{dp_0}{dt} = -\frac{1}{2}\frac{dp_1}{dt} + \frac{3c_0^2}{4\Delta x}(U_{\text{in}} - u_2). \tag{14}$$

The result for p_0 is plotted and compared as shown in Fig. 3 with the time-step$=5\times10^{-3}$ seconds.

6 Conclusions

A finite element model with laminar frequency-dependent friction has been developed. The finite element model retains the accuracy of the method of characteristics. Based on the finite element model, an electronic analogue methodology has been presented for the problem of fluid transients. The use of the equivalent electronic analogue circuit provides an alternative way to understand the mechanism of transient fluid flow and improve the frequency-dependent friction model mathematically.

Acknowledgments

The author is grateful to Prof. Jeffrey S. Marshall and the reviewers for their constructive comments and suggestions.

Appendix

Details of Abbreviations Used in the Ordinary Differential Eq. (13).

$$\mathbf{u}=\{u_2,u_4,\cdots,u_{2N}\}^T,\ \ \mathbf{p}=\{p_1,p_3,\cdots,p_{2N-1}\}^T,$$

$$\mathbf{y}=\{y_{1,2},y_{1,4},\cdot,y_{k,2N},y_{2,2},\cdots,y_{k,2N}\}^T,$$

$$\mathbf{N}=\{n_1,n_2,\cdots,n_k\}^T,\quad \mathbf{M}=\{m_1,m_2,\cdots,m_k\}^T,\boldsymbol{\Xi}=\{1,1,\cdots,1\}^T$$

$$\mathbf{A}=\begin{pmatrix} 10 & -12 & 2 & & & & & & & \\ -1 & 11 & -11 & 1 & & & & & & \\ & -1 & 11 & -11 & 1 & & & & & \\ & & \cdot & \cdot & \cdot & \cdot & & & & \\ & & & \cdot & \cdot & \cdot & \cdot & & & \\ & & & & \cdot & \cdot & \cdot & \cdot & & \\ & & & & & -1 & 11 & -11 & 1 & \\ & & & & & & -1 & 11 & -11 & \\ & & & & & & & -2 & 12 & \end{pmatrix}$$

$$\mathbf{B}=\begin{pmatrix} -12 & 2 & & & & & & & & \\ 11 & -11 & 1 & & & & & & & \\ -1 & 11 & -11 & 1 & & & & & & \\ & \cdot & \cdot & \cdot & \cdot & & & & & \\ & & \cdot & \cdot & \cdot & \cdot & & & & \\ & & & \cdot & \cdot & \cdot & \cdot & & & \\ & & & & -1 & 11 & -11 & 1 & & \\ & & & & & -1 & 11 & -11 & 1 & \\ & & & & & & -2 & 12 & -10 & \end{pmatrix}$$

$$\mathbf{C}=\{10,-1,0,\cdot,\cdot,\cdot,0,0,0\}^T \quad \mathbf{D}=\{0,0,0,\cdot,\cdot,\cdot,0,1,-10\}^T$$

$$\mathbf{E}=\{1,1,1,\cdot,\cdot,\cdot,1,1,1\}^T$$

$$\mathbf{F}=\begin{pmatrix} n_1\mathbf{I} & & & & \\ & n_2\mathbf{I} & & & \\ & & \cdot & & \\ & & & \cdot & \\ & & & & \cdot \\ & & & & n_k\mathbf{I} \end{pmatrix}.$$

The symbol $\otimes$ defines the Kronecker product of a vector $\mathbf{Z}=\{z_1,z_2,\cdots,z_k\}^T$ and a matrix $\mathbf{G}$, that is, $\mathbf{Z}\otimes\mathbf{G}\equiv\{z_1\mathbf{G},z_2\mathbf{G},\cdots,z_k\mathbf{G}\}^T$.

References

[1] Evangelisti, G., 1965, "Teoria generale del colpo d'ariete col metodo delle caratteristiche," L' Energía Elettrica, **42**, pp. 65–145.
[2] Evangelisti, G., 1969, "Waterhammer Analysis by the Method of Characteristics," L' Energía Elettrica, **46**, pp. 673–839.
[3] Gray, C. A. M., 1954, "The Analysis of the Dissipation of Energy in Water Hammer," Aust. J. Appl. Sci., **5**, pp. 125–131.
[4] Streeter, V. L., and Lai, C., 1962, "Water-Hammer Analysis Including Fluid Friction," J. Hydraul. Div., Am. Soc. Civ. Eng., **88**, pp. 79–112.
[5] Shu, J.-J., Burrows, C. R., and Edge, K. A., 1997, "Pressure Pulsations in Reciprocating Pump Piping Systems Part 1: Modelling," Proceedings of the Institution of Mechanical Engineers, Part I, Journal of Systems and Control Engineering, **211**, pp. 229–237.
[6] Wylie, E. B., and Streeter, V. L., 1978, *Fluid Transients*, McGraw-Hill, New York.
[7] Shu, J.-J., Edge, K. A., Burrows, C. R., and Xiao, S., 1993, "Transmission Line Modelling With Vaporous Cavitation," ASME Paper No. 93-WA/FPST-2.
[8] Shu, J.-J., 1995, "On Modelling Vaporous Cavitation," *Proceedings of the Second Academic Conference of Young Scientists*, China Association for Science and Technology, Beijing, China, pp. 124–135 (in Chinese).
[9] Rachford, H. H., Jr., and Ramsey, E. L., 1975, "Application of Variational Methods to Model Transient Flow in Complex Liquid Transmission Systems," SPE 5663, Society of Petroleum Engineers of AIME, 50th Annual Fall Meeting, Dallas, TX.
[10] Watt, C. S., Boldy, A. P., and Hobbs, J. M., 1980, "Combination of Finite Difference and Finite Element Techniques in Hydraulic Transient Problems," *Proceedings of the Third International Conference on Pressure Surges*, Canterbury, UK, BHRA Fluid Engineering, **1**, pp. 43–62.
[11] Paygude, D. G., Rao, B. V., and Joshi, S. G., 1985, "Fluid Transients Following a Valve Closure by FEM," *Proceedings of International Conference on Finite Elements in Computational Mechanics (FEICOM 85)*, Bombay, India, T. Kant ed., Pergamon Press, Elmsford, NY pp. 615–624.
[12] Wylie, E. B., and Streeter, V. L., 1993, *Fluid Transients in Systems*, Prentice-Hall, Englewood Cliffs, NJ.
[13] Galerkin, B. G., 1915, "Series Development for Some Cases of Equilibrium of Plates and Beams," Wjestnik Ingenerow Petrograd, **19**, pp. 897 (in Russian).
[14] Zielke, W., 1968, "Frequency-Dependent Friction in Transient Pipe Flow," ASME J. Basic Eng., **90**, pp. 109–115.
[15] Kagawa, T., Lee, I.-Y., Kitagawa, A., and Takenaka, T., 1983, "High Speed and Accurate Computing Method of Frequency-Dependent Friction in Laminar Pipe Flow for Characteristics Method," Trans. Jpn. Soc. Mech. Eng., Ser. B, **49**, pp. 2638–2644 (in Japanese).
[16] Horowitz, P., and Hill, W., 1980, *The Art of Electronics*, Cambridge University Press, Cambridge, UK.

[17] Zverev, A. I., 1967, *Handbook of Filter Synthesis*, John Wiley and Sons, New York.
[18] Lee, I.-Y., Kitagawa, A., and Takenaka, T., 1985, "On the Transient Behavior of Oil Flow Under Negative Pressure," Bull. JSME, **28**, pp. 1097–1104.
[19] Hairer, E., Nørsett, S. P., and Wanner, G., 1987, *Solving Ordinary Differential Equations, I: Nonstiff Problems*, Springer-Verlag, Berlin.
[20] Dormand, J. R., and Prince, P. J., 1980, "A Family of Embedded Runge-Kutta Formulae," J. Comput. Appl. Math., **6**, pp. 19–26.

Prediction of Centrifugal Slurry Pump Head Reduction: An Artificial Neural Networks Approach

Tahsin Engin[1]
Assistant Professor, Faculty of Engineering, Department of Mechanical Engineering, University of Sakarya, 54187 Sakarya, Turkey

Akif Kurt
Research Associate, Faculty of Engineering, Department of Industrial Engineering, University of Sakarya, 54187 Sakarya, Turkey
e-mail: akurt@sakarya.edu.tr

The feasibility of using artificial neural networks (ANN) in the prediction of head reduction of centrifugal pumps handling slurries is examined. An ANN model is proposed and compared with the empirical correlation given by the present authors earlier. The comparison showed that the ANN could successfully be used for the prediction of head reductions of centrifugal slurry pumps. The mean deviation between predicted and experimental values is 5.86% which is reasonable for slurry handling processes.
[DOI: 10.1115/1.1523062]

Introduction

It is well established that the performance of centrifugal pumps with slurries gets reduced in the presence of solids in the carrier liquid. The magnitude of the reduction is a function of concentration of solids in the mixture, physical properties of solids like their specific gravity, size and size distribution of particles, and pump size. For a given concentration of solids and volumetric flow rate at a constant shaft speed, the influence of slurry on a centrifugal pump performance is usually quantified by the head ratio (HR $=H_{slurry}/H_{water}$), and the efficiency ratio (ER$=E_{slurry}/E_{water}$). Another measure of the head reduction of a pump due to presence of solids in the carrying liquid is the head reduction factor (K $=1$-HR), which is widely used. Several correlations have been proposed in the literature to predict HR or K for a given operating condition, [1–7]. However, due to the complexity of the problem, they are usually restricted to narrow range of particular operating conditions. We seek an alternative model to estimate with acceptable accuracy the head reduction factor by using the artificial neural networks (ANN) method. This approach has received significant attention in recent years and it has been applied successfully to a wide range of problems, [9–17], because of its flexibility and easy implementation with a high-speed computer.

The objective of this paper is to evaluate the head reduction factor (K) of a centrifugal slurry pump using ANN. A total of 206 experimental data on slurry pumps with various solids materials available in the literature, [1,2,4–6,8], were utilized. It was found that the ANN model gives satisfactory predictions for almost all cases and leads to lesser prediction errors compared to conventional prediction tools.

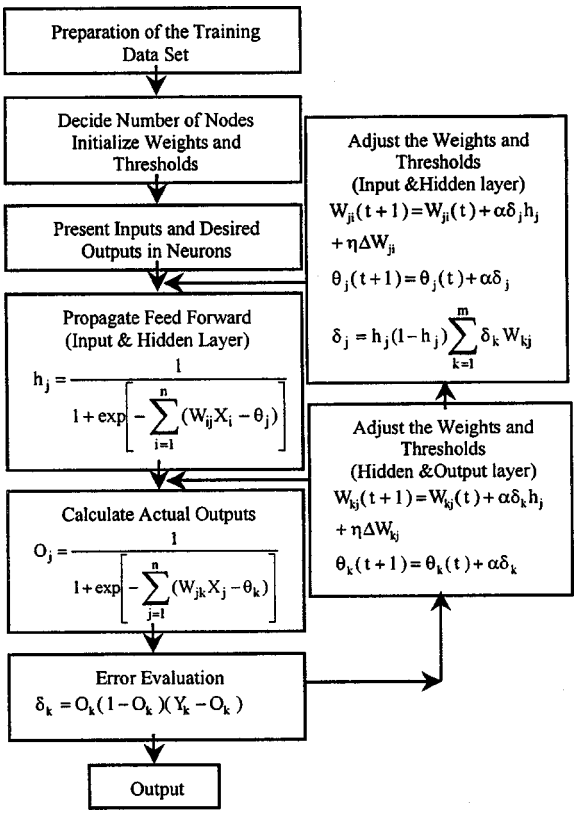

Fig. 1 Flow chart for the back-propagation learning algorithm

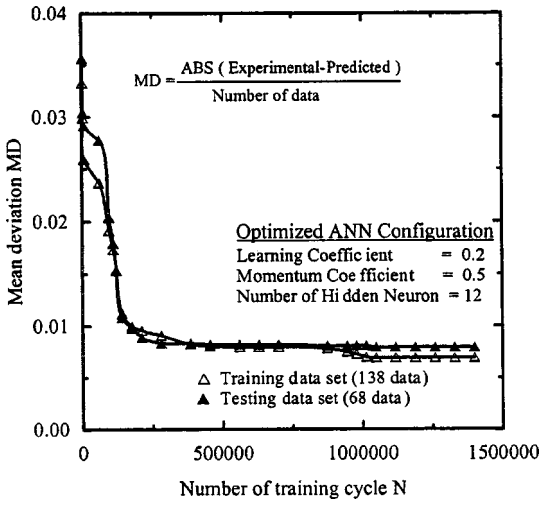

Fig. 2 Performance of proposed neural network architecture

[1]Corresponding author. Presently at the Department of Mechanical Engineering, ms. 312, University of Nevada, Reno, NV 89557. e-mail: engint@unr.nevada.edu.

Contributed by the Fluids Engineering Division for publication in the JOURNAL OF FLUIDS ENGINEERING. Manuscript received by the Fluids Engineering Division Aug. 30, 2001; revised manuscript received July 29, 2002. Associate Editor: B. Schiavello.

Table 1 Solids materials taken from the literature

Ref.	Solid Material	S	C_w(%) (min-max)	d_{50} (μm)	d_w (μm)	D (mm)	Q/Q_{BEP}
[1]	Sand-1	2.64	22.68-53.08	105	-	280	1.0
[1]	Sand-2	2.64	22.68-53.08	330	-	280	1.0
[1]	Sand-3	2.64	22.68-53.08	570	-	280	1.0
[1]	Sand-4	2.64	22.68-53.08	920	-	280	1.0
[1]	Sand-5	2.64	22.68-53.08	1400	-	280	1.0
[2]	Beach sand	2.67	8.85-63.86	295	-	371	0.4-1.0
[2]	River sand	2.64	13.93-56.45	1290	-	371	0.4-1.0
[2]	Ilmenite	4.63	16.11-61.57	170	-	371	0.4-1.0
[4]	Iron ore-B	4.15	27.93-37.27	1800	-	430	0.5-0.8
[4]	Perlite	2.34	33.06-54.93	350	-	430	0.5-0.8
[4]	Granite	2.67	17.31-30.71	3000	-	430	0.5-0.8
[5]	Zinc tailing	2.85	13.62-56.17	-	170.4	270	AV
[5]	Coal-A	1.48	33.94-47.74	-	900	270	AV
[6]	Sand-A	2.65	9.05-32.77	180	180	270	AV
[6]	Sand-B	2.65	6.51-27.91	230	230	270	AV
[6]	Sand-C	2.65	6.71-24.72	460	460	270	AV
[6]	Sand-D	2.65	6.64-56.02	230	230	270	AV
[6]	Sand-E	2.65	10.78-55.21	230	328	270	AV
[6]	Sand-F	2.65	6.72-44.60	362	400	270	AV
[6]	Coal-B	1.49	9.01-57.80	185	377	270	AV
[6]	Iron ore-A	4.35	2.51-12.59	663	663	270	AV
[6]	Mild Steel	6.24	5.33-23.20	230	230	270	AV
[6]	Zinc	5.51	3.67-9.47	455	482	270	AV
[8]	Coal-C1	1.625	15.84-20.67	-	14900	825	1.0
[8]	Coal-C2	1.562	25.31-29.25	-	15500	825	1.0
[8]	Coal-C3	1.716	27.23-36.15	-	15300	825	1.0
[8]	Coal-D1	1.520	23.58-29.66	-	16700	825	1.0
[8]	Coal-D2	1.756	38.46-42.68	-	17600	825	1.0
[8]	Coal-D3	1.759	43.17-48.67	-	17300	825	1.0
[8]	Coal-E1	1.827	18.87	-	17300	825	1.0
[8]	Coal-E2	1.772	30.72-33.12	-	16600	825	1.0
[8]	Coal-E3	1.754	42.16-45.57	-	15900	825	1.0
[8]	Gravel	2.60	21.44-28.59	-	26700	825	1.0

AV = averaged values over full range of flow rate

Artificial Neural Networks (ANN) and Implementation

Like a biological neuron, an ANN has the ability to adapt itself to changing environment and can solve problems involving complex nonlinear relationships, which do not lend themselves to conventional algorithmic solutions. An artificial neural network consists of input, hidden, and output neuron layers. An input layer receives data from the outside world and sends signals to subsequent layers. The hidden layer interprets signals from the previous layer to produce a result that is transmitted to the next layer. The output layer interacts with the outside world as the network's interpretation of the input data. Several neurons may exist in each layer. Each connector among the neurons has an associated scalar weight whose value can be modified during the training process of the neural network. The information processing of a neuron is performed through a simple set of mathematical operations. Each input signal X_i is first multiplied by a scalar weight W_{ij} and the weighted inputs are summed together to obtain x_j. The subscript ij refers to connection between ith and jth neurons. Therefore, the input to a jth neuron can be written as follows:

$$x_j = \sum_{i=1}^{n} (W_{ij} X_i - \theta_j) \tag{1}$$

where θ_j is a threshold value acting as a bias. The activation level of the neuron (x_j) should be modified by a transfer function. The most commonly used activation or transfer function is the sigmoid function, which is effectively used in back-propagation (BP) learning algorithm. The sigmoid function is given as

$$f(x_j) = \frac{1}{1 + e^{-x_j}} \tag{2}$$

Since this function has asymptotic limits of 0 and 1, all data to be used in ANN should be normalized to keep their values in this range. To achieve this, each parameter in the data set was divided by the largest value of that parameter group. A computer code was developed using the C^{++} language for iterative ANN calculations. The procedure is implemented through several stages, which involves data preparation, solution of network parameters and training data set, as well as network training. Figure 1 provides the flow chart used for BP learning algorithm. However, the interested reader is referred to the Haykin's textbook [18], for an account of the history of ANN and its mathematical background.

Several ANN architectures were designed and tested for the pump system using the software developed on a Pentium III 733

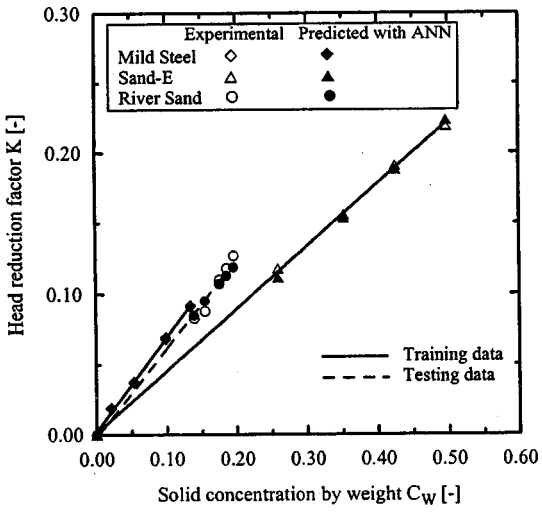

Fig. 3 Comparison between predicted and experimental head reduction factors

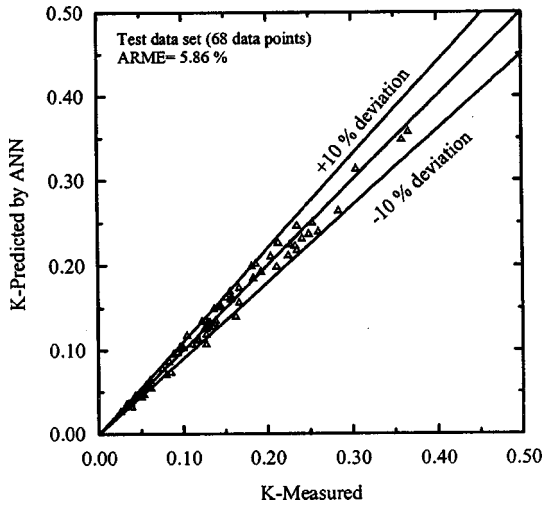

Fig. 4 Accuracy of ANN model for testing data set

MHz PC. It was found that the network architecture that best represents the problem has one hidden layer with 12 neurons. Also, the learning rate and momentum coefficient were optimized to be 0.2 and 0.5, respectively. Feed-forward fully connected networks with one hidden layer of neurons, having sigmoid transfer functions were used. Three input neurons (viz. specific gravity of solids S, concentration of solids by weight C_W, and relative particle diameter d/D), 12 hidden layer neurons and one output neuron, the head reduction factor K were considered.

A total of 206 data of head reduction factor K obtained experimentally by several researchers, [1,2,4–6,8], were gathered and classified. Thus, a data set covering a wide range of physical properties of solids (specific gravity $1.49 \leqslant S \leqslant 6.24$, average particle diameter 105 μm$\leqslant d_W$ or $d_{50} \leqslant 26700$ μm) with concentration by weight $C_W \leqslant 63.86$, and impeller diameter 270 mm$\leqslant D \leqslant 825$ mm, was provided. Then, the data set was divided into two groups: the first (138 data) was used as the training data set, and the second one (68 data) was used as the testing of data set. The solid materials and their physical properties are shown in Table 1.

The absolute relative mean error (ARME) was used to determine the performance of ANN, which is expressed as

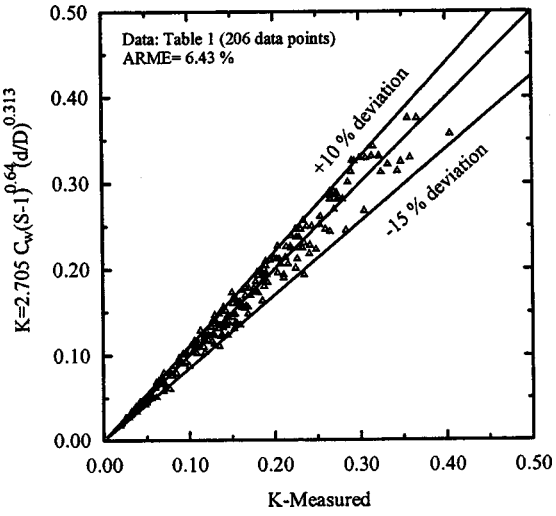

Fig. 5 Accuracy of the conventional correlation technique, [7], for prediction of head reduction factor

$$\text{ARME} = \frac{1}{N}\sum_{i=1}^{N}\left|100\frac{\text{Exp}_i - \text{Pred}_i}{\text{Exp}_i}\right| \tag{3}$$

where $N = 138$ for training data set, and $N = 68$ for testing data set.

Results and Discussions

The performance of the optimized ANN architecture is shown in Fig. 2. Such type of trend reflects the typical response of an ANN by BP with increasing of number of training cycle. At first, a sharp decrease in both mean deviations is observed until a certain number of training cycles is reached. It is clearly seen from this figure that each mean deviation remains unaltered at a lowest value after $N = 1{,}050{,}000$ approximately. The lowest mean deviations obtained are 0.007945 and 0.006923 for testing and training, respectively.

In order to test the applicability of the proposed ANN approach, variation of K with C_W for various solid materials were considered. Figure 3 shows a representative graph, comparing between the experimental and the predicted head reduction factors for three solids. As seen in Fig. 3, the training ability of the ANN appears to be very good since the training data points almost coincide with the corresponding experimental data for mild steel and sand-E. It is also clear from the same figure that the predicted values for testing of river sand show a good agreement with the experimental data. All the predicted head reduction factors for river sand are on the best-fitted curve (dashed line). The largest deviation of 6.50% in the predicted K for river sand occurs at a concentration of 19.57% by weight.

Figure 4 shows the accuracy of the proposed ANN model. The testing data set consists of 68 experimental values of K for the solid materials given in Table 1. The deviations between the experimental and the predicted values lie within $\pm 10\%$ band with ARME 5.86%. The most recent correlation in the literature, [7], which was given in the form of $K = 2.705 C_W (S-1)^{0.64} (d_w/D)^{0.313}$, produces an ARME of 6.43% for the whole data as shown in Fig. 5, which also indicates a data scattering in the range of -15% to $+10\%$. It was also observed that this correlation gave rise to ARME of 6.43 for training data set, and 6.86% for testing data set, respectively. None of the other correlations available in the literature, [1–6], could give better predictions compared to the proposed ANN model for both testing and training data sets. Taccani et al. [19] reported similar conclusions using data given by Kazim et al. [6]. It is therefore believed that the ANN approach may be a more reliable tool for prediction of the head reduction factors. The results showed that for the training data set, the deviations between the actual and trained values lie within the range of $\pm 10\%$ with ARME 4.41%. This implies that the ANN model exhibits a quite satisfactory harmony with the problem of prediction of the head reduction of centrifugal slurry pumps.

Conclusions

ANN was used as an alternative modeling technique, and appeared to be an enough accurate tool to predict the head reduction factors of centrifugal slurry pumps. A fully connected three layers feed-forward architecture was used for the ANN model. The network consisted of 3 input neurons, 12 hidden neurons, and 1 output neuron, and it was trained using back-propagation (BP) algorithm along with experimental slurry pump data from the literature. Comparing the ANN results with the experimental data, it can be seen that in general the head reduction factor for slurry pumps are modeled sufficiently well. The absolute relative mean errors (ARME) are found to be 4.41% and 5.86% for training and test data sets, respectively. It is therefore concluded that the artificial neural network approach has a great potential in the predicting head reduction and likely efficiency reduction for slurry

pumps. However, it should be noted that the ANN approaches are generally time-consuming to establish an optimal architecture to represent the physical problem.

Nomenclature

C_W = concentration of solids by weight
D = impeller diameter
d_{50} = mass median particle diameter
d_W = weighted mean particle diameter
E = pump efficiency
ER = Efficiency ratio $= E_{\text{slurry}}/E_{\text{water}}$
H = pump head
HR = head ratio $= H_{\text{slurry}}/H_{\text{water}}$
h_j = output of hidden layer
K = head reduction factor, $K = 1\text{-HR}$
m = number of output neurons
n = number of input/hidden neurons
N = number of training cycles
O_k = output of neuron in output layer
Q = pump flow rate
S = specific gravity of solid
t = time
W = scalar weight
X = input vector
x_j = activation level of neuron
Y_k = desired activation of output layer
α = learning rate
η = momentum coefficient
θ = threshold value
δ_j = error vector for each hidden layer neuron
δ_k = output layer error

References

[1] Vocadlo, J. J., Koo, J. K., and Prang, A. J., 1974, ''Performance of Centrifugal Pumps in Slurry Services,'' *Proc. Hydrotransport-3*, Paper J2, BHRA Fluid Engineering, pp. 17–32.

[2] Burgess, K. E., and Reizes, A., 1976, ''The Effect of Sizing, Specific Gravity and Concentration on the Performance of Centrifugal Pumps,'' Proc. Inst. Mech. Eng., **190-36/76**, pp. 391–399.

[3] Cave, I., 1976, ''Effects of Suspended Solids on the Performance of Centrifugal Pumps,'' *Proc. Hydrotransport-4, Paper H3*, BHRA Fluid Engineering, pp. 35–52.

[4] Sellgren, A., 1979, ''Performance of Centrifugal Pumps When Pumping Ores and Industrial Minerals,'' *Proc. Hydrotransport-6*, Paper G1, BHRA Fluid Engineering, pp. 291–304.

[5] Gahlot, V. K., Seshadri, V., and Malhotra, R. C., 1992, ''Effect of Density, Size Distribution, and Concentration of Solids on the Characteristics of Centrifugal Pumps,'' ASME J. Fluids Eng., **114**, pp. 386–389.

[6] Kazim, K. A., Maiti, B., and Chand, P., 1997, ''A Correlation to Predict the Performance Characteristics of Centrifugal Pumps Handling Slurries,'' Proc. Inst. Mech. Eng., **211A**, pp. 147–157.

[7] Engin, T., and Gur, M., 2003, ''Comparative Evaluation of Some Existing Correlations to Predict Head Degradation of Centrifugal Slurry Pumps,'' ASME J. Fluids Eng., **125**.

[8] Mez, W., 1984, ''The Influence of Solid Concentration, Solid Density and Grain Size Distribution on the Working Behavior of Centrifugal Pumps,'' *Proc. Hydrotransport-9*, Paper H1, BHRA Fluid Engineering, pp. 345–358.

[9] Kosko, B., 1991, *Neural Networks for Signal Processing*, Prentice-Hall, Englewood Cliffs, NJ.

[10] Fukushima, K., Miyake, S., and Ito, T., 1983, ''Neocognition: A Neural Network Model for a Mechanism of Visual Pattern Recognition,'' IEEE Trans. Syst. Man Cybern., **SMC-13**, pp. 826–834.

[11] White, H., 1988, ''Economic Prediction Using Neural Networks: The Case of IBM Daily Stock Returns,'' *Proceedings of the IEEE International Conference on Neural Networks*, Institute of Electrical and Electronic Engineers, San Diego, CA, pp. 41–58.

[12] Pu, H. C., and Hung, Y. T., 1995, ''Use of Artificial Neural Networks: Predicting Trickling Filter Performance in a Municipal Wastewater Treatment Plant,'' Environ. Manage. Health, **6**(2), pp. 16–27.

[13] Mansour, A., Karkoub, B., Osama, E., and Rabie, M. G., 1999, ''Predicting Axial Piston Pump Performance Using Neural Networks,'' Mech. Mach. Theory, **34**, pp. 1211–1226.

[14] Farshad, F. F., Garber, J. D., and Lorde, J. N., 2000, ''Predicting Temperature Profiles in Producing Oil Wells Using Artificial Neural Networks,'' Eng. Comput., **17**(6), pp. 735–754.

[15] Sinha, A. N., Mukherjee, P. S., and De, A., 2000, ''Assessment of Useful Life of Lubricants Using Artificial Neural Network,'' Indust. Lub. Tribol., **52**(3), pp. 105–109.

[16] Kalogirou, S. A., 2000, ''Applications of Artificial Neural Networks for Energy Systems,'' Appl. Energy, **67**, pp. 17–35.

[17] Mei, L., and Levermore, G. J., 2002, ''Simulation and Validation of a VAV System With an ANN Fan Model and a non-Linear VAV Box Model,'' Build. Environ., **37**, pp. 277–284.

[18] Haykin, S., 1994, *Neural Networks: A Comprehensive Foundation*, Macmillan, New York.

[19] Taccani, R., Pediroda, V., Reini, M., and Giadrossi, A., 2000, ''Slurry Pumping: Pump Performance Prediction,'' *Proceedings of the 25th Int. Conference on Coal Utilization and Fuel Systems*, Coal Technology Association, Clearwater, FL.